Transactions of the ASME

Journal of Heat Transfer

Journal of Heat Transfer (ISSN 0022-1481) is edited and published quarterly at the offices of The American Society of Mechanical Engineers, United Engineering Center, 345 E. 47th St., New York, N. Y. 10017. ASME-TWX No. 710-581-5267, New York. Second-class postage paid at New York, N. Y., and at additional mailing offices.

CHANGES OF ADDRESS must be received at Society headquarters seven weeks before they are to be effective. *Please send old label and new address.*

PRICES: To members, $30.00, annually; to nonmembers, $60.00. Single copies, $20.00 each. Add $5.00 for postage to countries outside the United States and Canada.

INDEXED by the Engineering Index, Inc.

Published Quarterly by The American Society of Mechanical Engineers
VOLUME 103 • NUMBER 3 • AUGUST 1981

ANNOUNCEMENTS

452 Second National Symposium on Numerical Methods in Heat Transfer
491 *HTD Best Paper of the Year*
507 Nominations for Heat Transfer Division Distinguished Service Award
545 Mandatory excess-page charges
590 Change of address form for subscribers

TECHNICAL PAPERS

409 Pioneering Contributions to Our Knowledge of Convective Heat Transfer: One Hundred Years of Heat Transfer Research (80-HT-137)
E. R. G. Eckert

415 Effect of Plenum Length and Diameter on Turbulent Heat Transfer in a Downstream Tube and on Plenum-Related Pressure Losses
S. C. Lau, E. M. Sparrow, and J. W. Ramsey

423 Analytic Prediction of the Friction Factor for Turbulent Flow in Internally Finned Channels
M. J. Scott and R. L. Webb

429 Heat Transfer in a Capillary Flow Emerging from a Reservoir
E. Papoutsakis and D. Ramkrishna

436 Effects of Axial Conduction and Convective Boundary Conditions in Slug Flow inside a Circular Tube
B. Vick and M. N. Özişik

441 Heat Transfer from a Plate Elevated above a Host Surface and Washed by a Separated Flow *Induced by the Elevation Step*
E. M. Sparrow, F. Samie, and S. C. Lau

448 Unsteady Stagnation Point Heat Transfer with Blowing or Suction
T. Sano

453 *Surface Contamination, Rejuvenation, and the Reproducibility of Results in Nucleate Pool Boiling*
K. A. Joudi and D. D. James

459 Destablization of Film Boiling Due to Arrival of a Pressure Shock—Part I: Experimental
A. Inoue and S. G. Bankoff

465 *Destabilization of Film Boiling Due to Arrival of a Pressure Shock—Part II: Analytical*
A. Inoue, A. Ganguli, and S. G. Bankoff

472 An Experimental Investigation of Boiling Heat Transfer of Flourocarbon R-11 Refrigerant for Concentric-Tube Thermosyphon
N. Seki, S. Fukusako, and K. Koguchi

478 Boiling Burnout During Crossflow over Cylinders, beyond the Influence of Gravity
M. Z. Hasan, M. M. Hasan, R. Eichhorn, and J. H. Lienhard

485 Density-Wave Oscillations in Sodium Heated Once-Through Steam Generator Tubes
H. C. Ünal

492 Application of Mixing Length Theory to Wavy Turbulent Liquid—Gas Interface
S. Levy and J. M. Healzer

501 A Numerical Solution to Dropwise Evaporation
J. J. Rizza

508 Cooling of Freely Falling Liquid Drops with a Shell of an Immiscible Volatile Liquid
Y. H. Mori, K. Nagai, H. Funaba, and K. Komotori

514 A Three-Dimensional Air-Vapor-Droplet Local Interaction Model for Spray Units
S. J. . Palaszewski, L. M. Jiji, and S. Weinbaum

522 Natural Convection from a Horizontal Cylinder—Laminar Regime
B. Farouk and S.İ. Güçeri

528 Transient Natural Convection Heat Transfer of Water with Maximum Density Effect and Supercooling (80-HT-74)
L. Robillard and P. Vasseur

535 Flow Structure with Natural Convection in Inclined Air-Filled Enclosures
S. J. M. Linthorst, V. M. M. Schinkel, and C. J. Hoogendoorn

540 Mixed Convection Heat Transfer from Horizontal Cylinders in the Crossflow of a Finite Water Layer
W. D. Bennon and F. P. Incropera

546 A Horizontal Flow Past a Partially Heated, Infinite Vertical Cylinder
L. S. Yao and F. F. Chen

552 Developing Laminar Free Convection in an Open Ended Vertical Annulus with a Rotating Inner Cylinder
M. A. I. El-Shaarawi and A. Sarhan

(*Contents continued on page 458*)

559 Laminar Mixed Convection in a Shrouded Fin Array
S. Acharya and S. V. Patankar

566 Combined Free and Forced Convection in Vertical Tubes with Radial Internal Fins
C. Prakash and S. V. Patankar

573 Some Fundamental Relationships for Tubular Heat Exchanger Thermal Performance
K. P. Singh

579 A General Theory of Wet Surface Heat Exchangers and its Application to Regenerative Evaporative Cooling
I. L. Maclaine-cross and P. J. Banks

586 *A Parametric Study of a Particulate Director Contact Heat Exchanger* (78-WA/HT-16)
R. Letan

591 Conduction of Heat across Rectangular Cellular Enclosures
J. Eftekhar, G. Darkazalli, and A. Haji-Sheikh

TECHNICAL NOTES

596 A Closed-Form Analytical Solution for Freezing Adjacent to a Plane Wall Cooled by Forced Convection
C. F. Hsu and E. M. Sparrow

598 Phase Change around a Circular Cylinder
V. J. Lunardini

600 Heat Conduction through "Yin-Yang" Bodies
J. H. Lienhard

601 Transient Thermal Expansion of Solids During Inert Heating, Phase Change, and Surface Gasification
L. W. Hunter

602 *Extension of the Adams-Welty Fluid Bed Heat Transfer Model to the Packed Bed Case*
R. L. Adams

604 *Thermal Storage Regenerator Parameters for Almost Constant Gas Discharge Temperature*
F. E. Romie

606 Effect of Knudson Number on Dropwise Condensation
H. Tanaka

527 Erratum on a previously published paper by C. E. Hickox

E. R. G. Eckert
University of Minnesota,
Department of Mechanical Engineering,
Minneapolis, Minn.
Honorary Mem. ASME

Pioneering Contributions to Our Knowledge of Convective Heat Transfer

One Hundred Years of Heat Transfer Research

This paper describes the development of our knowledge of heat transfer during the past 100 years. The foundations to a systematic and coherent body of knowledge were laid in 1880–1930. The contributions were applied to a variety of situations as they were encountered in new technical developments in 1930–1980.

Introduction

This year the American Society of Mechanical Engineers celebrates its 100th birthday and the Heat Transfer Division is pleased to join in this celebration. It is fitting at this occasion to take a look at the development of our knowledge of heat transfer during the past 100 years. The field of convective heat transfer developed especially rapidly during that period and will, therefore, be discussed in this paper.

It appears that the 100-year period can be divided into two equal parts. The foundations for a systematic and coherent body of knowledge were laid in the years 1880 to 1930 by the efforts of scientists and engineers in a number of countries and especially by the pioneering contributions of a few of them. The insight gained through these contributions were applied to an ever-widening variety of situations as they were encountered in new technical developments in the years 1930 to 1980. The present lecture will primarily dwell on early pioneering contributions which created the foundation on which those working in the field of heat transfer still build their research.

1880–1930: Fluid Mechanics

Convective heat transfer is intimately connected with fluid mechanics and it is interesting to realize that our understanding of fluid flow and, therefore, also of convective heat transfer has made a huge step forward 100 years ago. The fundamental laws of mechanics were, of course, already known since Isaac Newton and have been formulated for fluid flow in the Navier-Stokes equations. However, solutions to these equations could only be obtained for a few simple situations and even there they often did not agree with experimental results, for instance, with those describing the pressure drop connected with fluid flow through pipes. Neither did many of the experimental results correlate among themselves.

This was changed by a study by Osborne Reynolds, the results of which he reported on the 22nd of February 1880 together with a demonstration. The apparatus which he used for this purpose is shown in a figure from his paper [1] and is reproduced here in Fig. 1. Water was contained in a horizontal trough with glass walls. A glass tube was located horizontally inside the trough. It had a bell mouth on its left hand end and was connected on its right hand to a vertical pipe. Water could thus enter the tube from the trough and its discharge could be regulated by a valve. The flow rate of water was measured by a float on the water surface in the trough and an indicator connected to it. Reynolds explained that by normal viewing we cannot understand the details of the flow because water is transparent so that we cannot observe what happens inside it. He, therefore, introduced a small amount of colored fluid into the water at the tube entrance and observed what he called a color band as it moved through the tube after he had waited several hours before the start of the experiment to make sure that any disturbance in the water had died down. Sketches of what he observed are again taken from his paper as Fig. 2. Figure 2(*a*) shows that, at slow flow rate, the streak of colored water was completely straight and steady, indicating an ordered laminar flow. He observed that this persisted as the flow rate through the tube was increased until a certain value was reached where the colored streak changed its appearance quite suddenly to that shown in Fig. 2(*b*). This indicates that the color band started fluctuating and dispersing into the main flow. Reynolds also observed this flow with illumination by an electric spark. Figure 2(*c*) indicates that, with such an instantaneous illumination, waves and vortices are observed downstream of the location where the color band becomes unstable. Reynolds called this flow sinuous. Today we refer to it as turbulent. He repeated the experiments at different temperature levels and found that the transition occurred at lower flow rates as the temperature in the water increased.

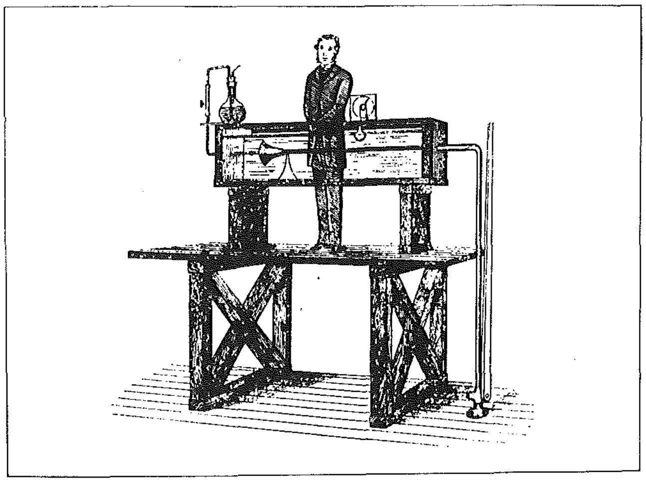
Fig. 1 Osborn Reynolds' demonstration setup

The fact that the viscosity of water decreases with temperature may have led him to the conclusion which he reported in a paper published in 1883 in the *Philosophical Transactions* [1]. There he argued that the characteristics of the flow are expected to be determined by the ratio of the inertia forces to the viscous forces in the fluid and he established as the ratio of these forces the expression

$$\frac{\rho v r}{\mu} \tag{1}$$

with ρ denoting the density of the water, v the mean velocity through the tube, r the tube radius and μ the viscosity of the water. He, therefore, concluded that the transition from laminar to turbulent flow should occur at a certain critical value of this dimensionless number. In the years between 1880 and 1883, he carried out a large number of experiments with tubes of different sizes and with different

---

Contributed by the Heat Transfer Division. This paper is based on an ASME Centennial Lecture given at the 19th Joint ASME/AIChE National Heat Transfer Conference, Orlando, Fla., July 27–30, 1980. Revised manuscript received by the Heat Transfer Division February 25, 1981. Paper No. 80-HT-137.

liquids and established that the transition to turbulence occurred at a critical number between 1900 and 2000, when it is based according to [1] on the tube radius. He also found that a dimensionless parameter obtained by dividing the resistance R of the flow through the tube by ρv^2 is proportional to a certain power of the parameter listed under [1] according to the expression

$$\frac{R}{\rho v^2} \sim \left(\frac{\rho v r}{\mu}\right)^{n-2} \qquad (2)$$

His own experiments as well as those of previous investigators correlated with the parameter $n = 1$ for laminar flow and $n = 1.723$ for turbulent flow except for some of Darcy's experiments with an incrusted pipe which resulted in the value $n = 2$. Reynolds also realized through his studies that the value of the critical parameter depends on the type of flow and in 1884 he published a table (see Table 1), in which he lists those factors which delay and those which advance transition to turbulence [2].

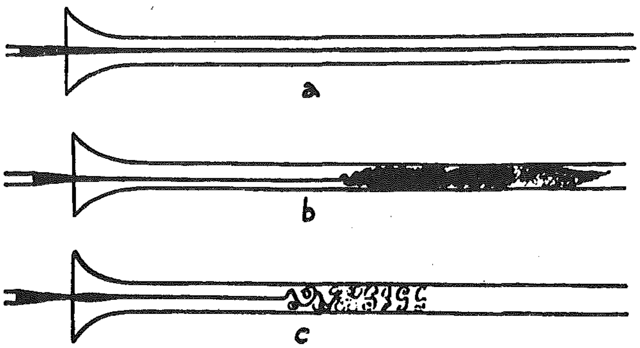

Fig. 2 Reynolds' sketches of flow observation

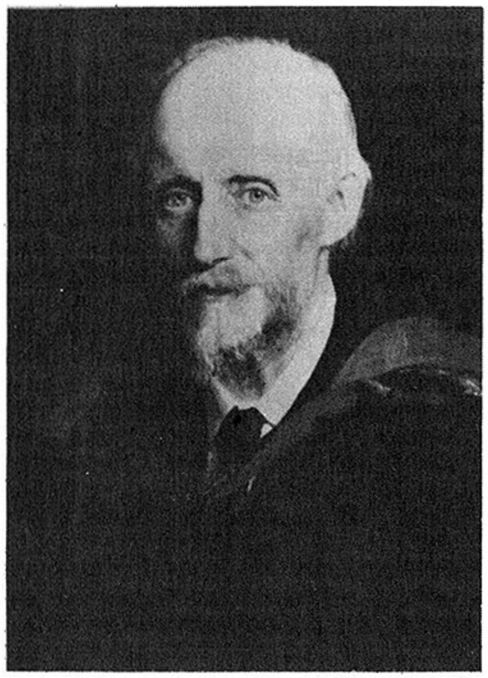

Fig. 3 Portrait of Osborn Reynolds (1904)

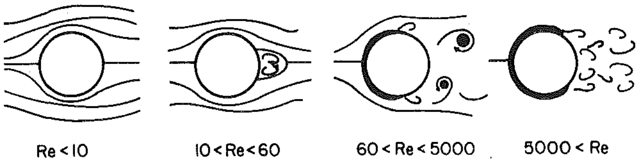

Fig. 4 Flow around a cylinder

Table 1

Circumstances conducive to	
Direct or steady motion:	Sinuous or unsteady motion:
1 Viscosity or fluid friction which continually destroys disturbances (treacle is steadier than water)	5 Particular variation of velocity across the stream, as when a stream flows through still water
2 A free surface	6 Solid boundary walls
3 Converging solid boundaries	7 Diverging solid boundaries
4 Curverature with the velocity greatest on the outside	8 Curvature with the velocity greatest on the inside

The importance of Reynold's contribution was readily recognized and he was invited to give a lecture on it at the Royal Institution as early as 1884. A reproduction of his portrait painted in 1904 and in the possession of the University of Manchester is shown as Fig. 3. The dimensionless parameter in equation (1) is referred to as Reynolds number with ample justification. Reynolds' studies provided the guideline for the correlation of experimental results in all the years up to the present and in this way advanced our understanding of fluid flow tremendously. Figure 4, as an example, presents sketches of the flow characteristics around a cylinder with circular cross section, indicating that they depend solely on Reynolds number and, therefore, are valid for any fluid, be it a liquid or a gas and for any cylinder diameter. Flow characteristics similar to those shown in Fig. 4 for flow around a sphere describe, for instance, the details of the flow around a small object like a tennis ball or a golf ball in the same way as flow around a large balloon or a storage tank for gas or liquids. Osborne Reynolds can, therefore, certainly be considered as a pioneer in the field of fluid mechanics and convective heat transfer.

Convective Heat Transfer

It certainly could be expected that the Reynolds number is also an important parameter for convective heat transfer processes. However, here the situation is more involved. Local temperature differences necessarily exist in the flow field and the fact that the properties influencing heat transfer depend on temperature complicates the situation. In addition, investigators probably were aware of the fact that experimental results were found to depend on the nature of the fluid beyond the influence expressed in the Reynolds number. The situation in convective heat transfer was, therefore, for many years similar to the one existing before 1880 in fluid mechanics. More and more experimental results became available but no general correlations could be obtained. This was changed by a paper which Wilhelm Nusselt published in 1915 and which was preceded by another paper in 1909. In both of them he applied dimensional analysis to the flow and energy transport equations.

In the paper published in 1909 [3], he reports the results of an analytical and experimental study of heat transfer caused by turbulent flow through a tube. He used a heat transfer coefficient, h, already introduced by Newton and defined by the equation

$$Q = hA\theta_w \qquad (3)$$

in which Q denotes the heat flux through the area A and θ_w is a characteristic temperature difference between the tube wall and the fluid. He then assumed that the heat transfer coefficient can be expressed as a product of the influencing parameters, each raised to a characteristic power. Assuming additionally that the properties on which the heat transfer depends can be considered as constants, he derived the following equation by dimensional analysis

$$h = C\frac{k_w}{d}\left(\frac{\rho v d}{\mu}\right)^m\left(\frac{\mu c}{k}\right)^n \qquad (4)$$

with C denoting a constant, k the thermal conductivity, c the specific heat of the fluid, and d a characteristic length. The other parameters have been defined before. He concludes from the energy equation that the two exponents, m and n, should have the same value. From experiments for turbulent heat transfer in a tube which he conducted with air, CO_2, and city gas and from experiments by M. Jakob with superheated steam he obtained the value 0.786 for m and 0.85 for n and he concluded that these values are sufficiently close to verify the conclusion $m = n$, and thus he derived the final relation

$$h = C\frac{k_w}{d}\left(\frac{\rho c v d}{k}\right)^m \tag{5}$$

Today we know that his value for n is too high, and that his conclusion, $m = n$, is not justified. He worried about the fact that the properties in this relation vary actually with temperature and proposed as an approximation to introduce the thermal conductivity at the wall temperature, where it is indicated by the subscript w, as well as the other properties at an average temperature in the bracketed parameter.

His second paper entitled "The Basic Law of Heat Transfer" [4] and published in 1915, is the more important one. In it he applies dimensional analysis to natural convection heat transfer, dropping the restriction that the heat flux is expressed as a product of the parameters raised to some power. He still considers the properties as constant with the exception of the density, the variation of which is expressed by a thermal expansion coefficient (Boussinesq assumption), and derives the following equation for the heat flow, Q, per unit time

$$Q = kd\theta_w\phi\left(\frac{k}{\mu c}, \frac{d^3\rho^2 g\beta\theta_w}{\mu^2}\right) \tag{6}$$

The gravitational acceleration, g, and the thermal expansion coefficient β appear in this equation in addition to the parameters defined before; d denotes a characteristic length.

This time he extends the thermal analysis to a gas in which the properties depend in the following way on the absolute temperature, T

$$\rho = \rho_0\left(\frac{T_0}{T}\right), \mu = \mu_0\left(\frac{T}{T_0}\right)^a$$

$$k = k_0\left(\frac{T}{T_0}\right)^b, c_p = c_{p0}\left(\frac{T}{T_0}\right)^c \tag{7}$$

The index, 0, refers to a characteristic fluid temperature. He derives the following result for the heat transfer coefficient, h

$$h = \frac{k}{d}\phi\left(\frac{d^3\rho^2 g}{\mu^2}, \frac{k}{\mu c_p}, \frac{T_w}{T_0}\right) \tag{8}$$

It took a considerable number of years before the relations derived by Nusselt were generally accepted. This may have been caused by the fact that heat transfer processes in engineering applications operate in general with fairly large temperature differences whereas the derivation of equations (4) and (6) hold strictly for a constant property fluid or for vanishingly small temperature difference. A book on heat transfer by A. Schack [5], the second edition of which appeared in 1940, devotes a considerable portion to an attempted proof that dimensional analysis does not work and the criticism raised in recent years against dimensionless relations of the type presented under the heading "The New Heat Transfer" [6] reflects the same objection. Relations of the form as derived by Nusselt, however, have in the meantime been widely accepted and are, today, a tool used generally by those working in heat transfer. The following names have been given to the dimensionless parameters appearing in the equations

$$\text{Nusselt number Nu} = \frac{hd}{k}$$

$$\text{Prandtl number Pr} = \frac{\mu c_p}{k} \tag{9}$$

$$\text{Grashof number Gr} = \frac{g\beta\rho^2 d^3\theta}{\mu^2}$$

and the expression for forced convection can thus be written as

$$\text{Nu} = f(\text{Re}, \text{Pr}) \tag{10}$$

and that for natural convection

$$\text{Nu} = f(\text{Gr}, \text{Pr}) \tag{11}$$

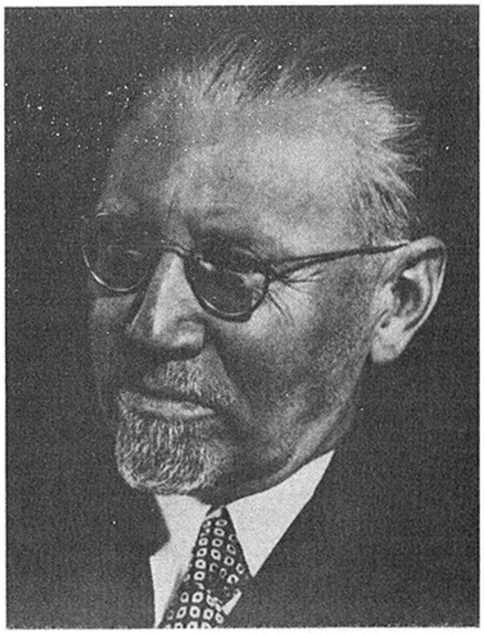

Fig. 5 Wilhelm Nusselt (~1940)

Heat transfer information has, in many cases, to be obtained by experiments and presentation of the results in the form of equations (10) and (11) is the means to unify and generalize them.

It is my opinion that the most important step in the analysis by Nusselt was the introduction of an ideal constant property fluid. Only in this way could he get to the simple general equations (10) and (11). The equations describing heat transfer in dimensionless parameters become more involved as soon as one attempts to consider the temperature dependence of the properties. Equation (8), derived by Nusselt, actually holds only for those gases which have the same value of the exponents, a, b, and c. The equation changes to the form

$$\text{Nu} = f\left(\text{Gr}, \text{Pr}, \frac{T_w}{T_0}, a, b, c\right) \tag{12}$$

when it is used to describe generally heat transfer in gases the properties of which vary according to the relations (7). This is evidence for the fact that dimensionless relations describing heat transfer become the more restricted the more accurately one tries to describe the fluid properties. The large value of relations of the form of equations (10) and (11) lies in their generality. They hold for groups of fluids with the same Prandtl number. They are exact in the limit of small temperature difference and experience has shown that they describe with fair approximation conditions at larger temperature differences when average values for the fluid properties are introduced. They are, today, found in any textbook, and Wilhelm Nusselt, therefore, can be considered as another pioneer in heat transfer (Fig. 5).

Heat/Mass Transfer

An important relation between heat transfer and mass transfer was derived by W. K. Lewis in 1922 [7]. The mass transfer process which he investigated was evaporation of a liquid into a gas stream. He defined a mass transfer coefficient, h_m, by an equation analogous to equation (3)

$$W = h_m A(c_w - c_0) \tag{13}$$

with W denoting the mass flux of vapor away from a liquid surface of area A, c denotes the vapor concentration (mass per unit volume of the mixture), and the indices, w and 0, indicate that the concentration should be introduced in equation (13) at the liquid surface and at a reference point in the gas stream, respectively. He established the relation

$$h_m = \frac{h}{\rho c_p} \tag{14}$$

between the mass transfer coefficient and the heat transfer coefficient.

In 1929 E. Schmidt presented a paper entitled "Evaporation and Heat Transfer" [8] in which he investigated the restrictions under which relation (14) is valid and in which he established the relations for the heat and mass transfer analogy by a dimensional analysis of the differential equations describing conservation of mass, momentum, and energy. He considered forced convection as well as natural convection. The thermodynamic and transport properties had again to be considered as constants. The main results reported in the paper by Schmidt can be formulated as the following rule for conversion of heat transfer relations to those describing mass transfer with the following dimensionless parameters

$$\text{Sherwood number Sh} = \frac{h_m L}{D} \tag{15}$$

$$\text{Schmidt number Sc} = \frac{\nu}{D} \tag{16}$$

The symbol D denotes the mass diffusion coefficient, L, characteristic length.

We will assume that a relation of the form (10) is available to describe a heat transfer process in forced convection. The Nusselt number in the heat transfer relation has then simply to be replaced by the Sherwood number and the Prandtl number by the Schmidt number for an analogous mass trasnfer process. This procedure is indicated in the following lines

$$\underset{\text{Sh}}{\cancel{\text{Nu}}} = \phi(\text{Re}, \underset{\text{Sc}}{\cancel{\text{Pr}}}) \tag{17}$$

The rule gives the correct relations for the limiting situation in which the differences in temperature and in concentration are vanishingly small, and it is valid for independent analogous heat and mass transfer situations as well as for a combined heat and mass transfer process. Schmidt also showed that the Lewis relation (14) follows from dimensional analysis for the condition Sc = Pr.

Two situations are treated separately in considering natural convection and the discussion is restricted to gases. In the first one, the analogy is established between a heat transfer process without mass transfer and an isothermal mass transfer process. Natural convection flow in the second process is generated by local differences in the density or the molecular weight, M, of the two components involved in mass transfer. Accordingly, a new mass transfer Grashof number is defined by the equation

$$\text{Gr}_m = \frac{gL^3}{\nu}\left(\frac{M_0}{M_w} - 1\right) \tag{18}$$

The process through which the heat transfer relation can be transformed to a mass transfer relation for a analogous process is sketched in the following

$$\underset{\text{Sh}}{\cancel{\text{Nu}}} = \Phi\,(\underset{\text{Gr}_m}{\cancel{\text{Gr}}},\ \underset{\text{Sc}}{\cancel{\text{Pr}}}) \tag{19}$$

If heat transfer and mass transfer occur in the same field, then the Grashof number takes on the form

$$\text{Gr}^* = \frac{gL^3}{\nu}\left(\frac{M_0 T_w}{M_w T_0} - 1\right) \tag{20}$$

and the process connecting the relation describing heat transfer with the one for mass transfer is sketched in the following line

$$\underset{\text{Sh}}{\cancel{\text{Nu}}} = (\text{Gr}^*, \underset{\text{Sc}}{\cancel{\text{Pr}}}, \underset{\text{Pr}}{\cancel{\text{Sc}}}) \tag{21}$$

which indicates that the Schmidt number and the Prandtl number have to be interchanged in the process.

Fig. 6 Ernst Schmidt (~1942)

In a paper published independently in 1930, Nusselt came to the same conclusions as Schmidt. He pointed out additionally that, in the dimensional analysis, one has to consider the boundary conditions in addition to the differential equations. The boundary condition in evaporation of vapor from a liquid surface into a gas stream, however, is different from the boundary condition describing heat transfer on a solid surface insofar as a convective mass flow occurs at the evaporating liquid surface whereas such a mass flow is absent at the heat transfer surface. In the meantime, transpiration cooling has found attention in the form of a cool gas ejected through a porous wall into a hot gas stream. In this case, a convective flow occurs at the porous surface and similarity in the boundary conditions is established to the mass transfer process described above.

The analogy between heat and mass transfer has in the meantime found wide application because more information is available on heat transfer than on mass transfer. It is also used in reverse direction to obtain heat transfer relations through mass transfer experiments which, in many situations, can be carried out more conveniently and with more accuracy than heat transfer experiments. The main contribution to this analogy is, in my opinion, the pioneer paper by E. Schmidt; a photograph of him is shown in Fig. 6.

Boundary Layers

Dimensional analysis provides the parameters with which experimental results can be generalized and it is very useful in its way; but it does not lead to an understanding of the detailed mechanisms and interactions of flow and heat transfer processes. Only mathematical analysis combined with well-planned experimentation can accomplish this. The analytical prediction of flow and heat transfer processes had to overcome two hurdles: A way had to be found to solve the Navier-Stokes equations and a proper model had to be conceived which describes the effect of turbulence.

Important contributions to both of these tasks are due to Ludwig Prandtl (Fig. 7). In his famous paper entitled "The Movement of Fluids with Very Small Friction" [10] and presented at the Third International Congress of Mathematicians at Heidelberg in 1904, he argues that the influence of a small viscosity of the fluid becomes noticeable only in regions with large transverse velocity gradients, primarily in those close to surfaces exposed to the flow, whereas the main body of the fluid can with good approximation be considered as frictionless. For its analysis, well developed methods were already available. The layers close to solid surfaces in which friction is important have to be thin in order to produce large transverse velocity

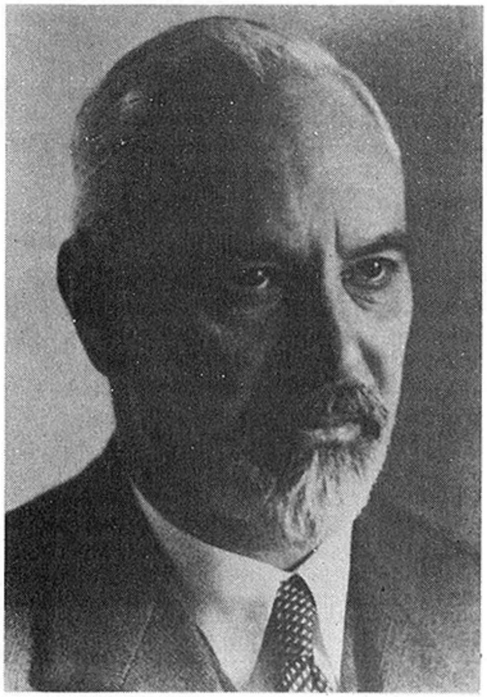

Fig. 7 Ludwig Prandtl (~1938)

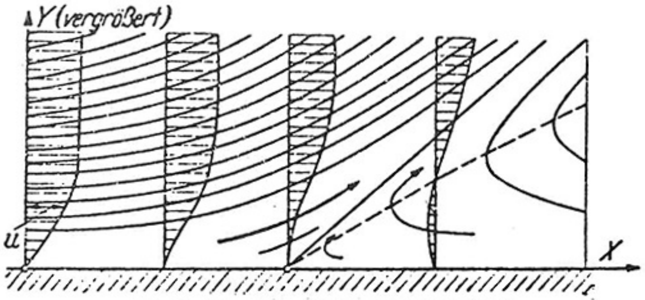

Fig. 8 Flow separation in a boundary layer

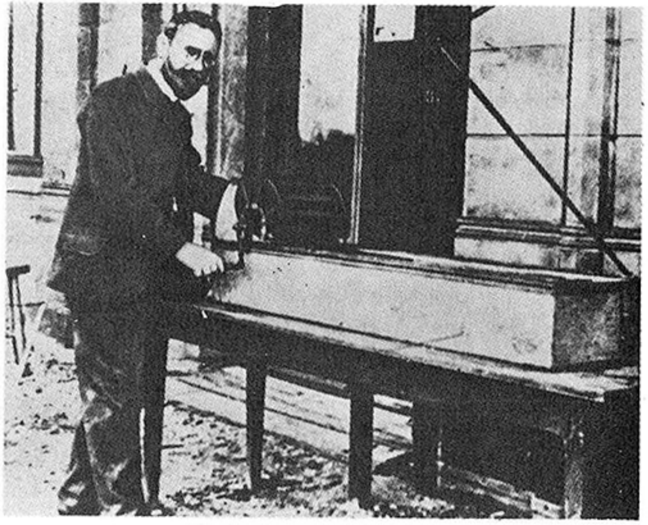

Fig. 9 Prandtl's water tunnel

gradients. On this basis, Prandtl simplified the Navier-Stokes equations to the differential equations describing laminar two-dimensional boundary layers. It took his student, H. Blasius, four more years to solve the boundary layer equations for steady laminar flow over a flat plate [11], but Prandtl presented a number of semi-quantitative flow fields obtained by quadrature. Among those was the one reproduced in Fig. 8, which is found in every textbook on fluid flow. It shows the onset of separation of a boundary layer in a region where the pressure increases in flow direction.

The paper which contains just eight equations also presents a number of photos obtained in a water tunnel. It is interesting to observe that the two contributions which advanced our understanding of fluid flow enormously, namely the one by Reynolds on transition to turbulence and the one by Prandtl on boundary layers, were both obtained by flow visualization using simple equipment. Figure 9 shows the water channel with a hand-operated paddle wheel in which Prandtl made his early studies.

Many more solutions to Prandtl's boundary layer equations have been obtained in the meantime. The analysis was extended to convective heat transfer by E. Pohlhausen, who introduced, in addition to Prandtl's velocity boundary layer, a thermal boundary layer within the temperature field adjacent to a heated surface. His paper [12] in 1921 treated in this way heat transfer between a solid body and a fluid with small friction and heat conduction; and in 1930, Pohlhausen solved the temperature and velocity boundary layer in free convection on a heated vertical plate in collaboration with Schmidt and Beckmann [13].

Turbulence

Ludwig Prandtl also provided an important impetus to the analysis of turbulent boundary layers with his mixing length hypothesis published in 1925 [14]. It served as a starting point for the development of the analysis of turbulent flow processes in the succeeding years. A contribution to the analysis of convective heat transfer had already been provided by Osborne Reynolds in 1874 [15] in a paper in which he postulated an analogy between turbulent transfer of momentum and heat. Ludwig Prandtl took up this idea in 1910 [16]. He recognized that Reynolds' analogy provides a satisfactory relationship between momentum and heat transfer caused by turbulent convection; but for many fluids, it is not satisfactory for an analogy between viscous momentum transport and heat transfer by conduction. To take care of this, he introduced a model with a sub-layer within the turbulent boundary layer. Prandtl's papers served as a starting point for later developments on turbulent flow and heat transfer.

1930–1980

The second period, the years from 1930 to 1980, is characterized by a tremendous growth of research in all fields of heat transfer. Workers from more and more countries joined in this activity and international cooperation developed strongly, furthered by International Heat Transfer Conferences—the first of which was held in 1950—which are now organized every fourth year. More than 400 papers were presented at the last conference, the Sixth International Heat Transfer Conference held in Toronto, Canada. The *International Journal of Heat Mass Transfer* and the International Centre for Heat and Mass Transfer, organized in Yugoslavia, also contributed to distribution of information on a worldwide scale.

A vigorous activity developed in the United States where national heat transfer conferences are held almost yearly with over 200 papers presented at the last one and where many other conferences provide sessions for the dissemination of heat transfer information. Two names stand out among the early scholars in this development: William H. McAdams (Fig. 10) of the Massachusetts Institute of Technology is the author of the book *Heat Transmission* [17] which first appeared in 1933. In this book McAdams collected, screened, and correlated the available information on heat transfer processes, supplemented it by his own research, and presented through three editions an up-to-date, concise, and unified picture of the state-of-the-art. He created a standard text which served the heat transfer community as a reference book through many years. Llewellyn M. K. Boelter (Fig. 11) started research in heat transfer in 1930 at the University of California, Berkeley. He had the gift of attracting talented students and implanting in them interest and love for engineering research. His lecture notes were printed under the name *Heat Transfer Notes* in 1933, 1940, and 1943 and were republished in book form in 1965 [18]. His associates influenced heat transfer research strongly through all the years and are still doing so.

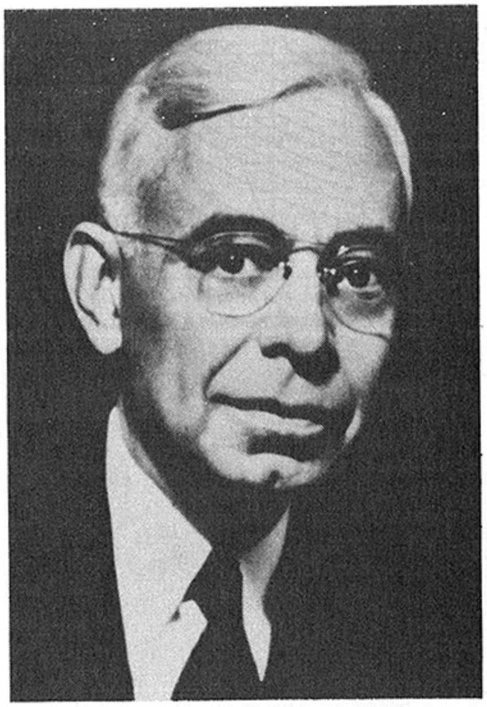

Fig. 10 William H. McAdams (~1950)

Fig. 11 Llewellyn M. K. Boelter (~1950)

Conclusion

Research activities in the last 50 years became so widespread that it is impossible to discuss the important contributions in the frame of this lecture. This growth is primarily due to the large variety of parameters which determine a heat transfer process. Table 2, in which parameters influencing a specific heat transfer process are listed, has been prepared to illustrate this. Examples of such parameters are arranged in four groups starting with the system or geometry describing a specific situation, followed by a second group listing the forces which determine fluid flow, and by a third group containing energy modes and energy transport mechanisms. The fourth group lists the fluids the properties of which influence convective heat transfer. Any combination using a parameter in each of the groups can determine a specific heat transfer situation and many of these combinations actually occur in engineering developments. In addition, several of the parameters in the same group may become involved in, for instance, combined natural and forced convection.

This raises the question of how a worker in the field can absorb, digest, and organize the overwhelming amount of information to which he is continuously exposed. I think that the pioneer contributions discussed in this paper show the way. All of them started out by simplifying the actual process, by neglecting parameters of minor impact, and by idealizing the fluids involved. Today electronic computers make it possible to describe a special heat transfer process in great detail and accuracy, but, we should not forget to cover in our research larger groups in a wide sweep and in this way to maintain a coherent and organic view of the whole field of heat transfer.

Table 2

1. **System:**
one component: rare
two component, solid-fluid, without phase change,
  solid in bulk: tube, flat plate, cylinder, sphere
  solid dispersed:$^{x)}$ porous matrix, grains, fibres
  solid dispersed,$^{x)}$ moving: fluidized bed, dust, soot
two component,$^{x)}$ solid-fluid, with phase change
  evaporation, boiling, condensation
two-component,$^{x)}$ fluid-fluid
more component:$^{x)}$ unsaturated porous media
2. **Forces**
  pressure
  inertia
  gravity
  centrifugal, Coriolis force
  electric, magnetic force
  surface tension
  molecular force
3. **Energy Mode and Energy Transport**
  kinetic
  chemical
  internal
  conduction
  convection
  diffusion
  diffusion-thermo
4. **Fluids**
  Newtonian—liquids, gases,
  Non-Newtonian
  plasma

x) considered as continua or particulates

References

1 Reynolds, O., "On the Experimental Investigation of the Circumstances which Determine Whether the Motion of Water Shall Be Direct or Sinuous, and the Law of Resistance in Parallel Channels," *Philosophical Transactions of the Royal Society*, Vol. 174, 1883, pp. 935–982.

2 Reynolds, O., "On the Two Manners of Motion of Water," *Proceedings of the Royal Institute of Great Britain*, 1884.

3 Nusselt, W., "Der Wärmeübergang in Rohrleitungen," *Zeitschrift Verein Deutscher Ingenieure*, Vol. 53, 1909, pp. 1750–1808.

4 Nusselt, W., "Das Grundgesetz des Wärmeüberganges," *Gesundheitsingenieur*, Vol. 38, 1915, pp. 477–482.

5 Schack, A., *Der Industrielle* Wärmeübergang, 2nd ed. 1940, Stahleisen, Düsseldorf.

6 Adjutori, E. F., *The New Heat Transfer*, Ventuno Press, Cincinnati, Ohio, Vol. 1, 1974.

7 Lewis, W. K., "The Evaporation of a Liquid into a Gas," *Mechanical Engineering*, Vol. 44, 1922, p. 445.

8 Schmidt, E., "Verdunstung und Wärmeübergang," *Gesundheitsingenieur*, Vol. 52, 1929, pp. 525–529.

9 Nusselt, W., "Wärmeübergang, Diffusion und Verdunstung, Z. angnew," *Mathematik und Mechanik*, Vol. 10, 1930, pp. 105–121.

10 Prandtl, L., "Grenzschichten und Widerstand" Verhandlungen des III, *Internationalen Mathematiker-Kongressses*, Heidelberg, 1904, pp. 484–491, Teubner, Leipzig, 1905.

11 Blasius, H., "Grenzschichten in Flüssigkeiten mit kleiner Reibung," *Zeitschrift fuer Mathematik und Physik*, Vol. 56, 1908, pp. 1–37.

12 Pohlhausen, E., "Der Wärmeaustausch zwichen festen Körpern und Flüssigkeiten mit kleiner Reibung" *Angewandte Mathematik und Mechanik* Vol. 1, 1921, p. 115.

13 Schmidt, E. and Beckmann, W., "Das Temperatur und Geschwindigkeitsfeld vor einer Wärme abgebenden, senkrechten Platte bei natürlicher Konvektion," *Forschung im Ingenieurwesen* Vol. 1, 1930, p. 391.

14 Prandtl, L., "Über die ausgebildete Turbulenz Zeitschr. angew," *Mathematik und Mechanik*, Vol. 5, 1925, p. 136.

15 Reynolds, O., "On the Extent and Action of the Heating Surface of Steam Generators," Proceedings of Literary and Philosophical Society, Manchester, Vol. 14, Session 1874–1875, pp. 81–85.

16 Prandtl, L., "Eine Beziehung zwischen Wärmeaustausch und Strömungswiderstand in Flüssigkeiten," *Physik Zeitschrift* Vol. 11, 1910, pp. 1072–1078.

17 McAdams, W. H., *Heat Transmission*, McGraw-Hill, New York, 1933.

18 Boelter, L. M. K., *Heat Transfer Notes*, McGraw-Hill, New York, 1965.

S. C. Lau
E. M. Sparrow
Fellow ASME

J. W. Ramsey
Department of Mechanical Engineering,
University of Minnesota,
Minneapolis, Minn 55455

Effect of Plenum Length and Diameter on Turbulent Heat Transfer in a Downstream Tube and on Plenum-Related Pressure Losses

A systematic experimental study was carried out to determine how the heat transfer characteristics of a turbulent tube flow are affected by the length and diameter of a cylindrical plenum chamber which delivers fluid to the tube. The net pressure loss due to the presence of the plenum was also measured. The experimental arrangement was such that the fluid experiences a consecutive expansion and contraction in the plenum before entering the electrically heated test section. Air was the working fluid, and the Reynolds number was varied over the range from 5,000 to 60,000. It was found that at axial stations in the upstream portion of the tube, there are substantially higher heat transfer coefficients in the presence of longer plenums. Thus, a longer plenum functions as an enhancement device. On the other hand, the plenum diameter appears to have only a minor influence in the range investigated (i.e., plenum diameters equal to three and six times the tube diameter). The fully developed Nusselt numbers are independent of the plenum length and diameter. With longer plenums in place, the thermal entrance length showed increased sensitivity to Reynolds number in the fully turbulent regime. The pressure loss coefficient, which compares the plenum-related pressure loss with the velocity head in the tube, increases more or less linearly with the plenum length. With regard to experimental technique, it was demonstrated that guard heating/cooling of the electrical bus adjacent to the tube inlet is necessary for accurate heat transfer results at low Reynolds numbers but, although desirable, is less necessary at higher Reynolds numbers.

Introduction

Turbulent heat transfer in circular tubes has been the subject of extensive study for many decades because the circular tube serves as a basic component in a wide variety of heat exchange devices. In general, fluid may be delivered to the tube from a broad range of sources, encompassing, for example, plenums of various geometric forms, upstream pipelines (either heated or unheated), and fittings of many types (e.g., tees, elbows). It may be expected that the tube heat transfer characteristics will be affected by the sources from which fluid is delivered, especially in the region of the tube adjacent to its inlet. The present research was undertaken to experimentally determine how the turbulent heat transfer characteristics of a heated tube respond to systematic variations of the length and diameter of an upstream plenum which delivers fluid to the tube. The pressure drop associated with the presence of the plenum was also measured, and flow visualization was employed for the observation of certain characteristics of the flow field.

In the heat transfer apparatus, a plenum chamber in the form of a circular cylinder is positioned immediately upstream of an electrically heated tube such that the tube and the plenum share the same axis. In turn, the working fluid, air, is delivered to the upstream end of the plenum via a tube which also shares the common axis of the plenum and the heated tube. Thus, the working fluid experiences a consecutive expansion and contraction prior to its entry into the heated test section tube.

The apparatus used for the pressure-drop studies is similar to that of the heat transfer experiments (and air is also the working fluid), except that the heated test section is replaced by an unheated tube instrumented with pressure taps. Flow visualization was conducted in an all-plexiglass apparatus with water as the working fluid.

Two plenums of different diameter D were employed during the experiments. Each plenum was designed and fabricated so that its streamwise length L could be varied. Relative to the diameter d of the test section tube, the investigated plenum configurations encompassed the range $\frac{1}{4} \leq L/d \leq 10$, respectively for $D/d = 3$ and 6. For each fixed plenum configuration investigated, experiments were conducted for Reynolds numbers ranging from 5000 to 60,000.

The heated test section was heavily instrumented to enable local heat transfer coefficients to be determined and, thereby, to facilitate identification of the effects of plenum geometry. Furthermore, the presentation of results is structured to highlight these effects. The total heat transfer presentation includes the thermal entrance region, the thermally developed regime, entrance length, and comparisons with the literature. With regard to fluid-flow aspects, the plenum-related pressure drop is presented in terms of a dimensionless pressure loss coefficient for the same range of parameters as were employed in the heat transfer experiments. The flow visualization observations were of a qualitative nature and are reported as such.

The experimental apparatus was designed and fabricated to provide heat transfer results of impeccable quality which can serve both as a guide to design and as a standard against which to compare candidate analytical models. In recognition of the potential injurious role of extraneous heat losses in airflow systems, a number of measures were instituted to defend against such losses. These include (1) near-zero contact between the heated test section and the plenum, (2) guard heating and cooling of the bus bars which deliver electrical power to the system, (3) suspension of the test section with thin nylon line, and (4) use of an insulation having a thermal conductivity less than that of air. In a sensitivity study, it was demonstrated experimentally that the absence of guard heating/cooling can have a substantial impact on the results in the thermal entrance region.

Attention will now be turned to the literature relevant to the subject under study. In general, a literature search failed to unearth any published research of the type reported in the present paper. However, to provide perspective, the general state of affairs with regard to upstream hydrodynamic conditions for turbulent tube-flow heat transfer will be briefly reviewed. With regard to analysis, it has been customary to avoid involvement with the actualities of the flow field upstream of the heated tube by imposing hydrodynamic boundary conditions

---

Contributed by the Heat Transfer Division for publication in the JOURNAL OF HEAT TRANSFER. Manuscript received by the Heat Transfer Division September 24, 1980.

at the tube inlet. Experiments have been reported in [1] and [2] for heated tubes to which flow is delivered via an abrupt or rounded contraction from a very large plenum, or via an adiabatic tube that is either straight (hydrodynamic development length) or curved (elbow or bend). In [2] and [3], a tee was used to convey the working fluid to the heated tube.

The heat transfer characteristics of a heated tube situated downstream of either an abrupt expansion or an abrupt contraction of finite diameter ratio were investigated in [4–8]. In all cases, the tube situated upstream of the change of section was sufficiently long so that the hydrodynamically developed conditions prevailed prior to the expansion or contraction. The case of a successive expansion and contraction (i.e., a plenum of finite length) upstream of a heated tube does not appear to have been investigated.

The Experiments

Heat Transfer Apparatus. The heat transfer apparatus will be described in sufficient detail to convey its main features and novel design aspects. A more detailed description, including design drawings, is available in [9].

The apparatus is an open-loop airflow system which is supplied by a dryer-equipped air compressor. Upon entering the loop, the air passes through a set of control valves, a filter, and a regulator, and then is ducted to a settling chamber which serves to damp the eddies induced by valves and elbows. From the settling chamber, the air enters and traverses a 65-diameters-long hydrodynamic development tube, the efflux of which discharges into the plenum chamber whose dimensions (length and diameter) are to be varied throughout the experiments. From the plenum, the air passes through the 76-diameters-long heated test section and the mixing chamber situated at its downstream end. The discharge from the mixing chamber is ducted to a rotameter and then passes into the room.

Apparatus Components. As noted earlier, the hydrodynamic development section, the plenum, and the test section all share a common axis. In addition, the development and test section tubes were cut from a single length of stainless steel tubing, the bore diameter of which, after internal honing to attain a smooth satin finish, was 2.36 cm (0.930 in.). The post-honing wall thickness of the test section tube (a parameter relevant to the ohmic heating) was 0.089 cm (0.035 in.) with a circumferential variation of ±0.002 cm (±0.0008 in.). The two plenum chambers used in the experiments were made of plexiglass, with respective internal diameters equal to 2.96 and 5.91 times that of the test section tube (nominally, 3 and 6 times).

To enable the streamwise length of the plenum chamber to be varied during the course of the research, its upstream end-face was designed so that it could be moved axially within the cylindrical wall of the chamber. An air seal between the cylindrical wall and the contacting edge of the end-face was achieved with a pair of O-rings. The end-face was rigidly attached to the downstream end of the hydrodynamic development tube, so that the axial movement of the face required a corresponding axial movement of the development tube. This movement was accommodated by a flexible coupling at the upstream end of the development tube.

Two thermocouples threaded through the upstream end-face of the plenum served to measure the air temperature just downstream of the plenum inlet. The thermocouples were positioned 180 deg apart, with the junctions placed in the mixing region of the incoming jet.

At the downstream end of the plenum, special precautions were taken to minimize possible extraneous heat conduction from the test section tube to the plenum end-face. These precautions were motivated by the concern that the plenum airflow, either impinging against or recirculating adjacent to the end-face, would induce an extraneous flow of heat out of the test section.

The first of the defenses against such extraneous losses is in the adopted structure of the end-face. The face consisted of two parts—an inner and an outer annular disk, of which only the former is relevant to the heat loss issue because of its contact with the test section tube. This disk was fabricated from rigid fiberglass circuitboard whose thickness was only 0.043 cm (0.017 in.). The inner diameter of the disk was made identical to the outer diameter of the test section tube, so that the disk could just slip over the tube. They were positioned so that their upstream faces lay in a continuous plane. The only thermal path between the tube and the disk was through their 0.043 cm (0.017 in.) interface. This is believed to be the very minimum that is consistent with structural integrity, especially when a nonmetallic, relatively low thermal conductivity material such as fiberglass is employed. A small fillet of silicone rubber was inserted just downstream of the disk to seal against air leaks—other defenses against air leaks are described in [9].

Immediately downstream of the fiberglass disk, a copper ring was soldered to the outer surface of the test section tube to serve as a distribution bus for the electric current used for the ohmic heating of the tube. The ring was beveled on its upstream face in such a way that it leaned away from the disk. To avoid ambiguity about the axial position where the ohmic heating began, the axial contact between the tube and the bus ring was kept as short as possible (axial contact length $\simeq \frac{1}{4}$ tube diameter). The ring also served as a hub against which three sharp-tipped nylon screws were tightened to ensure the alignment of the plenum and the test section tube.

Electric current was supplied to the copper bus ring by six rod-like copper conductors, each 0.476 cm ($\frac{3}{16}$ in.) in diameter and about 5.08 cm (2 in.) long. The rods, canted toward the downstream to avoid congestion adjacent to the plenum, emanated radially outward like the spokes of a wheel. The outer tip of each spoke was soldered to a heavy copper ring, which served as a terminal for a stranded copper cable from the power supply.

Each spoke was fitted with a differential thermocuple which enabled the existence of extraneous heat conduction along the spokes to be detected. To null out such extraneous heat flows, the outer copper ring was fitted with a water-carrying copper tube. The water temperature could be precisely controlled by a thermostatically regulated heating/cooling bath. This guard heating/cooling capability constituted a very important defense against extraneous losses/gains and, as will be demonstrated later, it served to insure the quality of the thermal entrance region results.

The test section tube itself was heavily instrumented with thermocouples. In an axial length extending eight diameters from the onset of heating, there were twelve thermocouple stations and, at each such station, four thermocouples were deployed at equal intervals around the circumference of the tube. Between the axial distances of 8 and 64 diameters from the inlet, there were 16 instrumented stations, each with two thermocouples. All thermocouples were of

Nomenclature

A_w = cross-sectional area of tube wall
c_p = specific heat of air
D = inside diameter of plenum chamber
d = inside diameter of tube
h = local heat transfer coefficient, equation (4)
K = pressure loss coefficient, equation (6)
k = thermal conductivity of air
k_w = thermal conductivity of stainless steel wall
L = axial length of plenum chamber
$\dot{m}$ = mass flow rate of air
Nu = local Nusselt number, hd/k
ΔP_p = net plenum-related pressure drop
Q_i = rate of convective heat transfer from control volume i to the fluid
Re = Reynolds number, $4\dot{m}/\mu\pi d$
T_b = local bulk temperature
T_w = local tube wall temperature
T_∞ = temperature of surroundings
V = mean air velocity in tube
x = axial coordinate measured from tube inlet
x_e = thermal entrance length
μ = viscosity
ρ = density

Subscript

fd = thermally fully developed

Superscript

$*$ = at plenum inlet

30-gage, calibrated copper and constantan wire, applied to the tube via spot welding and oriented so that the lead wires lay along the expected isothermal directions.

The final thermocouple station was situated twelve tube diameters from the downstream bus-bar assembly. That assembly was similar in structure to that of the upstream bus but was not guard heated or cooled because there was no need to do so (because it was too remote from the nearest measurement station).

The mixing chamber was mated to the downstream end of the test section. It consisted of a length of pvc pipe which housed a series of copper baffle plates. An array of holes was machined in each plate, and the pattern and size of the holes in the respective plates were designed to induce both radial and circumferential fluid motions. Three thermocouples situated downstream of the last baffle were used to measure the temperature of the air. Flexible tubing served to couple the discharge end of the mixing chamber to the rotameter used for flow metering.

As a further defense against extraneous heat losses (or gains), the plenum chamber, the test section, and the mixing chamber were situated within an insulation enclosure. The enclosure consisted of a plywood box with a 30.5 cm (1 ft) square cross section whose inner walls were lined with styrofoam sheet insulation. The styrofoam enclosed a space having cross-sectional dimensions of 21.6 × 21.6 cm (8.5 × 8.5 in.). Into this space was poured silica aerogel powder insulation whose thermal conductivity is about 85 percent that of air. The test section was suspended from the frame of the plywood box by monofilament nylon lines, and no other supports were employed.

Power Supply and Instrumentation. Electric power was supplied to the test section via a system which served to stabilize the voltage and to provide the high current and low voltage called for by the low-resistance test section. Test section voltage and current (both read as voltages) were measured by a true rms digital voltmeter (Keithly model 179). This type of meter was selected because of concern that possible departures from a sinusoidal wave form would introduce errors in the readings of other types of voltmeters.

All thermocouple emf's were read with a Fluke 2240B datalogger capable of programmable scanning. It provided a printed output with a smallest digit corresponding to 1 μV. The programming capabilities of the datalogger enabled the lengthy approach of the apparatus to thermal equilibrium to be monitored without human intervention. However, as a matter of course, the final attainment of equilibrium and the collection of data were always monitored and controlled by the experimenter. Both the datalogger and the aforementioned true rms voltmeter were new at the beginning of the research and were, therefore, under their calibration warranties.

The rate of air flow through the apparatus was measured by one of three rotameters, depending on the magnitude of the flow. All rotameters were calibrated against a secondary standard.

Pressure Measurement and Flow Visualization. A separate set of experiments were performed to determine the pressure drop due to the presence of the plenum chamber. For this purpose, the heated test section tube, its attached mixing chamber, and the insulation enclosure were removed from the airflow loop. A stainless steel tube (84 diameters long), that had been cut from the same length as the test section, was mated to the downstream end-face of the plenum via a plexiglass flange (the fiberglass disk remained with the heated test section). The tube was internally honed for smoothness and was equipped with pressure taps located sufficiently far downstream of the plenum so as to lie in the redeveloped flow regime. There was also a series of taps deployed along the hydrodynamic development tube (upstream of the plenum) which were employed in the determination of the plenum-related pressure drop.

The pressure signals were sensed by a Baratron solid-state capacitance-type pressure meter. The output of the Baratron was read with the aforementioned Keithly digital voltmeter. Pressure differences as small as 10^{-4} mm Hg could be detected by the Baratron. It, too, was new and under its warranty calibration during the duration of the experiments.

The flow visualization study was made prior to the heat transfer and pressure drop experiment. The specific focus of the visualization study was to detect the presence or absence of flow separation in the test section tube just downstream of the inlet cross section.

The visualization apparatus was made entirely of plexiglass and was equipped with dye injection taps both along the cylindrical wall of the plenum and along the upstream portion of the test section tube. Water was supplied to the apparatus from a constant-head tank suspended from the ceiling of the laboratory. The discharge from the apparatus was ducted to a weigh tank for flow metering.

Data Reduction

Heat Transfer Results. The procedures employed in deducing local heat transfer coefficients and Nusselt numbers will now be described. For the evaluation of the local heat transfer coefficient, the needed inputs are the local heat flux, wall temperature, and bulk temperature. Among these, only the local wall temperature is directly measured, so that the other quantities have to be obtained via data reduction.

The first step in the analysis is to envision the wall of the test section tube as being subdivided into axial segments of length Δx_i. Each such segment serves as a control volume for a heat balance. The axial boundaries of the respective control volumes are positioned midway between the adjacent temperature measurement stations. Thus, if x_{i-1}, x_i, and x_{i+1} denote the axial locations of successive wall temperature measurements, then the axial boundaries of the ith control volume are at $(x_{i-1} + x_i)/2$ and at $(x_{i+1} + x_i)/2$ and, correspondingly, the control volume length $\Delta x_i = (x_{i+1} - x_{i-1})/2$.

The energy transfers to and from a control volume include the following:

1 an internal heat source due to ohmic dissipation
2 convective heat transfer from the inner surface of the control volume to the airflow
3 heat loss from the outer surface of the control volume through the insulation to the ambient air
4 conduction heat transfer into the downstream face of the control volume from the adjacent portion of the tube wall
5 conduction heat transfer out of the upstream face of the control volume into the adjacent portion of the wall

Under steady-state conditions, these inflows and outflows are in balance. As will now be described, numerical values can be supplied to the heat balance equation for items 1, 3, 4 and 5, enabling the determination of the convective heat flow from the control volume to the fluid (item 2).

The ohmic dissipation for control volume i was determined by prorating the overall dissipation by the ratio $\Delta x_i/x_L$, where x_L is the length of the test section tube. For the heat loss through the insulation to the ambient, a conduction shape factor was found by setting up a two-dimensional finite difference network that spanned the two types of insulation (silica aerogel and styrofoam) and the surrounding wooden containment structure. A total of 1600 grid points were used to resolve the complex geometry which included both curved and straight boundaries. The details of this work are presented in [9]. With the shape factor available, the heat loss through the insulation was calculated by multiplying the shape factor with the temperature difference $(T_w(x_i) - T_\infty)$ and by the axial length Δx_i, where $T_w(x_i)$ is the measured wall temperature at x_i and T_∞ is the ambient temperature.

The axial conduction along the wall, items 4 and 5, was found by applying a central difference representation of Fourier's law. If A_w represents the cross-sectional area of the wall and k_w denotes the thermal conductivity of stainless steel (regarded as a function of temperature), then items 4 and 5 may be expressed as

$$k_w A_w (T_w(x_{i+1}) - T_w(x_i))/(x_{i+1} - x_i) \tag{1}$$

$$k_w A_w (T_w(x_i) - T_w(x_{i-1}))/(x_i - x_{i-1}) \tag{2}$$

Equations (1) and (2) were evaluated using the measured wall temperatures at stations x_{i-1}, x_i, and x_{i+1}.

The foregoing discussion has demonstrated that all contributions to the energy balance for a typical tube-wall control volume i can be evaluated from the experimental data, aside from the convection term.

Therefore, these operations yield the rate of convective heat transfer Q_i from the control volume to the fluid. The thus-determined Q_i for the successive control volumes are employed directly in the evaluation of the heat transfer coefficient and also for the computation of the local bulk temperature, as will now be described.

The axial distribution of the local bulk temperature was also found from a control volume analysis. For this analysis, the control volumes are cylinders of diameter d (equal to the tube diameter) and axial length Δx_i. The axial coordinates of the upstream and downstream faces of these control volumes are the same as those for the control volumes used earlier in the determination of the convective heat transfer rates Q_i.

For control volume i, let T^i_{in} be the bulk temperature of the fluid entering the control volume at its upstream face and T^i_{out} denote the fluid bulk temperature at the downstream face. Then,

$$T^i_{\text{out}} = T^i_{\text{in}} + Q_i/\dot{m}c_p \qquad (3)$$

Thus, with the already determined Q_i and the measured inlet bulk temperature, equation (3) can be used in a marching fashion to compute the fluid bulk temperature at all the control volume faces. Then, the bulk temperature $T_b(x_i)$ at any thermocouple measurement station x_i was found by linear interpolation between the faces of the corresponding control volume.

Then, with the information generated from the foregoing computations, the local heat transfer coefficient and Nusselt number at any station i was evaluated from

$$h_i = \frac{Q_i/A_i}{T_w(x_i) - T_b(x_i)}, \quad \text{Nu}_i = \frac{h_i d}{k_i} \qquad (4)$$

where $A_i = \pi d \Delta x_i$ and k_i is the thermal conductivity of air at $T_b(x_i)$. Although h_i may have the appearance of a "local average" heat transfer coefficient, it is, for the most part, a truly local coefficient. In this regard, it can be verified by carefully re-examining the foregoing data reduction procedure that the only quantity that is actually related to the finite axial length of the control volume is the axial conduction in the wall. Since the net axial conduction is only of significance at the first few measurement stations, it is only there that h_i is a local average. At all other points, h_i is strictly local.

The results will be parameterized by the Reynolds number defined as

$$\text{Re} = 4\dot{m}/\mu\pi d \qquad (5)$$

where μ is the viscosity corresponding to the mean bulk temperature of the air.

Variable fluid properties played only a minor role (e.g., maximum wall-to-bulk temperature difference about 11°C (20°F)). Nevertheless, for the reporting of fully developed Nusselt numbers, the foregoing definitions of Nu and Re were altered to respectively include k_{fd} and μ_{fd}, which correspond to the mean bulk temperature in the fully developed regime.

Pressure Drop Results. The net pressure drop due to the presence of the plenum chamber will be reported as a dimensionless pressure loss coefficient K whose evaluation will now be described. First, it may be recalled that there are pressure taps in the tubes both upstream and downstream of the plenum. These taps are so situated that for both the upstream and downstream regions, the respective p versus x distributions are straight lines. Envision next a graph where the p versus x data for a given run are plotted. Within the accuracy of the measurements, the aforementioned straight lines for the upstream and downstream regions are parallel but not colinear. Rather, there is a vertical separation between them (to be denoted by ΔP_p) which is due entirely to the presence of the plenum.

In terms of ΔP_p, the pressure loss coefficient is defined as

$$K = \Delta P_p/(\tfrac{1}{2}\rho V^2)^* \qquad (6)$$

The denominator of equation (6) is the velocity head corresponding to the density ρ^* of the fluid in the tube at the *inlet* of the plenum. For the evaluation of K, ΔP_p was determined from least-squares straight lines fitted to the pressure data, and the pressure needed for ρ^* was obtained via extrapolation from the upstream pressure data.

Results and Discussion

Basic Data. To illustrate the nature of the basic data collected during the experiments, Fig. 1 has been prepared. The figure shows wall and bulk temperature distributions for two data runs. The data points for the wall temperature distributions represent direct measurements. For the bulk temperature, only the inlet and exit values were directly measured, and these are identified by blackened data symbols. The other plotted points for the bulk temperature distribution were computed as described in the preceding part of the paper. Smooth curves are drawn through the data points for continuity; in the case of the bulk temperature, the faired curve is virtually indistinguishable from a straight line.

The wall and bulk temperature distributions shown in the lower part of the figure are typical of those for the overwhelming majority of the data runs. They are, in fact, exemplary specimens of what is expected for turbulent heat transfer in a uniformly heated tube. These distributions are exemplary from three standpoints: (1) they are remarkably free of data scatter, (2) the wall and bulk temperature distributions are precisely parallel in the downstream (fully developed) region, and (3) the computed bulk temperature distribution extrapolates almost exactly to the measured value at exit. With regard to the latter characteristic, it may be noted that in the majority of the data runs, overall energy balances closed to within one percent.

The results shown in the upper portion of Fig. 1 are unusual in that the wall temperature distribution exhibits an overshoot before attaining the fully developed straight-line increase. This overshoot was encountered only at the largest L/d (=10) and for Reynolds numbers of 7000 and lower. It can be attributed to the transition of the developing boundary layer from laminar to turbulent flow.

To illustrate the nature of the heat transfer coefficients measured here, a set of distribution curves for a given plenum geometry (D/d = 3, L/d = 10) is plotted in Fig. 2 in the form of h versus x/d. Results are shown for nine distinct Reynolds numbers between 5200 and 59,200. These results are distinguished by the general absence of scatter and by the true constancy of h in the thermally developed regime.

The distribution curves for Re > 10,000 display the classical shape that is characteristic of turbulent pipe flows, while the curves for Re ≤ 7000 are characterized by a slight undershoot prior to the attainment of the fully developed value. This undershoot is a reflection of the already-discussed wall temperature overshoot in Fig. 1.

An important observation in Fig. 2 is the absence of any indication of flow separation adjacent to the tube wall just downstream of the

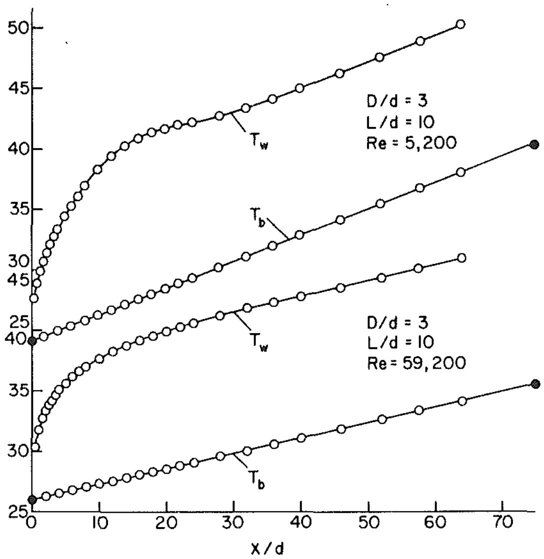

Fig. 1 Illustrative wall and bulk temperature distributions

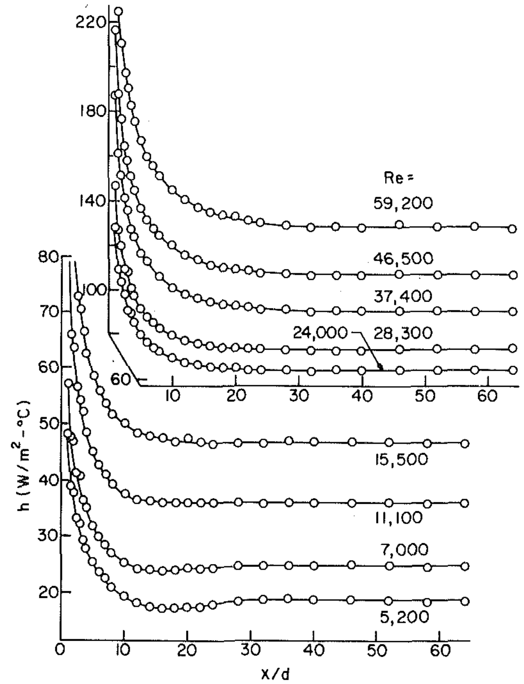

Fig. 2 Illustrative axial distributions of the heat transfer coefficient for parametric values of Reynolds number, $D/d = 3$ and $L/d = 10$

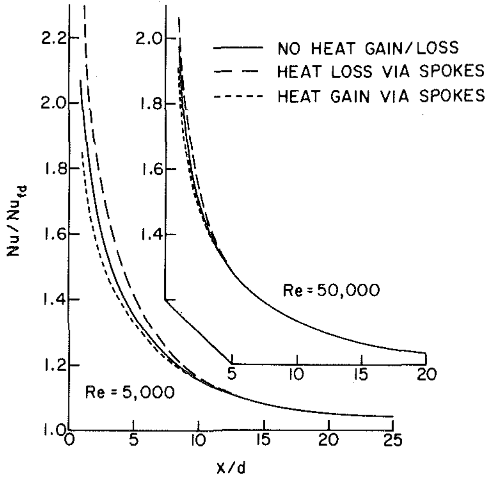

Fig. 3 Effect of guard heating/cooling on the axial distribution of the Nusselt number

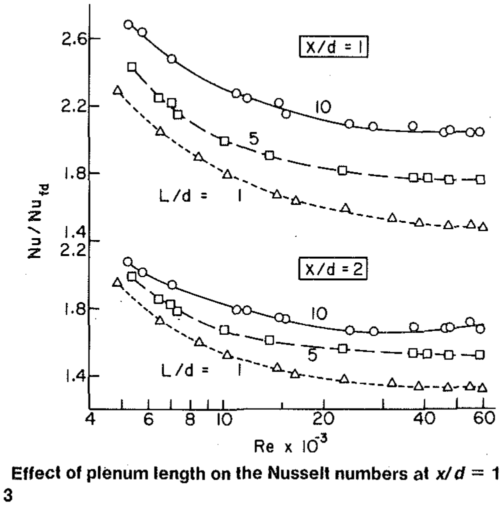

Fig. 4 Effect of plenum length on the Nusselt numbers at $x/d = 1$ and 2 for $D/d = 3$

inlet. The characteristic signature signalling the presence of such a separation region is an h versus x distribution which rises to a maximum at the point of flow reattachment and decreases thereafter. Clearly, such a pattern is not in evidence in the present results. Furthermore, the flow visualization studies did not reveal any separated regions within the test section tube.

Another basic issue of the research is the role of guard heating/cooling of the electrical bus adjacent to the tube inlet, and this issue is addressed in Fig. 3. The figure contains two panels in which results are respectively presented for a low and a high Reynolds number (Re = 5000 and 50,000). In each panel there are three curves of Nu/Nu_{fd} versus x/d, where Nu and Nu_{fd} respectively denote the local and fully developed Nusselt numbers. These curves have been faired through the experimental data, but the data have been omitted from the figure to avoid confusion.

One of the curves (the solid line) corresponds to the case where the guard heater/cooler is adjusted to null out extraneous heat transfer. The other curves correspond to ± 15 μV imbalances across the differential thermocouples installed on the copper current-carrying spokes. This imbalance is typical of that which would have occurred in the absence of guard heating.

The results speak for themselves—that is, guard heating is strictly necessary at low Reynolds numbers, but, while desirable, it is dispensable at Re = 50,000 or greater.

Plenum-Related Heat Transfer Enhancement. Attention will now be turned to the main focus of the research—the effect of plenum length and diameter on the heat transfer characteristics of a tube to which fluid is delivered by the plenum. Results documenting the plenum size effect will be presented in the next six figures, which will now be discussed sequentially.

The effect of plenum length for a fixed plenum diameter $D/d = 3$ is dealt with in Figs. 4 and 5. These figures encompass five individual graphs which pertain respectively to fixed axial stations $x/d = 1$, 2, 3, 5, and 8. At each station, Nu/Nu_{fd} is plotted as a function of Reynolds number for three different plenum lengths characterized by $L/d = 1$, 5, and 10. In this format, the effect of plenum length on the local heat transfer coefficient is readily identified by comparing the ordinates of the various L/d curves at a given Reynolds number.

From an examination of Figs. 4 and 5, it is seen that the plenum length has a decisive effect on the heat transfer coefficient when x/d is small, but the extent of the effect decreases with increasing downstream distance. At $x/d = 1$ and at the larger Reynolds numbers, the h value for $L/d = 10$ is about 40 percent greater than that for $L/d = 1$. The percentage increases are slightly smaller at lower Reynolds numbers. Thus, a relatively long plenum serves as an enhancement device.

At $x/d = 2$ and 3, heat transfer enhancement due to plenum length persists and is significant, but is smaller than that at $x/d = 1$. However, at $x/d = 5$, there is no apparent difference between the results for $L/d = 5$ and 10, and at this x/d the greatest enhancement in evidence due to the plenum length is about six percent. At $x/d = 8$, the curves tend to overlap, and while enhancement still persists at the larger Reynolds numbers, it is only a few percent. For still larger x/d

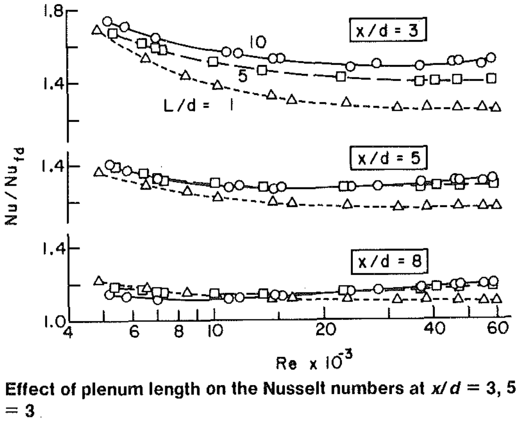

Fig. 5 Effect of plenum length on the Nusselt numbers at $x/d = 3$, 5, and 8 for $D/d = 3$

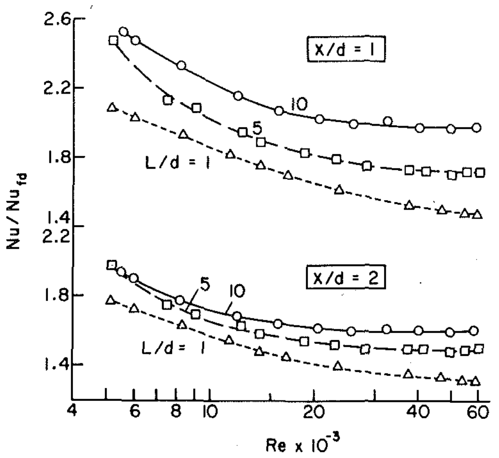

Fig. 6 Effect of plenum length on the Nusselt numbers at x/d = 1 and 2 for D/d = 6

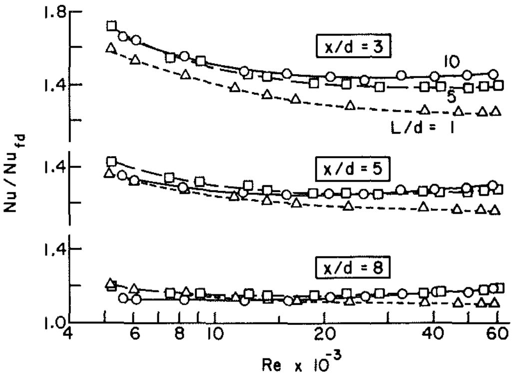

Fig. 7 Effect of plenum length on the Nusselt numbers at x/d = 3, 5, and 8 for D/b = 6

(not shown), all three curves collapse to the line $\mathrm{Nu/Nu}_{fd} = 1$.

A presentation similar to that of Figs. 4 and 5, but for a fixed plenum diameter $D/d = 6$, is provided by Figs. 6 and 7. The format of these figures is identical to those of the preceding figures. In actuality, the similarities between the two sets of figures are deeper than mere format. Aside from some minor differences in detail, the qualitative and quantitative behavior already identified for the $D/d = 3$ case appears to be reproduced for the $D/d = 6$ plenum.

To explore in greater detail the relationship between the results for the two plenum diameters, Fig. 8 has been prepared. This figure consists of two graphs, the upper of which conveys information for a fixed plenum length $L/d = 10$ while the lower is for the fixed length $L/d = 5$. In each graph, $\mathrm{Nu/Nu}_{fd}$ is plotted versus Reynolds number for both of the plenum diameters. The data for $D/d = 3$ are connected by faired curves but those for $D/d = 6$ are not fitted with curves to avoid the possible confusion of many closely positioned lines.

If attention is first given to the longest plenum $L/d = 10$, it is seen that the data at x/d = 1, 2, and 3 for the larger diameter plenum fall slightly below that for the smaller plenum, but the maximum deviations are only about five percent. At x/d = 5 and 8, the data for the two cases are coincident. Next, turning to the results for the intermediate length plenum $L/d = 5$ (lower graph), the same relationship between the Nusselt numbers for the two plenum diameters prevails but the deviations are even smaller. A comparison similar to that of Fig. 8 was also made for the shortest plenum $L/d = 1$ [9], and only very small diameter-related deviations were observed.

If consideration is now given to the findings of Figs. 4–8, it may be concluded that for the ranges investigated, plenum length has a much greater effect on the heat transfer coefficients than does plenum diameter. Indeed, considering the modest effect of plenum diameter, it appears that the results presented here are valid for all plenums with $D/d \geq 3$.

An alternative perspective on the plenum-related heat transfer enhancement is provided by Fig. 9. Here, $\mathrm{Nu/Nu}_{fd}$ is plotted versus x/d for three different Reynolds numbers, respectively Re = 6000, 15,000, and 50,000, in the three panels of the figure. Each panel contains curves for three plenum lengths, L/d = 1, 5, and 10, and the objective of the figure is to show how the entirety of the h versus x distribution curve is affected by the length of the plenum. The figure is for $D/d = 3$, but a similar figure for $D/d = 6$ conveys nearly identical results [9].

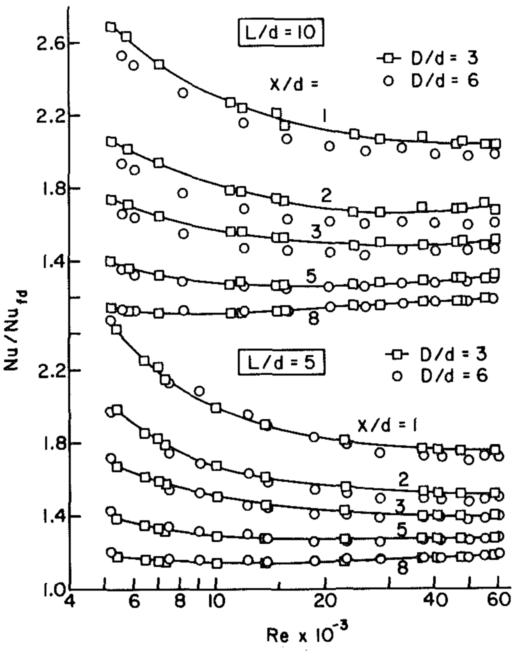

Fig. 8 Effect of plenum diameter on the Nusselt numbers at x/d = 1, 2, 3, 5, and 8 for L/d = 5 and 10

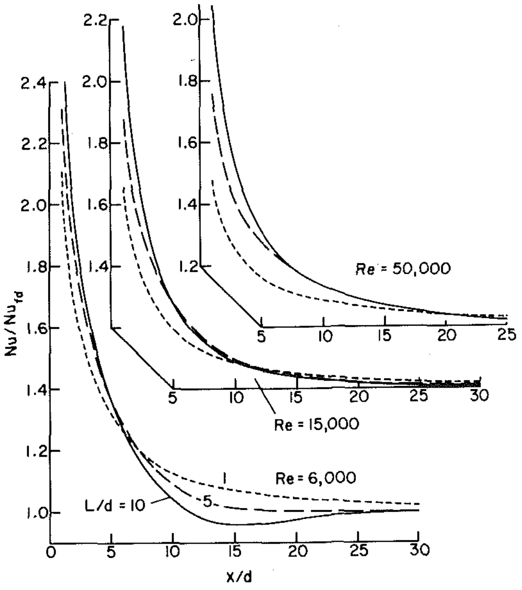

Fig. 9 Effect of plenum length on the axial distributions of the Nusselt number at Re = 6000, 15,000, and 50,000 for D/d = 3

The figure shows that at small x/d, the curves are ordered in a regular way with L/d, with that for the longest plenum being highest. However, the larger the L/d, the more rapidly do the curves drop off, and this causes all curves to ultimately cross. However, in the regions of the crossings, the $\mathrm{Nu/Nu}_{fd}$ values do not differ appreciably. The low-Reynolds-number curves (left-hand panel) are separated by as much as ten percent at downstream stations $x/d \sim 15$ owing to the absence or presence of the undershoot effect.

Before leaving Figs. 4–9, a brief comment appears appropriate about another enhancement mechanism, namely, the boundary layer development that gives rise to $\mathrm{Nu/Nu}_{fd}$ values well in excess of one in the entrance region. The figures show that entrance-region enhancement is greater at low Reynolds numbers than at high Reynolds numbers, a characteristic which does not appear to be well documented in the literature.

Thermal Entrance Lengths. The results presented in the preceding section, especially Figs. 2 and 9, suggest that the rapidity of the thermal development is affected by both the plenum geometry and the Reynolds number. To quantize the rate of thermal development, a thermal entrance length x_e has been defined as the distance from the test section inlet at which $\mathrm{Nu}/\mathrm{Nu}_{fd} = 1.05$. Dimensionless thermal entrance lengths x_e/d based on this definition are listed in Table 1.

It is seen from the table that the overall range of the thermal entrance length extends from 10 to 17 tube diameters. The plenum length appears to play a significant role in that the dependence of x_e/d on Re is affected by L/d. With a short plenum in place (i.e., $L/d = 1$), the thermal entrance length increases only very slightly with Reynolds number for $\mathrm{Re} \geq 20{,}000$, but is quite sensitive to Reynolds number at lower Re. These characteristics are similar to those expected when the plenum is absent (i.e., hydrodynamically developed flow at the inlet of the heated tube). On the other hand, for the two longer plenums ($L/d = 5$ and 10), there is an appreciable increase of x_e/d with Reynolds number for $\mathrm{Re} \geq 10{,}000$, while at lower Re the variation of x_e/d is slight. These marked differences in the characteristics of the thermal entrance length are reflective of flow field differences that are caused by the presence of the plenum.

Further inspection of Table 1 shows that the plenum diameter plays a secondary role. In general, the x_e values for the two plenum diameters do not differ by more than one tube diameter.

Literature Comparisons. The first of the literature comparisons is for the fully developed Nusselt number Nu_{fd}. Among the presently available predictive equations for Nu_{fd}, the widely quoted semi-empirical equation of Petukhov and Popov

$$\mathrm{Nu}_{fd} = \frac{(f/8)\mathrm{RePr}}{1.07 + 12.7(f/8)^{1/2}(\mathrm{Pr}^{2/3} - 1)} \tag{7}$$

$$f = (1.82\log\mathrm{Re} - 1.64)^{-2} \tag{8}$$

is regarded by many as being the most accurate. Equation (7) is purported [10] to be accurate to ±6 percent for Prandtl numbers between 0.5 and 200 and for the Reynolds number range from 10^4 to 5×10^6. To avoid massive data overlap, the present results for $D/d = 3$ and $D/d = 6$ have been plotted on separate graphs and respectively compared with equation (7). The two graphs are identical in all respects, and only that for $D/d = 3$ is presented here in Fig. 10.

The figure conveys two main messages. The first is that the fully developed Nusselt number is independent of L/d, and this is to be taken together with the aforementioned independence of Nu_{fd} from D/d. This finding confirms the expectation that given sufficient length of run, the specific details of the inlet velocity field will ultimately disappear so that the fully developed regime is truly universal.

Table 1 Thermal entrance lengths, x_e/d

D/d	Re	L/d 1	5	10
3	5000	16.5	11	9.5
	10,000	14	11	10
	20,000	12.5	12.5	12
	30,000	13	14	14
	40,000	13	15	15
	50,000	13.5	16	16
	60,000	13.5	16.5	16.5
6	5000	17	11	9.5
	10,000	15	11.5	10
	20,000	13	13.5	12
	30,000	13.5	15	13.5
	40,000	14	16	14.5
	50,000	14	16.5	15.5
	60,000	14.5	17	16

The other noteworthy feature of Fig. 10 is the excellent agreement of the present data with the Petukhov-Popov equation in the range $\mathrm{Re} \geq 10{,}000$, with a maximum deviation of five percent. At lower Reynolds numbers, the Petukhov-Popov equation departs more and more from the data, which is entirely expected because it is based on a fully turbulent model. It might also be noted that equation (7) is a slightly simplified version of the complete Petukhov-Popov equation (see equation (48) of ([10]). For airflow, the Nu_{fd} from the complete Petukhov-Popov equation is $2\frac{1}{2}$ percent lower than that from equation (7) at Re = 10,000, while for Re = 60,000 the complete equation gives a Nu_{fd} value that is 1.3 percent higher than that of equation (7). Therefore, the agreement of the present data with the complete Petukhov-Popov equation is even better than that in evidence in Fig. 10.

With regard to other comparisons with the literature, it has already been noted that there are no prior systematic studies of the effect of plenum geometry on heat transfer in a tube fed by the plenum. Thus, definitive comparisons of the present results with the literature are precluded. To enable limited comparisons to be made, a special set of experiments was performed in which L/d was set at its minimum possible value ($L/d = \frac{1}{4}$) consistent with the thermocouple installation in the plenum and with the avoidance of extraneous conduction between the upstream and downstream faces of the plenum. This arrangement was thought to be a close approximation for the case in which an already hydrodynamically developed flow enters a heated tube.

The results of those experiments (Re = 10,000 and 50,000, $D/d = 6$) are presented in Fig. 11 along with analytical predictions of [11] and [12] which correspond to turbulent flow in a uniformly heated tube with an axially unchanging velocity distribution. The predictions of [12] fall well below the data, and this tendency has been noted by others (e.g., [2]). On the other hand, for Re = 50,000, the predictions of [11] are in remarkably good agreement with the data. The agreement at Re = 10,000 is not as good, but the deviation might well be due, at least in part, to the gap associated with $L/d = \frac{1}{4} \neq 0$. The lower the Reynolds number, the more sensitive is the flow to the presence of such a gap.

The foregoing comparisons may be regarded both as a support of the present experimental technique as well as of the predictions of [10] and[11].

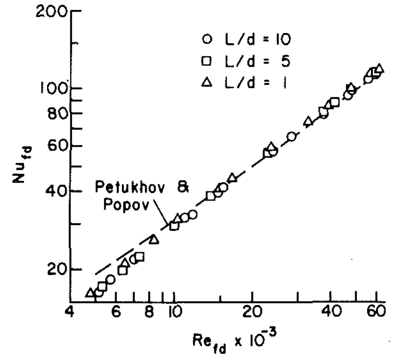

Fig. 10 Fully developed Nusselt numbers for $D/d = 3$

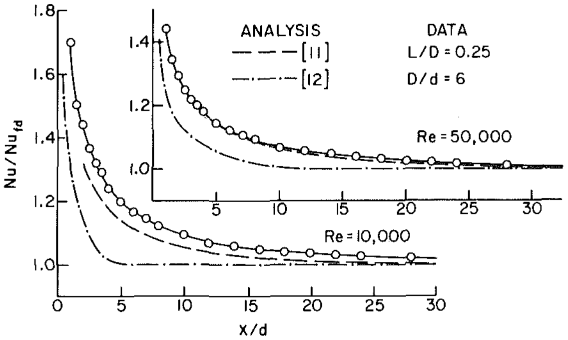

Fig. 11 Comparisons of measured Nusselt number distributions for L/d = 0.25 with analytical predictions corresponding to hydrodynamically developed flow in a uniformly heated tube

Table 2 Pressure loss coefficient K

(a) $D/d = 3$

$L/d = 1$		$L/d = 5$		$L/d = 10$	
Re	K	Re	K	Re	K
5700–6700	0.211	5900	0.722	5500	0.973
		6300	0.658	6200	0.935
8100	0.183	6700	0.628		
12,000	0.166	12,000	0.572	12,000	0.928
20,000	0.105	20,000	0.518	20,000	0.940
28,000	0.084	28,000	0.505	28,000	1.012
45,000	0.070	45,000	0.532	44,000	1.019
61,000	0.073	60,000	0.580	61,000	1.021
		(b) $D/d = 6$			
5700–6200	0.170	5600	0.680	5500	0.880
		5900	0.607	5800	0.831
6400	0.106	6800	0.539	6400	0.782
8000	0.107	8000	0.512		
12,000	0.101	12,000	0.460	12,000	0.797
21,000	0.084	21,000	0.423	21,000	0.819
28,000	0.077	28,000	0.420	29,000	0.832
45,000	0.074	45,000	0.430	45,000	0.921
53,000	0.091	59,000	0.461	59,000	0.941
59,000	0.110				

Plenum-Related Pressure Losses. As defined in equation (6) and discussed in the related text, the net pressure loss ΔP_p due to the presence of the plenum will be reported as a dimensionless loss coefficient K which is the ratio of ΔP_p to the velocity head in the tube at the plenum *inlet*. The experimentally determined values of K are listed in Table 2.

The most significant message of the table is the tight correlation between the magnitude of K and L/d. As L/d varies from 1 to 5 to 10, K varies, in global terms, from 0.1 to 0.5 to 1. This trend is entirely reasonable in that the two major contributions to K, the abrupt expansion at the plenum inlet and the abrupt contraction at the plenum exit, assert their separate identities more and more as L/d increases. However, even for $L/d = 10$, the K values listed in the table are less than the sum of the separate expansion and contraction coefficients.

With regard to Reynolds number effects, K varies somewhat irregularly when $\mathrm{Re} > 12{,}000$. At low Reynolds numbers, there is a general tendency of K to increase as Re decreases, with the greatest sensitivity in evidence for $L/d = 1$. In general, K is not very sensitive to D/d for the two values of D/d that were investigated.

Concluding Remarks

A systematic experimental study has been performed to determine the effect of plenum geometry on the turbulent heat transfer characteristics of a tube fed by the plenum. Measurements were also made of the plenum-related pressure drop. The experiments were designed and executed with painstaking care in order to provide a set of results of impeccable quality which can serve both as a guide to design and as a standard against which to compare candidate analytical models.

It was found that at axial stations in the near neighborhood of the tube inlet, the local heat transfer coefficients were higher for longer plenums. Thus, *a longer plenum functions as an enhancement device.* As an example of the enhancement, it may be noted that at $x/d = 1$, the heat transfer coefficient is 40 percent larger at a plenum length $L/d = 10$ than when $L/d = 1$. The extent of the enhancement decreases as x/d increases and can be regarded as negligible for $x/d \geq 8$. The plenum diameter appears to play a minor role with regard to the enhancement, so that the present results may be regarded as being applicable for all $D/d \geq 3$.

Thermal entrance lengths x_e, based on a five percent approach to complete thermal development, encompassed the range from 10 to 17 tube diameters for the investigated operating conditions. Longer plenums brought about a greater sensitivity of x_e to the Reynolds number in the fully turbulent regime but gave rise to a lesser sensitivity to Re in the low-Reynolds-number turbulent regime. The entrance lengths were not found to be sensitive to the plenum diameter.

The fully developed Nusselt numbers Nu_{fd} were independent of both the length and diameter of the plenum chamber. Excellent agreement prevailed between the measured Nu_{fd} values and those predicted by the Petukhov-Popov equation for $\mathrm{Re} \geq 10{,}000$, which is the range of applicability of the equation.

The pressure loss coefficient, which compares the plenum-related pressure loss with the velocity head in the tube, increased more or less linearly with the length of the plenum.

As a relevant adjunct to the main focus of the research, a study was performed to examine the role of guard heating/cooling at the electrical bus adjacent to the tube inlet. It was found that such heating/cooling was necessary for accurate Nusselt number results at low Reynolds numbers ($\mathrm{Re} \sim 5000$) and was desirable, but not strictly necessary at higher Reynolds numbers ($\mathrm{Re} \geq 50{,}000$).

Acknowledgment

This research was performed under the auspices of the Office of Naval Research (contract no. N00014-79-C-0621).

References

1 Boelter, L. M. K., Young, G., and Iverson, H. W., "An Investigation of Aircraft Heaters XXVII—Distribution of Heat Transfer Rate in the Entrance Section of a Circular Tube," NACA TN 1451, 1948.

2 Mills, A. F., "Experimental Investigation of Turbulent Heat Transfer in the Entrance Region of a Circular Conduit," *Journal of Mechanical Engineering Science*, Vol. 4, 1962, pp. 63–77.

3 Wesley, D. W. and Sparrow, E. M., "Circumferentially Local and Average Turbulent Heat Transfer Coefficients in a Tube Downstream of a Tee," *International Journal of Heat and Mass Transfer*, Vol. 19, 1976, pp. 1205-1214.

4 Ede, A. J., Hislop, C. I., and Morris, R., "Effect on the Local Heat Transfer Coefficient in a Pipe of an Abrupt Disturbance of the Fluid Flow: Abrupt Convergence and Divergence of Diameter Ratio 2/1," *Proceedings of the Institution of Mechanical Engineers*, London, Vol. 170, No. 38, 1956, pp. 1113–1126.

5 Ede, A. J., "Effect of an Abrupt Disturbance of the Flow on the Local Heat Transfer Coefficient in a Pipe," HEAT 164, National Engineering Laboratory, East Kilbride, Glasgow, Scotland, 1959.

6 Ede, A. J., Morris, R. and Birch, E. S., "The Effect of Abrupt Changes of Diameter on Heat Transfer in Pipes," NEL Report No. 73, National Engineering Laboratory, East Kilbride, Glasgow, Scotland, 1962.

7 Emerson, W. H., "Heat Transfer in a Duct in Regions of Separated Flow," *Proceedings of the Third International Heat Transfer Conference*, Vol. 1, 1966, pp. 267–275.

8 Zemanick, P. P. and Dougall, R. S., "Local Heat Transfer Downstream of Abrupt Circular Channel Expansion," ASME JOURNAL OF HEAT TRANSFER, Vol. 92, 1970, pp. 53–60.

9 Lau, S. C., "Effect of Plenum Length and Diameter on Turbulent Heat Transfer in a Downstream Tube and on Plenum-Related Pressure Losses," Ph.D. Thesis, Department of Mechanical Engineering, University of Minnesota, Minneapolis, Minnesota, 1980.

10 Petukhov, B. S., "Heat Transfer and Friction in Turbulent Pipe Flow with Variable Physical Properties," in *Advances in Heat Transfer*, Academic Press, New York, 1970, pp. 503–564.

11 Siegel, R. and Sparrow, E. M., "Comparison of Turbulent Heat Transfer Results for Uniform Wall Heat Flux and Uniform Wall Temperature," ASME JOURNAL OF HEAT TRANSFER, Vol. 82, 1960, pp. 152–153.

12 Deissler, R. G., "Analysis of Turbulent Heat Transfer and Flow in the Entrance Regions of Smooth Passages," NACA TN 3016, 1953.

M. J. Scott
Detroit Diesel Allison,
Detroit, MI

R. L. Webb
Associate Professor,
Department of Mechanical Engineering,
The Pennsylvania State University,
University Park, PA 16801

Analytic Prediction of the Friction Factor for Turbulent Flow in Internally Finned Channels

This work develops an analytical model for the friction factor with turbulent flow in internally finned channels. Such channels are an important class of enhanced heat transfer surfaces. Until this work, no analytical models for the turbulent friction factor have been proposed. The present model assumes the validity of the Law of the Wall and applies the logarithmic velocity distribution to the interfin and core regions of the flow. Theoretically based friction factor equations are developed for internally finned circular tubes and rectangular channels. The model predicts Carnavos data for 21 internally finned tubes within ±10 percent. Friction factor data were taken for five internally finned, rectangular channels. The analytical model predicts these data within ±10 percent, except for the case of a very high fin.

Introduction

This work is concerned with turbulent flow in internally finned channels. Circular internally finned tubes illustrated in Fig. 1 are of interest for heat exchanger application. Although internally finned tubes are commercially available in copper and aluminum, no analytical models are available for prediction of the heat transfer and friction characteristics. Work conducted by Carnavos between 1977 and 1979 has led to the development of an empirical correlation for the Nusselt number and friction factor as a function of the internal fin geometric parameters. Carnavos' 1977 paper [1] contains heat transfer and friction data for turbulent flow in 21 axial and helical finned tubes. Carnavos [1] initially attempted to correlate the data using the hydraulic diameter in the Dittus-Boelter heat transfer and Blasius friction factor equations. He found that the hydraulic diameter overpredicted the Nusselt number and friction factor. Carnavos developed empirical correction factors to the hydraulic diameter based correlation. The correction factor given by equations (1) and (2) are multiplied by the hydraulic diameter based correlations.

$$F_F = \frac{f}{f_H} = \left(\frac{S}{S_n}\right)^{0.5} \cos^{0.5}\alpha \tag{1}$$

$$F_H = \frac{\mathrm{Nu}}{\mathrm{Nu}_H} = \left(\frac{S}{S_n}\right)^{0.1} \left(\frac{A_n}{A}\right)^{0.5} \sec^3\alpha \tag{2}$$

Carnavos' 1979 study [2] used water and an ethylene glycol-water mixture as working fluids with eight of the original tubes and three additional helical finned tubes. The 1979 study replaced the $\cos^{0.5}\alpha$ in equation (1) by $\sec\,^3\alpha$. The air, water and glycol data were correlated within ±10 percent for $10{,}000 < \mathrm{Re}_H < 100{,}000$. The equation (1) and (2) correlations yielded $0.80 < F_F < 1.1$ and $0.64 < F_H < 0.96$. Thus, the hydraulic diameter correlations tend to overpredict the Nu and f. A hydraulic diameter model assumes that the velocity distribution is unaffected by the presence of the fins. The inaccuracy of the hydraulic diameter correlation apparently occurs because the velocity is reduced in the interfin region, relative to that in a smooth tube. The heat transfer and friction characteristics should depend on the dimensionless fin height (e/D) and on the interfin region aspect ratio, $(p - t)/e$. Equations (1) and (2) do not explicitly account for these geometric parameters.

Patankar, et al. [3] used a numerical model to predict the heat transfer and friction characteristics of axial internal fin tubes. This model employs an empirical constant to fit the results with Carnavos data [1].

Webb and Scott [4] used the equation (1) and (2) correlations to predict "optimum" geometric parameters (e/D and p/e) for axial and helical internally finned tubes. The optimum geometric parameters require minimum tube material for specified duty and operating constraints.

Ornatskii [5] recognized that the fins cause a reduced velocity in the interfin region, and developed an empirical equation relating the interfin and core region velocities to the average velocity in the channel. This work was performed using a flow channel which simulated a single interfin channel and an adjacent core region flow channel. Local and average velocities were measured in the two regions. The work was extended [6] to determine the resulting effects on heat transfer. Details of this work will be discussed in a later section.

Watkinson, et al. tested internally finned tubes with turbulent air [7] and water [8] and attempted to develop heat transfer and friction correlations. Their correlation uses the hydraulic diameter with a correction factor taken from Ornatskii, et al. [5]. They found different friction correlations for air and water. The correlations do not agree with those of Carnavos. Vasil'chenko and Barbaritskaya [9, 10] give empirical heat transfer and friction correlations for turbulent flow of transformer oil in aluminum internally finned tubes. Other internally finned tube data are reported by Hilding and Coogan [11] and Lipets, et al. [12].

This literature survey shows that the empirical Carnavos correlation [1, 2] represents the state-of-the-art, based on reliable data for air, water and water-glycol mixtures. The works of Carnavos and Watkinson show that the hydraulic diameter concept overpredicts the friction factor and heat transfer coefficients. Ornastskii's experiments show that the failure of the hydraulic diameter concept occurs because the velocity is slowed in the interfin region.

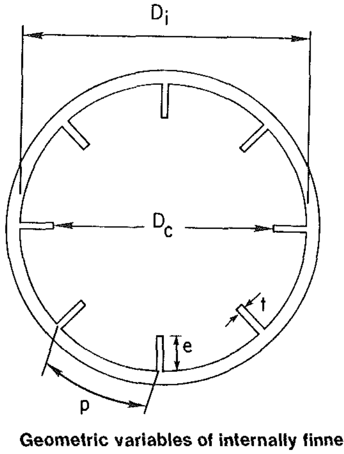

Fig. 1 Geometric variables of internally finned tube

Contributed by the Heat Transfer Division for publication in the JOURNAL OF HEAT TRANSFER. Manuscript received by the Heat Transfer Division August 11, 1980.

This work seeks to develop a theoretically based model for prediction of the friction factor with turbulent flow in internally finned channels. The successful completion of this objective will provide the basis for the development of a future analytical heat transfer model.

Theoretical Development for Circular Tubes

The theoretical model is based on the Law of the Wall [13]. The Law of the Wall assumes that the velocity distribution in the viscous influenced wall region is independent of the channel shape or pipe diameter. For the turbulence dominated wall region ($y+ > 26$) the algebraic form of the Law of the Wall is

$$\frac{u}{u^*} = 2.5 \ln \frac{yu^*}{\nu} + 5.5 \tag{3}$$

The friction factor in circular channels is well-predicted assuming equation (3) applies over the entire pipe radius. Equation (3) may be integrated over the pipe radius giving $\bar{u}/u^* \equiv \sqrt{2/f}$ which results in the friction factor equation

$$\sqrt{\frac{2}{f}} = 2.5 \ln \mathrm{Re}\sqrt{\frac{f}{2}} + 1.75 \tag{4}$$

Hartnett, et al. [14] and Brundrett [15] have predicted the friction factor in smooth square and rectangular channels by integrating equation (3) over the cross section. As discussed by Hartnett, et al., an approximation is introduced in this case, since secondary flows occur in such noncircular channels. Schlichting [16] describes the local flow structure in detail, based on Nikuradse's measurements. The secondary motion consists of fluid velocity components near the wall which flow toward the corner, and join to flow outward along the corner bisetrix. Schlichting [16] shows figures of this secondary flow field, based on Nikuradse's measurements in rectangular channels. The secondary flows augment the velocity in the corner region and cause the wall shear stress to vary from a maximum at the mid-point and drop sharply to zero in the vicinity of the corners. Both Hartnett, et al. and Brundrett ignore the effect of secondary flows in their analysis of rectangular channels.

The analysis of Hartnett, et al., uses an iterative procedure to draw a flow field of orthogonal constant velocity and gradient lines. Then, equation (3) is graphically integrated over the flow field. Their predicted results were in good agreement with data for 10:1 aspect ratio channels. But, the predicted values were 12 percent low for a 1:1 aspect ratio channel.

Brundrett uses a simpler procedure which models the rectangular channel as the combination of an infinite aspect ratio channel with half of a square channel at each end. Brundrett shows good agreement between theory and experiment for all channel aspect ratios, including the square duct.

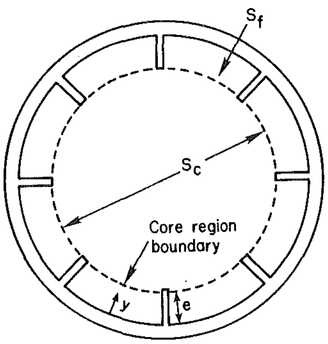

Fig. 2 Definition of interfin and core region flow areas

Due to the prior success in applying the Law of the Wall to rectangular channels we have chosen to apply the concept to internally finned tubes. However, substantial modifications in method are required to account for the more complex flow geometry. Figure 2 shows that the cross-sectional flow area (S) of a circular finned channel is divided into two flow areas: 1) the interfin region (S_f) for $0 < y \leq e$ and 2) the core region (S_c) for $y > e$. Thus,

$$S = S_f + S_c \tag{5}$$

Writing the continuity equation for the two flow regions yields

$$\bar{u}S = \bar{u}_f S_f + \bar{u}_c S_c \tag{6}$$

Dividing by u^* and using $\bar{u}/u^* \equiv \sqrt{2/f}$ allows equation (6) to be written as

$$\sqrt{\frac{2}{f}} = \frac{\bar{u}_f}{u^*}\frac{S_f}{S} + \frac{\bar{u}_c}{u^*}\frac{S_c}{S} \tag{7}$$

Expressions must now be developed for the interfin region velocity ($\bar{u}_f/u^*$) and the core region velocity ($\bar{u}_c/u^*$). Separate developments are necessary for each region. The development will be presented for an internally finned circular tube. Then, the analysis will be extended to the case of internally finned rectangular channels.

Interfin Region. The required assumptions are: (1) Secondary flows are neglected. (2) The interfin region is an open rectangular channel. (3) The velocity distribution between each wall and the corner bisectrix is given by equation (3).

Figure 3 shows the regions over which equation (3) is integrated. Different integrations are required for the three possible interfin region aspect ratios: 1) $e/b > 1$, 2) $e/b = 1$ and 3) $e/b < 1$. Symmetry is

Nomenclature

A = total heat transfer surface area
A_n = surface area based on nominal (smooth channel) area
a = one-half channel spacing in a rectangular channel
b = half the spacing between fins, $b = \frac{(p-t)}{2}$
b' = distance defined on Fig. 3, Case 3
d_{fh} = inter-fin hydraulic diameter, $d_{fh} = \frac{4be}{(b+e)}$
D_c = diameter of the core region
D_H = hydraulic diameter of a finned channel, $D_H = \frac{4A}{P_w}$
D_{HR} = hydraulic diameter of a smooth rectangular channel
D_i = inside diameter of a smooth tube; diameter to the base of the fins in a finned tube
e = fin height
e' = distance defined by Fig. 3, Case 1
f = fanning friction factor
n = number of fins in a tube
p = fin spacing
P_w = wetted perimeter
R = tube radius
Re_H = Reynolds number based on hydraulic diameter, $D_H\bar{u}/\nu$
S = actual minimum free flow area
S_c = flow area of the core region
S_f = flow area of the inter-fin region
S_n = flow area based on nominal (smooth channel) area
t = fin thickness
T = temperature
u = velocity
u_e = velocity at fin tip
u^* = shear velocity, $u^* = \sqrt{\tau_w/\rho}$
$\bar{u}$ = average velocity
$\bar{u}_c$ = average velocity in the core region
$\bar{u}_f$ = average velocity in the inter-fin region
Δu_e = shift in velocity profile for a finned channel, cf. equation (13)
w = half-width of rectangular channel
y = distance from a wall
z = distance from a wall
α = helix angle in a spiral fin tube measured from the tube axis
ν = kinematic viscosity
ρ = density
τ_w = average wall shear stress

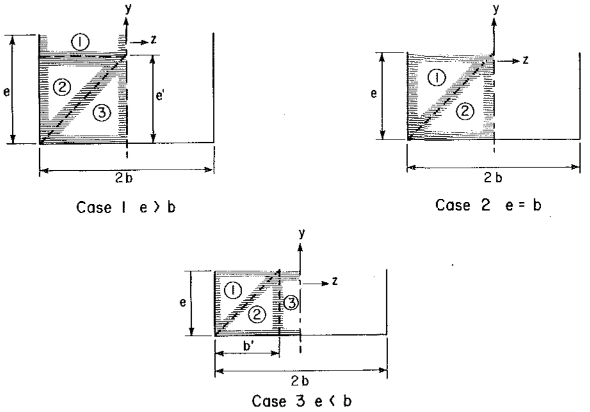

Case 1 e > b

Case 2 e = b

Case 3 e < b

Fig. 3 Integration areas for interfin region

employed, which simplifies the integrations. The integrations to be performed for each of the three cases are given by equations 8(a, b) and (c). For simplicity, let $B = 2.5$ and $A = 5.5$.

$$\frac{\overline{u}_f}{u*} = \frac{1}{eb}\left\{\int_0^b (e - e')\left[B \ln \frac{zu*}{\nu} + A\right] dz + \int_0^{e'} dy \int_0^{\frac{b}{e'}y}\left(B \ln \frac{zu*}{\nu} + A\right) dz + \int_0^b dz \int_0^{\frac{e'}{b}z}\left(B \ln \frac{yu*}{\nu} + A\right) dy\right\} \quad \text{for } (e > b) \tag{8a}$$

$$\frac{\overline{u}_f}{u*} = \frac{1}{eb}\left\{\int_0^e dy \int_0^{\frac{b}{e}y}\left(B \ln \frac{zu*}{\nu} + A\right)dz + \int_0^b dz \int_0^{\frac{e}{b}z}\left(B \ln \frac{yu*}{\nu} + A\right) dy\right\} \quad \text{for } (e = b) \tag{8b}$$

$$\frac{\overline{u}_f}{u*} = \frac{1}{eb}\left\{\int_0^e dy \int_0^{\frac{b'}{e}y}\left(B \ln \frac{zu*}{\nu} + A\right)dz + \int_0^{b'} dz \int^{\frac{e}{b'}z}\left(B \ln \frac{yu*}{\nu} + A\right) dy + \int_0^e (b - b')\left(B \ln \frac{yu*}{\nu} + A\right) dy\right\} \quad \text{for } (e < b) \tag{8c}$$

where

$$b = \frac{1}{2}(p - t) \tag{9}$$

$$p = \frac{\pi D_i}{n} \tag{10}$$

n is the number of fins and D_i is the diameter to the base of the fins, and e' and b' are defined in Fig. 3. By geometry, $e' = b$ and $b' = e$.

Equations (11a, b) and (c) are the integrated values of equations (8a, b) and (c). The equations are written in terms of the hydraulic diameters (D_H) and Reynolds number (Re_H) of the interfin region, which are defined in the Nomenclature.

$$\frac{\overline{u}_f}{u*} = \left[2.5 \ln\left(\frac{b}{D_H} \mathrm{Re}_H \sqrt{\frac{f}{2}}\right) - 1.25\frac{b}{e} + 3.0\right] \quad \text{for } (e > b) \tag{11a}$$

$$\frac{\overline{u}_f}{u*} = \left[2.5 \ln\left(\frac{e}{D_H} \mathrm{Re}_H \sqrt{\frac{f}{2}}\right) + 1.75\right] \quad \text{for } (e = b) \tag{11b}$$

$$\frac{\overline{u}_f}{u*} = \left[2.5 \ln\left(\frac{e}{D_H} \mathrm{Re}_H \sqrt{\frac{f}{2}}\right) - 1.25\frac{e}{b} + 3.0\right] \quad \text{for } (e < b) \tag{11c}$$

The Core Region. Equation (3) also applies to the core region ($y > e$). However, the velocity at $y = e$ is less than that which would occur at the same wall distance in a smooth tube due to the increased surface shear of the interfin region. Thus, the velocity in the core region is

$$\frac{u_c}{u*} = 2.5 \ln \frac{yu*}{\nu} + 5.5 - \frac{\Delta u_e}{u*} \tag{12}$$

where Δu_e is the shift of the velocity profile relative to the velocity at $y = e$ above a smooth surface. This velocity shift is given by

$$\Delta u_e = u_{es} - u_{ef} \tag{13}$$

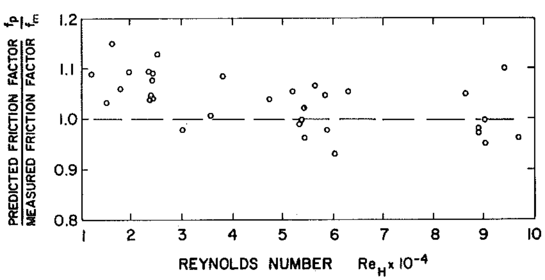

Fig. 4 Comparison of friction factor predicted by Table 1 equations with Carnavos data [1]

Table 1 Equations to be used in equation (7) to predict the friction factor for internally finned circular tubes

Case	$\frac{\overline{u}_f}{u*}$	$\frac{\overline{u}_c}{u*}$	$\frac{\Delta u_e}{u*}$
$e/b > 1$	equation (11a)	equation (16)	(14a)
$e/b = 1$	(11b)	equation (16)	(14b)
$e/b < 1$	(11c)	equation (16)	(14c)

The u_{ef} is the average velocity at the fin-tip and is obtained by integrating equation (3) to find the average velocity at $y = e$. The u_{es} is calculated from equation (3) at $y = e$. The resulting expressions for the three cases shown by Fig. 3 are:

$$\frac{\Delta u_e}{u*} = 2.5 \ln\left(\frac{e}{b}\right) + 2.5 \quad \text{for } (e > b) \tag{14a}$$

$$\frac{\Delta u_e}{u*} = 2.5 \quad \text{for } (e = b) \tag{14b}$$

$$\frac{\Delta u_e}{u*} = 2.5\frac{e}{b} \quad \text{for } (e < b) \tag{14c}$$

The existence of the velocity shift has been well-documented for flow over roughened surfaces and is discussed by Hinze [17].

The average core region velocity is found by integrating equation (12) over $e \leq y \leq R$

$$\frac{\overline{u}_c}{u*} = \frac{1}{A_c}\int_0^R 2\pi(R - y)\left(2.5 \ln \frac{yu*}{\nu} + 5.5 - \frac{\Delta u_e}{u*}\right) dy \tag{15}$$

The result of the integration is

$$\frac{\overline{u}_c + \Delta u_e}{u*} = \frac{{D_i}^2}{(D_i - 2e)^2} 2.5 \ln\left(\frac{D_i}{2D_H} \mathrm{Re}_H \sqrt{\frac{f}{2}}\right) - \frac{4(D_i e - e^2)}{(D_i - 2e)^2} 2.5 \ln\left(\frac{e}{D_H} \mathrm{Re}_H \sqrt{\frac{f}{2}}\right) - \frac{(\frac{3}{2}{D_i}^2 - 4D_i e + 2e^2)}{(D_i - 2e)^2} 2.5 + 5.5 \tag{16}$$

The term Δu_e in equation (16) is given by equations (14) for the interfin aspect ratio of interest.

Predicted Friction Factor. The theoretical friction factor is obtained by substituting equations (11) and (16) in equation (7). Table 1 summarizes the equations to be used for each of the three possible interfin aspect ratios.

Figure 4 shows the ratio of the predicted-to-measured friction factor based on the Table 1 equations and the data of Carnavos [1]. Carnavos' data are for 11 different axial internal-fin geometries. The agreement is within ±10 percent except for two data points. These points correspond to the low Reynolds number data for Carnavos tubes number 10 and 13. These tubes have thick fins and a small spacing between fins. The existence of a relatively thick viscous dominated flow may exist in the interfin regions. This flow condition would cause the present model to over-predict the friction factor.

The 11 tubes tested by Carnavos have $0.36 < e/b < 0.60$, and $0.02 < e/D < 0.29$. Therefore, the ability of the model to predict the $e/b > 1$ cases is not tested in Fig. 3. The assumption of rectangular shaped interfin channels is of questionable validity when $e/b > 1$ with large e/D. For this situation, a more precise formulation of equation (8*a*) should account for the decreasing channel width with distance from the wall. Wall curvature would not affect the core region equation (equation (16)) or the velocity shift equation (equation (14*a*)). The effect of wall curvature on $\bar{u}_f/u^*$ was examined by writing equation (8*a*) to account for wall curvature effects; this integral yields values of $\bar{u}_f/u^*$ 4 to 10 percent smaller than from equation (11*a*). When these smaller $\bar{u}_f/u^*$ values are substituted in equation (7), the friction factor will be reduced 2 to 5 percent. This correction would yield a very modest improvement for tubes 10 and 13. Fortunately, the case of large e/D_i and $e/b > 1$ is not a practical geometry (for circular tubes), and should not be encountered in practice.

Theory for Internally Finned Rectangular Channels

A procedure similar to the circular channel model may be applied to rectangular channels. The geometry of the rectangular channel is shown in Fig. 5. Equations (11*a*, *b*) and (*c*) apply equally for both channel shapes, since the interfin region is assumed to be of rectangular cross section. However, the core region velocity expression ($\bar{u}_c/u^*$) is different. In this case, equation (12) must be integrated over a rectangular channel, rather than a circular cross section. The result of the integration is

$$\frac{\bar{u}_c + \Delta u_e}{u^*} = \frac{(w - \frac{1}{2}a)a}{w(a-e)} 2.5 \ln\left(\frac{a}{D_H}\mathrm{Re}_H\sqrt{\frac{f}{2}}\right) + \frac{(a-e)}{2w} 2.5 \ln\left(\frac{a-e}{D_H}\mathrm{Re}_H\sqrt{\frac{f}{2}}\right) - \frac{(w + \frac{1}{2}e - a)e}{w(a-e)} \times 2.5 \ln\left(\frac{e}{D_H}\mathrm{Re}_H\sqrt{\frac{f}{2}}\right) - \left(1 + \frac{a}{2w}\right) 2.5 + 5.5 \quad (17)$$

The equations for the velocity shift (Δu_e) are obtained following a similar procedure for the rectangular shaped channel. The results of the integration are

$$\frac{\Delta u_e}{u^*} = 2.5\left(\frac{b}{e}\right) + \frac{e}{a} \quad \text{for } (e > b) \quad (18a)$$

$$\frac{\Delta u_e}{u^*} = 2.5 + \frac{e}{a} \quad \text{for } (e = b) \quad (18b)$$

$$\frac{\Delta u_e}{u^*} = 2.5\left(\frac{b}{e}\right) + \frac{b}{a} \quad \text{for } (e < b) \quad (18c)$$

Table 2 summarizes the equations to be used for the friction factor in an internally finned rectangular channel.

The equations for the circular and rectangular channels are different primarily because the average velocity in the core region (u_c) is different for the two channel shapes.

Experimental Program

Friction data were taken in a finned rectangular flow channel in order to provide further validation of the theoretical model. The test section was made from flat aluminum plates in which axial grooves were machined to insert 0.40 mm thick fins made of aluminum strip. A cross-sectional view of the test section is shown in Fig. 5 and the apparatus schematic is illustrated in Fig. 6. For all tests, the channel dimensions were $2w = 190.75$ mm and $2a = 19.69$ mm which gives an aspect ratio of 9.7:1. The range of test section dimensions tested is listed in Table 3.

Air was used as the working fluid and the flow rate spanned $5000 < \mathrm{Re}_H < 90{,}000$. The air flow rate was measured by a calibrated ASME orifice in a 52.5 mm dia pipe installed upstream of the test section. The air passed through a 760 mm long transition section having a 5.2 deg divergence angle before entering a 1840 mm length smooth rectangular entrance section. The 1840 mm length rectangular test section was connected to the rectangular entrance section by common side plates. The channel width and spacing of the entrance section were the same as those of the test section. The $2a$ and $2w$ dimensions used for data reduction were based on average values of 20 measurements of the channel width and 50 channel spacing measurements. The mean deviation of the channel width and spacing dimensions were 0.20 mm (0.1 percent) and 0.06 mm (0.3 percent), respectively. Static pressures were sensed by 1.6 mm dia holes drilled 95 mm from each end of the test section. At each axial location, three taps were drilled in the top plate and two were drilled in the bottom plate. The taps at each axial location were manifolded to yield the average static pressure at each axial location. A traveling-well micromanometer measured the difference between static pressure over the 1650 mm flow length between static taps.

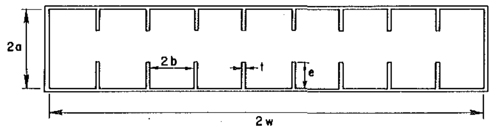

Fig. 5 Geometric variables of internally finned rectangular channel

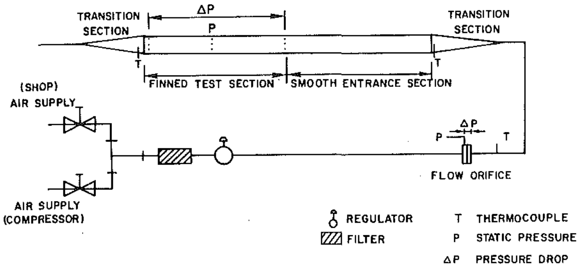

Fig. 6 Schematic of test apparatus

Table 2 Equations to be used in equation (7) for an internally finned rectangular channel

Case	$\frac{\bar{u}_f}{u^*}$	$\frac{\bar{u}_c}{u^*}$	$\frac{\Delta u_e}{u^*}$
$e/b > 1$	equation (11*a*)	equation (17)	equation (18*a*)
$e/b = 1$	(11*b*)	equation (17)	(18*b*)
$e/b < 1$	(11*c*)	equation (17)	(18*c*)

Table 3 Rectangular test sections tested

	Test Section Number					
	1	2	3	4	5	6
$\frac{e}{2a}$	smooth	0.115	0.211	0.211	0.211	0.405
$\frac{p}{e}$	—	1.690	0.918	1.836	3.673	1.915
$\frac{e}{t}$	—	5.65	10.40	10.40	10.40	19.95
D_H(mm)	35.70	13.40	7.75	14.38	24.53	14.89

The initial tests were performed on a smooth rectangular channel (test section 1). The measured friction factor is compared with the data of others [14, 17, 18] and our theoretical prediction, in Fig. 7.

The predicted friction factor for the smooth channel is obtained by integrating equation (3) over the regions illustrated in Fig. 8. The resulting analytical prediction for the smooth rectangular channel is

$$\sqrt{\frac{2}{f}} = 2.5 \ln\left(\frac{a+w}{w}\frac{\mathrm{Re}_H}{4}\sqrt{\frac{f}{2}}\right) - 2.5\left(1 + \frac{a}{2w}\right) + 5.5 \quad (19)$$

Equation (19) is in very close agreement with the model developed by Brundrett [15]. Equation (19) underpredicts the reference [14, 18] and [19] data 3 to 5 percent. The present data agree well with the referenced data for $\mathrm{Re}_H < 20{,}000$ but are about 15 percent high at Re_H

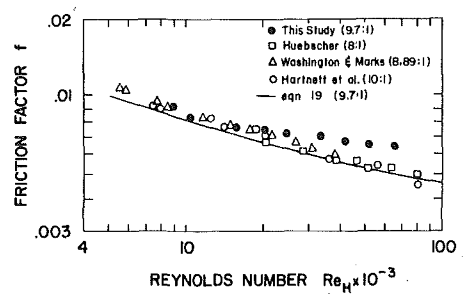

Fig. 7 Predicted and measured friction factors for smooth rectangular channel. Numbers in parentheses define channel aspect ratio

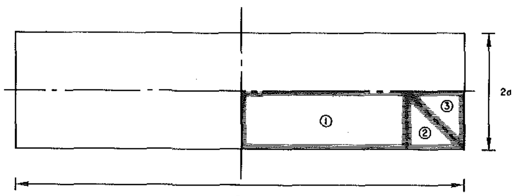

Fig. 8 Integration areas for smooth rectangular channel

= 80,000. The deviation at high Reynolds numbers suggests possible roughness effects.

Figure 9 shows the data obtained for the test sections listed in Table 3. It is interesting to note that the friction factors of the finned channels are higher than that of the smooth channel for some cases and lower in other cases. Figure 10 compares the predicted and measured friction factors. The predicted friction factors are based on the Table 2 equations. The theory predicts the present data within 10 percent for four of the five finned channels. The fifth case (test section 6) has very high fins and the friction factor is underpredicted 25 to 30 percent. In this case, the fin height occupies 81 percent of the channel spacing and the core region flow area is very small. Therefore, the model, which assumes distinctly different velocities in the interfin and core flow regions may become questionable. When the fins span the entire flow channel, the flow should be modeled as distinct noncircular flow channels.

The present theoretical equations predict the friction factor for internally finned circular and rectangular channels within ± 10 percent for typical geometries of interest.

Comparison with Ornatskii Model

Ornatskii [5] developed an empirical equation to relate the velocity in the interfin region ($\bar{u}_f$) to the average channel velocity ($\bar{u}$). His relation was derived from velocity distribution measurements in the special channel shape shown in Fig. 11. Air flow data were taken for $0.25 \le 2b/e \le 1.9$ with $7 < Re_H \times 10^{-4} < 25$. A similar channel was used for water flow data with $0.09 \le 2b/e \le 1.2$ with $3 < Re_H \times 10^{-4} < 10$. Velocity distributions were obtained for 25 channel configurations. Their experimental results were empirically correlated by equation (20).

$$\frac{\bar{u}_f}{u} = 1.22\left(\frac{2b}{D_i}\right)^{0.25}\left[1 - \exp\left(\frac{-3.8}{e}\,d_{fh}\right)\right] \qquad (20)$$

Dividing by u^* and using $\bar{u}/u^* = \sqrt{2/f}$, equation (20) is

$$\frac{\bar{u}_f}{u*} = 1.22\sqrt{\frac{2}{f}}\left(\frac{2b}{D_i}\right)^{0.25}\left[1 - \exp\left(\frac{-3.8}{e}\,d_{fh}\right)\right] \qquad (20a)$$

The predicted friction factor for an internally finned tube is obtained by substituting $\bar{u}_f/u^*$ from equations (11) into equation (20a). Figure 12 shows the ability of equation (20a) to predict the friction factor for Carnavos' internally finned tubes. The predicted values differ from the measured values by −25 percent to +19 percent. Ornatskii's semi-empirical model yields significantly poorer results than the present theoretical models defined by the equations in Tables 1 and 2.

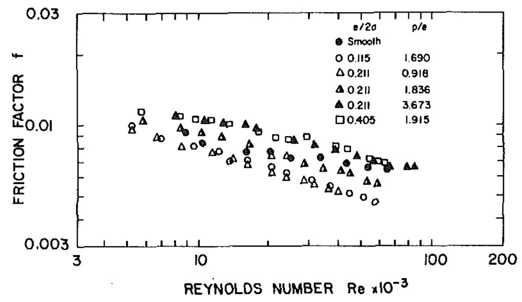

Fig. 9 Friction factors for smooth and internally finned rectangular channels

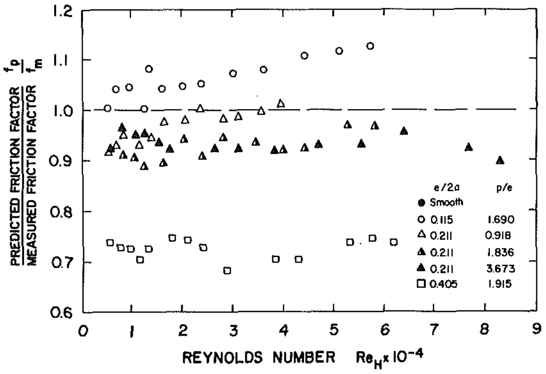

Fig. 10 Comparison of internally finned rectangular channel data predicted by Table 2 equations with experimental data

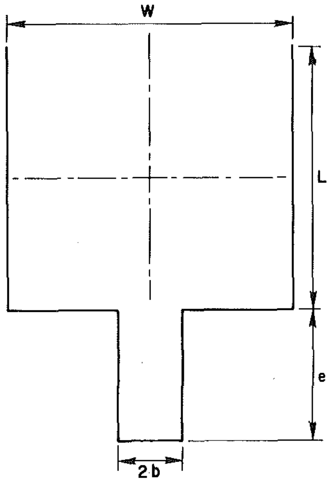

Fig. 11 Cross section of flow channel used by Ornatskii [5, 6]

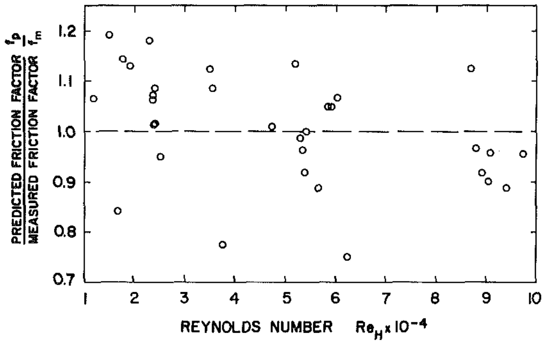

Fig. 12 Comparison of friction factor predicted by Ornatskii theory (equations (20a) and (11)) with Carnavos data [1]

Designer Correlation

Although the theoretical models summarized in Tables 1 and 2 provide quite accurate predictions of the friction factor, they may be cumbersome for design purposes. We have derived simple power law correlations, which may be used for design purposes. These correlations apply a geometric correction factor to the Blasuis friction correlation defined in terms of the hydraulic diameter. The correlation is derived by multiple regression analysis of the dimensionless variables.

For finned circular channels, the correlation is

$$f = \frac{0.056}{\mathrm{Re}_H{}^{0.25}}\left(\frac{e}{t}\right)^{0.057}\left(\frac{P}{D_i}\right)^{0.124}\left(\frac{e}{D_i}\right)^{-0.17} \tag{21}$$

Equation (21) correlates Carnavos data with ±10 percent.

The comparable correlation for finned rectangular channels is

$$f = \frac{0.139}{(\mathrm{Re}_H)^{0.25}}\left(\frac{p}{D_{HR}}\right)^{0.26} \tag{22}$$

Equation (22) correlates all of the finned rectangular channel data of the present study within ±10 percent, as shown in Fig. 13.

Conclusions

1 An analytical model was developed to predict the friction factor for turbulent flow in internally finned circular and rectangular channels. The model applies the logarithmic velocity distribution to the interfin and core regions of the flow.

2 The analytical model predicts the friction factors in both channel geometries within ±10 percent, except for very high fins.

3 The algebraic form of the analytic model is different for circular and rectangular channels due to the effect of channel shape on the average velocity in the core region.

4 The present theoretical model yields a more accurate prediction of the data than the semi-empirical model of Ornatskii, et al.

5 Simple power law friction correlations are also provided for design purposes.

6 The friction factor model should provide a basis for the future development of a theoretically based heat transfer equation.

Acknowledgments

This study was supported by Department of Energy Contract EG-78-S-02-4699.

References

1 Carnavos, T. C., "Cooling Air in Turbulent Flow with Internally Finned Tubes," *Heat Transfer Engineering*, Vol. 1(2), 1979, pp. 41–46.

2 Carnavos, T. C., "Heat Transfer Performance of Internally Finned Tubes in Turbulent Flow," *Advances in Enhanced Heat Transfer*, J. M. Chenoweth, J. Kaellis, J. W. Michel, and S. Shenkman, eds., ASME, New York, 1979, pp. 61–67.

3 Patankar, S. V., Ivanovic, M., and Sparrow, E. M., "Analysis of Turbulent Flow and Heat Transfer in Internally Finned Tubes and Annuli," ASME JOURNAL OF HEAT TRANSFER, Vol. 101, 1979, pp. 29–37.

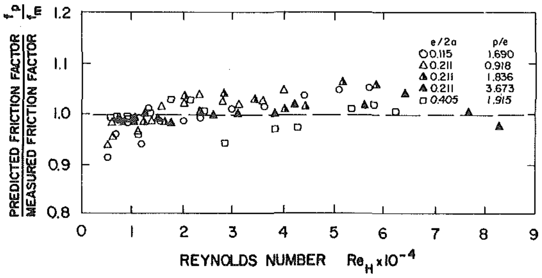

Fig. 13 Comparison of multiple regression curve fit (equation (22)) with internally finned rectangular channel data

4 Webb, R. L., and Scott, M. J., "A Parametric Analysis of the Performance of Internally Finned Tubes for Heat Exchanger Application," ASME JOURNAL OF HEAT TRANSFER, Vol. 102, 1979, pp. 38–44.

5 Ornatskii, A. P., Shcherbakuv, V. K., and Semena, M. G., "Investigation of Velocity Distribution in Tubes with Internal Longitudinal Fins," *Thermal Engineering*, Vol. 17(1), 1970, pp. 108–111.

6 Ornatskii, A. P., Shcherbakov, V. K., and Semena, M. G., "Investigation of Heat Transfer in Channels Between Fins of Tubes with Internal Longitudinal Fins," *Thermal Engineering*, Vol. 17(11), 1970, pp. 96–100.

7 Watkinson, A. P., Miletti, D. L., and Tarasoff, P., "Turbulent Heat Transfer and Pressure Drop of Internally Finned Tubes," *AIChE Symposium Series*, Vol. 69(131), 1973, pp. 94–103.

8 Watkinson, A. P., Miletti, D. L., and Kubanek, G. R., "Heat Transfer and Pressure Drop of Internally Finned Tubes in Turbulent Air Flow," *ASHRAE Transactions*, Vol. 81(1), 1975, pp. 330–349.

9 Vasil'chenko, Y. A., and Barbaritskaya, M. S., "Resistance with Nonisothermal Fluid Flow in Tubes with Longitudinal Fins," *Thermal Engineering*, Vol. 16(1), 1969, pp. 28–35.

10 Vasil'chenko, Y. A., and Barbaritskaya, M. S., "Heat Transfer in Tubes with Longitudinal Fins," *Thermal Engineering*, Vol. 16(5), 1969, pp. 105–109.

11 Hilding, W. E., and Coogan, C. H., Jr., "Heat Transfer and Pressure Loss Measurements in Internally Finned Tubes," *Symposium on Air-Cooled Heat Exchangers*, ASME, New York, 1964, pp. 57–85.

12 Lipets, A. U., Zholudov, Y. S., Lokshin, V. A., and Gromov, G. V., "The Temperature Regime and Hydraulic Resistance of Tubes with Internal Longitudinal Fins," *Heat Transfer-Soviet Research*, Vol. 1(5), 1969, pp. 86–94.

13 Hinze, J. O., *Turbulence* 2nd Ed., McGraw-Hill, New York, 1975, pp. 614–619.

14 Hartnett, J. P., Koh, J. C. Y., and McComas, S. T., "A Comparison of Predicted and Measured Friction Factors for Turbulent Flow through Rectangular Ducts," ASME JOURNAL OF HEAT TRANSFER, Vol. 84, 1962, pp. 82–88.

15 Brundrett, E., "Modified Hydraulic Diameter for Turbulent Flows," in *Turbulent Forced Convection in Channels and Bundles*, S. Kakac and D. B. Spalding, eds., Hemisphere, Washington, D.C., 1979, pp. 361–367.

16 Schlichting, H., *Boundary Layer Theory*, 7th Ed., McGraw-Hill, New York, 1979, pp. 612–615.

17 Hinze, J. O., *Turbulence*, 2nd Ed., McGraw-Hill, New York, 1975, pp. 635–637.

18 Huebscher, R. G., "Friction Equivalents for Round, Square and Rectangular Ducts," *Heating, Piping and Air Conditioning*, Vol. 19(12), 1974, pp. 127–135.

19 Washington, L., and Marks, W. M., "Heat Transfer and Pressure Drop in Rectangular Air Passages," *Industrial and Engineering Chemistry*, Vol. 29(3), 1937, pp. 337–334.

Eleftherios Papoutsakis[1]
Graduate Student.

Doraiswami Ramkrishna
Professor.

School of Chemical Engineering,
Purdue University,
West Lafayette, Ind. 47907

Heat Transfer in a Capillary Flow Emerging from a Reservoir

An extended Graetz problem is analyzed, with a semi-infinite axial domain and the Robin boundary condition on the heat-transfer wall. The heat-transfer problem examines a viscous fluid entering a cylindrical capillary from a reservoir. The capillary fluid is exchanging heat with the surrounding environment of prescribed temperature and thus the Robin boundary condition is employed on the wall. Since axial heat conduction is included in the analysis, a generalized Danckwerts boundary condition is shown to be most appropriate for the tube entrance. The energy equation is decomposed into a system of first-order partial differential equations, as in [4, 8, 9], to obtain a selfadjoint formalism. The Gram-Schmidt orthonormalization process is finally used to obtain what is technically an analytical solution, which is computationally simple and efficient. Other entrance boundary conditions are also discussed and analyzed.

1 Introduction

This work pertains to the temperature or concentration profile development in a fluid exchanging energy or mass with its surroundings as it flows into a long circular tube. Our most specific objective is the analysis of low Peclet number problems with semi-infinite heat- or mass-transfer sections, where the hydrodynamic problem may be decoupled from the heat- or mass-transfer problem. On the exchange wall we wish to specify the boundary condition of the third kind (Robin), where a linear combination of the heat flux and the temperature on the wall is prescribed. This boundary condition on the wall is for the most general and physically important case, where the wall containing the fluid conduit has a finite resistance to heat or mass transfer. The external fluid may be of constant temperature or may have a prescribed temperature distribution.

The specification of a semi-infinite axial domain derives from the fact that in a large number of problems of practical importance, what precedes the heat- or mass-exchange section is either not well defined physically (e.g., in biological systems [1–3]) or hydrodynamically very complex. For example, the fluid may enter the exchange section from an adiabatic reservoir or an adiabatic conduit of larger cross section, as is the case in viscous-fluid processing. A preceding adiabatic section of the same tubular cross section is one particular case that does not provide always the best description of the physical picture. The latter case leads to a boundary value problem with mixed boundary conditions (Neumann-Robin)[2] on the wall. That problem is discussed in [4], its solution culminating into solving an infinite set of algebraic equations. In view of the above discussion, in the present problem the fluid will be taken to flow into the circular tube from an adiabatic reservoir of large heat or mass capacity.

The corresponding hydrodynamic problem has been widely studied in the literature [5], its importance deriving from its applications in almost every industrial process involving transport of fluids. For flows of high Reynolds numbers, the velocity profile develops very slowly [5], so that the heat- or mass-transfer problem may not be decoupled from the hydrodynamic problem. However, in the case of low Reynolds numbers, the velocity profile develops rapidly; from the results of Vrentas and Duda [5], and possibly extrapolating to large values of their parameter β, even at $z = 0$, the velocity profile has essentially attained its fully-developed shape, except for a small core region around the centerline of the tube. It is therefore a good approximation to assume the fully developed velocity profile from the very beginning of the entrance region. Usual Reynolds numbers in viscous-fluid processing and many biological flows are of the order of 10^{-3} and the approximation of a fully developed flow at $z = 0$ is a typical one [2, 6]. However, small Reynolds numbers would result also in small Peclet numbers even for Schmidt or Prandtl numbers of the order of 10^4. Thus the validity of the model is not just restricted to the heat transfer problem in liquid metals. For the very low Peclet number regime, where the conductive terms dominate the heat transfer mechanism, the velocity profile approximation has a minimal effect on the solution of the problem. Although here we treat Newtonian flows only, extensions to fluids with any velocity profile may be realized in a straightforward manner from the analysis presented herein. The only difference will be computational, in the integration of the resulting eigenvalue problem (equation (21)). Thus, the methodology may apply to problems in experimental rheology, viscous fluid processing, heat transfer in liquid metals and mass transfer in biological systems. In the discussion and analysis that follow we discuss the heat transfer problem only, the analysis of the mass transfer problem being entirely analogous.

The problem under discussion may be looked upon as an extended Graetz problem, in that axial heat conduction is included in the analysis, so that it can be applied to low Peclet number flows. We consider as classical the problem without axial conduction but with any kind of a wall boundary condition. Past efforts on the extended Graetz problems, which have been discussed in detail by Shah and London [7], Papoutsakis [4] and Papoutsakis, et al. [8,9], were largely approximate. Truly analytical (and computationally efficient) solutions to extended Graetz problems with infinite axial domains were obtained in [8,9]. The Dirichlet-Dirichlet problem with a jump in the wall temperature at $z = 0$ was treated in [8]. The Neumann-Neumann problem was solved in [9]. The solutions to both the above problems were based on a selfadjoint formalism obtained by decomposing the energy equation into a pair of first order partial differential equations in the spirit of [10]. The decomposition was accomplished by defining an axial-energy flow function [8,9] based on physical arguments alone. This technique allowed analytical solutions to be obtained for the apparently non-selfadjoint extended Graetz problems.

Unfortunately, all extended Graetz problems with infinite axial domains and with the Robin wall boundary condition lead to mixed-boundary-value problems, which elude analytical solutions [4]. However, the extended Graetz problem with the Robin boundary condition on the wall and a semi-infinite axial domain admits a technically analytical solution, as it will be presently shown.

Yet, the treatment of the Robin wall boundary condition with a semi-infinite axial domain poses nontrivial difficulties, thus requiring further analysis. Specifically, the Robin boundary condition demands a nontrivial extension of the matrix differential operator that was used in our recent work [8, 9]; the semi-infinite axial domain introduces further difficulties whose resolution is even more demanding. The latter will become evident from the following analysis. This is indeed

---

[1] Currently Asst. Professor in the Department of Chemical Engineering, Rice University, Houston, Tex. 77001 (to whom all correspondence may be addressed).

[2] The Neumann boundary condition specifies the flux on the conduit wall (zero for adiabatic wall). In mixed boundary conditions, the first name refers to the upstream section and the second one to the heat- or mass-exchange section.

Contributed by the Heat Transfer Division for publication in the JOURNAL OF HEAT TRANSFER. Manuscript received by the Heat Transfer Division May 27, 1980.

the case where an apparently simpler problem (the present) is actually more complex and computationally demanding than some apparently more complex problems (the problems in [8, 9]).

The heat transfer problem for flow out of a reservoir and with Neumann wall boundary conditions (prescribed wall flux) has been addressed by Pirkle and Sigillito [11]; a flat temperature profile was employed as an entrance boundary condition. Variational techniques, leading to the solution of an infinite set of algebraic equations, were employed for the computation of the coefficients of expansion of the solution in terms of non-orthogonal eigenfunctions [11]. Hsu [12] treated the problem with a flat entrance temperature profile and the Robin wall boundary condition. The incorrectness and questionable computability of that solution have been discussed by Pirkle and Sigillito [13] and Michelsen and Villadsen [14], respectively. Finally, Sorensen and Stewart [15] solved the semi-infinite-domain problem with a Dirichlet wall boundary condition (prescribed wall temperature) and a generalized Danckwerts entrance condition (see below). That problem was meant as an approximation to the Neumann-Dirichlet problem and was treated by means of a collocation technique [15].

2 Analysis

2(*a*) Entrance Boundary Condition. In view of the discussion in the preceding section we consider the problem where a viscous fluid in a cylindrical capillary exchanges energy with its environment of constant temperature T_f through a wall of finite heat resistance. The viscous fluid is entering the capillary at low velocity from a reservoir of large heat capacity and constant temperature T_0.

In the formulation of an entrance boundary condition, the presence of a hydrodynamic entrance region represents an extraordinary degree of complexity even for an extensive numerical computation scheme. Consequently, we focus on situations that admit some important simplifications. Thus, we impose the restrictions of *low* Reynolds numbers for which the hydrodynamic entrance region is short and a Prandtl number large enough to preserve the uniformity of the temperature profile in this entrance region (except for peripheral distortions due to small amounts of heat transfer). The Peclet number, however, is assumed to be small enough to render axial conduction important (which is true for low enough Reynolds numbers). Next we ask that the reservoir be well stirred, have a large heat capacity, and be maintained at a *uniform* temperature T_0 *everywhere*, by which we imply that the mixing and its heat capacity are enough to overcome the axial gradient in temperature that will be induced by heat conduction at the outlet of the reservoir. Thus, if $z = 0$ is regarded as the capillary inlet, then for $z < 0$ the essentially uniform temperature field makes for negligible conduction whereas for $z > 0$ the heat transfer at the periphery will result in *axial* gradients near there and hence in axial conduction.

Summarizing, we have the situation of a virtually fully developed velocity profile at the outlet of the reservoir and a uniform temperature of T_0 with an energy efflux substantially by convection. On the capillary side, however, there is some axial conduction especially near the periphery. We have now two choices for the entrance boundary condition. Either we insist that the temperature be continuous so that the fluid will be entering at a uniform temperature T_0, in which case the situation is one of the *total* energy flux *entering* the capillary being different from that *leaving* the reservoir (implying a flux discontinuity), or we admit a temperature discontinuity by allowing the total flux to be continuous. Between these two options, the latter appears to us to be more reasonable since the procedure is in essence collapsing a finite but small region, where the temperature suffers a rapid change axially. Besides, the overall energy balance is intact. Indeed such idealizations are not foreign to analysis. We thus converge on the boundary condition

$$\lim_{z\to 0+}\left[-k\frac{\partial T}{\partial z}+\rho v_z(r)c_pT\right]=\rho v_z(r)c_pT_0 \tag{1}$$

Boundary condition (1) (which is a generalized Danckwerts type condition [16]) stands all by itself as an entrance condition for the type of physical applications that we discussed in the introduction. It has also been examined earlier [15] as a possible approximation to a mixed-boundary problem (Neumann-Dirichlet). In this context, it is in order to compare the present problem to the Neumann-Robin problem with regard to the temperature at $z = 0$. For the Neumann-Robin problem, the temperature at $z = 0$ will be lower than the temperature of the present problem at the same point. This is because of the high heat capacity of the reservoir. In other words, the fluid

Nomenclature

A_j^- = expansion coefficients, equations (30) and (36)
a_j^- = first argument of Kummer's functions; a constant, equation (46)
B = Biot number $\left(\equiv \dfrac{hR}{k}\right)$
B_j = a constant defined by equation (37)
C_j^+, C_j^- = integration constants corresponding to λ_j^- and λ_j^+, respectively, equations (26) and (27), respectively.
c_p = specific heat of a fluid at constant pressure
D = the domain of operator $\mathbf{L}_1$, equation (17)
E_k = the integral defined by equation (37)
$\mathbf{F}$ = the three-component-vector solution, equations (14) and (15)
$\mathbf{f}$ = a function in $\mathcal{H}$, equation (22)
$\mathcal{H}$, $\mathcal{H}_1$, $\mathcal{H}_2$ = Hilbert spaces
h = heat transfer coefficient for the tubular wall resistance.
k = thermal conductivity of the fluid
$\mathbf{L}_1$ = the linear matrix differential operator of equation (14); see also equation (15)
$M(, ,)$ = Kummer's function; the three blank spaces are for its first, second and third arguments, respectively, equation (45)
Nu = Nusselt number $\left(\equiv -\dfrac{k(\partial T/\partial r)r = R}{T_b - T_w}\cdot\dfrac{2R}{k}\right)$
Pe = Peclet number ($\equiv \rho c_p VR/k$)
R = radius of the tube (capillary)
$\mathcal{R}$ = the set of real numbers
r = radial variable (cylindrical coordinates)
T = fluid temperature
T_b = fluid bulk temperature
T_e = a given entrance-temperature distribution, equation (43)
T_f = ambient temperature
T_0 = fluid temperature in the reservoir
T_w = fluid temperature on the tubular wall
V = some characteristic velocity (a constant)
v = dimensionless axial velocity of the fluid
v_z = axial velocity of the fluid
z = axial variable
ϵ_{jk} = a constant, equations (34) and (42)
ζ = dimensionless z ($\equiv kz/\rho c_p VR^2$)
η = dimensionless r $\left(\equiv \dfrac{r}{R}\right)$
Θ = dimensionless T ($\equiv (T - T_f)/(T_0 - T_f)$)
Θ_e = dimensionless T_e, equation (43)
λ_j, λ_j^+, λ_j^- = eigenvalues, positive and negative eigenvalues, respectively
μ_j^- = the square root of $-\lambda_j^-$, equation (47)
Σ = dimensionless axial-energy-flow function, equation (7)
ρ = fluid density
ϕ = any function of η in $\mathcal{H}_2$
ϕ_1, ϕ_2, ϕ_3 = the first, second and third component, respectively of $\boldsymbol{\phi}$
$\boldsymbol{\phi}$ = any three component vector in $\mathcal{H}$
$\boldsymbol{\phi}_j$, $\boldsymbol{\phi}_j^+$, $\boldsymbol{\phi}_j^-$ = the three component eigenvectors corresponding to λ_j, λ_j^+, and λ_j^-, respectively
ϕ_{j1}, ϕ_{j2} = the first and second components, respectively, of $\boldsymbol{\phi}_j$
ϕ_{j1}^-, ϕ_{j2}^- = the first and second components, respectively, of $\boldsymbol{\phi}_j^-$
ψ = any function of η in $\mathcal{H}_2$
$\boldsymbol{\psi}$ = any three component vector in $\mathcal{H}$
ψ_j = a function of η, equation (34)
ψ_j' = non-normalized ψ_j
$\langle\ ,\ \rangle$ = the inner product of equation (16)
$(\ ,\ )$ = the inner product of equation (33)
$\|\cdot\|$ = the norm that corresponds to $\langle\ ,\ \rangle$
$|\cdot|$ = the norm that corresponds to $(\ ,\ )$

temperature at $z = 0$ for this problem will be lower than T_0 but somewhat higher than the fluid temperature of the Neumann-Robin problem. Also, the higher the Peclet number the lower the above temperature differences. Thus, for high Peclet numbers, the solutions of the three problems (i.e., the Neumann-Robin, the Danckwerts-entrance-condition and the uniform-temperature-entrance problems) will be the same.

Although entrance boundary condition (1) is used for the calculations presented in this paper, the generality of our solution methodology is demonstrated by solving the problem with other possible entrance conditions. These entrance conditions may include a specification of the axial flux or the temperature at $z = 0$.

The selfadjoint formalism presented here is useful for establishing the fact that the eigenvalues involved are real and an orthonormal basis is available in the space in which the differential operator is defined; yet, the solution to the boundary value problem is obtained as an expansion in terms of a part only of the above complete set of functions. The coefficients of expansion are however obtained by an application of the Gram-Schmidt orthogonalization process, which makes it *unnecessary* to solve an infinite set of algebraic equations. The selfadjoint formalism presented here naturally accommodates the entrance boundary condition, whether we use the Danckwerts boundary condition or the temperature or flux specification.

2(*b*) Formalism. In dimensionless form, the energy equation and the boundary conditions, assuming constant physical properties, negligible viscous dissipation, axisymmetry and in view of the above discussion, are given by,

$$-\frac{1}{\mathrm{Pe}^2}\frac{\partial^2\Theta}{\partial\zeta^2} - \frac{1}{\eta}\frac{\partial}{\partial\eta}\left(\eta\frac{\partial\Theta}{\partial\eta}\right) + v(\eta)\frac{\partial\Theta}{\partial\zeta} = 0 \qquad \begin{matrix} 0 < \eta < 1 \\ 0 < \zeta < \infty \end{matrix} \tag{2}$$

$$\lim_{\eta\to 0}\frac{\partial\Theta}{\partial\eta} = 0, \quad \text{all } \zeta \tag{3}$$

$$\frac{\partial\Theta}{\partial\eta}(\zeta, 1) + \mathrm{B}\Theta(\zeta, 1) = 0, \quad \text{all } \zeta \tag{4}$$

$$-\frac{1}{\mathrm{Pe}^2}\frac{\partial}{\partial\zeta}\Theta(0+, \eta) + v(\eta)\Theta(0+, \eta) = v(\eta), \quad \text{all } \eta \tag{5}$$

$$\Theta = \text{bounded}, \ \zeta \to \infty, \quad \text{all } \eta \tag{6}$$

Since axial and radial fluxes become zero for $z \to \infty$, boundary condition (6) implies that,

$$\lim_{\zeta\to\infty}\Theta = 0, \quad \text{all } \eta \tag{6a}$$

The dimensionless quantities are defined in the Nomenclature.

The motivation for the decomposition of the energy equation and the physical arguments used for the definition of the axial energy flow function may be found elsewhere [4, 8, 9]. In dimensionless form, the axial energy flow function is defined as,

$$\Sigma(\zeta, \eta) \equiv \int_0^\eta \left[-\frac{1}{\mathrm{Pe}^2}\frac{\partial\Theta}{\partial\zeta} + v(\eta')\Theta\right] 2\eta' d\eta' \tag{7}$$

Now the convective-diffusion process may be looked upon as a pair of first order differential equations describing how the axial energy flow varies with ζ and η. Thus, we have

$$\frac{\partial\Sigma}{\partial\zeta} = 2\eta\frac{\partial\Theta}{\partial\eta} \tag{8}$$

which expresses the fact that the axial change of energy flow results from radial conduction and

$$\frac{\partial\Sigma}{\partial\eta} = \left[-\frac{1}{\mathrm{Pe}^2}\frac{\partial\Theta}{\partial\zeta} + v(\eta)\Theta\right] 2\eta \tag{9}$$

which is obtained by differentiation from (7) and expresses the fact that the radial change of energy flow results from both axial convection and conduction of heat. Equation (9) may be rearranged to read as

$$\frac{\partial\Theta}{\partial\zeta} = \mathrm{Pe}^2 v(\eta)\Theta - \frac{\mathrm{Pe}^2}{2\eta}\frac{\partial\Sigma}{\partial\eta} \tag{10}$$

while from equations (7) and (6*a*) we obtain,

$$\lim_{\zeta\to\infty}\Sigma(\zeta, \eta) = 0, \quad \text{all } \eta \tag{11}$$

$$\Sigma(\zeta, 0) = 0, \quad \text{all } \zeta \tag{12}$$

We have now recast the problem into the pair of partial differential equations (8) and (10) in the two functions $\Theta(\zeta, \eta)$ and $\Sigma(\zeta, \eta)$ with boundary conditions given by (4, 5, 11) and (12). Note that (12) implies (3)[3] and (11) implies (6*a*) so that equations (3) and (6*a*) need not be included. Since it is important for the mathematical formalism to follow, we observe from (4) and (8) that

$$\frac{\partial}{\partial\zeta}\Sigma(\zeta, 1) = 2\frac{\partial\Theta}{\partial\eta}(\zeta, 1) = -2\mathrm{B}\Theta(\zeta, 1) \tag{13}$$

Equations (8), (10), and (13) now may be written in matrix notation as

$$\frac{\partial}{\partial\zeta}\begin{bmatrix}\Theta(\zeta, \eta) \\ \Sigma(\zeta, \eta) \\ \Sigma(\zeta, 1)\end{bmatrix} = \begin{bmatrix}\mathrm{Pe}^2 v(\eta) & -\dfrac{\mathrm{Pe}^2}{2\eta}\dfrac{\partial}{\partial\eta} & 0 \\ 2\eta\dfrac{\partial}{\partial\eta} & 0 & 0 \\ -2\mathrm{B}\lim\limits_{\eta\to 1} & 0 & 0\end{bmatrix}\begin{bmatrix}\Theta(\zeta, \eta) \\ \Sigma(\zeta, \eta) \\ \Sigma(\zeta, 1)\end{bmatrix} \tag{14}$$

Since equation (13) has already accounted for boundary condition (4), it is now possible to state the boundary conditions for (14) as given by (5, 11) and (12). Some notational brevity is achieved by denoting by $\mathbf{L}_1$ the *operator* in matrix form in equation (14). Also we denote by $\mathbf{F}(\zeta)$ the three component *vector* appearing on both sides of equation (14). Note that for *each* ζ this vector may be looked upon as an element of the linear space $\mathcal{H} \equiv \mathcal{H}_1 \oplus \mathcal{H}_2 \oplus \mathcal{R}$, which consists of ordered triplets of elements from the respective spaces $\mathcal{H}_1$, $\mathcal{H}_2$ and $\mathcal{R}$, the first two representing the spaces of functions, $f(\eta)$ and $g(\eta)$ defined in [0, 1], such that the Lebesque integrals $\int_0^1 f^2\eta d\eta < \infty$ and $\int_0^1 g^2 d\eta/\eta < \infty$, respectively, while $\mathcal{R}$ represents the space of the real numbers. Equation (14) is now written as

$$\frac{d}{d\zeta}\mathbf{F}(\zeta) = \mathbf{L}_1\mathbf{F}(\zeta) \tag{15}$$

The solution of the problem is now reduced to that of solving (15) subject to boundary conditions (5, 11) and (12).

The most interesting aspect of the operator $\mathbf{L}_1$ is that it gives rise to a selfadjoint problem although the original convective diffusion operator is nonselfadjoint. Indeed, if we define the *inner product* between two vectors

$$\boldsymbol{\phi} = \begin{bmatrix}\phi_1(\eta) \\ \phi_2(\eta), \\ \phi_3\end{bmatrix} \quad \boldsymbol{\psi} = \begin{bmatrix}\psi_1(\eta) \\ \psi_2(\eta) \\ \psi_3\end{bmatrix} \text{as}$$

$$\langle\boldsymbol{\phi}, \boldsymbol{\psi}\rangle = \int_0^1 \left[\frac{4}{\mathrm{Pe}^2}\phi_1(\eta)\psi_1(\eta)\eta + \phi_2(\eta)\psi_2(\eta)\frac{1}{\eta}\right] d\eta + \frac{1}{\mathrm{B}}\phi_3\psi_3 \tag{16}$$

and the following domain for $\mathbf{L}_1$,

$$D(\mathbf{L}_1) = \{\boldsymbol{\phi}\epsilon\mathcal{H}{:}\mathbf{L}_1\boldsymbol{\phi} \text{ (exists and) } \epsilon\mathcal{H},\ \phi_3 = \phi_2(1),\ \phi_2(0) = 0\} \tag{17}$$

it is shown in [4] that $\mathbf{L}_1$ is a symmetric operator in the Hilbert space

---

[3] Indeed, from (8), $2\lim\limits_{\eta\to 0}\dfrac{\partial\Theta}{\partial\eta} = \lim\limits_{\eta\to}\dfrac{1}{\eta}\dfrac{\partial\Sigma}{\partial\zeta}$, the right-hand side of which, using L'Hospital's rule, equals to: $\lim\limits_{\eta\to 0}\dfrac{\partial}{\partial\eta}\dfrac{\partial\Sigma}{\partial\zeta}\lim\limits_{\eta\to 0} = 1\dfrac{\partial}{\partial\zeta}\dfrac{\partial\Sigma}{\partial\eta}$ which by virtue of (7) and thus of (10) and (12), equals to $\lim\limits_{\eta\to 0}\dfrac{\partial}{\partial\zeta}\left[2\eta\left(-\dfrac{1}{\mathrm{Pe}^2}\dfrac{\partial\Theta}{\partial\zeta} + v(\eta)\Theta\right)\right] = 0$.

$\mathcal{H}$ of interest. Thus the selfadjoint (or Sturm-Liouville) eigenvalue problem is given by

$$\mathbf{L}_1\phi_j = \lambda_j\phi_j \tag{18}$$

from which we may obtain,

$$\mathrm{Pe}^2 v(\eta)\phi_{j1}(\eta) - \frac{\mathrm{Pe}^2}{2\eta}\phi_{j2}'(\eta) = \lambda_j\phi_{j1}(\eta) \tag{19}$$

$$2\eta\phi_{j1}'(\eta) = \lambda_j\phi_{j2}(\eta) \tag{20}$$

Therefore, the eigenvalue problem (18) implies, through (19, 20), and (17), that

$$\frac{1}{\eta}(\eta\phi_{j1}')' + \left[\frac{\lambda_j}{\mathrm{Pe}^2} - v(\eta)\right]\lambda_j\phi_{j1} = 0 \tag{21}$$

subject to the boundary conditions $\phi_{j1}(0) = 0$, $\phi_{j1}'(1) + \mathrm{B}\phi_{j1}(1) = 0$. $\mathbf{L}_1$ is neither positive definite nor negative definite and in fact possesses both positive eigenvalues $\{\lambda_j^+\}$ with corresponding eigenvectors $\{\phi_j^+\}$ and negative eigenvalues $\{\lambda_j^-\}$ with eigenvectors $\{\phi_j^-\}$. The two sets of eigenvectors normalized according to (16), together constitute an orthonormal basis in $\mathcal{H}$. It is worth noting that the eigenvalue problem (21) is the same as the eigenvalue problem obtained in the past [12] without recognizing the symmetric structure. The analysis herein justifies rigorously the implicit assumption made in [12] that the λ_j's are real since they are in fact the eigenvalues of a selfadjoint problem.

Before we proceed to the solution of the problem, the following expansion theorem is obtained from the eigenvalue problem, for any vector $\mathbf{f}\epsilon\mathcal{H}$,

$$\mathbf{f} = \sum_{j=1}^{\infty}\left[\frac{\langle\mathbf{f},\phi_j^+\rangle}{\|\phi_j^+\|^2}\phi_j^+ + \frac{\langle\mathbf{f},\phi_j^-\rangle}{\|\phi_j^-\|^2}\phi_j^-\right] \equiv \sum_{j=1}^{\infty}\frac{\langle\mathbf{f},\phi_j\rangle}{\|\phi_j\|^2}\phi_j \tag{22}$$

where

$$\|\phi\|^2 \equiv \langle\phi,\phi\rangle \tag{23}$$

2(*c*) The Solution. The solution of the problem, $\mathbf{F}(\zeta)$, is obtained in the form of series (22). To that effect the inner products indicated in the expansion coefficients of (22) must be obtained. Thus, since $\mathbf{F}\epsilon D(\mathbf{L}_1)$ we have,

$$\langle\mathbf{L}_1\mathbf{F}, \phi_j\rangle = \langle\mathbf{F}, \mathbf{L}_1\phi_j\rangle \tag{24}$$

and now using (15) and (18),

$$\frac{d}{d\zeta}\langle\mathbf{F}, \phi_j\rangle = \lambda_j\langle\mathbf{F}, \phi_j\rangle \tag{25}$$

from which we obtain, separately for the positive and negative eigenvalues,

$$\langle\mathbf{F}, \phi_j^+\rangle = C_j^+ e^{\lambda_j^+\zeta} \tag{26}$$

$$\langle\mathbf{F}, \phi_j^-\rangle = C_j^- e^{\lambda_j^-\zeta} \tag{27}$$

but since the solution is bounded for all ζ,

$$C_j^+ = 0, \quad \text{all } j \tag{28}$$

and also

$$C_j^- = \langle\mathbf{F}(0+), \phi_j^-\rangle \equiv A_j^-\|\phi_j^-\|^2 \tag{29}$$

Equation (28) expresses the fact that the eigenvectors that correspond to the positive eigenvalues are orthogonal to the solution, and thus to $\mathbf{F}(0+)$. From (22) and (26–29) now we have

$$\mathbf{F}(\zeta, \eta) = \sum_{j=1}^{\infty} A_j^- e^{\lambda_j^-\zeta}\phi_j^-(\eta) \tag{30}$$

where the expansion coefficients A_j^- must be determined. From (30) for $\zeta = 0$ and for the second vector components, we have

$$\Sigma(0+, \eta) = \sum_{j=1}^{\infty} \mathrm{A}_j^-\phi_{j2}^-(\eta) \tag{31}$$

while from equation (5) we obtain,

$$\Sigma(0+, \eta) = \int_0^\eta 2\eta' v(\eta')d\eta' \tag{32}$$

Since $\Sigma(0+, \eta)$ is known from (32), all that is required is to expand it in terms of the set $\{\phi_{j2}^-(\eta)\}$ for the determination of the A_j^-'s. This can be done by generating from $\{\phi_{j2}^-(\eta)\}$ an orthonormal set $\{\psi_j(\eta)\}$ by the Gram-Schmidt procedure (see, for example, Courant and Hilbert [17], pp. 3, 50). Note that $\{\phi_{j2}^-(\eta)\}$ is a linearly independent set, as may be readily inferred from the expansion theorem (22) and the linear independence of the set $\{\phi_j^-(\eta)\}$. The natural inner product to use for the Gram-Schmidt process is

$$(\phi(\psi), \psi(\eta)) = \int_0^1 \phi\psi\frac{1}{\eta}d\eta \tag{33}$$

that corresponds to Hilbert space $\mathcal{H}_2$. It is a simple computational procedure to determine constants $\{\epsilon_{jk}, j, k = 1, 2, 3, ..\}$ such that

$$\psi_j(\eta) = \sum_{k=1}^{j}\epsilon_{jk}\phi_{k2}^-(\eta) \tag{34}$$

as it will be seen subsequently. Since the set $\{\psi_j(\eta)\}$ is an orthonormal basis in $\mathcal{H}_2$, we have

$$\begin{aligned}\Sigma(0+, \eta) &= \sum_{j=1}^{\infty}(\Sigma(0+, \eta), \psi_j)\psi_j(\eta) = \sum_{j=1}^{\infty}\mathrm{B}_j\sum_{k=1}^{j}\epsilon_{jk}\phi_{k2}^-(\eta)\\ &= \sum_{k=1}^{\infty}\phi_{k2}^-(\eta)\sum_{j=k}^{\infty}\mathrm{B}_j\epsilon_{jk}\end{aligned} \tag{35}$$

Hence, from (31) and (35) we have

$$A_k^- = \sum_{j=k}^{\infty}\mathrm{B}_j\epsilon_{jk} \tag{36}$$

where

$$\mathrm{B}_j \equiv (\Sigma(0+, \eta), \psi_j) = \sum_{k=1}^{j}\epsilon_{jk}(\Sigma(0+, \eta), \phi_{k2}^-(\eta)) \equiv \sum_{k=1}^{j}\epsilon_{jk}E_k \tag{37}$$

The evaluation of E_k is discussed in detail in [4].

Now we turn to the evaluation of the set $\{\epsilon_{jk}\}$. From the Gram-Schmidt procedure we obtain for the non-normalized ψ_j,

$$\psi_j' = \phi_{j2}^- - \sum_{r=1}^{j-1}(\phi_{j2}^-, \psi_r)\psi_r \tag{38}$$

and then

$$\psi_j = \frac{\psi_j'}{|\psi_j'|} \tag{39}$$

where the norm in (39) derives from the inner product (33). Now, from (38) and (34) we obtain

$$\psi_j' = \phi_{j2}^- - \sum_{r=1}^{j-1}\sum_{s=1}^{r}\epsilon_{rs}(\phi_{j2}^-, \phi_{s2}^-)\sum_{k=1}^{r}\epsilon_{rk}\phi_{k2}^- \tag{40}$$

The summation range covered by r and k in (40) may be modified to read as,

$$\psi_j' = \phi_{j2}^- - \sum_{k=1}^{j-1}\phi_{k2}^-\sum_{r=k}^{j-1}\epsilon_{rk}\sum_{s=1}^{r}\epsilon_{rs}(\phi_{j2}^-, \phi_{s2}^-) \tag{41}$$

Thus, by virtue of (34) and (41), we obtain

$$\epsilon_{jk} = \begin{cases}\dfrac{1}{|\psi_j'|}, k = j, \text{ where } \psi_j' \text{ is given by equation (41)}\\[2ex] -\displaystyle\sum_{r=k}^{j-1}\epsilon_{rk}\sum_{s=1}^{r}\epsilon_{rs}(\phi_{j2}^-, \phi_{s2}^-)/|\psi_j'|, k = 1, 2, \ldots, j-1\end{cases} \tag{42}$$

Equation (42) is a recursive formula for the computation of the set $\{\epsilon_{jk}\}$ because we know $\epsilon_{11} = 1/|\phi_{12}^-|$. Considered as an infinite dimensional matrix, $\{\epsilon_{jk}\}$ is a lower triangular matrix in which the calculation of each row requires all the rows above it.

The computation of the integral $(\phi_{j2}^-, \phi_{s2}^-)$ is discussed in [4]. The defining equations for the bulk temperature, the Nusselt number and the asymptotic Nusselt number may be found in [4] or [8]. Expressions, suitable for computations, for the above quantities may be readily derived from their defining equations and equation (30) [4].

2(*d*) Other Entrance Conditions. If instead of the Danckwerts entrance condition (1), the entrance temperature $T_e(r)$ is prescribed at $z = 0$, the analysis up to equation (30) remains the same. From the first vector components of (30) at $\zeta = 0$ we would have

$$\Theta_e(\eta) \equiv \Theta(0+, \eta) = \sum_{j=1}^{\infty} A_j^- \phi_{i1}^-(\eta) \tag{43}$$

where $\Theta_e(\eta)$ is the dimensionless $T_e(r)$. For the determination of the A_j^-'s from (43) the Gram-Schmidt process must now be performed on the set $\{\phi_{j1}^-(\eta)\}$ with the inner product that corresponds to $\mathcal{H}_1$.

If the axial flux is specified at the entrance, from equation (30) we obtain,

$$\frac{\partial\Theta}{\partial\zeta}(0+, \eta) = \sum_{j=1}^{\infty} \lambda_j^- A_j^- \phi_{j1}^-(\eta) \tag{44}$$

and again the A_j^-'s are determined from (44) with the Gram-Schmidt process performed on the set $\{\phi_{j1}^-(\eta)\}$.

3 Computational Aspects

For the parabolic velocity profile the eigenvectors are computed using Kummer's functions [18], after transforming equation (21) into Kummer's equation [4, 8, 9, 18]. Thus, we have,

$$\phi_{j1}^-(\eta) = \exp\left(-\frac{\mu_j^-}{2}\eta^2\right) M(a_j^-, 1, \mu_j^-\eta^2) \tag{45}$$

where

$$a_j^- = \frac{1}{2}\left(1 - \frac{\mu_j^-}{2} - \frac{\mu_j^3}{2\mathrm{Pe}^2}\right) \tag{46}$$

$$\mu_j^- = (-\lambda_j^-)^{1/2} \tag{47}$$

while the eigenvalues are obtained from the characteristic equation,

$$(\mathrm{B} - \mu_j^-)M(a_j^-, 1, \mu_j^-) + 2\mu_j^- M'(a_j^-, 1, \mu_j^-) = 0 \tag{48}$$

obtained from boundary condition $\phi_{j1}'(1) + \mathrm{B}\phi_{j1}(1) = 0$, the real positive roots of which provide the μ_j^-'s. The computation of the eigenvalues has already been widely discussed in [4, 8, 9]. The expansion coefficients A_j^- of the problem are computed according to equation (36). It may be seen from the process of computing the set $\{\epsilon_{jk}\}$, that the computational effort increases much faster than linearly with the number of expansion coefficients to be computed. Thus, 11 expansion coefficients may be computed within 3–4 CP s on a CDC 6600 computer, 13 of them within 4–5 CP s and 15 of them within 8–12 CP 6600. Finally, the computation of 168 temperature points, typically used for either of the Figs. 1 and 2, required 1–1.5 CP 6600 s. It will be seen that the use of 11 terms for solution (30) provides an accuracy of better than 0.05 percent. It should be evident then that the analytical solution presented herein is also computationally very efficient.

4 Results

A number of negative eigenvalues has been presented in [12] for three different Biot numbers and various Peclet numbers. Further eigenvalues with their corresponding expansion coefficients may be found in [4]. Table 1 presents the expansion coefficients (computed with $j = 13$) for Pe = 5 and B = 1.

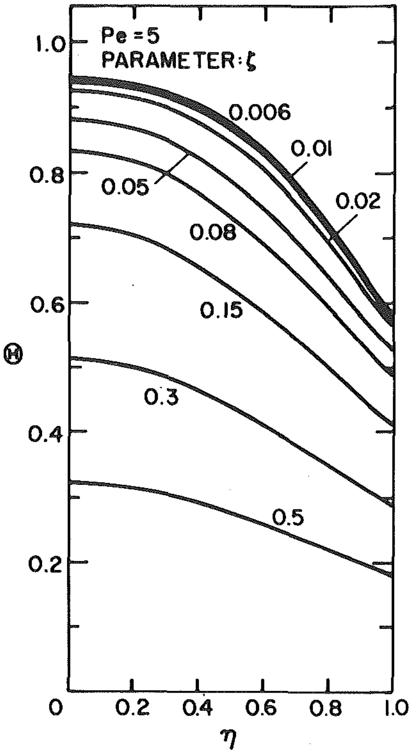

Fig. 1 Radial profiles of dimensionless temperature for various axial distances; Pe = 5

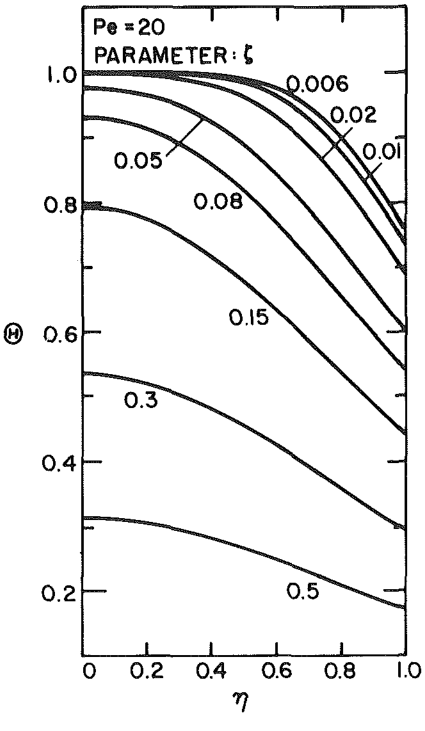

Fig. 2 Radial Profiles of dimensionless temperature for various axial distances; Pe = 20

A careful study of the construction of the expansion coefficients may reveal that, although the addition in the construction process of one or two terms may alter all the previous expansion coefficients, the changes are such that the net effect on the expansion of a quantity is minimal beyond a number of terms. Indeed, the maximum difference (usually in the entrance and the center of the tube) on the final computations with 14 and 18 terms was found to be less than 0.008 percent. The corresponding *maximum* difference between 11 and 15 term computations was found to be less than 0.03 percent. It may be concluded then that a solution with 11 series terms provides final accuracy of better than 0.05 percent with minimal computation time. The fast convergence of the series solution is primarily due to the fast decrease of the expansion coefficients; however, the decrease of the non-normalized eigenfunctions themselves [4] contribute to the fast series convergence in view of equation (30). An interesting point to note is that, unlike the Dirichlet [8] and the Neumann [9] problems,

Table 1 Expansion coefficient (A_j^-) corresponding to the eigenvalues λ_j^- for the Robin problem with Danckwerts entrance boundary condition; Pe = 5, j = 13

j	A_j^-
1	1.03234
2	−0.06927
3	−0.02683
4	0.02526
5	−0.01625
6	0.01017
7	−0.00656
8	0.00440
9	−0.00305
10	0.00218
11	−0.00158
12	0.00117
13	−0.00087

there exist two consecutive expansion coefficients with the same sign, except for Pe = ∞. Finally, note that for Pe = ∞ the expansion coefficients [4] are the same with those of the classical Graetz problem with Robin boundary conditions (see, for example [19]). Indeed, as discussed already in the introduction, for Pe = ∞ the Danckwerts boundary condition is equivalent to the uniform temperature boundary condition.

Figures 1 and 2 show radial temperature profiles for various axial distances, computed according to equation (30) for Pe = 5 and 20 respectively, both with B = 1. It can be shown, from further computational results in [4], that axial heat conduction may be neglected for Pe > 30.

Unlike the problem with Neumann boundary conditions [9], the length of the heating section becomes less important a factor in the analysis, since for dimensionless axial distance 1, the dimensionless temperature is almost zero. A heat exchange section of length 5–20 times the tube diameter is neither long nor unusual indeed particularly for the small Biot number used here. This feature derives from the nature of the boundary condition and it also exists for the problem with Dirichlet boundary conditions [8].

Figure 3 shows the dimensionless bulk temperature Θ_b as a function of the dimensionless axial variable, for three Peclet numbers, 5, 10 and ∞. The bulk temperature behavior shows a remarkable averaging of the axial conduction effect that may lead one to believe axial conduction not to be important for Peclet numbers higher than 10; the latter is not true as it was discussed above. Figure 4 shows a plot of the Nusselt number as a function of the dimensionless axial distance for three Peclet numbers, 5, 10 and 20. As it has been discussed in [20], the Nusselt number at $\zeta = 0$ becomes unbounded for Pe → ∞. However, the Nusselt numbers at $\zeta = 0$ are finite for all finite Peclet numbers, decreasing with decreasing Peclet numbers. In the contrary, the asymptotic Nusselt numbers increase with decreasing Peclet numbers. This creates the crossing of the Nusselt-number curves shown in Fig. 4. Note also that for Pe < 10 the Nusselt number curve shows a maximum occurring at an axial distance which increases with decreasing Peclet numbers. This fact is observed for the first time in a Newtonian Graetz problem.

Finally, Fig. 5 presents a plot of the asymptotic Nusselt number (Nu_{as}) as a function of the Peclet number. Thus, for Pe → 0, $\mathrm{Nu}_{as} \rightarrow 5.53$ and for Pe → ∞, $\mathrm{Nu}_{as} \rightarrow 4.125$. It is shown in [4] that the asymptotic Nusselt number is independent of the entrance boundary condition.

5 Discussion

The extended Graetz problems with a semi-infinite axial domain and either the Dirichlet or the Neumann boundary condition on the wall may be treated in an entirely analogous manner. The definitions of the proper matrix differential operators that correspond to $\mathbf{L}_1$, may be found in [8] and [9], respectively. What distinguishes $\mathbf{L}_1$ from the operators in [8, 9] is that the wall boundary condition (4) has been incorporated into the differential expression of $\mathbf{L}_1$ (equation (14)) by virtue of equation (13). This incorporation is necessary for a selfadjoint formalism. $\mathbf{L}_1$ is thus a 3 × 3 matrix operator in contrast to the 2 × 2 operators in [8, 9]; in the latter, the wall boundary conditions were accounted for by the proper definition of the domains of the operators. This non-trivial extension of the operators in [8, 9] to obtain $\mathbf{L}_1$ we found most instructive for the definition of the operators in the conjugated Graetz problems [21].

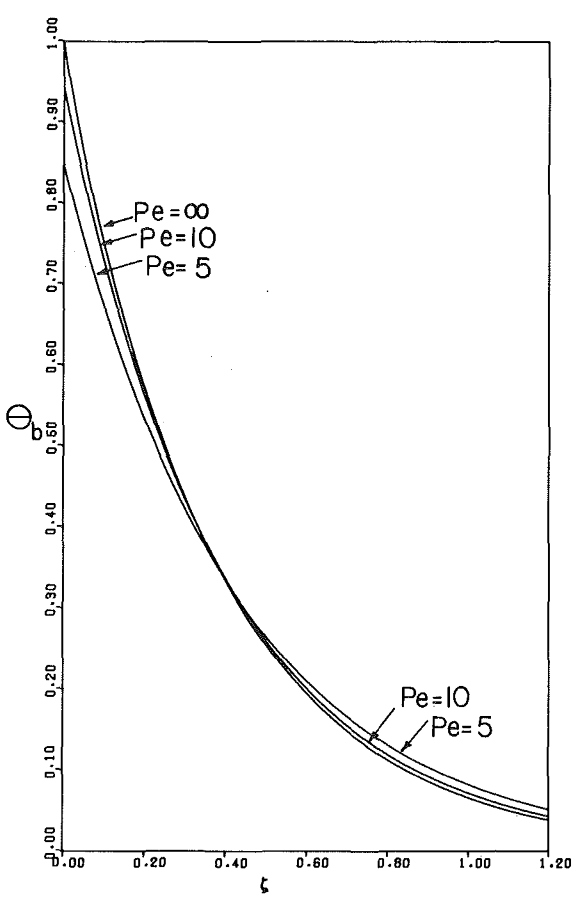

Fig. 3 Dimensionless bulk temperature Θ_b as a function of the axial distance for Pe = 5, 10, and ∞

The Dirichlet-Dirichlet [8] and Neumann-Neumann [9] problems had the unique feature that the wall-boundary conditions of the two sections ($z > 0$, $z < 0$) of the tube although physically different, were of the same type mathematically. This allowed analytical solutions to be obtained in terms of orthogonal functions, which resulted in the coefficients of expansion to be computed in the usual simple form of the classical Graetz problems. On the contrary, the Robin-Robin problem (and all problems with a different-type boundary condition on the wall of each section of the tube) lead to mixed-boundary problems, where the convenience of an analytical solution is lost. Yet, the semi-infinite problems, like the Robin problem presently discussed, lend themselves to technically analytical solutions, albeit not as efficient as those of [8, 9]. The nicety of these solutions derives from the fact that no variational techniques and/or infinite sets of algebraic equations must be used as in the past [11, 12]. The implications of the above is a solution with an improved accuracy and computational efficiency. Avoiding the use of variational techniques in handling the pointwise Danckwerts entrance boundary condition must be viewed as a particular accomplishment of the presented formalism. This derives from the fact that the pointwise Danckwerts condition is a linear combination of the heat flux and the temperature (equation (5)), with a coefficient of combination ($\upsilon(\eta)$) which is a function of the radial distance.

Acknowledgment

One of the authors (E.P.) is indebted to Purdue University, School of Chemical Engineering, for the financial assistance for the duration of this research. The computer facilities were generously provided by Purdue and Rice Universities.

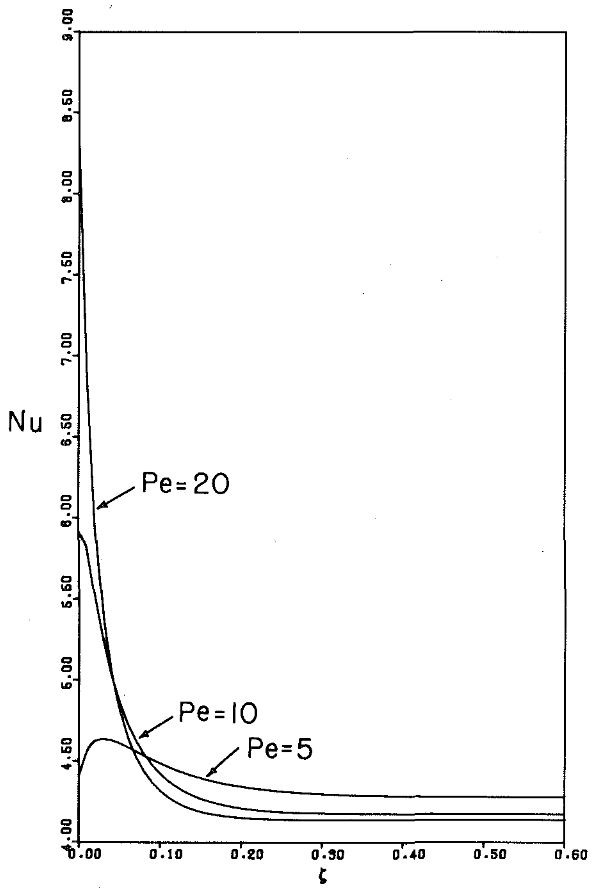

Fig. 4 **Nusselt number as a function of the axial distance for Pe = 5, 10, and 20**

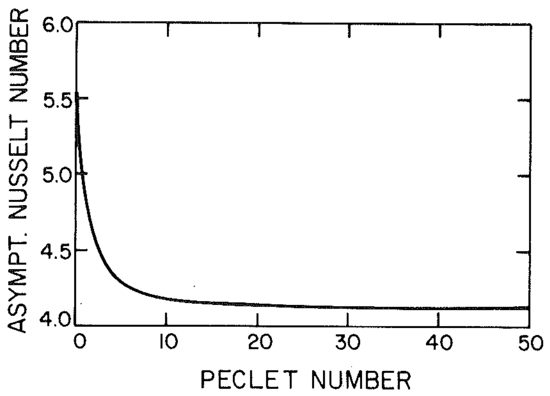

Fig. 5 **Asymptotic Nusselt number as a function of Peclet number**

References

1 Middleman, S., *Transport Phenomena in the Cardiovascular System*, Wiley-Interscience, New York, 1972.

2 Leonard, E. F. and Jorgensen, S. B., "The Analysis of Convection and Diffusion in Capillary Beds," *Annual Review of Biophysics and Bioengineering*, Vol. 3, 1974, pp. 293.

3 Davis, E. J., Cooney, D. O., and Chang, R., "Mass Transfer Between Capillary Blood and Tissues," *Chemical Engineering Journal*, Vol. 7, 1974, p. 213.

4 Papoutsakis, E., "The Solution of Boundary Value Problems in Diffusive Heat and Mass Transfer with Convection. Functional Analytic Methods," Ph.D. dissertation, Purdue University, W. Lafayette, Ind., 1979.

5 Vrentas, J. S., and Duda, J. L., "Flow of a Newtonian Fluid Through a Sudden Contraction," *Applied Scientific Research*, Vol. 28, 1973, p. 241.

6 Ybarra, R. M., and Eckert, R. E., "Viscous Heat Generation in Slit Flow," *AICHE Journal*, 1980, Vol. 26, 751.

7 Shah, R. K., and London, A. L., *Laminar Flow Forced Convection in Ducts. A Source Book for Compact Heat Exchanger Analytical Data. Advances in Heat Transfer*, Irvine, T. F. Jr. and Hartnett, J. P., Eds., Academic, New York, 1978.

8 Papoutsakis, E., Ramkrishna, D., and Lim, H. C., "The Extended Graetz Problem with Dirichlet Wall Boundary Conditions," *Applied Scientific Research*, Vol. 36, 1980, p. 13.

9 Papoutsakis, E., Ramkrishna, D., and Lim, H. C., "The Extended Graetz Problem with Prescribed Wall Flux," *AICHE Journal*, Vol. 26, 1980, p. 779.

10 Ramkrishna, D., and Amundson, N. R., "Boundary Value Problems in Transport with Mixed and Oblique Derivative Boundary Conditions. II. Reduction to First Order Systems," *Chemical Engineering Science*, Vol. 34, 1979, p. 309.

11 Pirkle, J. D. and Sigillito, V. G., "A Variational Approach to Low Peclet Number Heat Transfer in Laminar Flow," *Journal of Computational Physics*, Vol. 9, 1972, p. 207.

12 Hsu, C. J., "Exact Solution to Entry-Region Laminar Heat Transfer with Axial Conduction and the Boundary Condition of the Third Kind," *Chemical Engineering Science*, Vol. 23, 1968, p. 457.

13 Pirkle, J. C., and Sigillito, V. G., "Calculation of Coefficients in Certain Eigenfunction Expansions," *Applied Science Research*, Vol. 26, 1972, p. 105.

14 Michelsen, M. L., and Villadsen, J., "The Graetz Problem with Axial Heat Conduction," *International Journal of Heat Mass Transfer*, Vol. 17, 1974, p. 1391.

15 Sorensen, J. P., and Stewart, W. E., "Computation of Forced Convection in Slow Flow Through Ducts and Packed Beds.—I. Extensions of the Graetz Problem," *Chemical Engineering Science*, Vol. 29, 1974, p. 811.

16 Wehner, J. F., and Wilhelm, R. H., "Boundary Conditions of Flow Reactor," *Chemical Engineering Science*, Vol. 6, 1956, p. 89.

17 Courant, R., and Hilbert, D., *Methods of Mathematical Physics*, Vol. I, Interscience, New York, 1953.

18 Slater, S. L., *Confluent Hypergeometric Functions*, Cambridge Univ. Press, Cambridge, 1960.

19 Cooney, D. O., Kim, S. S., and Davis, E. J., "Analysis of Mass Transfer in Hemodialyzers for Laminar Blood Flow and Homogeneous Dialysate," *Chemical Engineering Science*, Vol. 29, 1974, p. 1731.

20 Papoutsakis, E., "Nusselt Numbers near the Entrance of the Heat-Exchange Section in Flow Systems," *AICHE Journal*, 1981, in press.

21 Papoutsakis, E., and Ramrishna, D., "Conjugated Graetz Problems. II. Fluid-Fluid Problems," *Chemical Engineering Science*, 1981, in press.

B. Vick
M. N. Özişik
Mechanical and Aerospace Engineering Department,
North Carolina State University,
Raleigh, N. C. 27650

Effects of Axial Conduction and Convective Boundary Conditions in Slug Flow inside a Circular Tube

An exact solution is presented for the temperature distribution and the local Nusselt number in slug flow of a low Péclét number fluid inside an infinitely long tube by including in the analysis the axial conduction in the fluid and convection from the walls for both the upstream and downstream regions. It is shown that the Péclét number and the relative magnitudes of the upstream and downstream Biot numbers significantly effect the local Nusselt number and the wall and mean fluid temperatures in the thermal entrance region. A particularly interesting result of the present investigation is the crossover of the wall and the mean fluid temperatures in such a manner as to give rise to a negative Nusselt number in the thermal entry region. Depending on the Péclét number and the relative magnitudes of the upstream and downstream Biot numbers, the negative Nusselt number can occur in the upstream or downstream region.

Introduction

The relative importance of axial heat conduction in flow inside a conduit depends on the magnitude of the Péclét number. For example, the axial conduction is negligible in comparison with radial conduction for flow inside a tube if the Péclét number is above 100. However, for liquid metals the Péclét number can be very low, hence the axial conduction can be important. The effects of axial conduction in heat transfer for liquids flowing inside tubes have been studied by several investigators [1–17]; but in all these investigations the problem was solved for very simple boundary conditions, such as a prescribed wall heat flux for the downstream region and insulated wall condition for the upstream region. However, when the upstream and downstream regions are subjected to convection with external environments at different temperatures, the relative magnitude of the Biot numbers for the upstream and downstream regions and the Péclét number are expected to influence the temperature distribution, hence the local Nusselt number, in the entrance region. Therefore, the objective of this work is to investigate the effects of the Biot and Péclét numbers on heat transfer at the entrance region of a circular tube.

Analysis

We consider incompressible, constant property fluid in slug flow inside a circular tube of radius r_0, lying in the axial domain $-\infty < z < \infty$. The tube has negligible wall thickness so that the axial conduction along the tube walls can be ignored. In the upstream region ($z < 0$), the environment is at a temperature $T_{1\infty}$, with a heat transfer coefficient h_1. In the downstream region ($z > 0$), the environment is at a temperature $T_{2\infty}$, with a heat transfer coefficient h_2. Figure 1 illustrates the geometry and coordinates. We assume a slug flow model for the velocity field. For liquids having very low Prandtl number, the temperature profile develops much faster than the velocity profile, hence the slug flow model is meaningful for the thermal entrance region problems. The mathematical formulation of this heat transfer problem, for the upstream ($\eta < 0$) and downstream ($\eta > 0$) regions, is now given in the dimensionless form as

$$\frac{1}{2}\frac{\partial \theta_i(\xi,\eta)}{\partial \eta} = \frac{1}{\xi}\frac{\partial}{\partial \xi}\left(\xi \frac{\partial \theta_i}{\partial \xi}\right) + \frac{1}{\mathrm{Pe}^2}\frac{\partial^2 \theta_i}{\partial \eta^2}, \quad \text{in } 0 < \xi < 1 \tag{1a}$$

$$\frac{\partial \theta_i(0,\eta)}{\partial \xi} = 0 \tag{1b}$$

$$\frac{\partial \theta_i(1,\eta)}{\partial \xi} + H_i\,\theta_i(1,\eta) = 0 \tag{1c}$$

$$\theta_1(\xi,-\infty) = 0,\ \theta_2(\xi,\infty) = 0 \tag{1d,e}$$

where $i = 1,2$, and throughout the analysis the subscript $i = 1$ will refer to the upstream region ($\eta < 0$) and $i = 2$ to the downstream region ($\eta > 0$).

The energy equations (1a) are coupled at $\eta = 0$ with the requirement that the temperatures and heat fluxes are continuous. These coupling conditions are given by

$$1 - \theta_1(\xi,0) = \theta_2(\xi,0) \tag{2a}$$

$$\frac{\partial \theta_1(\xi,0)}{\partial \eta} = -\frac{\partial \theta_2(\xi,0)}{\partial \eta} \tag{2b}$$

In the foregoing formulation, various dimensionless quantities are defined as

$$\theta_1(\xi,\eta) = \frac{T_{1\infty} - T_1(r,z)}{T_{1\infty} - T_{2\infty}},\ \theta_2(\xi,\eta) = \frac{T_2(r,z) - T_{2\infty}}{T_{1\infty} - T_{2\infty}},\ Pe = \frac{2\,r_0\,U}{\alpha},$$

$$H_1 = \frac{h_1 r_0}{k},\ H_2 = \frac{h_2 r_0}{k},\ \xi = \frac{r}{r_0},\ \eta = \frac{z/r_0}{\mathrm{Pe}} \tag{3}$$

The method of separation of variables is now applied to solve the coupled heat transfer problem defined by equations (1) and (2). Let $R_{im}(\xi)$ and $Z_{im}(\eta)$ be the separated functions in the radial variable ξ and the axial variable η, respectively. The solution for the temperatures $\theta_i(\xi,\eta)$ are constructed in the form

$$\theta_i(\xi,\eta) = \sum_{m=1}^{\infty} C_{im}\,R_{im}(\xi)\,Z_{im}(\eta),\ \begin{cases} i = 1 \text{ for } \eta < 0 \\ i = 2 \text{ for } \eta > 0 \end{cases} \tag{4}$$

Here the functions $R_{im}(\xi)$, (m = 1,2,. . .), satisfy the following eigenvalue problem

$$\frac{1}{\xi}\frac{d}{d\xi}\left(\xi \frac{dR_{im}}{d\xi}\right) + \beta_{im}{}^2 R_{im}(\xi) = 0, \text{ in } 0 < \xi < 1 \tag{5a}$$

$$\frac{dR_{im}(0)}{d\xi} = 0 \tag{5b}$$

$$\frac{dR_{im}(1)}{d\xi} + H_i\,R_{im}(1) = 0 \tag{5c}$$

where $i = 1,2$. The orthogonality condition for the eigenfunctions $R_{im}(\xi)$ is given by

$$\int_0^1 \xi\,R_{im}(\xi)\,R_{in}(\xi)\,d\xi = \begin{cases} 0 & \text{for } m \neq n \\ N(\beta_{im}) & \text{for } m = n \end{cases} \tag{6a}$$

where the normalization integral $N(\beta_{im})$ is defined by

---

Contributed by the Heat Transfer Division for publication in the JOURNAL OF HEAT TRANSFER. Manuscript received by the Heat Transfer Division January 16, 1981.

$$N(\beta_{im}) = \int_0^1 \xi\,[R_{im}(\xi)]^2\,d\xi \tag{6b}$$

The sets of functions, $R_{1m}(\xi)$ and $R_{2m}(\xi)$, are further related by the following relation (see appendix for proof)

$$\int_0^1 \xi\,R_{1n}(\xi)\,R_{2m}(\xi)\,d\xi = \left[\frac{H_1 - H_2}{\beta_{1n}{}^2 - \beta_{2m}{}^2}\right] R_{1n}(1)\,R_{2m}(1) \tag{7a}$$

which is valid for all m and n if $H_1 \neq H_2$. For the special case of $H_1 = H_2$, the eigenvalue problems given by equations (5), for $i = 1$ and 2, become identical. Then we have

$$\int_0^1 \xi\,R_{1n}(\xi)\,R_{2m}(\xi)\,d\xi = \begin{cases} 0 & \text{for } m \neq n \\ N(\beta_{1m}) = N(\beta_{2m}) \equiv N(\beta_m) & \text{for } m = n \end{cases} \tag{7b}$$

which is valid for $H_1 = H_2 \equiv H$.

The eigenvalue problem given by equations (5) is Bessel's equation of order zero and its solution satisfying the boundary condition (5*b*) is taken as

$$R_{im}(\xi) = J_0(\beta_{im}\xi) \tag{8a}$$

If this solution should satisfy the boundary condition (5*c*), the eigenvalues β_{im}, $(m = 1,2,3,\ldots)$, should be the solutions of the following transcendental equation

$$-\beta_{im}\,J_1(\beta_{im}) + H_i\,J_0(\beta_{im}) = 0 \tag{8b}$$

The normalization integral, $N(\beta_{im})$, is readily determined as

$$N(\beta_{im}) = \frac{1}{2}\,[J_0{}^2(\beta_{im}) + J_1{}^2(\beta_{im})] \tag{8c}$$

For the special case of $H_1 = 0$, $\beta_{10} = 0$ is also an allowable eigenvalue, corresponding to the eigenfunction $R_{10}(\xi) = 1$ with the resulting normalization integral $N(\beta_{10}) = \frac{1}{2}$. However, the possibility $H_2 = 0$ need not be considered as it leads to a trivial solution regardless of the value of H_1.

We now turn our attention to the separated functions $Z_{im}(\eta)$, $(m = 1,2,\ldots)$, in the axial variable η. It can be shown that the functions $Z_{im}(\eta)$ satisfy the differential equation

$$-\frac{1}{\mathrm{Pe}^2}\frac{d^2 Z_{im}}{d\eta^2} + \frac{1}{2}\frac{dZ_{im}}{d\eta} + \beta_{im}{}^2\,Z_{im}(\eta) = 0 \begin{cases} i = 1 \text{ for } \eta < 0 \\ i = 2 \text{ for } \eta > 0 \end{cases} \tag{9a}$$

subject to the conditions

$$Z_{1m}(-\infty) = 0,\; Z_{2m}(\infty) = 0 \tag{9b,c}$$

The solution of equations (9*a*) satisfying the conditions (9*b*,*c*) can be expressed as

$$Z_{im}(\eta) = e^{\gamma_{im}\eta},\; i = 1,2 \tag{10a}$$

where the exponents γ_{im} are given by

$$\gamma_{im} = \frac{1}{4}\,\mathrm{Pe}^2\left[1 - (-1)^i\sqrt{1 + \frac{16}{\mathrm{Pe}^2}\,\beta_{im}{}^2}\right] \tag{10b}$$

Having established the functional forms of the separated variables $R_{im}(\xi)$ and $Z_{im}(\eta)$, as given by equations (8*a*) and (10*a*), respectively, the dimensionless temperature functions $\theta_i(\xi,\eta)$, given by equation (4), take the form

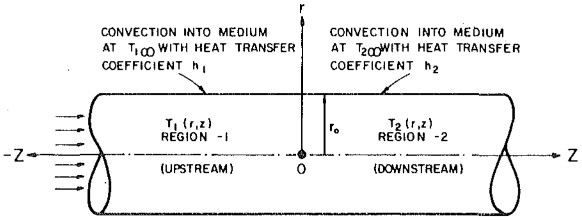

Fig. 1 Geometry and coordinates

$$\theta_i(\xi,\eta) = \sum_{m=1}^{\infty} C_{im}\,e^{\gamma_{im}\eta}\,J_0(\beta_{im}\xi), \begin{bmatrix} i = 1 \text{ for } \eta < 0 \\ i = 2 \text{ for } \eta > 0 \end{bmatrix} \tag{11}$$

If these solutions should satisfy the coupling conditions at $\eta = 0$, equations (2*a*,*b*) lead to

$$\sum_{i=1}^{2}\sum_{m=1}^{\infty} C_{im}\,J_0(\beta_{im}\xi) = 1 \tag{12a}$$

$$\sum_{i=1}^{2}\sum_{m=1}^{\infty} C_{im}\,\gamma_{im}\,J_0(\beta_{im}\xi) = 0 \tag{12b}$$

The expansion coefficients, C_{im}, can be determined from equations (12), by utilizing the orthogonality property of the eigenfunctions, as now described. We consider the analysis for the cases $H_1 = H_2 = H$ and $H_1 \neq H_2$ separately.

The Case $H_1 = H_2 = H$. For this special case, the eigenvalue problems, given by equations (5), are identical for $i = 1$ and 2, hence we have

$$\beta_{1m} = \beta_{2m} \equiv \beta_m \tag{13}$$

We now operate on both sides of equations (12*a*) and (12*b*) with the operator

$$\int_0^1 \xi\,J_0(\beta_n\xi)\,d\xi,$$

and utilize the orthogonality relations (6*a*, 7*b*) to obtain, respectively,

$$\sum_{i=1}^{2} C_{in}\,N(\beta_n) = \frac{H\,J_0(\beta_n)}{\beta_n{}^2} \tag{14a}$$

$$\sum_{i=1}^{2} C_{in}\,\gamma_{in} = 0 \tag{14b}$$

Here we made use of the transcendental equation (8*b*) to obtain the result given by equation (14*a*).

A simultaneous solution of equations (14) yields the expansion coefficients as

$$C_{in} = (-1)^i\left[\frac{\gamma_{3-i,n}}{\gamma_{1n} - \gamma_{2n}}\right]\left[\frac{H\,J_0(\beta_n)}{\beta_n{}^2\,N(\beta_n)}\right],\; (i = 1,2) \tag{15}$$

which is valid for $H_1 = H_2 = H$. The normalization integral, $N(\beta_n)$, is given by equation (8*c*).

Nomenclature

C_{im} = expansion coefficients
H_i = Biot numbers
h_i = heat transfer coefficients
k = thermal conductivity
$N(\beta_{im})$ = normalization integrals
$\mathrm{Nu}(\eta)$ = local Nusselt number
$\mathrm{Pe} = \frac{2r_0U}{\alpha}$ = Péclét number
$R_{im}(\xi)$ = separated radial functions
r = radial variable
r_0 = tube radius
$T_i(r,z)$ = temperature functions
$T_{i,b}(\eta)$ = bulk temperatures
$T_{i\infty}$ = environment temperatures
U = fluid velocity
$Z_{im}(\eta)$ = separated axial functions
z = axial variable
α = thermal diffusivity
β_{im} = eigenvalues
γ_{im} = exponents given by equation (10*b*)
$\theta_b(\eta)$ = dimensionless bulk temperature defined by equation (25)
$\theta_{i,b}(\eta)$ = dimensionless bulk temperatures
$\theta_i(\eta)$ = dimensionless temperatures
$\theta_w(\eta)$ = dimensionless wall temperature defined by equation (24)
$\eta = \frac{z/r_0}{\mathrm{Pe}}$ = dimensionless axial variable
$\xi = \frac{r}{r_0}$ = dimensionless radial variable

The case $H = 0$ need not be considered, since it leads to a trivial solution as discussed previously.

The Case $H_1 \neq H_2$. For this more general situation, we operate on equations (12*a*) and (12*b*) with the operator.

$$\int_0^1 \xi J_0(\beta_{1n}\xi)\, d\xi$$

and utilize the relations (6*a*, 7*a*) and (8*b*) to obtain, respectively,

$$C_{1n} N(\beta_{1n}) + \sum_{m=1}^{\infty} C_{2m} \left[\frac{H_1 - H_2}{\beta_{1n}^2 - \beta_{2m}^2}\right] J_0(\beta_{1n})\, J_0(\beta_{2m}) = \frac{H_1 J_0(\beta_{1n})}{\beta_{1n}^2} \qquad (16a)$$

$$C_{1n} N(\beta_{1n})\, \gamma_{1n} + \sum_{m=1}^{\infty} C_{2m}\, \gamma_{2m} \left[\frac{H_1 - H_2}{\beta_{1n}^2 - \beta_{2m}^2}\right] J_0(\beta_{1n})\, J_0(\beta_{2m}) = 0 \qquad (16b)$$

Similarly, we operate on equations (12*a*) and (12*b*) with the operator

$$\int_0^1 \xi J_0(\beta_{2n}\xi)\, d\xi$$

and utilize the relations (6*a*, 7*a*) and (8*b*) to obtain, respectively,

$$\sum_{m=1}^{\infty} C_{1m} \left[\frac{H_1 - H_2}{\beta_{1m}^2 - \beta_{2n}^2}\right] J_0(\beta_{1m})\, J_0(\beta_{2n}) + C_{2n} N(\beta_{2n}) = \frac{H_2 J_0(\beta_{2n})}{\beta_{2n}^2} \qquad (17a)$$

$$\sum_{m=1}^{\infty} C_{1m}\, \gamma_{1m} \left[\frac{H_1 - H_2}{\beta_{1m}^2 - \beta_{2n}^2}\right] J_0(\beta_{1m})\, J_0(\beta_{2n}) + C_{2n} N(\beta_{2n})\, \gamma_{2n} = 0 \qquad (17b)$$

We eliminate $C_{2n} N(\beta_{2n})$ between equations (17*a*,*b*) and rearrange the result in the form

$$\sum_{m=1}^{\infty} C_{1m} \left(1 - \frac{\gamma_{1m}}{\gamma_{2n}}\right) \left(\frac{\beta_{2n}^2}{\beta_{1m}^2 - \beta_{2n}^2}\right) J_0(\beta_{1m}) = \frac{H_2}{H_1 - H_2} \qquad (18a)$$

Similarly, the elimination of $C_{1n} N(\beta_{1n})$ between equations (16*a*,*b*) yields

$$\sum_{m=1}^{\infty} C_{2m} \left(1 - \frac{\gamma_{2m}}{\gamma_{1n}}\right) \left(\frac{\beta_{1n}^2}{\beta_{1n}^2 - \beta_{2m}^2}\right) J_0(\beta_{2m}) = \frac{H_1}{H_1 - H_2} \qquad (18b)$$

Equations (18*a*) and (18*b*), for $n = 1,2,3,\ldots$, provide an infinite set of simultaneous equations for the determination of the expansion coefficients C_{1m} and C_{2m}, for $m = 1,2,3,\ldots$. These equations can be written in matrix form as

$$\mathbf{A}_i\, \mathbf{C}_i = \mathbf{B}_i, \quad i = 1,2 \qquad (19)$$

where $\mathbf{A}_i$ is a square matrix whose elements are given by

$$A_{i,mn} = \left[\left(1 - \frac{\gamma_{im}}{\gamma_{3-i,n}}\right) \left(\frac{\beta_{3-i,n}^2}{\beta_{1m}^2 - \beta_{2n}^2}\right) J_0(\beta_{im})\right] \qquad (20a)$$

with subscript m designating the column and n designating the row.

$\mathbf{B}_i$ and $\mathbf{C}_i$ are the column vectors whose elements are given by

$$B_{i,n} = \frac{H_{3-i}}{H_1 - H_2} \qquad (20b)$$

$$C_{i,n} = C_{in} \qquad (20c)$$

where $i = 1$ or 2.

Once the expansion coefficients C_{1n} and C_{2n} are determined from the solution of the system of algebraic equations (19), the temperatures $\theta_i(\xi,\eta)$, $(i = 1,2)$, for the upstream and downstream regions, are computed according to equation (11).

A Special Case. When $H_1 = 0$, corresponding to an insulated upstream region, $\beta_{10} = 0$ is also an eigenvalue. Then equation (18*b*), for $n = 0$, becomes indeterminate and must be evaluated by L'Hospital's rule for $H_1 \to 0$, $\beta_{10} \to 0$. To evaluate this limit, equation (18*b*), for $n = 0$, is rearranged so that the term H_1/β_{10}^2 appears on the right-hand side and H_1 is replaced by $\beta_{10} J_1(\beta_{10})/J_0(\beta_{10})$ according to the transcendental equation (8*b*). The application of L'Hospital's rule reduces equation (18*b*), for $H_1 \to 0$ and $\beta_{10} \to 0$, to

$$\sum_{m=1}^{\infty} C_{2m} \left(1 - \frac{\gamma_{2m}}{\gamma_{10}}\right) \frac{1}{\beta_{2m}^2} J_0(\beta_{2m}) = \frac{1}{2H_2} \qquad (21)$$

The Nusselt Number. Once the temperature distributions $\theta_i(\xi,\eta)$, $(i = 1,2)$, in the fluid are known, the local Nusselt number, $\mathrm{Nu}(\eta)$, for the upstream or downstream region, is determined from its definition, given by

$$\mathrm{Nu}(\eta) = -\frac{2\dfrac{\partial\theta_i(1,\eta)}{\partial\xi}}{\theta_{i,b}(\eta) - \theta_i(1,\eta)} = \frac{2H_i\, \theta_i(1,\eta)}{\theta_{i,b}(\eta) - \theta_i(1,\eta)} \qquad (22a)$$

where the subscript $i = 1$ for $\eta < 0$ and $i = 2$ for $\eta > 0$; and equation (1*c*) is utilized to obtain the alternative form of the numerator. The dimensionless bulk or mean temperature, $\theta_{i,b}(\eta)$, is defined as

$$\theta_{i,b}(\eta) = 2\int_0^1 \xi\, \theta_i(\xi,\eta)\, d\xi = 2H_i \sum_{m=1}^{\infty} C_{im}\, e^{\gamma_{im}\eta} \frac{J_0(\beta_{im})}{\beta_{im}^2} \qquad (22b)$$

and the dimensionless wall temperature, $\theta_i(1,\eta)$ is given by

$$\theta_i(1,\eta) = \sum_{m=1}^{\infty} C_{im}\, e^{\gamma_{im}\eta} J_0(\beta_{im}) \qquad (22c)$$

For the special case of $H_1 = 0$, we have $\beta_{10} = 0$ as an eigenvalue. Then, equation (22*b*), for the limiting case of $H_1 \to 0$, $\beta_{10} \to 0$, is evaluated by replacing $H_1 J_0(\beta_{10})$ by $\beta_{10} J_1(\beta_{10})$ according to the transcendental equation (8*b*), and applying L'Hospital's rule. We find

$$\theta_{1,b}(\eta) = C_{10}\, e^{\gamma_{10}\eta} = C_{10}\, e^{\mathrm{Pe}^2\eta/2} \qquad (23)$$

where we utilized equation (10*b*) to relate γ_{10} to $\mathrm{Pe}^2/2$.

Results and Discussion

Before presenting numerical results for the temperature distribution and the local Nusselt number, we discuss briefly the physical significance of the present mathematical modelling in relation to heat exchanger applications. Consider a heat exchanger tube having an unheated (or uncooled) hydrodynamic entrance region confined to the domain $\eta < 0$, followed by an applied heat transfer region confined to $\eta > 0$. Considerable amount of heat transfer takes place between these two regions by axial conduction in the fluid through the cross-section at $\eta = 0$ if the Péclét number is low. Therefore, the temperature of the fluid at $\eta = 0$ is not known a priori. In the present modelling, it is assumed that the fluid enters the tube with a temperature $T_{1\infty}$ at an axial location sufficiently away from the origin of the axial coordinate, $\eta = 0$, where the applied heat transfer section begins. The boundary condition of the present analysis, for the upstream region, $\eta < 0$, implies that the temperature of the external ambient is the same as the fluid inlet temperature, $T_{1\infty}$, and that the external Biot number is H_1. At the beginning of the heat transfer section, $\eta = 0$, a step change occurs in the external ambient temperature from $T_{1\infty}$ to $T_{2\infty}$, while the external Biot number for the downstream region, $\eta > 0$, is taken as H_2. Clearly, several special cases are obtainable from such general boundary conditions. For example, $H_1 = 0$ represents an adiabatic upstream condition; $H_2 \to \infty$ corresponds to a prescribed uniform wall temperature for the downstream region; and $H_1 = H_2 \equiv H =$ finite represents equal Biot numbers for the upstream and downstream regions while $T_{1\infty} \neq T_{2\infty}$.

Numerical calculations are performed to determine the dimensionless bulk temperatures, $\theta_{i,b}(\eta)$, the wall temperatures, $\theta_i(1,\eta)$, and the local Nusselt number, $\mathrm{Nu}(\eta)$, for both the upstream ($\eta < 0$) and the downstream ($\eta > 0$) regions, for several different values of the Péclét number and the Biot numbers, H_1 and H_2. The temperatures $\theta_{i,b}(\eta)$ and $\theta_i(1,\eta)$, given by equations (22*b*) and (22*c*) converge faster for longer values of Péclét number and $|\eta|$; but the convergence becomes slower for larger values of H_1 and H_2. Except for extreme cases, 20 to 30 terms in the series give sufficiently accurate results.

For convenience in the discussion of the numerical results, we consider the external ambient for the upstream region ($\eta < 0$) hot and that for the downstream region ($\eta > 0$) cold; that is $T_{1\infty} > T_{2\infty}$.

In the presentation of the results for temperatures in graphical form, we defined a new dimensionless wall temperature, $\theta_w(\eta)$, as

$$\theta_w(\eta) = \begin{cases} 1 - \theta_1(1,\eta) & \text{for } \eta < 0 \\ \theta_2(1,\eta) & \text{for } \eta > 0 \end{cases} \tag{24}$$

and a new dimensionless bulk fluid temperature, $\theta_b(\eta)$, as

$$\theta_b(\eta) = \begin{cases} 1 - \theta_{1,b}(\eta) & \text{for } \eta < 0 \\ \theta_{2,b}(\eta) & \text{for } \eta > 0 \end{cases} \tag{25}$$

The notations $\theta_w(\eta)$ and $\theta_b(\eta)$ are used in all graphical presentations. The physical significance of the definitions given by equations (24) and (25) is envisioned better by recalling the definitions of $\theta_1(\xi,\eta)$ and $\theta_2(\xi,\eta)$ given by equation (3).

Figure 2 shows the dimensionless wall and bulk fluid temperatures plotted as a function of the dimensionless axial distance, η, for $H_1 = 0$, $H_2 = 20$, at Péclét numbers 1, 5 and 200 for the upstream region. Figure 3 is a similar plot for the downstream region. As expected, the effects of axial conduction are strongly pronounced at the thermal entry region where lowering the Péclét number lowers the temperatures. At high Péclét number, Pe = 200, the effects of axial conduction are unnoticeable.

Figures 4 and 5 are prepared to illustrate the effects of the variation of the Péclét number on the local Nusselt number for the downstream region. Figure 4 is for $H_1 = 0, H_2 = 1$, while Fig. 5 is for $H_1 = 0, H_2 = 20$. We note that in both of these figures, the curves for different Péclét numbers have crossover regions. These crossing regions are shifted toward $\eta = 0$ as the Biot number for the downstream region, H_2, is increased. These curves show that at the beginning of the heat transfer section, $\eta = 0$, decreasing the Péclét number decreases the local Nusselt number. The reason for such a trend is that as the Péclét number is reduced, the effects of axial conduction in the fluid become more pronounced, which in turn causes the development of the temperature profile to begin further into the upstream region. As a result, the fluid entering the heat transfer region becomes more thermally developed, thus reducing the Nusselt number for fluids with a smaller Péclét number. These figures also show a crossover of the curves, thus indicating an apparent reversal of the dependence of the Nusselt number on the Péclét number in the region between the crossover area and the thermally developed zone. This trend is not representative of the actual physical situation in the real z-coordinates, since the true axial distance z has been scaled off by the Péclét number. If the curves were not stretched in proportion to the Péclét number, such a crossover would not have occurred in the graphs. It is also to be noted that the crossover of the curves in these figures takes place over a finite region rather than at a specific point.

Figure 6 shows the effects of the variation of the downstream Biot number, H_2, on the local Nusselt number for the downstream region. Increasing the downstream Biot number increases the downstream Nusselt number at the thermal entry region, but this effect is reversed as the Nusselt number approaches its fully developed value.

Figures 7 and 8 show the effects of the variation of the upstream Biot number on the dimensionless wall and mean fluid temperatures for both the upstream and the downstream regions. We note that in Fig. 7, the wall temperature and the mean fluid temperature cross each other and, by the definition of the Nusselt number, this crossover point corresponds to an infinite Nusselt number. The region after the crossing point, where $\theta_b(\eta) > \theta_w(\eta)$ while the heat flow is still from

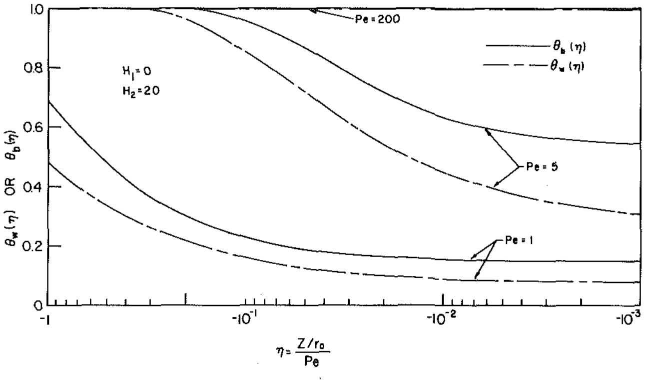

Fig. 2 Dimensionless wall and bulk temperature for the upstream region, $\eta < 0$ (effects of Péclét number)

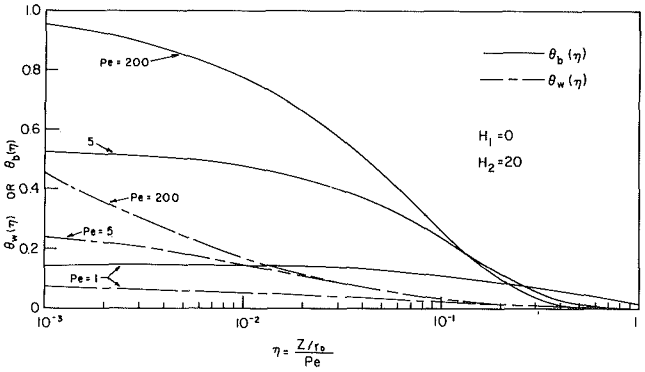

Fig. 3 Dimensionless wall and bulk temperatures for the downstream region, $\eta > 0$ (effects of Péclét number)

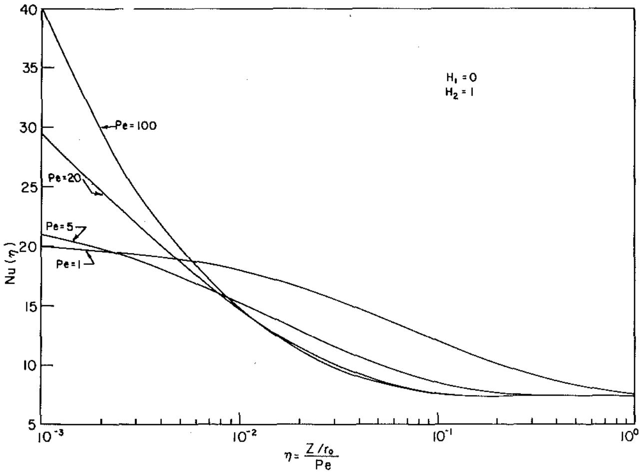

Fig. 4 Local Nusselt number for the downstream region, $\eta > 0$

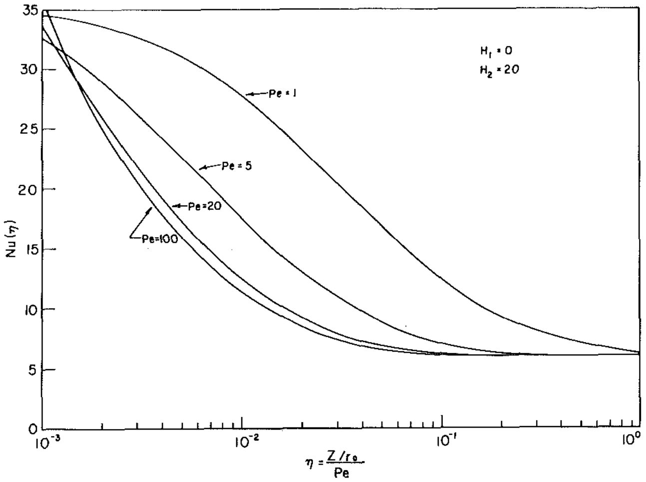

Fig. 5 Local Nusselt number for the downstream region, $\eta > 0$

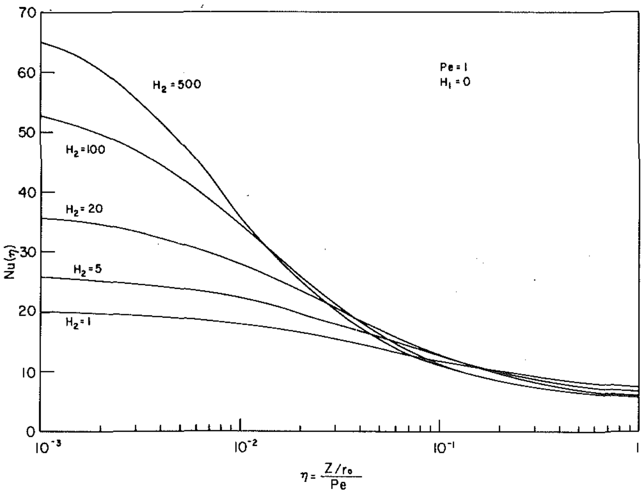

Fig. 6 Local Nusselt number for the downstream region, $\eta > 0$

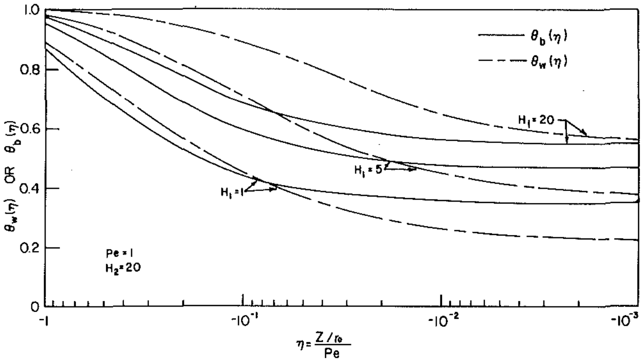

Fig. 7 Dimensionless wall and bulk temperatures for the upstream region. $\eta < 0$ (effects of H_1)

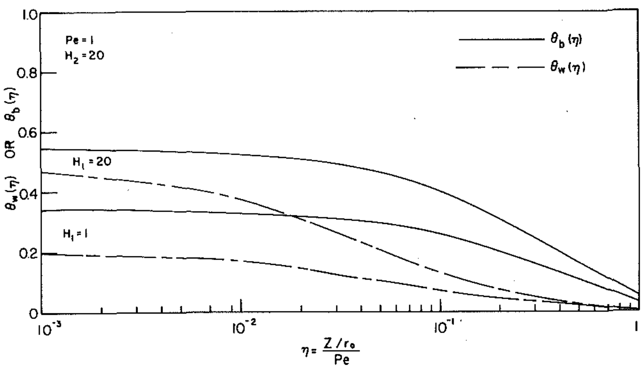

Fig. 8 Dimensionless wall and bulk temperature for the downstream region, $\eta > 0$ (effects of H_1)

the hot surrounding into the fluid, corresponds to a negative Nusselt number. The crossover point is shifted towards the origin, $\eta = 0$, as H_1 is increased. Clearly, the negative Nusselt number resulting from such a peculiar temperature distribution is caused by axial conduction in the fluid. The crossover point may occur in the upstream or downstream regions depending on the relative magnitudes of H_1 and H_2. When $H_1 = H_2 = \infty$, the crossover point should occur at $\eta = 0$.

Since experimental data on laminar heat transfer for liquid metals in the thermal entrance region are meager, no comparison of the present results has been made with the experiments. The analytical results presented here may help to assess the importance of axial heat conduction on heat transfer in a fluid at the thermal entrance region.

Acknowledgment

This work was supported in part by the National Science Foundation through the Grant ENG. 77-12949.

References

1 Singh, S. N., "Heat Transfer by Laminar Flow in a Cylindrical Tube," *Applied Scientific Research*, Section A, Vol. 7, 1957–1958, pp. 325–340.

2 Agrawal, H. C., "Heat Transfer in Laminar Flow Between Parallel Plates at Small Péclét Numbers," *Applied Scientific Research*, Section A, Vol. 9, 1960, pp. 177–189.

3 Hennecke, D. K., "Heat Transfer by Hagen-Poiseuille Flow in the Thermal Development Region with Axial Conduction," *Wärme-Stoffübetragung Bd.*, Vol. 1, 1968, pp. 177–184.

4 Verhoff, F. H., and Fisher, D. P., "A Numerical Solution of the Graetz Problem with Axial Conduction," ASME JOURNAL OF HEAT TRANSFER, Vol. 95, 1973, pp. 132–134.

5 Michelsen, M. L., and Villadsen, J., "The Graetz Problem with Axial Conduction," *International Journal Heat Mass Transfer*, Vol. 17, 1974, pp. 1391–1402.

6 Campo, A., and Auguste, J. C., "Axial Conduction in Laminar Pipe Flows with Nonlinear Wall Heat Fluxes," *International Journal Heat Mass Transfer*, Vol. 21, 1978, pp. 1597–1607.

7 Hsu, Chia-Jung, "Theoretical Solutions for Low-Péclét-Number Thermal-Entry-Region Heat Transfer in Laminar Flow Through Concentric Annuli," *International Journal Heat Mass Transfer*, Vol. 13, 1970, pp. 1907–1924.

8 Hsu, Chia-Jung, "An Exact Analysis of Low-Péclét-Number Thermal-Entry-Region Heat Transfer in Transversely Nonuniform Velocity Fields," *AIChE Journal*, Vol. 17, No. 3, May 1971, pp. 732–740.

9 Davies, E. J., "Exact Solutions for a Class of Heat and Mass Transfer," *Canadian Journal of Chemical Engineering*, Vol. 51, 1973, pp. 562–572.

10 Smith, C. E., Faghri, M., and Welty, J. R., "On the Determination of Temperature Distribution in Laminar Pipe Flow with a Step Change in Wall Heat Flux," ASME JOURNAL OF HEAT TRANSFER, Vol. 97, 1975, pp. 137–139.

11 Jones, A. S., "Extensions to the Solutions of the Graetz Problem," *International Journal of Heat Mass Transfer*, Volume 14, 1971, pp. 619–623.

12 Jones, A. S., "Laminar Forced Convection at Low Péclet Number," *Bulletin of the Australian Mathematical Society*, Vol. 6, 1972, pp. 83–105.

13 Jones, A. S., "Two-Dimensional Adiabatic Forced Convection at Low-Peclet Number," *Applied Scientific Research*, Vol. 25, 1972, pp. 337–348.

14 Deavours, C. A., "An Exact Solution for Temperature Distribution in Parallel Plate Poiseuille Flow," ASME JOURNAL OF HEAT TRANSFER, Vol. 96, 1974, pp. 489–495.

15 Bayazitoğlu, Y., and Özişik, M. N., "On the Solution of Graetz Type Problems and Axial Conduction," *International Journal of Heat Mass Transfer*, Vol. 23, 1980, pp. 1399–1402.

16 Vick, B., Özişik, M. N., and Bayazitoğlu, Y., "A Method of Analysis of Low Peclet Number Thermal Entry Region Problems with Axial Conduction," *Letters in Heat Mass Transfer*, Vol. 7, 1980, pp. 235–248.

17 Vick, B., and Özişik, M. N., "An Exact Analysis of Low Péclēt Number Heat Transfer in Laminar Flow with Axial Conduction," *Letters in Heat Mass Transfer*, Vol. 8, 1981, pp. 1–10.

APPENDIX

Proof of Equation (7*a*). We write equation (5*a*) for $R_{1n}(\xi)$ and $R_{2m}(\xi)$

$$\frac{1}{\xi}\frac{d}{d\xi}\left[\xi\frac{dR_{1n}}{d\xi}\right] + \beta_{1n}{}^2 R_{1n}(\xi) = 0 \qquad (1a)$$

$$\frac{1}{\xi}\frac{d}{d\xi}\left[\xi\frac{dR_{2m}}{d\xi}\right] + \beta_{2m}{}^2 R_{2m}(\xi) = 0 \qquad (1b)$$

We operate on equation (1*a*) with the operator $\int_0^1 \xi R_{2m}(\xi)\,d\xi$ and equation (1*b*) with the operator $\int_0^1 \xi R_{1n}(\xi)\,d\xi$, subtract the results and integrate by parts to obtain

$$(\beta_{1n}{}^2 - \beta_{2m}{}^2)\int_0^1 \xi R_{1n} R_{2m}\,d\xi = -\int_0^1 R_{2m}\frac{d}{d\xi}\left(\xi\frac{dR_{1n}}{d\xi}\right)d\xi + \int_0^1 R_{1n}\frac{d}{d\xi}\left(\xi\frac{dR_{2m}}{d\xi}\right)d\xi = \left[R_{1n}\frac{dR_{2m}}{d\xi} - R_{2m}\frac{dR_{1n}}{d\xi}\right]_{\xi=1} \qquad (2)$$

If $H_1 \neq H_2$, the right-hand side of equation (2) is evaluated by utilizing the boundary condition (5*c*). Then equation (2) becomes

$$\int_0^1 \xi R_{1n}(\xi) R_{2m}(\xi)\,d\xi = \left[\frac{H_1 - H_2}{\beta_{1n}{}^2 - \beta_{2m}{}^2}\right] R_{1n}(1) R_{2m}(1) \qquad (3)$$

which is the result given by equation (7*a*).

Heat Transfer from a Plate Elevated above a Host Surface and Washed by a Separated Flow Induced by the Elevation Step

E. M. Sparrow
Fellow ASME

F. Samie
S. C. Lau
Department of Mechanical Engineering,
University of Minnesota,
Minneapolis, Minn. 55455

Wind tunnel experiments were performed to determine heat transfer coefficients and fluid flow patterns for a thermally active surface elevated above a parallel host surface. The step-like blockage associated with the elevation causes flow separation and recirculation on the forward portion of the thermally active surface. Four parameters were varied during the course of the experiments, including the angle of attack of the oncoming airflow relative to the surface, the step height, the extent of the host surface which frames the active surface (i.e., the skirt width), and the Reynolds number. Flow visualization studies, performed with the oil-lampblack technique, showed that the streamwise extent of the separation zone increases with decreasing angle of attack, with larger step heights and skirt widths, and at higher Reynolds numbers. At larger angles of attack, separation does not occur. The experimentally determined heat transfer coefficients were found to increase markedly due to the flow separation, and separation-related enhancements as large as a factor of two were encountered. The enhancement was accentuated at small angles of attack, at large step heights and skirt widths, and at high Reynolds numbers. A main finding of the study is that the separation-affected heat transfer coefficients are generally greater than those for no separation, so that the use of the latter may underestimate the heat transfer rates. For an application such as a retrofit solar collector, such an underestimation of the wind-related heat loss would yield an optimistic prediction of the collector efficiency.

Introduction

This paper is concerned with the heat transfer characteristics and related patterns of fluid flow for a plate that is inclined to an airstream, with part of the plate surface being washed by a separated, recirculating flow. The physical situation under consideration is depicted schematically in the upper diagram of Fig. 1. As shown there, a heat transfer surface is elevated above a host surface such that the two surfaces are parallel to each other and are inclined to an airflow. The mounting arrangement of the elevated surface presents a step-like blockage to the oncoming flow. The flow attempts to climb the step but, because of its inability to turn sharp corners, separated regions, containing recirculating fluid, occur. One such separated region is situated on the forward portion of the heat transfer surface, while a second zone of separation occurs at the intersection of the step and the host surface. In general, literature information on separated, recirculating flows indicates that the corresponding heat transfer coefficients are decisively different from those for flows which move in the mainstream direction.

While the study of the aforementioned physical situation can be regarded as basic research on a complex external flow, it also bears a clear relationship to the design of flat plate solar collectors, as will now be elaborated. Flat plate collectors are highly susceptible to heat losses, as witnessed by the fact that their efficiencies are on the order of 50 percent or lower. One of the significant heat loss paths is via forced convection from the upper cover plate of the collector to the wind which passes over the collector. Consequently, heat transfer coefficients for airflow over surfaces which are geometrically similar to collector surface configurations are needed for a proper appraisal of wind-related heat losses.

The situation is particularly complex in the case of a collector that is installed on the roof of an existing building (i.e., retrofit installation). In that case, there is little likelihood that the upper surface of the collector will be flush with the surface of the roof. Rather, the collector will be mounted atop the roof, so that its upper surface is elevated above the plane of the roof. With respect to the oncoming airflow, the thus-mounted collector presents a step-like blockage to the flow.

In light of the foregoing discussion, it is evident that the configuration to be studied here serves to model the retrofit installation of a solar collector. Thus, in addition to their basic research content, the present results should have application to solar collector design.

There is no information in the solar literature about wind-related heat transfer coefficients which takes account of the elevation of the collector above a host surface, nor are there related results in the basic heat transfer literature. Until the recent past, solar texts and compendiums (e.g., [1–3]) recommended the equation $h_w = a + bV^n$ for the wind-related heat transfer coefficient, where V is the wind velocity and a, b, and n are empirical constants. This equation, based on experiments for airflow parallel to a heated plate, is actually inappropriate for solar applications. It does not take account of either the orientation of the wind vector with respect to the collector plate or of the streamwise length of the collector plate. Recent experiments [4–6] have dealt with these issues and have yielded a dimensionless

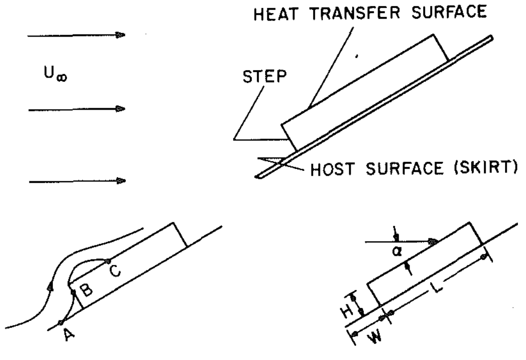

Fig. 1 Diagrams showing the physical situation, nomenclature, and perceptions of the separation zones

---

Contributed by the Heat Transfer Division for publication in the JOURNAL OF HEAT TRANSFER. Manuscript received by The Heat Transfer Division September 12, 1980.

correlation for h_w. However, neither the aforementioned inappropriate equation nor the new dimensionless correlation take account of the recirculating flow which washes the upper surface of an elevated collector.

Very recently [7], it was demonstrated that the use of an inappropriate wind-related heat transfer coefficient could have a marked effect on the predicted performance of a flat plate solar collector.

The present research encompassed two complementary portions, both of which dealt with the configuration pictured in Fig. 1. One of these was the determination of heat transfer coefficients for the elevated surface. The other was a flow visualization study which was focused on revealing the pattern of fluid flow adjacent to the elevated surface.

The heat transfer coefficients were determined indirectly from mass transfer measurements and by subsequent application of the well-established analogy between heat and mass transfer [8]. For the mass transfer measurements, the naphthalene sublimation technique was used. Relative to direct heat transfer measurements, the advantages of the naphthalene technique lie in the absence of extraneous losses via structure and supports, easier attainment of boundary condition uniformity, and generally higher accuracy. The heat transfer boundary condition analogous to that of the mass transfer experiments is uniform wall temperature. The flow visualization studies were performed by employing the oil-lampblack technique.

The experiments were carried out in a low-turbulence, subsonic wind tunnel, with a plate of square planform being used as the active mass transfer surface. Four parameters were varied during the course of the experiments. Three of these are geometrical parameters and are illustrated in the lower right of Fig. 1. They include: (1) the angle of attack α of the oncoming airflow relative to the plate surface, (2) the height H of the step, and (3) the width W of the portion of the host surface which frames the active mass transfer surface. Both H and W will be reported in terms of dimensionless ratios, H/L and W/L respectively, where L is the streamwise length of the elevated mass transfer surface (L was held fixed for the experiments). The fourth parameter is the Reynolds number Re. The experiments were conducted so that for fixed values of H/L, W/L, and Re, the angle of attack α was varied systematically and served as the independent variable against which the heat (mass) transfer results are plotted.

The format chosen for the presentation of the heat transfer results enables ready identification of the range of operating conditions where flow separation plays a significant role; the deviations of the separation-affected coefficients from those for separation-free flow are also clearly portrayed. The visualization studies revealed the boundary of the separated region on the active surface as well as the streamline patterns of the flow adjacent to the surface.

The Experiments

Experimental Apparatus. The mass transfer model used in the experiments is shown in pictorial view in Fig. 2. In essence, the model consists of a naphthalene-filled cavity situated atop a flat plate. The metallic portion of the model (i.e., all parts of the model aside from the naphthalene) is a one-piece unit which was machined from a single block of aluminum. As seen in the figure, the walls of the cavity frame the exposed surface of the naphthalene. The 0.117-cm (0.046-in.) thickness of the frame was the minimum that could be machined consistent with the attainment of straight walls, uniform thickness, and a smooth exposed edge. Also shown in the diagram is the 45-degree beveled leading edge of the model (i.e., the edge which thrusts forward into the airflow); the purpose of the beveling was to avoid bluntness effects.

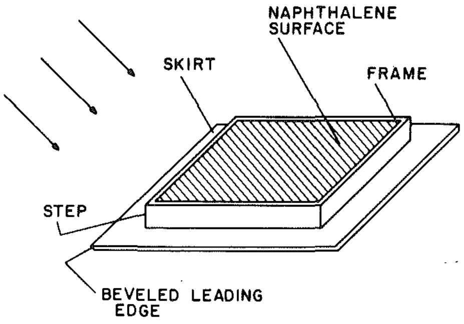

Fig. 2 Pictorial view of the mass transfer model

The dimensions of the model were chosen so as to avoid excessive blockage of the 61 × 30.5 cm (2 × 1 ft) cross section of the wind tunnel. Experience has indicated that when the blockage is small (~ three percent or less), the results of wind tunnel experiments can be applied without correction for flows in large unbounded domains. To fulfill this constraint, the base plate, the projected area of which is the blockage area, was initially fabricated as a 8.89 × 8.89 cm (3.5 × 3.5 in.) square. The elevated surface (i.e., the naphthalene surface plus the thickness of the framing walls of the cavity) was also a square, with dimensions 6.35 × 6.35 cm (2.5 × 2.5 in.) thereby leaving a 1.27 cm (0.500 in.) skirt all around. As initially fabricated, the step height was 1.27 cm (0.500 in.). The thickness of the base plate, selected to be the minimum consistent with strength and structural considerations, was 0.159 cm ($\frac{1}{16}$ in.).

As was noted in the Introduction, the step height and the skirt width were varied during the course of the investigation. With regard to the step height, it was reduced to 0.846 cm (0.333 in.) after the completion of the data runs for the initial height. Subsequently, when the runs for the second step had been completed, the height was reduced once again, this time to 0.423 cm (0.167 in.). These height reductions were accomplished by machining the edges of the cavity wall with a milling machine.

With regard to the skirt width, the visualization studies revealed that only the portion of the skirt which thrusts forward into the oncoming stream has a significant effect on the flow pattern on the mass transfer surface. Therefore, changes in width were made only for that part of the skirt. On completion of the planned data runs with the original skirt, it was removed (by milling) and replaced by a 2.54 cm (1.000 in.) skirt which was held in place by rivets which were anchored within the naphthalene cavity. A final set of runs was made with the forward skirt removed altogether.

The geometric characteristics of all the variants of the mass transfer model are listed in Table 1 in terms of the quantities H, W, and L that are defined in the lower diagram in Fig. 1. The range of the angle of attack α is also indicated in the table.

The model was mounted in the test section of the wind tunnel by means of a sting which was suspended from the upper wall of the tunnel. A swivel-type coupling situated at the forward end of the sting enabled the angle of incidence α to be set and maintained at any value between 0 and 90 deg, with the angle being read with a protractor. The

Nomenclature

c_p = specific heat
$\mathcal{D}$ = diffusion coefficient
H = step height, Fig. 1
h = average heat transfer coefficient
h^* = value of h for nonseparated flow
j = Colburn j-factor, equations (2) and (3)
j^* = j-factor value for nonseparated flow
K = average mass transfer coefficient, equation (1)
K^* = value of K for nonseparated flow
L = streamwise length of active surface
$\dot{m}$ = rate of mass transfer per unit area
Pr = Prandtl number
Re = Reynolds number, $U_\infty L/\nu$
Sc = Schmidt number
U_∞ = free stream velocity of oncoming flow
X_r = distance of reattachment line from leading edge of active surface
W = width of forward-thrusting skirt
α = angle of attack, Fig. 1
ν = kinematic viscosity
ρ = density
ρ_{nw} = naphthalene vapor density at active surface
$\rho_{n\infty}$ = naphthalene vapor density in free stream

Table 1 Geometric characteristics of the mass transfer models

H/L	W/L	α (deg)
1/5	1/5	15–60
1/7.5	1/5	15–60
1/15	1/5	15–60
1/15	1/2.5	15–60
1/15	0	15–60

coupling mated with a socket-like fixture that had been machined into the underside of the base surface of the model. The sting supported the model from the rear—the rear support being chosen to avoid disturbing the flow over the windward surfaces of the model.

Mass Transfer Surface. The naphthalene test surface was produced by a casting process utilizing a two-part metallic mold. One of the parts is the aluminum model itself, while the other is a thick, highly polished stainless steel plate. To initiate the casting process, the solid naphthalene contained in the model cavity from a prior data run is removed by melting and subsequent evaporation. Then, the model is placed face down on the stainless steel plate so that the rear surface of the base plate is up while the open end of the cavity is down (and blocked by the steel plate). A funnel is implanted in an aperture in the upfacing surface to facilitate the pouring of molten naphthalene into the cavity. Risers in the form of small diameter tubes are also implanted in holes in the upfacing surface to facilitate the escape of air displaced from the cavity by the molten naphthalene.

Once the naphthalene had solidified, the two parts of the mold were separated, exposing the naphthalene surface that had been cast against the highly polished stainless steel plate. The quality of the cast naphthalene surface was uniformly excellent—equal to that of the plate against which it was cast.

A new mass transfer surface was cast for each data run using fresh (previously unused) reagent-grade naphthalene. Once the casting had been made, the pouring aperture and the air-escape holes were carefully sealed with a pressure-sensitive tape, thereby ensuring that the test surface would be the only naphthalene surface exposed to the airflow in the wind tunnel.

A cover, made of plexiglass, was designed to fit over the entire elevated portion of the model (i.e., both the test surface and the step). When locked in place by two spring-loaded clamps which pressed the flange of the cover against the base plate, the cover served to provide an air-tight seal around the test surface. This seal served to prevent sublimation during the preparatory stage of the data run, as will be described shortly.

Instrumentation and Experimental Procedure. For the determination of the mass (heat) transfer coefficients and their correlation with the airflow, six quantities were measured for each data run. The amount of mass transferred during the course of the run was obtained from weighings of the model immediately before and immediately after the run. For the weighing, a vernier-equipped Mettler analytical balance was employed; the balance had a smallest scale division of 0.1 mg and a total weighing capacity of 200 g. The temperature of the airflow adjacent to the model was measured with an ASTM-certified 0.1°F thermometer positioned just downstream of the model. The accuracy of the thermometer was verified by comparisons with a secondary standard.

To determine the free stream velocity of the air approaching the model, a retractable impact tube was used in conjunction with a wall static tap. The impact and static pressures were conveyed via plastic tubing to the ports of a Baratron solid-state capacitance-type pressure meter capable of discriminating pressure differences to 10^{-4} mm Hg. The output of the pressure meter was read with a digital voltmeter. The impact tube–wall tap combination was checked against a Pitot tube with integral pressure taps, with a resulting agreement within one percent. For the static pressure in the test section of the wind tunnel, the Baratron was used to measure the tunnel static relative to ambient, and the ambient pressure was read from a precision barometer. The duration of the data run was read with a stop watch to within one second, while the angle of attack was set with the aid of a protractor.

As noted earlier, a new naphthalene test surface was cast for each data run. To prepare for a run, airflow was initiated in the wind tunnel, and the controls were set to yield the desired Reynolds number. The tunnel was operated in the open-circuit mode, with air being drawn from the building and exhausted to the outdoors. This mode of operation ensured that the air approaching the model would be free of naphthalene vapor and, since the fan is positioned downstream of the test section, there was no preheating of the air.

The tunnel was allowed to operate for about an hour to attain steady state. At that point of time, the model was weighed and the cover applied and clamped in place. The thus-capped model was then affixed on the sting in the wind tunnel and the angle of attack α was set. Previous experience had demonstrated that the capped model achieved a steady temperature equal to that of the flowing air within a half hour. During the equilibration period, the air velocity and temperature were carefully monitored for constancy. Then, after the passage of a half hour (or longer) the impact tube was retracted, and the data run proper was initiated by uncapping the model and starting the stop watch.

Temperatures were read and recorded at frequent intervals during the data run. The duration of the run was selected so that the amount of mass transfer could be measured accurately while limiting the average recession of the surface to 0.0025 cm (0.001 in.). Depending on the operating conditions, 100 to 200 mg were sublimed, and run times ranged from 20 to 75 min.

To conclude the run, the wind tunnel hatch was opened, and the model cap was applied and clamped. The mass of the model was immediately measured. Before the tunnel was turned off, a calibration procedure was executed to correct for any ambiguities in mass transfer during the model's installation in and removal from the wind tunnel. The airspeed was also measured prior to shutdown.

Flow Visualization. As noted earlier, the oil-lampblack technique was employed to enable visualization of the flow field adjacent to the elevated surface. Lampblack is a very fine black powder now primarily available as an ingredient of paint. It mixes readily with oil, and the mixture, when brushed on a surface, produces a smooth, glossy-black coating. The fluidity of the mixture can be regulated by the selection of the viscosity of the oil and by the proportions of the oil and the lampblack powder. These proportions also have a significant effect on the degree of definition of the flow pattern that can be achieved with the method. The degree of fluidity of the mixture is an especially relevant factor when the flow adjacent to an inclined surface is to be visualized, as is the case in the present investigation. In such a situation, the mixture will sag under the action of gravity, unless it is sufficiently stiff.

The general procedure for using the technique is to brush the oil-lampblack mixture on a surface and then to expose the surface to the airflow whose characteristics are to be studied. Ideally, under the action of the shear stresses exerted by the flow, the mixture will move along the surface, following the paths of the fluid particles that pass adjacent to the surface. These path lines will appear as streaks on the surface. In regions of low shear stress (e.g., at separation, reattachment, or stagnation), the mixture will remain stationary, so that such regions show themselves as black streak-free zones on the surface.

For all of the visualization runs, the elevated surface was coated with white, plasticized contact paper in order to obtain the highest possible contrast for the black streak lines and the black low-shear zones. In order to attain the clearest possible patterns, the bulk of the visualization work was performed at the highest Reynolds number investigated (~70,000), which also corresponded to the highest shear stress. Some observations made at lower Reynolds numbers will also be reported.

Results and Discussion

The presentation of results will begin with the information obtained from the flow visualization studies, with the heat (mass) transfer results to follow.

Flow Visualization Results. To provide guidance for the interpretation of the visualization results, attention will be directed to the diagram at the lower left of Fig. 1. This diagram shows a perception of the expected separation zones associated with the presence of the step. These separation zones are created because the flow is unable to turn the sharp corners at both the bottom and top of the step. Within each separation zone, there is a recirculating flow.

Of particular interest is the point C where the mainflow reattaches to the elevated surface. Downstream of C, the fluid adjacent to the surface moves in the streamwise direction, whereas upstream of C (within the separation bubble), the fluid adjacent to the surface moves upstream. Thus, C is a point of zero shear, and it should appear as a dark spot in the oil-lampblack visualization (actually as a line when the plate is viewed head-on rather than from the side). Similarly, points A and B, which respectively correspond to separation and reattachment, should also appear as black lines.

These expectations were actually realized during the visualization runs. All three lines were observed, but primary attention was focused on the reattachment at C since the heat (mass) transfer is directly affected by the extent of the separated zone which washes the forward part of the elevated surface.

Illustrative flow-visualization photographs showing head-on views of the elevated surface are presented in Fig. 3. These photographs correspond to the highest Reynolds number of the experiments (70,000), to the intermediate step height ($H/L = 1/7.5$), and to the intermediate skirt width ($W/L = 1/5$). In the upper row, the successive photographs (left to right) are for angles of attack α of 15, 20 and 30 deg, while the lower photographs are for α values of 40, 45, and 50 deg. These photographs show the traces of the streamlines adjacent to the surface as well as the reattachment line. In some of the photographs, extraneous black regions caused by sagging of the oil-lampblack mixture are visible.

By inspection of Fig. 3, it is seen that the reattachment line moves forward toward the leading edge and finally disappears as the angle of attack increases. This decrease in the size of the separated region with angle is altogether reasonable and reflects the decrease of the projected step height as seen by the oncoming flow. The reattachment line is more or less parallel to the leading edge, indicating a nearly two-dimensional flow pattern in the neighborhood of reattachment. Indeed, in the recirculation region, the streamlines are straight and parallel. Even downstream of reattachment, the flow is nearly two-dimensional except near the side edges of the surface. As the size of the separation zone shrinks with increasing angle, three-dimensionality becomes more evident.

As noted earlier, the bulk of the flow visualization runs were made at the highest Reynolds number (~70,000) because the relatively high shear stresses provided the most sharply etched flow pattern traces. For this Reynolds number and for all step heights and skirt widths investigated, the reattachment distance (i.e., distance between the leading edge of the elevated surface and the reattachment line) was measured. The reattachment distance, to be termed X_r, is a direct index of the size of the separated region. It was measured directly from the visualization patterns on the model surface (not from photographs).

Dimensionless reattachment distances X_r/L are plotted in Figs. 4 and 5 as a function of the angle of attack α. Figure 4 conveys results for parametric values of the step height H/L at a fixed skirt width $W/L = 1/5$, whereas Fig. 5 is for a fixed step height $H/L = 1/15$ with the skirt width serving as the parameter. Turning first to Fig. 4, it is seen that the trend of reattachment distance decreasing with angle, as evidenced earlier by the photographs of Fig. 3, is reaffirmed. At the smaller angles of attack, the reattachment distance is quite sensitive to the step height, increasing as the step height increases. On the other hand, for angles of 30 deg and larger, the reattachment distance is more or less independent of the height of the step. At angles of 50 deg

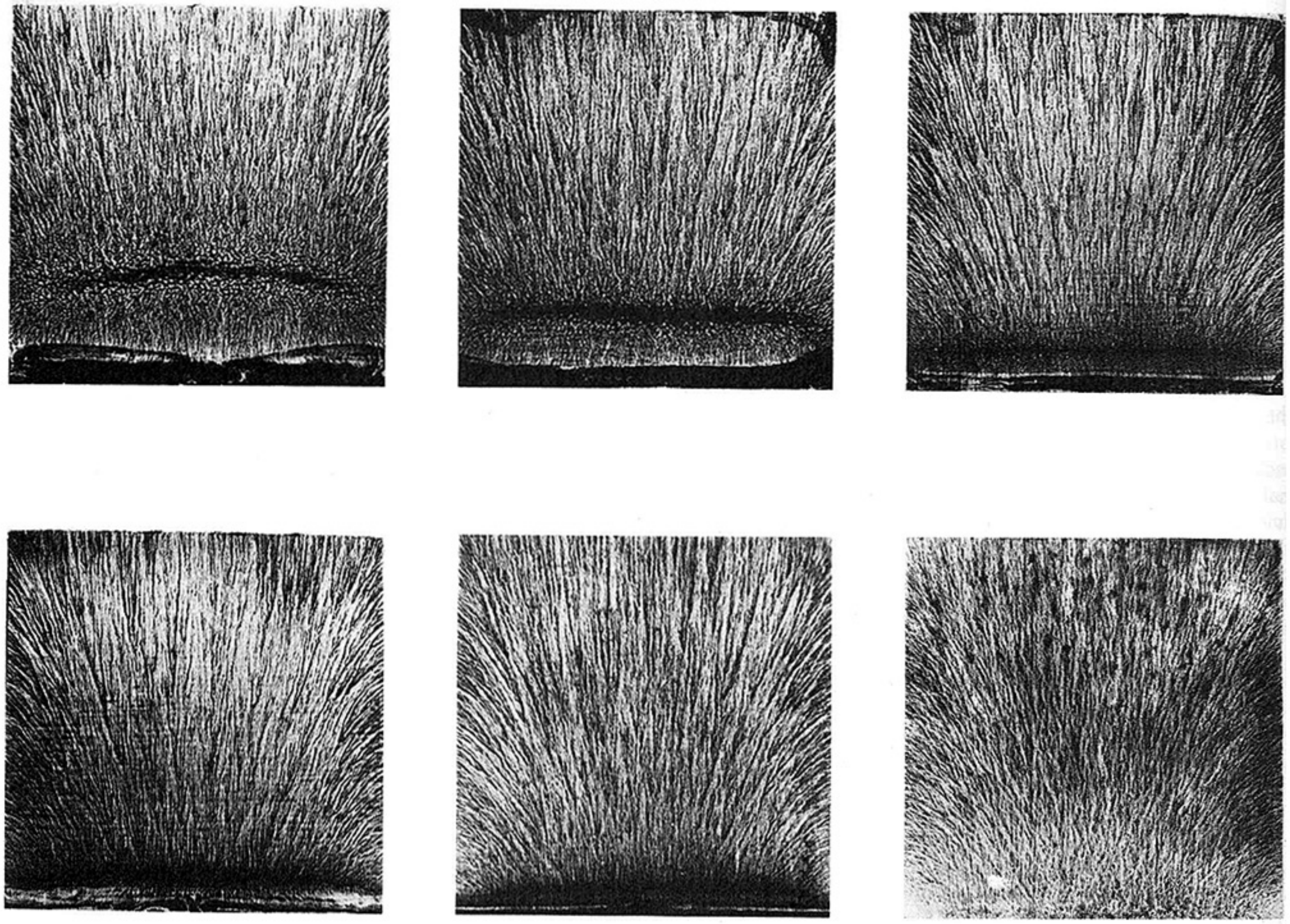

Fig. 3 Illustrative flow-visualization photographs; Re~ 70,000, $H/L = 1/7.5$, and $W/L = 1/5$. Upper row (left-to-right), $\alpha = 15$, 20, and 30°; lower row (left-to-right), $\alpha = 40$, 45, and 50°

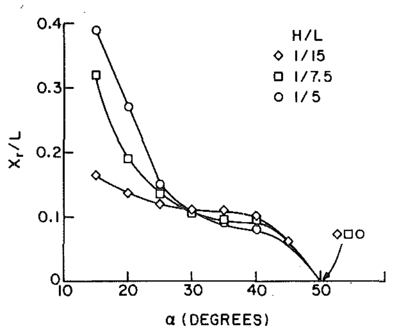

Fig. 4 Reattachment distances for various step heights at a skirt width $W/L = 1/5$ and Re ~ 70,000

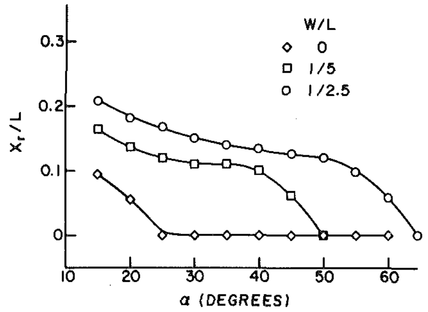

Fig. 5 Reattachment distances for various skirt widths at a step height $H/L = 1/15$ and Re ~ 70,000

or larger, separation could not be detected.

As a supplement to the data presented in Fig. 4, additional visualization runs were performed over a range of Reynolds numbers at various fixed angles of attack. In general, there was a tendency for the reattachment distance to increase with the Reynolds number, rather rapidly at first and then very slowly. The X_r/L values of Fig. 4 are more or less applicable for Reynolds numbers in the range 45,000 to 70,000.

The results of Fig. 5 show that the reattachment distance is quite sensitive to the width of the skirt that thrusts forward from the base of the step. In general, the greater the skirt width, the larger the reattachment distance. In addition, separation persists at larger angles of attack for wider skirts. For the no-skirt case, the reattachment distance is generally small, and separation does not occur at angles of 25 deg or greater.

Brief observations will be made about points A and B (lower left, Fig. 1), which are the anchor points of the separation zone at the foot of the step. Point A moves slowly forward toward the step as the angle of attack increases. At angles of 40 deg and larger, a stagnation line first appears on the skirt and, as the angle increases, the stagnation line and the separation line markedly interact. Point B, which is situated at mid-height at low angles, moves up the step as the angle increases and finally disappears. This disappearance coincides with the condition that no separation occurs on the elevated surface.

With regard to the relation of the visualization results to heat (mass) transfer, it may be expected that the larger the separation zone, the greater the transfer. This expectation is based on the belief that at the Reynolds numbers investigated, the separated region will contain a vigorously recirculating fluid. Consequently, high rates of transfer are expected at low angles of attack, high steps, wide skirts, and high Reynolds numbers.

Dimensionless Heat (Mass) Transfer Parameters. The interchangeability of heat and mass transfer results, which has been noted at various points throughout the paper, will now be formalized. First, a mass transfer coefficient K is defined as

$$K = \dot{m}/(\rho_{nw} - \rho_{n\infty}) \tag{1}$$

where $\dot{m}$ is the rate of mass transfer per unit surface area, and ρ_{nw} and $\rho_{n\infty}$ are the densities of naphthalene vapor at the mass transfer surface and in the free stream. A convenient dimensionless version of the mass transfer coefficient is given by the Colburn j-factor

$$j = (K/U_\infty)\mathrm{Sc}^{2/3} \tag{2}$$

in which U_∞ is the free stream velocity and Sc is the Schmidt number (analogous to the Prandtl number). There is also a j-factor for heat transfer given by

$$j = (h/\rho c_p U_\infty)\mathrm{Pr}^{2/3} \tag{3}$$

According to the Colburn Analogy, the j values for heat and mass transfer are equal at any given value of Reynolds number.

The exponent 2/3 of Pr and Sc in equations (2) and (3) bears some discussion in view of the fact that for certain operating conditions, a portion of the plate surface is covered by a zone of flow separation. Within the knowledge of the authors, the effect of Pr (or Sc) on heat (mass) transfer coefficients in separated flows has not yet been definitively correlated. There is evidence, however, that the 2/3 power may not be too far off the mark. In [9], the Nusselt number for a cylinder in crossflow (a situation where about half the surface is washed by a separated flow) was correlated with $\mathrm{Pr}^{0.37}$, which corresponds to $(h/\rho c_p U_\infty)\mathrm{Pr}^{0.63}$ = constant at a given value of Reynolds number. In the range of Pr or Sc between 0.7 and 2.5, which encompasses the Prandtl number for heat transfer in air and the Schmidt number for naphthalene diffusion in air, there is little difference between a $\mathrm{Pr}^{2/3}$ dependence or a $\mathrm{Pr}^{0.63}$ dependence. However, to minimize the issue of which exponent is appropriate, most of the results are presented in a ratio form which eliminates the presence of the thermophysical properties.

The j-factor for mass transfer was evaluated from equations (1) and (2) by using the experimental data. To determine $\dot{m}$, the change in mass during a data run was divided by the duration of the run and the mass transfer surface area. The determination of ρ_{nw} involves a two-step process. First, the naphthalene vapor pressure p_{nw} at the wall was evaluated from the Sogin relation [10] with the measured temperature as input. Then, with p_{nw} and with the temperature, ρ_{nw} was calculated from the perfect gas law. With regard to $\rho_{n\infty}$, the complete absence of naphthalene vapor in the free stream gives $\rho_{n\infty} = 0$.

The Schmidt number appearing in equation (2) was evaluated from its definition

$$\mathrm{Sc} = \nu/\mathcal{D} \tag{4}$$

Since the naphthalene vapor concentration is minute, the kinematic viscosity can be taken as that of pure air. The diffusion coefficient $\mathcal{D}$ was calculated from Skelland's formula [11]. For the operating conditions of the experiments, Sc $\sim$2.55.

The Reynolds number, which served to parameterize the results, was defined as

$$\mathrm{Re} = U_\infty L/\nu \tag{5}$$

in which L is the streamwise length of the test surface.

Heat (Mass) Transfer Results. To help identify a format which would be most effective in displaying the effects of flow separation, working graphs were prepared in which j was plotted as function of the angle of attack α for a fixed Reynolds number and for fixed geometry. It was observed from these graphs that j varied with α in the range of small and intermediate α, but that j was essentially a constant at larger α. This latter behavior confirms a prior finding [4, 6] that j is a very weak function of α in separation-free flow. It was further observed that in the range where j was nearly independent of α, it was also relatively insensitive to the specifics of the model geometry (i.e., step height, skirt width).

These characteristics suggested a presentation format that is exemplified by any one of Figs. 6 to 9. Consider, for example, Fig. 8. This figure corresponds to a fixed Reynolds number, Re = 50,000, and to a fixed skirt width, $W/L = 1/5$. In the figure, j/j^* is plotted as a function of the angle of attack α for parametric values of the step height $H/L = 1/5, 1/7.5$, and 1/15. The quantity j^* is equal to the average of the j values that fall in the α-independent portion of the data range. Aside from the secondary effect of geometry in the α-independent regime, j^* corresponds to the j value for separation-free flow at the Reynolds number in question.

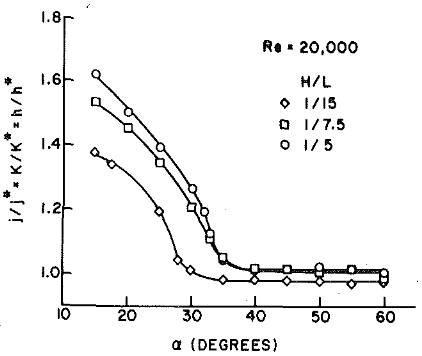

Fig. 6 Heat (mass) transfer coefficients for various step heights at a skirt width W/L = 1/5; Re = 20,000 and j^* = 0.00603

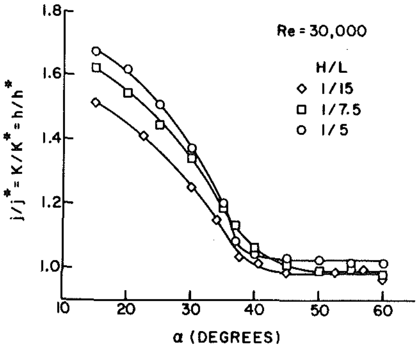

Fig. 7 Heat (mass) transfer coefficients for various step heights at a skirt width W/L = 1/5; Re = 30,000 and j^* = 0.00492

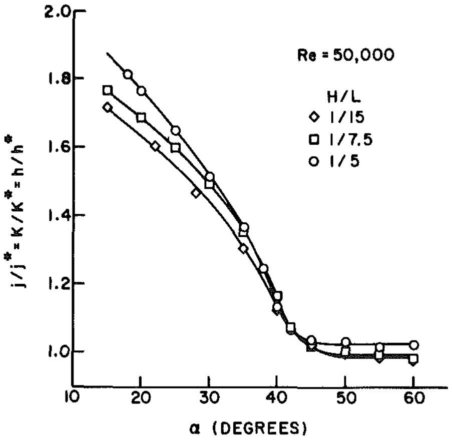

Fig. 8 Heat (mass) transfer coefficients for various step heights at a skirt width W/L = 1/5; Re = 50,000 and j^* = 0.00379

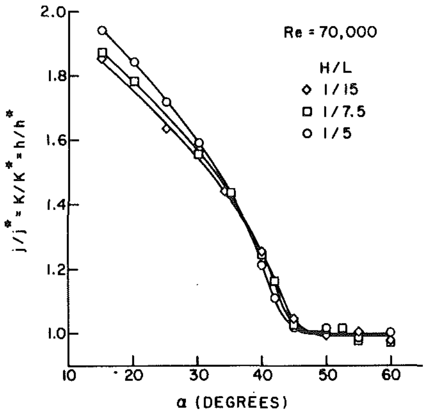

Fig. 9 Heat (mass) transfer coefficients for various step heights at a skirt width W/L = 1/5; Re = 70,000 and j^* = 0.00329

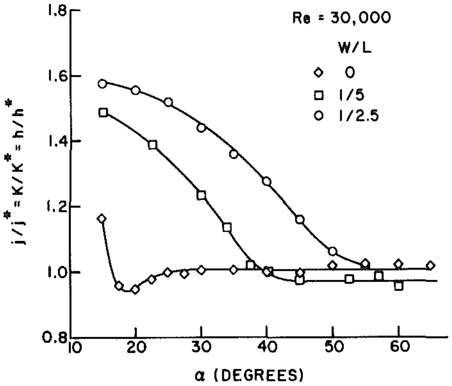

Fig. 10 Heat (mass) transfer coefficients for various skirt widths at a step height H/L = 1/15; Re = 30,000 and j^* = 0.00495

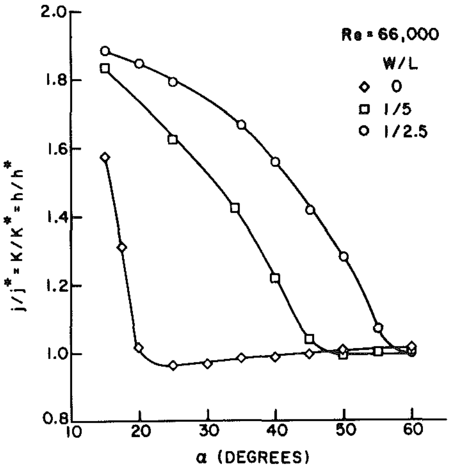

Fig. 11 Heat (mass) transfer coefficients for various skirt widths at a step height H/L = 1/15; Re = 66,000 and j^* = 0.00337

In light of the foregoing, it is evident that deviations of j/j^* from unity are indicative of the effect of flow separation on the heat transfer coefficient. Furthermore, since j and j^* correspond to the same Reynolds number and to the same thermophysical properties, it follows that $j/j^* = K/K^* = h/h^*$. The ordinates of the figures have been labeled to reflect these equalities.

Figures 6 to 9 convey results for j/j^* versus α for a fixed skirt width W/L = 1/5, with each successive figure corresponding to a fixed Reynolds number equal to 20,000, 30,000, 50,000, and 70,000. The data in each figure are parameterized by the step height H/L, and curves have been faired through the data to provide continuity.

The striking feature of these figures is the large values of j/j^* that are encountered as the angle of attack decreases. These increases in j/j^* can be directly attributed to the enlargement of the separated region that was displayed in Figs. 3 to 5. For the operating conditions of the experiments, separation-induced increases in heat transfer coefficient of almost a factor of two are in evidence.

As shown in the figures, the highest heat transfer coefficients are attained at the smallest of the investigated angles of attack, α = 15 deg. As α increases, the transfer coefficient decreases monotonically and levels off to the separation-free value, with the leveling-off taking place in the α range 35–45 deg, depending on the operating conditions.

With regard to step height, higher steps give rise to progressively greater enhancement of the heat transfer coefficient at those α values where there is significant enhancement. However, at lower enhancements, there is some crossing of the curves for the various step heights, but in that range the enhancements caused by the different step heights are not very different. These trends with step height tend to reflect the variation of the reattachment distance with step height as portrayed in Figs. 4 and 5.

From a careful examination of Figs. 6 to 9, a number of significant Reynolds-number-related effects can be identified. First of all, the general level of enhancement increases as the Reynolds number increases. This is due to the increased vigor of the recirculating flow in the separation zone. Second, there is a diminished sensitivity to variations of step height at higher Reynolds numbers. Finally, enhancement persists to higher angles of attack at larger Reynolds numbers. Thus, for example, at Re = 70,000, enhancement persists to α = 45 deg, while at Re = 20,000, enhancement has effectively ceased at 35 deg, for the higher steps and at 25–30 deg for the lowest step.

Attention may now be turned to the effect of skirt width on the heat transfer coefficient, with the step height being held fixed at H/L = 1/15. These results are presented in Figs. 10 and 11, which correspond respectively to Re = 30,000 and 66,000. In each figure, j/j^* is plotted as a function of α for parametric values of the forward-thrusting skirt width W/L = 1/2.5, 1/5, and 0. The results shown in these figures convey a clear message, namely, that the separation-related enhancement of the heat transfer coefficient is markedly affected by the skirt width.

Not only is the magnitude of j/j^* significantly affected by skirt width, but also is the range of angles of attack at which enhancement occurs. Both the magnitude of the enhancement and the angles to which enhancement persists are increased as the skirt width becomes greater.

The curves for the two non-zero skirt widths have similar shapes. It is interesting to note that there is a definite tendency for these curves to come together at smaller angles as well as at larger angles. The enhancement effects for the wider of the two skirts persist to angles that are 10–15 deg larger than for the narrower skirt.

The characteristics evidenced by the no-skirt case are altogether different from those for the finite-width skirts. First of all, there is no significant enhancement of the heat transfer coefficient for angles greater than 15–20 deg. Furthermore, an undershoot is in evidence at lower angles, whereby the heat transfer coefficient falls slightly below the large-angle separation-free value.

It is not surprising that there are such different trends when a skirt is absent and when a skirt is present. These differences can be attributed to differences in the respective flow fields. Thus, for example, the separated region at the foot of the step (between points A and B, Fig. 1, lower left) is no longer present when there is no skirt. Furthermore, a stagnation line which would otherwise lie in the skirt may shift to the step when the skirt is absent.

In common with the trends of earlier figures, the effect of higher Reynolds numbers, as evidenced in Figs. 10 and 11, is to increase the degree of enhancement and to extend the range of angles where enhancement occurs.

Concluding Remarks

The research reported here was aimed at determining heat transfer coefficients for a thermally active surface elevated above a host surface. Supplementary flow visualization experiments, intended to provide insights into the patterns of fluid flow adjacent to the surface, were also carried out.

The visualization studies demonstrated the presence of a region of flow separation which blankets the forward part of the elevated surface. Fluid recirculation within the separated region was inferred from the streak lines on the surface. The streamwise extent of the separated region was found to increase with decreasing angle of attack. On the other hand, at larger angles of attack, separation does not occur. Separated regions of greater extent were encountered at larger step heights and for greater widths of the skirt which thrusts forward into the flow. There is also a tendency toward larger separated regions at higher Reynolds numbers. Since, at the Reynolds numbers investigated, the separation zone contains vigorously recirculating fluid, larger separated regions give rise to higher heat transfer coefficients.

At a fixed Reynolds number and for fixed geometry (i.e., fixed step height and skirt width), the heat transfer coefficient increases monotonically with decreasing angle of attack. Separation-related enhancements of the heat transfer coefficient as large as a factor of two were encountered. At larger angles of attack, where there is no flow separation, the heat transfer coefficient is essentially independent of angle and of geometry.

Higher steps give rise to progressively greater heat transfer enhancement at angles where there is significant enhancement. The degree of enhancement is markedly increased as the skirt width increases and, in addition, the enhancement persists to larger angles of attack. In the absence of a skirt, there is very little enhancement.

The Reynolds number plays a significant role in the separation-induced enhancement. The degree of enhancement is greater and enhancement persists to larger angles at higher Reynolds numbers. On the other hand, with increasing Reynolds number the heat transfer coefficients become less sensitive to variations in step height.

With regard to applications, it may be concluded that the use of literature information for non-separated-flow heat transfer coefficients will generally provide a low estimate of the surface heat transfer rate. For solar collectors, such a low estimate will yield an optimistic prediction of the collector efficiency.

As a final observation, it should be pointed out that a wind tunnel is not able to model, in all details, the fluid flow conditions that are encountered in the outdoor environment, e.g., unsteadiness and turbulence characteristics. On the other hand, owing to the variability of the outdoor environment, it is unrealistic to think in terms of a universal set of fluid flow conditions for solar collectors (the specification of the mean wind speed does not characterize unsteadiness or turbulence). Thus, model experiments of any kind, whether performed in a wind tunnel or outdoors, can only approximate any particular solar collector application. While it is well to keep such concerns in mind, it is still necessary to employ the results of model experiments for solar collector design. In this light, the present results merit consideration for incorporation into solar collector design calculations.

Acknowledgment

This research was performed under the auspices of the American Society of Heating, Refrigerating, and Air-Conditioning Engineers.

References

1. Duffie, J. A., and Beckman, W. A., *Solar Energy Thermal Processes*, Wiley, New York, 1974, p. 83.
2. Jordan, R. C. and Liu, B. Y. H., eds., *Application of Solar Energy for Heating and Cooling of Buildings*, ASHRAE, New York, 1977, Chapter 8.
3. Krieth, F., and Krieder, J. F., *Principles of Solar Engineering*, McGraw-Hill, New York, 1978, p. 139.
4. Sparrow, E. M., and Tien, K. K., "Forced Convection at an Inclined and Yawed Flat Plate—Application to Solar Collectors," ASME JOURNAL OF HEAT TRANSFER, Vol. 99, 1977, pp. 507–512.
5. Tien, K. K., and Sparrow, E. M., "Local Heat Transfer and Flow Field Characteristics for Airflow Oblique or Normal to a Flat Plat," *International Journal of Heat and Mass Transfer*, Vol. 22, 1979, 349–360.
6. Sparrow, E. M., Ramsey, J. W., and Mass, E. A., "Effect of Finite Plate Width on Heat Transfer and Fluid Flow about an Inclined Rectangular Plate," ASME JOURNAL OF HEAT TRANSFER, Vol. 101, 1979, pp. 199–204.
7. Ramsey, J. W., and Charmchi, M., "Variances in Solar Collector Performance Predictions due to Different Methods of Evaluating Wind Heat Transfer Coefficients," ASME JOURNAL OF HEAT TRANSFER, Vol. 102, 1980, pp. 766–768.
8. Eckert, E. R. G., "Analogies to Heat Transfer Processes," in *Measurements in Heat Transfer*, E. R. G. Eckert and R. J. Goldstein, eds., Hemisphere, Washington, 1976.
9. Zukauskas, A., "Heat Transfer from Tubes in Crossflow," in *Advances in Heat Transfer*, Vol. 8, Academic Press, New York, 1972, pp. 93–160.
10. Sogin, H. H., "Sublimation from Disks to Air Streams Flowing Normal to their Surfaces," *Trans. ASME*, Vol. 80, 1958, pp. 61–69.
11. Skelland, A. H. P., *Diffusional Mass Transfer*, Wiley, New York, 1974, p. 51.

Unsteady Stagnation Point Heat Transfer with Blowing or Suction

Takao Sano
Department of Mechanical Engineering,
University of Osaka Prefecture,
Sakai, Osaka, Japan

The effects of blowing and suction on unsteady heat transfer at a stagnation point due to a step change in wall temperature are examined. Two asymptotic solutions for the temperature field at large and small Prandtl numbers are presented. It is shown that the asymptotic solution for large Prandtl number gives sufficiently accurate results for the surface heat transfer even for the moderate values of Prandtl number if Euler transformation is applied to the series.

1 Introduction

The thermal response behavior of laminar steady flows at a front stagnation point due to a step change in wall temperature or in wall heat flux has been investigated by several authors [1–4]. The present paper extends this problem to the case with a uniform blowing or suction at the surface. This extension has already been made by Jeng [5]. The method of solution adopted by Jeng is to obtain two asymptotic solutions respectively valid for small and large time, which are joined together at some moderate value of time. However, the matching seems unsatisfactory especially for small Prandtl number and the method for obtaining the large-time solution has a drawback of the lack of uniqueness [4]. Jeng gave the numerical results only for the case of blowing and only for Pr = 0.01 and 0.7. The latter restriction on the value of Pr is probably due to the fact that the convergence of the series for the parameters which are included in the large-time solution as functions of Pr becomes poor when Pr is large.

In the present paper, in order to study the effects of blowing and suction on unsteady heat transfer process for a wide range of Pr, we obtain asymptotic solutions for large and small Prandtl numbers for the case of a step change in wall temperature. These solutions are uniformly valid for all time and it is found that the solution for large Pr is valid even for moderate values of Pr if its convergence is improved by the Euler transformation.

2 Governing Equations

Consider steady, incompressible, laminar flows near a front stagnation point of a two-dimensional or axisymmetrical body. We assume that there is a uniform blowing or suction through the surface. Initially, the surface of the body and the fluid are at the same temperature T_∞, whereupon at time $t = 0$ the surface temperature is suddenly changed to a constant value T_w. By introducing the following variables

$$\eta = y\left(\frac{2^iK}{\nu}\right)^{1/2} \qquad \tau = \frac{2^iKt}{\Pr},$$
$$\psi = \left(\frac{\nu K}{2^i}\right)^{1/2}\left(\frac{x}{L}\right)^i x f(\tau, \eta), \tag{1}$$
$$\theta = (T - T_\infty)/(T_w - T_\infty),$$

where x and y are the coordinates along and normal to the body, ν the kinematic viscosity of the fluid, L the characteristic length of the body, K a constant related to the velocity u_p just outside the boundary layer by $u_p = Kx$, i a constant being zero for plane flow and one for axisymmetrical flow, T the temperature of the fluid and ψ the stream function defined by

$$u = \left(\frac{L}{x}\right)^i \frac{\partial\psi}{\partial y} \qquad v = -\left(\frac{L}{x}\right)^i \frac{\partial\psi}{\partial x}$$

u and v being velocities in the x and y directions, respectively, the governing equations for the velocity and the temperature fields can be written as [2]

$$f''' + ff'' + 2^{-i}(1 - f'^2) = 0, \tag{2}$$

$$\frac{\partial\theta}{\partial\tau} = \theta'' + \Pr f\theta', \tag{3}$$

where prime denotes differentiation with respect to η, and the initial and boundary conditions as

$$\theta = 0 \quad \text{for } \tau = 0,$$
$$f = f_0, f' = 0, \theta = H(\tau) \quad \text{for } \eta = 0 \tag{4}$$
$$f' \to 1, \theta \to 0 \quad \text{as } \eta \to \infty,$$

where $H(\tau)$ is the Heaviside step function. Positive values of f_0 correspond to suction and negative ones to blowing. The momentum equation (2) has already been solved numerically by several authors [6–8]. In the following sections, we shall obtain asymptotic solutions of (3) for small and large Prandtl numbers.

3 Asymptotic Solution for Small Prandtl Number

We first consider the case of small Pr. Assuming that θ may be expanded as

$$\theta = \theta_0(\tau, \eta) + \Pr\theta_1(\tau, \eta) + \Pr^2\theta_2(\tau, \eta) + \ldots, \tag{5}$$

and substituting this into (3), we have

$$\frac{\partial\theta_0}{\partial\tau} - \theta_0'' = 0, \tag{6}$$

$$\frac{\partial\theta_1}{\partial\tau} - \theta_1'' = f\theta_0', \tag{7}$$

etc. The solutions of these equations can easily be obtained by using the Laplace transformation technique. The final result for the wall temperature gradient is

$$-(\theta')_{\eta=0} = (\pi\tau)^{-1/2} + \Pr\left[\frac{1}{2}\left(\frac{\tau}{\pi}\right)^{1/2} + \frac{\beta}{2} + (\pi\tau)^{-1/2}\int_0^\infty (f - \eta - \beta)e^{-\eta^2/\tau}d\eta\right] + 0(\Pr^2), \tag{8}$$

where

$$\beta = \lim_{\eta\to\infty}(f - \eta). \tag{9}$$

It is seen that, as $\tau \to \infty$, $(\theta')_{\eta=0}$ becomes infinite, that is, (8) and hence (5) are singular for large τ. The reason for the failure of the expansion (5) at large τ can be explained as follows. At an early stage (when $\tau = 0(1)$) in the unsteady heat transfer process, the thermal layer is confined to the velocity boundary layer (inner region) near the surface, where the effect of convection on temperature is small and the equation (3) and the expansion (5) are adequate for describing the temperature field. As τ becomes larger, however, the thermal layer diffuses into the "outer region" outside the momentum layer where, no matter how small Pr is, both the convection and conduction terms are of the same order of magnitude. It is the existence of this outer region which prevents the expansion (5) from becoming a uniformly valid approximation to the temperature.

Contributed by The Heat Transfer Division for publication in the JOURNAL OF HEAT TRANSFER. Manuscript received by The Heat Transfer Division May 11, 1979.

In order to obtain a uniformly valid solution, we shall use the method of matched asymptotic expansions. From the argument stated above, it is reasonable to construct two expansions valid in the large-time region in addition to (5); one is an "inner expansion" valid in the inner region and the other an "outer expansion" valid in the outer region. These expansions are constructed in such a way that: (1) The inner expansion satisfies the boundary condition on the surface. (2) The outer expansion satisfies the boundary condition at infinity. (3) The two expansions match identically in the overlapping domain in space where both expansions are valid and also match the small-time solution (5) at small values of τ^*, τ^* being a time variable in the large-time region.

As the time variable in the large-time region, we introduce τ^* such as

$$\tau^* = \mathrm{Pr}\tau \equiv 2^i Kt, \tag{10}$$

in terms of which the energy equation can be written as

$$\mathrm{Pr}\frac{\partial\theta^*}{\partial\tau^*} = \theta^{*\prime\prime} + \mathrm{Pr}f\theta^{*\prime}, \tag{11}$$

where

$$\theta^*(\tau^*, \eta) = \theta(\tau, \eta). \tag{12}$$

(11) is an inner equation valid in the inner region. In the outer region, we introduce following variables

$$\xi = \mathrm{Pr}^{1/2}\eta,\ F(\xi) = \mathrm{Pr}^{1/2}f(\eta),\ \Theta^*(\tau^*, \xi) = \theta^*(\tau^*, \eta), \tag{13}$$

in terms of which the energy equation may be written as

$$\frac{\partial\Theta^*}{\partial\tau^*} = \ddot{\Theta}^* + F(\xi)\dot{\Theta}^*, \tag{14}$$

where the dot denotes differentiation with respect to ξ. Since, in this region, η is very large, the stream function F is expressed by the following asymptotic form:

$$F \sim \xi + \beta\mathrm{Pr}^{1/2} + (\exp-), \tag{15}$$

where (exp−) denotes exponentially small terms. Neglecting the terms, (14) becomes

$$\frac{\partial\Theta^*}{\partial\tau^*} = \ddot{\Theta}^* + (\xi + \beta\mathrm{Pr}^{1/2})\dot{\Theta}^*. \tag{16}$$

Since the small-time solution decays exponentially as $\eta \to \infty$, the following matching condition holds as an initial condition for Θ^*:

$$\lim_{\tau^*\to 0} \Theta^* = 0. \tag{17}$$

Therefore, application of the Laplace transformation

$$\bar{\Theta}^* = \int_0^\infty \Theta^* e^{-p\tau^*}d\tau^*, \tag{18}$$

to (16) yields

$$\ddot{\bar{\Theta}}^* + (\xi + \beta\mathrm{Pr}^{1/2})\dot{\bar{\Theta}}^* - p\bar{\Theta}^* = 0. \tag{19}$$

The solution of (19) satisfying the boundary condition at infinity is expressed as an expansion in terms of $\mathrm{Pr}^{1/2}$ as follows:

$$\begin{aligned}\bar{\Theta}^* = {} & A_0\nabla_p(\xi) + \mathrm{Pr}^{1/2}\{-A_0\beta\nabla_{p-1}(\xi) + A_1\nabla_p(\xi)\} \\ & + \mathrm{Pr}\left\{\frac{A_0\beta^2}{2}\nabla_{p-2}(\xi) - A_1\beta\nabla_{p-1}(\xi)\right\} + \mathrm{Pr}^{3/2}\left\{-\frac{A_0\beta^3}{6}\nabla_{p-3}(\xi)\right. \\ & \left. + \frac{A_1\beta^2}{2}\nabla_{p-2}(\xi) - A_2\beta\nabla_{p-1}(\xi) + A_3\nabla_p(\xi)\right\} + 0(\mathrm{Pr}^2),\end{aligned} \tag{20}$$

where

$$\begin{aligned}\nabla_p(\xi) = {} & \left(\frac{\pi}{2}\right)^{1/2}\left\{{}_1F_1\left(-\frac{p}{2}, \frac{1}{2}, -\frac{\xi^2}{2}\right)\Big/ 2^{p/2}\Gamma\left(\frac{p}{2}+1\right)\right. \\ & \left. -\xi\,{}_1F_1\left(-\frac{p}{2}+\frac{1}{2}, \frac{3}{2}, -\frac{\xi^2}{2}\right)\Big/ 2^{(p-1)/2}\Gamma\left(\frac{p}{2}+\frac{1}{2}\right)\right\},\end{aligned} \tag{21}$$

${}_1F_1(a, b, x)$ being the confluent hypergeometric function [9], and A_n's are unknown constants to be determined through the following matching condition:

$$\lim_{\eta\to\infty}\theta^* = \lim_{\xi\to 0}\Theta^*\left(\text{or, } \lim_{\eta\to\infty}\bar{\theta}^* = \lim_{\xi\to 0}\bar{\Theta}^*\right). \tag{22}$$

In view of (20), the inner expansion should be of the form

$$\begin{aligned}\theta^* = {} & \theta_0^*(\tau^*, \eta) + \mathrm{Pr}^{1/2}\theta_1^*(\tau^*, \eta) + Pr\theta_2^*(\tau^*, \eta) \\ & + Pr^{3/2}\theta_3^*(\tau^*, \eta) + 0(\mathrm{Pr}^2).\end{aligned} \tag{23}$$

Substituting this into (11) yields the following equations for θ_n^*:

$$\begin{gathered}\theta_0^{*\prime\prime} = \theta_1^{*\prime\prime} = 0, \\ \theta_n^{*\prime\prime} = -f\theta_{n-2}^{*\prime} + \frac{\partial\theta_{n-2}^*}{\partial\tau^*}\ (\text{for } n \geq 2).\end{gathered} \tag{24}$$

Solutions of these equations satisfying the boundary condition on the surface are

$$\begin{gathered}\theta_0^* = 1 + a_0(\tau^*)\eta, \\ \theta_1^* = a_1(\tau^*)\eta, \\ \theta_2^* = a_0(\tau^*)\left(\int_0^\eta \eta f d\eta - \eta\int_0^\eta f d\eta\right) + \frac{1}{6}\frac{da_0}{d\tau^*}\eta^3 + a_2(\tau^*)\eta, \\ \theta_3^* = a_1(\tau^*)\left(\int_0^\eta \eta f d\eta - \eta\int_0^\eta f d\eta\right) + \frac{1}{6}\frac{da_1}{d\tau^*}\eta^3 + a_3(\tau^*)\eta,\end{gathered} \tag{25}$$

Matching condition (22) determines the unknown constants A_n and a_n. Only the final result for the wall temperature gradient calculated from the inner solution is shown below.

$$\begin{aligned}-(\theta^{*\prime})_{\eta=0} = {} & \left\{\frac{2}{\pi(1-e^{-2\tau^*})}\right\}^{1/2}\mathrm{Pr}^{1/2} \\ & + \frac{2\beta\mathrm{Pr}\{E(\sqrt{1-e^{-2\tau^*}}) - e^{-2\tau^*}K(\sqrt{1-e^{-2\tau^*}})\}}{\pi(1-e^{-2\tau^*})} \\ & + \left(\frac{2}{\pi}\right)^{1/2}\left\{\gamma(1-e^{-2\tau^*})^{-1/2} - \frac{2\beta^2 I(\tau^*)}{\pi}\right\}\mathrm{Pr}^{3/2} + \mathrm{O}(\mathrm{Pr}^2),\end{aligned} \tag{26}$$

where

$$\begin{gathered}\gamma = \int_0^\infty (f - \eta - \beta)d\eta, \\ I(\tau^*) = \int_0^{\sqrt{1-e^{-2\tau^*}}} \frac{\sqrt{1-k^2}\{2E(k) - (2-k^2)K(k)\}}{k^3\sqrt{1-e^{-2\tau^*}-k^2}}dk,\end{gathered} \tag{27}$$

Nomenclature

f, F = dimensionless stream function
f_0 = value of f at the surface of the body
i = constant being zero for plane flow and one for axisymmetrical flow
K = proportionality constant related to the velocity outside the boundary layer
L = characteristic length
p = parameter in Laplace transform
Pr = Prandtl number
s = parameter in Laplace transform
t = time
T = temperature
u = velocity in x direction
v = velocity in y direction
x = coordinate along the body measured from the front stagnation
y = coordinate normal to the body
β = constant defined in (9)
γ = constant defined in (27)
ζ = dimensionless coordinate defined in (30)
η = dimensionless coordinate defined in (1)
$\theta, \theta^*, \Theta^*, \hat{\theta}$ = dimensionless temperature
ν = kinematic viscosity
ξ = dimensionless coordinate defined in (13)
$\tau, \tau^*, \hat{\tau}$ = dimensionless time
ψ = stream function

Subscripts

s = steady-state
w = condition at wall surface
∞ = free stream condition

$K(k)$ and $E(k)$ being the complete elliptic integrals of the first and the second kind, respectively. It is easy to show that the large-time solution (26) matches with the small-time solution (8) and gives for $\tau^* \to \infty$ the steady-state solution which has already been obtained by the present writer [10].

When $\tau = O(1)$, the surface heat transfer may be calculated from (8), and when $\tau^* = O(1)(\tau = O(\mathrm{Pr}^{-1}))$ from (26). It is, however, possible to construct from (8) and (26) a single composite expansion which is valid uniformly for all values of time.[1] Employing the so-called "additive composition method" [11], we get

$$
\begin{aligned}
-(\theta')_{\eta=0} = {} & \left\{\left(\frac{2}{\pi(1-e^{-2\tau^*})}\right)^{1/2} - \frac{1}{2}\left(\frac{\tau^*}{\pi}\right)^{1/2}\right\}\mathrm{Pr}^{1/2} \\
& + \left[(\pi\tau)^{-1/2}\int_0^\infty f e^{-\eta^2/\tau} d\eta - \frac{\beta}{2} \right. \\
& \left. + \frac{2\beta\{E(\sqrt{1-e^{-2\tau^*}}) - e^{-2\tau^*}K(\sqrt{1-e^{-2\tau^*}})\}}{\pi(1-e^{-2\tau^*})}\right]\mathrm{Pr} \\
& + \left[\left(\frac{2}{\pi}\right)^{1/2}\left\{\gamma(1-e^{-2\tau^*})^{-1/2} - \frac{2\beta^2 I(\tau^*)}{\pi}\right\} \right. \\
& \left. - \gamma(\pi\tau^*)^{-1/2}\right]\mathrm{Pr}^{3/2} + O(\mathrm{Pr}^2). \qquad (28)
\end{aligned}
$$

For calculating β, γ, and the integral included in (28), we need the numerical values of the stream function f. For $i = 0$, Evans [7] obtained numerical solutions of f for several valus of f_0. For $i = 1$, on the other hand, they are obtained only for $f_0 = 0$ [6] and hence the calculation of the integral and constants mentioned above is performed only for this special case. The calculated results for β and γ are shown in Table 1.

4 Asymptotic Solution for Large Prandtl Number

We shall now proceed to obtain the asymptotic solution of (3) for large Prandtl number. When Pr is large, the thickness of thermal layer is much thinner than that of viscous layer, so that the velocity field in the thermal layer may be expressed by the following series form:

$$
f = f_0 + \left(\frac{f_0''}{2}\right)\eta^2 + \frac{f_0'''}{6}\eta^3 + \frac{f_0^{(iv)}}{24}\eta^4 + \dots, \qquad (29)
$$

where subscript 0 denotes the values of functions at $\eta = 0$. We assume that $f_0 \neq 0$. Introducing the following variables

$$
\zeta = \mathrm{Pr}\eta,\ \hat{\tau} = \mathrm{Pr}^2\tau,\ \hat{\theta}(\hat{\tau}, \zeta) = \theta(\tau, \eta), \qquad (30)
$$

and substituting (29) and (30) into (3), we have

$$
\frac{\partial\hat{\theta}}{\partial\hat{\tau}} = \frac{\partial^2\hat{\theta}}{\partial\zeta^2} + \left(f_0 + \frac{f_0''}{2}\zeta^2\mathrm{Pr}^{-2} + \frac{f_0'''}{6}\zeta^3\mathrm{Pr}^{-3} + \frac{f_0^{(iv)}}{24}\zeta^4\mathrm{Pr}^{-4} + \dots\right)\frac{\partial\hat{\theta}}{\partial\zeta}. \qquad (31)
$$

Assuming that $\hat{\theta}$ may be expressed as

$$
\hat{\theta} = \hat{\theta}_0(\hat{\tau}, \zeta) + \hat{\theta}_1(\hat{\tau}, \zeta)\mathrm{Pr}^{-1} + \hat{\theta}_2(\hat{\tau}, \zeta)\mathrm{Pr}^{-2} + \dots, \qquad (32)
$$

and substituting this into (31), we have

$$
\begin{aligned}
& \frac{\partial\hat{\theta}_0}{\partial\hat{\tau}} - \frac{\partial^2\hat{\theta}_0}{\partial\zeta^2} - f_0\frac{\partial\hat{\theta}_0}{\partial\zeta} = 0, \\
& \frac{\partial\hat{\theta}_1}{\partial\hat{\tau}} - \frac{\partial^2\hat{\theta}_1}{\partial\zeta^2} - f_0\frac{\partial\hat{\theta}_1}{\partial\zeta} = 0, \qquad (33) \\
& \frac{\partial\hat{\theta}_2}{\partial\hat{\tau}} - \frac{\partial^2\hat{\theta}_2}{\partial\zeta^2} - f_0\frac{\partial\hat{\theta}_2}{\partial\zeta} = \frac{f_0''}{2}\zeta^2\frac{\partial\hat{\theta}_0}{\partial\zeta}, \\
& \frac{\partial\hat{\theta}_3}{\partial\hat{\tau}} - \frac{\partial^2\hat{\theta}_3}{\partial\zeta^2} - f_0\frac{\partial\hat{\theta}_3}{\partial\zeta} = \frac{f_0'''}{6}\zeta^3\frac{\partial\hat{\theta}_0}{\partial\zeta} + \frac{f_0''}{2}\zeta^2\frac{\partial\hat{\theta}_1}{\partial\zeta},
\end{aligned}
$$

Table 1 Numerical values of β and γ

	f_0	β	γ
	−3	−4.8585	2.590
	−1	−1.9450	0.7234
	−0.5	−1.2810	0.5081
$i = 0$	0	−0.6479	0.3595
	0.5	−0.0423	0.2584
	1	0.5407	0.1895
	3	2.7329	0.0678
$i = 1$	0	−0.8046	0.5360

The solutions of (33) satisfying the initial and boundary conditions can easily be found by using the Laplace transformation technique. The final result for $\hat{\theta}_0$ is

$$
\hat{\theta}_0 = \frac{1}{2}\left\{\mathrm{erfc}\left(\frac{\zeta\hat{\tau}^{-1/2} + f_0\hat{\tau}^{1/2}}{2}\right) + e^{-f_0\zeta}\mathrm{erfc}\left(\frac{\zeta\hat{\tau}^{-1/2} - f_0\hat{\tau}^{1/2}}{2}\right)\right\}, \qquad (34)
$$

which represents the temperature distribution in the limit $\mathrm{Pr} \to \infty$. It should be noted that, when $f_0 < 0$, $\hat{\theta}_0 \to 1$ as $\hat{\tau} \to \infty$, that is, the solution (34) does not satisfy the boundary condition at infinity when $\hat{\tau} \to \infty$. This means that for the case of blowing the expansion (32) is invalid in the outer region when both $\hat{\tau}$ and ζ are infinitely large, and that an outer expansion, which is not obtained in the present paper, prevails there. This failure of (32) at large $\hat{\tau}$ and large ζ is due to the fact that, as $\hat{\tau}$ increases, the thermal boundary layer, which initially adheres to the wall, becomes to be blown away from the surface due to the convective effect of the injected fluid and the approximate equation (29) for f becomes to be invalid in the thermal boundary layer. In the injection layer near the surface, (29) is still a valid approximation for f even when $\hat{\tau}$ is large and (32) is valid for all values of $\hat{\tau}$.

The solutions of (33) are obtained up to $\hat{\theta}_4$, which are not shown here to save space, and it is found that, for $f_0 < 0$, $\hat{\theta}_n \to 0 (n \geq 1)$ as $\hat{\tau} \to \infty$. This means that, when $\hat{\tau}$ is large, deviation of the value of $\hat{\theta}$ from unity is exponentially small in the injection layer and the temperature drop from unity to zero occurs only in the thermal boundary layer far from the surface. The result for the wall temperature gradient is

$$
\begin{aligned}
-(\theta')_{\eta=0} = {} & \frac{f_0}{2}\left\{\frac{1}{\sqrt{\pi}T} + \mathrm{erfc}(-T)\right\}\mathrm{Pr} \\
& + \frac{f_0''}{f_0^2}\left\{-\left(\frac{1}{2} + \frac{T}{\sqrt{\pi}}\right)e^{-T^2} + \mathrm{erfc}(-T)\right\}\mathrm{Pr}^{-1} \\
& + \frac{f_0'''}{f_0^3}\left\{-\left(\frac{T^2}{2} + \frac{T}{\sqrt{\pi}} + \frac{1}{2}\right)e^{-T^2} + \mathrm{erfc}(-T)\right\}\mathrm{Pr}^{-2} \\
& + \left[\frac{f_0''^2}{2f_0^5}\left\{\left(\frac{4T^5}{15\sqrt{\pi}} - \frac{T^4}{2} - \frac{4T^3}{3\sqrt{\pi}} - T^2 - \frac{2T}{\sqrt{\pi}} - 1\right)e^{-T^2} + \mathrm{erfc}(-T)\right\}\right. \\
& \left. + \frac{f_0^{(iv)}}{2f_0^4}\left\{\left(\frac{-4T^3}{3\sqrt{\pi}} - T^2 - \frac{2T}{\sqrt{\pi}} - 1\right)e^{-T^2} + \mathrm{erfc}(-T)\right\}\right]\mathrm{Pr}^{-3} \\
& + O(\mathrm{Pr}^{-4}), \qquad (35)
\end{aligned}
$$

where

$$
T = \frac{f_0}{2}\sqrt{\hat{\tau}}. \qquad (36)
$$

It is seen that, when $f_0 < 0$, $(\theta')_{\eta=0} \sim O(\mathrm{Pr}^{-\infty})$ as $\hat{\tau} \to \infty$, that is, for the case of blowing, the wall temperature gradient becomes to be exponentially small as $\mathrm{Pr} \to \infty$ and $\hat{\tau} \to \infty$.

5 Discussion

Using the asymptotic solutions obtained in the preceding sections, we calculate the wall temperature gradient for Pr ranging from 0.01 to 100 and for f_0 from −3 to 3. (For axisymmetrical case, the small Prandtl number results are not obtained since the numerical values for f, which are necessary for calculating the temperature field, have

---

[1] According to Van Dyke [11], the construction of a single uniformly valid composite expansion can be carried out in a large variety of ways and their results may be different because of the non-uniqueness of the composite expansion; but they will all be equivalent to the order of accuracy retained.

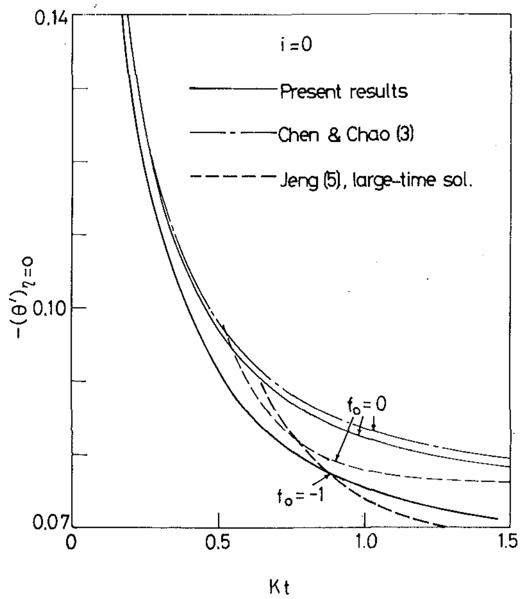

Fig. 1 Comparison of the present results with the previous works at Pr = 0.01

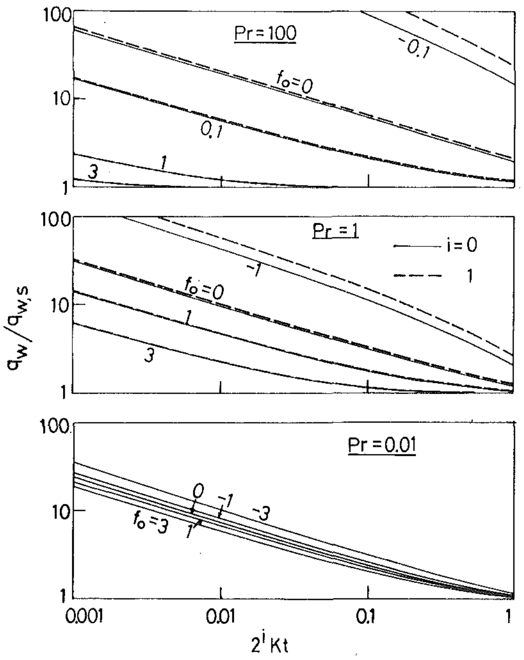

Fig. 2 Effect of f_0 on heat transfer response

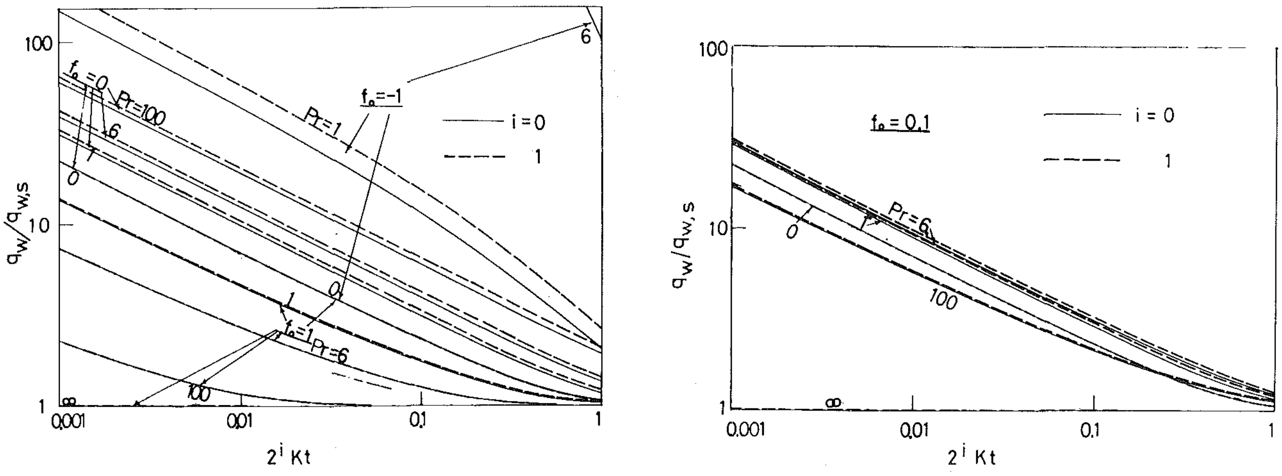

Fig. 3(a) **Fig. 3(b)**

Fig. 3 Effect of Prandtl number on heat transfer response

not yet been given.) It is found that for sufficiently large or small Pr the present results for $\tau \rightarrow \infty$ agree well with the numerical ones given for steady state [8] and that the convergence of the asymptotic solutions is better for smaller values of time. For moderate value of Pr, we apply the Euler transformation to the asymptotic solution for large Pr. The Eulerized series shows good convergence even for Pr = 0.7 when τ^* is smaller than about 1.5.

In Fig. 1, our small Prandtl number results for plane flow are compared with those[2] obtained previously at Pr = 0.01 and $f_0 = -1,0$. It is seen that the results of Jeng [5] are not satisfactory. Figure 2 shows the effect of mass transfer on the variation of the ratio $q_w/q_{w,s}$ with time for Pr = 0.01, 1 and 100, where q_w is the instantaneous wall heat flux and $q_{w,s}$ the steady-state value of q_w. The results for $f_0 = 0$ are obtained using the solution in [4]. It is seen from Fig. 2 that the response time of heat transfer increases monotonously as f_0 decreases from positive values (suction) to negative ones (blowing) and the effect of mass transfer is larger for larger value of Pr. The reason why the effect of mass transfer on the response time is small for small Pr is that when Pr is small the thickness of momentum layer is much smaller than that of thermal layer and the change in the velocity distribution due to mass transfer at the surface has small effect on the temperature field. In Fig. 3, on the other hand, the effect of the Prandtl number on the ratio $q_w/q_{w,s}$ is shown for some values of f_0. It is seen that for the case of blowing and for impermeable surface the response time increases monotonously with increasing Prandtl number, while for the case of suction the trend is reversed provided that f_0 is larger than some threshold value f_0^*. The exact value of f_0^* can not be determined in the present paper. For $0 < f_0 < f_0^*$, the response time is not a monotonous function of Pr; it is maximum at some value of Pr (depending on the value of f_0) and decreases as Pr $\rightarrow 0, \infty$. This aspect may be considered as the transitional one between the two diametrically opposite trends described above. It is also seen from Fig. 3 that blowing has greater effect on $q_w/q_{w,s}$ for axisymmetrical than for the two-dimensional case, as is already noted by Jeng, but that the effect of suction is almost the same for both cases.

References

1 Cess, R. D., and Sparrow, E. M., "International Developments in Heat Transfer," *Trans. ASME*, Part II, Sec. B, 1961, p. 468.

2 Chao, B. T., and Jeng, D. R., "Unsteady Stagnation Point Heat Transfer," ASME JOURNAL OF HEAT TRANSFER, Vol. 87, 1965, p. 221.

3 Chen, J. L., and Chao, B. T., "Thermal Response Behavior of Laminar Boundary Layer in Wedge Flow," *International Journal of Heat Mass Transfer*, Vol. 13, 1970, p. 1101.

---

[2] The author wishes to thank one of the referees, who kindly made available to the author the numerical data of Chen and Chao [3].

4 Jeng, D. R., Lee, M. H., and De Witt, K. J., "The Final Approach to Steady State in Nonsteady Stagnation Point Heat Transfer," *Journal of Engineering Mathematics*, Vol. 10, 1976, p. 173.

5 Jeng, D. R., "Unsteady Heat Transfer in Laminar Boundary Layers," Ph.D. thesis in mechanical engineering, University of Illinois, 1965.

6 Hartree, D. R., "On an Equation Occurring in Falkner and Skan's Treatment of the Equations of the Boundary Layer," *Proceedings of the Cambridge Philosophical Society*, Vol. 33, 1937, p. 57.

7 Evans, H. L. "Mass Transfer through Laminar Boundary Layer-8. Further Solutions to the Velocity Equation," *International Journal of Heat Mass Transfer*, Vol. 5, 1962, p. 373.

8 Elzy, E., and Sisson, R. M., "Tables of Similar Solutions to the Equations of Momentum, Heat and Mass Transfer in Laminar Boundary Layer Flow," Bulletin No. 40, Engng. Experiment Station, Oregon State Univ., Carvallis, 1967.

9 Slater, L. J., *Confluent Hypergeometric Functions*, Cambridge University Press, 1960.

10 Sano, T., "Forced-Convection Heat Transfer in Laminar Boundary Layer at Low Prandtl Number," Bulletin of Univ. Osaka Prefecture, Series A, Vol. 21, 1972, p. 27.

11 Van Dyke, M., *Perturbation Methods in Fluid Mechanics*, Parabolic, 1975.

K. A. Joudi
Lecturer, Department of Mechanical Engineering,
University of Basrah, Basrah, Iraq

D. D. James
Lecturer, Department of Mechanical Engineering,
UMIST, Manchester, England

Surface Contamination, Rejuvenation, and the Reproducibility of Results in Nucleate Pool Boiling

Contamination of stainless steel boiling surfaces at nucleation sites by corrosion products in water, and by oxide deposits in methanol are investigated experimentally. Reproducibility of boiling data is achieved by nitrogen sparging of test liquids and employing inert components in the apparatus. Heating surface rejuvenation is effected by boiling in refrigerant R-113. The order of testing a surface with various liquids is investigated.

Introduction

The important feature of any reliable scientific investigation is that the results obtained should be reproducible at different times under similar conditions. A feature which is peculiar to nucleate boiling, more so than the other regimes of heat transfer, is the difficulty encountered in controlling the condition of the heat transfer surface, and also maintaining the chemical purity of both the surface and the boiling liquid. A consequence of this difficulty is reflected in the inconsistency and scatter of experimental data caused by the "time-in-use" or so-called aging of a surface on which boiling occurs.

Details of how the effect of aging is overcome are not usually given in the majority of the published literature, except for general remarks to the effect that the data were taken after the surface had aged. Generally, surfaces which have been in service for long periods of time require higher temperature differences to maintain the same heat flux. Rohsenow and Choi [1] attribute this trend to either added resistance of an oxide or deposited layer, or to the decrease in cavity size resulting from mild oxidation. Localized deposits of corrosion products at nucleation sites have been cited by Nestrueva, et al. [2] in experiments involving boiling heat transfer with water. They reported that the formation of oxide film, and deposition of corrosion products was the most probable reason for the considerable scatter of the available data on heat transfer in developed boiling.

This work describes an attempt to systematically inhibit and possibly eliminate surface contamination under boiling conditions so that results from boiling experiments over a period of time are reproduced and can be relied on. The use of nitrogen sparging as an oxygen-induced corrosion preventer is an innovation which will be of interest to those concerned with reproducibility of results in boiling heat transfer. Heat transfer data are reported for stainless steel surfaces boiling in three liquids; Analar[1] water, methanol and refrigerant R-113 over a pressure range including 0.25 atm., 0.5 atm., and atmospheric pressure.

Description of the Equipment

The experimental apparatus and instrumentation are shown schematically in Fig. 1. A test liquid was boiled from an electrically heated horizontal rectangular stainless steel plate housed in a cubical stainless steel boiling chamber with clear inside dimensions of 210 mm on all sides. An auxiliary heater made of resistance wire in silica glass tube was used to bring the test liquid to boiling and maintain it at saturation temperature during low heat flux operation. Hot vapours were conducted to a stainless steel condenser, and the condensate was returned to the boiling chamber, through the base plate, by glass tubing. Nitrogen gas which was used for sparging water and methanol during experiments, was bubbled through a 6 mm glass tube fitted flush in a corner of the base plate of the boiling chamber and positioned 80 mm from the nearest edge of the test specimen.

The flow rate of nitrogen was kept to a minimum during tests such that it did not influence the natural convection currents and liquid circulation to and from the heating surface. Nitrogen bubbles did not induce bubble generation from the heating surface and did not appear to have an observable effect on the boiling process.

A test surface was fitted with a 6 mm thick "pure natural" rubber backing piece which provided thermal insulation as well as sealing. These items were then placed on an Araldite block which fitted over two gold plated brass electrodes as shown in Fig. 2. The surface temperature was determined from the average indication of ten Chromel-Alumel thermocouples attached to the base of the test specimen, and situated so as to measure the temperature distribution across the length and width of the sample. Measured temperature profiles indicated that approximately 96 percent of the boiling area was isothermal.

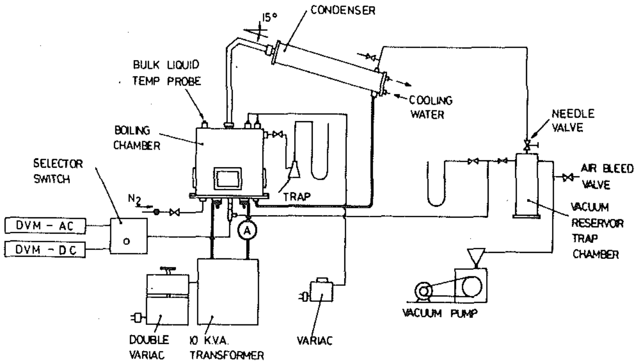

Fig. 1 Schematic diagram of experimental apparatus

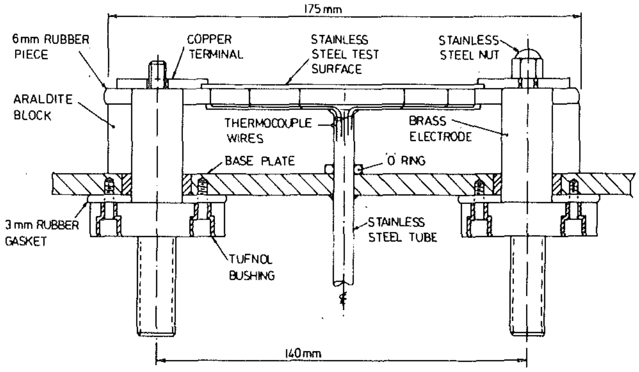

Fig. 2 Test surface assembly

---

[1] Analar water is a double de-ionized commercial product obtained from British Drug Houses.

Contributed by the Heat Transfer Division for publication in the JOURNAL OF HEAT TRANSFER. Manuscript received by the Heat Transfer Division December 14, 1979.

Tests were carried out with flat specimens of varying surface roughness, made of type EN 58E stainless steel measuring nominally 100 × 50 × 1.6 mm. The variation in surface roughness was produced by a vaqua blasting technique, which consists of the impingement on the surface at high pressure of an alumina particle suspension in water.

Low pressure operation was achieved by evacuating the system from the cold end of the condenser which reduced loss of vapor to a negligible level. Pressure inside the chamber was regulated by a throttling needle valve connected to a vacuum reservoir-trap chamber. System and vacuum pump pressures were measured with mercury-in-glass manometers.

Heating of the test surface was accomplished by the passage of a heavy a-c current through the specimen at low voltage from a transformer which was regulated by a double variac.

The apparatus was dismantled completely at the conclusion of each experiment and cleaned dry of all the residue of the test liquid. Prior to each experiment, the test surface was cleaned with acetone before the introduction of the test liquid. A more detailed description of the apparatus, instrumentation and measurement is given by Joudi and James [3].

Surface Contamination and Associated Experimental Refinements

Contamination as referred to here is not the normal tarnishing of a surface which causes what is known as aging in boiling research. Rather, it is the appearance of small circular "doughnut" shaped spots, of approximately 0.5 mm in diameter, at the base of boiling bubbles. In fact, the total number of nucleation sites can be assessed by counting the number of these spots at the end of a test. In this work it was observed that, generally, these spots became larger and darker in color with prolonged or more vigorous boiling. Two different forms of surface contamination were encountered, the first with methanol, and the other with water, each of which was used as a test liquid boiling on stainless steel test surfaces. The two types of contamination are described separately, together with the consequent refinements of the experimental apparatus which were employed to combat the contamination.

The photograph in Fig. 3 was obtained using a Scanning Electron Microscope (SEM), and shows spots which were incurred by methanol contamination. Small sections of a methanol contaminated surface were examined, for analysis, at high resolutions in an SEM, and at even higher resolutions under an Electron Probe Microanalyzer (EPM). Figure 4 represents a scan with the EPM across the edge of a crater (spot) from the outside to the center of the crater, showing zinc ion concentration. The peak of the graph, above background noise, was a result of concentration of zinc deposit on the surface, the density of which diminished as the scan approached the clean centre of the crater. With the EPM contamination spots were analyzed for concentrations of iron, copper, nickel, chrome, magnesium, lead, manganese and zinc. Of these elements, only zinc was detected, and upon comparing its content to a standard, approximately 2.5 percent zinc was found in the annular space.

Figure 5 is a qualitative analysis obtained with the SEM of the constituent elements, immediately under the electron beam of a test section containing methanol contamination spots. The very high peaks correspond to the presence of the parent stainless steel material, i.e., iron, nickel and chrome. The smaller peaks represent other elements, and in particular zinc, which is present in all its phases. An aluminium peak is evident and is caused by deflections from the specimen's aluminium mounting stub, whilst a small sulphur peak is attributed to the parent stainless steel material, which more often than not, contains small amounts of sulphur. Identification of the elements present is accomplished by determining the energies of the peaks in the spectrum. A marker is positioned on to each peak shown

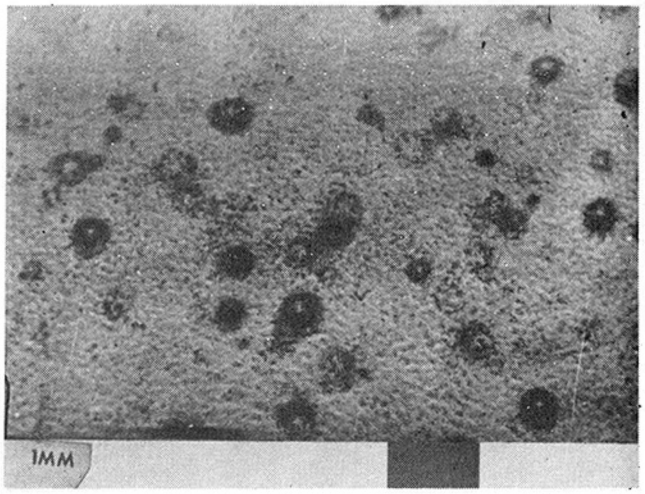

Fig. 3 Evidence of heating surface contamination

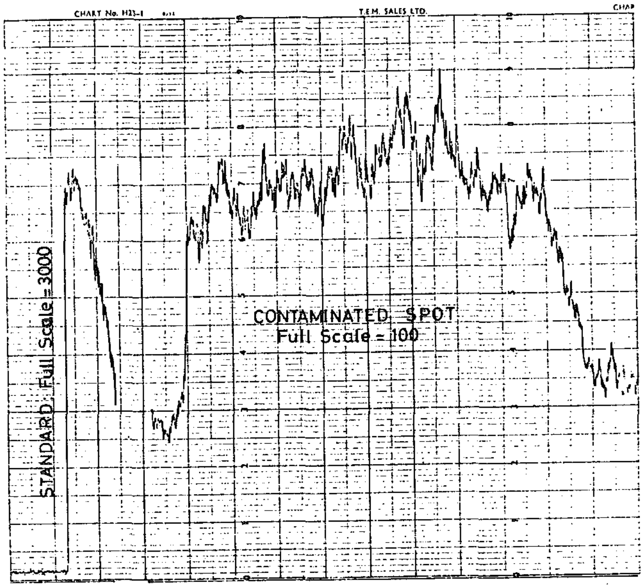

Fig. 4 Electron probe microanalyser: scan of surface contamination

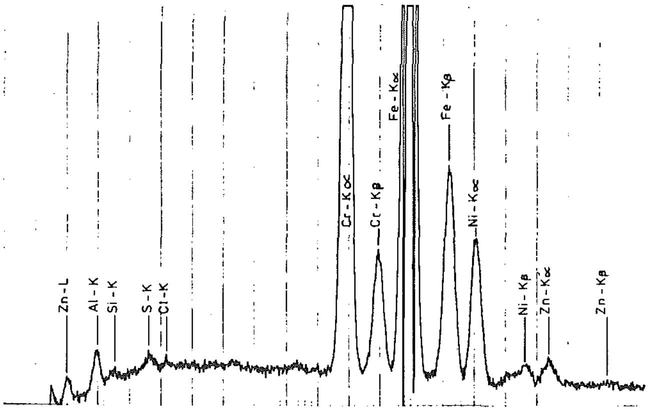

Fig. 5 Scanning electron microscope: analysis of a contamination spot

Nomenclature

q/A = heat flux
T_w = heated surface temperature
T_{sat} = liquid saturation temperature

in the spectrum and direct readout is obtained of the energy level of the peak.

The above analyses indicate clearly the presence of zinc in the spots of contamination which are produced by the boiling of methanol. The source of zinc is the dezincification of brass, which comprises a copper rich phase and a zinc rich phase. Zinc ions dissolve in the boiling methanol forming a white coloured zinc oxide, which precipitates on the boiling surface at the base of bubbles, once its concentration exceeds a certain value. The generation of boiling bubbles accentuates precipitation, and in particular at the base of bubbles where the surface is hottest. This type of contamination was totally eliminated by replacing all the original brass fittings of the boiling chamber with stainless steel fittings, and by gold plating the brass electrodes and the copper terminals of each test piece. Another necessary measure was the distillation of methanol prior to its use in a boiling test, thus eliminating possible dissolved solids.

The second type of surface contamination was localized corrosion, which was encountered with water boiling on the stainless steel heating samples. Microscopically, a vaqua blasted test surface is very rough and contains innumerable irregularities that could be considered as pits, as can be observed from Fig. 6. Stainless steel is a ferrous alloy, and in a smooth surface the distribution of alloys is uniform. However, on a rough surface the distribution of alloys is nonuniform, and a higher concentration of iron is obtained in pits, which consequently makes them more readily corrosive. From the microscopic pits in the surface, iron ions dissolve in the boiling water to form ferrous oxide with the oxygen dissolved in the water. This corrosion product appears on the surface at the mouth of the pit as ferric oxide (rust) and an accumulation of this product forms a small brown spot.

Corrosion spots with water occurred at the base of bubbles, as did those of methanol contamination. The shape of these spots was exactly the same as those of Fig. 3. Pits were not only a source of iron ions but also acted as bubble nucleation sites. In fact, the ebullition cycle of a bubble acted as a pump for ion transportation from inside the pit to the cavity mouth, while the successive dryout and rewetting at the base of a bubble stream provided an excellent condition for the supply and deposition of the corrosion products. Ross [4] reviewed the effects of heat transfer on the corrosion phenomenon, and stated that special features were introduced with boiling from a heated surface. Accelerated reaction rates between liquid and surface were suggested as a consequence of dryout and rewetting of the surface by a boiling liquid. In addition, electric heating of the test surface together with the use of dissimilar metals under boiling conditions might possibly set up a galvanic action, which would make matters worse. The extent of such a reaction could not be assessed, however, and no apparent effect of a galvanic action was observed.

Corrosion spots could not be analyzed by a Scanning Electron Microscope, because the presence of iron in a spot would be masked by the abundant iron of the parent stainless steel material. Peaks, similar to those of Fig. 5, for contaminant material would not be obtained. This would be particularly the case when the thickness of the corrosion product is less than 10 μm, which in fact was the situation encountered in this work.

To reduce the rate of corrosion of the stainless steel, oxygen dissolved in the water must be removed. A general approach for the removal of dissolved oxygen from water has been to employ prolonged nitrogen sparging of the water in a packed column. Nitrogen mechanically removes the dissolved oxygen by mixing with and replacing it.

In the present work, double de-ionized Analar water was sparged with nitrogen for several hours before using it in a test. Bubbling with nitrogen was continued inside the rig for the duration of a test. This also provided an inert nitrogen atmosphere inside the rig, which minimized possible redissolution of oxygen in the condensing vapors. The use of double de-ionized water with adequate nitrogen sparging eliminated corrosive contamination of the heat transfer test surface.

Several components of the apparatus, employed at the preliminary stage of experimentation, were subsequently found incompatible with one or more of the boiling test liquids, or were contributing to the contamination of test surfaces.

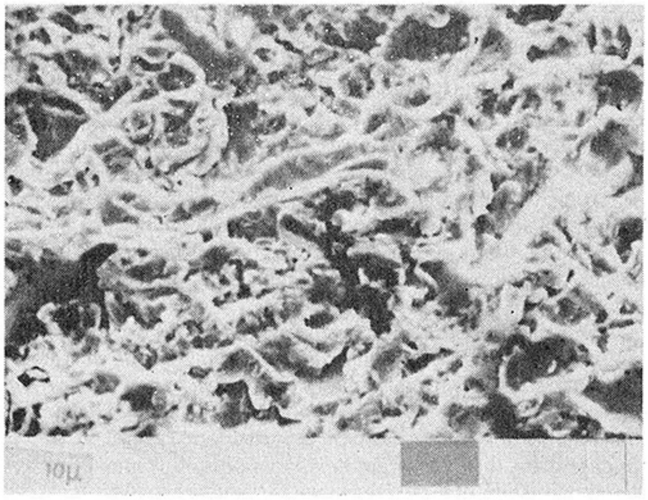

Fig. 6 Electron micrograph of surface finish

Consequently, all the brass and copper electrical terminals were gold plated, all fittings were manufactured from glass and stainless steel, silicone rubber was used for gaskets and pure natural rubber para B was used to seal the underside of the test specimen. It was found necessary to pre-treat the rubber prior to installation. Full information covering these experiments is recorded by Joudi [5].

Results and Discussion

Conditions of surface contamination appeared in the form of small spots at nucleation sites when a stainless steel test surface was boiled in water or methanol. In water the spots were the result of localized corrosion of the surface, whereas in methanol these spots were the result of the deposition of zinc oxide at bubble sites. Reproducibility of boiling data was established for several stainless steel test surfaces and experimental conditions. However, for the purpose of this presentation typical results of only one specimen are presented.

As a consequence of surface contamination, higher temperature differences were continually required for a given value of heat flux. This was true not only from test to test, but also at any one power input setting. In a single test, the surface temperature continued to increase with time as the contamination became more severe with sustained boiling.

Refrigerant R-113 which is sometimes used as a strong cleaning agent, was found to cause a reversal of the pattern of surface aging. A surface which was originally boiled in water and then in R-113, and then boiled again in water exhibited a marked increase in the number of bubbles. In the latter test (with water) this augmentation in bubble population was accompanied by a substantial reduction in surface temperature for the same values of heat flux as those originally obtained in the initial test. This phenomenon will be termed "rejuvenation" of a boiling surface and is illustrated in Fig. 7, together with the effect of surface contamination.

It would facilitate interpretation of Figs. 7 and 8 if the sequence of experimental runs is presented at this point. Tests were conducted in the chronological order listed in the following table.

Fig.	Curve	Run	Liquid	Notes
7	I W	1	Water	Fresh surface
8	I R	1,2	R-113	
7	II W	1	Water	Rejuvenation
	III W	1	Water	
	IV W	1,2,3	Water	Nitrogen sparged water
8	II R	3,4	R-113	
9	V W	1,2	Water	Second rejuvenation

The data presented in Fig. 7 were obtained with a flat specimen of surface roughness 0.67 μm in boiling water at atmospheric pressure. Curve I W was obtained by boiling the fresh surface in de-ionized—

three times distilled water. For this test, laboratory tap water was first distilled, then de-ionized in a "Permutit Mark 7" de-ionizer, and finally twice distilled in an all glass apparatus. The test was carried out in the rig with its final refinements incorporated for the reduction of contamination, but the liquid was not sparged with nitrogen. At the conclusion of this experiment with the fresh specimen, faint brown spots were observed on the surface as a result of localized corrosion. According to well established reports (e.g., Rohsenow and Choi [1]) in the published literature concerning the performance of a boiling surface, the results obtained with this fresh specimen should give lower temperatures, for the same heat flux, than subsequent experiments.

This surface was next boiled in refrigerant R-113 on two consecutive days for a minimum of three hours per test, to investigate whether or not contamination with this liquid would occur. As can be observed in Fig. 8 curve I R, the results are reproduced remarkably well in the two tests with R-113. It has been reported by Akagawa, et al. [6], among others, that refrigerant R-113 as well as other organic refrigerants decompose at very high temperatures under conditions of film boiling. Fouling on platinum heating wires was observed and measured to be 0.1–2 μm in thickness depending on the degree of decomposition of the liquid refrigerant and the severity of contamination. However, it was also reported that at temperatures below 100°C, R-113 was very stable, and that no deposit was built up in nucleate boiling. In the present work almost exact reproducibility was obtained for tests with refrigerant R-113 and no contamination of any sort was encountered with this liquid. In fact, its cleaning action is thought to dissolve possible contaminants which might have built up on the surface during tests with other liquids.

The surface was next boiled in double de-ionized Analar water in order to determine whether this high purity water would alleviate the corrosion problem. Contamination was still present but to a slightly lesser extent. However, the remarkable change in the boiling surface performance was striking as can be seen in curve II W of Fig. 7. A substantial reduction in ($T_W - T_{\mathrm{sat}}$) has occurred as a result of the intervening experiment with boiling R-113. The test surface rejuvenated with a noticeable increase in bubble population accompanied by a decrease in bubble diameter as compared with the results of the fresh surface (curve I W). These differences were visually observed. The so-called ageing effect is thus reversed. As mentioned above, surface rejuvenation is attributed to the dissolution in R-113 of contaminants which reduce cavity size or choke the cavity mouth. Further, refrigerant R-113 cleanses the surface of oxide film thus activating cavities that would otherwise be inactive. A similar hypothesis was put forth by Turton [7] concerning the behaviour of a stainless steel tube in boiling water and refrigerant R-11 under the influence of increased gravity and pressures higher than atmospheric. However, Turton explained what might be called a rejuvenation of the surface in successive tests with water as being the result of contamination which changed the wetting properties of the surface. Such contamination was said to increase the effective cavity size and reduce the superheat required for nucleation. Contamination being the cause of surface rejuvenation in water seems very unlikely in the light of what has been put forward, and also in what follows.

Another attempt was made to eliminate surface corrosion, this time by using distilled double de-ionized Analar water. The results of the experiment are shown in curve III W of Fig. 7. The shift in the curve to the right may be caused by the contamination of the surface incurred in the previous experiment of Curve II W, even though the surface was thoroughly cleaned with acetone prior to the test. In spite of the liquid being distilled and double de-ionized, localized corrosion still occurred although to a much lesser extent.

The result of the first test with nitrogen sparged Analar water is shown in curve IV W of Fig. 7. Again, a small shift of the curve to the right is observed due to the contamination produced in the previous test (Curve III W). However, at the end of this particular experiment no visible traces of corrosion spots whatsoever could be detected on the surface. Corrosion was inhibited due to the deoxygenation of the water by the sparged nitrogen gas, which removed the dissolved oxygen as described earlier.

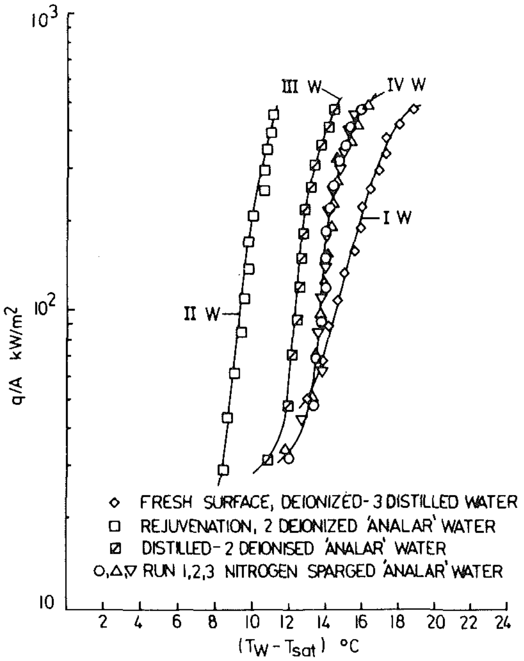

Fig. 7 Surface rejuvenation, contamination, and reproducibility of boiling data with water

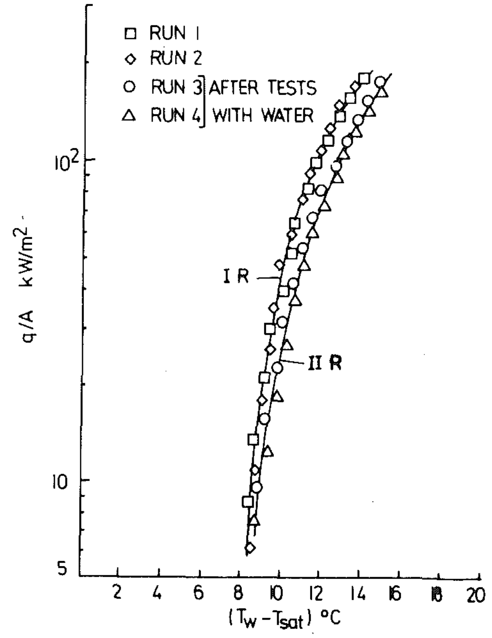

Fig. 8 Effect of order of testing of liquids on boiling data of R-113

The successive step-wise change in the characteristic performance of a surface, such as shown in curves II W, III W and IV W of Fig. 7, is what may be attributed by some investigators to so-called aging of a surface, particularly concerning boiling experiments with water. Fand and Keswani [8] report on the particulars of the ageing problem associated with sub-cooled boiling of water from a stainless steel tube. They stated that a set of five experimental measurements corresponding to five increasing values of heat flux were repeated in total again and again until the test cylinder was aged; that is, until two consecutive sets of five measurements were negligibly different. It was reported that this situation occurred after six hours of operation, and the data presented at one heat flux value for two consecutive sets of measurements indicated a difference of approximately 0.7°F between the two measurements. Furthermore, after aging the surface was activated only for the minimum time sufficient to gather data. It would not be wise to speculate, but in the light of what has been mentioned concerning contamination, it would not be unreasonable to assume that some degree of surface contamination was taking place, the results of which were being attributed to the so-called aging effect.

In experiments with copper tubes boiling in refrigerant R-11, Gorenflo [9] reported that constant values of heat transfer coefficient were obtained only after 60–80 hr of continuous boiling, and that the final value was approximately 12 percent less than that obtained with a fresh surface. No assessment was made of the surface condition, but for copper such a trend would most probably be due to extensive tarnishing and oxidation of the surface.

A second test (run 2, curve IV W) of three hours duration with nitrogen sparged Analar water and the same surface was conducted four days after the first run. Immediately after this second test, the power input to the specimen was turned off for one hour whilst the liquid was continually boiled by the auxiliary heater and sparged with nitrogen. After this period, another test run (No. 3) was then carried out, the results of which together with those of run No. 2 are shown in Fig. 7, curve IV W. It can be clearly observed that leaving the surface clean and dry for four days between runs 1 and 2, and that also the prolonged boiling of test runs 2 and 3 did not affect the reproducibility of results. The variation in ($T_w - T_{\text{sat}}$) for the same heat flux in runs 1, 2 and 3 with nitrogen sparged Analar water was less than 0.5°C, which is well within the experimental accuracy of ± 0.4°C.

It is well known that corrosion cannot be completely eliminated. However, localized corrosion of the test surfaces employed in this work was inhibited to a large degree by using nitrogen sparged double deionized Analar water, such that experimental data obtained within several hours or indeed several days of operation can be totally relied upon and reproduced. In the light of this, the concept of a so-called aging effect should be critically scrutinized, particularly for boiling experiments in water.

Due to the rejuvenation of the surface for experiments with water (curves I W and II W, Fig. 7), it was considered important to investigate the influence of the order of boiling of the liquids. Two test runs (3 and 4 curve II R, Fig. 8) were made with refrigerant R-113 on two consecutive days, one run per day, after all the tests with water mentioned above had been completed. As can be observed from Fig. 8, curve II R, the data are remarkably reproducible for these two particular tests but are not the same as those previously obtained (curve I R). The difference between the two curves is the result of a change in surface condition due to the intervening tests with water.

The next logical step was to determine whether the surface would again rejuvenate in water after the last tests with R-113. Two further tests (runs 1,2 curve V W) were carried out with N_2 sparged Analar water the results of which are shown in Fig. 9. A second rejuvenation did occur with a visually observed increase in bubble population and a reduced bubble diameter, as was the case for the first rejuvenation test (curves I W and II W, Fig. 7). However, the change in surface performance in this case was much less pronounced than that of Fig. 7. The data of run 2 Fig 9 are closer to the values of the reproducible experiments with water (curve IV W, Fig. 7) than those of run 1. It thus appeared as if the surface was aging, without corrosion.

Tests with boiling pure methanol were then conducted after the liquid had been distilled in an all glass apparatus with considerable care being taken to minimize absorption of water moisture from the atmosphere, for which methanol has a very high affinity. Distilled pure methanol was sparged with nitrogen, only inside the pool boiler for the duration of an experiment. Reproducibility of data with boiling methanol is illustrated in Fig. 10 for all operating pressures. The time intervals between the successive tests, as indicated in the figure, are of the order of days and weeks.

Changes in surface performance obtained by increasing and decreasing the power input in established boiling were encountered with all the test liquids. For the range of heat flux in fully developed boiling, the surface temperature with increasing power input was slightly lower than that obtained with decreasing power input for the same value of heat flux. The difference in temperature at any one setting was between 0.25 and 0.5°C. This small variation was systematic and present in all experiments and was attributed solely to the effect of the heat capacity of the heat surface assembly. On this basis, data were recorded only for decreasing heat flux, so that consistent values of surface temperature would be obtained.

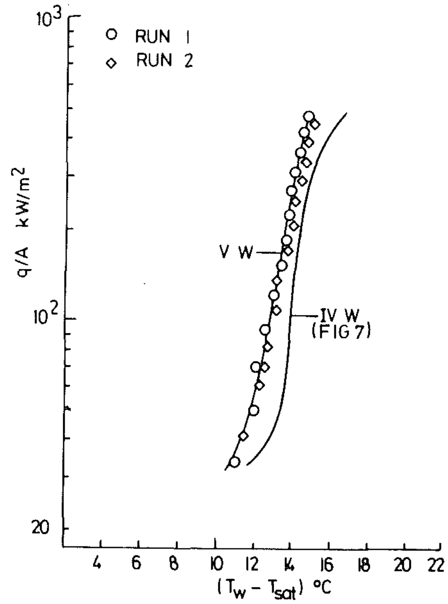

Fig. 9 Second rejuvenation of surface in water

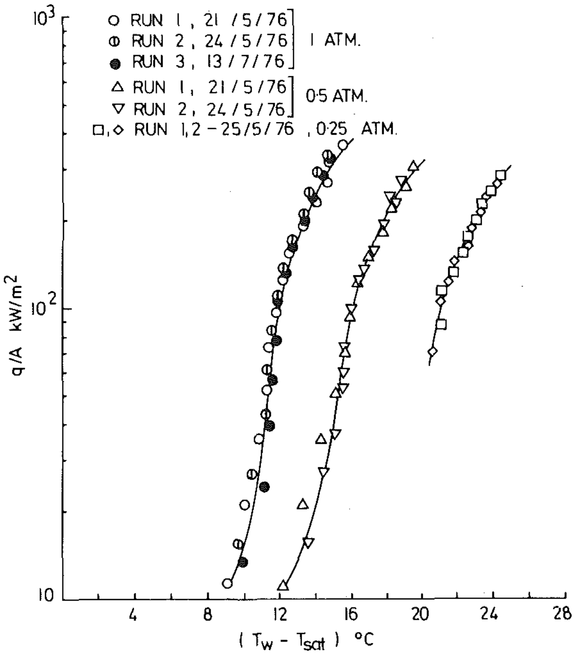

Fig. 10 Reproducibility of data in boiling with methanol

Due to the changes in surface performance associated with the order of boiling of the liquids, it is recommended that tests with surface liquid combinations described in this work be carried out firstly with refrigerant R-113 then with methanol, and lastly with water.

Conclusions

Contamination of a heating surface should not be associated with the so-called ageing effect of a boiling surface. Localized corrosion of a stainless steel heating surface in boiling water can be inhibited by nitrogen sparging of double de-ionized water.

Dezincification of brass components and contamination of a test surface in methanol can be totally eliminated by gold plating the brass, distilling the methanol, and employing rig components which are nonreactive with methanol.

Rejuvenation of a stainless steel heating surface can be effected by boiling the surface in a strong cleaning agent such as refrigerant R-113 which dissolves surface contaminants.

The order of boiling of liquids on a given test surface can result in variation in boiling characteristics with each liquid due to rejuvenation or oxide film deposit on the surface.

Acknowledgments

Thanks are due to Dr. J. A. Richardson of the Corrosion and Protection Centre, UMIST, for much useful discussion.

References

1 Rohsenow, W. M. and Choi, H. Y., *Heat, Mass and Momentum Transfer*, Prentice Hall, International, London, 1961.

2 Nestrueva, E. I., Romanovskii, I. M., and Kashinskii, V. I., "Some Aspects of Heat Exchange During Boiling," *Teploenergetika*, Vol. 23, No. 6, (1976), p. 12.

3 Joudi, K. A., and James, D. D., "Incipient Boiling Characteristics at Atmospheric and Sub-Atmospheric Pressures," ASME JOURNAL OF HEAT TRANSFER, Vol. 99, 1977, p. 398.

4 Ross, T. K., "Corrosion and Heat Transfer—a review, *"British Corrosion Journal,"* Vol. 2, 1967, p. 131.

5 Joudi, K. A., "Surface Geometry Variations in Nucleate Pool Boiling," Ph.D. Thesis, UMIST, Manchester, UK, 1977.

6 Akagawa, K., Sakaguche, T., and Fujii, T., "Influence of Fouling on Boiling Heat Transfer to Organic Coolants," 5th Int. Heat Transfer Conference, Tokyo. JSME, Vol. IV, Paper No. B1.6, 1974, p. 25.

7 Turton, J. S., "The Effects of Pressure and Acceleration on Pool Boiling of Water and Arcton 11," *International Journal Heat Mass Transfer*, Vol. 11, 1968, p. 1295.

8 Fand, R. M. and Keswain, K., "The Influence of Sub-Cooling on Pool Boiling Heat Transfer from a Horizontal Cylinder to Water," *Proceedings 5th International Heat Transfer Conference Tokyo*, JSME, Vol. IV, Paper No. B1.3, 1974, p. 11.

9 Gorenflo, D., "Zum Wärmeübergang bei der Blasenverdampfung an Rippenrohren," Diss T. H. Karlsruhe, W. Germany, 1966.

Destabilization of Film Boiling Due to Arrival of a Pressure

Shock: Part I Experimental[2]

A. Inoue[1]
S. G. Bankoff

Chemical Engineering Department,
Northwestern University,
Evanston IL 60201

Transient heat transfer from an electrically-heated 3 mm o.d. horizontal tube, initially in subcooled film boiling, was measured immediately after passage of a shock wave of 1–5 × 10^5 N/m^2 over-pressure. The fluids tested were Freon-113 and 95 percent ethanol-5 percent water at initially 0.5–2 × 10^5 N/m^2 at 22–24°C. Transient heat transfer rates, averaged over 0.5–1 ms after vapor film collapse, ranged up to 20 times the steady-state value. The maximum transient flux occurred at supercritical contact temperatures, with frequently a minimum in the range of contact temperatures between the homogeneous nucleation and the critical temperature. Photography at 5000 frames/s showed apparently complete vapor film collapse within one or two frames, followed by re-establishment of film boiling in ∼1 ms, and eventually nucleate boiling in ∼100 ms. The surface temperature which gave the highest peak transient flux shifted appreciably with increasing shock pressure, which indicates some compressibility even after "contact" was made. Implications for vapor explosions are discussed.

1 Introduction

Violent, or even explosive, boiling may result when a very hot liquid, such as molten UO_2, steel or aluminum, is mixed rapidly with a colder, vaporizable liquid, such as sodium or water. Such processes, designated generically as fuel-coolant interactions (FCI), are of concern in the nuclear reactor field, among others. It is believed that an important step in the triggering of small-scale explosions and in the triggering and propagation of large-scale explosions consists of the destabilization of the film boiling resulting from coarse premixing of the two liquids. Destabilization is thought to be favored by a decrease in the fuel or coolant temperature (or both), increase in relative velocity of the two fluids, or by a sudden increase in pressure. However, the time scales for the pressure rise in explosive boiling are 0 (10^{-4}) s, so that it is very difficult to obtain quantitative information in liquid-liquid systems. It seemed likely, therefore, that useful information concerning the mechanics of triggering and propagation might be obtained by studying the transient heat transfer behavior of an horizontal electrically-heated nickel tube, initially in film boiling with respect to the surrounding subcooled liquid, upon arrival of a moderate pressure shock wave. In this part the experimental results with Freon-113 and ethanol over a range of initial pressure, final pressures, shock rise times, and surface temperatures are presented. The second part deals with a theoretical treatment of the vapor film collapse process.

There seem to be no previous studies with which the present results can be directly compared. In the general area of liquid-solid film boiling destabilization, Bradfield [1] and Stevens and Witte [2] plunged a hot graphite cylinder and a hot silver sphere, respectively, into cold water, and observed that a very rapid destabilization of film boiling (termed a "transplosion") occurred when the wall temperature cooled to a threshold value, usually above the critical temperature. In a different vein, a pseudofilm boiling phenomenon has been observed above the critical pressure of water, due to the rapid variation of specific heat in the neighborhood of the pseudocritical temperature [3].

2 Equipment and Procedure

A low-pressure vertical shock tube was constructed for measuring destabilization of film boiling on a horizontal nickel heater by plane shocks of up to 2 MPa overpressure (Fig. 1). It consisted of a test section constructed of thin-walled 50 mm o.d. stainless steel tubing separated from a high-pressure driver section by a thin mylar membrane. The pressure in the driver section was controlled by a regulating valve from 0–2 MPa. The membrane was broken by means of a piston actuated by a solenoid valve with a time delay adjusted by means of a needle valve. This time delay was necessary to prevent the electrical noise produced by opening the valve from contaminating the pressure transducer signals.

Prior to breaking the membrane the liquid was circulated at a low velocity by a pump through an external heat exchanger to maintain a constant temperature. When the shock was generated it traveled about 0.3 m down the test section through nitrogen and 0.11 m through the liquid before reaching the heated tube, and then an additional meter through the liquid column to reach the bottom of the shock tube. Some metallic sponge was placed at the bottom of the test section to reduce the reflection of the shock.

A sidearm with a second diaphragm similarly controlled (MV2) was available for adjusting the shape of the pressure pulse, but was not used in this series of experiments.

The test section could be maintained initially at sub-atmospheric pressures by means of a vacuum pump protected by a cold trap. Just before starting each experimental run, the main test section was isolated from the circulation loop by the magnetic valves, after which the shock was generated. The steady-state pressures in the driver section and in the test section were measured by high precision pressure gauges, which were also used for calibration of the pressure transducer for transient measurements of the shock pressure. The thermocouple for measurement of the liquid temperature was placed below the glass section. The initial test section pressure could be controlled from the vapor pressure of the liquid to 0.5 MPa.

A series of orifices was used to control the pressure rise time. Assuming a first-order response of the form

$$P_\infty(t) = P_I + (P_F - P_I)\,(1 - \exp(-t/\tau_p)) \qquad (1)$$

the time constant could be varied from $\tau_p = 8 \times 10^{-5}$ s with no orifice to $\tau_p = 0.344$ s for a 1.58 mm orifice.

The test heater on which film boiling was established consisted of a centerless-ground nickel tube 3.0 mm o.d., 20–25 mm in length and 0.06–0.08 mm in thickness. The tube was silver-soldered at its ends to 4 mm dia copper busbars which entered the test section through

---

[1] Associate Professor, Research Laboratory for Nuclear Reactors, Tokyo Institute of Technology, O-okayama, Meguro-ku, Tokyo, Japan.

[2] This work was supported by the U. S. Department of Energy.

Contributed by the Heat Transfer Division and presented at the 19th AIChE/ASME National Heat Transfer Conference, July 27 to 30, 1980, Orlando, Fla. Revised Manuscript received by the Heat Transfer Division November 7, 1979.

teflon seals. The nickel tube was heated by passing direct current from six 200 amp-hr 6 V truck batteries connected in parallel. The current was controlled by a water-cooled stainless steel trombone rheostat with copper busbar slides driven by individual lead screws. In view of the significant axial heat losses to the busbars, 0.1 mm nickel wire leads were spot welded across the center 10 mm span for voltage measurements of the isothermal portion of the tube.

The time-dependent test heater power and average temperature were determined by measuring the current and voltage drop across the center section of the heater tube by means of a double bridge circuit. It was necessary to provide a bypass current sufficiently large to avoid burnout at the transition from nucleate to film boiling (Fig. 2). Details of the circuit design are given in Appendix I. The transient pressure was measured 70 mm above the test heater by a piezoelectric transducer with 2 μs rise time; 250 Khz resonance frequency; 700 N/m^2 resolution. The travel time of the shock from the transducer to the test heater was about 0.05 ms for a shock speed of 1500 m/s. The shunt voltage drop, the bridge unbalance voltage and the pressure transducer output were recorded on an FM tape recorder with a maximum frequency response of 5 KHz. The temperature of the test section, the pressure, the heat transfer coefficient and the heat flux were then calculated by playing the tape recorder into an analog computer at $\frac{1}{32}$ speed. The computer output was recorded on an oscillograph. Additional experimental details are given elsewhere [4].

The instantaneous heat flux, q_m, was calculated from a heat balance:

$$q_m = q_{ss} - M_t \frac{dT_m}{dt} \tag{1}$$

where q_{ss} is the steady power to the test heater per unit surface area; M_t is the mass of the test heater per unit surface area; and T_m is the average temperature of the center portion of the test heater. The heat transfer coefficient, h, was then computed from q_m and $\Delta T_m = T_m - T_\ell$. The peak transient heat flux, q_p, was estimated by fitting a tangent to the T_m versus t trace immediately after passage of the shock. Usually this trace exhibited a linear decrease over the first 0.5–1.5 ms. The thermal boundary layer thickness in a nickel slab is ~0.3 mm after 1 ms, so that the assumption of uniform metal temperature in the heater tube is acceptable. A more detailed analysis is given in Appendix II.

3 Experimental Results

Figures 3 and 4 illustrate the effect of the initial metal temperature on the pressure transducer and the heater temperature signals as a function of time after the passage of a sharp shock (rise time 80 ms). The vapor film disappears completely in 1–2 frames at 5000 frames/s. With an initial metal temperature of 195°C the film begins to be re-established after several milliseconds, but is collapsed again by the reflected shock from the bottom. This repeats several times. At no time is nucleate boiling visible, as evidenced by the absence of a milky appearance due to scattered light. With an initial metal temperature of 331°C, the liquid-solid "contact" time is shorter, and the vapor film which then forms is more stable. Nucleate boiling commences in times of order 10^2–10^3 ms.

Additional pressure and temperature traces are given in reference [4]. In general the temperature behavior just after the shock appears to fall into three classifications depending upon the initial wall temperature, T_{mo}, the shock pressure rise $\Delta P = P_F - P_I$, the pressure rise time, τ_p and the initial test section pressure P_I:

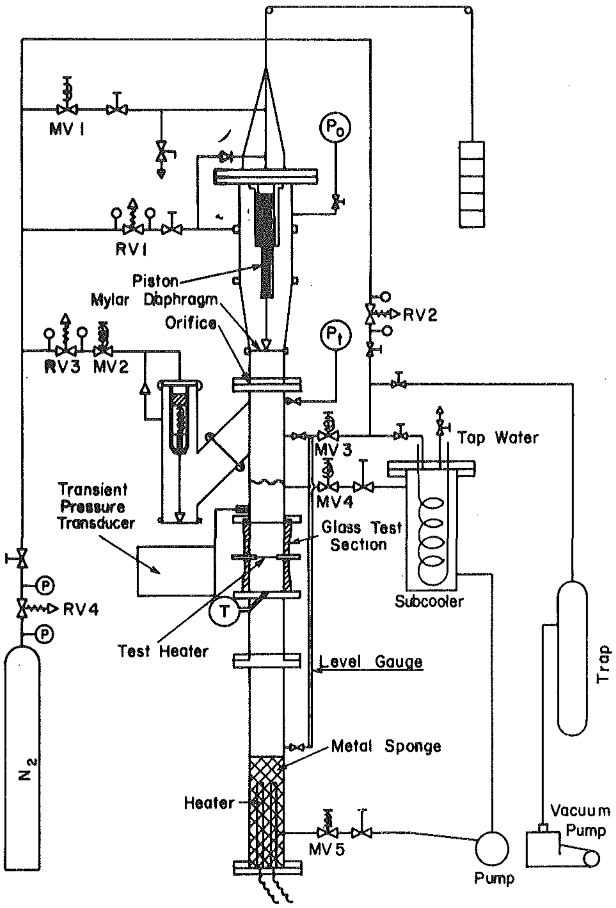

Fig. 1 Sketch of shock-tube experimental facility: T = temperature thermocouple; P = pressure gauge

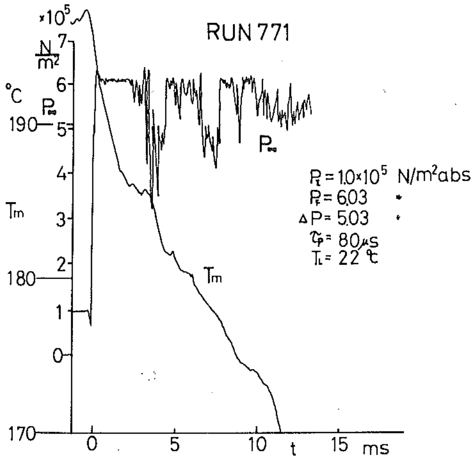

Fig. 2 Boiling curves under steady-state and transient conditions

Nomenclature

Mt = mass of heated tube per unit external surface area
P_I = initial pressure of test section
P_F = final pressure of test section
q = surface heat flux of heated tube
q_p = peak surface heat flux after shock passage
T = temperature
T_i = calculated interfacial contact temperature
T_m = average temperature of center portion of heated tube
T_{mo} = heated tube initial average temperature of center portion of heated tube
T_{sn} = spontaneous nucleation temperature
τ_p = pressure rise time

Subscripts

crit = critical
Homo = Homogeneous nucleation (same as spontaneous nucleation for well-wetting surface)
ℓ = liquid
max = maximum

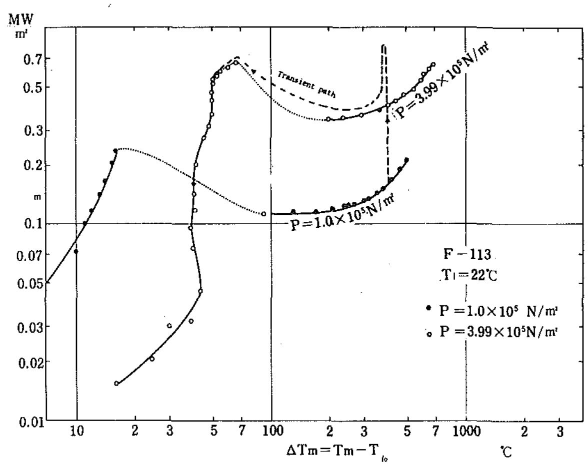

Fig. 3 Time histories of pressure 7 cm above heated tube and the metal temperature for sharp shock in freon 113 at the initial temperature 195°C

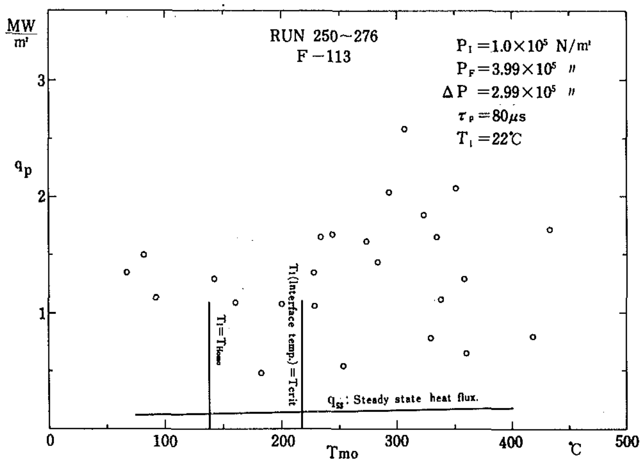

Fig. 5 Peak heat flux versus initial metal temperature at shock pressure $\Delta P = 2.99 \times 10^5$ N/m², pressure rise time $\tau_p = 80$ μs for freon-113

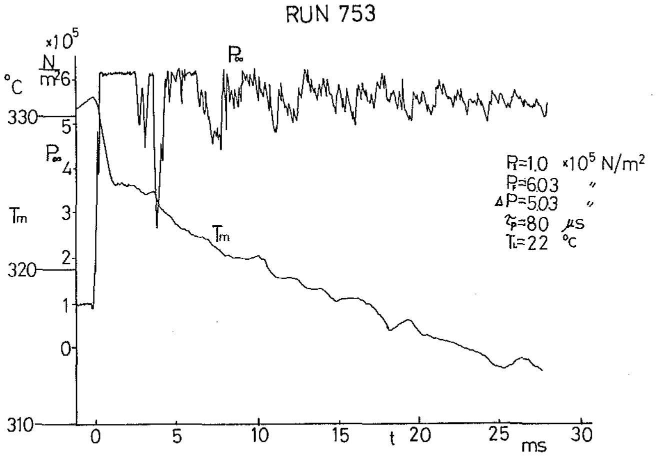

Fig. 4 Same as Fig. 3, except the initial metal temperature 331°C

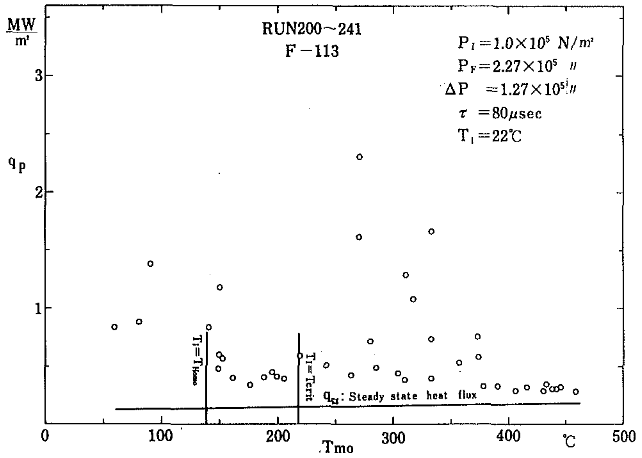

Fig. 6 Same as Fig. 5, except $\Delta P = 1.27 \times 10^5$ N/m²

1 No significant temperature change, corresponding to the ratio of the peak heat flux to the steady-state film boiling heat flux $q_p/q_{ss} < 1.5$, found under conditions where $\tau_p > 3.3$ ms; $T_{mo} \gg 300$°C or $T_{mo} \ll 300$°C

2 Slow temperature decrease but no rapid decrease in the initial 1 ms: $q_p/q_{ss} \sim 5$

3 A sharp temperature drop in less than 1 ms after the shock with $q_p/q_{ss} > 5$

There were no sharp transitions between each classification. The last category is favored by the following conditions: $T_{mo} = 250$–350°C, corresponding to reduced temperatures $T_r = 1.07$–1.28; $\Delta P_F/\Delta P_I > 3$; and $\tau_p < 0.15$s. The last two parameters seem to be more important than the other two. More detailed information concerning these parametric effects can be obtained by investigating the peak heat flux just after the shock.

The data for a large number of runs are summarized in the form of peak heat flux, q_p, as a function of the initial metal temperature, T_{mo}. Figure 5 shows the results for a sharp shock with Freon-113 initially at atmospheric pressure. There is a considerable scatter of q_p, partly due to errors in fitting a tangent to the curve of $T_m(t)$ at $t = 0$, and partly due to random variations in the initial vapor film thickness at the time of shock passage. Nevertheless, it is clear that the peak heat flux increases sharply with initial metal temperature *above* the critical temperature up to about 300°C and then begins to decrease. Since the interfacial contact temperature, T_i, is within 10°C of T_{mo}, this implies that very high heat fluxes can be obtained in the absence of true liquid-solid contact. It may be noted that Zyszkowski [5] also observed that a violent interaction with a molten copper drop in water occurs at a much higher theoretical contact temperature than the critical temperature of the liquid. However, the actual surface temperature may have been subcritical, due to the presence of a thick surface oxide layer. Similar results have been reported by Ando and Caldarola [11]. In the present tests the oxide layer, if any, was of negligible thickness on the polished nickel surface, and there seems to be no doubt that the initial contact temperature was supercritical. The maximum of q_p around $T_{mo} \sim 300$°C is thus independent of nucleation and bubble growth phenomena, which control the behavior below $T_{\rm crit}$. The heat flux maximum can be explained by the opposing tendencies represented by the increased temperature driving force for heat transfer versus the increased vapor film stability as the metal temperature increases. This is consistent with measurements of liquid-solid contact in steady-state film boiling of water from a gold-plated surface [6]. An attempt to make similar measurements here with an ethanol-water mixture was unsuccessful due to vibration of the fine electrical-resistivity probe after passage of the shock.

It is also interesting that q_p may exhibit an apparent minimum in the range $T_{sn} \leq T_i \leq T_{\rm crit}$, where T_{sn} is the spontaneous (in this case homogeneous) nucleation temperature, $T_{\rm Homo}$. This is the case with Freon 113, but not with 95 percent ethanol-5 percent water. The appearance of this minimum is the opposite of the behavior observed with liquid-liquid contacts, where this range is explosive, providing coarse premixing followed by a trigger (vapor film collapse) is achieved. There is, however, a simple and consistent explanation. Above T_{sn} film boiling is re-established very rapidly. With a solid (constant-area) surface this may correspond to decreased heat transfer below $T_{\rm crit}$, depending on the thermal properties of the solid and liquid. However, a liquid surface can exhibit very rapid increase in contact area due to pressure-driven local mixing, and hence increased energy transfer.

Figures 5 to 7 show the effect of the shock pressure, P_F, with an initial pressure P_I = 0.1 mPa, and all other conditions remaining constant. One finds that $T_{\max}$, the temperature at which the maximum q_p appears, increases with ΔP, the shock pressure jump, as shown in Table 1.

The effect of reducing the initial test section pressure, P_I, by a factor of two can be seen by comparing Fig. 8 with Fig. 5. It is seen that the heat transfer coefficient is increased by roughly a factor of two, indicating again closer approach of the liquid to the wall, with the peak heat transfer coefficient being roughly proportional to the initial mass of vapor per unit area of heater surface. This suggests that the relevant parameter may be P_F/P_I, rather than ΔP. This is in agreement with the experimental results of Sharon and Bankoff [9] for molten metal-water interactions, and also with the theoretical model, to be described in Part II. Figure 9 shows the effect of the pressure rise time, which was varied by employing orifices of different diameters. The peak flux becomes quite high for small τ_p, as shown for τ_p = 80 μs and 125 μs. For τ_p > 3.3 ms, q_p is less than twice the steady-state value, and is not strongly affected by T_{mo} or τ_p. One concludes that evaporation from the approaching liquid surface becomes important with slow rise times, but is negligible for fast rise times until the intervening vapor film becomes very thin.

The collapse of the vapor film was photographed at 5000 frames per second. The collapse of the vapor film appears to be completed at 0.1–0.3 ms after the shock. This is the same time interval during which the very sharp temperature drop and peak heat flux are observed. It is not possible to determine from these films whether the vapor film is completely or partially collapsed, but no liquid-vapor interface is visible. This condition continues until about 0.7 ms after the shock when the formation of a vapor layer becomes apparent. No small bubbles are observed during this time, as would be indicated by light scattering, and it would appear that nucleate boiling does not occur, as might be expected when $T_{io} > T_{hn}$.

The peak flux just after the shock for 95 percent ethanol-5 percent water at T_{mo} of 341°C is only slightly higher than for F-113 at 295°C, as shown by comparing Figs. 5 and 10, despite the fact that the thermal conductivity of the ethanol is three to five times greater than for Freon-113 in the liquid and vapor states. The minimum in q_p for $T_m < T_{\text{crit}}$ is also not apparent. The reasons for these differences in behavior are not known, but may be related to wetting properties, as well as thermal properties, of the fluid.

4 Discussion and Conclusions

The completeness of initial collapse of the vapor film will be discussed in more detail in Part II. We note here, however, that the observed maximum average heat fluxes can be accounted for heat conduction through a high-pressure vapor layer of 10^{-7} to 10^{-8} m thickness. Since the surface roughnesses are $0(10^{-7}$ m), at least partial liquid-solid "contact" is expected. We define contact here as the absence of an intervening vapor phase. Thus, at any particular location the local pressure may be above the critical pressure, which corresponds to local contact, or below the critical pressure, in which case a vapor layer can exist. True liquid-solid contact can exist only when $T_i < T_{\text{crit}}$. For $T_i > T_{\text{crit}}$ the fluid compressibility is significant in the neighborhood of the solid surface. Hence one would expect that the space- and time-average contact efficiency would increase with ΔP, as shown in Table 1.

One can draw from these results the important conclusion that the energy transfer in triggering and early propagation of vapor explosions occurs by rapid fragmentation and formation of new contact area *during* the elementary propagation cycle.

Another conclusion relates to the upper bound of metal vs. coolant temperature interaction zone (TIZ) reported by Reynolds, et al. [8] for small quantities of tin poured into water. The results of Table 1 suggest that this upper bound, corresponding to the establishment of effective contact, can be shifted upwards by a shock wave, corresponding to an energetic trigger. This is confirmed by recent mea-

Table 1

ΔP, MPa	$T_{\max}$, °C
0.13	270
0.30	300
0.50	330

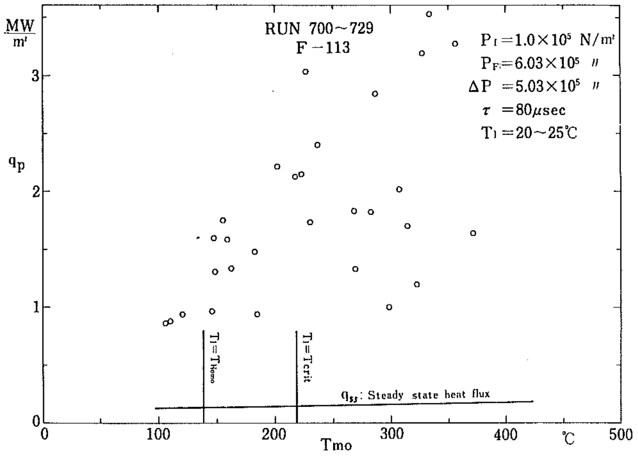

Fig. 7 Same as Fig. 5, except ΔP = 5.03 × 10^5 N/m²

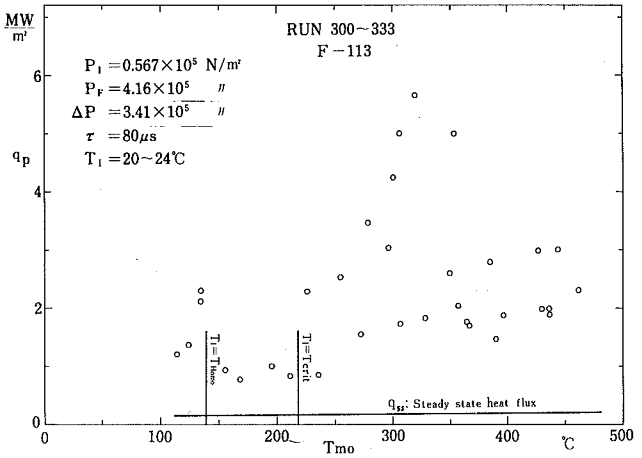

Fig. 8 Same as Fig. 5, except initial test section pressure P_I = 0.567 × 10^5 N/m²abs, ΔP = 3.41 × 10^5 N/m²

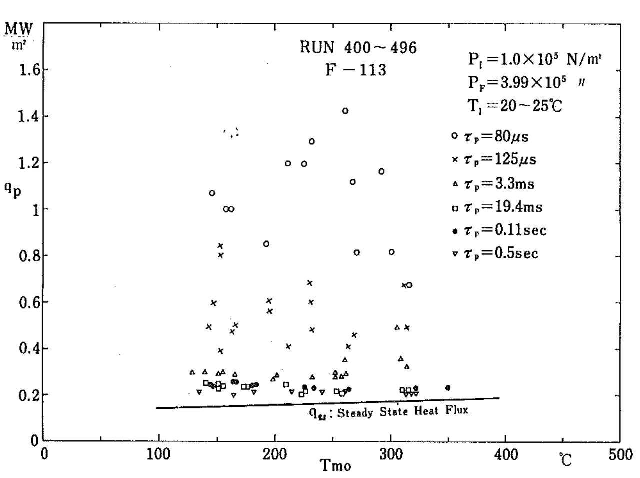

Fig. 9 Same as Fig. 5, except pressure rise time constant τ_p varied from 80 μs to 0.5 s

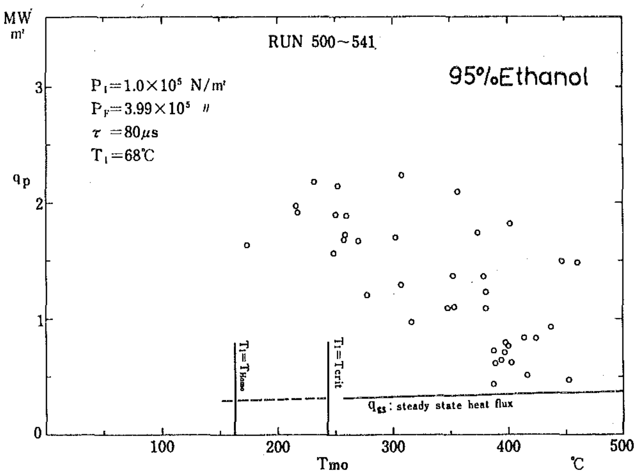

Fig. 10 Same as Fig. 5, except 95 percent ethanol-5 percent water at the liquid temperature 68°C

surements by Sharon and Bankoff [9] in a shock tube of liquid metal/water interactions with initially established film boiling. In fact, the plots of heat flux immediately after shock passage versus metal temperature shown in Figs. 5–10 are remarkably similar to plots of peak pressure versus metal temperature in molten tin-lead alloy/water interactions following shock wave passage (Sharon and Bankoff [9]).

These results further imply that vapor explosions can propagate in the supercritical contact temperature, but subcritical pressure, range, with only a weak pressure shock as the initial triggering event. In fact, no large-scale explosions have been reported when $T_i < T_{\text{crit}}$, and nearly all peak pressures obtained to date have been below the coolant critical pressure (Amblard and Jacobs [12]).

One can carry this reasoning one step further, and suggest that vapor explosions are nearly always propagated by boiling, or boiling-like, mechanisms. This means that at subcritical pressures behind the shock front mixing and fragmentation result from bubble growth and collapse. At supercritical pressures regions of large density variations can also exist, giving rise to similar behavior. However, the fact that "contact" is not uniform means that large pressure gradients *tangential* to the interface can exist. This may be the principal mechanism for rapid mixing. A simplified model for local mixing due to local variations in contact pressure is the "splash" theory of Ochiai and Bankoff [10].

References

1 Bradfield, W. S., "On Liquid-Solid Contact in Stable Film Boiling," Rpt. No. 36, State Univ. of New York, College of Engineering, Stony Brook, 1965.

2 Stevens, J. W., and Witte, L. C., "Destabilization of Vapor Film Boiling around Spheres," *International Journal of Heat Mass Transfer*, Vol. 16, 1973, pp. 669–678.

3 Hebel, W., and Decreton, M., "Mechanisms of Critical Heat Flux in a Stagnant Water Annulus," 2nd Multiphase Flow and Heat Transfer Symposium—Workshop, Miami Beach, Fla., Apr. 1979.

4 Inoue, A., and Bankoff, S. G., "Destabilization of Film Boiling due to Arrival of a Pressure Shock," Rpt. C00-2512-13, Chem. Eng. Dept., Northwestern Univ., Evanston, Ill., 1978; also in *Topics in Two-Phase Heat Transfer and Flow*, S. G. Bankoff, ed., ASME, N.Y., 1978, pp. 77–88.

5 Zyszkowski, W., "Experimental Investigation of Fuel-Coolant Interaction," *Nuclear Technology*, Vol. 33, 1977, pp. 40–59.

6 Yao, S. C., and Henry, R. E., "An Investigation of the Minimum Film Boiling Temperature on Horizontal Surfaces," ASME JOURNAL OF HEAT TRANSFER, Vol. 100, May 1978, pp. 260–267.

7 Hsu, Y. Y., and Graham, R. W., *Transport Processes in Boiling and Two-Phase Systems*, McGraw-Hill, New York, 1976.

8 Reynolds, J. A., Dullforce, T. A., Peckover, R. S., and Vaughan, G. J., "Fuel-Coolant Interactions—Some Basic Studies at the UKAEA Culham Laboratory," Paper SNI 6/2, Proc. Third Spec. Meeting on Sodium/Fuel Interaction in Fast Reactors, Tokyo, 1976.

9 Sharon, A., and Bankoff, S. G., "Fuel-Coolant Interaction in a Shock Tube with Initially-Established Film Boiling," *Proceedings ANS/ENS International Meeting on Fast Reactor Safety*, Seattle, Wash., Vol. 4, 1979, pp. 1796–1810.

10 Ochiai, M., and Bankoff, S. G., "A Local Propagation Theory for Vapor Explosions," Paper SNI 6/3, *Proceedings Third Special Meeting on Sodium/Fuel Interactions in Fast Reactors*, Tokyo, Japan 1976.

11 Ando, M., and Caldarola, L., paper presented at OECD CSNI Joint Interpretation Exercise on Selected Fuel-Coolant Interaction Experiments, Karlsruhe, Germany, Dec. 1980.

12 Amblard, M., and Jacobs, H., "Fuel-Coolant Interactions: The CORECT II VO₂-Na Experiment," *Proceedings ANS/ENS International Meeting on Fast Reactor Safety*, Seattle, Wash., Vol. 3, 1979, pp. 1512–1519.

APPENDIX I

Heating and Temperature Measurement Circuit

The power to be dissipated increased with heater temperature in constant-current heating, since the resistance increases with temperature, possibly resulting in departure from nucleate boiling (DNB). Therefore, insofar as possible a constant-voltage power circuit is desired. Another consideration is that the ends of the heated nickel tube will be cooler than the center portion, due to heat losses to the copper busbars to which the tube is attached.

To measure the average temperature of the uniform central region, a double bridge method was used. The bridge elements consisted of the test heater resistance R_t ($\sim 0.7 - 1.0 \times 10^{-3}\ \Omega$); a precision shunt resistance R_s ($5 \times 10^{-5}\ \Omega$); a variable bypass resistance, $R_b = R_t$, and a slide resistance R_v ($0.003 - 0.186\ \Omega$), made from 3 ft lengths of water-cooled stainless-steel tubing; a standard resistance R_c ($5\ \Omega$); and a decade box reading to four digits ($0 - 999.9\ \Omega$).

We assume that the resistance of the copper cables and the contact resistance of each connection can be neglected.

The resistance of the nickel heater is

$$R_t = R_{to}\,(1 + \alpha \Delta T_m), \tag{I-1}$$

where α is the temperature coefficient of resistivity, R_{to} is the test heater resistance at the DNB temperature and ΔT_m is the temperature rise of the heater above the DNB temperature. In this case it can be shown that

$$\frac{[Q]}{[Q_0]} = (1 + \alpha \Delta T_m) \left(\frac{1}{1 + \dfrac{K_1 \alpha}{1 + K_2} \Delta T_m} \right)^2 \tag{I-2}$$

where

$$K_1 = \frac{R_{to}}{R_s + R_{to}}$$

$$K_2 = \frac{R_b R_v}{(R_b + R_v)\,(R_s + R_{to})}$$

and $[Q_o]$ is the heater power at DNB, while $[Q]$ is the power at a temperature other than DNB.

In the present case $K_1 = 0.95$ (when $R_{to} = 10^{-3}\ \Omega$ at DNB), $R_b \div R_{to}$ and $R_v \gg R_{to}$

Therefore $K_x \div 1$. It then follows that

$$\frac{[Q]}{[Q_o]} = (1 + \alpha \Delta T_m) \left(\frac{1}{1 + 0.475\,\Delta T_m} \right)^2 \tag{I-3}$$

The curve of $[Q]/[Q_o]$ is shown in Fig. 10. From the intersection of the power curve with the film boiling curve it is seen that the temperature at DNB is limited to 520°C. However, in actuality the resistances of the copper cable and contacts are of the same order as that of the heater and the actual circuits, so that in the present equipment about a 20 percent decrease in power is measured at DNB.

APPENDIX II

Test Heater Surface Temperatures

As noted above, the average wall temperature of the nickel tube is determined by measuring the electrical resistance. The nonuniformity in the temperature in the axial direction can be avoided by measuring the resistance only of the central portion of the tube, but the radial differences may be significant under highly transient conditions.

a Temperature Difference at Steady-State. The temperature difference at steady-state between the mean metal temperature and the wall surface temperature is given by the steady-state heat conduction equation. For a steady-state surface heat flux $q_{ss} = 100$ w/cm², $\overline{T}_m - T_w = \frac{1}{3}\dot{Q}\,\delta_m{}^2/k_m = 0.40°\mathrm{C}$, where the tube wall thickness $\delta = 0.07$ mm, $\overline{T}_m$ is the average metal temperature and T_w is the wall surface temperature. This difference is therefore negligible for heat fluxes in the film boiling regime in this experiment (14–19 w/cm² for $T_w = 450°\mathrm{C}$).

b Temperature Difference under Transient Conditions.

$$\frac{\partial T_m}{\partial t} = \alpha_m \frac{\partial^2 T_m}{\partial x^2} + \frac{\dot{Q}}{\rho_m C_{pm}} \qquad \text{(II-1)}$$

$$\text{I.C. } T_m(x, 0) = T_w(0) + \tfrac{1}{2}\frac{\dot{Q}}{k_m}(\delta_m{}^2 - x^2)$$

$$\text{where: } k_m = \rho_m C_{pm}\alpha_m$$

$$B.C. \text{ at } x = 0\text{: } \left.\frac{dT_m}{dx}\right|_{x=0} = 0 \qquad \text{(II-2)}$$

$$\text{at } x = \delta\text{: } T_m(\delta, t) = T_w(t)$$

The space-averaged Laplace transform solution $[\overline{T}_m(p)]$ of equation (II-1) with conditions (II-2) is

$$\begin{aligned}
[\overline{T}_m(p)] - [T_w(p)] &= \frac{1}{3}\frac{\dot{Q}}{x_m}\delta_m{}^2\frac{1}{p} \\
&\quad + \left\{\frac{e^{q_m\delta_m} - e^{-q_m\delta_m}}{(e^{q_m\delta_m} + e^{-q_m\delta_m})^{\delta_m q_m}} - 1\right\}[T_w(p)] \\
&\quad + \frac{T_w(0)}{}\left\{\frac{e^{-q_m\delta_m} - e^{q_m\delta_m}}{(e^{q_m\delta_m} + e^{-q_m\delta_m})\,\delta_m q_m} - 1\right\} \\
&= \frac{1}{3}\frac{Q}{k_m}\delta_m{}^2\frac{1}{p} + \left\{1 - \frac{1}{\delta_m q_m}(1 - e^{-2q_m\delta_m})\sum_{n=0}^{\infty}(-1)^n e^{-2nq_m\delta_m}\right\}. \\
&\qquad \left(\frac{T_w(0)}{p} - [T_w(p)]\right) \qquad \text{(II-3)}
\end{aligned}$$

where

$$q_m \equiv \frac{p}{\sqrt{\alpha_m}}$$

(*i*) *Step Response of* $\overline{T}_m(t)$.

Let $T_w(t) = T_w(0) - \Delta T_w H(t)$ (II-4)

where $H(t) = 0, \quad t = 0$

$H(t) = 1, \quad t > 0$

Substituting Laplace transform of equation (II-4) into equation (II-3):

$$\begin{aligned}
[\overline{T}_m(p)] &= \frac{1}{3}\frac{\dot{Q}}{k_m}\delta_m{}^2\frac{1}{p} \\
&\quad + \frac{\Delta T_w}{p}\left(1 - \frac{1 - e^{-2q_m\delta_m}}{\delta_m q_m}\sum_{n=0}^{\infty}(-1)^n e^{-2nq_m\delta_m}\right) \qquad \text{(II-5)}
\end{aligned}$$

If we take $n = 0$ and 1, since we are only interested in small time behavior, and perform the inverse transformation, equation (II-5) gives

$$\begin{aligned}
\frac{\overline{T}_m(t) - T_w(t)}{\Delta T_w} &= 1 - \frac{2}{\sqrt{\pi}}\sqrt{t^*}\,(1 - 2\,e^{-1/t^*} + e^{-4/t^*}) \\
&\quad + 4\left(\operatorname{erf}\frac{1}{\sqrt{t^*}} - \operatorname{erf}\frac{2}{\sqrt{t^*}}\right) \qquad \text{(II-6)}
\end{aligned}$$

where

$$t^* = \frac{\alpha_m t}{\delta_m{}^2}$$

If this function is approximated by e^{-t^*/τ^*}, the time constant τ^* is

$$\tau^* = 0.33 \quad \text{or} \quad \tau = 0.33\frac{\delta_m{}^2}{\alpha_m} \qquad \text{(II-7)}$$

For the heated tube $\tau = 0.33\,(0.007)^2/0.1496 = 0.11$ ms, so that the time lag between the average and surface temperature may be neglected.

(*ii*) *Temperature Difference during Ramp Transient.* To get actual surface temperature $T_w(t)$ from the average metal temperature $\overline{T}_m(t)$, by rearranging equation (II-3):

$$\begin{aligned}
[T_w(p)] - \frac{T_w(0)}{p} - \frac{1}{3}\frac{\dot{Q}}{k_m}\delta_m{}^2\frac{1}{p} &= \delta_m q_m\,(1 + e^{-2q_m\delta_m})\sum_{n=0}^{\infty} e^{-2q_m\delta_m} \\
&\quad \times \left\{[\overline{T}_m(p)] - \frac{\overline{T}_m(0)}{p}\right\} \qquad \text{(II-8)}
\end{aligned}$$

We truncate the series after the first term for a short transient:

$$\begin{aligned}
[T_w(p)] - \frac{T_w(0)}{p} - \frac{1}{3}\frac{\dot{Q}}{k_m}\delta_m{}^2\frac{1}{p} &= \delta_m q_m\,(1 - e^{-2q_m\delta_m}) \\
&\quad \left\{[\overline{T}_m(p)] - \frac{\overline{T}_m(0)}{p}\right\} \qquad \text{(II-9)}
\end{aligned}$$

By inverse transformation of equation (II-9)

$$\begin{aligned}
T_w(t) - T_w(0) - \frac{1}{3}\frac{\dot{Q}}{k_m}\delta_m{}^2 \\
= \mathcal{L}^{-1}\left[[\delta_m q_m\,(1 - e^{-2q_m\delta_m})\left([\overline{T}_m(p)] - \frac{\overline{T}_m(0)}{p}\right)\right] \qquad \text{(II-10)}
\end{aligned}$$

If $\overline{T}_m(t)$ is approximated as a ramp function, $\overline{T}_m(t) = \overline{T}_m(0) - \Delta\dot{T}_m t$, in the initial stage of the transient, one obtains, by substituting the Laplace transform of $\overline{T}_m(t)$ into equation (II-10),

$$\begin{aligned}
\frac{T_w(t) - T_w(0) - \frac{1}{3}\frac{\dot{Q}}{k_m}\delta_m{}^2}{\Delta T_m\,\delta_m{}^2/\alpha_m} &= \mathcal{L}^{-1}\left[[-\delta_m q_m(1 - e^{-2q_m\delta_m})\,\Delta\dot{T}_m\frac{1}{2p}\right] \\
&= -\frac{2}{\sqrt{\pi}}\sqrt{t^*}\,(1 - e^{-\frac{1}{t^*}} + 2\operatorname{erfc}\tfrac{1}{t^*} \qquad \text{(II-11)}
\end{aligned}$$

or

$$\frac{T_w(t) - \overline{T}_m(t) - \dot{Q}\delta_m/2k_m}{\Delta T_m\delta_m{}^2/\alpha_m} = t^* - \frac{2}{\sqrt{\pi}}\sqrt{t^*}\,(1 - e^{-\frac{1}{t^*}}) \qquad \text{(II-12)}$$

In our case

$$\begin{aligned}
T_w(t) - \overline{T}_m(t) - \frac{1}{2}\frac{Q}{k_m}\delta_m{}^2 \\
= 3.3 \times 10^{-4}\,\Delta\dot{T}_m\left(t^* - \frac{2}{\sqrt{\pi}}\sqrt{t^*}\,(1 - e^{-\frac{1}{t^*}})\right) \qquad \text{(II-13)}
\end{aligned}$$

or,

$$\leq 3.3 \times 10^{-4}\,\Delta\dot{T}_m \times 0.3$$

In the present experiments, the maximum of $\Delta\dot{T}_m$ immediately after passage of the shock was found to be 10240°C/s at $\dot{Q}\delta_m = 19$ w/cm². In this case, the maximum difference of temperature is $T_w(t) - \overline{T}_m(t) \leq 1.06°\mathrm{C}$, and hence is negligible.

Destabilization of Film Boiling Due to Arrival of a Pressure Shock[2]

Part II: Analytical

A. Inoue
Associate Professor,
Research Laboratory for Nuclear Reactors,
Tokyo Institute of Technology,
O-okayama, Meguro-ku,
Japan

A. Ganguli[1]
S. G. Bankoff
Chemical Engineering Department,
Northwestern University,
Evanston, Ill. 60201

Vapor explosions are believed to be triggered by the rapid collapse of film boiling of coolant in contact with molten fuel, probably due to local pressure waves from an initially small interaction. In Part I of this work the heat transfer during the first two ms after passage of a shock past a hot nickel tube surrounded by subcooled Freon-113 or ethanol was studied. The following important results were obtained: (1) The peak heat flux exhibits a maximum of a heater surface temperature of 280–350°C, depending upon the strength of the shock. This is well above the critical temperature, so that nucleation considerations are irrelevant. (2) The maximum of the peak heat flux envelope depends upon the shock ΔP, indicating that only partial contact is made upon collapse of the vapor film. (3) The collapse is rapid (1–2 frame at 5000 f/s), and is produced by relatively weak shocks ($\Delta P \doteq 2$–3 atm.). In the present work, the vapor film collapse is studied analytically, in order to obtain additional insight into the mechanism. A Lagrangian transformation due to Hamill and Bankoff is introduced to immobilize the moving boundary, and a polynomial temperature distribution in the transformed mass variable is assumed in the vapor region, as well as in the liquid region. This leads to a set of coupled nonlinear ordinary differential equations in the three regions, which are solved numerically. Two models were developed: (1) A detailed model, taking into account the Knudsen layers at the vapor-liquid and vapor-solid interfaces, and (2) a simplified model, in which these layers were neglected, and a linear temperature profile in the Lagrangian vapor phase variable was assumed. It is found that the initial vapor mass is a key variable determining whether collapse is achieved. In practice, this is a stochastic variable due to bubble departure, which explains the observed heat flux data scatter. The analytical results are in general agreement with the experimental data.

1 Introduction

Violent, or even explosive, boiling may result when a very hot liquid, such as molten UO_2, steel or aluminum, is mixed rapidly with a colder, vaporizable liquid, such as sodium or water. Such processes, designated generically as fuel-coolant interactions (FCI), are of concern in the nuclear reactor field, among others. It is believed that an important step in the triggering of small-scale explosions and in the triggering and propagation of large-scale explosions consists of the destabilization of the film boiling resulting from coarse premixing of the two liquids. Destabilization is thought to be favored by a decrease in the fuel or coolant temperature (or both), increase in relative velocity of the two fluids, or by a sudden increase in pressure. However, the time scales for the pressure rise in explosive boiling are $0\ (10^{-4})$ s, so that it is very difficult to obtain quantitative information in liquid-liquid systems. On the other hand, studies on the collapse of Leidenfrost boiling of single drops of ordinary fluids, such as ethanol or Freon, on molten Woods metal or solid metal surfaces due to a rapid increase in pressure indicate little difference in behavior [1]. Presumably this is due to high interfacial tension of the liquid metal relative to either the vapor or liquid, which tends to inhibit liquid-liquid mixing in this configuration. It seemed likely, therefore, that useful information concerning the mechanics of triggering and propagation might be obtained by studying the transient heat transfer behavior of an horizontal electrically-heated nickel tube, initially in film boiling with respect to the surrounding subcooled liquid, upon arrival of a moderate pressure shock wave.

Inoue and Bankoff [1] have reported experimental results with two liquids over a range of initial pressures, final pressures, shock rise times and surface temperatures. This paper presents two theoretical treatments of the vapor film collapse process, which are compared with the experimental data.

2 Model

Complete and simplified models are developed for the approach of the vapor-liquid interface toward the solid surface after the shock has passed. The aim of this analysis is to study the effect of several parameters on the peak heat flux and to estimate the possibility of direct contact.

Even the complete model represents a first-order approach to the actual phenomenon, which is considerably more complex. The surface roughnesses are of order 2μ, so that the calculation loses physical meaning for vapor layer thicknesses $\leq 1\ \mu$. In addition, the unstable vapor-liquid interface generates random waves, which may be quite large in amplitude compared to the small vapor layer thickness. Also, an unstable vapor dome forms at the top of the heated horizontal tube, releasing vapor bubbles nearly periodically, while the vapor layer at the bottom stagnation point is quite thin prior to the shock arrival. Hence the actual film collapse is expected to be asymmetric, which is not taken into account in these calculations. Finally, physical properties of the fluid (Freon 113) are either extrapolated from a low pressure, low temperature range (for vapor) or assumed constant (for liquid). Since the rise in gas pressure and temperature is considerable (often to supercritical values), this might cause some error in the results.

Since the characteristic lengths of the phenomenon are much smaller than the heater diameter, curvature effects can be neglected and the problem is treated in rectangular coordinates. The principal difficulty in solution arises from the fact that the moving boundary is induced by external forces and not by heat transfer. This sets it apart from other moving boundary heat conduction problems with change of phase and eliminates similarity solutions. Since it is probably impossible to get an analytical solution, numerical methods were used after simplifying or eliminating some of the equations. The complete model is shown in Fig. 1 and the following assumptions were made: (1) Metal temperature is uniform. (2) Molecular transport layers exist at both ends of the vapor layer. (3) No heat storage in the molecular layers. (4) Vapor follows the ideal gas law. (5) Pressure inside the vapor film is uniform. (6) Volumetric heat release rate in

---

[1] Present address: Heat Transfer Research, Inc., Alhambra, Calif.

[2] This work was supported by the U.S. Department of Energy.

Contributed by the Heat Transfer Division for publication in the JOURNAL OF HEAT TRANSFER. Manuscript received by the Heat Transfer Division November 7, 1980.

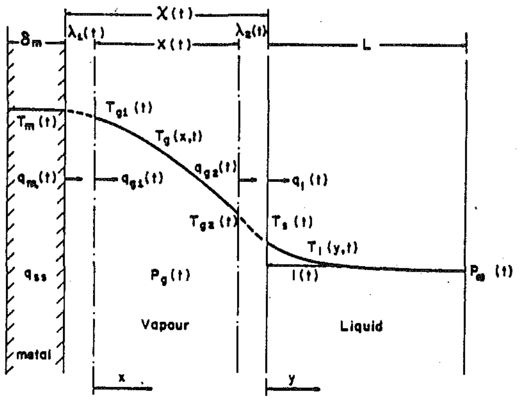

Fig. 1 Sketch of the model

metal is constant. (7) All viscous dissipation and gravity effects are negligible. (8) Constant liquid properties. (9) Velocity of vapor purely radial during collapse.

Assumption (1) has been justified by the analysis reported in Part I. Assumption (2) is required because (*a*) the influence of the Knudsen number becomes dominant when the vapor film gets thin, and (*b*) the heat flux, which goes toward infinity when the vapor thickness approaches zero, can be limited by considering the molecular transport mechanism. The third assumption is justifiable in view of the large heat flow and the negligibly small heat capacity involved. Assumption (4) is expected to hold since the gas is highly superheated. The fifth, seventh and eighth assumptions are customary, and assumption (6) reflects our experimental condition. Assumption (9) takes into account the short collapse times. Later, we will impose additional restrictions, as required to facilitate the solution. Thus, an energy balance on the metal tube gives:

$$q_m(t) = q_{ss} - \rho_m C_{pm}\, \delta_m \frac{dT_m(t)}{dt} \tag{1}$$

where the steady-state heat flux is

$$q_{ss} = \frac{I^2 R_t}{\pi D L_t} = \text{constant} \tag{2}$$

and

$$T_m(0) = T_{mo} = \text{given} \tag{3}$$

Considering the metal side molecular transport layer, the Knudsen treatment shows that the heat flux, $q_m(t)$, at the wall interface region is given by [2, 3, 4]:

$$q_m\,(t) = \frac{\alpha}{2}\frac{\gamma+1}{\gamma-1}\left(\frac{R}{2\,\pi\, M_g}\right)^{1/2} \frac{P_g(t)}{\sqrt{T_{g1}\,(t)}}\,(T_m(t) - T_{g1}\,(t)) \tag{4}$$

According to assumption (3) this also represents the heat flux at the left-hand edge of the vapor conduction zone. The thickness of this layer can be assumed to be one half of the mean free path of gas molecules [5], so that

$$\lambda_1(\overline{T}_{g1}\,(t), P_g(t)) = \frac{1}{2\sqrt{2}\, sn} \tag{5}$$

The collision cross section, s $(=\pi d^2)$, does not change in the present range of temperatures and pressures. The number density, n, however, is a function of the gas temperature and pressure. $\overline{T}_{g1}(t)$ is taken to be the average temperature in this layer:

$$\overline{T}_{g1}(t) = \tfrac{1}{2}\,(T_m(t) + T_{g1}(t)) \tag{6}$$

The mass of this molecular transport layer, is given by:

$$M_{\lambda 1} = M'_g n\, \lambda_1 = \frac{M'_g}{2\sqrt{2}\, s} = M_0 = \text{constant} \tag{7}$$

since the collision cross section remains constant during the transient period.

Using the ideal gas law in the definition of the mean free path, one finds

$$\lambda_1(t) = \frac{\overline{T}_{g1}(t)\, P_g(0)}{\overline{T}_{g1}(0)\, P_g(t)}\,\lambda_0 \tag{8}$$

where λ_0 is half the mean free path at $P_g(0)$, $\overline{T}_{g1}(0)$ and can be determined easily. λ_0 is about 300 to 400 Å at NTP.

The mass and thickness of the liquid side molecular layer can be found similarly. Inside the vapor conduction region, the mass balance and energy balance equations can be written, in view of assumption (7), as [5]:

$$\frac{\partial \rho_g}{\partial t} + \frac{\partial}{\partial x}\,(\rho_g u_g) = 0 \tag{9}$$

Nomenclature

A_i = profile coefficient, equation (31) for i = 0, 1, 2
B_i = profile coefficient, equation (62) for i = 0, 1, 2
C_p = specific heat at constant pressure
C_v = specific heat at constant volume
D = diameter of heated tube
H = enthalpy
I = current
k = thermal conductivity
ℓ = thickness of transient boundary layer in liquid
L_t = length of heated tube
$L\infty$ = length of liquid column
m = Lagrangian coordinate in vapor layer
$\dot{m}_c$ = condensation mass flux, molecular
$\dot{m}_e$ = evaporation mass flux, molecular
$\dot{m}_t = \dot{m}_c - \dot{m}_e$
M = total mass of gas in conduction layer
M'_g = molecular mass of Freon-113
M_g = molar mass of Freon-113
$M_{\lambda 1,2}$ = mass of the Knudsen layer at left, right
n = number density of molecules in gas
P = pressure
P_∞ = pressure far from the heater
P_F = final test section pressure
P_I = initial test section pressure
$\Delta P = P_F - P_I$
q = transient heat flux
q_p = peak heat flux, maximum of q_m
q_{ss} = steady state heat flux
R = molar gas constant
R_t = resistance of heated tube
s = collision cross section of gas molecules
t = time
$t_{B,C}$ = time for first bounce, collapse
$T_{\ell 0}$ = steady-state liquid temperature profile
$T_{\ell\infty}$ = initial liquid temperature far from the heater (or outer edge of boundary layer)
T'_ℓ = perturbation in T_ℓ, equation (53)
T_{m0} = initial metal temperature
u = velocity
x = coordinate direction, Fig. 1
X = vapor conduction layer thickness
y = coordinate direction, Fig. 1
α = thermal accommodation coefficient
α = thermal diffusivity
$\beta_g = \dfrac{\rho_g k_g}{C_{pg}}$
$\gamma = C_p/C_v$
Γ = latent heat
$\delta_{\text{sat,sub}}$ = initial vapor film thickness for saturated or subcooled boiling
δ_m = thickness of heated tube
λ = half of mean free path
μ = viscosity
ρ = density
σ = condensation or evaporation coefficient
$\sigma_{c,e}$ = condensation, evaporation coefficient
ψ = Landau transformation variable, equation (23)
τ_p = pressure rise time constant
$\chi = X + \lambda_1 + \lambda_2$, total vapor film thickness

Subscripts

avg = average
m = metal
g = vapor
g_1, g_2 = vapor properties at points shown in Fig. 1
ℓ = liquid
0 = initial value
s = saturation

$$\rho_g C_{pg}\left(\frac{\partial T_g}{\partial t} + u_g \frac{\partial T_g}{\partial x}\right) = \frac{\partial}{\partial x}\left(k_g \frac{\partial T_g}{\partial x}\right) \qquad (10)$$

where

$$\rho_g \equiv \rho_g(x, t); \quad u_g \equiv u_g(x, t) \qquad (11)$$

$$T_g \equiv T_g(x, t) \qquad (12)$$

Using the Lagrangian coordinate system employed by Hamill and Bankoff [6]

$$m(x, t) = \int_0^x \rho_g dx \qquad (13)$$

$$M(t) = \int_0^{X(t)} \rho_g dx \qquad (14)$$

the continuity equation then becomes

$$\frac{\partial m}{\partial t} + \rho_g u_g = 0 \qquad (15)$$

and the convective term can be eliminated from the energy equation, which reads:

$$\frac{\partial T_g}{\partial t} = \beta_g \frac{\partial^2 T_g}{\partial m^2} \qquad (16)$$

where

$$\beta_g = \frac{\rho_g k_g}{C_{pg}} \equiv \beta_g(P_g) \qquad (17)$$

$$T_g \equiv T_g(m, t) \qquad (18)$$

It is found that $\rho_g k_g$ is nearly constant over a wide temperature range, for a particular pressure, so that β_g is not a function of temperature. The boundary conditions are:

$$T_g(0, t) = T_{g1}(t) \qquad (19)$$

$$q_{g1}(t) = -\rho_g k_g \left.\frac{\partial T_g}{\partial m}\right|_{m=0} \qquad (20)$$

$$T_g(M, t) = T_{g2}(t) \qquad (21)$$

$$q_{g2}(t) = -\rho_g k_g \left.\frac{\partial T_g}{\partial m}\right|_{m=M} \qquad (22)$$

To eliminate the moving boundary condition at $m = M(t)$ we make use of the Landau transformation [6]:

$$\psi = \frac{m(x, t)}{M(t)} \qquad (23)$$

The energy equation then becomes:

$$\frac{\partial T_g}{\partial t} - \frac{\psi}{M}\frac{dM}{dt}\frac{\partial T_g}{\partial \psi} = \beta_g \frac{1}{M^2}\frac{\partial^2 T_g}{\partial \psi^2} \qquad (24)$$

where

$$T_g \equiv T_g(\psi, t) \qquad (25)$$

The boundary conditions are:

$$T_g(0, t) = T_{g1}(t) \qquad (26)$$

$$q_{g1}(t) = -\frac{\rho_g k_g}{M}\left.\frac{\partial T_g}{\partial \psi}\right|_{\psi=0} \qquad (27)$$

$$T_g(1, t) = T_{g2}(t) \qquad (28)$$

$$q_{g2}(t) = -\frac{\rho_g k_g}{M}\left.\frac{\partial T_g}{\partial \psi}\right|_{\psi=1} \qquad (29)$$

Upon integrating the energy equation from $\psi = 0$ to $\psi = 1$, one obtains:

$$\frac{\partial}{\partial t}\left(\int_0^1 T_g d\psi\right) - \frac{1}{M}\frac{dM}{dt}\left(\int_0^1 \psi \frac{dT_g}{d\psi} d\psi\right) = \frac{\beta_g}{M^2}\left(\left.\frac{\partial T_g}{\partial \psi}\right|_{\psi=1} - \left.\frac{\partial T_g}{\partial \psi}\right|_{\psi=0}\right) \qquad (30)$$

In view of the number of boundary conditions available, a quadratic profile in ψ is chosen for T_g [7]:

$$T_g(\psi, t) = A_0(t) + A_1(t)\,\psi + A_2(t)\,\psi^2 \qquad (31)$$

To satisfy the boundary conditions in T_g, this becomes:

$$T_g(\psi, t) = T_{g1}(t) + (T_{g2}(t) - T_{g1}(t) - A_2(t))\,\psi + A_2(t)\,\psi^2 \qquad (32)$$

Substitution of the above profile into the integral energy equation and a little simplification results in

$$\frac{dT_{g1}}{dt} + \frac{dT_{g2}}{dt} - \frac{1}{3}\frac{dA_2}{dt} - \frac{1}{M}\frac{dM}{dt}\left(T_{g2} - T_{g1} + \frac{A_2}{3}\right) = \frac{4A_2\beta_g}{M^2} \qquad (33)$$

The boundary conditions on the conduction heat flux at the left and right hand edges of the conduction zone become:

$$q_{g1}(t) = -\frac{\rho_g k_g}{M}(T_{g2} - T_{g1} - A_2) \qquad (34)$$

$$q_{g2}(t) = -\frac{\rho_g k_g}{M}(T_{g2} - T_{g1} + A_2) \qquad (35)$$

For the molecular transport layer on the right-hand side, the absolute condensation mass flux, $\dot{m}_c$, and the absolute evaporation mass flux, $\dot{m}_e$, are obtained from kinetic theory [8]:

$$\dot{m}_c = \sigma_c P_g(t)\sqrt{\frac{M_g}{2\pi R\, T_{g2}(t)}} \qquad (36)$$

$$\dot{m}_e = \sigma_e P_s(t)\sqrt{\frac{M_g}{2\pi R\, T_s(t)}} \qquad (37)$$

In general, $\sigma_c = \sigma_e = \sigma$ and the net condensation mass flux is

$$\dot{m}_t = \dot{m}_c - \dot{m}_e = \sigma\sqrt{\frac{M_g}{2\pi R}}\left(\frac{P_g}{\sqrt{T_{g2}}} - \frac{P_s}{\sqrt{T_s}}\right) \qquad (38)$$

and, for $M(t) \geq 0$,

$$\dot{m}_t = -\frac{dM}{dt} \qquad (39)$$

The net energy flux at the vapor-liquid interface, $q_i(t)$, is

$$q_i(t) = \dot{m}_t H_g(T_s(t), P_s(t)) + \dot{m}_c(H_g(T_{g2}(t), P_g(t)) - H_g(T_s(t), P_s(t))) \qquad (40)$$

Then the heat flux to the bulk liquid, from an interfacial energy balance on the deposition layer, is

$$q_\ell(t) + \dot{m}_t H_\ell((T_s(t), P_s(t)) = q_i(t) \qquad (41)$$

where $H_g(T, P)$ and $H_\ell(T, P)$ are the vapor and liquid enthalpies, and

$$\Gamma = H_g(T_s, P_s) - H_\ell(T_s, P_s) \qquad (42)$$

since $P_g(t)$ is not very different from $P_s(t)$, so that $H_g(T_s, P_s)$ is nearly equal to $H_g(T_s, P_g)$. Therefore,

$$q_\ell(t) = \dot{m}_t\Gamma + \dot{m}_c C_{pg}(T_{g2}(t) - T_s(t)) \qquad (43)$$

where Γ is the latent heat of evaporation at the saturation temperature. After substitution of the appropriate quantities, one obtains,

$$q_\ell(t) = \sigma\sqrt{\frac{M_g}{2\pi R}}\left\{\left(\frac{P_g(t)}{\sqrt{T_{g2}(t)}} - \frac{P_s(t)}{\sqrt{T_s(t)}}\right)\Gamma + \frac{P_g(t)}{\sqrt{T_{g2}(t)}}C_{pg}(T_{g2}(t) - T_s(t))\right\} \qquad (44)$$

On the other side of this molecular transport region, the energy balance becomes, including energy transfer by mass transfer:

$$\dot{m}_t H_g(T_{g2}, P_g) + q_{g2}(t) - q_i(t) = \tfrac{1}{2} M_{\lambda 2} C_{pg}\frac{d(T_{g2}(t) + T_s(t))}{dt} \cong 0 \qquad (45)$$

In the liquid the momentum equation is, assuming cylindrical compression of liquid

$$\frac{d^2\chi(t)}{dt^2} + a\left(\frac{d\chi(t)}{dt}\right)^2 = \frac{P_g(t) - P_\infty(t)}{\rho_\ell b} \tag{46}$$

where $P_\infty(t) = P_I + \Delta P(1 - \exp(-t/\tau_p))$

$$\chi(t) = X(t) + \lambda_1(t) + \lambda_2(t) \tag{47a}$$

$$a = \frac{2}{D}\left\{1 - \tfrac{1}{2}\left(1 - \frac{1}{Y^2}\right)\right\}; \quad b = \frac{D}{2}\,\ell n\, Y; \quad Y = L_\infty/D \tag{47b,c}$$

The energy equation, using a coordinate y which is fixed to the moving interface, becomes for short times,

$$\frac{\partial T_\ell}{\partial t} = \alpha_\ell \frac{\partial^2 T_\ell}{\partial y^2} \tag{48}$$

with the initial and boundary conditions

$$T_\ell(y, 0) = T_{\ell 0}(y) \tag{49}$$

$$T_\ell(0, t) = T_s(t) \tag{50}$$

$$T_\ell(\ell(t), t) = T_{\ell 0}(\ell(t)) \tag{51}$$

$$-k_\ell \left.\frac{\partial T_\ell}{dy}\right|_{y=\ell(t)} = -k_\ell \left.\frac{dT_{\ell 0}}{dy}\right|_{y=\ell(t)} = q_{ss} \tag{52}$$

where $\ell(t)$ is the transient thermal boundary layer thickness in the liquid. Next, we put

$$T_\ell(y, t) = T_{\ell 0}(y) + T'_\ell(y, t) \tag{53}$$

with

$$\frac{\partial^2 T_{\ell 0}(y)}{\partial y^2} = 0 \tag{54}$$

and $B.C.$

$$T_{\ell 0}(0) = T_s(0) \tag{55}$$

$$T_{\ell 0}(\ell_0) = T_{\ell\infty} \tag{56}$$

Substituting equation (53) into equation (48), one obtains

$$\frac{\partial T'_\ell(y, t)}{\partial t} = \alpha_\ell \frac{\partial^2 T'_\ell(y, t)}{\partial y^2} \tag{57}$$

with the initial condition:

$$T'_\ell(y, 0) = 0 \tag{58}$$

and boundary conditions:

$$T_\ell(0, t) = T_s(t) - T_{\ell 0}(0) = T_s(t) - T_s(0) \tag{59}$$

$$T'_\ell(\ell(t), t) = 0 \tag{60}$$

$$-k_\ell \left.\frac{\partial T'_\ell(y, t)}{\partial y}\right|_{y=\ell(t)} = 0 \tag{61}$$

Assuming a polynomial profile in the liquid [7] of the form

$$T'_\ell(y, t) = B_0(t) + B_1(t)\left(\frac{y}{\ell(t)}\right) + B_2(t)\left(\frac{y}{\ell(t)}\right)^2 \tag{62}$$

and satisfying the boundary conditions, one obtains

$$T'_\ell(y, t) = (T_s(t) - T_s(0))\left(1 - \frac{y}{\ell(t)}\right)^2 \tag{63}$$

Applying the integral method to equation (57), the energy equation becomes

$$\frac{1}{3}\frac{d}{dt}\{(T_s(t) - T_s(0))\,\ell(t)\} = \alpha_\ell \frac{2}{\ell(t)}(T_s(t) - T_s(0)) \tag{64}$$

and

$$q_\ell(t) = -k_\ell\left(\frac{\partial T_\ell(y, t)}{\partial y}\right)_{y=0} = q_{ss} - k_\ell\left(\frac{\partial T'_\ell(y, t)}{\partial y}\right)_{y=0}, \tag{65}$$

or using equation (63)

$$q_\ell(t) = q_{ss} + \frac{2k_\ell}{\ell(t)}(T_s(t) - T_s(0)). \tag{66}$$

The Clausius-Clapeyron equation at the interface is

$$\frac{dT_s(t)}{dt} = \frac{RT_s^2(t)}{M_g \Gamma P_s(t)}\frac{dP_s(t)}{dt}. \tag{67}$$

From the ideal gas law

$$\int_0^{\chi(t)} P_g(t)\, dx = \frac{R}{M_g}\int_0^{\chi(t)} \rho_g(x, t)\, T_g(x, t)\, dx \tag{68}$$

After integration and simplification, one finds

$$P_g(t)\,\chi(t) = \frac{1}{2}\frac{R}{M_g}\Big\{M_\lambda\,(T_m(t) + T_{g1}(t) + T_{g2}(t) + T_s(t)) + M(t)(T_{g2}(t) + T_{g1}(t) - \frac{1}{3}A_2(t))\Big\} \tag{69}$$

3 Calculation

Two computer codes were constructed, based on the above model, the second being a simplified version. Both of them indicated the same trends and showed the same order values in the peak heat flux and peak gas pressure when a parameter survey was run to check the effect of T_{m0}, P_I, ΔP and τ.

The following equation was used from the analysis of Baumeister and Hamill [9] to determine an initial film thickness:

$$\chi(0) = \frac{D}{2}\left[\exp\left\{4.35\left(\frac{k_g \mu_g\,(T_{m0} - T_{s0})}{\Gamma' D\,\rho_g \sigma_g}\right)^{1/4}\right\} - 1\right] \tag{70}$$

where,

$$\Gamma' = \Gamma\left\{1 + \frac{19}{20}\frac{C_{pg}\,(T_{m0} - T_{s0})}{\Gamma}\right\} \tag{71}$$

This value of the initial film thickness, however, always came out to be larger than that calculated by the steady-state pure conduction equation. The difference is attributed to turbulence and surface waves which increase the effective gas thermal conductivity. A superficial gas thermal conductivity $k_g{}^*$ was thus defined to satisfy the following boundary conditions

$$k_g{}^* = k_{g0} = \frac{q_{ss}\,\chi(0)}{(T_{m0} - T_{s0})} \text{ at } \chi \geq \chi\,(0) \tag{72}$$

$$k_g{}^* = k_g \text{ at } \chi \leq \chi_{\text{cond}} \tag{73}$$

and to produce a smooth fit, as a function of χ between $\chi(0)$ and χ_{cond}. Here, χ_{cond} represents the smaller film thickness calculated from the pure conduction equation:

$$\chi_{\text{cond}} = \frac{k_g}{q_{ss}}(T_{m0} - T_{s0}) \tag{74}$$

and k_g is the actual gas thermal conductivity which is a function of the average gas temperature and pressure. Thus, for $\chi_{\text{cond}} < \chi(t) < \chi(0)$ one obtains:

$$k_g{}^*(\overline{T}_g, P_g) = k_g(\overline{T}_g, P_g) + (k_{g0} - k_g(\overline{T}_g, P_g))\left\{\frac{\chi(t) - \chi_{\text{cond}}}{\chi(0) - \chi_{\text{cond}}}\right\}^{1.5} \tag{75}$$

A value of 1.5 was chosen for the exponent after finding that significant changes in q_p did not occur if the exponent was taken as 1.0 or 2.0. In our experimental condition, a and b in equation (49 b,c) are 500 and 0.003, respectively.

(a) Simplified Model. If one neglects heat storage in the gas film by setting β_g $(= \rho_g k_g/C_{pg}) \rightarrow \infty$, one obtains $A_2(t) = 0$, which means that the temperature profile in the gas is linear in ψ. This simplifies the equation set considerably.

Secondly, the molecular transport layer on the gas-liquid interface was suppressed and a simple heat balance was used to determine the rate of condensation or evaporation.

Two different methods were used to determine the heat flux in the liquid, in addition to the one reported above. One follows the Duhamel's integral approach, while the other is based on a general profile method, as shown in reference [10]. All three gave nearly the same results, and the last one was chosen for calculations, being the quickest. Thus, the final set of equations is:

$$q_{ss} - \rho_m C_{pm} \delta_m \frac{dT_m}{dt}$$

$$= \frac{\alpha}{2\sqrt{2}} \frac{\gamma + 1}{\gamma - 1} \sqrt{\frac{R}{\pi M_g}} \frac{P_g}{\sqrt{T_{g1}}} (T_m - T_{g1})$$

$$= \frac{\rho_g k_g}{M} (T_{g1} - T_s) = q_\ell + \frac{dM}{dt} \Gamma \qquad (76a,b,c)$$

$$q_\ell = k_\ell \rho_\ell C_{p\ell} \frac{d}{dt} \left\{ \frac{(T_s - T_{\ell\infty})^2}{q_\ell} \right\} \qquad (77)$$

$$\frac{d^2\chi}{dt^2} + a \left(\frac{d\chi}{dt} \right)^2 = \frac{P_g - P_\infty}{\rho_\ell b}; \quad a = 500, b = 0.003 \qquad (78)$$

$$\frac{dT_s}{dt} \left\{ \frac{2\Gamma\, M_g{}^2 P_g \chi}{R^2 T_s{}^2} \right\} + \frac{d\chi}{dt} \left\{ \frac{2\, M_g P_g}{R} \right\} - \frac{dM}{dt} \{2\, T_s\} = 0 \qquad (79)$$

T_{g1} is found from equation (76b), which is an intermediate balance of equations (76), the step-by-step heat balance for the whole system. Equation (77) represents heat transfer on the liquid side, while equation (78) governs the motion of the liquid under the pressure gradient. Equation (79) is the combined form of the ideal gas law and the Clausius-Clapeyron equation, after differentiation. This system of five nonlinear first-order ordinary differential equations was solved numerically for T_m, T_s, M, q_ℓ and χ as a function of time explicitly.

(b) Complete Model. Since the Knudsen layer equations are algebraic in form they were converted to differential equations by appropriate differentiation, where necessary. Finally, a system of ten non-linear ordinary differential equations are obtained, which can be solved numerically for T_m, T_{g1}, T_{g2}, T_s, A_2, P_g, P_s, M, ℓ and χ as a function of time. The Runge-Kutta-Gill method with double precision was used in the numerical calculation. The initial time step was 10^{-5} s but the step size decreased automatically, depending on the magnitude of the time derivative $\dot{\chi}$ and χ itself in the region of rapid change. Final forms are rather lengthy and are given in reference [12].

4 Results

(a) Simplified Model. A parametric survey was run to check the effect of T_{m0}, P_I, ΔP and τ on the behavior of the gas film after passage of the shock. The time history of the heat flux, film thickness and gas pressure were calculated for each parameter. The results are quite sensitive to the initial film thickness, which is actually a stochastic variable, due to surface waviness and bubble breakoff. For these calculations, the stopping criterion was arbitrarily set at $\chi \leq 0.1\ \mu$, corresponding to the estimated surface roughness, which might play an important role during an actual vapor-liquid contact on microscale. However, the film always bounced back before reaching this cut-off value and computations were continued until the second rebound occurred. In these cases, the left hand-side molecular transport layer had practically no effect and T_{g1} was always within 1°C of T_m.

Figure 2 shows the effect of shock pressure. Bounce times varied from 0.1 to 0.2 ms for ΔP values of 0.1–0.35 MPa. The heat fluxes increased by an order of magnitude or more, but stayed high over a rather short period only. The gas pressure always remained below critical, the value of which is 3.37 MPa for Freon 113. The trends shown are as expected.

(b) Complete Model. In this case the parametric survey involved two additional parameters, i.e. α and σ. It was found that changes in α from 1.0 to 0.05 were of negligible effect, so that α was chosen to be 1.0 always. The calculations are continued up to $\chi \leq 0.1\ \mu$, but unlike the previous case, complete collapse was predicted for a few cases.

Figure 3 shows the effect of the condensation-evaporation coefficient, σ, on the peak heat flux, q_p, the minimum film thickness, χ_p, and the peak gas pressure, P_p. The results are quite independent of σ for ΔP = 0.2 MPa but there is a significant change if ΔP = 0.3 MPa.

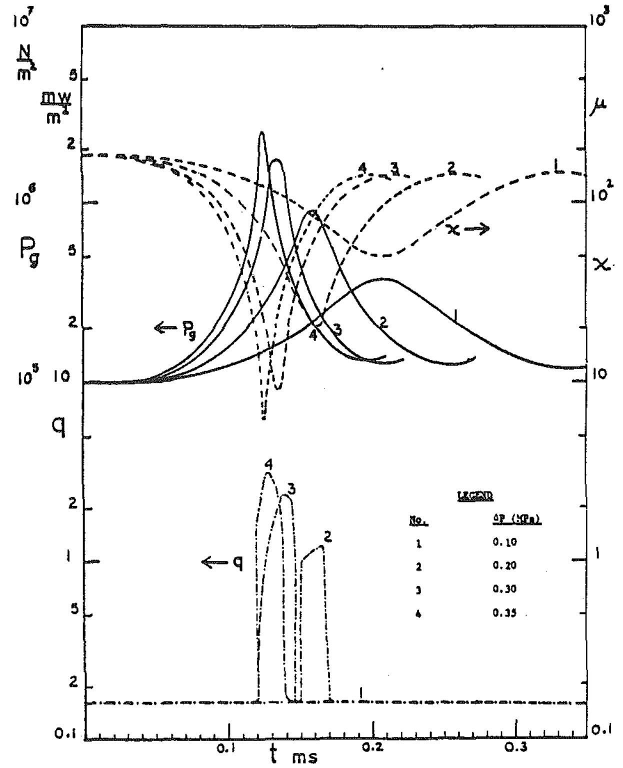

Fig. 2 Simplified model results. Time history of q, P and χ for changing ΔP. T_{m0} = 300°C, P_I = 0.1 MPa, $\tau_p{}^\zeta$ = 80 μs, T_ℓ = 22°C. q_{ss} = 0.16 Mw/m^2

Measured values of σ for Freon-113 have not been reported. However, some early experiments have shown that σ becomes very low for antisymmetric molecules. Heideger and Boudart [10] found σ to be 0.05 for glycerol while Delaney, et al. [11] reported a value of ~0.03 for water. Assuming Freon molecules to be antisymmetric one might therefore expect σ to be around 0.05. If these molecules were symmetric, σ would be higher. However, the noncondensible gases present in the system would lower its value considerably, by adding to the interfacial resistance. Very minute quantities of noncondensibles are required for a large reduction in σ, as they get concentrated while the vapor film is condensing. Therefore, σ = 0.05 was chosen for further computations to check the effects of ΔP, P_I, τ and T_{m0}. Figure 4 shows the time history of the variables for changing ΔP, and can be compared directly with Fig. 2, since identical conditions were used for both. The trends are quite similar, except that the gas film apparently collapsed for ΔP = 0.35 MPa, and no bouncing was detected for ΔP = 0.1 MPa, within about 0.25 ms. Figure 5 is a plot of these peak values against ΔP. The dashed and the solid lines show the results of Figs. 2 and 4, respectively. The experimental ranges of q_p are shown by vertical lines, and are found to be in the same range. For shocks with ΔP > 4 atm., very high heat fluxes with supercritical gas pressures and partial contacts are predicted, according to Fig. 5.

Figure 6 shows the effect of P_I. These calculations indicate that the gas film would collapse for P_I < 0.1 MPa, producing rather high heat fluxes and gas pressures exceeding the critical. This is also in agreement with Fig. 5, since a high value of ΔP = 0.34 MPa was used. The bounce or collapse time of ~0.13 ms was independent of P_I. The experimental q_p values agree with theory for P_I = 0.1 MPa. They are much lower for P_I = 0.057 MPa, which is not unexpected. A sharp peak whose half width value is less than 10 μs cannot be detected by the experimental measurement circuit and the measured peak is therefore greatly attenuated.

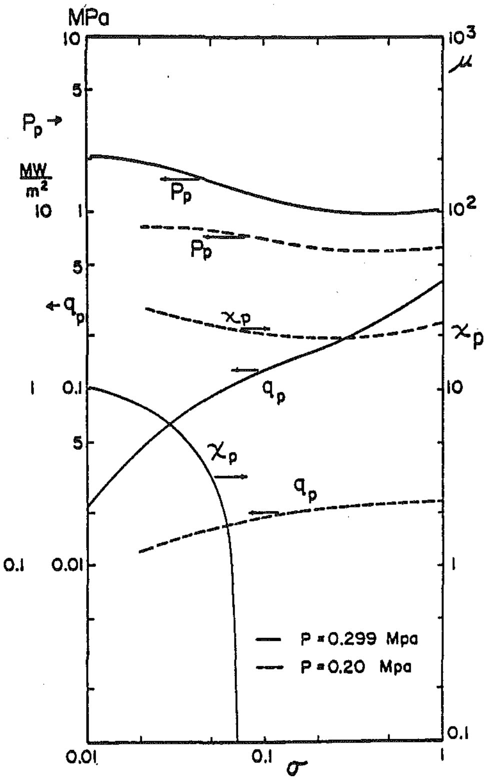

Fig. 3 Complete model results. Effect of condensation-evaporation coefficient. q_p, P and χ_p versus σ. T_{m0} = 300°C, P_l = 0.1 MPa, τ_p = 80 μs, T_ℓ = 22°C, q_{ss} = 0.16 Mw/m² and ΔP = 0.299 and 0.22 MPa

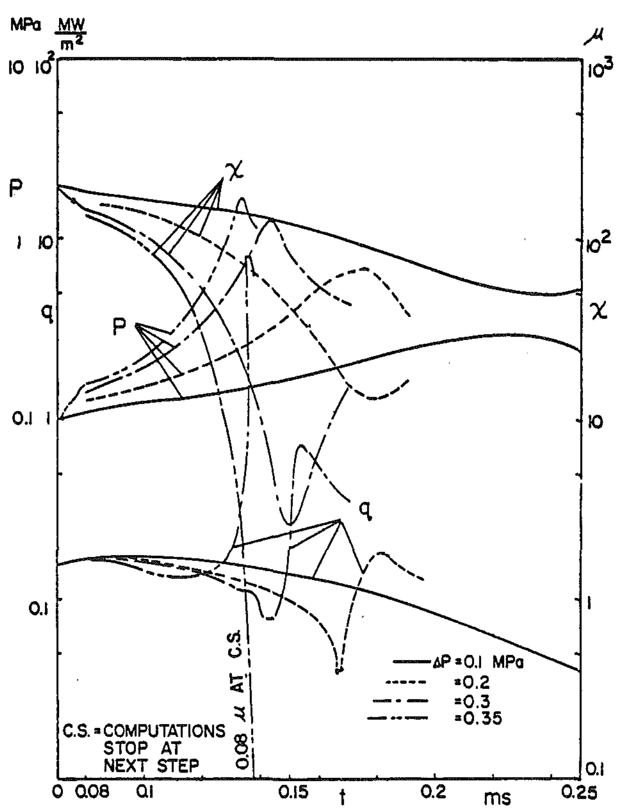

Fig. 4 Same as Fig. 2, except for complete model with σ = 0.05

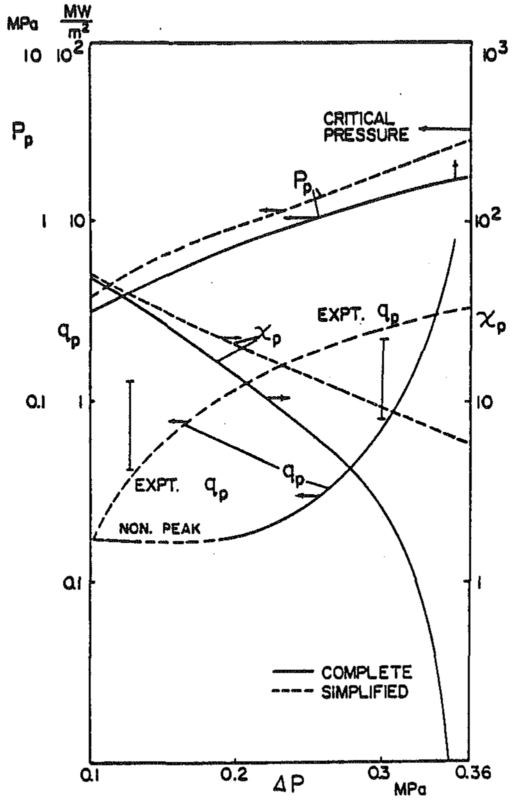

Fig. 5 Comparison of results of Figs. 2 and 4. q_p, P_p and χ_p versus ΔP for both models. Same condition as Figs. 2 and 4

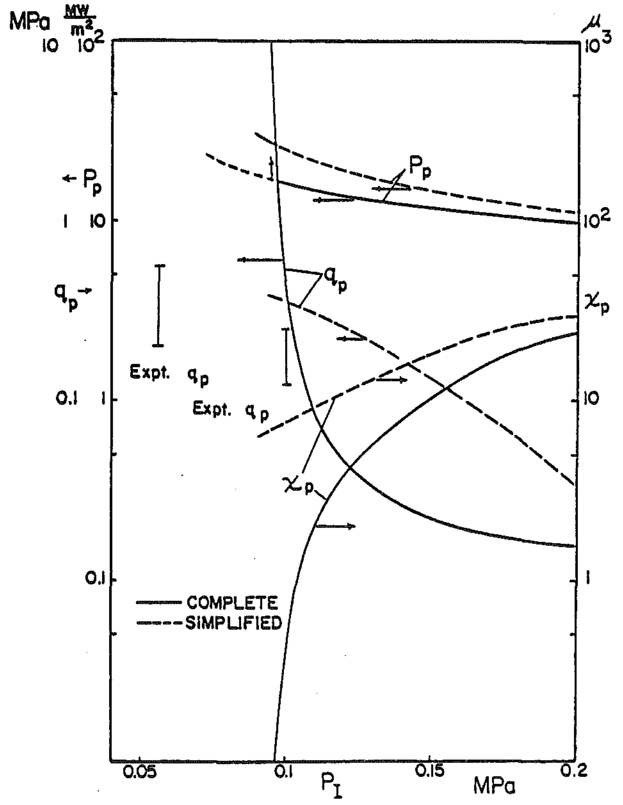

Fig. 6 Comparison of q_p, P_p and χ_p versus P_l for simplified and complete models. Same conditions as Fig. 2 except for changing P_l. T_{m0} = 300°C, ΔP = 0.341 MPa, τ_p ± 80 μs, T_ℓ = 22°C and Q_{ss} = 0.16 Mw/m²

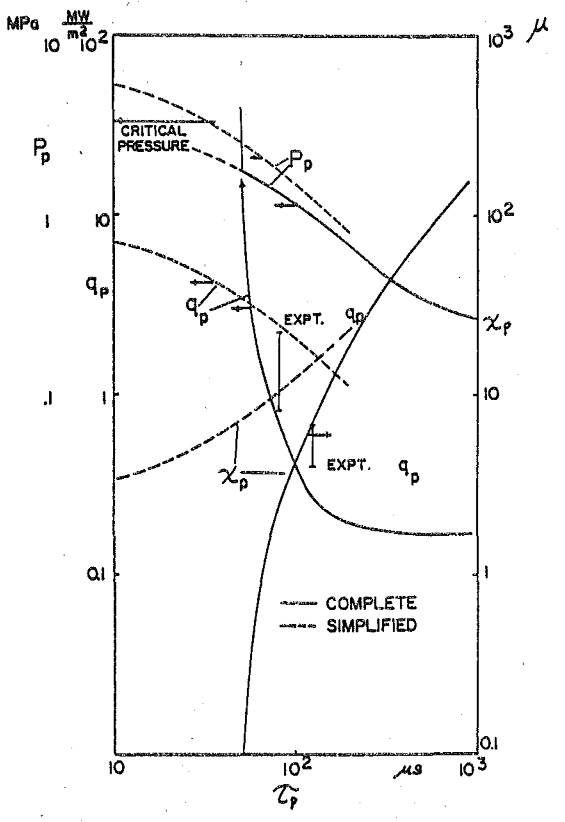

Fig. 7 Comparison of q_p and P_p and χ_p versus τ_p for both models. Same conditions as Fig. 2 except for changing τ_p, $T_{m0} = 300°C$, $P_l = 0.1$ MPa, $\Delta P = 0.299$ MPa, $T_\ell = 22°C$ and $q_{ss} = 0.16$ Mw/m²

Figure 7 shows the effect of the pressure rise time constant, τ. It shows good agreement with experimental q_p values at $\tau = 80$ and 120 μs.

The solid lines in Fig. 8 show two plots of q_p versus the initial metal temperature, T_{m0}, in the sensitive range for the film collapse or bouncing of $\Delta P = 2.99$ and 0.32 MPa, respectively. However, when the initial vapor film thickness is chosen to be about twice that calculated by the Baumeister and Hamill correlation [9]. (Since the correlation gives an initial film thickness which is about half the average thickness calculated from the initial heat flux and metal temperature, the computational results, shown by the dotted lines are quite different. This illustrates the powerful effect of the initial film thickness on the tendency for the vapor film thickness to collapse below about 0.08 μ, corresponding to the Knudsen layer thickness (cf. Fig. 4).)

The experimental points are generally bracketed by the two sets of curves. It appears therefore that by a reasonable adjustment of the assumed initial vapor film thickness the calculated q_p versus T_{m0} curves can be made to follow the data trends, but that the behavior is quite sensitive. Further, it is recognized that the initial vapor film thickness, and hence collapse, is far from uniform from top to bottom.

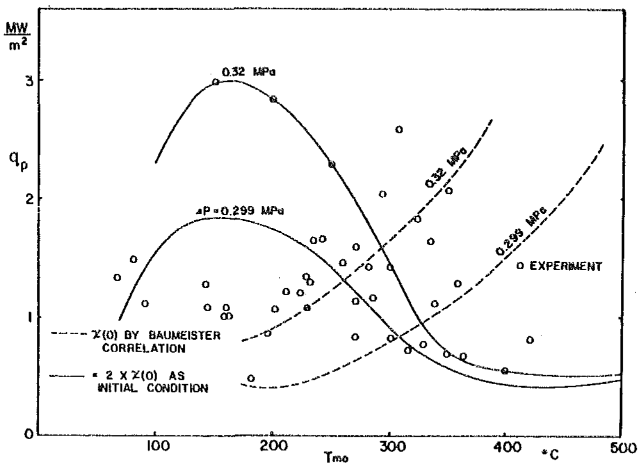

Fig. 8 q_p versus T_{m0} for the complete model and two values of the initial film thickness. Also compared with experimental data points. $P_l = 0.1$ MPa, $\Delta P = 0.299$ MPa and 0.32 MPa, $\tau_p = 80$ μs, $T_\ell = 22°C$ and $\sigma = 0.05$

6 Conclusions

1 Two models for destabilization of film boiling around a heated cylinder by a sudden increase in ambient pressure are presented. The more complete model takes into account heat transfer in all three phases—solid, vapor and liquid—as well as the Knudsen layers on the liquid and solid surfaces. The simplified model neglects heat storage in the vapor film and the Knudsen layer at the liquid surface. Both models predict peak fluxes in general agreement with those found experimentally, but the complete model is considered more reliable, since it predicts vapor film collapse under conditions where the simplified model predicts a "bounce" (minimum vapor film thickness), and where experimentally it is known that collapse takes place.

2 The experimental data scatter is most probably due to random variations in film thickness at the instant of shock arrival, as seen from an analytical sensitivity study. There is also an experimental averaging of the peak heat flux data due to instrument limitations.

3 Effective direct "contact" between solid and liquid, with only a thin intervening layer of supercritical fluid, is attainable by shocks with rise times of order 0.1 ms-1 ms and pressure ratios less than 10. Collapse times of the order of 0.1 ms can be expected, which is adequate for efficient fuel-coolant interactions.

4 When the thickness of the vapor layer becomes less than 1μ, the vapor pressure increases to more than 10 MPa and reaches supercritical pressures under some conditions. The transient local pressure in the thin vapor layer might cause fragmentation and mixing of fluids near the interface.

References

1 Inoue, A., and Bankoff, S. G., "Destabilization of Film Boiling Due to Arrival of a Pressure Shock. Part I: Experimental," Report No. C00-2512-13, Chemical Engineering Dept., Northwestern University, Evanston, Ill, 1978.

2 Loeb, L. B., *The Kinetic Theory of Gases*, McGraw Hill, New York, 1927.

3 Patterson, G. N., *Molecular Flow of Gases*, John Wiley and Sons, New York, 1956.

4 Alofs, D. J., Flagan, R. C., and Springer, G. S., "Density Distribution Measurements in Rarefied Gases Contained between Parallel Plates at High Temperature Differences," *Physics of Fluids*, Vol. 14, 1971, pp. 529–533.

5 Bird, R. B., Stewart, W. E., and Lightfoot, E. N., *Transport Phenomena*, John Wiley and Sons, New York, 1960.

6 Hamill, T. D. and Bankoff, S. G., "Growth of a Vapour Film at a Rapidly Heated Plane Surface," *Chemical Engineering Science*, Vol. 18, 1963, pp. 355–364.

7 Goodman, T. R., "The Heat Balance Integral and its Application to Problems Involving a Change of Phase," *Trans. ASME*, Vol. 80, 1958, pp. 335–342.

8 Collier, J. G., *Convective Boiling and Condensation*, McGraw Hill, New York, 1972.

9 Baumeister, K. J., and Hamill, T. D., "Laminar Flow Analysis of Film Boiling from a Horizontal Wire," NASA TN D-4035, July 1967, p. 44.

10 Heidegger, W. J., and Boudart, M., "Interfacial Resistance to Evaporation", *Chemical Engineering Science*, Vol. 17, 1962, pp. 1–10.

11 Delaney, L. J., Houston, R. W. and Eagleton, L. C., "The Rate of Vaporization of Water and Ice," *Chemical Engineering Science*, Vol. 19, 1964, pp. 105–114.

12 Inoue, A., Ganguli, A., and Bankoff, S. G., "Destabilization of Film Boiling Due to Arrival of a Pressure Shock Part II: Analytical," Rpt. No. C00-1512-15, Chemical Engineering Dept., Northwestern University, Evanston, Ill., 1978.

N. Seki
Professor.

S. Fukusako
Associate Professor.

K. Koguchi
Graduate Student.

Department of Mechanical Engineering,
Hokkaido University,
Sapporo 060, Japan

An Experimental Investigation of Boiling Heat Transfer of Fluorocarbon R-11 Refrigerant for Concentric-Tube Thermosyphon

The characteristics of the boiling heat transfer for a concentric-tube open thermosyphon are examined in detail. Fluorocarbon R-11 refrigerant as a testing fluid is utilized. Out of a number of possible controlling variables, the effects of the heat flux, the void ratio, and the diametric ratio of the concentric-tube on the heat-transfer performance are determined. From the present experimental results it is demonstrated that total heat flux can be appropriately predicted by a superposition of the heat flux due to the available correlations for free convection and due to the correlations experimentally determined for boiling heat flux.

Introduction

Recent recognition of the finite nature of fossil fuels such as natural gas and oil has led inevitably to an urgent call for the development of alternative energy resources.

From a practical point of view, the potential for utilization of geothermal energy has extensively been described in several references, for instance, Hayakawa [1]. The major use of the geothermal energy up to now has been power produced from steam-dominated or from liquid-dominated reservoirs. The great potential of geothermal energy, which is probably to be found in locations of normal geothermal gradient, would be expected to be devoted, for instance, to melt snow on roads in the northern cold districts.

A number of important problems, however, remain to be resolved before utilization of such energy in very low density becomes feasible. Especially, the means of energy transport to the surface is of prime importance in economical and technical evaluation of the heat-removal from such a very low-density geothermal energy.

A two-phase open thermosyphon, which utilizes buoyancy force and phase change of liquid contained in a vertically long tube, may be considered to be one of the convenient devices to achieve this, because a power supply and a pump to circulate the working fluid are not required, and, furthermore, the low cost and simplicity of construction of the device are quite advantageous. It is well known that the high performance of the two-phase heat-transfer system is attributed to the fact that it utilizes mainly the heat-transfer characteristics of phase change which are more efficient means of heat transfer than those of single-phase.

In addition to the aforementioned expectation, it was recently shown by Seki, et al. [2] that the markedly decreased heat-transfer performance under impeded or similar flow conditions can significantly be improved by installing an additional inner tube which could be occupied by the downward return-flow in this concentric-tube open thermosyphon.

There have been few investigations on the two-phase thermosyphon other than those reported in the open literature [3–10] and thus it appears that the fundamental design information and operating technique of the system may be not satisfactory. Cohen and Bayley [3] conducted a series of experiments using hollow thermosyphon tubes in a rotating jig which were filled with water in quantities ranging from 0 to 100 percent of the tube volume. They reported that over a wide range the heat transferred from the heated section to the cooled section of the thermosyphon is independent of the quantity of coolant enclosed. Long [4] tried to use the closed two-phase thermosyphon as a thermal rectifier to keep permafrost. Chato [5] investigated analytically the general problem of condensing thermosyphon in a variable acceleration field, and concluded that the effects of temperature difference and the Prandtl number are similar to those in other condensing problems. The possible application of heat transfer by evaporative cooling of a liquid metal under high centrifugal acceleration to turbine blade cooling was demonstrated by Genot and LeGrives [6]. A study of a two-phase thermosyphon with large filling quantity was done by Larkin [7]. In his study it was pointed out that it was not possible to develop a precise relationship for boiling and condensing heat-transfer coefficients, but an appreciable knowledge of the process was gained. A recent study of the two-phase thermosyphon was carried out by Lee and Mital [8]. They performed an experimental study using water and fluorocarbon R-11 refrigerant as testing fluids, and evaluated the effects of many possible controlling variables on the heat-transfer characteristics of a two-phase thermosyphon. McDonald, et al. [23] investigated the characteristic operating behavior of a two-phase thermosyphon loop which they are proposing as an efficient waste heat recovery system and found that the optimum performance is mainly concerned with the orientations of the evaporator and condenser tubes. A simulation of the behavior of the thermosyphon loop was made by Ali and McDonald [24], who indicated that the agreement between the simulated performance and experimental data is very good. McDonald and Ali [25] also presented the results of a number of loop simulations which were carried out to illustrate typical behavior of thermosyphon loops as various parameters are changed.

Experiments of the heat-transfer performance and the critical heat flux for a single-tube open thermosyphon using water, ethyl-alcohol, normalhexane, and carbontetrachloride as testing fluids were conducted by Kusuda and Imura [9, 10]. They claimed that the heat transfer for their thermosyphon is greater than that of pool-boiling, while the critical heat flux has a tendency to become small, and that the heat-transfer coefficient is nearly independent of the tube length and tube diameter, and also of the flow-pattern characteristic.

From the foregoing literature survey, it is apparent that very little is known about the boiling heat-transfer characteristics of the concentric-tube open thermosyphon of the present system, and especially about the fundamental informations which are essential to apply the system in extraction of thermal energy from deep in the earth and in bringing it to the surface thermal plant.

The objective of the present paper is, therefore, to make an experimental study into the heat-transfer performance of a stationary open thermosyphon having a concentric annulus, so-called the present concentric-tube open thermosyphon. In particular, the effects of the heat flux, the void ratio, and the diametric ratio of concentric tube were extensively investigated.

Contributed by the Heat Transfer Division for publication in the JOURNAL OF HEAT TRANSFER. Manuscript received by the Heat Transfer Division July 3, 1980.

Experimental Apparatus and Procedures

A schematic diagram of the experimental set up is depicted in Fig. 1. The main heat-transfer loop of the concentric-tube open thermosyphon consists of a vertical concentric cyclinder as test section where both the top and bottom of inner tube are opened, a main electrical resistance heater assembly, a guard heater, a reservoir, and associated instrumentations.

The copper outer tube of 100.0 mm i.d. and 2 mm thickness with 2000 mm length was utilized. Values of the annular-space width ranging from 5.7 to 34.0 mm were employed by using vinyl chloride tubes with diameters of 32.0, 48.0, 60.0, 66.6, 76.0, and 88.6 mm with 2000 mm length as the inner tube. Between the copper outer tube and the cooling reservoir a lucite tube 100.0 mm in length was installed for visual observation of boiling behavior in the annulus. Closure of the outer tube was performed by screwing a threaded cap into the bottom end, which also carried a brass tube to a drain valve.

The surface temperature of the outer tube was uniformly maintained at a constant temperature by using nine independent and controllable main heaters, which were respectively surrounded by corresponding guard heaters to eliminate the heat loss from the main heaters to the environment. These heaters were made of electric resistance rod (chromel-iron wire 1.6 mm in diameter) wound around the outer tube surface. All heaters were supplied with electric power through separate circuits from a variable transformer rated 10 KVA, 100 V, respectively. The heat from the test section was removed at the reservoir through a heat exchanger consisting of coiled copper tubing and a temperature-controlled coolant.

Measurements of wall-surface temperature were obtained from thermocouples carefully plugged into the tube wall at stations corresponding to the center plane of each heating coil. In addition, a long slender shielded probe with thermocouple was axially traversed along the axis of the tube to measure the core temperature of the working fluid in the inner tube. Outputs of these thermocouples were continuously recorded on YOKOGAWA Multiplex Recorders. Power to the main heaters subdivided were measured by means of ammeters and voltmeters provided for each heating coil.

The pressure inside the thermosyphon was measured at the reservoir by a pressure gauge. Measurements of the mean void ratio, which is defined as the ratio of the vapor space to the total volume of the annulus, were undertaken by using a Hg-manometer measuring the pressure difference between the bottom and open end of the concentric-tube thermosyphon. In the procedure mentioned above, it was assumed that the head of the fluid friction in the rising two-phase flow could be neglected comparing with the gravity head of the two-phase flow (maximum ratio of the fluid-friction head to the gravity one was approximately evaluated to be less than 1.0 percent).

Before starting actual experiments, the thermosyphon system was thoroughly cleaned by repeated washing with acetone followed by water. After the system had been perfectly dried, the charge valve was opened, and the flow of the working fluid was initiated. Special care was taken to insure that there were no air bubbles within the concentric tube. Power then was supplied to both the main and guard heaters. The power to main heaters was increased in steps up to a desired wall-temperature. Continuous thermocouple readings were made on the temperatures in the total system.

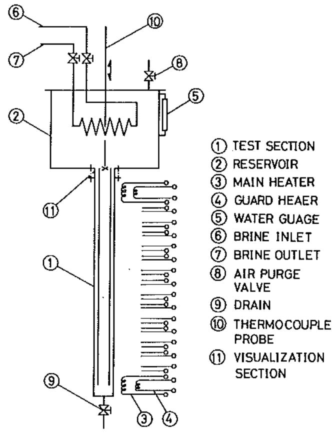

Fig. 1 Schematic diagram of experimental set up

In a series of experiments, a fresh fluorocarbon R-11 refrigerant packed in 20 kg vessel, which has been preserved in the temperature-controlled room at 15°C, was always charged to the thermosyphon system.

Results and Discussions

In all, 104 experimental runs were conducted for the various temperatures of heated outer tube. Measurements were made as the temperatures of heated outer tube varied from 15.6 to 52.5 °C. All physical properties were based on the arithmetic mean temperature of the heated outer tube and that of the entrance-fluid into inner tube. A more complete documentation of the data is included in [26].

Visual Observation. Qualitative visual observations were conducted to examine the effect of the presence of inner tube on the boiling phenomena which take place near the open end of the single-tube open thermosyphon or the concentric-tube one.

Flow visualization for the boiling phenomena of the single-tube open thermosyphon and the vertical narrow annular channel has been studied extensively by previous investigators [9–11]. The present observations were mainly focused on the flow-exit phenomena with boiling near the open end of the concentric-tube open thermosyphon.

For a single-tube open thermosyphon using fluorocarbon R-11 refrigerant as a working fluid, it was assessed that the present results observed may be approximately similar to those of Kusuda and Imura [9] using pure water as working fluid. It was observed that bubbles generated along the heated tube rise without coalescence and carried back some of the cool fluid (flow downward), as schematically shown in Fig. 2(*a*). Kusuda and Imura [9], furthermore, claimed that onset of bubble coalescence and accompanying pulsation throughout the whole channel occurs as the heat flux is increased. Such a phenomenon, however, was not observed within the range of present experimental parameters examined. This is mainly attributed to both the

Nomenclature

a = inner radius of heated tube, $D/2$
d_i = inner diameter of inner tube
d_o = outer diameter of inner tube
D = inner diameter of heated tube
g = gravitational acceleration
L = tube length of thermosyphon
p = dimensionless pressure normalized by atmospheric pressure
q = total heat flux from heated tube
q_b = heat flux due to boiling heat transfer
q_{ex} = measured heat flux
q_c = heat flux due to free convective heat transfer
q_{cal} = calculated heat flux based on equations (2) or (3), (4) + equations (5), (6), respectively
r = equivalent heat-transfer radius, $(D^2 - d_0{}^2)/(2D)$
t_a = dimensionless temperature based on inner radius, $g\beta\Delta T a^3/(\nu\kappa)$
t_r = dimensionless temperature based on equivalent heat-transfer radius, $g\beta\Delta T r^3/(\nu\kappa)$
T_e = temperature of entrance-fluid at open end of thermosyphon
T_s = temperature of saturated fluid
T_w = temperature of heated surface
ΔT = temperature difference between heated wall and entrance-fluid, $T_w - T_e$
ΔT_s = temperature difference between heated wall and saturated fluid at open end of thermosyphon, $T_w - T_s$
α_b = boiling heat-transfer coefficient, $q_b/(T_w - T_s)$
β = coefficient of volumetric expansion
κ = thermal diffusivity
λ = thermal conductivity
μ = viscosity
ν = kinematic viscosity

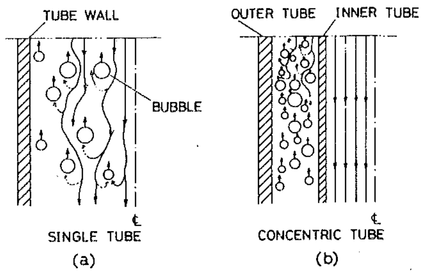

Fig. 2 **Schematic drawing of flow pattern near open end of thermosyphon**

differences of the working fluid and the dimension of the heated tube (Kusuda and Imura [9] used a markedly small channel of the rectangular section of 300 mm in length and 50 mm in width).

On the other hand, as will be appreciated by an inspection of Fig. 1, for the concentric-tube open thermosyphon the primary effect of heating the outer tube should be to cause flow upward along the wall of the tube due to the buoyancy effect and an associated return flow downward in the inner tube via continuity. It was, thus, observed that the cool fluid without bubbles in the inner tube comes down to the bottom while the hot fluid with a number of bubbles due to evaporation rises up the annulus like the pure free convection in the concentric-tube open thermosyphon. It was, furthermore, found that with small d_0 (large annular space) some of the cool fluid (flow downward) tends to enter into the annulus, hence a serious interaction between the ascending flow with bubbles and the descending cool fluid occurs near the open end of the annulus, as will be shown in Fig. 2(*b*). It was also observed that for large d_0 (small annular space) a three-dimensional flow with bubbles occurs near the place where the tube meets the reservoir.

The effects of annular-space width on the boiling heat transfer in a vertical annular channel was extensively studied by Ishibashi and Nishikawa [11]. They showed that the boiling phenomena without any coalescence of bubbles when the annular space is greater than 5 mm in width are closely similar to those of pool boiling along the vertical surface, while for annular space smaller than 5 mm in width the bubbles tend to coalesce and continue to grow further to large size and are accompanied by pulsation at low frequency as the annular space becomes smaller than 2.7 mm in width.

Therefore, the fact that the coalesced bubbles could not be obtained in the range of present experimental parameters examined (annular space $\geqq$ 5.7 mm in width) appears to be well consistent with results obtained by Ishibashi and Nishikawa [11].

Temperature Distributions. Typical temperature distributions in the inner tube (flow downward) and in the annulus (flow upward) for the concentric-tube open thermosyphon are shown in Fig. 3, where d_0 denotes the outer diameter of the inner tube. The ordinate is the fluid temperature of the core in the inner tube or in the annulus, while the abscissa is the actual distance from the bottom of the thermosyphon. The dotted line in the figure indicates the saturation-temperature distribution of the working fluid which is evaluated by taking the local static pressure into account.

It is quite natural that the heating of the outer tube will cause a flow upward in the annulus due to buoyancy and an associated return flow downward in the inner tube via continuity, as pointed out earlier. The temperature of the fluid in the annulus is, thus, expected to increase as the fluid flows up along the outer tube. It is, however, clear that the temperature of the fluid in the annulus increases initially with an increase in axial distance from the bottom, goes through a maximum at a certain distance from the bottom, and then decreases with further increase in *L*. This phenomenon may be physically understood by considering that after the temperature of the fluid in the annulus becomes identical to the saturation temperature at a certain distance from the bottom, boiling within the working fluid becomes possible in the annulus, depending upon the gradient of the saturation pressure-temperature relationship of the fluid.

On the other hand, the temperature of the fluid in the inner tube appears to be quite uniform until the cool fluid turns upward from the inner tube into the annulus, thus indicating that the heat transferred between upward and downward flows is unexpectedly quite small. It should be, thus, noted that for the concentric-tube open thermosyphon there might be two different flow regimes with and without boiling in working fluid even if the working fluid at the entrance section of the inner tube is completely saturated.

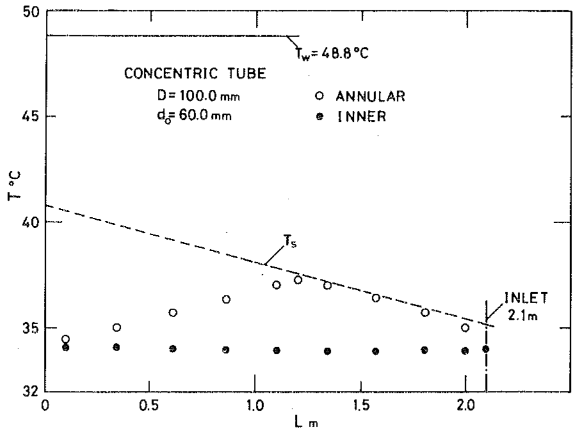

Fig. 3 **Distributions of core-fluid temperature for concentric-tube thermosyphon**

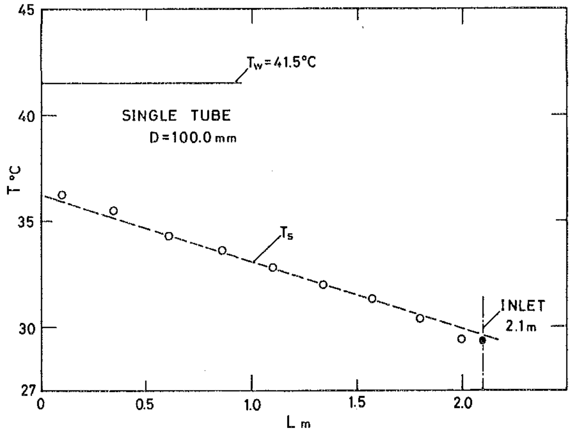

Fig. 4 **Distribution of core-fluid temperature for single-tube thermosyphon**

Figure 4 shows a typical temperature distribution of the working fluid along the core of a single-tube open thermosyphon without an inner tube. The difference between temperature distributions of Figs. 3 and 4 is quite evident. The temperature distribution mentioned above is closely in accordance with that of the saturation pressure-temperature relationship, which reveals that the boiling within the working fluid may take place throughout the thermosyphon tube. Such a trend as shown in Fig. 4 was also reported by Kusuda and Imura [9] who conducted an experimental study on a single-tube open thermosyphon under the condition of uniform heat flux.

Boiling Heat-Transfer Curve. As pointed out earlier, it appears that the process of the boiling with free convection in a vertical annulus heated from outside may be still more complicated than that of common boiling in a pool, because the vapor-bubbles cannot rise freely from a submerged heater, but are constrained to rise in a relatively narrow space, becoming more and more crowded and displacing more liquid. It is firstly, however, natural to evaluate the characteristics of boiling heat transfer for the present thermosyphon in the form of conventional boiling curve. In the present study, to more clearly investigate the transition regime from the free convection to the developed boiling, ΔT may be firstly defined as the temperature difference between the heated surface temperature and the inlet fluid temperature at the open end of the thermosyphon.

Figure 5 shows the heat transfer rate q as a function of the temperature difference ΔT. As will be seen in Fig. 5, the q increases at a moderate rate with ΔT, while at approximately ΔT = 13°C and ΔT

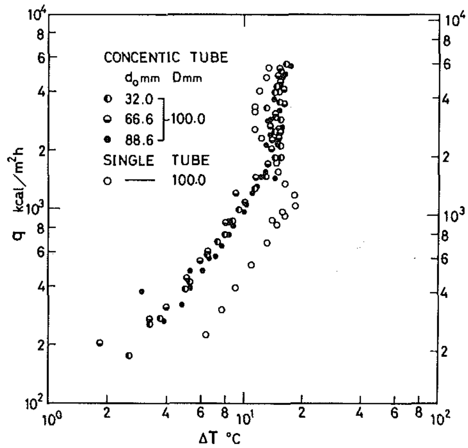

Fig. 5 Boiling curves showing departure from free convection heat transfer

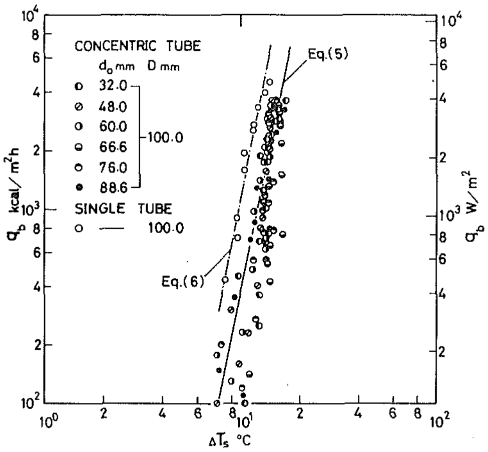

Fig. 6 q_b versus ΔT_s

= 18°C for the concentric-tube and the single-tube open thermosyphons, respectively, the rate of the increase becomes to a great extent larger. It was reported by Seki, et al. [12] that for the concentric-tube thermosyphon of closed system, bubbles take place only on a few selected spots of the heating surface in the range of smaller ΔT than about 10°C. It is, thus, expected that the smaller number of bubbles may have a minor contribution on heat transfer and that the heat-transfer rate may be mainly governed by free convection in the annulus. However, the number of spots on which bubbles start becomes larger with an increase in ΔT, and at a temperature difference beyond about $\Delta T = 13°C$ heating surface is so densely populated with bubbles that their separation may cause an appreciable stirring action in the ascending fluid which gives rise to an increase of the heat transfer. This might be considered to be the reason for steeper increase of the q in the region $\Delta T > 13°C$.

Of interest is the fact that for the single-tube open thermosyphon after the so-called inception of developed boiling, ΔT decreases rapidly with an increase in q, yielding a marked neck of boiling curve, as will be clearly seen in Fig. 5. Such a great overshooting of ΔT at near the inception of developed boiling appears to be caused by the rapid transition from the subcooled boiling to saturated pool boiling due to the more serious stirring-action of the bubbles which may take place more successively with an increase in heat flux. It should be noted that in the range of the developed boiling the temperature of entrance-fluid at the open end of the thermosyphon-tube was nearly maintained at the saturated one under the prescribed pressure in the reservoir. For the concentric-tube open thermosyphon, on the other hand, this trend was not observed because subcooled fluid turns upward from the inner tube into the annulus at the bottom of the concentric-tube even if the working fluid at the entrance section of the inner tube is completely saturated, as will be suggested from the saturation-temperature relationship in Fig. 3.

Correlation of Boiling Heat Transfer. The present experimental results were firstly examined to be correlated using a similar method to that adopted by previous investigators [13–16] for correlating forced-convection boiling heat-transfer data. It was assumed that in the case of boiling with free convection the convection effects can be superimposed on the bubble motion effects, and the total heat flux thus is

$$q = q_b + q_c \tag{1}$$

The free covective heat-transfer rate was calculated from the experimentally determined values by Seki, et al. [2] as follows, for the concentric-tube open thermosyphon

$$q_c = 0.980 \frac{\lambda}{r} t_r^{0.25} \Delta T \ (1 \times 10^5 \leq t_r) \tag{2}$$

$$q_c = 0.197 \frac{\lambda}{r} t_r^{0.388} \Delta T \ (t_r < 1 \times 10^5) \tag{3}$$

for the single-tube open thermosyphon

$$q_c = 0.0158 \frac{\lambda}{a} t_a^{0.443} \Delta T \ (8 \times 10^6 \leq t_a) \tag{4}$$

where r denotes the equivalent heat-transfer radius, t_r the dimensionless parameter based on r, a the inner radius of the heated tube, and t_a the dimensionless parameter based on a, respectively, as will be defined in Nomenclature. The combination of equations (1) and (2–4) results in q_b, representing that portion of the heat-transfer rate which is only due to bubble-motion effects.

The resulting graph of q_b versus ΔT_s is shown in Fig. 6. In the present study, ΔT_s may be defined as the temperature difference between the heated surface temperature T_w and saturation temperature T_s at the open end of the thermosyphon under the prescribed pressure of the reservoir. As will be shown in Fig. 6, it is elucidated that the points representing q_b-versus-ΔT_s could be correlated approximately by a straight line on a log-log plot for both the single-tube and the concentric-tube open thermosyphons, respectively. Furthermore, it can be seen that the heat-transfer rate for the single-tube open thermosyphon is greater than that for the concentric-tube open one in the whole range of parameter studied, yielding a clear contrast to the tendency in the free-convection region (see equations (2–4)).

This characteristic may be understood by the fact that for the single-tube open thermosyphon the boiling within the working fluid would be taking place axially throughout the whole tube because the temperature of fluid is closely in accordance with that of the saturation pressure-temperature relationship, while for the concentric-tube open thermosyphon there exist two kinds of flow regimes with and without boiling even if the working fluid at the open end of the thermosyphon is completely saturated, namely, developed boiling might be taking place only on an upper portion of the heating surface, as pointed out earlier in Fig. 3.

It is elucidated from the Fig. 6 that the present experimental results using fluorocarbon R-11 refrigerant as a working fluid can be correlated by following equations in the range of parameters investigated.

For the concentric-tube open thermosyphon

$$q_b = 3.85 \times 10^{-3} (\Delta T_s)^5 \tag{5}$$

For the single-tube open thermosyphon

$$q_b = 1.21 \times 10^{-1} (\Delta T_s)^5 \tag{6}$$

As elucidated above, it is thus evident that ΔT_s is also an important variable controlling the nature and the rate of the heat-transfer process in the regime with boiling for the present system as well as for the common boiling in pool. The exponent in equations (5) and (6) stands in good accordance with values reported in [17].

Boiling Heat-Transfer Coefficients. It may be of great interest to compare the present experimental results with those for the pool boiling reported by Nishikawa, et al. [18, 19], who extensively investigated the effects of the saturation pressure on the pool-boiling heat transfer using fluorocarbon R-11 and R-113 refrigerants as working

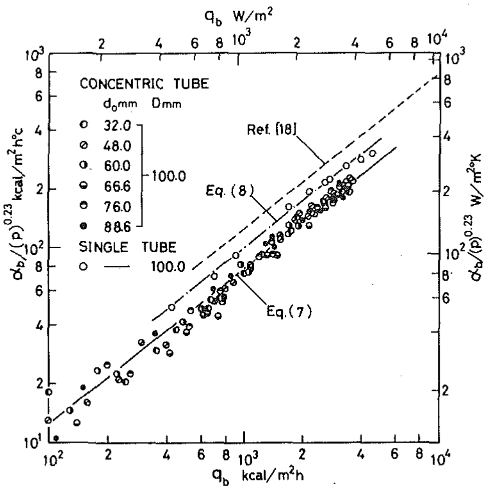

Fig. 7 Correlations of boiling heat transfer data

fluids. It appears that this comparison may give an evaluation for the boiling heat-transfer performances of the present thermosyphons.

The heat-transfer coefficient α_b as a function of heat flux q_b is shown in Fig. 7, where p denotes the dimensionless pressure normalized by the atmospheric pressure, thus taking into account the saturation pressure. In the present program p is varied from 1.0 to 1.65. For the calculation of α_b in term of $q_b/(T_w - T_s)$ the saturation temperature T_s at the open end of the thermosyphon was utilized.

From an inspection of this figure, the slope of the present experimental results for both the concentric-tube and the single-tube open thermosyphons seem to be in closely good accordance with that of Nishikawa, et al. [18, 19], though the operating conditions are quite different. It is, however, clear that the heat-transfer coefficients for the present thermosyphon are rather small as compared to that of Nishikawa, et al. [18, 19], within the whole range examined. This may be attributed to the fact that in the case of the present program the evaluation of the saturation temperature at the open end of the thermosyphon is utilized, namely, that the smallest value of T_s varying along the heated surface is adopted. It would be furthermore found that the present results for the single-tube open thermosyphon might be in good accordance with that of Nishikawa, et al. [18, 19] if the average of T_s which varies axially corresponding to the saturation pressure-temperature relationship would be utilized.

Hence, it appears to be concluded that the boiling heat-transfer performance for the single-tube open thermosyphon using the fluorocarbon R-11 as a testing fluid at least may qualitatively be quite similar to that for the common pool boiling of fluorocarbon R-11 refrigerant. Simple correlations which may satisfy the boiling heat-transfer performances of fluorocarbon refrigerant for both the concentric-tube and the single-tube open thermosyphons are given as follows, respectively.

For the concentric-tube open thermosyphon

$$\alpha_b = 0.311(q_b)^{0.8}(p)^{0.23} \tag{7}$$

For the single-tube open thermosyphon

$$\alpha_b = 0.398(q_b)^{0.8}(p)^{0.23} \tag{8}$$

Effect of Diametric Ratio of Concentric-Tube on Boiling Heat Transfer. Now, in addition to the matters mentioned above, it appears to be of importance to investigate the effect of the diameter of the inner tube on the boiling heat-transfer performance for the concentric-tube open thermosyphon. As will be seen from Figs. 5–7, it seems that the boiling heat fluxes may show no significant dependency on the diameter of inner tube (i.e., the width of annular space) for the concentric-tube thermosyphon investigated in this study.

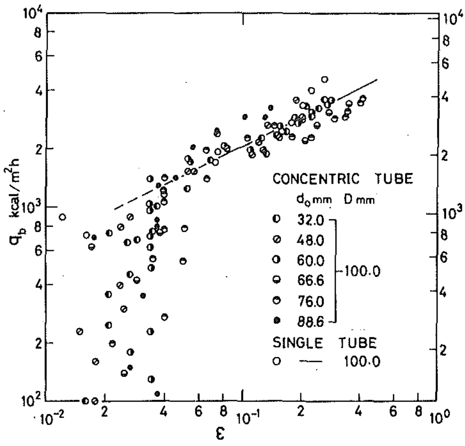

Fig. 8 q_b versus ϵ

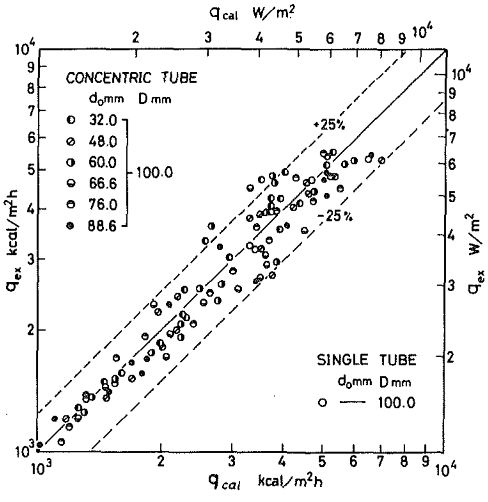

Fig. 9 Comparison of q_{ex} with q_{cal}

Ishibashi and Nishikawa [11] studied the effect of the width of vertical annular channel heated from inside unlike the present system on the boiling heat-transfer characteristics by using pure water as a testing fluid, and found that for the annular spaces less than 2.7 mm in width the heat-transfer coefficient has a tendency to markedly increase with a decrease in width due to occurrence of the coalescence of bubbles, while for the annular spaces greater than 5.1 mm in width the rate of increase of the coefficient is relatively small. Hence, it appears to be reasonable that the boiling heat transfer for the concentric-tube open thermosyphon may be nearly independent of the diameter of inner tube (i.e., the width of annular space) because in the present program width of the annular space ranged from 34.0 to 5.1 mm.

Effect of Void Ratio on Boiling Heat Transfer. An attempt was made to consider the relationship between the boiling heat flux and the mean void ratio for the present thermosyphon. In Fig. 8 is plotted the boiling heat flux q_b as a function of the mean void ratio ϵ, which is the ratio of the vapor space to the total volume of the annulus. It can be seen in this figure that the boiling heat flux increases steeply at first with an increase in mean void ratio; thereafter, it increases with a gentle slope of dependency on the mean void ratio.

In the range of q_b greater than 10^3 kcal/m^{2}h, it may appear that $q_b{}^2 \propto \epsilon$. This relationship is similar to that obtained by Nishikawa [20] for pool boiling experiments using a heated plate facing upwards, namely, $q_b{}^2 \propto n$, where n denotes the number of vapor columns. Gaertner, et al. [21] claimed that for the fully developed boiling regime the relationship of $d_0 \cdot n = C_1$ may be obtained, where d_0 is defined as diameter of a bubble just leaving the heated surface, and C_1 as a uniform constant. On the other hand, it was pointed out by Nishikawa, et al. [20] and Jakob [22] that for the various heated surfaces, boiling heat fluxes, and working fluids, $d_0 \cdot f$ is a uniform constant, where f denotes the frequency of bubble formation. It may be quite natural to suppose here that the mean void ratio ϵ is in proportion to $d_0 \cdot n \cdot f$.

According to the matters mentioned above, thus, it may be proven that $\epsilon \propto n$. Therefore, it is concluded that the relationship of $q_b{}^2 \propto \epsilon$ for the present thermosyphon shown in Fig. 8 might be quite similar to that of Nishikawa [20] in the range of parameters examined.

Finally, for confirmation, all the data which encompass the boiling heat-transfer process within the working fluid were reproduced in Fig. 9 using the abscissa as q_{cal} (equations (2) or (3, 4) + equations (5, 6), respectively). It may be seen that for both the concentric-tube and the single-tube open thermosyphons using fluorocarbon R-11 refrigerant as a testing fluid, calculated and experimental values agree within an average deviation of approximately ±25 percent.

Conclusions

Boiling heat-transfer characteristics were experimentally investigated for fluorocarbon R-11 refrigerant in the concentric-tube open thermosyphon. Varying the different parameters while maintaining uniform temperature along the heated outer tube, boiling data have been obtained. It is concluded from the present experimental results that total heat flux can be appropriately predicted by a superposition of the convective heat flux given by available correlations (equations (2) or (3, 4)) and pure boiling heat flux given by available correlations (equations (5, 6)). For design purposes for the concentric-tube and the single-tube open thermosyphons these correlations may be utilized.

Acknowledgment

The authors are indebted to Mr. Y. Usami for his help in the experiments.

References

1 Hayakawa, M., "Geothermal Energy," *NHK Books*, 114, Nippon Hoso Kyokai, 1977.

2 Seki, N., Fukusako, S., and Koguchi, K., "Single-Phase Heat Transfer Characteristics of Concentric-Tube Thermosyphon," *Wärme- und Stoffübertragung*, 14, 1980, pp. 189–199.

3 Cohen, H., and Bayley, F. J., "Heat Transfer Problems of Liquid Cooled Gas Turbine Bladed," *Proceedings Institute Mechanical Engineers*, 169, 1955, pp. 1063–1080.

4 Long, E. L., "The Long Thermophile", *Proceedings Permafrost International Conference*, 1963, pp. 487–491.

5 Chato, J. C., "Condensation in a Variable Acceleration Field and the Condensing Thermosyphon," ASME *Journal of Engineering Power*, Vol. 87, 1965, pp. 355–360.

6 Genot, J., and LeGrives, E., "Transfert de Chaleur des Ailettes de Turbine," *Fourth International Heat Transfer Conference*, Paris, HE 2.2, 1970.

7 Larkin, B. S., "An Experimental Study of a Two-Phase Thermosyphon Tube," 70-CSME-6, 84th Annual Meeting, Engng, Institute of Canada, Ottawa, 1970.

8 Lee, Y., and Mital, U., "A Two-Phase Closed Thermosyphon," *International Journal of Heat Mass Transfer*, 15, 1972, pp. 1673–1707.

9 Kusuda, H., and Imura, H., "Boiling Heat Transfer in an Open Thermosyphon (1st Report)," *Bulletin of JSME*, 16, 1973, pp. 1723–1733.

10 Kusuda, H., and Imura, H., "Boiling Heat Transfer in an Open Thermosyphon (2nd Report)," *Bulletin of JSME*, 16, 1973, pp. 1734–1740.

11 Ishibashi, E., and Nishikawa, K., "Boiling Heat Transfer in Narrow Space (1st Report)," *Trans. JSME*, 33, 1967, pp. 121–129.

12 Seki, N., Fukusako, S., Cheng, K. C., and Kawabe, H., "Heat Transfer Characteristics of Double Tube Thermosyphon," *Proceedings of Brasilian Energy Congress*, Rio de Janeiro, A-5, 1978, pp. 43–53.

13 Rohsenow, W. M., "Heat Transfer with Evaporation," Lectures at Symposium on Heat Transfer, University of Michigan, 1953, pp. 101–1491.

14 Clark, J. A., and Rohsenow, W. M., "Local Boiling Heat Transfer to Water at Low Reynolds Numbers and High Pressures," ASME JOURNAL OF HEAT TRANSFER, Vol. 76, 1954, pp. 553–562.

15 Bergles, A. E., and Rohsenow, W. M., "The Determination of Forced-Convection Surface-Boiling Heat Transfer," ASME JOURNAL OF HEAT TRANSFER, Vol. 86, 1964, pp. 365–372.

16 Blall, T. A., and Adt. Jr, R. R., "An Experimental Investigation of Boiling Heat Transfer and Pressure-Drop Characteristics of Freon 11 and Freon 113 Refrigerants," *AIChE Journal*, Vol. 10, 1964, pp. 369–373.

17 McAdams, W. H., *Heat Transmission*, 3rd edition, McGraw-Hill, New York, 1963.

18 Nishikawa, K., Fujita, K., and Hidaka, S., "Nucleate Boiling Heat Transfer of Fluorocarbon Refrigerants (1st Report)," Preprint of National Heat Transfer Symposium of Japan, 1977, pp. 130–132.

19 Nishikawa, K., Fujita, K., Ota, H., and Hidaka, S., "Nucleate Boiling Heat Transfer of Fluorocarbon Refrigerants (2nd Report)," Preprint of National Heat Transfer Symposium of Japan, 1978, pp. 148–150.

20 Nishikawa, K., "Effect of Surface Roughness on Boiling Heat Transfer," *Trans. JSME*, Vol. 20, 1954, pp. 808–815.

21 Gaertner, R. N., and Westwater, J. W., "Nobel Method for Determining Nucleate Boiling Sites," *Chemical Engineering Progress Symposium.*, Ser., Vol. 55, 1959, pp. 58–61.

22 Jakob, M., *Heat Transfer*, Vol. 1, 1949, John Wiley, New York.

23 McDonald, T. W., Hwang, K. S., and Diciccio, R., "Thermosiphon Loop Performance Characteristics: Part 1. Experimental Study," *ASHRAE Transaction*, Vol. 83, 1977, pp. 250–259.

24 Ali, A. F. M., and McDonald, T. W., "Thermosiphon Loop Performance Characteristics: Part 2. Simulation Program," *ASHRAE Transactions*, Vol. 83, 1977, pp. 260–278.

25 McDonald, T. W., and Ali, A. F. M., "Thermosiphon Loop Performance Characteristics: Part 3. Simulated Results," *ASHRAE Transactions*, Vol. 83, 1977, pp. 279–287.

26 Koguchi, K., "Heat-Transfer Characteristics of Concentric-Tube Thermosyphon," M. S. Thesis, Department of Mechanical Engineering, Hokkaido University, Sapporo, Japan, 1979.

M. Z. Hasan[1]
Research Assistant,
School of Engineering and Applied Science,
University of California,
Los Angeles, Calif.
Assoc. Mem. ASME

M. M. Hasan
Research Assistant,
Assoc. Mem. ASME

R. Eichhorn
Dean of Engineering,
Fellow ASME

J. H. Lienhard[1]
Professor,
Mechanical Engineering Department,
University of Houston,
Houston, Tex. 77004
Fellow ASME

Boiling and Phase Change Laboratory,
Mechanical Engineering Department,
University of Kentucky,
Lexington, KY 40506

Boiling Burnout During Crossflow over Cylinders, beyond the Influence of Gravity[2]

New observations of burnout during the upflow and downflow of isopropanol and methanol over horizontal cylinders are added to previous observations. A criterion is developed to determine whether or not gravity influences burnout in any such flow. A prediction that depends on one empirical constant is then developed to predict burnout when gravity is not influential. Those of the existing data that are uninfluenced by gravity are represented within ±20 percent by the prediction. It is also shown that a low-speed downflow can cause the hydrodynamic burnout to be replaced with a very inefficient buoyancy burnout mechanism.

Introduction

Most industrial heat removal by flow boiling has been done *within* tubes, or in the axial channels separating tubes within closely packed tube bundles. However, there is increasing interest in the high heat fluxes that can be achieved in the *crossflow* of liquids over single tubes and tube bundles. Our concern is that of predicting the peak heat flux, or "burnout" in such flows.

Previous Work. Many previous experimenters have provided observations of the burnout heat flux for crossflows over single cylinders. Those data that appear to be free of such nuisance variables as end-mounting influences, short aspect ratio effects, etc., include Vliet and Leppert's water data [1, 2], Cochran and Andracchio's Freon 113 data [3], Min's water and methanol data [4], Eichhorn's isopropanol data [5], and Yilmaz and Westwater's Freon-113 data [6]. If there are other data, we are either unaware of them or do not have enough documentation to deal with them here.

The work of Lienhard and Eichhorn [5] provided a strategy for predicting the peak heat flux on single cylinders with the help of a mechanical energy stability criterion. They observed that burnout occurs when more kinetic energy relative to the flow, $\rho_g u_g (u_g{}^2/2)\,\alpha D$, enters the wake than surface energy $2\sigma u_\infty$, is consumed by it. (See Fig. 1. See also [5] or the discussion in [7]. This analysis gave

$$\frac{u_g}{u_\infty} = \left(\frac{4}{\alpha \mathrm{We}_g}\right)^{1/3} \tag{1}$$

where[3] $\mathrm{We}_g \equiv \rho_g u_\infty{}^2 D/\sigma$. A simple energy balance gives

$$q_{\max} = \rho_g h_{fg}\,(u_\infty + u_g)\,\frac{A_{\text{jet}}}{A_{\text{heater}}} \tag{2}$$

so

$$\phi \equiv \frac{\pi q_{\max}}{\rho_g h_{fg} |u_\infty|} = \alpha\left[1 + \frac{u_g}{u_\infty}\right] = \alpha + \frac{(2\alpha)^{2/3}}{\mathrm{We}_g{}^{1/3}} \tag{3}$$

The one problem that remained was the evaluation of the jet contraction factor, α. The existing data seemed to suggest that, for low velocity flows, α was close to unity, and for high velocity flows it was

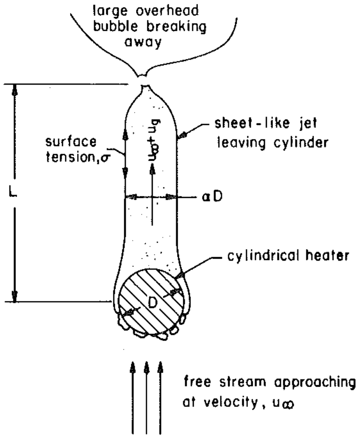

Fig. 1 Schematic diagram of vapor removal process during boiling on a cylinder in a liquid crossflow

$$\alpha \simeq \text{constant}\,(\rho_f/\rho_g)^{3/4}$$

The Scaling of Gravity and Heater Diameter. The flow in all previous experiments was upward over the cylinder so that gravity aided vapor removal. Normally, the Froude number, which might be defined as

$$\mathrm{Fr} \equiv \sqrt{\rho_f u_\infty{}^2/gD(\rho_f - \rho_g)} \simeq u_\infty/\sqrt{gD} \tag{4}$$

determines whether or not gravity actually exerts an influence on the flow. Typically, a value of Fr >10 suggests that gravity ceases to be a major influence on the flow. Only the data of Yilmaz and Westwater, and some isolated points of Min's, and Vliet and Leppert's satisfy this criterion.

Lienhard and Eichhorn's prediction did not take account of the influence of gravity and unfortunately the data in [1–5] all fell in the range: $0.76 < \mathrm{Fr} < 16.4$. Their correlation might well predict results that would be different if the gravity field were altered.

There is a second influence that is connected to gravity, and that is *local* surface tension—surface tension forces that are related to bubble behavior at the heater surface. Such bubbles might have a role in shaping the liquid-vapor interface (and in determining α) at low velocity, but not at high velocity. Gravity will also have a role in shaping these bubbles. Thus there should also be an influence of the liquid Weber number, We_f

$$\mathrm{We}_f \equiv \frac{\rho_f u_\infty{}^2 D}{\sigma} \sim \frac{\text{liquid inertia}}{\text{capillary force}} \tag{5}$$

---

[1] Most of this study was done while J. H. Lienhard and M. Z. Hasan were at the University of Kentucky.

[2] This work was supported by the National Science Foundation under Grant ENG77-25029.

[3] Symbols not defined in context or in Fig. 1 are conventional ones. They are defined in the Nomenclature.

Contributed by the Heat Transfer Division for publication in the JOURNAL OF HEAT TRANSFER. Manuscript received by the Heat Transfer Divison July 24, 1980.

if We_f is small—say less than 10.

We have carefully studied the dependence of ϕ on both Fr and We_f. For upflow, the existing ϕ data correlate reasonably well with We_f, even when We_f is as low as 10. For downflow, there is a diameter effect of Fr and ϕ does not correlate with either Fr or We_f alone unless both parameters are large. From our observations, however, the demarcation between gravity dependent burnout and gravity independent burnout becomes independent of diameter when $|u_\infty|$ is large enough. If this is to be the case, the point of demarcation must be governed by a parameter, made up of Fr and We_f, that does not depend on D. We designate this parameter (similar to a Kutataladze number) as G:

$$G \equiv \sqrt[4]{\mathrm{We}_f \mathrm{Fr}^2} = \sqrt[4]{\frac{\rho_f{}^2 u_\infty{}^4}{g(\rho_f - \rho_g)\sigma}} \simeq \frac{u_\infty}{\sqrt[4]{g\sigma/\rho_f}} \qquad (6)$$

The Region of Gravity-Influenced Behavior. We assume that equation (3) is correct for predicting the burnout heat flux, whether or not gravity influences are present. It should only fail when such influences become so extreme as to replace the hydrodynamic stability mechanism with some other kind of burnout mechanism. Therefore, the influence of gravity will merely be that of changing the magnitude of the contraction factor, α, in equation (3).

Objectives of the Present Work. The previous considerations point to the need for more experiments, and a more comprehensive theory, than are now available. We therefore aim to

1 Provide observations of $q_{\max}$ in both upflow and downflow over cylinders, with Fr being varied from $\ll -10$ to $\gg +10$, and We_f from near zero to $\gg 10$.

2 Use these data to identify a critical value of $|G| = G_c$, above which gravity exerts no influence.

3 Determine α for flows for which $|G| > G_c$.

4 Provide a general prediction or correlation of ϕ for $|G| > G_c$.

The Prediction of $q_{\max}$ in the High-Speed Limit

The Prediction of α. Figure 2 shows a control volume located around the cylindrical heater. We can neglect viscous influences because the liquid flow around the cylinder is almost a pure slip-flow. The vapor "lubricates" the liquid flow around the cylinder so the only significant drag force, F, exerted on it is *pressure* drag. Then a momentum balance gives

$$\Sigma(\text{forces and momentum fluxes to right}) = F(N/m)$$

or

$$\rho_f u_\infty{}^2 L - \rho_f u_\infty{}^2(L - \alpha D) - \rho_g(u_g + u_\infty)^2 \alpha D - \rho_f u_\infty{}^2 \alpha D\left[1 - \frac{\rho_g}{\rho_f}\left(\frac{u_g}{u_\infty} + 1\right)\right] + 2\sigma = F \qquad (7)$$

Simplifying this equation and introducing the notations: $r \equiv \rho_f/\rho_g$, $\mathrm{We}_g \equiv \rho_g u_\infty{}^2 D/\sigma$, $\mathrm{We}_f \equiv \rho_f u_\infty{}^2 D/\sigma$, $C_D \equiv F/\rho_f u_\infty{}^2 D$, and $\phi/\alpha = 1 + u_g/u_\infty$, we obtain a relation between α and F and C_D:

$$-\phi\left(\frac{\phi}{\alpha} - 1\right) = rC_D - \frac{2}{\mathrm{We}_g} = r\left(C_D - \frac{2}{\mathrm{We}_f}\right) \qquad (8)$$

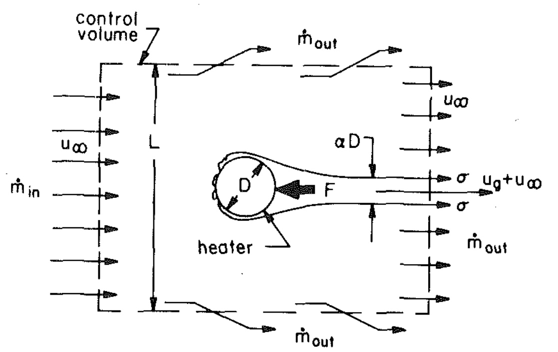

$$\dot{m}_{\text{in left}} = \rho_f u_\infty L$$

$$\dot{m}_{\text{out right}} = \rho_f u_\infty (L - \alpha D) + \rho_g (u_g + u_\infty)\alpha D$$

$$\dot{m}_{\text{out sides}} = \dot{m}_{\text{in left}} - \dot{m}_{\text{out right}} = \rho_f u_\infty \alpha D - \rho_g (u_g + u_\infty)\alpha D$$

$$= \rho_f u_\infty \alpha D\left[1 - \frac{\rho_g}{\rho_f}\left(\frac{u_g}{u_\infty} + 1\right)\right]$$

Fig. 2 Control volume around heater, and mass balance

We can only complete the derivation when we can predict C_D. However, consider one preliminary result of this balance. The mechanical energy stability criterion, equation (3), makes it clear that for high liquid velocities ($\mathrm{We}_g \to$ large) the dimensionless heat flux, ϕ, must approach α. Under those circumstances C_D must also approach zero in accordance with equation (8). Such a result matches our expectation because, at high heat flux, vapor moves at a speed close to u_∞ and blankets almost all of the cylinder, the no slip conditions disappears, and the flow approaches a perfect potential flow of liquid around the cylinder.

Notice, too, that the drag is composed of three contributions:

$$C_D = \underbrace{\frac{2}{\mathrm{We}_f}}_{\substack{\text{surface tension}\\ \text{contribution}\\ \text{(always positive)}}} + \left[-\frac{\phi}{r}\left(\frac{\phi}{\alpha} - 1\right)\right] \qquad (9)$$

liquid momentum cont. (always positive).

vapor thrust contribution (always negative).

When we substitute actual numbers in equation (9), in the next section, we shall see that the vapor jet exerts a thrust, driving the heater into the flow throughout most, if not all, of the velocity range. Thus C_D is generally negative.

The evaluation of C_D. The drag coefficient consists of two parts. The first one is explicitly $2/\mathrm{We}_f$ and the other becomes, with the help of equation (3),

$$-\frac{\alpha}{r}\frac{\phi}{\alpha}\left(\frac{\phi}{\alpha} - 1\right) = -\left(2\frac{\alpha}{r}\right)^{2/3} \frac{1}{\mathrm{We}_f{}^{1/3}}\left[\left(\frac{4}{\alpha}\right)^{1/3} \frac{r^{1/3}}{\mathrm{We}_f{}^{1/3}} + 1\right]$$

This can be rearranged into

$$\frac{\phi}{r^{1/3}}\left(\frac{\phi}{r} - 1\right) - \frac{(2\alpha)^{2/3}}{(\mathrm{We}_f)^{1/3}} = \left(\frac{16\alpha/r}{\mathrm{We}_g{}^2}\right)^{1/3} \qquad (10)$$

Nomenclature

A_{jet}; A_{heater} = cross-sectional area of vapor jet leaving heater; area of the heater itself

C = empirical constant defined in equation (11)

C_D = drag coefficient, $F/\rho_f u_\infty{}^2 D$

D = diameter of heater

F = drag force exerted on the cylinder in the direction of flow (may be negative)

Fr = Froude number, $\sqrt{\rho_f u_\infty{}^2/gD(\rho_f - \rho_g)} \simeq u_\infty/\sqrt{gD}$

G = gravity influence parameter, $\sqrt{\mathrm{We}_f \mathrm{Fr}^2} \simeq u_\infty/\sqrt[4]{g\sigma/\rho_f}$ (positive or negative depending upon whether u_∞ is directed upward or downward)

G_c = critical value of $|G|$ below which gravity influences the flow

g = acceleration of gravity

h_{fg} = latent heat of vaporization of boiled fluid

u_∞; u_g = velocity of liquid relative to the cylinder (positive in the upward direction); velocity of vapor in the jet *relative to the liquid* moving at u_∞

$q_{\max}$ = the burnout, or peak, heat flux on the cylinder

$r = \rho_f/\rho_g$

We_f, We_g = Weber numbers, $\rho_f u_\infty{}^2 D/\sigma$, and $\rho_g u_\infty{}^2 D/\sigma$, respectively

α = jet contraction factor (width of vapor jet/D)

ρ_f, ρ_g = saturated liquid and vapor densities of boiled fluid, respectively

σ = surface tension of the boiling fluid

ϕ = dimensionless peak heat flux, $\pi q_{\max}/\rho_g h_{fg}|u_\infty|$

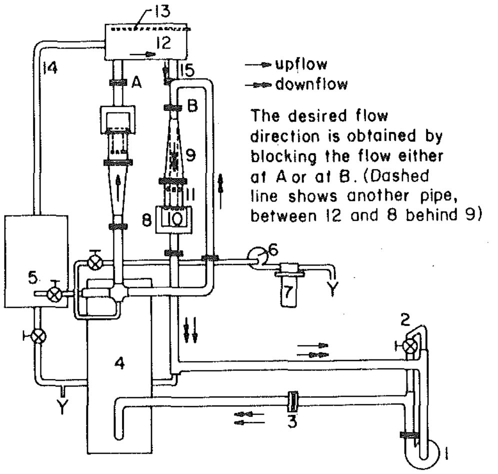

The desired flow direction is obtained by blocking the flow either at A or at B. (Dashed line shows another pipe, between 12 and 8 behind 9)

Fig. 3 A schematic diagram of the experimental facility (1) 200 gpm centrifugal pump (2) by-pass (3) orifice-meter (4) heater (5) drain drum (6) filter pump (7) filter (8) test chamber (9) diffuser (10) glass window (11) nozzle (12) overhead tank (13) condenser coil (14) overflow pipe (15) bubble removal pipe for downflow, liquid return pipe for upflow

Finally we recall from [5] that α was guessed to vary as $r^{3/4}$. That may or may not have been accurate, but we do expect the exponent of the r dependence of α to be on the order of unity. In any event, $(\alpha/r)^{1/3}$ will exhibit very weak dependence on α or r, if it exhibits any. Therefore, we seek a relation of the form:

$$\frac{\phi}{r^{1/3}}\left(\frac{\phi}{\alpha}-1\right)-\frac{(2\alpha)^{2/3}}{(\mathrm{We}_f)^{1/3}}=\frac{C}{\mathrm{We}_g{}^{2/3}} \qquad (11)$$

at high velocity, where C is an empirical constant.

The High-Velocity Prediction of ϕ. Substituting equation (3) in equation (11) and solving the resulting quadratic formula for ϕ, we obtain

$$\alpha^{1/3}=C(r/16)^{1/3} \qquad (12)$$

Substituting equation (12) in (3), we get

$$\phi=\frac{C^3 r}{16}+\frac{C^2}{4}\left(\frac{r^2}{\mathrm{We}_g}\right)^{1/3} \qquad (13)$$

It now remains only to determine C from experimental data.

There are now three orders of business to be resolved:

- We must measure $q_{\max}$ over a wide variety of conditions in both upflow and downflow to identify G_c.
- We must use the data for $|G| > G_c$ to establish the value of C using equations (3) and (11).
- We must then determine whether or not equation (13) predicts observed values of $q_{\max}$ accurately, based on the empirical value of C.

Experiment

The hot flow loop described in [4] and [5] and redesigned by M. Z. Hasan and M. M. Hasan has been used for the present tests. Complete descriptions of the apparatus and experimental procedure are given in [8]. Figure 3 is a schematic diagram of the system. The test section (elements 8, 9, 10 and 11) is shown in its right-side-up, upflow position on the left and in its up-side-down, downflow position on the right:

for upflow: Flange A remains open and flow returns down pipe 15. Flange B is blanked off. The test section is replaced with a neutral run of pipe on the right.

for downflow: Flange A is blanked off and B is open. The test section is replaced with a neutral run of pipe on the left.

The system is designed to accommodate a variety of organic liquids or water. The 2.54 cm wide, two-dimensional nozzle, shown in two views in Fig. 4, delivers liquid at velocities (u_∞) up to 2.6 m/s over a 10.16 cm span. (The cylinder is not shown in place between holders, 4). The nozzle was designed according to the method of Cheers [10] and the velocity profile above it is within 2 percent of being uniform, with the flow virtually free of turbulence. The velocity is inferred from a calibrated ASME orifice meter. All data presented here were obtained in the same nozzle configuration.

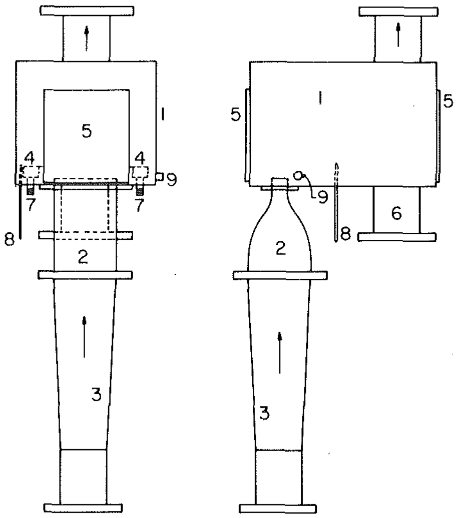

Fig. 4 Test section (to approximate scale only) (1) test chamber (2) nozzle (10.16 cm × 2.54 cm) (3) diffuser (7.66 cm circular to 10.16 cm square section) (4) brass seat for holding device (5) glass windows (6) bubble removal pipe for downflow case. (7) power leads (8) thermometer (9) pressure measurement tap

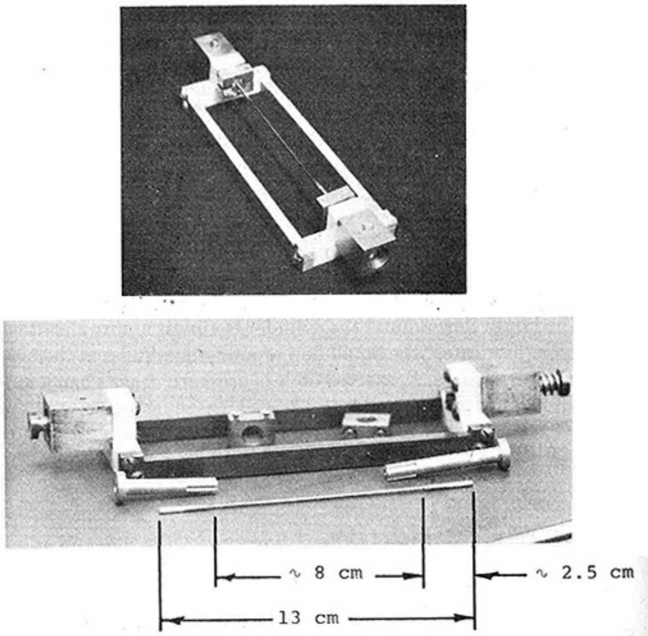

Fig. 5 The test-heater holding-device, giving about 8 cm unobstructed active heater length

The cylindrical heaters were of 14, 20, and 24 gage Nichrome wire. Each one was 13 cm in length with the two ends electroplated with a tapered copper sheath to provide good electrical connections and to minimize end effects. This defined an active unplated length that varied from wire to wire but stayed in the neighborhood of 8 cm. Figure 5 shows a heater wire.

Alternating current was applied to the wires in small steps. The burnout was noted both visually and by a sudden drop of applied current that accompanied it. (The resistance of the wire was carefully obtained prior to the tests.) The probable error of $q_{\max}$ was about ±2.2 percent based on the component measurements and the reproducibility of observations at any condition was found to be within ±2.5 percent.

At each condition, a plot of $q_{\max}$ against liquid subcooling was made and extrapolated over the last 1°C to zero subcooling. Thus all data are reported here for saturated liquid.

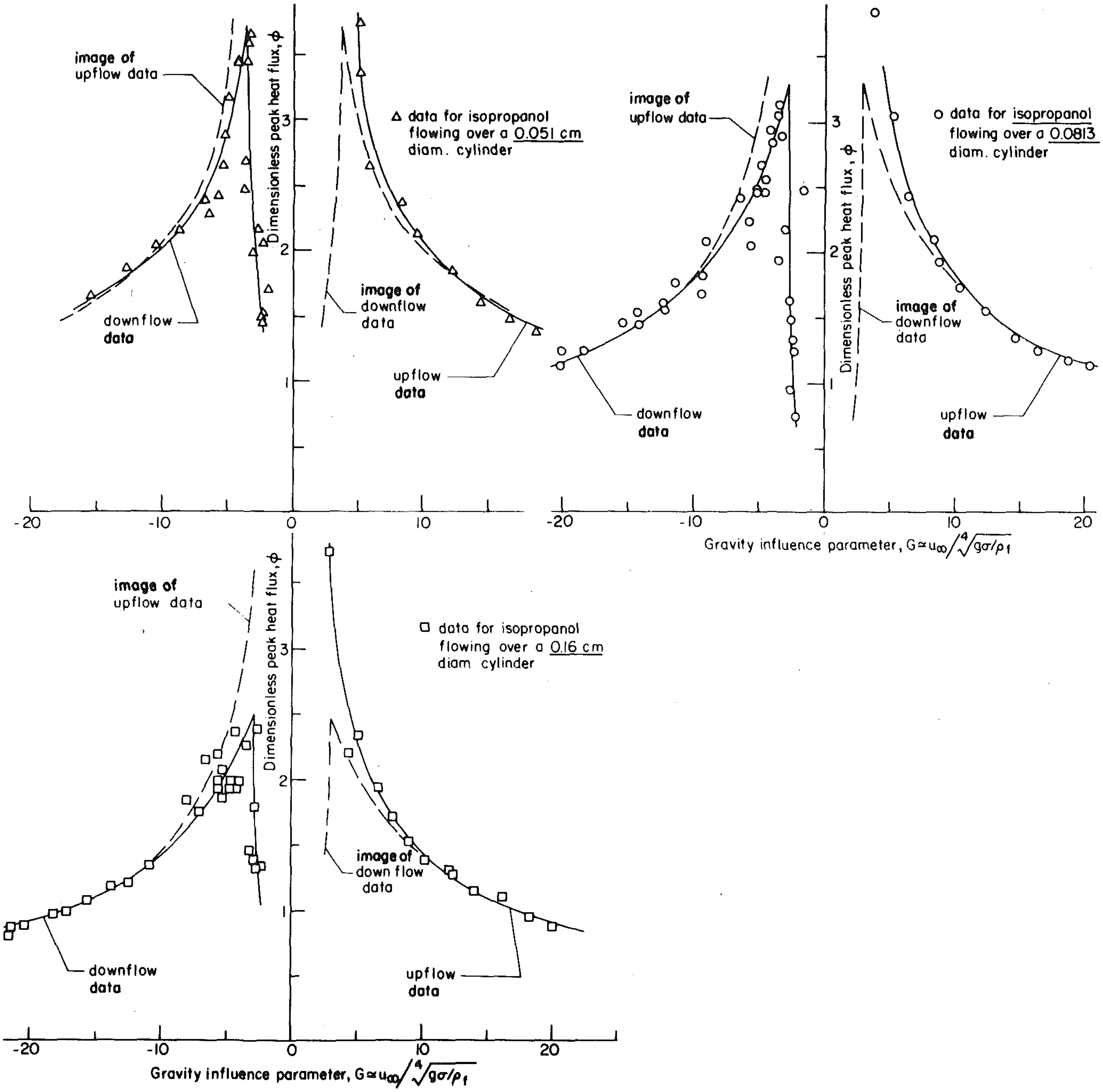

Fig. 6 Influence of gravity on burnout

Results and Discussion

The Identification of the Regime of Gravity Influence. The collected data for the present experiments are tabled in Appendix A. The table includes the raw data ($q_{\max}$, u_∞, and D) and it includes their dimensionless reductions in the form of ϕ, Fr, G, We_f, and $\mathrm{We}_g^{-1/3}$. It also includes the contraction factor, α, calculated by trial and error from known values of ϕ and $\mathrm{We}_g^{-1/3}$ using equation (3). The reader should be warned that neither ϕ_{pred} nor α are offered as valid for $|G| < G_c$.

The dimensionless burnout heat flux is plotted against G for several cases in Fig. 6. Downflow is interpreted as the case for which u_∞ is negative, so downflow data are plotted on left side, in each case. Notice that for $|G| > 10$ the curves are almost perfect mirror images. This is demonstrated by fairing curves through the data on each side, and then dashing the right-hand curve in on the left side, and vice versa. Consequently we identify the critical gravity influence parameter as

$$G_c = 10.$$

Notice that the data diverge only modestly in the range $10 > |G| > 3$. But, for $-3 < G < 0$, ϕ plunges abruptly and drastically. We believe that in the range $10 > |G| > 3$ burnout continues to obey the mechanical energy stability criterion, but that α is altered by gravity in ways that are not reflected in equation (11).

When G is between -3 and zero in a downflow, a dramatic change is evident in the vapor wake. We observed that it became very thick—almost triangular with the apex at the wire. This large, oddly-shaped bubble is suspended in the flow around the wire. As u_∞ is decreased, $q_{\max}$ drops far below the value predicted (see e.g., [9]) for pool boiling. Our data include $q_{\max}$ values as small as 18 percent of the pool boiling limit.

These low values of $q_{\max}$ reflect a burnout model quite different from the hydrodynamic stability limit. Burnout occurs, in this case, as the result of a balance between the rate of buoyant rise of the vapor slug around the cylinder and the downward velocity of the liquid. One would have to be able to predict the equilibrium diameter of such a slug, and the heat transfer through it as well, to determine the mini-

Table 1 Combined raw and reduced data

u_{∞} $\frac{m}{s}$	q_{max} $\frac{MW}{m^2}$	$\phi_{expt.}$	$We_g^{-1/3}$	We_f	Fr	G	α	$\phi_{pred.}$
Isopropanol, r = 334.76; diameter = 0.150 cm								
0.279	0.585	4.490	4.000	5.2	2.30	2.29	0.498	
0.350	0.615	3.763	3.442	8.2	2.89	2.88	0.468	
0.515	0.650	2.703	2.661	17.8	4.25	4.23	0.402	
0.623	0.685	2.355	2.344	26.0	5.14	5.12	0.385	
0.808	0.730	1.935	1.971	43.7	6.66	7.79	0.339	
1.082	0.770	1.524	1.622	78.4	8.92	8.89	0.320	
1.233	0.800	1.389	1.487	101.9	10.16	10.13	0.309	1.383
1.333	0.808	1.298	1.411	119.1	10.99	10.95	0.298	1.328
1.476	0.865	1.255	1.319	146.0	12.17	12.12	0.305	1.261
1.682	0.885	1.127	1.209	189.6	13.87	13.82	0.289	1.182
1.942	0.915	1.009	1.098	252.7	16.01	15.95	0.274	1.102
2.202	0.972	0.945	1.010	324.9	18.15	18.09	0.272	1.038
2.407	0.990	0.881	0.952	388.2	19.84	19.77	0.262	0.996
Isopropanol, r = 334.76; diameter = 0.081 cm								
0.290	0.770	5.686	4.792	3.0	3.25	2.38	0.554	
0.350	0.775	4.742	4.227	4.4	3.93	2.88	0.502	
0.437	0.785	3.847	3.646	6.9	4.90	3.59	0.450	
0.610	0.865	3.037	2.919	13.5	6.84	5.01	0.424	
0.796	0.900	2.421	2.444	22.9	8.93	6.54	0.381	
0.991	0.970	2.096	2.112	35.5	11.12	8.14	0.370	
1.065	0.955	1.920	2.013	41.0	11.95	8.75	0.346	
1.230	0.990	1.724	1.829	54.7	13.80	10.10	0.332	1.630
1.467	1.060	1.547	1.626	77.9	16.46	12.05	0.326	1.483
1.760	1.100	1.338	1.440	112.1	19.74	14.46	0.304	1.349
1.942	1.130	1.246	1.349	136.5	21.79	15.95	0.296	1.283
2.233	1.225	1.175	1.229	180.4	25.05	18.34	0.300	1.196
2.435	1.270	1.117	1.160	214.5	27.32	20.00	0.297	1.146
Isopropanol, r = 334.76; diameter = 0.050 cm								
0.261	0.925	7.589	6.037	1.5	3.73	2.14	0.620	
0.273	0.900	7.060	5.860	1.7	3.90	2.24	0.581	
0.375	0.830	4.740	4.741	3.1	5.35	3.08	0.433	
0.425	0.865	4.358	4.362	4.0	6.06	3.49	0.428	
0.462	0.928	4.301	4.126	4.8	6.60	3.80	0.451	
0.465	1.000	4.605	4.108	4.8	6.64	3.82	0.500	
0.607	0.955	3.369	3.439	8.2	8.67	4.99	0.401	
0.610	1.070	3.756	3.428	8.3	8.71	5.01	0.469	
0.812	1.000	2.637	2.833	14.7	11.59	6.67	0.360	
0.985	1.095	2.381	2.491	21.7	14.06	8.09	0.364	
1.145	1.130	2.113	2.253	29.3	16.35	9.41	0.347	
1.455	1.355	1.994	1.920	47.3	20.78	11.95	0.384	1.696
1.458	1.250	1.836	1.918	47.5	20.82	11.98	0.343	1.695
1.722	1.287	1.600	1.716	66.2	24.59	14.15	0.322	1.549
2.010	1.385	1.476	1.548	90.2	28.70	16.51	0.322	1.427
2.248	1.462	1.393	1.437	112.9	32.10	18.47	0.322	1.347
Isopropanol, r = 321.51; diameter = 0.163 cm								
-0.527	0.600	2.362	2.516	20.2	-4.17	-4.33	0.356	
-0.615	0.610	2.058	2.270	27.5	-4.86	-5.05	0.332	
-0.678	0.650	1.989	2.127	33.4	-5.36	-5.57	0.341	
-0.784	0.690	1.826	1.930	44.7	-6.20	-6.44	0.338	
-0.808	0.540	1.387	1.892	47.5	-6.39	-6.63	0.237	
-0.836	0.700	1.737	1.850	50.8	-6.61	-6.86	0.331	
-1.298	0.830	1.327	1.379	122.5	-10.26	-10.66	0.315	1.267
-1.474	0.855	1.204	1.267	158.0	-11.66	-12.10	0.301	1.188
-1.853	0.960	1.075	1.088	249.6	-14.65	-15.22	0.300	1.062
-2.044	0.980	0.995	1.019	303.8	-16.16	-16.78	0.289	1.013
-2.156	1.015	0.977	0.984	338.0	-17.05	-17.70	0.291	0.989
-2.421	1.035	0.887	0.910	426.1	-19.15	-19.88	0.276	0.936
-2.543	1.075	0.877	0.881	470.2	-20.11	-20.88	0.279	0.916
Isopropanol, r = 321.51; diameter 0.158 cm								
-0.348	0.300	1.789	3.352	8.5	-2.79	-2.86	0.168	
-0.476	0.455	1.983	2.721	16.0	-3.82	-3.91	0.253	
-0.542	0.518	1.983	2.495	20.7	-4.35	-4.45	0.282	
-0.692	0.560	1.679	2.120	33.8	-5.56	-5.68	0.271	
Isopropanol, r = 321.51; diameter = 0.158 cm (continued)								
-0.794	0.624	1.631	1.934	44.4	-6.38	-6.52	0.289	
-0.915	0.635	1.440	1.760	59.0	-7.35	-7.51	0.271	
-2.570	0.985	0.795	0.884	465.5	-20.64	-21.10	0.245	0.918
Isopropanol, r = 321.51; diameter = 0.152 cm								
-0.197	0.320	3.371	4.962	2.6	-1.61	-1.62	0.250	
-0.267	0.170	1.321	4.052	4.8	-2.19	-2.19	0.084	
-0.332	0.210	1.313	3.504	7.5	-2.72	-2.73	0.102	
-0.418	0.455	2.259	3.005	11.8	-3.42	-3.43	0.269	
-0.502	0.465	1.922	2.660	17.1	-4.11	-4.12	0.249	
-0.577	0.530	1.906	2.424	22.6	-4.73	-4.74	0.276	
-0.618	0.550	1.847	2.316	25.9	-5.06	-5.08	0.279	
-0.663	0.610	1.909	2.210	29.8	-5.43	-5.44	0.308	
Isopropanol, r = 321.51; diameter = 0.081 cm								
-0.209	0.250	2.482	5.884	1.6	-2.35	-1.72	0.127	
-0.231	0.215	1.931	5.504	1.9	-2.59	-1.90	0.096	
-0.273	0.095	0.722	4.925	2.7	-3.06	-2.24	0.027	
-0.284	0.170	1.242	4.796	2.9	-3.19	-2.33	0.061	
-0.290	0.185	1.324	4.730	3.0	-3.25	-2.38	0.068	
-0.321	0.230	1.487	4.420	3.7	-3.60	-2.64	0.089	
-0.327	0.150	0.952	4.366	3.9	-3.67	-2.69	0.047	
-0.332	0.266	1.625	4.322	4.0	-3.72	-2.73	0.104	
-0.362	0.380	2.178	4.080	4.7	-4.06	-2.97	0.172	
-0.394	0.550	2.897	3.856	5.6	-4.42	-3.24	0.280	
-0.433	0.652	3.124	3.621	6.8	-4.86	-3.56	0.338	
-0.440	0.645	3.042	3.582	7.0	-4.94	-3.61	0.330	
-0.482	0.660	2.840	3.371	8.4	-5.41	-3.96	0.323	
-0.509	0.720	2.935	3.251	9.4	-5.71	-4.18	0.354	
-0.545	0.675	2.570	3.106	10.7	-6.11	-4.48	0.310	
-0.563	0.665	2.451	3.039	11.5	-6.32	-4.62	0.298	
-0.591	0.760	2.668	2.943	12.6	-6.63	-4.85	0.350	
-0.604	0.720	2.474	2.900	13.2	-6.78	-4.96	0.320	
-0.612	0.725	2.458	2.875	13.5	-6.86	-5.03	0.321	
-0.682	0.670	2.038	2.675	16.8	-7.65	-5.60	0.269	
-0.696	0.746	2.224	2.639	17.5	-7.81	-5.72	0.309	
-0.706	0.760	2.234	2.614	18.0	-7.92	-5.80	0.315	
-0.775	0.900	2.410	2.456	21.7	-8.69	-6.36	0.377	
-1.050	1.055	2.085	2.006	39.8	-11.78	-8.62	0.388	
-1.108	0.975	1.826	1.935	44.4	-12.43	-9.10	0.337	
-1.108	0.900	1.685	1.935	44.4	-12.43	-9.10	0.302	
-1.372	1.165	1.762	1.678	68.0	-15.39	-11.27	0.376	1.477
-1.447	1.085	1.556	1.620	75.7	-16.23	-11.88	0.329	1.436
-1.480	1.145	1.605	1.596	79.1	-16.60	-12.15	0.349	1.419
-1.702	1.184	1.443	1.454	104.7	-19.09	-13.98	0.333	1.319
-1.722	1.280	1.542	1.442	107.1	-19.32	-14.14	0.368	1.311
-1.850	1.300	1.458	1.375	123.7	-20.75	-15.19	0.358	1.264
-2.202	1.320	1.244	1.224	175.2	-24.70	-18.08	0.325	1.158
-2.407	1.445	1.246	1.154	209.3	-27.00	-19.77	0.345	1.108
-2.407	1.300	1.121	1.154	209.3	-27.00	-19.77	0.300	1.108
Isopropanol, r = 321.51; diameter 0.051 cm								
-0.267	0.265	2.059	5.831	1.6	-3.77	-2.19	0.098	
-0.322	0.335	2.159	5.147	2.4	-4.55	-2.64	0.124	
-0.386	0.500	2.688	4.561	3.4	-5.46	-3.17	0.201	
-0.398	0.700	3.650	4.469	3.6	-5.63	-3.27	0.321	
-0.458	0.545	2.469	4.069	4.8	-6.48	-3.76	0.207	
-0.501	0.830	3.438	3.833	5.7	-7.08	-4.11	0.360	
-0.643	0.820	2.646	3.245	9.4	-9.09	-5.28	0.306	
-0.703	0.818	2.414	3.058	11.2	-9.94	-5.77	0.290	
-0.763	0.840	2.284	2.896	13.2	-10.79	-6.27	0.286	
Isopropanol, r = 321.51; diameter 0.050 cm								
-0.220	0.180	1.698	6.678	1.1	-3.14	-1.81	0.061	
-0.273	0.200	1.520	5.783	1.7	-3.90	-2.24	0.063	
-0.279	0.200	1.490	5.707	1.7	-3.98	-2.29	0.063	
-0.279	0.195	1.450	5.700	1.7	-3.98	-2.29	0.060	

Table 1 (Continued)

u_∞ $\frac{m}{s}$	q_{max} $\frac{MW}{m^2}$	$\phi_{expt.}$	$We_g^{-1/3}$	We_f	Fr	G	α	$\phi_{pred.}$
-0.355	0.340	1.987	4.854	2.8	-5.07	-2.92	0.119	
-0.418	0.725	3.599	4.353	3.9	-5.97	-3.43	0.326	
-0.440	0.727	3.428	4.207	4.3	-6.28	-3.61	0.318	
-0.502	0.830	3.431	3.853	5.6	-7.17	-4.12	0.356	
-0.596	0.910	3.168	3.437	7.9	-8.51	-4.89	0.368	
-0.618	0.860	2.888	3.354	8.5	-8.82	-5.07	0.332	
-0.826	0.950	2.387	2.765	15.2	-11.79	-6.78	0.323	
-1.039	1.075	2.147	2.034	38.2	-18.69	-10.75	0.334	1.728
-1.235	1.200	2.016	2.114	34.0	-17.63	-10.14	0.350	1.784
-1.519	1.360	1.858	1.842	51.5	-21.69	-12.47	0.365	1.593
-1.835	1.460	1.651	1.624	75.1	-26.20	-15.07	0.356	1.439
Methanol, r = 615.11; diameter = 0.151 cm								
1.171	1.370	2.717	1.936	84.9	9.62	9.41	0.580	
1.327	1.482	2.593	1.781	108.9	10.90	10.66	0.594	2.498
1.658	1.470	2.059	1.536	169.8	13.62	13.32	0.508	2.232
1.672	1.590	2.208	1.527	172.9	13.74	13.44	0.560	2.223
1.820	1.600	2.042	1.443	204.8	14.95	14.63	0.534	2.131
Methanol, r = 615.11; diameter = 0.081 cm								
1.214	1.606	3.073	2.327	48.9	13.62	9.76	0.561	
1.369	1.850	3.139	2.147	62.1	15.36	11.00	0.631	2.888
1.583	2.025	2.971	1.949	83.1	17.76	12.72	0.650	2.680
1.744	2.150	2.863	1.827	100.8	19.56	14.02	0.661	2.548
1.855	2.210	2.767	1.754	114.1	20.81	14.91	0.659	2.469
Methanol, r = 615.11; diameter = 0.051 cm								
1.242	1.670	3.123	2.673	32.2	17.56	9.98	0.489	
1.369	1.980	3.359	2.505	39.1	19.35	11.00	0.583	3.284
1.638	2.240	3.176	2.223	56.0	23.16	13.16	0.617	2.980

mum value of $q_{\max}$ in this case. We make no attempt here to predict such burnout, nor do we claim to identify the transition to this mechanism using $G = -3$. A correct general criterion would doubtless be more complicated. The data for $-3 < G < 0$ do not correlate on either Fr or We_f alone and they are insufficient to justify their being represented as a function of G.

The Evaluation of C. The left-hand side of equation (11) is plotted against $We_g^{-1/3}$ in Fig. 7, based on only those data from the present study (and those from [1] and [5])[4] for which $|G| > 10$. They give a remarkably straight line on logarithmic coordinates and fix the constant C—the slope—as 0.245.

The Prediction of ϕ. Using $C = 0.245$ we obtain the final high speed formula for the dimensionless peak heat flux, from equation (13).

$$\phi = 0.000919 \left[1 + \frac{16.3}{We_f^{1/3}}\right] \tag{14}$$

Predicted values of ϕ are compared with all observed values for $|G| > 10$ in Fig. 8. The data are represented well within ±20 percent by equation (14). Two Westwater data are high, but they were obtained under about 6°C subcooling.

Figure 9 shows dimensional values of $q_{\max}$ as a function of u_∞ for 0.16 cm dia. cylinders in isopropanol. The prediction of $q_{\max}$ from equation (14) is included as a solid line on the curve, in the range $|G| > 10$. The low velocity behavior ($|G| < 10$) is sketched in as a dash-dot line. Notice the discontinuity of the dash-dot line in low-velocity downflow, and notice how far below ($q_{\max}$) pool boiling the burnout heat flux falls.

Both Fig. 6 and Fig. 9 suggest that the present correlation will be valid for G's substantially below 10 in upflows. We opt for caution and make no such claim here, since we lack a rationale for doing so.

The Magnitude of α. Equation (12) gives

$$\alpha = 0.000919\, r \tag{15}$$

For high values of r this formula gives values of α that exceed unity. Values of α significantly greater than unity are probably not really attained. It is more likely that α simply reaches an upper limit of about unity and stays there, in accordance with the assumption [5] that $\alpha \simeq 1$ for slow flows. We should also note that α is velocity-independent when $|G|$ is large.

Conclusions

1 The influence of gravity on the peak heat flux during boiling from a single horizontal cylinder in a crossflow becomes inconsequential when $|G| > 10$.

2 The peak heat flux in this case is given within ±10 percent by equation (14).

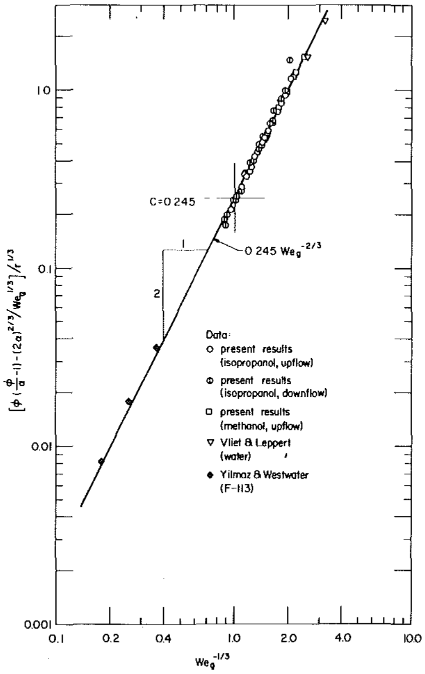

Fig. 7 Correlation of the liquid and vapor momentum contributions to the drag on a cylinder during boiling

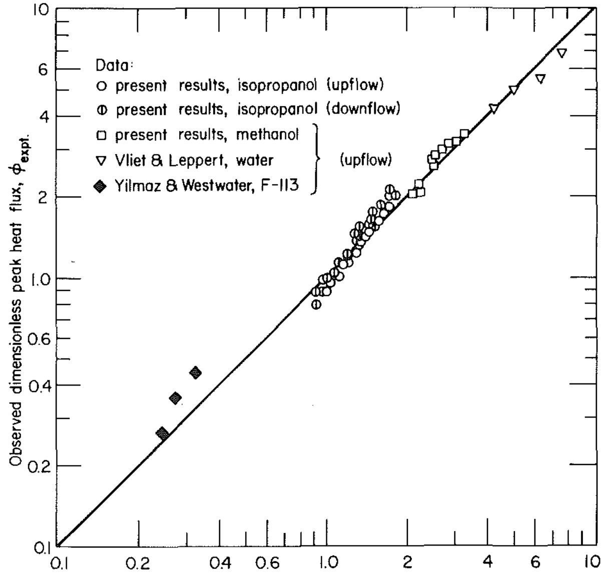

Fig. 8 Comparison of high-speed burnout prediction with experimental data

---

[4] Data from the other sources fall in the range $|G| < 10$.

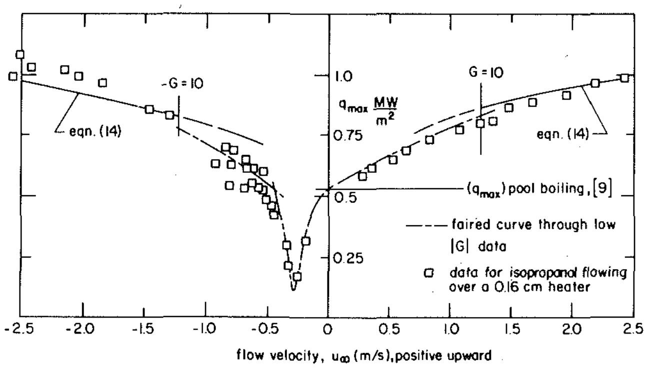

Fig. 9 Typical behavior of data in dimensional coordinates

3 The drag coefficient in this case is

$$C_D = \frac{2}{We_f} - \frac{0.245}{We_f^{2/3}} - \frac{0.0150}{We_g^{1/3}} \qquad (9a)$$

4 When $|G|$ is reduced sufficiently far below 10 the hydrodynamic stability criterion for burnout is replaced by a buoyancy criterion. When this occurs, q_{max} can fall far below the pool boiling limit, instead of exceeding it, in the downflow case.

5 α is velocity-independent and equal to $0.000919r$, when $|G| > 10$.

Acknowledgment

We are grateful to Gene Ungar and E.B. Yates for their help with the present experiment.

References

1 Vliet, G. C., and Leppert, G., "Critical Heat Flux for Nearly Saturated Water Flowing Normal to a Cylinder," ASME JOURNAL OF HEAT TRANSFER, Vol. 86, No. 1, 1964, pp. 59–67.

2 Leppert, G., and Pitts, C. C., "Boiling," in *Advances in Heat Transfer* T. F. Irvine, Jr., and J. P. Hartnett, eds., Vol. 1, Academic Press, New York, 1964.

3 Cochran, T. H., and Andracchio, C. R., "Forced Convection Peak Heat Flux on Cylindrical Heaters and Refrigerant 113," NASA D-7553, Feb., 1974.

4 Min, T. K., "Boiling on Cylinders in Cross Flow—Low Velocity Peak Heat Flux Measurements for Water and Methanol," Master's Thesis, University of Kentucky, Mechanical Engineering Department, 1975.

5 Lienhard, J. H., and Eichhorn, R., "Peak Boiling Heat Flux on Cylinders in a Cross Flow," *International Journal of Heat Mass Transfer*, Vol. 19, 1976, pp. 1135–1142.

6 Yilmaz, S., and Westwater, J. W., "Effect of Velocity on Heat Transfer to Boiling Freon-113," JOURNAL OF HEAT TRANSFER, Vol. 102, No. 1, 1980, pp. 26–31.

7 Lienhard, J. H., *A Heat Transfer Textbook*, Prentice-Hall, Englewood Cliffs, N.J., 1981.

8 Hasan, M. Z., "Peak Boiling Heat Flux in Upflow and Downflow across Single Cylindrical Heaters," Master's Thesis, University of Kentucky, Mechanical Engineering Department, 1980.

9 Sun, K. H., and Lienhard, J. H., "The Peak Pool Boiling Heat Flux on Horizontal Cylinders," *International Journal of Heat Mass Transfer*, Vol. 13, 1970, pp. 1425–1439.

10 Cheers, F., "Note on Wind Tunnel Contractions," Aeronautical Research Council, Reports and Memoranda No. 2137, Mar 1945.

Density-Wave Oscillations in Sodium Heated Once-Through Steam Generator Tubes

H. C. Ünal
Central Technical Institute TNO,
P.O. Box 342,
7300 AH Apeldoorn, The Netherlands

Inception conditions of density-wave oscillations were determined in two sodium heated once-through steam generator tubes, i.e., in a 44.43 m long helical coil of 0.018 i.d. and in a tube of 0.0131 m i.d., comprised of a 9.40 m long vertical- and an 11.05 m long, V-shaped horizontal tube. The operating conditions on the water/steam side for the experiments were: pressure: 6–19.1 MN/m^2; mass velocity 187–1020 kg/m^2 s; inlet subcooling: 3.2–168 K; outlet steam quality: 1.15–2.38. The 306 data obtained and the 74 data found in the literature from sodium and electrically heated once-through steam generator tubes were correlated within 7.5 percent accuracy for 98 percent of the time. The R.M.S. error for all the 380 data is 3.33 percent. The observed density-wave oscillations are time-delay oscillations and the length of the superheated steam region and the transit time in this region practically govern the mechanism of these oscillations. An empirical relation has also been established for this mechanism.

1 Introduction

A particular type of dynamic instability, i.e., Density-Wave Oscillations (DWO), jeopardizes the safety of a sodium heated steam generator, a crucial component of the LMFBR cooling system. These oscillations cause flow maldistribution among the tubes or inside the tubes, and thermal cycling at the upper tube plate and at the dryout location. The DWO are low-frequency oscillations of which the period is of the same order of magnitude as the transit time of a fluid particle in a steam generator tube. The DWO are due to multiple regenerative feedback between the flow rate, the vapor generation rate and the pressure drop [1–2]. The DWO have been extensively studied for comparatively short electrically heated tubes [1–2], but not for sodium heated once-through steam generator tubes. The DWO data for the latter are also scarce in literature. Furthermore stability models in the form of computer programs generally do not fit the data from sodium or gas heated once-through steam generator tubes well [3–4]. By using the 88 data of [4–10] obtained for quite a wide range of operating conditions in six different sodium or electrically heated once-through steam generator tubes (i.e., $1272 \leq L_h/d \leq 9502$ and $X > 1$), a correlation was established in [11] to predict the inception conditions of the DWO. In that correlation, the effect of inlet throttling could not be taken into account for $L_h/d \leq 4118$ due to lack of data.

The main purpose of the present study is to report the results of the experiments carried out to determine the inception conditions of the DWO in two sodium heated once-through steam generator tubes. One of these was a tube of total length 20.45 m and 0.0131 m i.d., comprised of a 9.40 m long vertical and an 11.05 m long V-shaped horizontal tube. The other was a 44.43 m long helical coil of 0.018 m i.d. By-pass pipes were built around both test tubes in order to keep the total pressure drop constant in the tubes. The experiments were carried out in such a way that the effects of all operating conditions and inlet throttling on the stability could be determined. For this purpose, the outlet steam quality at the inception of the DWO was measured within about 2.5 percent accuracy for most of the tests carried out in the first tube and within about 6 percent accuracy for the tests carried out in the latter. The 306 data obtained and the 74 data given in [5–10] for long sodium or electrically heated once-through steam generator tubes were correlated within about these accuracies.

From the results of the experiments carried out in both test tubes, it was concluded that the outlet steam quality at the inception of the DWO is a function of pressure for a given inlet throttling whereas the effects of all the other operating conditions on the steam quality are of secondary importance. The above phenomenon as well as the mechanism of the DWO observed in the test tubes were explained. An empirical relation has been established for the multiple regenerative feedback mechanism, which causes the DWO in the test tubes.

2 Experimental Apparatus and Procedure

2.1 The Loop. The flow diagram of the heat transfer loop used is shown in Fig. 1, where the high-pressure part of the loop is drawn in heavy lines and the low-pressure part in fine lines. The main specifications of the loop are reported in [5, 12]. During high pressure operation, the pressure is regulated by an automatic control valve and the piston pump. The deaerator then serves as an expansion tank. The volume of the high pressure part of the loop was approximately 0.05 m^3, excluding the test tube and by-pass. The sodium in the loop was heated electrically. The maximum available power was about 0.5 MW, including the power of the preheater. Two test tubes, a Ferritic steel Test Tube (FTT) and a stainless steel Helically Coiled test Tube (HCT) were used in the loop described briefly above to determine the inception conditions of the DWO. At the inlet and outlet of each test tube, headers were mounted. Between these two headers, a vertical by-pass pipe of 49.3 mm i.d. was installed; thus the total pressure drop in each test tube was approximately constant. The by-pass pipe is not shown separately in Fig. 1, but it is included in the part indicated as test section. The total length of a test tube was the length between the inlet header and the outlet header. Flow control valves and flow meters were mounted at a test tube just after the inlet header.

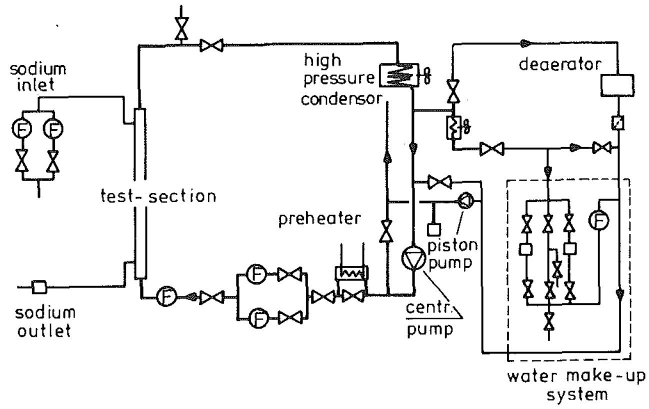

Fig. 1 Flow diagram of heat transfer loop

Contributed by the Heat Transfer Division for publication in the JOURNAL OF HEAT TRANSFER. Manuscript received by the Heat Transfer Division October 30, 1979.

2.2 FTT. This 20.45 m long test tube of 0.01312 m i.d. and 0.0171 m o.d. was manufactured from stabilized ferritic steel, 10CrMoNb-Ni9.10, and consisted of a 9.40 m vertical and an 11.05 m V-shaped horizontal tube. The sodium side surrounding the test tube was constructed of 4 annuli. From the base, these were respectively 10.25, 4, 3, and 2 m long. The inner wall of each annulus was formed by the test tube. The i.d. of the outer tube of each annulus was 0.0297 m. The annuli were connected by approximately 0.5 m long adiabatic circular tubes of 0.0297 m i.d. A 0.80 m long piece at the inlet and a 0.40 m long piece at the outlet of the test tube were not heated. The flow orientation was upward in the water/steam side and downward in the sodium side. By means of two flow control valves mounted at the inlet of the test tube, the value of the inlet throttling coefficient was adjusted between 54.7 and 382.9. This coefficient (i.e., total of the pressure loss coefficients of the two flow control valves and a flow meter between these valves) was based on the tube diameter. For given openings of the valves, this coefficient was taken as the average of the values obtained in all tests carried out with the same openings.

2.3 HCT. This 44.43 m long test tube of 0.018 m i.d. and 0.026 m o.d. was manufactured from stainless steel-316 and was placed concentrically in another helical coil of 0.049 m i.d. The flow on the sodium side was downward in the annulus between these coils, and upward in the test tube. A 2.0 m long piece at the inlet and a 2.3 m long piece at the outlet of the test tube were not heated. The helix angle of the test tube was 7.77 deg and the coil diameter was 1.50 m. For 41 percent of the tests, the value of inlet throttling was adjusted between 223 and 665 by means of two flow control valves fitted at the inlet of the test tube. For the calculation of the inlet throttling coefficient, the same procedure was used as described for FTT. For the rest of the tests, these valves were not mounted and in this case the throttling of the flow was solely due to the turbine flow meter at the inlet of the test tube, and $K = 15\text{–}27$.

2.4 Instrumentation. Both test tubes were heavily instrumented. It is sufficient to mention here that both on the sodium side and water/steam side, inlet and outlet temperatures, outlet pressure, inlet mass flow, and the temperature along the test tube at 11.05, 15.05 and 18.05 m axial positions in FTT and at 8.84, 13.59, 18.35, 23.10, 27.86, 32.62, 35, 37.37 and 39.75 m axial positions in HCT were measured with precalibrated instruments. Sodium-side temperatures in FTT were also measured at 12 additional axial positions. All the measurements were collected with an on-line data acquisition system and processed by a Hewlett-Packard-2116 B computer. Outlet temperatures both on the sodium side and on water/steam side, and the inlet temperature, inlet mass flow and outlet pressure on the water/steam side, and the pressure drop in the by-pass pipe were simultaneously recorded with a six-channel line recorder.

Both water/steam and sodium-side temperatures were measured with stainless-steel sheathed chromel-alumel thermocouples of 1 mm o.d. Maximum error in measuring these temperatures was 1.2 K. Both water/steam-side and sodium-side mass flows were measured with turbine flow meters, which had errors less than 1 percent. Water/steam-side outlet pressure was measured with a dead-weight balance manometer, which had a maximum error of 0.03 MN/m^2.

2.5 Experimental Procedure. The inception conditions of the DWO are, by definition, the operating conditions of the stable test run made just before the run in which the DWO appear. In order to generate the DWO, steam quality at the outlet of the test tube was increased by very small increments for most of the tests by increasing only the sodium-side inlet temperature. For a few tests, the DWO were created by decreasing only water/steam-side pressure. The DWO were detected by observing the recordings of the water/steam side mass flow on the six-channel recorder. When the first diverging mass flow oscillations appeared on the recorder, the operating conditions of the previous stable run were specified as the inception conditions of the DWO. It was also ensured that the observed oscillations fulfilled the three conditions: (1) that they reach a limit cycle and thereafter stay sustained (2) that they disappear when the sodium-side inlet temperature is decreased or when the water/steam side pressure is increased (3) that their period is of about the same order of magnitude as the transit time of a fluid particle in the test tube.

For 82 percent of the tests carried out in FTT and 45 percent of the tests carried out in HCT, the sodium-side inlet temperature was increased in steps of 5 K or the water/steam side outlet pressure was decreased in steps of 0.25 MN/m^2. For the rest of the tests, the increment or the decrement in the aforesaid temperature and pressure was respectively in 10 K and 0.56 MN/m^2 steps.

Most of the tests were carried out systematically; in other words the effects on the outlet steam quality at the inception of the DWO of the water/steam side inlet subcooling, mass velocity, outlet pressure and inlet throttling, and the ratio of the mass flow in the sodium side to that in the water/steam side were investigated at several pressure levels (i.e., $P = 14$, 16 and 18 MN/m^2). For this purpose, the outlet steam quality at the inception of the DWO was measured for several values of one of the aforesaid parameters, while the other parameters were kept constant and the measurements were repeated at several pressure levels. At the DWO-runs, the water/steam side outlet temperature did not fluctuate and was constant. For these runs, this temperature was considerably higher than the saturation temperature at system pressure. The above implied the presence of pure steam at the outlet of a test tube. Therefore, the outlet steam quality (i.e., thermodynamic steam quality) at the inception of the DWO was determined with measured outlet temperature and pressure, using a Steam Table.

Nomenclature

A = cross-sectional area of steam generator tube (m^2)
a = transit time of a fluid particle (s)
a^+ = dimensionless transit time
D = coil diameter (m)
d = tube inside diameter (m)
G = mass velocity at the inception of DWO on water/steam side (kg/m^2 s)
g = acceleration of gravity (m/s^2)
K = inlet throttling coefficient
h = enthalpy at the inception of DWO on water/steam side (J/kg)
ΔH = dimensionless inlet subcooling enthalpy $(1 - h_i/h_{\text{sat}})$
L = length (m)
l = length of a heat transfer region (m)
N = summation of pressure loss coefficients of bends along a straight tube or a serpentine
P = outlet pressure at the inception of DWO (N/m^2)
P_r = reduced outlet pressure (i.e., P divided by critical pressure)
ΔP = pressure drop (N/m^2)
Q = power at the inception of DWO (W)
Re = Reynolds number at the inception of DWO
r = latent heat of evaporation for water (J/kg)
T = temperature at the inception of DWO on water/steam side (K)
t = temperature at the inception of DWO on sodium side (K)
ΔT_{sub} = inlet subcooling on water/steam side (K)
W = mass flow at the inception of DWO (kg/s)
X = outlet steam quality (i.e., thermodynamic quality) at the inception of DWO, based on thermal equilibrium
y = axial coordinate; $y = 0$ at the begin of superheated steam region (m)
ρ = average density in a heat transfer region (kg/m^3)

Subscripts

a = adiabatic length
b = boiling region
h = heated length
i = inlet condition
M = measured
n = sodium side
P = predicted
p = preheat region
S = beginning of the superheated steam region
s = superheated steam region
sat = liquid phase at the state of saturation
t = total length or total power developed in superheated steam region
v = vapor phase at the state of saturation
w = water/steam side

Table 1 Range of operating conditions for the tests

Test tube	P MN/m^2	G kg/m^2 s	W_n/W_w	K	H_i kJ/kg	X	Number of data
FTT	7.6–13.5	439–1020	10.4–19.9	54.7–382.9	898–1257	1.37–1.68	16
	13.6–14.5	486–910	8.8–19	54.7–196.6	768–1416	1.47–1.79	46
	14.6–15.5	498–951	8.8–18.2	54.7–122.9	990–1440	1.58–1.83	26
	15.6–16.5	493–890	10.1–18.1	54.7–106.9	980–1475	1.66–1.94	27
	16.6–17.5	507–648	12.5–17.6	54.7–69.9	981–1471	1.78–1.95	22
	17.6–19.0	526–683	10.6–16.9	54.7–107.9	826–1472	1.97–2.20	23
HCT	6.0–8.0	225–678	11.4–23.7	16–223	856–1083	1.15–1.49	8
	8.0–10.0	187–731	8.6–22.6	16–665	845–1387	1.29–1.73	22
	10.1–12.0	246–644	9.5–28.3	15–450	669–1421	1.37–1.83	29
	12.1–14.0	260–726	9.9–29.5	15–450	720–1431	1.49–1.96	35
	14.1–16.0	262–755	8.8–26.4	17–450	857–1470	1.58–2.04	28
	16.1–19.1	294–768	11.7–22.2	15–223	862–1487	1.82–2.38	24

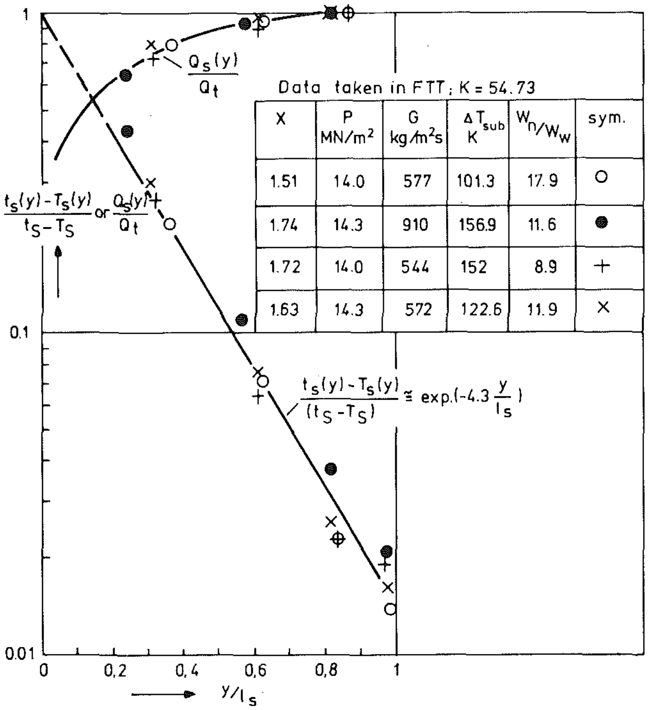

Data taken in FTT; K = 54.73

X	P MN/m^2	G kg/m^{2}s	ΔT_{sub} K	W_n/W_w	sym.
1.51	14.0	577	101.3	17.9	○
1.74	14.3	910	156.9	11.6	●
1.72	14.0	544	152	8.9	+
1.63	14.3	572	122.6	11.9	×

Fig. 2 Profiles of the dimensionless temperature difference between the sodium and water/steam side and the dimensionless power along the superheated steam region

Demineralized water with an oxygen content of less than 15 ppb, a conductivity of less than 0.5 μS/cm and a pH between 8.5 and 9 was used during the tests.

In total 2240 tests were carried out. In 160 tests with FTT and in 146 tests with HCT, the DWO were observed. The range of operating conditions for the tests are summarized in Table 1, and are fully given in [12]. The by-pass ratio varied between 0.1 and 13 for FTT tests and between 2.2 and 12 for HCT tests. At the inception of the DWO, the sodium-side inlet temperature was only a few degrees higher than the water/steam side outlet temperature.

The period of the observed mass flow oscillations was between 1.3 and 7 s in FTT and between 2.8 and 13.5 s in HCT. Peak-to-peak amplitudes of these oscillations varied from 30 to 200 percent of the mass flow recorded at the least stable test run. The water/steam side outlet temperature did not oscillate.

In the tests carried out in FTT with high inlet subcoolings, the outlet pressure also oscillated. The peak-to-peak amplitude of these oscillations was up to a few percent of the outlet pressure and their period was equal to that of the mass flow oscillations. There was a phase difference between these two oscillations. In the tests carried out with low inlet subcoolings, no pressure oscillations were observed, nor in the tests carried out with high inlet subcoolings and very small by-pass ratios. The tests carried out in HCT were less susceptible to pressure oscillations than those carried out in FTT. The generation of pressure oscillations is explained as follows: The amount of highly superheated steam produced in a test tube varies periodically. This superheated steam condenses completely in the cold water in the upper header coming from the by-pass. This causes variation of the pressure, since the volume of the high-pressure part of the loop is small, as mentioned before.

During all the stable test runs for which $X > 0$, mass flow oscillations with small irregular periods and amplitudes were always present in both test tubes. These irregular mass flow oscillations were assumed to be caused by the noise created by the flow in the rather small diameter by-pass pipe. Because of these irregular mass flow oscillations, inlet mass flow in the water/steam side was measured at one-second intervals for 10 seconds and the arithmetic average of the measurements was considered.

3 Discussion of the Results

3.1 The Mechanism of the DWO. The observed DWO in both test tubes are time delay oscillations. The length of the superheated steam region and the transit time in this region are of vital importance for the mechanism of the DWO. In order to show this, the following relation between the reduced outlet pressure, inlet throttling coefficient and the ratio of the length of the superheated steam region to the total tube length is established from the data taken in FTT at the inception of the DWO:

$$l_s/L_t = C_1(1+K)^{0.028}\,(0.95 + 0.079\,P_r) \qquad (1)$$

where $C_1 = 0.626$. The data reduction methods used throughout the paper are given in [12–13]. Equation (1) predicts l_s/L_t within about 12 percent accuracy from these data. So the length of the superheated steam region at the inception of the DWO is approximately constant for given outlet pressure and inlet throttling. The effect of the outlet pressure on this length is minute and that of inlet throttling is considerable but not of paramount importance. A similar result is also obtained from HCT tests with the value of C_1 in equation (1) equal to 0.688. With the exception of 17 data taken mostly at low pressures when the irregular mass flow oscillations were comparatively large, equation (1) predicts the length of the superheated steam region at the inception of the DWO also within 12 percent accuracy for the data obtained in HCT. The aforesaid length is *considerable*. For example for $P = 14$ MN/m^2, it is equal to about 35.6 m if $K = 223$ and to 33.3 m if $K = 20$ in HCT and to 14.3 m if $K = 54.7$ in FTT. C_1 in equation (1) appears to be dependent on the tube length.

In all the tests at the inception of the DWO, the difference between the sodium side and water/steam side temperatures decreased approximately exponentially along the superheated steam region, as illustrated in Fig. 2 for the few test runs carried out in FTT. This is due to the behavior of the specific heat of steam in the vicinity of the saturation temperature at high pressures. The power developed along the superheated steam region is also given in Fig. 2, which shows that in the last 50 percent of this region or beyond the about 15 m point along the test tube almost no heat is transferred to the water/steam side. During most of the tests only the sodium-side inlet temperature was increased by small increments. This resulted in a gradual increase in the length of the superheated steam region and a decrease in the lengths of the preheat and boiling regions. From the above, the significance of the length of the superheated steam region for the mechanism of the DWO is obvious: In order to trigger the multiple regenerative feedback mechanism which generates the DWO in a test tube when outlet pressure and inlet throttling are kept constant, the length of the superheated steam region has to reach a constant value. Thereafter the DWO appear and the multiple regenerative feedback mechanism begins to operate. Inlet throttling delays this mechanism in accordance with equation (1); i.e., the length of the superheated steam region required to initiate DWO increases with increasing inlet throttling coefficient.

In order to determine the relation for the mechanism of the DWO, the transit times of a fluid particle in all the different heat transfer regions in a steam generator tube have to be considered. The transit time of a fluid particle in a heat transfer region is

$$a = l\rho/G \tag{2}$$

This transit time is transformed into a nondimensional form as follows:

$$a^+ = (ga^2/l)^{1/2} = (l\rho^2 g/G^2)^{1/2} \tag{3}$$

The term in parentheses in equation (3) is the reciprocal of the Froude number and shows the ratio of gravity to inertia force.

With the data taken in FTT, the following empirical relation has been established between the inlet throttling coefficient, outlet pressure and the transit times at the inception of the DWO in the preheat, boiling and superheated steam regions:

$$\frac{(1/a_s^+) + (1/a_p^+)}{(1/a_s^+) + (1/a_p^+) + (1/a_b^+)} = C_2(1+K)^{-0.028}\,(0.855 - 0.15\,P_r) \tag{4}$$

where $C_2 = 1$. Equation (4) is shown in Fig. 3 for the data from FTT. This figure shows that the L.H.S. of equation (4) is practically constant at the inception of the DWO for given outlet pressure and inlet throttling. Inlet throttling delays the DWO in accordance with equation (4) i.e., the length of the superheated steam region increases with increasing inlet throttling coefficient, as explained in [13]. The use of different two-phase flow models for the evaluation of a_b in equation (4) did not practically alter the value of C_2.

Equation (4) has only been checked with 16 data taken in HCT for the pressure range $13.9 \leq P(\mathrm{MN/m^2}) \leq 14.3$. For these data G = 262–675 kg/m^2 s; ΔT_{sub} = 20.4–168 K; X = 1.49–1.96. If the value of C_2 in equation (4) is taken as 0.921, this equation fits the data within 6 percent accuracy.

From the above, it is concluded that the observed DWO are "time-delay oscillations," that the inlet throttling delays the mechanism of the DWO and that C_2 in equation (4) seems to be weak function of (L_t/d).

Equation (4) gives the mechanism of the DWO in FTT and in HCT if these tubes operate in the once-through mode. It follows that in order to initiate the multiple regenerative feedback mechanism which generates the DWO in these tubes, the condition expressed by equation (4) has to be fulfilled.

For a steam generator tube for which $X \leq 1$, a_s^+ in equation (4) must not be considered. In this case, this equation was checked with the 8 data reported in [14] for a very short electrically heated tube of L_t/d = 153. These data were taken for $4.1 \leq P(\mathrm{MN/m^2}) \leq 8.3$ and $0.087 \leq \Delta H \leq 0.131$. The value of C_2 in equation (4) for the data were 0.44 with an accuracy of 10 percent.

Provided that the R.H.S. of equation (4) is determined for a reasonable amount of data taken in tubes of different geometries, the equation may serve a stability model since it includes the mechanism of the DWO. Both equation (1) and equation (4) were established to show some phenomena related to the DWO in two once-through steam generator tubes. Thus they are not for general use, and their application should be restricted to the conditions similar to those used in the present experiments.

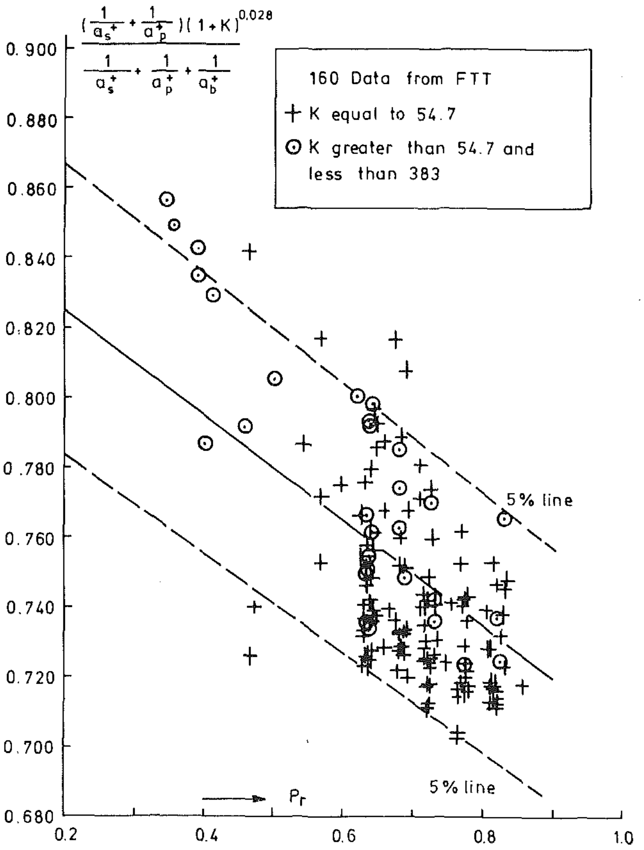

Fig. 3 **Verification of the mechanism of the DWO in accordance with equation (4)**

3.2 The Outlet Steam Quality at the Inception of the DWO. This steam quality appears to be almost solely a function of outlet pressure for a given inlet throttling in both test tubes. The effects of all the other operating conditions on the aforesaid steam quality seem to be of secondary importance. In the works reported in [6, 14], a similar conclusion has been drawn.

The reason why the outlet steam quality at the inception of the DWO is constant, can be explained as follows: Average density in the superheated steam region at the inception of the DWO was solved from equation (4), and was correlated within about 12 percent accuracy for 129 data taken in FTT, for which K = 54.7, with the equation below

$$\rho_s = 3.62 + 82.76\,P_r \tag{5}$$

Assuming that the density is equal to that calculated using the average temperature in the superheated steam region, the outlet steam quality at the inception of the DWO was determined within 0.4 percent accuracy by the use of equation (5) and a Steam Table, as given below

$$X = 0.721 - 0.764\,\ln[(1-P_r)P_r^{0.3}] \tag{6}$$

With four exceptions, equation (6) fits the aforesaid data within 8 percent accuracy. The R.M.S. error for all the data is 4.2 percent. From this, it is concluded that outlet steam quality (or temperature) at the inception of the DWO is practically a function of pressure for given inlet throttling and geometry, and that the effects on the inception of the DWO of other operating conditions are of secondary importance. For the length of the superheated steam region, the same conclusion was also drawn. It follows from the above that the superheated steam region dominates the mechanism of the DWO in both the test tubes and equation (4) seems to give this mechanism well.

4 Correlation of Data

The present data and the data available from the literature are correlated using the results given in Sections 3.1 and 3.2 in two different ways for practical applications. For this purpose, dimensional analysis is used. The dimensionless numbers which fully characterize the dynamics of two-phase flow are numerous and it is practically impossible to take all of them into account when correlating the data [15]. Furthermore, as indicated in [16], the use of the Buckingham and Rayleigh methods of dimensional analysis will give dimensionless groups, but their physical significance is not evident. The use of differential equations allows one to interpret physically the dimensionless groups thus derived, but provides no information on the fundamental mechanism of the process [16]. Thus, the experiment is the only safe basis for the selection of the dimensional variables for the correlation of the DWO data. As concluded from [17], the logical grouping of these variables into dimensionless groups can then be accepted without hesitation. In this case, however, the physical significance of these dimensionless groups may not be evident [16].

The present experiments clearly demonstrate that the most significant dimensional variables for the inception of the DWO in a once-through steam generator tube are total or heated tube length, outlet temperature, outlet pressure and pressure drop due to inlet throttling. For the present experiments $L_h \cong L_t$. These variables are transformed into dimensionless numbers such as L/d, the ratio of tube length to tube diameter, X, outlet steam quality, P_r, reduced pressure and K, inlet throttling coefficient. The importance of the first mentioned three dimensionless numbers on the mechanism of the DWO is due to fact that they characterize the length of the superheated steam region and the transit time of a fluid particle in this region. As demonstrated in the preceding sections, these are of vital importance for the mechanism of the DWO in a once-through steam generator tube. The importance of the inlet throttling coefficient on this mechanism is due to distribution of the pressure losses along the tube: The total of these pressure losses is constant and the DWO are time-delay oscillations. The experiments of Quandt [14] carried out in a steam generator tube in which no superheated steam was produced show that the inlet subcooling also influences the inception conditions of the DWO. This is logical, since subcooling characterizes the length of the boiling (or preheat) region in this tube. The inlet subcooling can be nondimensionalized as ΔH, the dimensionless inlet subcooling enthalpy.

It follows from the above that it seems sufficient to consider five dimensionless numbers, i.e., L/d, X, P_r, K and ΔH for the correlation of the DWO data. Therefore, a correlation (i.e., equation (7)) was first established using the above dimensionless numbers. This equation applies both to a steam generator tube in which no superheated steam is produced and to a once-through steam generator tube. This correlation should be very useful for many practical applications since it includes a few operating conditions. It is also an accurate correlation.

For some special applications in engineering practice, improvements in the accuracy are considered very useful for predicting the inception conditions of the DWO, especially for a once-through steam generator tube. This can be achieved if the second-order variables are also considered for the correlation of the DWO data. These variables, in their nondimensional form, are W_n/W_w, the ratio of sodium-side mass flow to water/steam side mass flow and Re_v, the Reynolds number for flow in the superheated steam region. The first dimensionless number influences the length of the superheated steam region and the latter accounts for the variation of water/steam-side mass flow. Thus a second correlation (i.e., equation (8)) was established considering the aforesaid five dimensionless numbers, i.e., L/d, X, P_r, ΔH, K, and W_n/W_w and Re_v. The correlation thus obtained is indeed more accurate than the first correlation, but applies only to once-through steam generator tubes.

4.1 First Correlation. The previous correlation of the author [11] predicts the power at the inception of the DWO from the present data well, i.e., within 8 percent accuracy for 90 percent of the time if the effect of inlet throttling is taken into account using the formula given below

$$X = X_c(1 + K)^{C_4} \tag{7}$$

where

$$C_4 = 0.07\text{–}0.017.10^{-3}\, L_h/d \quad \text{for } L_h/d \le 4118 \tag{7.1}$$

$$C_4 = 0 \quad \text{for } L_h/d > 4118 \tag{7.2}$$

The R.M.S. error for all the 306 data is 5.44 percent. X_c in equation (7) is the outlet steam quality at the inception of the DWO given in [11], and the effect on this steam quality of inlet throttling could not be taken into account for $L_h/d \le 4118$ due to lack of data. The correlation reported in [11] predicts the power at the inception of the DWO within 6.5 percent accuracy from the 88 once-through steam generator data considered in [11]. It has to be noted here that it is sufficient to know only two operating conditions, i.e., P and T_i to determine equation (7) for given (L_h/d) and K.

4.2 Second Correlation. Since 5.44 percent R.M.S. error is not considered sufficiently accurate for once-through steam generator applications, the present data and the 74 data reported in [5–10] were recorrelated. The evaluation of these 74 data is given in [12–13]. The range of geometries and operating conditions for these data are summarized below: Geometry: circular straight tubes, a coil, a serpentine and a test tube consisting of a 10 m long vertical and an 8.84 m long, V-shaped horizontal tube; arrangement of the test tube: tubes of large capacity steam generators; tubes around which a by-pass is built; two or three tubes arranged in parallel; heating conditions: electrically or sodium heated; L_t = 10–223.3 m; d = 7.86–29.9 mm; D = 0.8 m; ΔT_{sub} = 23.9–245.9 K; G = 118–1365 kg/m^2 s; X = 1.01–1.69; P = 4.3–17.3 MN/m^2; K = 0–2882.

For the correlation of the data, the effect on the outlet steam quality at the inception of the DWO of each operating condition, namely, P, W_n, W_w, ΔT_{sub} and G, and inlet throttling was determined separately as expressed by equations (8.1) to (8.6) with the aid of the very accurate data obtained in FTT. For this purpose, these operating conditions were used in dimensionless form, i.e., P_r, W_n/W_w, ΔH and Re_v, respectively. Thereafter a correlation was established for all the data obtained in FTT. By comparing this correlation with the data from HCT and the data reported in [5–10], the effect of inlet throttling coefficient on the tube length and the effect of the friction factor on the steam quality at the inception of the DWO were determined by expressions given by equations (8.7) to (8.9). The term in the denominator of equation (8.9) is practically identical to Blasius's friction factor for straight tubes and the first two terms in the numerator are the friction factor for helical coils [18]. The last term in the numerator represents loss coefficients of the bends along a straight tube or a serpentine. The final correlation obtained is

$$X = A_1A_2A_3A_4A_5A_6 \tag{8}$$

where

$$A_1 = 0.131\text{–}0.135 \ln[(1 - P_r)P_r^{0.2}] \tag{8.1}$$

$$A_2 = 1\text{–}0.005\, W_n/W_w \tag{8.2}$$

$$A_3 = 1 + 0.13\, \Delta H \tag{8.3}$$

$$A_4 = \mathrm{Re}_v^{0.125} \tag{8.4}$$

$$A_5 = [1 + K/(L_t/d)^{0.37}]^{C_5} \tag{8.5}$$

$$C_5 = 0.11 \quad \text{for FTT} \tag{8.6}$$

$$C_5 = 0.175\text{–}4.2.10^{-5}(L_t/d) \quad \text{for } L_t/d \le 4167 \tag{8.7}$$

$$C_5 = 0 \quad \text{for } L_t/d > 4167 \tag{8.8}$$

$$A_6 = \{[A_7 + 0.029(d/D)^{0.5} + (Nd/L_t)^{1.18}]/A_7\}^{0.79} \tag{8.9}$$

$$A_7 = 0.304\, \mathrm{Re}_v^{-0.25} \tag{8.10}$$

If the steam quality at the outlet of a once-through steam generator tube exceeds the outlet steam quality predicted by equation (8), the DWO appear in the tube. The power at the inception of the DWO is expressed by the equation

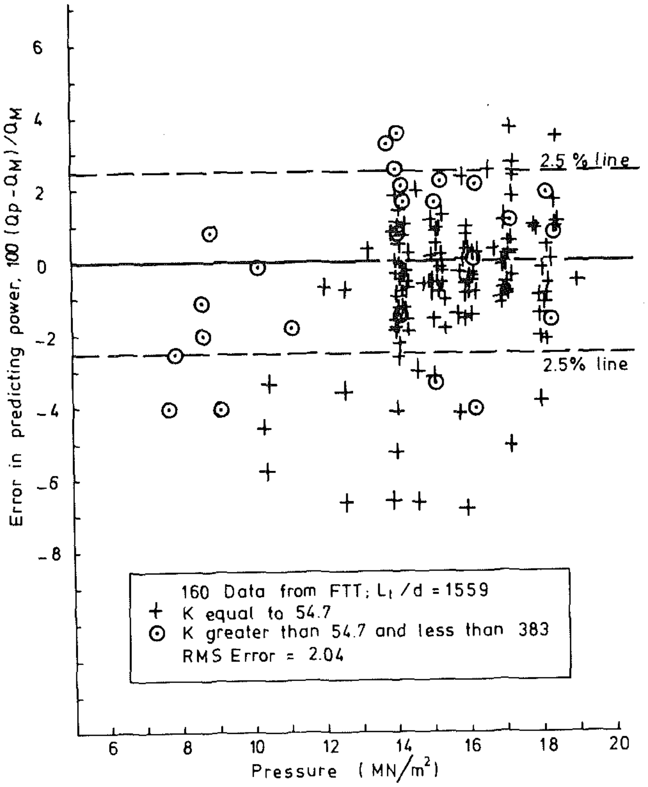

Fig. 4 Errors in predicting power in accordance with equation (9) for the data taken in FTT

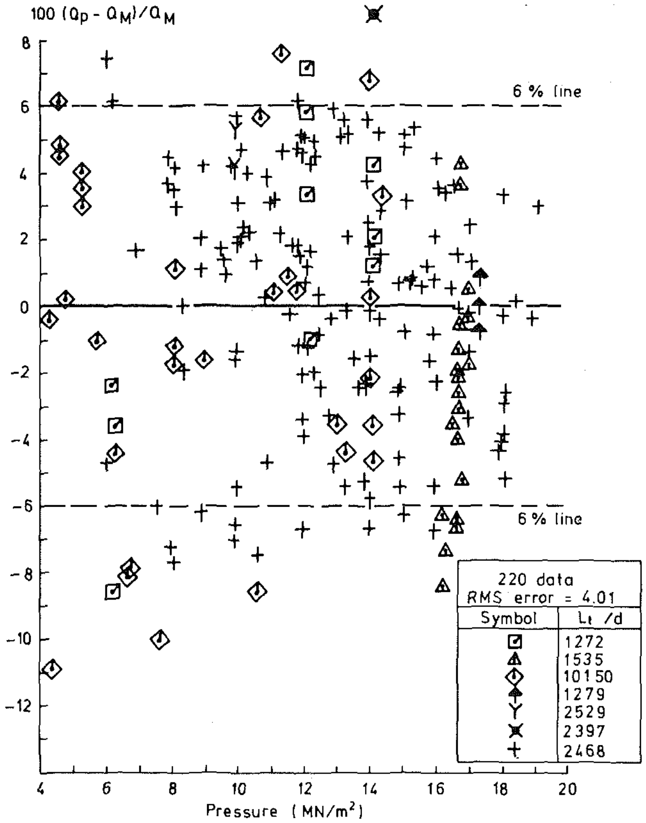

Symbol	Lt /d
◘	1272
▲	1535
◇	10150
✦	1279
Y	2529
✖	2397
+	2468

Fig. 5 Errors in predicting power in accordance with equation (9) for the data taken in HCT and data of [5-10]

$$Q = GA(h_{\text{sat}} - h_i + rX) \tag{9}$$

where X is given by equation (8). The results of comparison of the data from FTT, and data from HCT and the data reported in [5-10] with equations (8) and (9) are given in Figs. 4 and 5, respectively. Equation (9) predicts the power at the inception of the DWO within 7.5 percent accuracy for 98 percent of the time. The R.M.S. error for all the 380 data is 3.33 percent.

As mentioned, 82 percent of the data obtained in FTT were very accurate. For these data, equation (9) predicts the power at the inception of the DWO within 2.5 percent, as shown in Fig. 4. It is then concluded from equations (8) to (8.4) that the effect of the operating conditions on the steam quality at the inception of the DWO is small with the exception of pressure for long once-through steam generator tubes. The data analyzed in Fig. 5 and equation (6) also confirm this conclusion.

The effect on X of inlet throttling seems to decrease with increasing (L_t/d) and disappears beyond $L_t/d > 4167$; in other words this effect stays within the experimental accuracy for $L_t/d > 4167$. For the data reported in [9-10] from a very long tube of $L_t/d = 10150$, the inlet throttling coefficient varies between 237 and 2882. These data are shown in Fig. 5.

The second correlation is recommended for sodium and electrically heated once-through steam generator tubes of $1272 \leq L_t/d \leq 10150$ for the following range of operating conditions: $P = 4.3$–19.1 MN/m^2; $G = 118$–1365 kg/m^2 s; $\Delta T_{\text{sub}} = 3.2$–$245.9$ K; $X = 1.01$–2.38; $K = 0$–2882. With the exception of coil, $D = \infty$ in A_6.

As discussed in [11], a stability model in the form of a long computer program can not, in general, predict the power at the inception of the DWO better than to about 10 percent. It is known that the accuracy of stability models presented so far in the literature can be much less than 10 percent. It must be remembered, however, that an empirical correlation lacks generality and is, as a rule, invalid outside its range. Nevertheless, if the mechanism of the DWO described before is considered, it seems that the present correlations are not much susceptible to the aforesaid invalidity.

5 Summary and Conclusions

- DWO were investigated in two sodium heated once-through steam generator tubes of $L_t/d = 1559$ and 2468. The observed DWO are time-delay oscillations. For the mechanism of these oscillations, an empirical relation has been established. The length of the superheated steam region and the transit time of a fluid particle in this region are of vital importance for the aforementioned mechanism.
- The 306 data obtained and the 74 data reported in the literature have been correlated to predict the power at the inception of the DWO within 7.5 percent accuracy for 98 percent of the time. The R.M.S. error for all the 380 data is 3.33 percent. The established correlation is recommended for sodium and electrically heated once-through steam generator tubes of $1272 \leq L_t/d \leq 10150$ for the following range of operating conditions: $P = 4.3$–19.1 MN/m^2; $G = 118$–1365 kg/m^2 s; $\Delta T_{\text{sub}} = 3.2$–$245.9$ K; $X = 1.01$–2.38; $K = 0$–2882.
- This study shows that the inception conditions of the DWO can be predicted with simple equations, thus eliminating the use of time-consuming complicated stability correlations in the form of a computer program for a wide range of operation conditions and geometries, as considered here. Further verification of the work presented is recommended.

Acknowledgment

This study is a government sponsored work carried out by TNO. The author wishes to express his gratitude to Messrs. K. A. Warschauer, A. R. Braun and M. L. G. van Gasselt for their encouragement during the preparation of this work. The loop was operated by Mr. A. J. C. Spierings.

References

1 Bouré, J. A., Bergles, A. E., and Tong, L. S., "Review of Two-Phase Flow Instability," *Nuclear Engineering and Design*, Vol. 25, 1973, pp. 165-192.

2 *Proceedings of the Symposium of Two-Phase Flow Dynamics*, EUR-4288e, Vol. I and Vol. II, 1969.

3 Fallows, T., Hitchcook, J. A., Jones, R. C., Lis, J., and Northover, E. W., "A Study of Oscillatory Instabilities in the Parallel Channels of A High Pressure

Once-Through Boiler Rig," *Proceedings of the International Conference-Boiler Dynamics and Control in Nuclear Power Stations,* The British Nuclear Energy Society, 1973, pp. 14.1–14.8.

4 Waszink, R. P., and Efferding, L. E., "Hydrodynamic Stability and Thermal Performance Test of a 1-MWt Sodium-Heated Once-Through Steam Generator Model," ASME *Journal of Engineering for Power*, Vol. 96, 1974, pp. 189–200.

5 Ünal, H. C., "An Investigation of the Inception Conditions of Dynamic Instabilities in Sodium Heated Steam Generator Pipes," in *Two-Phase Flows and Heat Transfer*, edited by S. Kakac and T. N. Veziroglu, Vol. 3, pp. 1425–1443, Hemisphere Publishing, 1977.

6 Ünal, H. C., Van Gasselt, M. L. G., and Ludwig, P. W. P. H., "Dynamic Instabilities in Tubes of a Large Capacity, Straight-Tube, Once-Through Sodium Heated Steam Generator," *International Journal of Heat and Mass Transfer*, Vol. 20, 1977, pp. 1389–1399.

7 Brasz, J., "Hydrodynamic Instability and Performance Degradation of a Straight-Tube Sodium Heated Steam Generator," *Proceeding of Condensed Papers of the Meeting—Two-Phase Flow and Heat Transfer Symposium-Workshop*, Ft. Lauderdale-Fla, Oct. 18–20, 1976, edited by T. N. Veziroglu, University of Miami, 1976, pp. 183–189.

8 Sano, A., Kanamori, A., and Tsuchiya, T., "Operating Experiences with 1 MW Steam Generator," Paper Presented at IAEA Study Group Meeting on Steam Generators for LMFBR's, Bensberg, October 14–17, 1974.

9 Deam, R., and Murray, J., "The Prediction of Dynamic Stability Limits in Once-Through Boilers Using DYMEL," Paper Presented at European Two-Phase Group Meeting, Erlangen, 31st May–4th June 1976.

10 Deam, R., Personal communication.

11 Ünal, H. C., "Correlations for the Determination of the Inception Conditions of Density-Wave Oscillations for Forced and Natural Circulation Steam Generator Tubes," ASME JOURNAL OF HEAT TRANSFER, Vol. 102, 1980, pp. 14–19.

12 Ünal, H. C., "Some Aspects of Two-Phase Flow, Heat Transfer and Dynamic Instabilities in Medium and High Pressure Steam Generators," Ph.D. Thesis submitted to Technological University of Delft, The Netherlands (to be published on March 18, 1981).

13 Ünal, H. C., "Density-Wave Oscillations in Sodium Heated Once Through Steam Generator Tubes," CTI-TNO Report, Ref. Nr. 79-06976, July 1979.

14 Quandt, E. R., "Analysis and Measurements of Flow Oscillations," *Chemical Engineering Progress Symposium Series*, Vol. 57, Nr. 32, 1961, pp. 111–126.

15 Ishii, M., and Jones, O. C., Jr., "Derivation and Application of Scaling Criteria for Two-Phase Flows," in *Two-Phase Flows and Heat Transfer*, edited by S. Kakac and F. Mayinger, Vol. 1, pp. 163–185, Hemisphere Publishing Corporation, 1977.

16 Knudsen, J. G., and Katz, D. L., *Fluid Dynamics and Heat Transfer*, McGraw Hill, New York, 1958, p. 143.

17 McAdams, W. H., *Heat Transmission,* McGraw Hill, New York, 1954, p. 135.

18 Ito, H., "Friction Factors for Turbulent Flow in Curved Pipes," ASME *Journal of Basic Engineering*, June 1959, pp. 123–134.

S. Levy
J. M. Healzer

S. Levy, Inc.,
Campbell, Calif.

Application of Mixing Length Theory to Wavy Turbulent Liquid—Gas Interface[1]

A fully developed and adiabatic two-phase annular model with liquid entrainment is derived for flow in a pipe with negligible gravity effects. The model is based upon application of the single phase mixing length theory to a wavy liquid-gas interface. The model subdivides the flow cross section into three regions: a liquid film, a gas core of constant density, and a transition wavy layer between them. The combination of a constant velocity and a density varying exponentially with distance from the wall is employed in the transition layer. This approach plus appropriate logarithmic velocity distributions in the liquid film and gas core make it possible to specify the two-phase pressure drop, volume fraction, wave velocity, and thickness of the liquid film and transition layer. The liquid entrainment is obtained in terms of the exponent of the density profile in the transition layer, and interface stability considerations are used to express this entrainment parameter semiempirically in terms of an apparent Weber number and density ratio. Comparisons of the model are made with air-water and steam-water test data, and the results generally are satisfactory over a wide range of conditions and for all the important characteristics of this flow pattern.

Introduction

Wavy liquid-gas interfaces are found in many practical two-phase flow applications involving annular flow patterns. A very large number of models have been proposed in the literature to deal with such an interface. One large family of solutions range from the classical hydrodynamic treatment of surface, gravity and wind waves [1] and extends to the most recent application of the nonlinear Korteweg-de Vries equation to describe small but finite amplitude longwaves [2]. Another large group of solutions relies upon empirically based formulations to describe the drag coefficient of the waves or the increased friction at the interface [3–6]. In this paper, it is proposed to deal with the turbulent structure of the flow at the liquid-gas interface and to extend the accepted single phase mixing length turbulent theory to describe it.

The characteristics of a turbulent liquid-gas interface are depicted in Fig. 1(*a*) for an annular flow pattern in a pipe of radius R. It consists of a liquid film at the channel wall with a central core of gas containing liquid droplets. The liquid film and gas core are separated by a transition layer of liquid waves. For the present model, the liquid-gas arrangement is simplified as shown in Fig. 1(*b*). At any position z along the direction of flow, the elements of the flow pattern are described as follows:

Liquid Film. The liquid film thickness is Y_f. The velocity in the liquid film is u_f and varies from zero at the wall to U_f at the edge of the liquid film. The density in the film is taken as liquid density, ρ_L.

Transition Layer. The transition layer extends from the edge of the liquid film to the edge of the core, Y_t. The velocity in the transition layer, u_t, varies from the velocity at the edge of the liquid film to that at the edge of the core. In this model, the density in the transition layer is assumed to decrease exponentially across the layer, starting at the liquid density, ρ_L, at the liquid film and decreasing to the core density, ρ_c, at the outer edge of the core. As shown by the later application of the mixing length theory, the transition layer velocity is found to be a constant and is taken as the liquid wave velocity, U_w.

Core. The central core extends from the edge of the transition layer to the center of the flow passage. The core velocity, u_c, varies from the velocity, U_t, at the edge of the core, Y_c, to a maximum value in the center of the flow passage. The density in the core, ρ_c, is taken as constant.

The advantage to dividing the annular flow pattern into the above regions is that both the core and the liquid film can be treated using single phase mixing length turbulent flow concepts. The transition layer can be modeled with a relatively simple extension of these same concepts.

For steady-state turbulent flow, neglecting gravitational forces, the momentum equation reduces to the familiar Reynolds expression for shear stress, τ. In a fully developed flow of variable density, the shear stress can be written as [7]

$$\tau = 1_u 1_{\rho u} \frac{du}{dy}\frac{d(\rho u)}{dy} \tag{1}$$

where the mixing lengths 1_u and $1_{\rho u}$ are assumed to be functions of y. If they are taken to be such that

$$1_u 1_{\rho u} = F^2(y)\left(1 - \frac{y}{R}\right) \tag{2}$$

there results for $\tau = \tau_w\,(1 - y/R)$

$$\tau_w = F^2(y)\frac{du}{dy}\frac{d(\rho u)}{dy} \tag{3}$$

where τ_w is the wall shear stress.

For a constant density fluid, equation (3) reduces to the well-known Prandtl expression for wall shear stress if we assume that [8]

$$F^2(y) = k^2 y^2 \tag{4}$$

where k is the mixing length constant.

For application to the present model, equation (3) is solved for each of the three separate flow regions depicted in Fig. 1(*b*) (liquid film extending to Y_f, transition layer between Y_f and Y_t, and the core spanning from Y_t to the center of the pipe). The solutions will yield not only the pressure drop and the volume fractions occupied by the gas and liquid, but they will specify the amount of liquid entrained beyond the liquid film. This quantity is most important in many practical applications such as the prediction of critical heat flux. Also predictions will be developed for the liquid and gas velocity and density distributions, for the liquid and transition layer thicknesses,

---

[1] This work was sponsored by the Electric Power Research Institute (EPRI) under Research Project 1380-1 and their support is gratefully acknowledged.

Contributed by the Heat Transfer Division for publication in the JOURNAL OF HEAT TRANSFER. Manuscript received by the Heat Transfer Division July 2, 1980.

and for the transition layer constant velocity (taken to be the wave velocity).

Before employing equation (3) to obtain such solutions, it is useful to first review typical approaches which have been used in the past and discuss their modeling assumptions for an annular flow pattern.

Previous Interface Assumptions and Solutions

Many different interface assumptions have been employed previously. They tend to fall into three classes:

- discontinuous density interface and continuous velocity interface.
- discontinuous density and velocity interface.
- empirical interface relations.

The solutions have dealt with varying types of two or three fluid systems and include:

Two Fluid Systems. A liquid film and a gas core with no liquid drops; or a liquid film and a gas core with entrained liquid droplets.

Three Fluid Systems. A liquid film, entrained liquid drops in the gas, and a gas core; or a liquid film, a transition layer, and a gas core with entrained liquid droplets.

In the simplest case of two completely separate fluids and a discontinuous density interface, the liquid and gas velocity are assumed equal at the interface. If we assume that $F^2(y) = k^2y^2$ as in single phase turbulent flow, there results

$$\left.\begin{aligned} u_L{}^+ &= \frac{1}{k}\ln\frac{y}{Y_f} + U_f{}^+, \quad y \leqq Y_f \\ u_G{}^+ &= \frac{1}{k}\ln\frac{y}{Y_f} + U_f{}^+\sqrt{\frac{\rho_G}{\rho_L}}, \quad y \geqq Y_f \end{aligned}\right\} \qquad (5)$$

where Y_f is the liquid film thickness and u^+ and $U_f{}^+$ are shear stress velocities.

$$u^+ = u\Big/\sqrt{\frac{\tau_w}{\rho}}, \quad U_f{}^+ = U_f\Big/\sqrt{\frac{\tau_w}{\rho_L}} \qquad (6)$$

The subscripts G and L are used to indicate that the gas and liquid properties and density are used in equations (5) and (6).

Equations (5) have been integrated by many investigators to predict two-phase annular flow and in several instances they have been modified to take into account the effects of gravity [9, 10, 11]. The solutions have been found to do an adequate job on the liquid film but to do poorly in predicting the gaseous pressure drop or interface friction factor. This is not too surprising since the gaseous shear stress velocity at the interface, $U_G{}^+$ is equal to

$$U_G{}^+ = U_f{}^+\sqrt{\frac{\rho_G}{\rho_L}} \qquad (7)$$

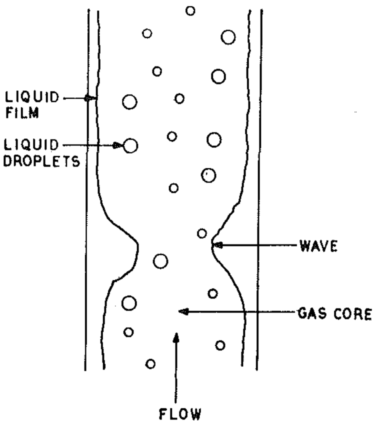

Fig. 1(a) Annular flow pattern

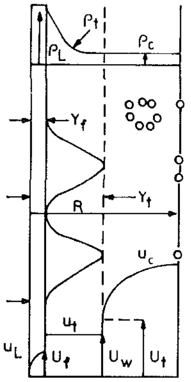

Fig. 1(b) Annular flow pattern model

Since in most experiments performed $\rho_G/\rho_L \ll 1$ one would calculate $U_G{}^+$ values well below 5.[2] Since a value of shear stress velocity below 5 is associated with laminar flow (8), the assumption of equal liquid and gas velocity at the interface implies the hardly practical possibility of a laminar gas condition ($U_G{}^+ < 5$) atop a turbulent liquid layer ($U_f{}^+ > 14$). The gas interface will, in fact, be turbulent and the gaseous pressure drop should be expected to exceed the predictions from equation (5).

One way to correct this situation is to assume not only a discon-

---

[2] For example, for $\rho_G/\rho_L = 0.0025$ and $U_f{}^+ = 15$, $U_G{}^+ = 0.75$.

Nomenclature

C_e = liquid concentration beyond base liquid film
D = pipe diameter
E = entrainment cross flow rate
F = function describing mixing length
f_{is} = interface friction factor
G = mass flow per unit pipe area
K = function defined by equation (31)
k_e = cross flow entrainment coefficient
k = mixing length constant
k_s = equivalent surface roughness
l_u = velocity mixing length
$l_{\rho u}$ = mass rate mixing length
N_{Re} = Reynolds number for gas flow only ($G_G D/\mu_G$)
P = pressure
R = pipe radius
U_f = velocity at edge of liquid film
U_t = velocity at edge of core
U_w = wave velocity
u = local velocity
u^+ = nondimensional shear velocity ($u^+ = u/\sqrt{\tau_w/\rho}$)
Y_f = thickness of base liquid film
Y_t = distance to outermost edge of transition layer
Y_w = distance to center of gravity of transition layer
y = distance from wall
y^+ = nondimensional distance ($y^+ = y\sqrt{\tau_w/\rho}/\mu$)
z = distance along pipe
β = density function exponent
μ = viscosity
ρ = density
σ = surface tension
τ = shear stress
τ_w = wall shear stress

Subscripts

c = core
e = entrained liquid
f = liquid film
G = gas
L = liquid
TPF = two-phase friction
t = transition layer
wf = just beyond liquid film
wt = just short of core

Superscripts

$-$ = average over

tinuous density but also a discontinuous velocity at the interface. In this case

$$u_G{}^+ = \frac{1}{k}\ln\frac{y}{Y_f} + U_G{}^+, \quad U_G{}^+ \gg U_f{}^+\sqrt{\frac{\rho_G}{\rho_L}} \tag{8}$$

It is interesting to note that if as in single phase flow one assumes $U_G{}^+ = 5.5$, equation (8) becomes with $k_s = 3.32\ Y_f$

$$u_G{}^+ = \frac{1}{k}\ln\frac{y}{k_s} + 8.5 \tag{9}$$

With the constant 8.5, equation (9) corresponds to single phase flow in a rough pipe with a sand roughness k_s [8]; and, in two-phase flow with $U_G{}^+ = 5.5$ the gas flow tends to behave as in single phase flow in a rough pipe with a sand roughness k_s equivalent to 3.32 times the liquid thickness. This is not very different from the Wallis empirical approach of using four times the liquid film thickness [5]. It is important to note, however, that the velocity discontinuity at the interface is very substantial since

$$\frac{U_G}{U_f} = \frac{5.5}{U_f}\sqrt{\frac{\rho_L}{\rho_G}} \tag{10}$$

and it is doubtful that such conditions will exist and preserve the assumed density discontinuity.

For that reason, several investigators have recognized the need to break the liquid film into two regions. A continuous liquid base layer is employed which is in contact with the wall and it supports an intermittent, wavy layer of variable density. The model developed by Moeck and Stachiewicz [12] is typical of such derivations and it employs a two-dimensional film and a one-dimensional droplet laden gas core. Others [13] have chosen to break the core into the gas itself and a separate liquid droplet field. In all formulations of this type, several empirical correlations are necessary to describe the interface. They include relations for the base liquid film thickness, the interface friction factor, the droplet size and a droplet deposition coefficient. Of particular interest are the semi-empirical works of Wallis [5], Levy [4], and Moeck [6], which showed that the interface friction factor depends only upon the liquid film thickness. In this final class of solutions for annular flow, the predictions can be expected to be more accurate but they cannot deal with the details of the flow and density structures and must concentrate upon properties averaged over large portions of the flow cross section.

It is the purpose of this investigation to deal with the detailed flow distributions and to limit the number of empirical correlations necessary to predict liquid entrainment.

Proposed Interface Solution

It is proposed in this section to examine the velocity and density discontinuity at the interface. By introducing equation (6) into equation (3) and nondimensionalizing, there results

$$\left(\frac{du^+}{dy/Y_f}\right)^2 = \frac{Y_f{}^2}{F^2} + \frac{1}{4}u^{+2}\left(\frac{d\ln\rho/\rho_L}{dy/Y_f}\right)^2 \tag{11}$$

$$\frac{du^+}{dy/Y_f} = \overset{+}{\underset{-}{}}\sqrt{\frac{Y_f{}^2}{F^2} + \frac{1}{4}u^{+2}\left(\frac{d\ln\rho/\rho_L}{dy/Y_f}\right)^2} \tag{12}$$

The first major difference from single phase flow is that equation (12) can admit to the two roots, + and − in two-phase flow. The reason is that in single phase flow u^+ and the fluid velocity always increase away from the wall. In two phase flow, the density ρ is decreasing away from the liquid interface. We can, in fact, visualize two types of distribution. The first one is such that ρ decreases slowly beyond the interface and u and u^+ are going up beyond the liquid interface. This type of distribution is characteristic of bubbly flow. The second type of distribution would be one in which the density decreases rapidly in a transition layer from the liquid interface to a gas core and the shear stress velocity u^+ would be decreasing in the transition layer. Within the gas core, the density can be assumed to be relatively constant and is equal to ρ_c and the shear stress velocity distribution within the core would be characteristic of turbulent flow and increasing with distance from the wall. The distribution just described is that of annular flow with liquid entrainment, except that it includes a transition layer within which the density was allowed to vary continuously from the liquid to the gas core value. To the authors' knowledge, such an approach with a decreasing u^+ in the transition layer has not been considered in the past. In order to more specifically illustrate the preceding comment let us assume beyond the liquid film

$$\left.\begin{aligned}\frac{\rho}{\rho_L} &= \left(\frac{y}{Y_f}\right)^{-\beta}\\ F^2 &= k^2y^2\end{aligned}\right\} \tag{13}$$

where β is a positive exponent and k is the so-called mixing length constant. Equation (11) becomes:

$$\left(\frac{du^+}{dy/Y_f}\right)^2 = \left(\frac{Y_f}{y}\right)^2\left[\frac{1}{k^2} + \frac{1}{4}u^{+2}\beta^2\right] \tag{14}$$

and

$$\frac{du^+}{\sqrt{u^{+2} + (2/k\beta)^2}} = \pm\frac{\beta}{2}\frac{d\,y/Y_f}{y/Y_f} \tag{15}$$

Equation (15) can be integrated with $u^+ = U_{wf}{}^+$ just beyond the interface,[3]

$$\frac{u^+ + \sqrt{u^{+2} + (2/k\beta)^2}}{U_{wf}{}^+ + \sqrt{U_{wf}{}^{+2} + (2/k\beta)^2}} = \left(\frac{y}{Y_f}\right)^{\pm\frac{\beta}{2}} \tag{16}$$

Let us now consider two types of density profile. For $\beta > 1$ and preferably $\beta \gg 1$ we have a rapid decrease of the density beyond the interface, which is typical of annular flow with liquid entrainment. If u^+ is kept turbulent or u^+ at least exceeds 5, $u^{+2} \gg (2/k\beta)^2$ with k taken close to the accepted value of 0.4, equation (16) simplifies approximately to

$$\frac{u^+}{U_{wf}{}^+} = \left(\frac{y}{Y_f}\right)^{\pm\frac{\beta}{2}} \tag{17}$$

Using the density distribution of equation (13), the corresponding velocity ratio is for the positive root,

$$\frac{u}{U_w} = \left(\frac{y}{Y_f}\right)^{\beta} \tag{18}$$

or for the negative root,

$$\frac{u}{U_w} = 1 \tag{19}$$

If one utilizes the positive root, it would mean that u^+ increases as $(y/Y_f)^{\beta/2}$ in the transition layer and that the velocity slip between liquid film and gas core would be greater than that calculated from equations (5) and (8). Also, examination of the velocity data of Cohen [14] obtained for turbulent air flowing over a horizontal liquid film reveals that u^+ is decreasing in the transition layer.[4] On this basis, the annular flow with liquid entrainment can only satisfy equation (12) with a minus sign and there results

$$\frac{u^+ + \sqrt{u^{+2} + (2/k\beta)^2}}{U_{wf}{}^+ + \sqrt{U_{wf}{}^{+2} + (2/k\beta)^2}} \cong \frac{u^+}{U_{wf}{}^+} = \left(\frac{y}{Y_f}\right)^{-\frac{\beta}{2}} = \sqrt{\frac{\rho}{\rho_L}} \tag{20}$$

Under such conditions, it is worthwhile to note that the fluid velocity is relatively constant in the transition layer and equal to a velocity U_w beyond just the interface.

It is also worthwhile to note that the same result is obtained without assuming the form of F^2 as long as

---

[3] In this definition, liquid properties are used because of closeness to interface, which accounts for subscript f.

[4] In reference [14], at a given y^+ the measured values of u^+ in the air layer fall below the values obtained from equation (30) which apply to the liquid film.

$$\frac{Y_f^2}{F^2} \ll \frac{1}{4} u^{+2} \left(\frac{d \ln \rho/\rho_L}{d\, y/Y_f}\right)^2$$

Equation (11) then leads to the only acceptable solution in the transition layer, or

$$u^+ (\rho/\rho_L)^{1/2} = \text{constant}, \beta > 1$$

Let us next consider the value of U_w. At the edge of the gas core the velocity is equal to U_w and the corresponding shear stress velocity U_{wt}^+ is

$$U_{wt}^+ = U_w \Big/ \sqrt{\frac{\tau_w}{\rho_c}} = \sqrt{\frac{\rho_c}{\rho_L}} \frac{U_w}{\sqrt{\tau_{w/\rho_L}}} = \sqrt{\frac{\rho_c}{\rho_L}}\, U_{wf}^+ \qquad (21)$$

If the velocity U_w at the edge of the transition layer is taken to be that of the liquid at the edge of the liquid film or U_f ($U_{wt}^+ = U_f^+ \sqrt{\rho_c/\rho_L}$), one could again be faced with the anomaly of U_{wt}^+ falling below 5 because $\rho_c/\rho_L \ll 1$ and the gas core would be starting with a laminar interface. Because this does not make sense physically U_w must be taken greater than U_f and the transition layer with a continuous density distribution and a constant velocity U_w requires a step jump in velocity at the edge of the liquid film to achieve a turbulent interface.

The interface equations and mixing length turbulence behavior are, therefore, suggesting presence of a transition layer of constant velocity with a rapid decrease in density from liquid to gas core and with a step jump in velocity over that of liquid film. This, in fact, is the representation that one would get of the wavy layer above the liquid if averaged over long periods of time. It has been found that disturbance waves can travel above the liquid film at velocities much greater than those in the liquid film and that they protrude several times above the liquid film thickness. The equations developed herein attempt to describe such a layer but averaged over long periods of time.

Solutions for Annular Flow with Liquid Entrainment

As shown in Fig. 1, let us assume that the flow cross section can be broken down into three regions: a liquid film of thickness Y_f, a transition layer extending from Y_f to Y_t, and a gas core from Y_t to the pipe center with a constant density ρ_c. As previously noted, in the transition layer, the velocity u_t is constant so that

$$u_t = U_w = U_{wt}^+ \sqrt{\frac{\tau_w}{\rho_c}}, \quad Y_f < y < Y_t \qquad (22)$$

The mass flow rate in the transition region per unit area of pipe, G_t is obtained from equations (22) and (13) and

$$\frac{G_t/\rho_L}{\sqrt{\tau_w/\rho_c}} = 2\, U_{wt}^+ \frac{Y_f}{R} \left[1 - \left(\frac{Y_f}{Y_t}\right)^{\beta-2}\right] \frac{1}{\beta - 1} + 2\, U_{wt}^+ \left(\frac{Y_f}{R}\right)^2 \frac{1}{2-\beta} \left[1 - \left(\frac{Y_f}{Y_t}\right)^{\beta-2}\right] \qquad (23)$$

In the gas core, the velocity distribution is obtained from a single phase type relation or

$$u_c^+ = \frac{1}{k} \ln \left(\frac{y}{Y_t}\right) + U_t^+ \qquad (24)$$

and the mass flow rate in the gas core per unit pipe area G_c is given by

$$\frac{G_c/\rho_c}{\sqrt{\tau_w/\rho_c}} = U_t^+ \left(1 - \frac{y_t}{R}\right)^2 + \frac{2}{k} \left[\frac{Y_t}{R} - 0.75 - \frac{1}{4}\left(\frac{Y_t}{R}\right)^2 + \frac{1}{2} \ln \frac{R}{Y_t}\right] \qquad (25)$$

Also, because of equation (13), there results

$$\frac{\rho_c}{\rho_L} = \left(\frac{Y_t}{Y_f}\right)^{-\beta} \qquad (26)$$

Because the velocity u is relatively constant in the transition layer we can assume that the liquid and gas velocities are equal in that layer. The same assumption can be made in the gas core where the density was taken as constant. The total amount of liquid entrainment per unit pipe area, G_e is equal to the sum of liquid entrained in the gas core and liquid in the transition layer. It is equal to

$$G_e = \left[G_c \left(\frac{\rho_L}{\rho_G} - \frac{\rho_L}{\rho_c}\right) + G_t \left(\frac{\rho_L}{\rho_G} - \frac{\rho_L}{\bar{\rho}_t}\right)\right] \frac{\rho_G}{\rho_L - \rho_G} \qquad (27)$$

It is important to note that in this model the liquid in the transition zone or wave zone is assumed to be entrained. This is a reasonable approach since this liquid is moving at velocities well in excess of those in the liquid film and close to the gas velocity. The total gas flow per unit pipe area G_G is equal to the sum of the gas flowing in the core and the transition zone. It is equal to

$$G_G = \left[G_c \left(\frac{\rho_L}{\rho_c} - 1\right) + G_t \left(\frac{\rho_L}{\bar{\rho}_t} - 1\right)\right] \frac{\rho_G}{\rho_L - \rho_G} \qquad (28)$$

so that

$$\frac{G_e}{G_G} = \frac{\left(\frac{\rho_L}{\rho_G} - \frac{\rho_L}{\rho_c}\right) + \frac{G_t}{G_c}\left(\frac{\rho_L}{\rho_G} - \frac{\rho_L}{\bar{\rho}_t}\right)}{\left(\frac{\rho_L}{\rho_c} - 1\right) + \frac{G_t}{G_c}\left(\frac{\rho_L}{\bar{\rho}_t} - 1\right)} \qquad (29)$$

Equations (23, 25, 27) and (29) mean that the ratio G_e/G_G is a function of the density ratios ρ_L/ρ_G, ρ_L/ρ_c, the liquid film thickness ratio Y_f/R and the parameter β. Finally, the solution in the liquid film proceeds as in single phase flow. It is subdivided into three regions: a liquid laminar region extending to $y_L^+ = 5$, a liquid transition region extending from $y_L^+ = 5$ to $y_L^+ = 30$, and a turbulent liquid region extending beyond $y_L^+ = 30$ [8]. The velocity u_L^+ is given by [8]

$$\begin{aligned} u_L^+ &= y_L^+ & y_L^+ &\leqq 5 \\ u_L^+ &= -3.05 + 5 \ln y_L^+ & 5 \leqq y_L^+ &\leqq 30 \\ u_L^+ &= 2.5 \ln y_L^+ + 5.5 & y_L^+ &\geqq 30 \end{aligned} \qquad (30)$$

where y_L^+ is a nondimensional distance equal to $y_L \sqrt{\tau_w/\rho_L}/\rho_L/\mu_L$ with μ_L being the liquid viscosity. The liquid film mass flow rate per unit area of pipe, G_f is obtained by integrating equation (30) so that

$$\frac{G_f/\rho_L}{\sqrt{\frac{\tau_w}{\rho_L}}} = \frac{2}{R^{+2}} K\,(Y_f^+, R^+) = 2 \int_0^{y_f+/R+} \left(1 - \frac{y^+}{R^+}\right) \frac{\rho}{\rho_L}\, u^+ d \left(\frac{y^+}{R^+}\right) \qquad (31)$$

where

$$K(Y_f^+, R^+) = \frac{1}{2} R^+ Y_f^{+2} - \frac{1}{3} Y_f^{+3}, \quad \text{for } Y_f^+ < 5$$

$$K(Y_f^+, R^+) = 12.51R^+ - 10.45 - 8.05R^+ Y_f^+ + 2.775\, Y_f^{+2} + 5R^+Y_f^+ \ln Y_f^+ - 2.5\, Y_f^+ \ln Y_f^+, \quad \text{for } 5 < Y_f^+ < 30$$

$$K(Y_f^+, R^+) = 3R^+Y_f^+ - 63.9R^+ - 2.125\, Y_f^{+2} - 1.25\, Y_f^{+2} \ln Y_f^+ + 2.5R^+Y_f^+ \ln Y_f^+ + 573.21, \quad \text{for } Y_f^+ > 30$$

with

$$R^+ = \frac{R\sqrt{\tau_w/\rho_L}}{\mu_L}\, \rho_L$$

The preceding equations make it possible to predict annular flow with liquid entrainment. If the parameters k, U_{wt}^+, β, U_L^+, ρ_L/ρ_c, ρ_L/ρ_G are specified, the solution can proceed as follows:

1 Assume a value of Y_f/R, calculate Y_t/Y_f from equation (26) and G_t/G_c from equation (23) and (25). The entrained ratio G_e/G_G follows from equation (29).

2 The ratio G_G/G_c is calculated from equation (28) and the term $G_c/\rho_c/\tau_w/\rho_c$ obtained from equation (25). An interface friction factor results such that

$$\frac{G_G/\rho_G}{\sqrt{\tau_w/\rho_G}} = \frac{(G_G/G_c)\,(G_c/\rho_c)\sqrt{\frac{\rho_c}{\rho_G}}}{\sqrt{\tau_w/\rho_c}} = \sqrt{\frac{2}{f_{is}}} \qquad (32)$$

where f_{is} is the interface friction factor based upon the superficial gas velocity in the pipe, G_G/ρ_G. Equation (32) makes it possible to calculate the wall shear stress τ_w, i.e. the corresponding two-phase frictional pressure drop $(dp/dz)_{\text{TFP}}$ for a given value of G_G or

$$\left(\frac{dp}{dz}\right)_{\text{TPF}} = \frac{2\tau_w}{R} = \frac{1}{R} f_{is} \rho_G \left(\frac{G_G}{\rho_G}\right)^2 \qquad (33)$$

3 The average fluid density is obtained by integrating the density over each of the three regions in the pipe [17].

4 Finally, for a given value of the total gas flow rate G_G, the non-dimensional liquid film thickness $Y_f{}^+$ is obtained from

$$Y_f{}^+ = Y_f \frac{\sqrt{\frac{\tau_w}{\rho_L}}\rho L}{\mu_L} = \frac{Y_f}{R}\frac{R\,G_G}{\mu_L}\frac{\sqrt{\tau_w/\rho_G}}{G_G/\rho_G}\sqrt{\frac{\rho_L}{\rho_G}} \tag{34}$$

and the liquid film flow rate G_f is obtained from equation (31).

5 The calculations are repeated with different values of Y_f/R and one can generate the desired values of liquid entrainment, friction and head losses for any specified value of gas and liquid flow rate and core density.

Specifications of Parameters k, $U_t{}^+$, $U_{wt}{}^+$

Before predictions can be made, it is necessary to select appropriate values for the parameters k, $U_t{}^+$, and U_w. We shall take $k = 0.4$[5] as in single phase flow. This is a reasonable assumption since at the limit of $\rho_L = \rho_G$, k must assume that value. Similarly $U_t{}^+$ will be taken as $U_t{}^+ = 5.5$ to again obtain the correct single phase profile at the limit of $\rho_L = \rho_G$. The parameter U_w corresponds to the constant velocity to be employed in the transition layer. As pointed out before, it is also taken to be the wave velocity in this transition zone. It is specified as follows:

1 The position Y_w of the center of mass of the transition layer is found by writing

$$\frac{Y_w}{Y_f} = \left(\frac{\rho_L}{\bar{\rho}_t}\right)^{1/\beta} \tag{35}$$

where $\bar{\rho}_t$ is the mean density in the transition layer.

2 The shear stress velocity at the edge of the liquid film is $U_f{}^+$ and the shear stress velocity at the edge of the transition layer is $U_t{}^+$. By assuming a straight line between $U_f{}^+$ and $U_t{}^+$, the shear stress velocity at the position Y_w can be calculated and it is taken to be the wave shear stress velocity $U_w{}^+$. There results

$$U_w{}^+ = U_w/\sqrt{\tau_w/\bar{\rho}_t} = U_f{}^+ - \frac{U_f{}^+ - 5.5}{\left(\frac{Y_t}{Y_f} - 1\right)}\left(\frac{Y_w}{Y_f} - 1\right) \tag{36}$$

and the corresponding wave velocity U_w is obtained.

The validity of equation (36) can be checked against experimental data for the wave velocity for which Y_t, Y_f, and the pressure drop have been reported. From the ratio Y_t/Y_f one can calculate a value of β from equation (26). The values of $\bar{\rho}_t/\rho_L$ and $U_f{}^+$ can also be computed which specify the wave velocity U_w. All the measured and predicted wave velocities are shown in Figure 2 and the correspondence between tests (15, 3, 16) and predictions is good.

Correlation for Parameter β

The parameter β is most important to the proposed solutions. In the original study performed for EPRI [17], constant values of the parameter β were first employed together with and without liquid present in the gas core. The solutions revealed that:

- the model had many of the correct characteristics observed in tests
- that the simplified assumption of no liquid in the core had a minor impact upon the prediction
- that the parameter β which describes overall liquid entrainment needed to vary with gas flow rate and liquid surface tension.

It was then surmised that the value of β is controlled by interface stability consideration. In other words, for a given gas and liquid flow rate, the amount of liquid entrained and its distribution in the core should be such that the liquid-core interface is stable. Interface stability relations have been developed by several authors [18] and they yield

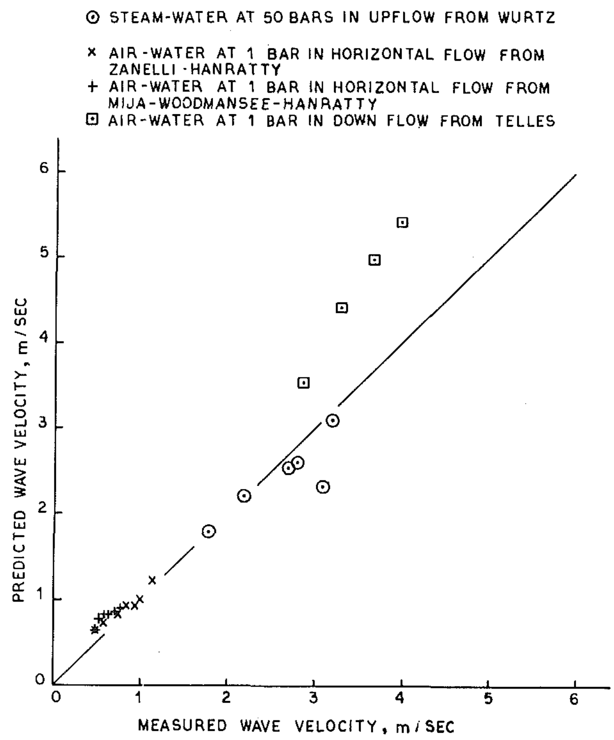

Fig. 2 Measured and predicted wave velocities

$$\lambda \propto \frac{\sigma\,(\rho_L + \rho_c)}{\rho_L\,\rho_c}\frac{1}{(\bar{u}_c - \bar{u}_f)^2} \tag{37}$$

where λ is the interface wave length, σ the surface tension and $\bar{u}_c$ and $\bar{u}_f$ are the average core and film velocities. One can visualize the possibility of employing equation (37) together with previously defined relations to specify β or ρ_c. In this study, equation (37) will be employed in a much more narrow way, that is to define nondimensional parameters upon which β might depend. If one assumes that $\bar{u}_c \gg \bar{u}_f$, equation (37) becomes with $\bar{u}_c = G_c/\rho_c$

$$\lambda \propto \frac{\left(1 + \frac{\rho_c}{\rho_L}\right)}{\frac{\rho_c}{\rho_L}}\frac{\sigma}{\rho_L}\left(\frac{\rho_c}{G_c}\right)^2 \tag{38}$$

As suggested by Tippets [18], the wavelength λ of the disturbance can be taken proportional to the mixing length. It is also expected that the wave length λ decreases as Y_t/Y_f increases and goes to infinity when $Y_t = Y_f$ or $\rho_L = \rho_G$, and across the transition layer, one can write

$$\lambda \propto k\,Y_f \Big/ \left(\frac{Y_t}{Y_f} - 1\right) \tag{39}$$

so that with the approximation $G_c/\rho_c \approx G_G/\rho_G$ there results

$$\frac{\rho_c/\rho_L}{1 + \rho_c/\rho_L} \propto \frac{\left(\frac{Y_t}{Y_f} - 1\right)}{Y_f/R}\left(\frac{\rho_G}{\rho_L}\right)^2 \frac{\sigma}{k\,R}\frac{\rho_L}{G_G{}^2} \tag{40}$$

Equation (40) contains a new non-dimensional parameter (σ/kR) $(\rho_L/G_G{}^2)(Y_t/Y_f - 1)$. It was pointed out after equation (29) that

$$\frac{G_e}{G_G} \propto F\left(\frac{\rho_G}{\rho_L}, \beta, \frac{Y_f}{R}, \frac{\rho_c}{\rho_L}\right) \tag{41}$$

and compatibility between equations (40) and (41) suggests

$$\beta \propto f\left[\frac{\sigma}{kR}\frac{\rho_L}{G_G{}^2}\left(\frac{Y_t}{Y_f} - 1\right)\right] \tag{42}$$

---

[5] Plots of $u_c{}^+$ versus y^+ from some velocity measurements in the gas core have given a straight line with a slope varying from 0.4 to 0.1 (See Chemical Engineering, Vol. 19, pp. 665–682) and this has been interpreted that k in equation (24) should vary accordingly. It should be noted that equation (24) used here expresses $u_c{}^+$ in terms of y/Y_t and that Y_t depends upon β, the gas and liquid density and the wall shear stress, thus allowing for the variation of the slope observed in test data when plotted in terms of $u_c{}^+$.

Physically, it is expected that β should decrease with $\sigma/kR\ \rho_L/G_G{}^2\ (Y_t/Y_f - 1)$.

The exact form of equation (42) was developed empirically and it was found that with $Y_t/Y_f = (\rho_L/\rho_G)^{1/\beta}$ the relation

$$\beta = 1 + \sqrt{\left[\left(\frac{\rho_L}{\rho_G}\right)^{1/\beta} - 1\right]\frac{2\sigma}{kD}\frac{\rho_L}{G_G{}^2}} \qquad (43)$$

gave satisfactory agreement with the entrainment data of Gill and Hewitt [19].

It should be pointed out that in developing equation (43) the liquid entrained G_e in the proposed analytical solutions with $\rho_c = \rho_G$ was set equal to the measured values for simplification purposes. As pointed out in [17] making $\rho_c \neq \rho_G$, while keeping the total amount of entrained liquid constant, does not have a major effect upon the results and the simplification is warranted for ease of calculations. It should also be noted that no great effort was expended to optimize the form of equation (43) in view of some of the approximations introduced; yet, the proposed model gives superior results to previously published correlations.

Comparison to Test Results

Of particular interest is liquid entrainment because it is the parameter least satisfactorily correlated to-date. This parameter is sometimes expressed as a cross flow rate perpendicular to the flow direction. Such an entrainment cross flow rate E is proportional to the liquid concentration C_e beyond the liquid film with $E = k_eC_e$ and $C_e = G_e/(G_G/\rho_L + G_e/\rho_L)$. Two types of correlations have been proposed to-date for the entrainment cross flow rate. Paliev and Filippovich [20] employed the parameter $(\mu_L G_G/\rho_G\sigma)^2\ (\rho_G/\rho_L)$. This grouping was shown by Styrikovich, et al. [21] not to be acceptable for their steam-water tests. The second approach developed at Harwell relies upon the grouping $\tau_w Y_f/\sigma$ which gives the ratio of the disruptive shear forces on the liquid film to the stabilizing surface tension forces. An alternate proposed by Whalley, et al. [22] is to replace the liquid film thickness Y_f with the effective roughness height k_s. Such correlations have been found to be preferable but they still leave much to be desired because data scatter is still substantial.

The results obtained for the entrainment rate G_e from the solutions proposed herein together with equation (43) are shown in Figs. 3 to 7. Figure 3 shows the predictions together with the data of Gill and Hewitt [19]. The correspondence is very good with the deviation at most being 50 percent and generally being within 20 percent. As can be observed from Fig. 3, the ratio G_e/G_G increases with gas flow rate G_G and approaches the homogeneous curve at very high gas mass rates. At very high quality the data tend to fall below predictions. For such points, $Y_f{}^+$ falls well below 30 and equation (38) is not valid for $Y_f{}^+ < 30$. An increase in β is necessary below $Y_f{}^+ = 30$ and the liquid entrainment can be expected to decrease when the liquid film is not fully turbulent [17].

Let us next consider the prediction of the thickness of the transition layer or height of the waves. In line with the approximation developed to correlate liquid entrainment one sets $\rho_c = \rho_G$ so that

$$\frac{Y_t}{Y_f} = \left(\frac{\rho_L}{\rho_G}\right)^{1/\beta} \qquad (44)$$

For air-water mixtures, $\rho_L/\rho_G \gg 1$, β tends to be large (between 4 and 8) so that the density decreases rapidly in the transition layer. The base liquid film Y_f is, therefore, not very different from the measured mean liquid thickness and one can use the measured mean liquid thickness for Y_f to compare the measured ratio of Y_t/Y_f to the predicted one from equation (44). For the Harwell data, most measurements have been taken with air mass flow rates between 50 and 100 kg/m^2 s and the corresponding values of β are between 3.5 and 5.0. Equation (44) gives ratios of Y_t/Y_f of 3.8 and 6.8 which agree very well with the data given in reference [12] of 4.0 to 6.5. In the case of Hanratty and co-workers the air flow was set constant at 90 cm/s. This corresponds to a value of β of 9.3 for a gas density of 1.2 kg/m^3. Many of the runs were, however, performed with very thin films so that $Y_f{}^+ < 30$ and the corresponding β value would be in excess of 9.3. Values of 2.1 and less would result for Y_t/Y_f which compare favorably with the experimental results of 2.0 to 3.30. The slow increase in Y_t/Y_f noted in the Hanratty experiments reinforces the view that an increasing β parameter in the region of $U_f{}^+$ below 30 would be more appropriate. In the case of Telles [15] data, Y_t/Y_f was reported to be between 2.5 and 2.6 versus the prediction of 3 and less depending upon whether $Y_f{}^+$ is above or below 30. Finally, Charvonia developed a plot of Y_t/Y_f with values ranging from 2.8 to 3.4. The corresponding model predictions are 3.7 and less and they again bracket most of the data.

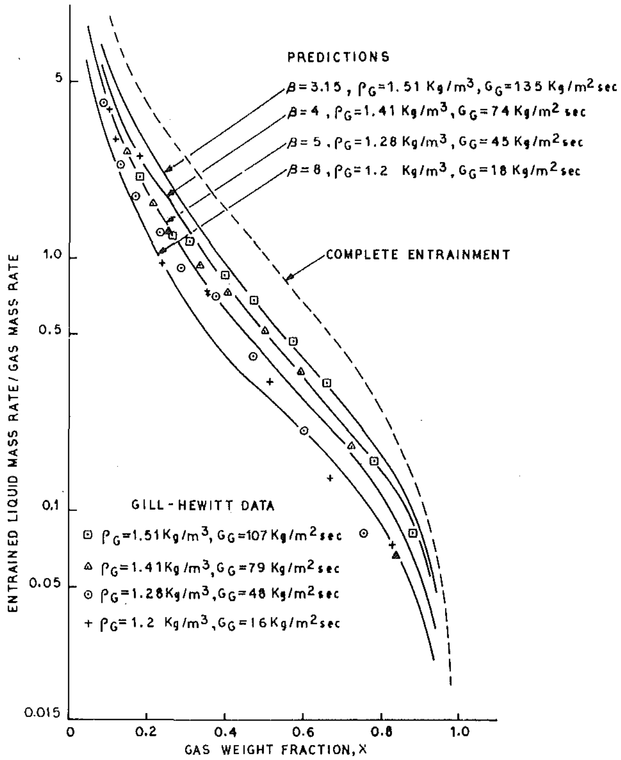

Fig. 3 Comparison of entrainment model to Gill-Hewitt data

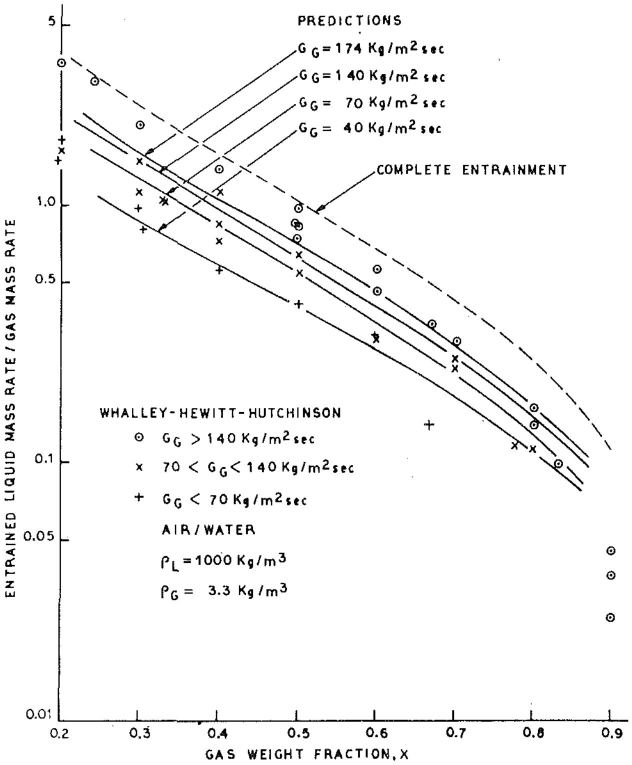

Fig. 4 Comparison of entrainment model to Whalley data

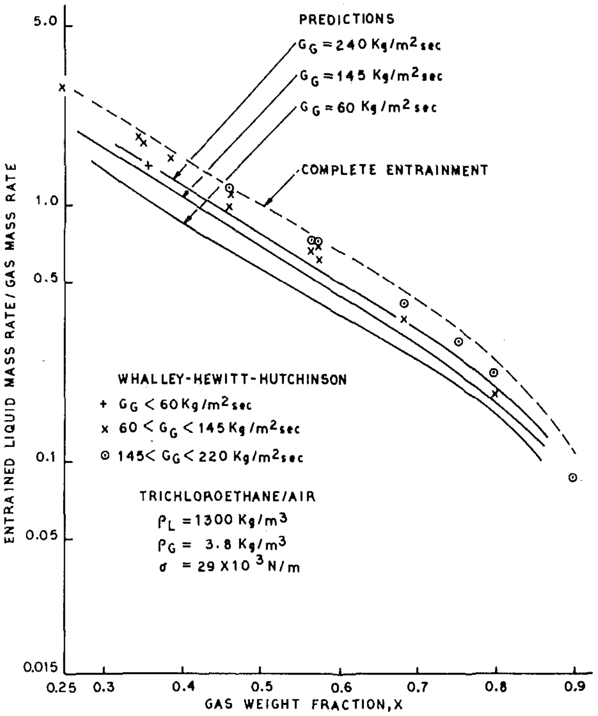

Fig. 5 Comparison of entrainment model to Whalley data

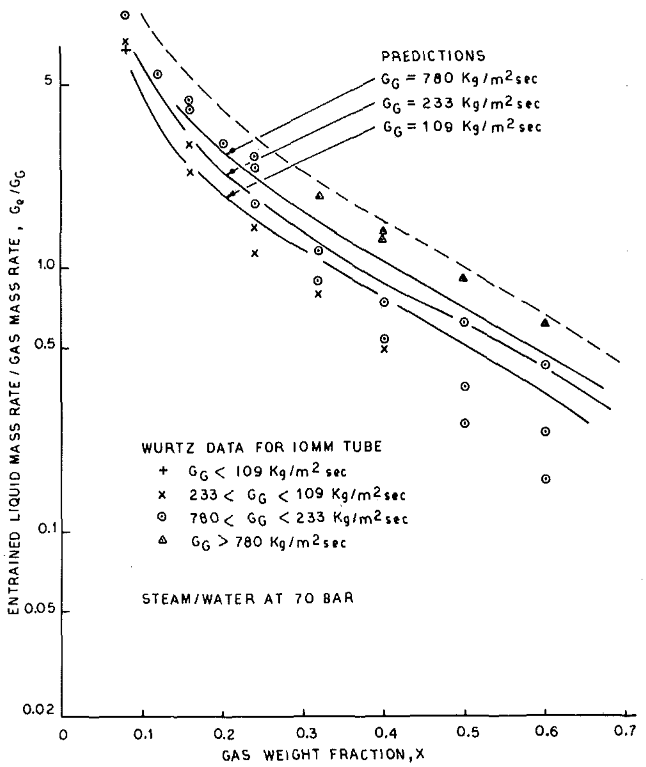

Fig. 6 Comparison of entrainment model to Wurtz data

In the case of high pressure stream-water mixtures, the parameter β is much lower. For example at 70 bars β tends to vary between 1.3 and 2.0 and the density decreases slowly in the transition layer, making it difficult to differentiate between the base liquid film thickness Y_f, the mean liquid thickness and the edge of the transition layer, Y_t. This is illustrated in Fig. 8 where the data of Subbotin [23] are reproduced for the minimum film and maximum film thickness. The ratio of maximum to minimum film is shown on the same plot. From equation (43), one can calculate approximate values of β and the predicted ratio of Y_t/Y_f is shown. At high quality the film thickness may be small enough to possibly fall below $Y_f^+ = 30$ and the ratio Y_t/Y_f decreases.

The trend and absolute values are seen to be satisfactory. Similar acceptable comparison was obtained with the data of Würtz. In Würtz's case Y_t/Y_f ranged from 6.5 to 17 and tended to slightly exceed the model predictions. This is not unexpected because as pointed out before the correlation for β was based upon measured liquid entrainments and should lead to Y_f values in excess of the minimum or base liquid film thickness.

Let us next consider the wave velocity. The model predicts the ratio of U_w to G_G/ρ_G for given values of β and gas weight fraction. By again using the simplifications of $\rho_c = \rho_G$, values of the wave velocity U_w were calculated to match a few of the test results of Whalley, Hewitt and Hutchinson and Würtz. The results are shown in Table 1. For air-water tests the model is 10 to 20 percent high while for steam-water the model is 30 to 50 percent high. Part of this discrepancy might be explained by realizing that a much more accurate value of U_w would have resulted from

$$U_w = \frac{\displaystyle\int_{Y_f/R}^{Y_t/R} \rho u \left(1 - \frac{y}{R}\right) d\,\frac{y}{R}}{\displaystyle\int_{Y_f/R}^{Y_t/R} \rho \left(1 - \frac{y}{R}\right) d\,\frac{y}{R}} \tag{45}$$

Equation (45) would give smaller values of U_w than those obtained by employing the velocity at Y_w from equations (35) and (36) and this would be particularly true for low β values.

In the case of frictional pressure drop, several good and approximate correlations have been developed for the interfacial friction factor.

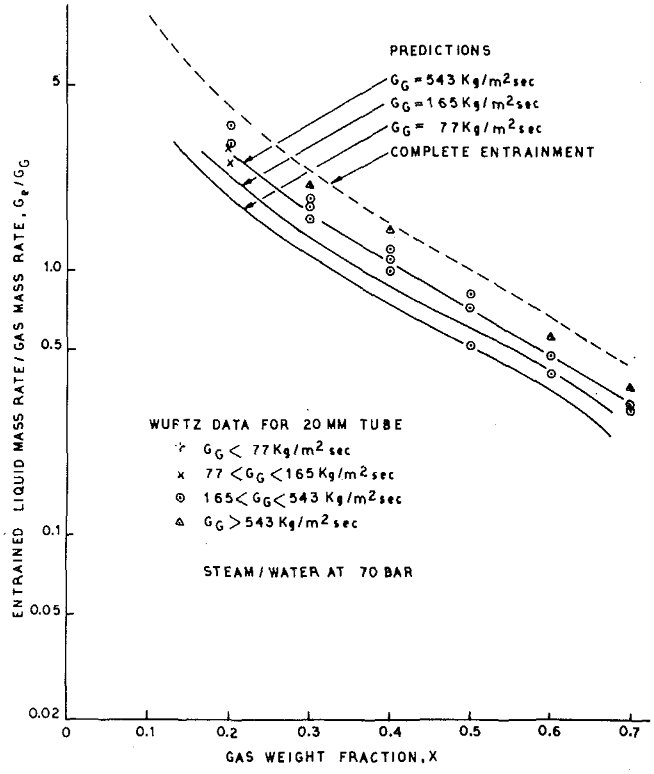

Fig. 7 Comparison of entrainment model to Wurtz data

The correlations of Wallis, Moeck and Levy have been shown to be satisfactory over a wide range of test conditions and it is proposed to compare the present model with such empirical correlations. In Fig. 9 the ratios of interface friction factor to single gas phase friction factor predicted for $\beta = 3.15$ and 4 is plotted. The results correspond to air

Table 1 Prediction of Wave Velocity

G_G (kg/m^2 s)	G_L (kg/m^2 s)	ρ_L (kg/m^3)	ρ_G (kg/m^3)	σ (N/m)	Measured U_w (m/s)	Predicted U_w (m/s)
142.4	15.9	1000	3.26	73.1×10^{-3}	3.74	3.54
126.6	31.8	1000	3.29	73.1×10^{-3}	3.57	4.45
78.9	79.9	1000	3.26	73.1×10^{-3}	2.90	3.82
62.7	94.8	1000	3.30	73.1×10^{-3}	2.60	3.38
100.0	400.0	742	36.00	17.7×10^{-3}	1.80	2.30
150.0	350.0	742	36.00	17.7×10^{-3}	2.20	3.20
200.0	300.0	742	36.00	17.7×10^{-3}	2.50	3.60
250.0	250.0	742	36.00	17.7×10^{-3}	2.80	4.10
300.0	200.0	742	36.00	17.7×10^{-3}	3.10	4.60
350.0	150.0	742	36.00	17.7×10^{-3}	3.20	4.70
150.0	600.0	742	36.00	17.7×10^{-3}	2.60	4.00
225.0	525.0	742	36.00	17.7×10^{-3}	3.20	4.80
300.0	450.0	742	36.00	17.7×10^{-3}	3.60	5.30
375.0	375.0	742	36.00	17.7×10^{-3}	3.90	6.10
450.0	300.0	742	36.00	17.7×10^{-3}	4.30	6.50

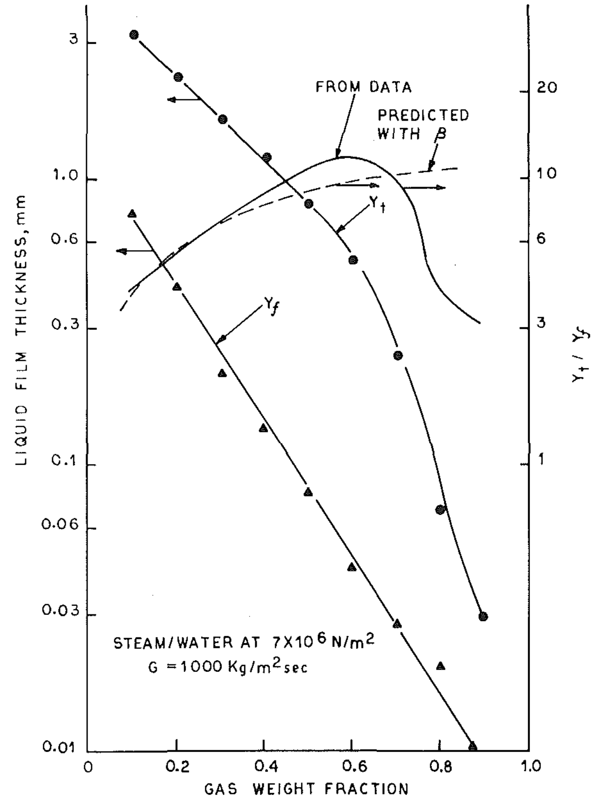

Fig. 8 Wave height prediction for steam-water

flow rates of 135 and 74 kg/m^2 s by Gill and Hewitt in a pipe of 0.0318 m in diameter. The proposed model is seen to bracket the available correlations and even slightly exceeds the Wallis correlation at high flow rates. A similar comparison is given in Fig. 10 for steam-water mixtures at 70 bars. Plots are given for β values of 1.31 and 1.70 corresponding to mass flow rates of 90 and 542 kg/m^2 s in a 20 mm tube. Again the analyses bracket the previously proposed correlations and would give good agreement with the steam-water data of Subbotin which were found to match the Wallis correlation.

An interesting facet of Figs. 9 and 10 is that they show that as the fluid density ratio decreases the parameter β decreases thus bringing the interface frictional curves together. Another interesting facet would be that the present model would predict increased friction factor with fluids of reduced surface tension, a result noted by several two-phase flow investigators.

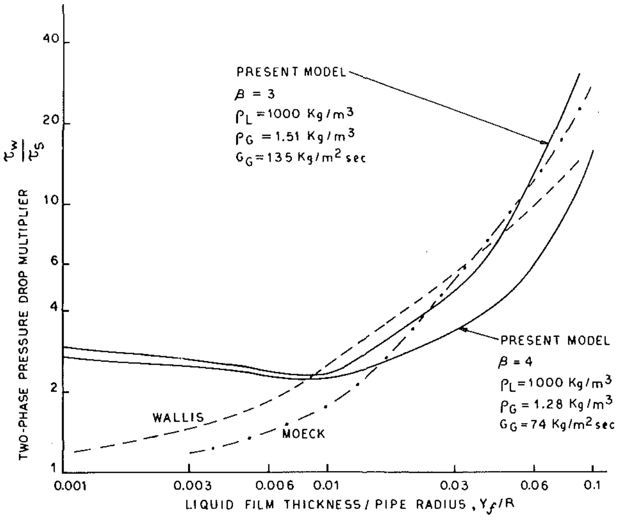

Fig. 9 Comparison of present model to empirical friction correlations for air-water

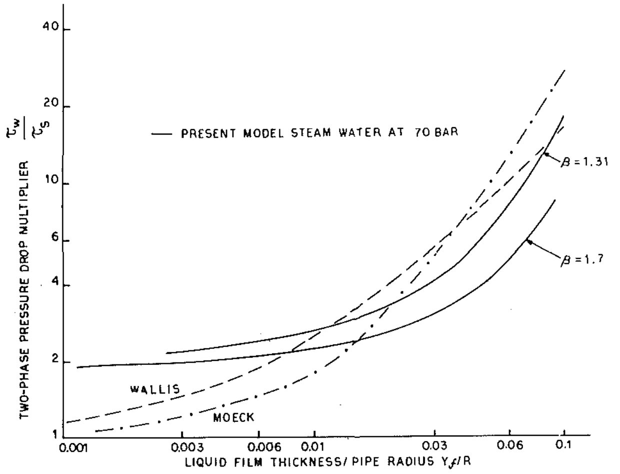

Fig. 10 Comparison of present model to empirical friction correlations for steam-water

As a final check of the model let us compare the predicted film thicknesses to measured values. Plots are given in Fig. 11 for air-water mixture while Figure 12 deals with steam-water mixtures at 70 bars. Here again the assumption is made that Y_f corresponds to liquid film thickness. The comparisons are satisfactory especially when one

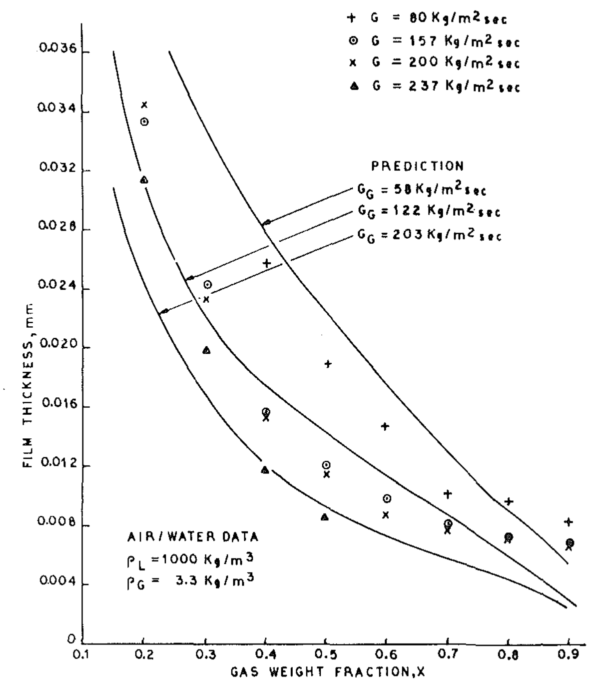

Fig. 11 Comparison of liquid film model to air-water data

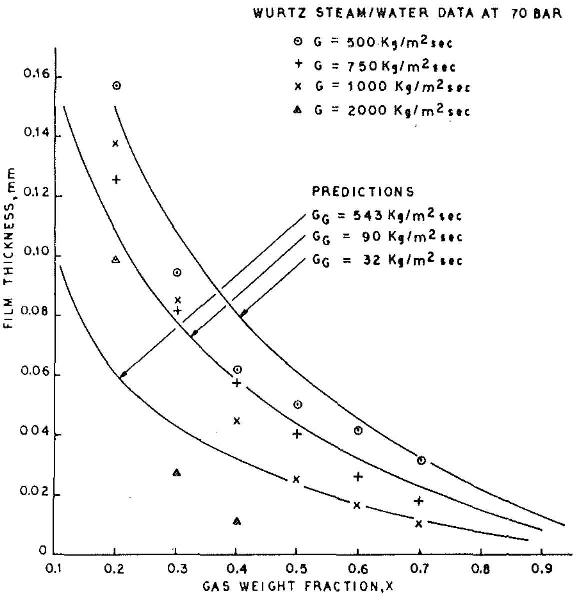

Fig. 12 Comparison of liquid film model to steam-water data, in 20 mm tube

realizes that the simplification has been made that the core contains no liquid droplets.

In summary, the proposed model is seen to give good agreement with available data over a wide range of parameters and fluids.

Simplified Model

A simplified version of the preceding model is developed in reference [17]. It relies upon simplified and semiempirical expressions for the two-phase friction factor and for the entrained flow rate in terms of the parameter β. The simplified model gives good agreement with the data.

Conclusions

1 A new model has been developed to predict two-phase annular flow with liquid entrainment. The model requires a single empirical *entrainment parameter β which is obtained from test data. This parameter* β defines the density variation above the base liquid film and is specified in terms of nondimensional grouping inferred from interface stability considerations.

2 The model exhibits good agreement with test data when compared to other available correlations and is capable of handling a variety of fluids including variation in surface tension, fluid pressure, and tube diameter.

3 The model gives good agreement with test data for many other parameters, including liquid film thickness, friction pressure drop, interface wave height and velocity.

4 Because the model is based upon detailed velocity and density distributions it could be applied to more complex geometries.

References

1 Lamb, H., *Hydrodynamics*, Dover Publications, New York, 1932.

2 Banerje, S., and Chan, A. M. C., "Separated Flow Models—I. Analysis of the Averaged and Local Instantaneous Formulations," *International Journal of Multiple Flow*, Vol. 6, No. 1–2, 1980.

3 Miya, M., Woodmanseee, D., and Hanratty, T., "A Model for Roll Waves in Gas-Liquid Flow," *Chemical Engineering Science*, Vol. 26, 1971.

4 Levy, S., "Prediction of Two-Phase Annular Flow with Liquid Entrainment," *International Journal of Heat Mass Transfer*, Vol 9, 1966.

5 Wallis, G. B., "Annular Two-Phase Flow, Part 1: A Simple Theory," ASME *Journal of Basic Engineering*, 1970, pp. 59–82.

6 Moeck, E. O., "Annular Dispensed Two-Phase Flow and Critical Heat Flux." *Atomic Energy of Canada Limited-3656*, 1970.

7 Levy, S., "Prediction of Two-Phase Pressure Drop and Density Distribution From Mixing Length Theory," ASME *Journal of Heat Transfer*, Vol. 85, 1963, p. 1973.

8 Schlichting, H., *Boundary Layer Theory*, McGraw-Hill, New York, 1960, pp. 488, 508, 523.

9 Anderson, G. H., and Mantzouranis, B. G., "Two-Phase (Gas Liquid) Flow Phenomena—I. Pressure Drop and Hold-Up for Two-Phase in Vertical Tubes," *Chemical Engineering Science*, Vol. 12, 1960, p. 109.

10 Dukler, A. E., "Fluid Mechanics and Heat Transfer in Vertical Falling Film Systems," *Chemical Engineering Progress Symposium Service*, Vol. 56, No. 30, 1960.

11 Hewitt, G. F., "Analysis of Annular Two-Phase Flow. Applications of the Dukler Analysis to Vertical Upward Flow in a Tube," *Atomic Energy Research Establishment*, R-3680, 1960.

12 Moeck, E. O., and Stachiewicz, J. W., "A Droplet Interchange Model for Annular-Disperse, Two-Phase Flow," *International Journal of Heat Mass Transfer*, Vol. 15, 1972, p. 637.

13 Saito, T., "Multi-Fluid Modeling of Two-Phase Flow and Heat Transfer; Application to CHF Prediction for BWR Conditions," Ph.D. Thesis, University of Wisconsin, 1977.

14 Cohen, L. S., *Interaction Between Turbulent Air and Flowing Liquid Film*, Ph.D. Thesis, University of Illinois, 1964.

15 Rae, J., "A Model for Interface Waves in Two-Phase Flow," *Atomic Energy Research Establishment*, Harwell TP 611, HTFS RS 156.

16 Wurtz, J., "An Experimental and Theoretical Investigation of Annular Steam-Water Flow in Tubes and Annuli at 30 to 90 Bar," Riso National Laboratory, Denmark, 1978.

17 Levy, S., and Healzer, J. M., "Prediction of Annular Liquid-Gas Flow With Entrainment—Cocurrent Vertical Pipe Flow With No Gravity," EPRI NP-1409, May 1980.

18 Tippets, F. E., "Critical Heat Fluxes and Flow Patterns in High Pressure Boiling Water Flows," ASME Paper No. WA-162, 1962.

19 Gill, L. E., and Hewitt, G. F., "Further Data on the Upwards Annular Flow of Air-water Mixtures," *Atomic Energy Research Establishment*, R-3935, 1962.

20 Paleev, I. I., and Filipovich, B. S., "Phenomena of Liquid Transfer in Two-Phase Dispersed Annular Flow," *International Journal of Heat Mass Transfer*, Vol. 9, 1966.

21 Styrikovich, M. A., et al. *Wave Pattern and Liquid Film Burnout with Cocurrent Vapor Flow*, International Heat Transfer Conference, Toronto, Canada, 1978.

22 Whalley, P. B., Hewitt, G. F., and Hutchinson, P., "Experimental Wave and Entrainment Measurements in Vertical Annular Two-Phase Flow," *Atomic Energy Research Establishment*, R-7521, 1973.

23 Subbotin, V. I., et al., *Integrated Investigation Into Hydrodynamic Characteristics of Annular-Dispersed Steam-Liquid Flows*, International Heat Transfer Conference, Toronto, Canada, 1978.

A Numerical Solution to Dropwise Evaporation

J. J. Rizza
Professor of Engineering,
Mechanical Engineering Faculty,
California State University, Fullerton,
Fullerton, Calif. 92634
Mem. ASME

A numerical solution is presented for spray evaporation on the surface of a spray evaporator. Excess temperatures below the Leidenfrost transition temperature are considered along with the nonisothermal wall condition. The combination of a high thermal conductivity and low heat capacity for the evaporator wall material, as well as the time-dependent boundary conditions, dictates a quasi-steady-state solution to this evaporator phenomenon. A numerical solution to the conduction equation and boundary conditions is given. A dimensionless evaporation time is computed, and from this a flooding index is developed. The flooding index is shown to be related exponentially to the droplet diameter and wetting ratio. The functional correlation between the heat transfer coefficient for the spray and the wetting ratio is verified from previously published experimental data.

Introduction

How liquid droplets impact and evaporate on warm surfaces is of interest in a number of areas of engineering; e.g., spray evaporators, cooling of turbine blades and the cooling of hot metal ingots, to name a few. The evaporation of impacted droplets has received considerable attention in the literature for the so-called Leidenfrost phenomenon; i.e., for large excess temperatures, the difference between the surface temperature and the evaporant saturation temperature [1–3]. The prediction of the transition Leidenfrost temperature is of current importance in fast breeder-liquid metal cooled reactors and in cryogenic systems. The evaporation of impacted droplets below the Leidenfrost transition temperature also has been studied for a number of years, although not to the same degrees as the Leidenfrost phenomenon [4–6].

The configuration most often considered in experimental studies for the surface heat transfer is one in which there is little or no thermal resistance within the wall of the spray evaporator or evaporating surface; i.e., the isothermal wall condition. When the droplet diameter before impact is of the same order of magnitude as the evaporator wall thickness, the thermal resistance between the transport fluid and the evaporating droplet can not be neglected; i.e., the nonisothermal wall condition is applicable. This phenomenon is characterized by a significant reduction in wall temperature below the impacted droplet. Temperature reductions up to 30°C are reported in [5] for droplet sizes as large as 600 μm. Similar surface temperature depressions are reported by [1] for a nonisothermal surface made of pyrex glass. When the evaporating droplet is in this configuration, it is not only the evaporation rate from the droplet surface that determines the rate of heat transfer, but is the combined transfer from the transport fluid through the wall to the evaporating droplet which must be considered.

The present investigation is a study of the evaporation of impacted droplets on the surface of a spray evaporator at excess temperatures below the Leidenfrost transition temperature and for the nonisothermal wall condition. The droplet evaporation times are considered, and from them an evaporator flooding index is developed. The flooding of an evaporator surface is of importance in the overall performance of the spray evaporator relative to the maintenance of dropwise evaporation over filmwise evaporation and to the effective utilization of the spray evaporant; i.e., reduction of evaporant runoff.

Analysis

Local Temperature Depressions. It is possible to estimate approximately the combination of parametric values that will produce the nonisothermal wall condition on the surface of a spray evaporator by considering a simplified evaporation model for the impacted droplet. When a liquid droplet impacts a warm surface, it begins to evaporate on contact by drawing heat from the surface directly below the impacted droplet. The energy immediately available for evaporation is equal to the change in internal energy of the surface directly below the impacted droplet. This internal energy change is limited by the surface temperature change; i.e., from its initial value to the evaporant saturation temperature. The internal energy change can be represented by

$$\Delta E = c_w \rho_w A_w \ell \Delta T \tag{1}$$

where c_w and ρ_w are the specific heat and density of the wall material. The effective heat transfer surface area, A_w, will in general be greater than the contact surface area between the droplet and the wall. The wall thickness is denoted by ℓ and the local temperature depression by ΔT. The energy required to evaporate the droplet is related to the phase change energy and the sensible heat. If the droplet is given to be at its saturation temperature at impact, the required energy is given by

$$\Delta E = \rho_f A_d \, b \, h_{fg} \tag{2}$$

where b and A_d are the impacted droplet thickness and surface contact area. Upon combining equations (1) and (2), an expression for the local temperature depression is obtained.

$$\Delta T = (\rho_f h_{fg}/c_w \, \rho_w) \, (A_d/A_w) \, (b/\ell) \tag{3}$$

If the volume of the droplet before impact is equated to the volume after impact, a relationship results for the disk-shaped impacted droplet thickness

$$b = 2d/3 \, \alpha^2 \tag{4}$$

where α represents the droplet spreading ratio. This is defined as the ratio of the droplet diameter after impact to the diameter before impact.

If the effective heat transfer surface area is taken to be roughly four times the contact area and if equations (3) and (4) are combined, the following expression can be written for the local temperature depression. This area is thermally equivalent to a much larger area since the temperature is inversely related to distance.

$$\Delta T = (\rho_f \, h_{fg}/c_w \, \rho_w) \, (d/\ell) \, (1/6 \, \alpha^2) \tag{5}$$

A typical value for the first ratio in the above expression for a combination of water and a number of metals is approximately 800/1. A representative value for the spreading ratio is about 4/1 [4,5]. If these values are used in equation (5), the following results.

$$\Delta T = 8.5 \, (d/\ell) \, ^\circ\mathrm{C} \tag{6}$$

The above expression demonstrates the effect of droplet diameter on the wall temperature distribution. If the droplet diameter before impact is small relative to the wall thickness, then the local temperature depressions are also small; i.e., the isothermal wall condition. There is sufficient sensible heat in this case within the wall to evaporate the droplet. However, if the droplet diameter is equal to or

---

Contributed by the Heat Transfer Division for publication in the JOURNAL OF HEAT TRANSFER. Manuscript received by the Heat Transfer Division July 14, 1980.

greater than the wall thickness, then the local temperature depressions will be large. There is insufficient sensible heat in this case within the wall to evaporate the droplet. Heat must be transferred from the transport fluid, the thermal resistance between the transport fluid and the evaporating droplet; and the local temperature field within the evaporator wall must be considered in the overall evaporation process, i.e., the nonisothermal wall case.

Flooding Index. The continual maintenance of dropwise evaporation on the surface of a spray evaporator is desirable in order to *maximize the heat transfer rate and minimize the required evaporant* flow rate for a given operating condition. Flooding causes a liquid film to form on the evaporator surface, thereby producing a thermal barrier between the warm surface and the impacting evaporant droplets, resulting in a reduction in overall performance for the spray evaporation process. The *ability to understand and predict evaporator* flooding is useful in the design and analysis of a spray evaporator system.

The evaporator flooding index for the total evaporator is defined as the ratio of the mass flow rate of the evaporant spray to the evaporating mass flow rate; i.e.,

$$\phi = \dot{m}/(q/h_{fg}) \tag{7}$$

When ϕ is greater than unity, on average for the total evaporator surface, the system will become flooded. More insight on the flooding index can be gained if it is viewed at the local level or at a single evaporation site; i.e., a small portion of the evaporator surface which serves as an evaporation region for a single impacted droplet at a given point in time. Locally the flooding index can be defined as a time ratio; i.e., *the ratio of the average evaporation time for a single droplet at* a given site to the average time between impacting droplets at that same site.

$$\phi = t/t^* \tag{8}$$

The average time between impacting droplets can be represented by the ratio of the total number of evaporation sites on average to the number of droplets generated per unit time within the spray.

$$t^* = N/\dot{N} \tag{9}$$

The number and size of the evaporation sites on the evaporator surface are dependent on the characteristics of the spray nozzle and its distance from and orientation to the evaporator surface. A fogging nozzle will produce a large number of small droplets dispersed over a wide area; i.e., a large cone angle. Thus, the evaporation sites will be many and relatively small. As the nozzle is moved away from the surface, the droplet density in the direction perpendicular to the flow becomes less; i.e., larger evaporation sites. However, the droplet density in the direction of the flow, i.e., the average time between impacting droplets, remains approximately constant. There is an interdependence among the above parameters and the flooding index; e.g., consider the special case when the total evaporator surface constitutes the evaporation site. The time between impacting droplets would be very short, and the surface at the point of droplet impact would become flooded for most evaporant flow rates, i.e., even a small number of droplets can cause local flooding if the spray distribution is adverse.

The average number of droplets generated per unit time can be represented by the ratio of the evaporant mass flow rate to the average droplet mass.

$$\dot{N} = 6\dot{m}/d^3 \pi \rho \tag{10}$$

The average number of evaporation sites is given by the ratio of evaporator surface area to the evaporation site area; i.e.,

$$N = A/4R^2 \tag{11}$$

The average time between impacting droplets can be redefined from equations (9, 10) and (11) as follows.

$$t^* = A\, d^3 \pi \rho/24\dot{m} R^2 \tag{12}$$

It is convenient to define a dimensionless evaporation time for the evaporating droplet. This is defined as the ratio of the actual evaporation time to the minimum or ideal evaporation time; i.e., the time *required for evaporation if the site were totally wetted by the droplet.* This ideal time is obtained by taking the ratio of the droplet phase change energy to the ideal heat transfer rate at the site based on total wetting.

$$t_I = h_{fg}\,(\rho \pi d^3/6)/4h' R^2 \Delta T_{st} \tag{13}$$

where h' is the transport fluid heat transfer coefficient and ΔT_{st} is the difference between the transport fluid and evaporant temperature. The nondimensional evaporation time becomes

$$\tau = 24\, t\, h' R^2 \rho \Delta T_{st}/h_{fg} \pi d^3 \tag{14}$$

where τ and t are the nondimensional and dimensional evaporation times, respectively. The flooding index can now be placed in final form by combining equations (8, 12) and (14).

$$\phi = \tau\, h_{fg} \dot{m}/h' A\, \Delta T_{st} \tag{15}$$

where it remains to determine τ as a function of the system parameters.

Nomenclature

a = thermal diffusivity of the evaporator wall
A = surface area
b = impacted droplet thickness
B = nondimensional impacted droplet thickness
c = specific heat of the evaporator wall
d = droplet diameter before impact
E = a quantity of heat
h = enthalpy
h' = heat transfer coefficient, transport fluid
h^* = heat transfer coefficient, evaporant
k = thermal conductivity of the evaporator wall
ℓ = evaporator wall thickness
m = droplet mass
M = nondimensional droplet mass
$\dot{m}$ = evaporant mass flow rate
N = number of evaporation sites
$\dot{N}$ = average number of droplets generated per unit time
q = heat flow rate
Q = nondimensional heat flow rate
q' = heat flux
Q' = nondimensional heat flux
r = radial direction, cylindrical coordinates
r = impacted droplet radius
R = evaporation site radius
t = evaporation time
T = temperature
t^* = average time between impacting droplets at a given location
z = axial direction, cylindrical coordinates
α = spreading ratio, droplet diameter after impact to droplet diameter before impact
β = wetting ratio, $\alpha d/2R$
Δ = difference between two values of the same parameter
η = nondimensional radial direction
θ = nondimensional temperature, equation (18*c*)
λ = nondimensional axial direction
ρ = density
τ = nondimensional evaporation time, equation (14)
ϕ = flooding index, equations (7) and (15)

Subscripts

d = droplet
f = liquid evaporant
fg = difference between vapor and liquid component
g = vapor evaporant
i = a grid point
I = ideal
s = saturation point
st = difference between transport fluid state and evaporant saturation point
t = transport fluid
w = evaporator wall

Droplet Evaporation Times. Consider an impacted disk-shaped droplet on the surface of a spray evaporator; the droplet is heated from below by a warm transport fluid. The droplet lies at the center of an evaporation site of radius, R. The heat conduction diffusion equation governs the flow of heat within the evaporator wall.

$$\frac{\partial^2 T}{\partial r^2} + \frac{1}{r}\frac{\partial T}{\partial r} + \frac{\partial^2 T}{\partial z^2} = \frac{1}{a}\frac{\partial T}{\partial t} \tag{16}$$

where T denotes the temperature at any point within the wall and a represents the thermal diffusivity of the wall material. The associated boundary conditions on the evaporation site are given by the following relationships:

$$\text{at } r = R \qquad \partial T/\partial r = 0 \tag{17a}$$

$$\text{at } r = 0 \qquad \partial T/\partial r = 0 \tag{17b}$$

$$\text{at } z = 0 \qquad \partial T/\partial r = -h'\,[T_t - T(r,0,t)]/k \tag{17c}$$

$$\text{at } z = \ell \qquad \partial T/\partial z = 0 \text{ for } r > r_d\,(t) \tag{17d}$$

$$\text{at } z = \ell \qquad T = T_s \text{ for } r < r_d\,(t) \tag{17e}$$

The instantaneous impacted droplet radius, $r_d(t)$, is time-dependent and varies with the rate of heat transfer. Fig. 1, a sketch of the heat flow lines for the above configuration at a given point in time, reveals that the flux lines are highly concentrated at the outer radii of the droplet, thereby causing the droplet to evaporate from the outer radius inward toward the droplet center. This is in addition to the evaporation from the upper surface of the droplet. Equation (16) is made dimensionless by the following relations and equation (14).

$$\eta = r/R \tag{18a}$$

$$\lambda = z/\ell \tag{18b}$$

$$\theta = [T_t - T\,(r,z,t)]/\Delta T_{st} \tag{18c}$$

The diffusion equation now becomes

$$\frac{\partial^2 \theta}{\partial \eta^2} + \frac{1}{\eta}\frac{\partial \theta}{\partial \eta} + \left(\frac{R}{\ell}\right)^2 \frac{\partial^2 \theta}{\partial \lambda^2} = \left(\frac{R^2}{a t_I}\right)\frac{\partial \theta}{\partial \tau} \tag{19}$$

The boundary conditions transform as follows:

$$\text{at } \eta = 1 \qquad \partial\theta/\partial\eta = 0 \tag{20a}$$

$$\text{at } \eta = 0 \qquad \partial\theta/\partial\lambda = 0 \tag{20b}$$

$$\text{at } \lambda = 0 \qquad \partial\theta/\partial z = h\,\ell\,\theta(r,0)/k \tag{20c}$$

$$\text{at } \lambda = 1 \qquad \partial\theta/\partial z = 0 \text{ for } \eta > r_d(t)/R \tag{20d}$$

$$\text{at } \lambda = 1 \qquad \theta = 1 \text{ for } \eta < r_d(t)/R \tag{20e}$$

The convective heat transfer between the transport fluid and droplet occurs through the evaporator wall. Thus, the conventional choice of driving potential for the transport fluid convective process is the temperature difference between the inner wall temperature, i.e., $T\,(r,z,t) = T\,(r,o,t)$, and the transport fluid temperature, where $z = o$ denotes the position of the inner wall in contact with the transport fluid and $z = \ell$ denotes the outer wall position in contact with the impacted droplet. The convective heat transfer coefficient is taken to have a constant value. The variation in h' due to changes in the fluid properties caused by the nonisothermal wall would be small.

It is demonstrated above that for the nonisothermal wall condition the temperature below the impacted droplet is depressed by the evaporating droplet; i.e., there is insufficient sensible heat within the wall to evaporate the droplet and heat must be transferred directly from the transport fluid.

The thermal contact conductance between the impacted droplet surface in contact with the evaporator wall and the internal thermal conductance of the impacted droplet are taken to be large compared to the conductance within the thermal boundary layer of the transport fluid. Thus, the temperature at the interface is taken to be approximately equal to the saturation temperature.

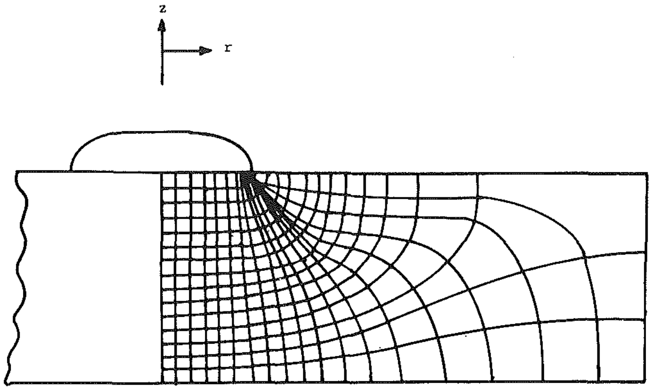

Fig. 1 Heat-flow lines and isotherms for an impacted droplet on an evaporator surface

A worse case approximation can be developed for the above condition by assuming that all of the heat flows through the impacted droplet thickness and that the heat transfer through the droplet conforms to one-dimensional steady flow. A simple thermal circuit can be setup which includes the transport fluid boundary layer conductance, the wall conductance and the conductance within the impacted droplet for both convection and conduction. The amount of convective mixing within the droplet is dependent on the impact kinetic energy, two-phase pumping and natural convective currents. A nominal value of unity is taken for the Nusselt number. This approximate one-dimensional model indicates that the conductances within the impacted droplet is 50 times larger than the conductance within the transport fluid boundary layer for the case of a stainless steel walled evaporator and for the spray evaporation parameters consider in this paper. For an aluminum walled evaporator it is about 3.5 times larger. However for a copper wall the approximate model predicts a value of only 1.5 times as large. It should be noted however, that for the actual three-dimensional unsteady model a large portion of the heat is not transferred through the droplet but at the outer radius, as can be seen in Fig. 1. In addition at the beginning phases of evaporation, when the one-dimensional model predicts the lowest droplet conductance, the droplet is in a state of excitement due to the impact kinetic energy. Finally, the conductance of the droplet is continually increasing due to the reduction in droplet diameter and thickness.

Thus, for a very high wall thermal conductivity, such as copper, the relative thermal conductance through the impacted droplet and transport fluid boundary layer may be such that the interface temperature would be more than a few degrees above the saturation temperature as might be expected for the general case of the nonisothermal wall condition. This is dependent on the level of convective activity within the impacted droplet caused by the impact kinetic energy, two-phase pumping and natural convective currents. Since the saturation temperature represents a more general approach this value has be selected. For special cases a pseudo-saturation temperature can be defined to include the increase in interface temperature.

The model was first developed in three-dimensional rectangular coordinate system (x,y,z) but soon after changed to a two-dimensional cylindrical coordinate system (r,z). The incremental increase in accuracy for the three-dimensional space did not justify the longer computer run times, particularly in view of the errors associated with matching the boundary conditons for the disk shape droplet in a rectangular space and the computer roundoff error associated with the longer run times. However, it should be noted that the ideal evaporation time is defined by equation (13) in terms of the square based evaporation site rather than a cylindrical site as used for the computer solution since there was no need to make this approximation for the normalization of the evaporation times and flooding index.

An order of magnitude study of equation (19) reveals that the diffusion equation reduces to the Laplace equation. The combination of a high thermal conductivity and low heat capacity for the evaporator wall material indicates that changes in the storage energy, i.e., wall internal energy changes, are small when compared to the droplet phase change energy. The magnitude of the coefficient on the time derivative term (the energy storage term) in equation (19), i.e., R^2/at_I, causes that term to be small when compared to the remaining three terms of the equation. This can be demonstrated formally by rearranging the terms in equation (19) and estimating the order of the magnitude of each term. This is done by noting that each of the nondimensional variables, i.e., η, λ, τ and θ, has an order of magnitude of unity and the first and second derivatives have orders of magnitude of unity and $1/\epsilon$, respectively, where ϵ denotes a small incremental value. A review of the isotherms and heat flow lines sketch, i.e., Fig. 1, supports this position. From equation (19),

$$\frac{\partial^2\theta}{\partial\eta^2}+\frac{1}{\eta}\frac{\partial\theta}{\partial\eta}+\left(\frac{R}{\ell}\right)^2\left[\frac{\partial^2\theta}{\partial\lambda^2}-\left(\frac{\ell^2}{at_I}\right)\frac{\partial\theta}{\partial\tau}\right]=0 \qquad (21a)$$

$$0\,(1/\epsilon)+0(1)+\left(\frac{R}{\ell}\right)^2\left[0(1/\epsilon)-\left(\frac{\ell^2}{at_I}\right)0(1)\right]=0 \qquad (21b)$$

$$\frac{\partial^2\theta}{\partial\eta^2}+\frac{1}{\eta}\frac{\partial\theta}{\partial\eta}+\left(\frac{R}{\ell}\right)^2\frac{\partial^2\theta}{\partial\lambda^2}=0 \qquad (21c)$$

where 0( ) denotes order of magnitude. Typically, ℓ^2/at_I would vary between 0(1) and 0(0.1) for a nonisothermal wall evaporator, depending on the evaporator wall material and thickness and droplet size.

However, it should be noted that the solution to equation (21*c*) is still time-dependent, since the boundary conditions, equations (20*d*) and (20*e*), are time-dependent. The solution to the above set of equations does lend itself most readily to a numerical/computer solution. However, before this can be accomplished, equation (20) must be defined in more detail.

The instantaneous droplet radius is dependent on the droplet mass and thickness at any given point in time. The initial mass of the impacted droplet can be written in terms of the droplet radius and thickness.

$$m(0)=\pi\, r_d^2\,(0)\; b\,(0)\,\rho \qquad (22a)$$

where $m(0)$, $r_d(0)$ and $b(0)$ are the initial droplet mass, radius and thickness, respectively. The initial droplet mass can also be described in terms of the droplet diameter before impact.

$$m(0)=\pi\, d^3/6 \qquad (22b)$$

The instantaneous droplet mass during the evaporation process is represented by

$$m(t)=\pi\, r_d^2\,(t)\; b\,(t)\,\rho \qquad (23)$$

It is convenient to define an instantaneous nondimensional droplet mass by taking the ratio of equations (22*a*) and (23).

$$M(t)=(r_d(t)/R)^2\,(b(t)/b(0))\,(1/\beta^2) \qquad (24)$$

The wetting ratio, β, is defined as the ratio of the impacted droplet diameter to the diameter of the evaporation site; i.e.,

$$\beta=\alpha\, d/2R \qquad (25)$$

The incremental droplet mass evaporated within a given time increment is determined from the heat transferred at the interface between the inner wall and the transport fluid. Once the steady-state temperature field is determined for a given time increment, the heat transfer along the wall can be found by summing the incremental heat flow for each spacial grid point.

$$q=\sum h'\,A_i\,(T_t-T_i) \qquad (26a)$$

where T_i and A_i are the temperature and heat transfer surface area at a grid point. It is helpful in the development of the numerical solution to define the above heat flow in terms of a nondimensional surface area and temperature.

$$q=\sum h'\,[\pi R^2\,(\eta_{i+1}^2-\eta_i^2)]\,\Delta T_{st}\,\theta_i \qquad (26b)$$

The above relation can be rearranged to define a dimensionless heat flow along the wall.

$$Q=\sum\,(\eta_{i+1}^2-\eta_i^2)\,\theta_i \qquad (26c)$$

Now, having defined the heat transferred during a given time increment, it is possible to describe the incremental mass evaporated during this time increment.

$$\Delta m=q\;\Delta t/h_{fg} \qquad (27a)$$

If equations (14, 22*b*) and (26*b*) are combined, a dimensionless incremental droplet mass is obtained.

$$\Delta M=Q\Delta\tau \qquad (27b)$$

The numerical solution is terminated when the sum of the incremental dimensionless masses is equal to unity; i.e., when the droplet has been completely evaporated. Equation (27*b*) gives the incremental time associated with each incremental decrease in mass based on the total heat transferred in each time increment. As the droplet evaporates, the droplet radius decreases and less surface area of the evaporation site is wetted, thereby reducing the heat flow to the droplet. For each incremental change in droplet radius, a new steady-state temperature field must be computed, as well as an updated value of the heat flow. If either the incremental time or droplet mass is selected as the independent incrementing parameter, the droplet radius, in nearly all cases, will fall between two grid points. Therefore, it is far more conveneint to select the droplet radius as the independent incrementing parameter and have it change in nonfractional increments of the grid spacing, usually one grid space at a time. The incremental time and mass now become dependent parameters.

Equation (24) shows that the dimensionless droplet mass is dependent on both the droplet radius and thickness. As indicated above, the heat flux lines are highly concentrated at the outer droplet radii; however, in the center or middle regions of the droplet, the flux lines are quite uniform and nearly equally spaced. Thus, there is a reduction in droplet thickness in the middle region of the droplet which contributes to the droplet mass reduction, in addition to the mass evaporated in the outer radii; i.e., the region of highly concentrated flux lines. The incremental change in droplet thickness in the middle regions of the droplet is determined by evaluating the average heat flux at the interface between the droplet and the evaporator surface.

The incremental droplet thickness is given by

$$\Delta b=q'\;\Delta t/h_{fg}\;\rho \qquad (28a)$$

where q' is the average heat flux in the droplet middle region and ρ is the droplet density. However, it should be noted that the droplet mass and energy are conserved by equations (27) and (24) and not solely by equation (28*a*). If equation (28*a*) is divided by the initial droplet thickness, a nondimensional thickness is defined.

$$\Delta B=q'\;\Delta t/h_{fg}\;\rho\; b(0) \qquad (28b)$$

It is convenient to nondimensionalize the heat flux and incremental time in the above relation by making use of equations (18*b*) and (18*c*).

$$q'=(k\;\Delta T_s/\ell)\;\partial\theta/\partial\lambda \qquad (29a)$$

and be rearranging the above, a dimensionless heat flux is defined

$$Q'=q'/(k\;\Delta T_s/\ell) \qquad (29b)$$

or in more compact form

$$Q'=\partial\theta/\partial\lambda \qquad (29c)$$

When equations (14, 25, 28) and (29) are combined, the dimensionless droplet thickness becomes

$$\Delta B=Q'\;\Delta\tau\;\beta^2/(h'\;\ell/k) \qquad (30)$$

The assumption of approximate uniform droplet thickness is made above even though there exists a large nonuniformity in the droplet heat flux relative to droplet radius. The combined fluid action of the liquid droplet and droplet surface tension force causes the droplet to maintain its original disk shape. The surface tension forces are relatively high for these size droplets, when compared to other forces such as the force due to gravitation and droplet fluid acceleration [5]. The fluid can easily adjust to any local changes in droplet thickness for the relative space and time increments of the droplet. The fluid acceleration required to maintain a steady, uniform droplet thickness would be very small since the Reynolds number for this type of fluid motion within the droplet would be about unity or in the creeping flow regime.

Numerical Solution Outline. The combination of a high thermal conductivity and a low heat capacity for the evaporator surface material, as well as the time-dependent boundary conditions, dictates a quasi-steady-state solution to this evaporation phenomenon. The complex characteristics of the time-dependent boundary conditions suggest that a numerical approach provides the best possibility for a solution. The computer program proved to be long running, since for each time increment a steady-state numerical solution to the Laplace equation was required. In addition, a variety of droplet sizes relative to the evaporator wall thickness were considered and a number of different values for the wetting ratio (see Fig. 2). The following list of equations represents a summary of the relationships used in the final solution.

$$\frac{\partial^2\theta}{\partial\eta^2} + \frac{1}{\eta}\frac{\partial\theta}{\partial\eta} + \left(\frac{R}{\ell}\right)^2 \frac{\partial^2\theta}{\partial\lambda^2} = 0 \qquad (21c)$$

$$\text{at } \eta = 1 \qquad \partial\theta/\partial\eta = 0 \qquad (20a)$$

$$\text{at } \eta = 0 \qquad \partial\theta/\partial\eta = 0 \qquad (20b)$$

$$\text{at } \lambda = 0 \qquad \partial\theta/\partial z = h\ \ell\ \theta\ (r,0)/k \qquad (20c)$$

$$\text{at } \lambda = 1 \qquad \partial\theta/\partial z = 0 \text{ for } \eta > r_d(t)/R \qquad (20d)$$

$$\text{at } \lambda = 1 \qquad \theta = 1 \text{ for } \eta < r_d(t)/R \qquad (20e)$$

$$Q = \sum (\eta_{i+1}^2 - \eta_i^2)\ \theta_i \qquad (26c)$$

$$\Delta M = Q\Delta\tau \qquad (27b)$$

$$Q' = \partial\theta/\partial\lambda \qquad (29c)$$

$$\Delta B = Q'\ \Delta\tau\ \beta^2/(h'\ \ell/k) \qquad (30)$$

$$\tau = 24\ t\ h'R^2\rho\Delta T_{st}/h_{fg}\ \pi\ d^3 \qquad (14)$$

$$\eta = r/R \qquad (18a)$$

$$\lambda = z/\ell \qquad (18b)$$

$$\theta = [T_t - T\ (r,z,t)]/\Delta T_{st} \qquad (18c)$$

$$\phi = \tau\ h_{fg}\dot{m}/h'\ A\ \Delta T_{st} \qquad (15)$$

$$\beta = \alpha\ d/2R \qquad (25)$$

Equation (21*c*), the dimensionless Laplace equation, was placed into a difference equation form, along with the associated boundary conditions given in equation (20). A particular droplet diameter, evaporation site radius and spreading coefficient were selected to generate a single point for Fig. 2. An appropriate grid size was selected, and the time-dependent boundary conditions were defined based on the parameters selected. The initial temperature field was determined from equations (20) and (21*c*). With this information, equation (26*c*) is used to determine the heat flow rate between the transport fluid and the evaporator inner surface. The droplet was reduced by decreasing the droplet radius by one grid spacing. The incremental change in mass, resulting from the radius reduction, is combined with the calculated heat flow rate in order to determine the time increment from equation (27). The time increment is expanded to account for the change in mass due to the change in droplet thickness as determined in equation (30). A running sum is maintained on the evaporation times and on the evaporated droplet mass. For each incremental change in droplet radius, a new temperature field is computed using the Laplace equation and the updated boundary conditions; i.e., the time-dependent conditions equations (20*d*) and (20*e*). A new heat flow rate and time increment are computed for each new radii. The solution continues until the evaporated mass is equal to the initial droplet mass. This may occur when the droplet radius becomes zero, i.e., at the center grid point, or if the droplet thins out first, i.e., the instantaneous droplet thickness becomes zero.

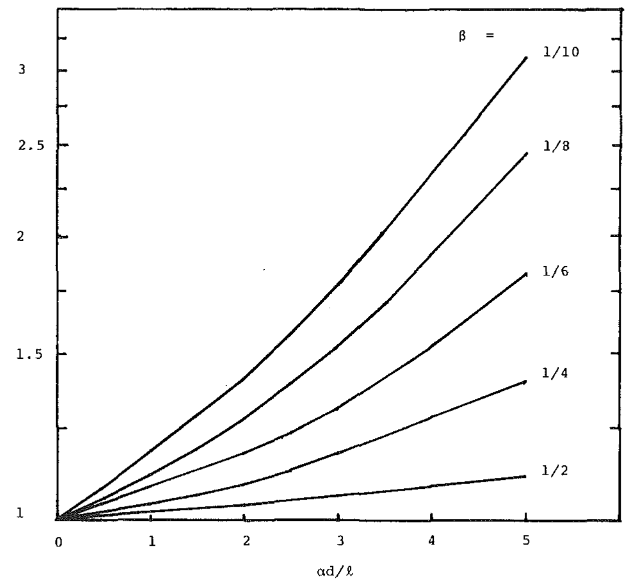

Fig. 2 Dimensionless droplet evaporation times for various wetting ratios and relative droplet sizes

The numerical procedure used for solving Laplace's equation was to transform the differential equation into a difference equation. This was accomplished with the use of first central-difference approximations for the first and second partial derivatives of the nondimensional temperature with respect to the nondimensional distances in the *r* and *z* directions. In a like manner, the partial derivatives of the boundary conditions were transformed. The error associated with the first central-difference approximations is related to the truncated terms of a Taylor series and is approximately equal to the square of the grid size dimension. The nondimensional grid size used in the final solution varied between 1/10 and 1/40 for the *r* direction, depending on the size of the impacted droplet relative to the evaporation site, and 1/5 in the *z* direction. Grid sizes as small as 1/100 and 1/10 for the *r* and *z* direction, respectively, were tried in the initial checkout phase of the program. The worst case truncation error would be 4 percent, based on the largest grid size of 1/5 in the *z* direction. The number of iterations required for convergence varied between 200 and 500; the condition placed on convergence was a less than 1 percent change on all the temperatures within the field. Since the solution is on a closed domain, roundoff errors are not a factor, except on the last iteration of the solution.

Figure 2 presents the dimensionless evaporation times versus the relative impacted droplet diameter for various values of the wetting ratio. This family of curves represents the complete numerical solution to the above system of equations. The two parameters associated with the evaporant are the wetting ratio β and the relative impacted droplet diameter $\alpha d/\ell$. A total of 25 conditions were selected based upon typical spray evaporation conditions. The parameters β and $\alpha d/\ell$ varied as follows: 1/10, 1/8, 1/6, 1/4, 1/2 for β and 1, 2, 3, 4, 5 for $\alpha d/\ell$. The incorporation of equation (30) into the numerical solution requires the selection of a value for the dimensionless spray evaporator parameter $h'\ell/k$. This parameter is similar in appearance to the Nusselt number but different in its function. Here k is the thermal conductivity of the wall and not of the transport fluid, and ℓ is not a characteristic dimension for the transport fluid flow but the wall thickness of the evaporator. The value selected for this parameter is 0.036, which is typical for spray evaporators.

Results and Discussion

The fraction of heat transfer surface area covered by the impacted droplets on the evaporator surface is relatively small; e.g., in [4] this fraction was measured experimentally and reported to vary from 0.015

to 0.196 or in terms of the wetting ratio β from 0.122 to 0.443. The quantity of heat transferred from the transport fluid directly below the inner radii or droplet base compared to the heat transferred to the outer radii or the peripheral heat transfer is approximately proportional to the fractional wetted surface area, except as the droplet radius becomes very small. When the initial droplet diameter is nearly equal to the evaporation site diameter, the ratio of peripheral to base heat transfer, as well as the unwetted to wetted surface area ratio, is near unity. As the droplet evaporates, more of the surface becomes unwetted and the heat transfer ratio increases. The calculated values for this ratio ranged between 3 and 6. As the droplet radius becomes very small, temperature gradients in the radial direction cannot be maintained to support the large variations in heat flux and the ratio again approaches unity.

The assumption of a time-dependent impacted droplet radius was made in the above model development based on the calculated high heat fluxes in the outer droplet radii. Under a certain set of conditions, a constant radius model can be assumed [4]. However, it should be noted that the presence of a high heat flux at the outer radii of the evaporating droplet is more a result of the solution rather than an assumption, even if a constant radius model is selected. However, how the solution is finally carried out does depend on the droplet evaporation dynamics model selected. A constant radius model requires the assumption that the droplet will thin out independent of a high non-uniformity of heat flux and independent of a strong droplet surface tension action. As the droplet diameter becomes small relative to the evaporation site diameter, the concentration of heat flux in the outer radii becomes less. The average droplet sizes considered in [4] are relatively small, ranging between 51 to 99μ, so that the non-uniformity in heat flux would be less pronounced. In addition, the evaporator surface geometry selected by [4] makes the surface less of a nonisothermal wall than a typical spray evaporator surface, further reducing the nonuniformity in heat flux.

Figure 2 demonstrates the strong dependency of the droplet diameter on the evaporation times and on the flooding index defined in equation (15). Typically, $\alpha d/\ell$ would vary between 2 and 3 for a spray evaporator and spray nozzle generating droplets of about 300 μm in diameter. However, these values can easily be outside the 2 to 3 range for droplets less than 200μ on the low end and for droplets greater than 600μ on the high end of the range. The droplet sizes considered in [4] would place the value of $\alpha d/\ell$ below 2 for most spray evaporators. The wetting ratio, β, is spray nozzle-dependent and varies not only with position within the spray but with the distance between the nozzle and the evaporator surface. Typical values for β of 0.122 to 0.443 are reported in [4] for a variety of nozzles. If the above values are considered, the dimensionless evaporator times, from Fig. 2, would vary between 1.05 and 1.50; i.e., a 5 to 50 percent increase in evaporation time due to the wall and transport fluid thermal resistance.

The family of curves in Fig. 2 can be represented, within 5 percent, by a single relationship for values of $\alpha d/\ell$ between 0 and 2.5. A log-log plot of the average slope of each curve within the above range indicates a linear correlation among the slope values or an actual exponential relationship among the slopes. Thus, the dimensionless evaporation times in the above range of $\alpha d/\ell$ are given by

$$\tau = \exp\left[(0.0075\ \alpha d/\ell)/\beta^{1.34}\right] \tag{31}$$

Upon combining equations (15) and (31), a relationship for the flooding index results.

$$\phi = h_{fg}\,\dot{m}\,\exp\left[(0.0075\ \alpha d/\ell)/\beta^{1.34}\right]/h'\,A\,\Delta T_{st} \tag{32}$$

for values of $\alpha d/\ell$ from 0 to 2.5 only.

Therefore, for a given evaporator, the flooding index is a function of only two major parameters; i.e., the wetting ratio, β, and the relative impacted droplet diameter, $\alpha d/\ell$. The functional validity of equation (32) relative to the wetting ratio parameter can be demonstrated with the use of the experimental data reported in [4].

The heat flux on the evaporating surface is given by

$$q/A = h_{fg}\,\dot{m}/A \tag{33a}$$

and the heat transfer coefficient for the spray is defined as

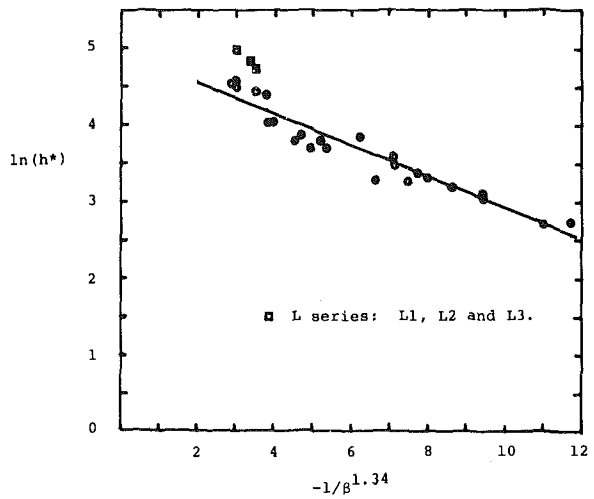

Fig. 3 Functional correlation for the wetting ratio and the spray heat transfer coefficient

$$h^* = (q/A)/\Delta T_{st} \tag{33b}$$

Combining equations (32) and (33) for ϕ equal to unity, i.e., for the maximum heat flux value just before flooding occurs, gives the following functional correlation for the heat transfer coefficient and the wetting ratio, β,

$$\ln(h^*) \propto (-1/\beta^{1.34}) \tag{34}$$

A proportionality relationship results since the wetting ratio parameter functional validity in equation (32) is being verified and not the validity of the combined relative impacted droplet diameter and wetting ratio parameters. Fig. 3 demonstrates the validity of equation (34) based on experimental data presented in [4].

The ordinate axis values for Fig. 3 are computed by taking the natural log of the values in column 7, titled h (kW/m^{2}K), presented in Table 2 of [4]. The abscissa values are developed from the values in column 11, titled ϵ Meas. In [4] ϵ Meas. denotes the measures value of the fractional heat transfer area covered or wetted by the droplets. Since β represents the wetting ratio or the ratio of the impacted droplet diameter, αd, to the evaporation site diameter, $2R$, ϵ is equal to β^2. The square root of the values in column 11 are taken and then raised to the 1.34 power. The abscissa values are computed by taking the reciprocal of these last values.

The 28 data points reported by [4] are plotted in Fig. 3 with the exception of run number C1 (as identified by [4]), coordinates (16.7, 2.77) which are off the graph in Fig. 3. This data run represents a very light spray. The heat flux for C1 was reported to be 47.8 kW/m^2 compared with the average heat flux of 782 kW/m^2 for all 28 runs. The second lowest or the next highest value of heat flux to C1 was run number A1, 75.9 kW/m^2 or 58 percent greater than C1. Run A1 does correlate well with the other data, coordinates (11.8, 2.72); see Fig. 3. If the analytical value of the wetting ratio computed by [4] is used for run number C1 rather than the experimental value, the correlation is improved by a significant factor. The coordinates for C1 would now be (14, 2.77); the correct correlation should be (14, 2.20) based on the wetting ratio.

Also worth noting is the correlation of the complete L series, i.e., runs L1, L2 and L3, which lie more off line than do the remainder of the other data points; see Fig. 3. The L series represent a combination of a high wetting ratio and a low total volume flow rate from the nozzle. The wetting ratios for L1, L2 and L3 were 0.392, 0.434 and 0.402, respectively, compared to a maximum of 0.443 and an average value of 0.308 for all 28 runs. The liquid volume flow rate for the type L nozzle was 0.68 cm^3/s, the lowest flow rate of the 14 nozzles considered. The cone angle for the L nozzle was 45 deg. The average flow rate for the 14 nozzles was 1.5 cm^3/s. The second lowest or next highest flow rate to the L nozzle was the type C nozzle at 0.89 cm^3/s or 31 percent greater than the L nozzle. The cone angle for the C nozzle was 80 deg. The combination of these two nozzle parameters, high droplet density on the evaporating surface and low nozzle flow rate produced a highly concentrated spray with the narrow 45 deg cone angle and may have produced some local flooding of the evaporation surface.

Acknowledgment

This paper presents the results of research performed under a NASA-ASEE Summer Faculty Fellowship Program at the Johnson Spacecraft Center in Houston, Texas.

References

1 Baumeister, K. J., and Simon, F. F., "Leidenfrost Temperature—Its Correlation for Liquid Metals, Cryogens, Hydrocarbons and Water," ASME JOURNAL OF HEAT TRANSFER, Vol. 95, No. 2, 1973, pp. 166–172.

2 Pedersen, C. O., "An Experimental Study of the Dynamic Behavior and Heat Transfer Characteristics of Water Droplets Impinging Upon a Heated Surface," *International Journal of Heat Mass Transfer*, Vol. 13, 1970, pp. 369–381.

3 Wachters, L. H. J., Smulders, L., Vermeulen, J. R., and Kleiweg, H. C., "The Heat Transfer from a Hot Wall to Impinging Mist Droplets in the Spheroidal State," *Chemical Engineering Science*, Vol. 21, 1966, pp. 1231–1238.

4 Bonacina, C., Del Gindice, S., and Comini, G., "Dropwise Evaporation," ASME JOURNAL OF HEAT TRANSFER, Vol. 101, 1979, pp. 441–446.

5 Rizza, J. J., "Triple-Point Pressure Evaporation of Impacted Droplets," *Journal of Spacecraft and Rockets*, AIAA, Vol. 16, No. 4, 1979, pp. 210–213.

6 Toda, S. and Uchida, H., "A Study of Mist Drops on a Heated Surface at High Temperatures and High Heat Fluxes," Fourth International Heat Transfer Conference, Paris-Versailles, 1970.

Yasuhiko H. Mori
Kyuichiro Nagai[1]
Hitoshi Funaba[2]
Kazunari Komotori

Department of Mechanical Engineering,
Keio University,
3-14-1 Hiyoshi, Kohoku-ku, Yokohama 223
Japan

Cooling of Freely Falling Liquid Drops with a Shell of an Immiscible Volatile Liquid

An augmentation of evaporative cooling of liquid drops falling freely through the atmosphere has been attempted by attaching them with some amount of immiscible volatile liquid. An experimental study was performed for a water/n-pentane system, the water either being pure or containing a small amount of surfactant. The cooling rate was found to be strongly augmented provided the volatile liquid (n-pentane) engulfed almost completely the liquid which was to be cooled (water). The dependences of the cooling rate on the initial drop temperature, volume ratio of the volatile liquid to the other in each drop, air temperature and humidity were examined.

Introduction

The cooling of liquid drops while falling freely through an atmosphere of lower temperature is the most commonly used operation in an evaporative cooling system. The cooling rate will increase strongly if some amount of volatile liquid is so attached to each drop as to envelop it thoroughly or partly. This technique may be applicable in some limited situations in which, for example, some means are available to recover economically the evaporated volatile species or the evaporated volatile species are permitted to be discarded into the atmosphere from both economical and ecological points of view. A crowd of such "composite drops" each of which consists of two immiscible liquids may be formed by, for example, an impingement of liquid jets generated by a couple of adjoining nozzles. Gibson, et al. [1, 2] made a spray of composite drops by making a pair of brine jets impinge at an acute angle upon a Freon jet locating in between, the freeze desalination being the object of their study. Though they evaluated experimentally the overall performance of such a novel spray freezer, the characteristics of heat and mass transfer from each drop have been analyzed neither experimentally nor theoretically.

This paper provides an experimental examination on the cooling of single composite drops falling freely in an air which contains in its bulk a negligible amount of the volatile species evaporating from the drops. The cooling rate is primarily controlled by the evaporation rate of the volatile liquid, which in turn should depend on the configuration of drops, i.e. how the volatile liquid is situated in each composite drop. The possible configuration for a specific combination of liquids can readily be predicted from the surface and interfacial tensions as described below. The dependence of the cooling rate on the configuration has been confirmed in the experiments and will be shown later.

Prediction of Configurations

Here we consider the interaction of two immiscible liquid drops brought into contact in a gas phase. The problem is similar to those dealt with by Torza and Mason [3, 4] and Mori [5], the former being concerned with the interaction of two immiscible liquid drops in a third immiscible liquid and the latter with the configuration of gas-liquid two-phase bubbles in a second immiscible liquid. For convenience, the less volatile liquid which is to be cooled is designated as liquid A and the volatile liquid is designated as liquid B. Possible configurations after the contact of the two liquids are shown schematically in Fig. 1. These are:

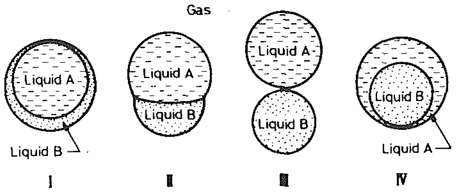

Fig. 1 Possible configurations of composite drops

I The drop of liquid A is entirely enclosed by the liquid B.

II The drop of liquid A and the drop of liquid B connect to each other so that a line bounding the three phases is formed.

III The liquid A-liquid B interface cannot form spontaneously; i.e. the drops remain separated by the gas without forming a composite drop.

IV The drop of liquid B is entirely enclosed by the liquid A, opposite to case I.

We assume that the configurations are determined solely by the three interfacial tensions; σ_A (liquid A-gas), σ_B (liquid B-gas) and σ_{AB} (liquid A-liquid B). The effects of shear on falling drop surfaces, drop oscillations, etc. are neglected. Thus, it can be shown, through a similar deduction as described by Mori [5], that the above configurations are provided respectively under the following conditions.

$$\left.\begin{array}{ll} \text{I} & S_A < 0, S_B > 0, S_G < 0, \\ \text{II} & S_A < 0, S_B < 0, S_G < 0, \\ \text{III} & S_A < 0, S_B < 0, S_G > 0, \\ \text{IV} & S_A > 0, S_B < 0, S_G < 0 \end{array}\right\} \tag{1}$$

where S_A, S_B, S_G are the spreading coefficients defined as

$$\left.\begin{array}{l} S_A = \sigma_B - (\sigma_A + \sigma_{AB}), \\ S_B = \sigma_A - (\sigma_B + \sigma_{AB}), \\ S_G = \sigma_{AB} - (\sigma_A + \sigma_B). \end{array}\right\} \tag{2}$$

Some of the inequalities given in (1) can be eliminated, since they are satisfied automatically if some other inequalities are satisfied. Furthermore, we know that S_G is negative for any combination of actual liquids; this suggests that the case III is unreal. In other words, once drops of different liquids contact each other, they will never separate spontaneously. Thus the criteria for the configurations of composite drops become

$$\left.\begin{array}{ll} \text{I} & S_B > 0, \\ \text{II} & S_A < 0, S_B < 0, \\ \text{IV} & S_A > 0. \end{array}\right\} \tag{3}$$

It is readily presumed that the configuration I is the most favorable for the purpose of cooling liquid A. On the contrary, the volatile liquid

---

[1] Present address: Hitachi Consumer Products Research Center, Yokohama

[2] Present address: Ina Seito Co., Ltd., Tsukuba

Contributed by the Heat Transfer Division for publication in the JOURNAL OF HEAT TRANSFER. Manuscript received by The Heat Transfer Division September 22, 1980.

B hardly contributes to the cooling of liquid A in case of configuration IV. The configuration II is situated between the above two limiting cases.

The exact prediction of configuration for a specific combination of liquids is not always easy because of the difficulty to know the accurate values of interfacial tensions under such a condition that each liquid is saturated with the other and particularly at elevated temperatures. Following are typical examples in which rather reliable predictions are possible based on the criteria (3): (i) The combination of water (A) and a light hydrocarbon (B) in which the equilibrium value of S_B is generally close to zero will yield either configuration I or configuration II in which only a small portion of the surface of liquid A is not covered by the liquid B; (ii) a drop of a liquid metal (A) will be completely enclosed by the shell of water (B), i.e. configuration I will be available; (iii) a nonvolatile mineral oil (A) will completely engulf a drop of water (B) resulting in configuration IV. In short, the proposed process is favorable for the cooling of liquids with large surface tensions.

In the experiments described below, the combination of water (A) and n-pentane (B) was used. A small amount of surfactant (sodium oleate) was added in some runs to the water phase to change the configuration of composite drops. In case of no surfactant in water phase, a shell of pentane covered almost the whole surface of water phase, though we could not confirm whether it was truly configuration I or not. An addition of the surfactant to the water phase reduced the fraction of water surface covered by n-pentane resulting in the composite drops of typical configuration II.

Experimental Equipment and Procedure

The experimental setup is schematically shown in Fig. 2. It consists of a column containing the conditioned air, an air conditioning equipment, a water feeding unit, a n-pentane feeding unit, and a drop catcher that could be positioned at any elevation to catch the drop and to measure its temperature. The column was 170 mm × 170 mm in cross section and 3 m in height, being sheathed by another square column. Through a gap between the columns the air whose temperature had been regulated was circulated to insure a uniform temperature distribution inside the inner column. The air whose temperature T_∞ and humidity ϕ had been regulated to specified values (T_∞: 20 ~ 31 °C, ϕ: 20 ~ 100 percent) flowed downward in the inner column at about 60 mm/s to maintain a constant environment (humidity and vapor pressure of n-pentane).[3] The temperature of the air measured by copper-constantan thermocouples at three heights in the column never deviated over ±0.3 K around a specified level during each run. The humidity was measured at the entrance of the column by use of a wet and dry bulb hygrometer, which was removed before each run to prevent the addition of water vapor from its wet bulb to the air flowing into the column. Water deionized and distilled and n-pentane of reagent grade were fed to the nozzles facing each other as shown in Fig. 3 at specified flow rates, they came into contact with each other at nozzle tips, and then fell down in the column one by one as a form of composite drops. The water temperature was controlled by an electronic system in which a silicon transistor was applied as a heater and a sensor simultaneously [6]. The temperature monitored by a sheathed copper-constantan thermocouple inserted in the nozzle at 3 mm from its tip was regarded as the nominal initial temperature of liquid A, T_{Ai}; the temperature in the region closer to the nozzle tip was found to fluctuate due to the evaporation of pentane contacting with the water so that it could not be employed as the standard of the initial water temperature. T_{Ai} was regulated to either 50 °C or 31 °C with a fluctuation less than ± 0.2 K during each run; the former being higher and the latter lower than the saturation temperature of pentane under the atmospheric pressure, 36.1 °C. The pentane feeding unit was so carefully designed that the pentane never contacted with any material other than glass and Teflon. All joints in the unit, e.g., those at the inlet and outlet of the flowmeter, were immersed in pools of water to prevent tiny air bubbles from being entrained into the flowing pentane through minute gaps in those joints due to capillarity. The temperature of pentane was not controlled artificially. The

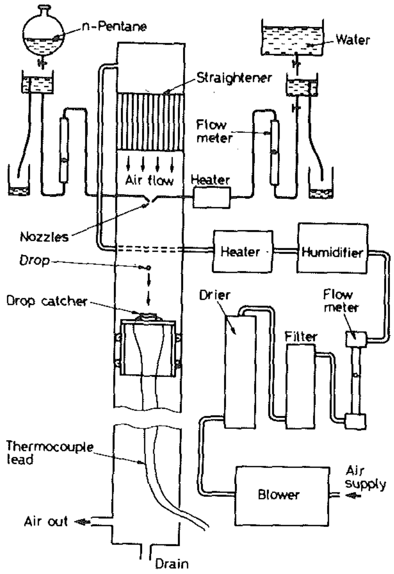

Fig. 2 Schematic of experimental setup

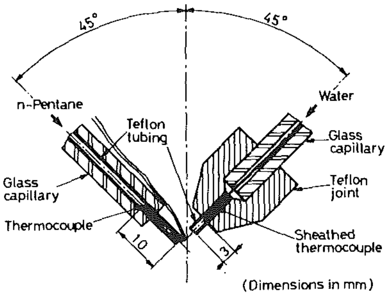

Fig. 3 Construction of nozzles

---

[3] The air velocity (≃60 mm/s) was much smaller than the fall velocity of drops except at very small falling distances (≪10 mm), and thus its effect on the drop cooling must have been negligible with a good approximation.

Nomenclature

A = liquid which is to be cooled
B = volatile liquid
c_{pA} = specific heat capacity of liquid A
H = falling distance from nozzle tips
Δh_{vB} = specific latent heat of vaporization of liquid B
S_A, S_B, S_G = spreading coefficients defined in equation (2)
T_A = maximum temperature inside a drop
T_{Af} = temperature of liquid A in a composite drop when the attached liquid B has just vanished
$T_{Af}{}^*$ = ideal value of T_{Af} given by equation (4)
T_{Ai} = initial temperature of liquid A
$T_{A0} = \lim_{H\to 0} T_{A(H)}$
$T_A{}'$ = adiabatic saturation temperature of air-liquid A system
$T_B{}'$ = adiabatic saturation temperature of air-liquid B system
T_∞ = air temperature
Γ = cooling efficiency defined in equation (5)
Δ_i, Δ_0 = indices of cooling augmentation defined by equations (6) and (7)
ζ_i = volume flow ratio of liquid B to liquid A
ρ_A, ρ_B = densities of liquid A and of liquid B
σ_A, σ_B, σ_{AB} = surface tension of liquid A saturated with liquid B, surface tension of liquid B saturated with liquid A, and interfacial tension of liquid A-liquid B interface
ϕ = relative humidity of air

temperature measured by a thermocouple locating in the nozzle at 10 mm away from the tip varied between 8 and 18 °C depending on the flow rate of pentane, while the flow rate of water and T_{Ai} were held constant, because a part of pentane crept up the outside wall of the nozzle made of Teflon and evaporated there, resulting in the cooling of the nozzle. However, the effect of the variation in pentane temperature on drop cooling was estimated to be sufficiently small and was neglected in this study.

The volume fraction of pentane in each composite drop at the moment of its departure from the nozzles could not be specified exactly because some fraction of pentane evaporated before the departure. Thus, we use the ratio of pentane flow rate to water flow rate, ζ_i, as the nominal value of initial volume fraction of pentane. The experiments were designed to provide data for varying ζ_i while water volume in each composite drop and the frequency of drop departure were held almost constant; this was accomplished by shifting slightly the positions of two nozzle tips relative to each other correspondingly with the variation of pentane flow rate under a constant water flow rate. The equivalent spherical diameter of water phase in a composite drop and of a water drop was 3.5 ± 0.1 mm throughout the experiments except a special run in which water drops of 3.2 mm dia were used for the convenience of comparison of the result with Yao and Schrock's result [9] with 3 mm dia drops. The frequency of drop departure was 1.04 to 1.20 Hz.

To measure properly the variation in a certain representative temperature (e.g., the maximum temperature or mean temperature) of water in drops with the falling distance was a crucial problem in this study. The method of Yao and Schrock [9], i.e., collecting drops in a small dewar—which could be positioned at any elevation in the column—to measure the mean temperature, was not applicable for composite drops. Thus we attempted to measure the maximum temperature by the following method.

The drop catcher as illustrated in Fig. 4 was mounted on a specially designed carrier that enabled us to move the catcher in three directions independently by drawing wires from outside of the column. A copper-constantan thermocouple of 30 μm dia was stretched rigidly at the entrance of a center hole (of 3 mm dia, a little smaller than the drop diameter) of the catcher into which drops were to be swallowed. It was confirmed with such a catcher configuration that the water phase in a composite drop contacted the junction of the thermocouple with little time delay when the drop entered the catcher almost concentrically, and then it slowly drained off the catcher through the center hole. When a drop entered the catcher off its center, there was a larger time delay of the contact between the drop and the thermocouple junction; this should have resulted in a lower temperature exhibited by the thermocouple. The thermo voltage was amplified by a d-c amplifier (Model 6L3-1, San'ei Instruments Co., Ltd.) and then recorded by an electromagnetic oscillograph (Visigraph FR-201, San'ei Instruments Co., Ltd.). Thus, the periodical peaks on the oscillogram were expected to represent the maximum temperature T_A of water in the drops at a falling distance H measured from the nozzle tips to the thermocouple junction, if the drops entered the catcher concentrically and if the response rate of the thermocouple was high enough. In practice, the heights of peaks were scattered to some extent because of the eccentricity of impingement point to the center of the catcher being different from drop to drop; and thus the maximum of a large number (160 to 620 depending on H) of peaks sampled successively at a specified H was assumed to represent T_A at that H. The response rate of the thermocouple was considered to be high enough based on the following facts.

By increasing the feeding speed of oscillopaper up to 1 m/s so that the detailed shape of each peak could be revealed, it was found that the thermo voltage reached a maximum asymptotically in about 4 ms after the start of its rise, which was enough short compared to the duration of the thermocouple junction staying in the water phase in a drop, and then fell slowly relative to the rate of rise up to the aforementioned maximum. The responding characteristics were also examined by preheating the thermocouple with a power transistor attached to the catcher till the level of thermo voltage while the thermocouple junction was not in contact with drops came close to the level of peaks on the oscillogram. Such a preheating was found to hardly affect the level of peaks themselves: this indicates that the level of peaks represented with enough accuracy the maximum temperature inside drops irrespective of the preheating.

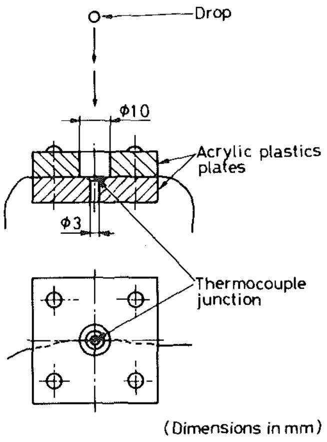

Fig. 4 Drop catcher detail

Further details of the experimental equipment and procedure are described in references [7] and [8].

Results and Discussion

Results are shown in Figs. 5 to 9 in the form of T_A versus falling distance from the tips of nozzles, H. Except Fig. 9, the results are for pure pentane-water system without surfactant. In every figure data on composite drops ($\zeta_i > 0$) are given together with the corresponding data on water drops ($\zeta_i = 0$) for the convenience of comparison. The data on water drops agree well with those of Yao and Schrock [9] who measured the mean drop temperature instead of the maximum temperature T_A inside drops. The fact that little difference is found between T_A we measured and the mean temperature Yao and Schrock did, may be ascribed to a mixing of water due to oscillation of drops. Composite drops are apparently characterized by a large temperature drop till their departure from the tips of nozzles due to a partial evaporation of attached pentane as well as by the cooling rates which are much higher than those of water drops, while falling through the air, due to the evaporation of residual pentane.

Dependence on Initial Volume Fraction of n-pentane, ζ_i. The sheath of pentane in a composite drop must have some thermal resistance to heat flow from the hot water core to the surrounding depending on its thickness. The calculation by assuming a concentric pentane shell around a spherical water core and a radial conduction predicts the resistance of the pentane shell being dominant in the present heat transfer process at least in an early stage of the fall of the drop. In practice, however, ζ_i did not affect the cooling rate, as shown in Figs. 5 and 6, except that the cooling curve for $\zeta_i = 0.3$ began to deviate increasingly from those for larger ζ_i's at about 0.2 m of the falling distance probably due to the complete consumption of the pentane. This fact indicates that the thermal resistance of the pentane layer was negligibly small.

A high-speed cine-photography [8] revealed that the major part of the pentane formed a convexo-concave lens covering a limited area of the surface of water core while the residual surface area was covered with a thin film of pentane. The lens revolved quickly round the water core while falling, probably resulting in a continual supply of pentane to the film region where the pentane was quickly consumed by evaporation. Such a configuration and a motion of the pentane as described above were presumed to be the cause that minimized the resistance of the pentane layer.

It is noticed in Fig. 5 that the cooling rate for $\zeta_i = 0.3$ in the range $H > 0.2$ m agrees with that for water drops with nearly the same instantaneous T_A. This indicates that the attached pentane had evaporated almost completely till $H = 0.2$ m as described before and that the cooling of drops in the further range resulted from the evaporation of water. The cooling rates for $\zeta_i = 0.43$ and 0.74 agree

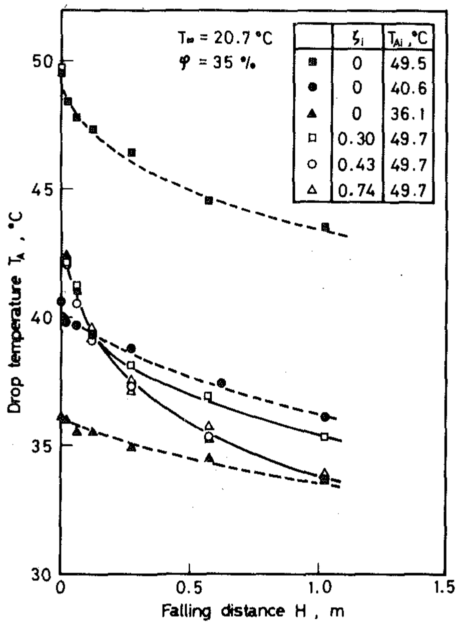

Fig. 5 Dependence on initial volume fraction of pentane ($T_{Ai} \simeq 50$ °C)

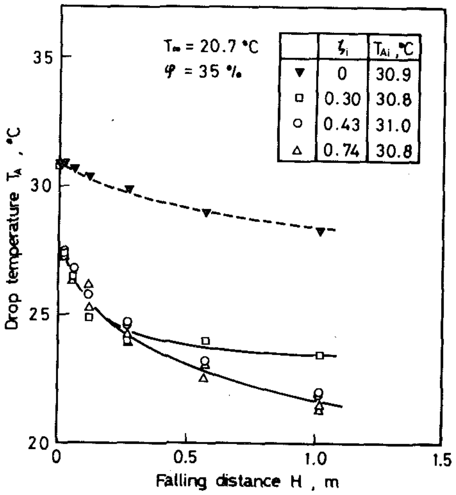

Fig. 6 Dependence on initial volume fraction of pentane ($T_{Ai} \simeq 31$ °C)

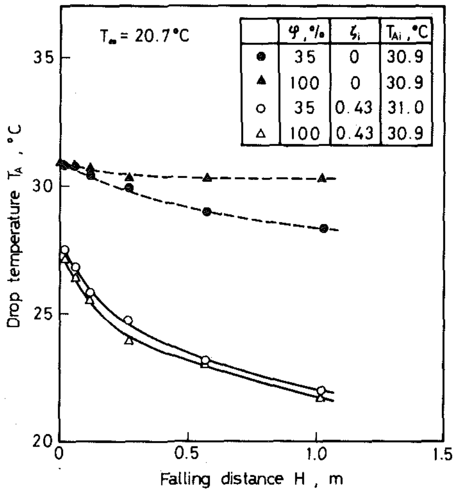

Fig. 7 Dependence on relative humidity

with each other and are appreciably higher than those for water drops with similar T_A's throughout the whole range of H in the present experiments; this indicates that the cooling was due to evaporation of pentane throughout the whole range of H.

Dependence on Humidity and Temperature of Air. Figures 7 and 8 show the variations of cooling curves with the relative humidity ϕ and the temperature T_∞ of the air. The cooling curves for composite drops were not affected by ϕ and T_∞ whenever some amount of pentane remained in the drops, but the cooling rate for water drops was appreciably reduced with an increase of ϕ from 35 to 100 percent (Fig. 7) and was slightly reduced with an increase of T_∞ from 21 to 31 °C (Fig. 8) due to the suppressions of mass transfer (i.e., latent heat transfer) and of sensible heat transfer respectively. This fact clearly indicates that the cooling of composite drops is dominated by the latent heat transfer due to the evaporation of pentane.

Effect of Drop Configuration. The effect of an addition of sodium oleate to water phase is demonstrated in Fig. 9. The addition of sodium oleate resulted in a decrease of cooling rates for both water drops and composite drops. The decrease of cooling rate for water drops may be ascribed to the suppression of oscillation of drops while falling. The high-speed cine-photography showed that the addition of sodium oleate caused a 20 percent reduction of frequency and a little increase of amplitude of the oscillation of water drops in the range of $H \leq 0.2$ m; the effect on the oscillation of composite drops was less remarkable. The decrease of cooling rate for composite drops due to the addition of sodium oleate is much more drastic. Such a decrease seems to be primarily ascribed to the change in the configuration of composite

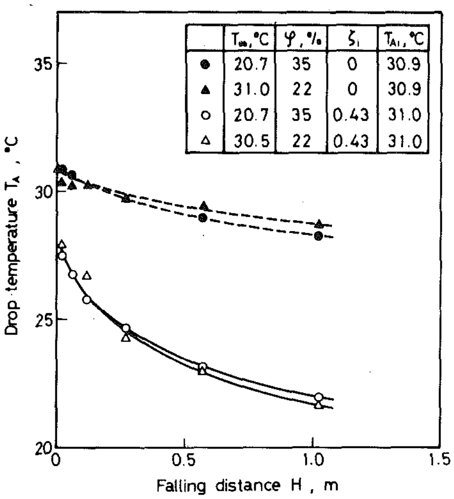

Fig. 8 Dependence on air temperature

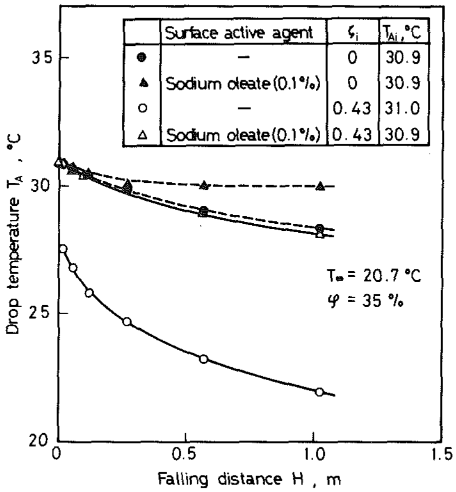

Fig. 9 Effect of addition of a surfactant to water phase

drops as described before, i.e. from configuration I (or configuration II with a very small surface area not covered by pentane) to the typical configuration II, resulting in disappearance of the surface area covered with a thin film of pentane where the internal resistance to heat transfer must be very small. Further, the cine-photography suggested that the mobility of the pentane lens round the water core was appreciably suppressed, probably being related to the presence of the three-phase contact line. Hence, it is reasonably presumed that the cooling rate was remarkably reduced due to an increased internal resistance of the pentane layer which was thicker and less mobile as well as a decreased area of pentane-air interface providing an appreciably larger resistance to the diffusion of pentane vapor.

Cooling Efficiency. The absolute cooling limit for water drops is given by the adiabatic saturation temperature for air-water system (i.e., wet bulb temperature), T_A', while that for composite drops is given by the adiabatic saturation temperature for air-pentane system, T_B'. The former is, for example, 12.3 °C under the condition that $T_\infty = 20$ °C and $\phi = 35$ percent, and the latter was roughly measured to be as low as −15 °C under the same T_∞ and the vanishing pentane concentration in the free-stream air. In practice, the temperature T_{Af} which the water temperature attains in a composite drop when the attached pentane has just vanished is restricted by ζ_i and may be higher than T_A' in some cases. If $T_{Af} > T_A'$, the drop will be further cooled gradually in the succeeding fall in the air by the evaporation of water; and if $T_{Af} < T_A'$, the drop will be heated up to T_A'. Hence, T_{Af} may desirably be predicted from the practical point of view. If the pentane supplied to the nozzle is completely used to cool the water, T_{Af} is equal to $T_{Af}{}^*$ given by

$$T_{Af}{}^* = T_{Ai} - \frac{\zeta_i\, \rho_B\, \Delta h_{vB}}{\rho_A\, c_{pA}}\,. \tag{4}$$

In practice, T_{Af} must be somewhat higher than $T_{Af}{}^*$, because some fraction of pentane evaporates during the formation of a composite drop cooling the nozzle and the air, and because a much smaller fraction may be lost due to the sensible heat transfer from the air to pentane surface if the temperature at pentane surface becomes lower than T_∞ in the course of the fall of the drop. Here we define the cooling efficiency Γ as

$$\Gamma = \frac{T_{Ai} - T_A}{T_{Ai} - T_{Af}{}^*}\,, \tag{5}$$

which is plotted against the falling distance in Fig. 10. It is presumed that the pentane attached to each drop vaporized completely during its fall till $H \simeq 0.2$ m for the case $\zeta_i = 0.3$ as described before. It is seen in Fig. 10 that at this falling distance

$$\Gamma = 0.3 \sim 0.4 : T_{Ai} \simeq 31\ ^\circ\mathrm{C} \text{ and}$$
$$\Gamma = 0.6 \sim 0.7 : T_{Ai} \simeq 50\ ^\circ\mathrm{C}.$$

It should be noted that Γ depends on the condition of formation of composite drops. Higher flow rates of pentane and water shorten the period of drop formation, and thus will result in a decrease of the initial loss of pentane. Hence, the cooling efficiencies as shown here are expected to be appreciably raised in practical cooling systems operated at much higher flow rates of liquids.

Evaluation of Cooling Augmentation. Though the cooling rate of composite drops being appreciably higher than that of water drops can readily be recognized in Figs. 5 to 9, the extent of augmentation is not quantitatively specified there. Since the cooling of composite drops depends on many factors, no definite method of quantitative evaluation of augmentation can be presented. Under each condition (a combination of liquids, T_{Ai}, T_∞, ϕ, ζ_i and drop size are specified), however, the augmentation may be evaluated by use of specific temperature fall $(T_{Ai} - T_A)/(T_{Ai} - T_\infty)$ of composite drops to that of water drops with almost the same T_{Ai} at each falling distance H. The dependence of

$$\Delta_i = \frac{(T_{Ai} - T_A)/(T_{Ai} - T_\infty)_{\text{composite drop}}}{(T_{Ai} - T_A)/(T_{Ai} - T_\infty)_{\text{water drop}}} \tag{6}$$

on H is shown in Fig. 11 for the runs presented in Figs. 5 and 6. Here the cooling augmentation of drops at the nozzle tip and that during

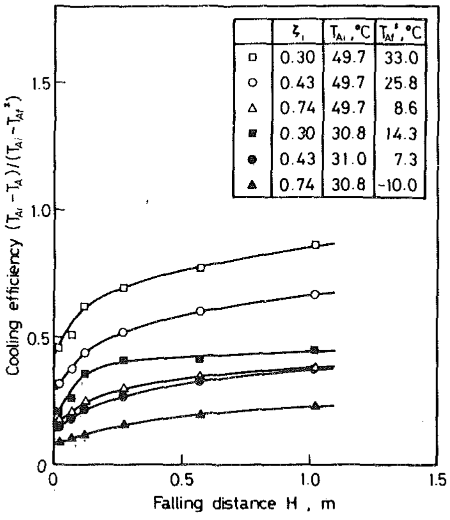

Fig. 10 Cooling efficiency

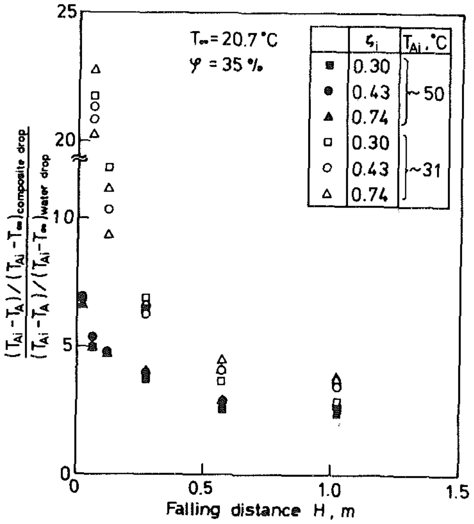

Fig. 11 Total cooling augmentation

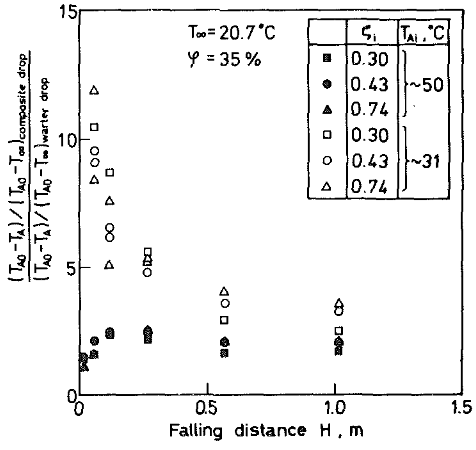

Fig. 12 Cooling augmentation of drops during their free fall

their free fall are evaluated in the gross. The latter may rather be evaluated by using

$$\Delta_0 = \frac{(T_{A0} - T_A)/(T_{A0} - T_\infty)_{\text{composite drop}}}{(T_{A0} - T_A)/(T_{A0} - T_\infty)_{\text{water drop}}}, \tag{7}$$

where $T_{A0} = \lim_{H \to 0} T_A(H)$ is obtained by the extrapolation of T_A versus H relation in each run, and is lower to some extent than T_{Ai} for composite drops and practically the same with T_{Ai} for water drops. In Fig. 12 Δ_0 is evaluated for composite and water drops with almost the same T_{Ai}, though it should be done, in principle, for those with same T_{A0}. A proper evaluation of Δ_0 for composite and water drops with same T_{A0} would give higher values than those given in Fig. 12.

The extent of augmentation represented by such an index as Δ_i or Δ_0 becomes more remarkable as T_{Ai} (or T_{A0}) decreases, causing a suppression of water evaporation. It should be kept in mind that Δ_i (or Δ_0) goes to infinity as T_{Ai} (or T_{A0}) approaches T_A', the adiabatic saturation temperature. If T_{Ai} (T_{A0}) decreases further beyond T_A', Δ_i (Δ_0) becomes negative and loses the meaning as an index of cooling augmentation.

Concluding Remarks

The possibility of augmentation of the evaporative cooling of falling drops by attaching them with some amount of an immiscible, more volatile liquid has been considered and examined experimentally. Dependences of cooling rate on various factors and the extent of available augmentation were exemplified for water drops of 3.5 mm dia sheathed by *n*-pentane. Following are principal findings that seem to be not specific for such a system but of general nature.

The cooling is intensely augmented on the condition that the spreading coefficient of the volatile liquid on the other which is to be cooled is positive or at least around zero, so that the volatile liquid encloses almost completely the other. The layer of the volatile liquid hardly adds to thermal resistance even if its thermal conductivity is fairly low because of its motion round a drop. Consequently the initial volume fraction of the volatile liquid does not affect the temperature history of each drop while the volatile liquid is remaining on the drop surface but it determines the total temperature fall attained when the volatile liquid has vanished.

Acknowledgment

The authors greatly appreciate the help and advice afforded by Dr. Y. Tochitani in constructing the experimental setup. K. Higeta is also acknowledged for his help, particularly in the high-speed cine-photography. H. Mitsuyoshi, Y. Ueno and K. Ishimitsu partially assisted the experiments. This work has been sponsored in part by the Grant in Aid for Scientific Research of the Ministry of Education of Japan under Grant 375113.

References

1 Gibson, W., Emmermann, D., Grossman, G., Johnson, R., Modica, A., and Pallone, A., "Spray Freezer and Pressurized Counterwasher for Freeze Desalination," *Proceedings of the Fourth International Symposium on Fresh Water from the Sea*, Heidelberg, Sept. 1973, Vol. 3, pp. 343–345.

2 Johnson, W. E., Fraser, J. H., Gibson, W. E., Modica, A. P., Grossman, G., and Stepakoff, G. L., "Spray Freezing, Decanting, and Hydrolysis as Related to Secondary Refrigerant Freezing," Office of Saline Water, Research and Development Progress Report No. 786, 1972.

3 Torza, S., and Mason, S. G., "Coalescence of Two Immiscible Liquid Drops," *Science*, Vol. 163, 1969, pp. 813–814.

4 Torza, S., and Mason, S. G., "Three-Phase Interactions in Shear and Electrical Fields," *Journal of Colloid and Interface Science*, Vol. 33, 1970, pp. 67–83.

5 Mori, Y. H., "Configurations of Gas-Liquid Two-Phase Bubbles in Immiscible Liquid Media," *International Journal of Multiphase Flow*, Vol. 4, 1978, pp. 383–396.

6 "Temperature Limiter for Small Variations," *Electronic Engineering*, Vol. 49, No. 590, Apr. 1977, p. 23.

7 Nagai, K., "Cooling of Freely Falling Liquid Drops with a Shell of an Immiscible Volatile Liquid," (in Japanese), M. Eng. thesis, Keio University, Yokohama, March 1979.

8 Funaba, H., "Cooling of Freely Falling Liquid Drops with a Shell of an Immiscible Volatile Liquid," (in Japanese), B. Eng. thesis, Keio University, Yokohama, March 1980.

9 Yao, S.-C., and Schrock, V. E., "Heat and Mass Transfer from Freely Falling Drops," ASME JOURNAL OF HEAT TRANSFER, Vol. 98, 1976, pp. 120–126.

S. J. Palaszewski
Bell Laboratories,
Member of Technical Staff,
Whippany Road,
Whippany, NJ 07981
Assoc. Mem. ASME

L. M. Jiji
Professor.

S. Weinbaum
Professor.

The City College of the
City University of New York,
Department of Mechanical Engineering,
Convent Avenue at 138th Street,
New York, NY 10031
Mem. ASME

A Three-Dimensional Air-Vapor-Droplet Local Interaction Model for Spray Units

An approximate fully three-dimensional numerical model for predicting the detailed flow and thermal characteristics of spray units is presented. The new model differs from all previous analyses of spray cooling systems in that it determines the local variation in the dry-bulb temperature, absolute humidity and the air streamlines throughout the flow field encompassing the spray umbrella and the effect of this local variation on drop cooling. The conservation equations to determine the local absolute humidity, velocity and dry-bulb temperature of the air-vapor phase are written in Lagrangian form where the droplets are treated as spatially varying sources of mass, momentum and energy. The analysis takes into consideration stable and unstable meteorological conditions, turbulent mixing in the atmospheric surface layer and nonuniform upwind and local air-velocity profiles. The numerical model is of intrinsic interest because it demonstrates the feasibility of computing a three-dimensional, two-phase flow field without the use of excessive computer time. Model predictions of droplet return temperature along the spray centerline were compared with data for the Spraco 1751 nozzle. Good agreement was observed.

Introduction

In recent years, spray cooling systems have received favorable attention from the power industry as an alternative to cooling towers for the dissipation of waste heat from electric generating plants. Spray cooling systems have a number of advantages over cooling towers. These include economy of construction, ease of maintenance and the ability to control the rate of heat dissipation by selectively shutting off or turning on any number of spray modules. Factors of land availability, environmental considerations and the inability of current theoretical models to accurately predict their performance are the major reasons why spray cooling systems for waste heat dissipation have had very limited use to date. Ryan and Myers [1] underscore the uncertainty in current theories by an example calculation where the number of required spray units for a given design criteria varies by a factor of 2.5 depending on the theoretical model used. A magnitude of uncertainty of this order is intolerable in view of the substantial capital costs of each spray module. The purpose of this paper is to demonstrate the feasibility of solving a three-dimensional, two-phase flow field by using a comprehensive and accurate numerical finite difference model which requires little computer time. The model considers for the first time the local changes in the air-vapor phase due to the presence of the spray and the effect of these local changes on the energy released by the droplets.

Existing theoretical models for predicting the performance of spray units and systems have been based in large measure on approximate solutions to Merkel's equation for the energy transfer of an individual droplet from the moment it leaves the nozzle until it returns to the canal. The driving potential for the energy loss due to convective and evaporative cooling at the drop surface is the instantaneous difference in the total heat function (enthalpy of air-vapor phase minus the liquid enthalpy of the vapor fraction at the adiabatic saturation temperature) between the drop temperature and the local wet-bulb temperature. Merkel's equation neglects radiation losses from the drop and assumes that its thermal relaxation time is short compared to the trajectory time. Soo [2] has shown that both are reasonable approximations for typical spray units.

The principal difficulty in evaluating Merkel's equation is that the local wet-bulb temperature can change significantly as the air is heated and gains moisture while passing through the spray. The local wet-bulb temperature is a complicated function of the time history of the mass, momentum and energy exchange experienced by the air-vapor element from the moment it approaches the spray to the time it reaches its present position. It also depends on the meteorological conditions in the lower part of the earth's boundary layer. The problem is further complicated by the fact that particle trajectories and air-vapor streamlines differ substantially, as shown schematically in Fig. 1, which illustrates that a vapor bubble does not follow the drop as assumed by Elgawhary [3] and Frediani and Smith [4].

In view of the above complexities, different approximations have been introduced for obtaining the local wet-bulb temperature. The two limiting approximations are that the wet-bulb temperature is given by upstream ambient conditions [2] or that the air is saturated

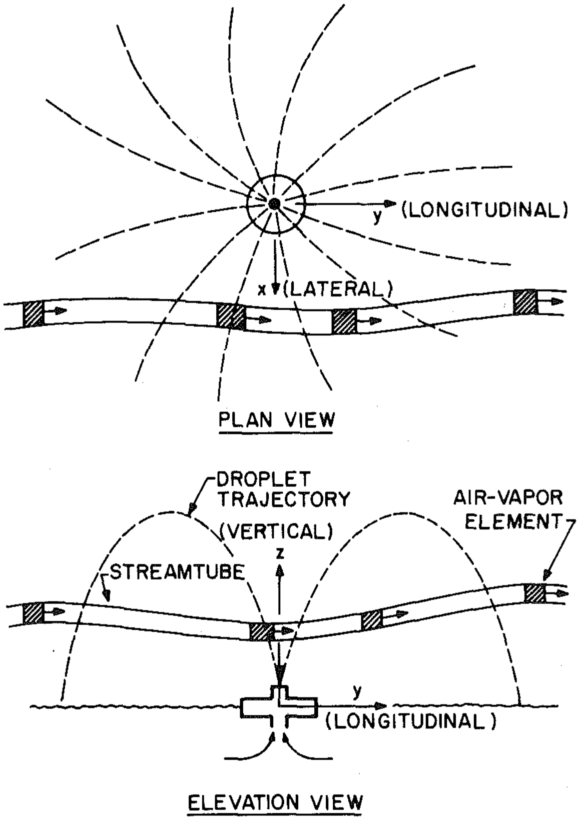

Fig. 1 Trajectory of a fluid element as it crosses the spray field

---

Contributed by the Heat Transfer Division for publication in the JOURNAL OF HEAT TRANSFER. Manuscript received by the Heat Transfer Division July 14, 1980.

in the spray domain [5]. Other investigators have introduced an appropriate constant average wet-bulb temperature [6, 7], or have utilized convective-diffusion theory (incorporating an experimentally obtained spray heat release parameter NTU) to determine a dimensionless interference factor f relating the local wet-bulb temperature to the initial droplet and ambient wet-bulb temperatures [8, 9]. The latter models in particular provide useful engineering estimates of dimensionless groups, denoted by NTU or SER, which characterize the total energy released by the droplets. No previous model has attempted to theoretically predict the local variation in wet-bulb temperature or the three-dimensional streamline patterns of the air-vapor phase, two important objectives of the present finite difference model. The streamline patterns obtained from the solution are particularly instructive since they show how the droplet drag and buoyancy forces affect the air-vapor circulation in the spray as a function of wind speed and atmospheric stability.

While the more comprehensive model developed herein eliminates the need for empirical factors such as effective droplet diameter or an average wet-bulb temperature, it does use the empirical correlation equations of Ranz and Marshall [10] for the convective heat and mass transfer from the drop and an eddy viscosity model for the turbulent diffusion of mass, momentum and energy in the air-vapor mixture. In essence, one has replaced an ad hoc empirical correction factor by fluid equations with an approximation for local transport properties. The important advantages of using the latter approach are that one obtains a picture of the air-vapor flow field and can calculate the heat loss for a droplet along any particular trajectory in the spray umbrella. Furthermore, since the exit conditions for one spray unit provide the entrance conditions for the next spray unit in the pass, one has eliminated the need for additional empirical correction factors between rows in a spray system. One important limitation of the model formulation is that the ambient air is assumed to be in motion. The numerical calculations give reasonable results provided the air velocities induced by droplet drag and buoyancy are of the same order as the local wind speed. For typical power plant spray units this implies a minimum wind speed of approximately 1.0 m/s.

Another important consideration in predicting spray unit performance is the droplet size distribution. For the 56 kW Powered Spray Module manufactured by the Ceramic Cooling Tower Company that is examined in the present paper, the droplets are relatively monodispersed and an effective Sauter-mean diameter is used. For sprays exhibiting a distribution of drop sizes, a single effective drop size may not be satisfactory. These cases are easily treated in the framework of the present model by dividing the droplet size distribution into discrete intervals and calculating the particle trajectories for each interval. Thus the analysis of the Spraco 1751 nozzle described later in the paper considers five different droplet sizes each with a different ejection angle.

Two complementary papers are in progress. The first of these papers deals with the application of the basic model presented in this study to the performance and design optimization of individual spray units. The second paper analyzes the interaction between spray units in a module or a pass.

Model Description

At present, finite difference solution schemes do not exist for solving the Navier-Stokes equations in three dimensions, even without the added complications of the turbulent transport terms or the additional terms due to the droplet phase. One thus needs to devise an approximate set of model equations which retain the three-dimensional character of the flow field and droplet trajectories but which can be solved in a few minutes on a large capacity high speed computer. Short computational times are essential if the computer code is to be used for spray design and optimization.

The minimum requirements of the model are that it:

1 accurately calculate the trajectories of the droplets released in any direction with respect to the incoming wind profile taking into account the instantaneous local difference in velocity and direction between the air-vapor and droplet phases (see Fig. 1),

2 determine the three-dimensional path of an air-vapor element through the spray umbrella and the change in local dry-bulb

Nomenclature

A = cross-sectional area of streamtube
C_D = drag coefficient
C_p = constant pressure specific heat
c = number characterizing the size of an air element
D = diffusion coefficient
d = droplet diameter
d_c = droplet diameter upon canal re-entry
g = gravitational acceleration
H_0 = surface heat flux
h = droplet heat transfer coefficient
h_D = droplet mass transfer coefficient
h_f = enthalpy of water at saturation temperature
i = enthalpy of air − vapor mixture
$\mathbf{j}$ = unit vector in the wind direction (longitudinal)
k = thermal conductivity
k' = von Karman's constant
K_h = turbulent thermal conductivity of air
K_m = turbulent viscosity of air
K_{wv} = turbulent thermal diffusivity of water vapor in air
ℓ = lateral dimension of streamtube
L = latent heat of vaporization of water
L_{mo} = Monin-Obukhov length scale = $-\rho_a C_{pa} T_{db} u_*^3/(k' g H_0)$
M = droplet mass
m = vertical dimension of streamtube
N = total number of trajectories
n = number of droplets in an air-vapor element
$\dot{n}_j$ = number of droplets ejected from the nozzle per unit time for a given trajectory
NTU = number of transfer units
Pr = Prandtl number = $\mu_a C_{pa}/k_a$
$\dot{Q}$ = rate of heat transfer from a spray unit
Re = Reynolds number = $\rho_a d|\mathbf{v} - \mathbf{u}|/\mu_a$
s = distance along a streamline or drop trajectory
Sc = Schmidt number = $\mu_a/(\rho_a D)$
SER = spray energy release
T = temperature, $T^* = (T - T_{wb\infty})/(T_{do} - T_{wb\infty})$
T_c = spray cold water temperature at canal re-entry
T_{do} = spray supply temperature
T_{ra} = reference temperature
t = time
U_∞ = wind speed
$\mathbf{u}$ = air velocity vector
u_* = friction velocity
V = volume of a finite air-vapor element
$\mathbf{v}$ = droplet velocity vector
v_0 = initial speed of the mean size drop
x = horizontal space coordinate perpendicular to the wind direction
y = horizontal space coordinate in the wind direction
Z, z = vertical distance above canal surface
z_0 = roughness height
β_T = coefficient of thermal expansion of air
ϵ = prescribed tolerance for convergence of spray heat transfer from successive iterations
θ = droplet discharge angle in the horizontal plane (measured from the x-axis)
μ = viscosity
ρ = density
ϕ = spray discharge angle in the vertical plane measured from the x-y plane
ω = absolute humidity

Superscript

$*$ = dimensionless variable

Subscripts

0 = initial value at nozzle discharge
$2m$ = ambient value at a $2m$ height
∞ = ambient value at any height
a = air
av = air-vapor mixture
d = droplet
db = dry bulb
i = droplet size in size distribution
j = trajectory number
k = iteration number
s = saturated air
v = water vapor
wb = wet bulb
y = horizontal space coordinate in the wind direction
z = vertical space coordinate

temperature and absolute humidity along this path taking into account droplet drag, buoyancy, forces due to thermal gradients in the air-vapor phase, the local convective and evaporative losses from the droplets and the turbulent mixing of the gaseous phase,

3 include basic meteorological conditions such as the stability of the atmospheric surface winds both in the incoming velocity profile and in the expressions for the turbulent transport coefficients.

Two reasonable approximations which greatly simplify the field equations for the air-vapor phase are that the pressure field is uniform and that turbulent transport is of the boundary layer type (only turbulent diffusion normal to the earth's surface is considered). With these two approximations, the differential equations for the air-vapor phase change from elliptic to parabolic form, provided the droplets can be treated as known sources of mass, momentum and energy. Unfortunately, the droplet source terms are not known since they depend on the local velocity and wet and dry-bulb temperatures of the air-vapor phase. Thus, an iterative solution procedure must be adopted in which the lowest order solution for the droplet trajectories and temperature is based on ambient conditions. This iterative procedure will be described in more detail later. The important point to be made here is that for each iteration the droplet source terms can be computed, the air-vapor differential equations treated as a parabolic system and a finite difference forward marching scheme employed.

The governing equations that have been adopted for the air-vapor phase differ from conventional boundary layer equations in several important respects. Although the pressure field is neglected, the momentum equation contains nontrivial components both normal to the canal surface and in the lateral direction (see Fig. 1). The transverse forces are generated by buoyancy and droplet drag components normal to the wind direction. A novel computational scheme is used for calculating the transverse velocity components and streamline displacements and is described in detail by Palaszewski [11]. Secondly, because the droplet trajectories are distinct, the source terms for mass, momentum and energy are distributed along discrete surfaces in the air-vapor space. To calculate the number density of droplets along each surface one must account for both the divergence of the trajectories with distance from the spray nozzle and the droplet velocity variation along each trajectory. This kinematics problem must first be solved and the spatial distribution of the droplets stored in the computer before the source terms can be calculated in the air-vapor differential equations. Thirdly, the duration of a droplet in an air-vapor element traversing the spray envelope depends on the local relative velocity difference between the phases.

These particular features of the spray flow field motivate the use of a Lagrangian coordinate description in which each air-vapor element is followed along a rectangular streamtube whose cross-sectional area changes with the local speed and whose side dimensions are obtained by considering the transverse momentum equations. The interaction between streamtubes occurs through the kinematic displacement of streamlines required from continuity and turbulent diffusion. In a typical calculation, a rectangular grid of 10 by 20 streamtubes is used to describe the air-vapor flow field on one side of the symmetry plane of the spray. The surfaces representing the locus of points of droplet trajectories are divided into anywhere from 30 to 100 discrete segments. This brief description covers the essential features of the model formulation. The governing equations for the droplets and air-vapor elements are summarized below. A more detailed description of the method of solution and the finite difference procedure is given by Palaszewski [11]. The equations are written in dimensional form so that the individual terms can be easily recognized. The dimensionless forms of the governing equations are given in [11]. These equations are useful in performing parametric studies aimed at improving the efficiency of spray units.

Conservation Equations

Conservation of Mass for a Droplet. To determine the amount of evaporation that a droplet experiences during its time in flight, one relates the time rate of change of droplet mass to the evaporative flux across the concentration boundary layer of the droplet:

$$dM/dt = -\rho_a h_D \pi d^2[\omega_s(T_d) - \omega]. \qquad (1)$$

The mass transfer coefficient h_D is determined by an empirical correlation given by Ranz and Marshall [10]:

$$h_D = (D/d)[2 + 0.6(\mathrm{Re})^{1/2}(\mathrm{Sc})^{1/3}]. \qquad (2)$$

Conservation of Droplet Momentum. Droplet velocities are determined by applying Newton's law for a particle. Consideration is taken of gravitational forces and the drag induced by the local vector-velocity difference between the droplet and the air-vapor continuum. The resulting equation is:

$$M d\mathbf{v}/dt = M\mathbf{g} - (C_D \rho_a \pi d^2/8)|\mathbf{v} - \mathbf{u}|(\mathbf{v} - \mathbf{u}) \qquad (3)$$

where [12]:

$$C_D = 0.44 = \text{drag coefficient for Re} > 1000 \qquad (4a)$$

$$C_D = (24/\mathrm{Re})(1 + 0.15\,\mathrm{Re}^{0.687}),\ \mathrm{Re} \le 1000. \qquad (4b)$$

A droplet trajectory is found from:

$$d\mathbf{s}_d/dt = \mathbf{v}. \qquad (5)$$

Conservation of Energy for a Droplet. Taking into consideration surface convection and evaporation, and neglecting temperature gradients within the droplet, the energy balance gives

$$-MC_{pd}dT_d/dt = \pi d^2 h(T_d - T_{db}) + \pi d^2 \rho_a h_D(\omega_s(T_d) - \omega)L. \qquad (6)$$

The terms on the right hand side of equation (6) are the energy given up by the droplet due to convection and evaporation, respectively.

The heat transfer coefficient h is obtained from an empirical correlation for a droplet given by Ranz and Marshall [10]:

$$h = (k_a/d)[2 + 0.6(\mathrm{Re})^{1/2}(\mathrm{Pr})^{1/3}]. \qquad (7)$$

Water Vapor Continuity Equation. To determine the variation of absolute humidity along any air-vapor streamline in the spray field, species conservation along a streamline is required. Conservation of mass for the water vapor in a fluid element gives:

$$\rho_a V d\omega/dt = \rho_a \pi d^2 n h_D[\omega_s(T_d) - \omega] + \rho_a V K_{wv} \partial^2\omega/\partial z^2 \qquad (8)$$

where

$d\omega/dt$ is the total derivative following the fluid motion.

The first term on the right hand side of equation (8) represents the droplets as sources of water vapor to the air-vapor elements. The second term is the net efflux of water vapor across the boundaries of the element due to turbulent diffusion.

If an element is considered to have the shape of a rectangular parallelpiped, the volume of an element can be characterized by an equivalent cube, whose side dimension is some multiple of the initial mean droplet diameter:

$$V = (cd_0)^3. \qquad (9)$$

Equation (8) is integrated along the gas-phase streamlines to determine ω. These streamlines are obtained from the momentum equation for the air-vapor element.

Conservation of Air Momentum. The velocity of an air-vapor element is found from a Lagrangian form of the momentum equation. Forces on the element are droplet drag, buoyancy and turbulent shear. The air momentum equation can be written as

$$\begin{aligned}\rho_a V d\mathbf{u}/dt = {} & (n\rho_a C_D \pi d^2/8)|\mathbf{v} - \mathbf{u}|(\mathbf{v} - \mathbf{u}) \\ & - \rho_a \beta_T V\mathbf{g}(T_{db} - T_{db\infty}) + \rho_a V K_m(\partial^2 u_y/\partial z^2)\mathbf{j}\end{aligned} \qquad (10)$$

Air Continuity Equation. The continuity equation for the air-vapor phase is formulated for a rectangular streamtube. The cross-sectional area of the streamtube upwind of the spray is given by the frontal area of an air-vapor element. This area changes as the element moves through the spray domain according to:

$$\rho_a u_y A = \rho_a U_\infty A_\infty \tag{11}$$

where the cross-sectional area of a streamtube is given by:

$$A = \ell m. \tag{12}$$

The lateral and vertical streamtube dimensions and velocity components are obtained by utilizing a ratio of the lateral and vertical components of the air momentum equation as detailed by Palaszewski [11]. The air-vapor streamline itself is found from:

$$d\mathbf{s}_a/dt = \mathbf{u}. \tag{13}$$

Air Energy Equation. Neglecting conduction in comparison with turbulent diffusion of heat, one can write for conservation of energy along an air-vapor streamline:

$$\begin{aligned}\rho_a V di/dt = n\pi d^2 h(T_d - T_{db}) + n\pi d^2 L h_D \rho_a(\omega_s(T_d) - \omega) \\ + \rho_a C_{pa} V K_h \partial^2 T_{db}/\partial z^2.\end{aligned} \tag{14}$$

The terms on the right hand side of equation (14) represent convective and evaporative heat transfer from the droplets and turbulent diffusion of heat in that order. The enthalpy i of an air-vapor mixture is given by:

$$i = C_{pa}(T_{db} - T_{ra}) + \omega[h_f(T_{wb}) + L(T_{wb}) + C_{pv}(T_{db} - T_{wb})]. \tag{15}$$

After substituting equation (15) into equation (14) and dropping small terms, equation (14) becomes:

$$\begin{aligned}\rho_a V C_{pav} dT_{db}/dt = \rho_a \omega V C_{pv} dT_{wb}/dt + n\pi d^2 h(T_d - T_{db}) \\ + \rho_a C_{pa} V K_h \partial^2 T_{db}/\partial z^2\end{aligned} \tag{16}$$

where,

$$C_{pav} = C_{pa} + \omega C_{pv}. \tag{17}$$

Meteorological Considerations

The initial upwind profiles of dry-bulb temperature and absolute humidity can be considered uniform since the variation of these quantities is small over heights typical of sprays (5 m). The wind velocity profile is given [13] as:

$$U_\infty(z) = u_*/k'\left[\ell n\left(\frac{z}{z_0} + 1\right) + \psi(z)\right]. \tag{18}$$

$\psi(z)$ takes on different forms depending on the stability condition of the atmosphere [13]. Values of the turbulent transport properties and the turbulent length scale L_{mo} are given in [13]. While the spray heat and moisture release will affect atmospheric stability, the effect of changes in stability are assumed small compared to convection and evaporation in determining drop and air-vapor temperatures.

Iterative Solution Technique

To obtain the lowest order solution for the droplet velocities, locations, temperatures, and sizes, one considers the local environment of the drops to be that of the ambient air-vapor phase. The calculation of local air-vapor velocities, streamlines, temperatures and humidities can then be performed by using the droplet solutions to evaluate the droplet source terms appearing in the air-vapor conservation equations. These first order air-vapor solutions yield a correction to the local environment of the drops, and are utilized in the next iteration on the droplet phase as detailed below.

Droplet trajectories and air-vapor streamlines cross at many locations in the spray domain. The velocity, temperature and humidity of the air-vapor element as it crosses a given droplet trajectory describes the local environment of the droplets at this location. By assigning the first order solutions for the air-vapor properties to locations along each droplet trajectory where the trajectories and streamlines cross, one obtains the first order corrections to the air-vapor phase along each trajectory. One can now solve the droplet equations again, using the corrected local values of the air-vapor properties instead of the ambient values. The resulting solutions for droplet location, velocity, temperature and size are used to evaluate the mass, momentum and energy source terms appearing in the air-vapor phase equations. Hence, one can obtain the second order solution for the gas phase and again assign the new air-vapor properties to the droplet trajectories where they cross the gas-phase streamlines. This completes the second order solution for the two-phase system.

The above iterative solution procedure is repeated until successive iterations on the droplet phase yield values of the rate of heat transfer from the spray that fulfill the following convergence criteria:

$$\frac{\dot{Q}_k - \dot{Q}_{k-1}}{\dot{Q}_{k-1}} \le \epsilon. \tag{19}$$

A maximum of four iterations are required. The total heat transfer from the spray is given by:

$$\dot{Q}_k = \frac{\rho_d C_{pd} \pi}{6} \sum_{j=1}^{N} \dot{n}_j [T_{do} d_{oj}{}^3 - T_{cj} d_{cj}{}^3] \tag{20}$$

A numerical fourth-order Runge-Kutta technique was used to solve the coupled set of droplet and air-vapor equations. The model can be applied at wind speeds above approximately 1.0 m/s. For lower wind speeds, continuity cannot be satisfied since the spray-air momentum interaction causes a reversal of the air-vapor velocities, which indicates a condition of recirculation.

Spray Characteristics

The present model is capable of predicting the local air-vapor velocity, absolute humidity and temperature fields of a spray unit, in addition to the droplet trajectories, velocities, temperatures and sizes. To demonstrate this capability, spray field characteristics are shown for a single spray of the Powered Spray Module (PSM) manufactured by the Ceramic Cooling Tower Company. A typical spray module is aligned parallel to the edge of a cooling canal. The module is powered by a 56 kW pump. Each nozzle sprays approximately 9470 liters of water per minute. The nozzles are located 0.91 m (3.0 ft) above the water surface, and produce a spray pattern with a maximum height of 6.1 m and a radius of 6.1 m at the water surface in the absence of wind. The initial droplet velocity is 11.64 m/s and the spray discharge angle is 74 deg [14].

In the theoretical model, droplets were discharged from 36 sites around the nozzle perimeter, producing a droplet trajectory every 10 deg.

The spray was assumed to be monodisperse. The value of the initial droplet diameter (d_0 = 1.5 cm) was obtained by varying the drop diameter until the single particle momentum equation (3) yielded the experimentally measured trajectory [14].

Figures 2 to 5 show model predictions of the detailed air-vapor droplet flow field of a spray unit. All results are for typical summer ambient design conditions. The atmosphere was assumed to be extremely unstable under strong solar insolation.

Figure 2 shows the trajectories of droplets ejected from the PSM at initial angles of $\theta_0 = -85$ deg and $\theta_0 = 85$ deg in the x-y plane for the condition of low wind. Also shown are a number of air-vapor streamlines traversing the spray domain near the centerline (y-axis) of the PSM. The effect of the upwind droplets in blocking the air-vapor flow is seen by the rising of the streamlines upwind of the nozzle. Continuity demands that the streamlines rise due to the reduced air-vapor velocity and the small lateral forces of the droplets on the air (the streamlines are not deflected very much laterally). Downwind of the nozzle, the droplets speed up the air and force the streamlines to descend. Figure 2 also reveals the effect of buoyancy on the streamline pattern. Near $y^* = -0.39$, the droplets following the upwind trajectory have a horizontal velocity component which is small compared to the vertical component, since the droplets are falling almost vertically. One would therefore expect little blockage of the

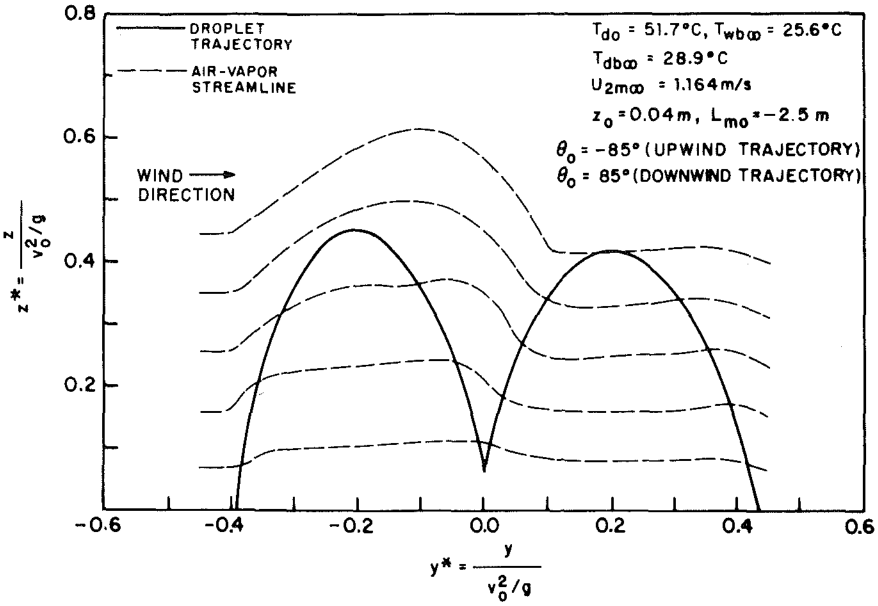

Fig. 2 Air-vapor streamlines near centerline of PSM for low wind (elevation view)

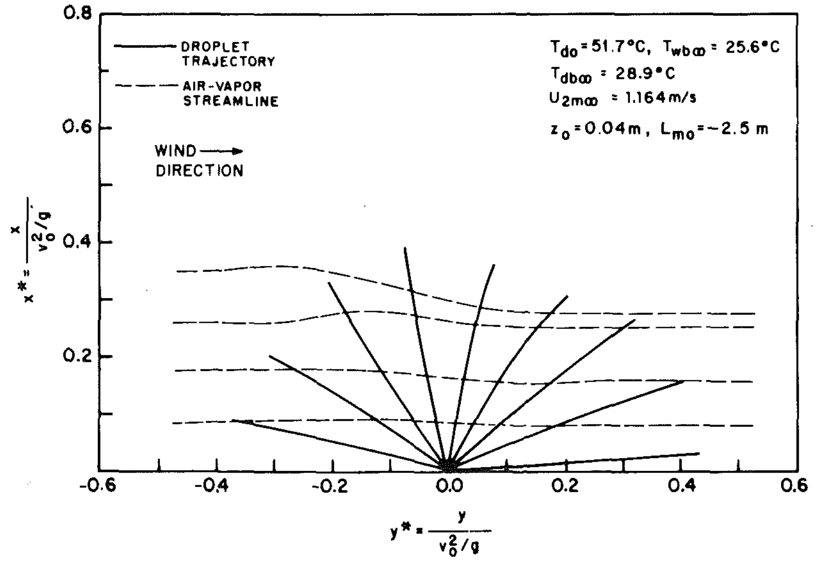

Fig. 3 Air-vapor streamlines initially at a 2m height upwind of PSM (plan view). Low wind

air-vapor flow near the lowest streamline in Fig. 2, and consequently, little rise of this streamline near $y^* = -0.39$. These expectations are borne out in the figure. However, at $y^* = -0.39$ the other streamlines, which have not as yet interacted with the spray, are seen to rise substantially. This effect is due to the buoyancy force produced by the heated air near the lowest streamline which has undergone thermal interaction with the droplets near $y^* = -0.39$.

The streamlines at $y^* = 0.0$ have not seen the downwind droplets. As stated above, the effect of the downwind droplets is to speed up the air and cause the streamlines to descend. However, one notices the streamlines descending before the air-vapor elements interact with the downwind droplets. This results from turbulent diffusion of heat from the hot air-vapor elements near the top of the spray to the cooler ambient free stream.

Figure 3 is a plan view of the PSM spray field at low wind. Droplet trajectories are plotted for half the spray domain. Air-vapor streamlines initially at a 2 meter height are also shown. One can readily see the small effect of drag on the droplets at low wind since the droplet trajectories lie essentially in vertical planes. The lateral entrainment of air by the spray is revealed by the compression of the streamlines downwind of the nozzle. Vertical air entrainment can be seen from Fig. 2 where the uppermost streamline is lower downwind of the spray than upwind, indicating the tendency of the spray to pull ambient air downward. This entrainment of ambient air is required to satisfy continuity. Vertical entrainment results from cooling of the air-vapor flow due to turbulent diffusion of heat from the air-vapor elements, as well as the acceleration of the air-vapor flow by the downwind droplets. Lateral entrainment is due exclusively to momentum interaction between air-vapor and droplets. The lateral and vertical entrainment by the spray at low wind indicates that more air participates in the local mass, momentum and energy interaction with the spray than initially enters the spray domain with the ambient wind. The ability of the model to predict this effect obviates the need for empirical entrainment coefficients used by other investigators.

Figure 4 shows typical absolute humidity profiles near the PSM centerline for low wind. Upwind of the spray, the absolute humidity profile is uniform. As air enters the spray, it is progressively humidified, and exhibits the developing profiles depicted in Fig. 4. The lower boundary condition on the profiles is the saturated humidity at the temperature of the canal water. Dry-bulb temperature profiles, al-

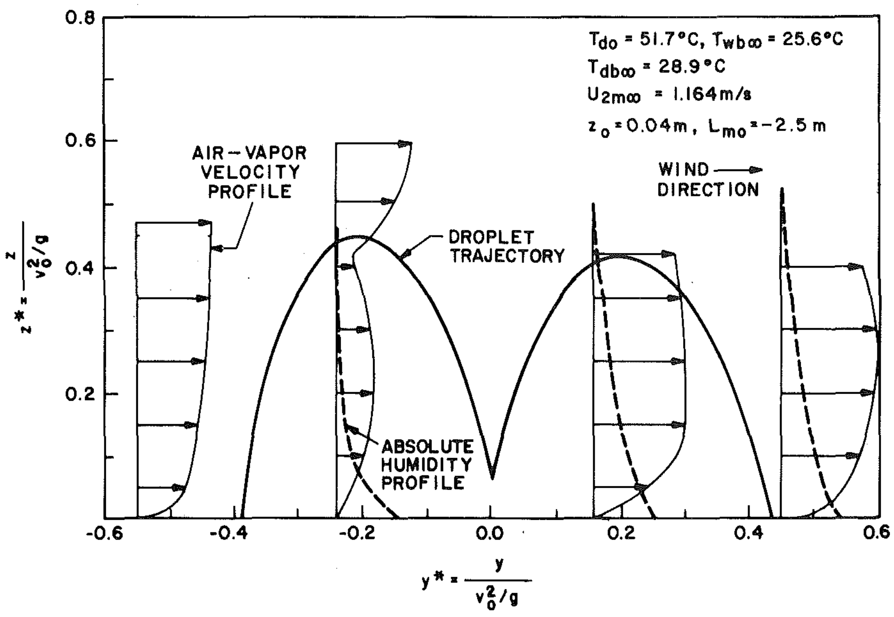

Fig. 4 Absolute humidity and air-vapor velocity profiles near centerline of PSM for low wind

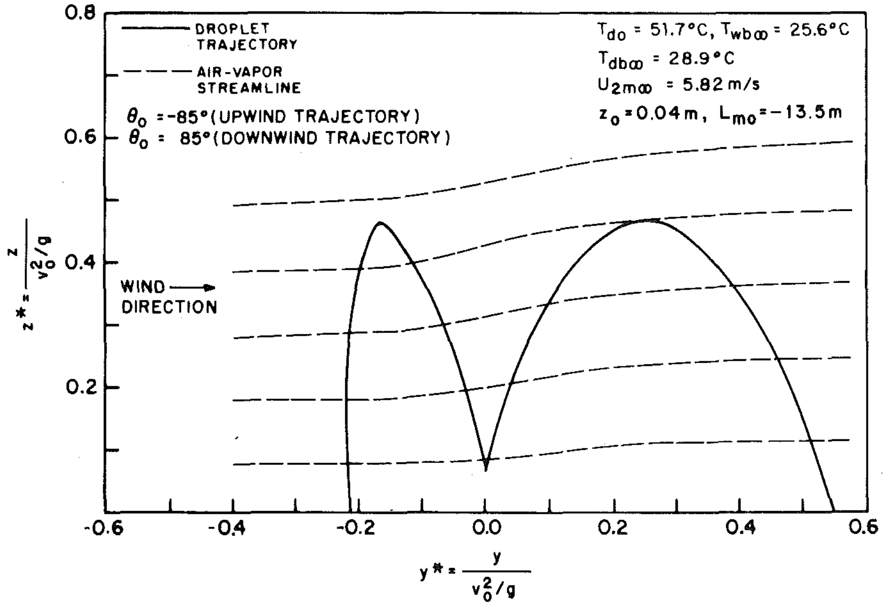

Fig. 5 Air-vapor streamlines near centerline of PSM for high wind (elevation view)

though not shown, exhibit similar behavior to the absolute humidity profiles.

Figure 5 shows PSM droplet trajectories and air-vapor streamlines for high wind conditions. One observes the substantial distortion of the droplet trajectories at high wind whereas droplet drag on the air causes little deflection of the air-vapor streamlines. Streamline spacing is wider downwind of the spray than upwind indicating that no significant entrainment has taken place. Absolute humidity and dry-bulb temperature profiles develop more slowly at higher wind speeds. The greater air flow through the spray at high wind results in local conditions closer to ambient conditions.

Comparisons with Data

The present model was compared with data [15] obtained for the Spraco 1751 nozzle in an outdoor laboratory facility located at the Richmond Field Station, University of California at Berkeley. The spray produced by this nozzle differs from that produced by the PSM in that the droplets exhibit a pronounced size distribution and are ejected at different angles depending on their size and discharge direction (upwind or downwind). The nozzle was mounted 1.52 m (5.0 ft) above the pond surface. The flow rate of water through the nozzle was 200.6 l/min (53.0 gal/min) at a nozzle pressure of 51.0 KPa (7.4 psig). The maximum height of the spray above the pond at this nozzle pressure and zero wind speed is 4.0 m, and the maximum spray radius at the pond surface is 4.9 m. To collect the sprayed water, catch pans were placed on the pond surface along the longitudinal axis (see Fig. 1). Cold spray temperatures were measured in the catch pans for different wind speeds, ambient psychrometric conditions and droplet discharge temperatures.

Five discrete droplet diameters from the measured size distribution, their discharge angles, and the mass fraction of the total spray flow rate for each size, were used as input to the model [11].

In the model, droplets were discharged from ten sites around the nozzle perimeter. All five droplet sizes were discharged from each site.

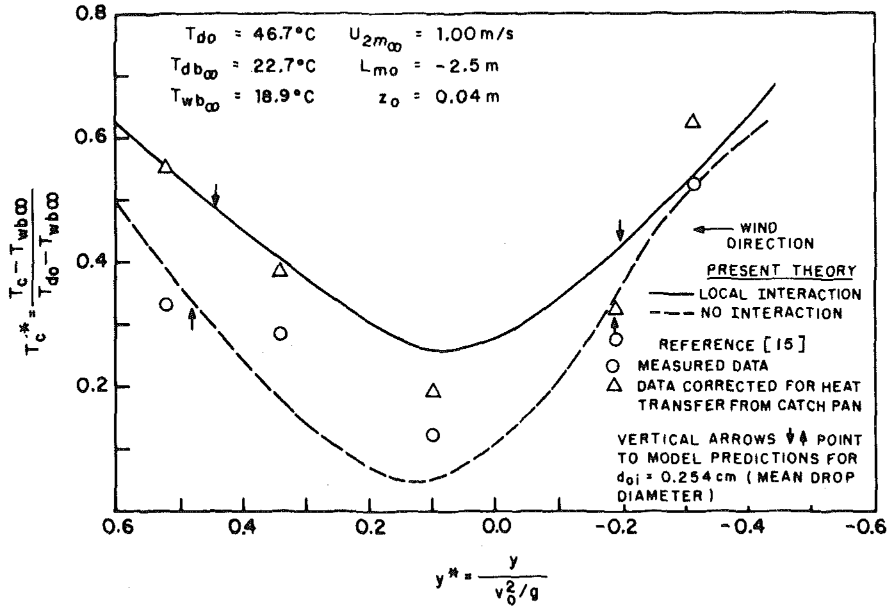

Fig. 6 Centerline droplet return temperature for Spraco 1751 nozzle ($U_{2m\infty}$ = 1.00 m/s)

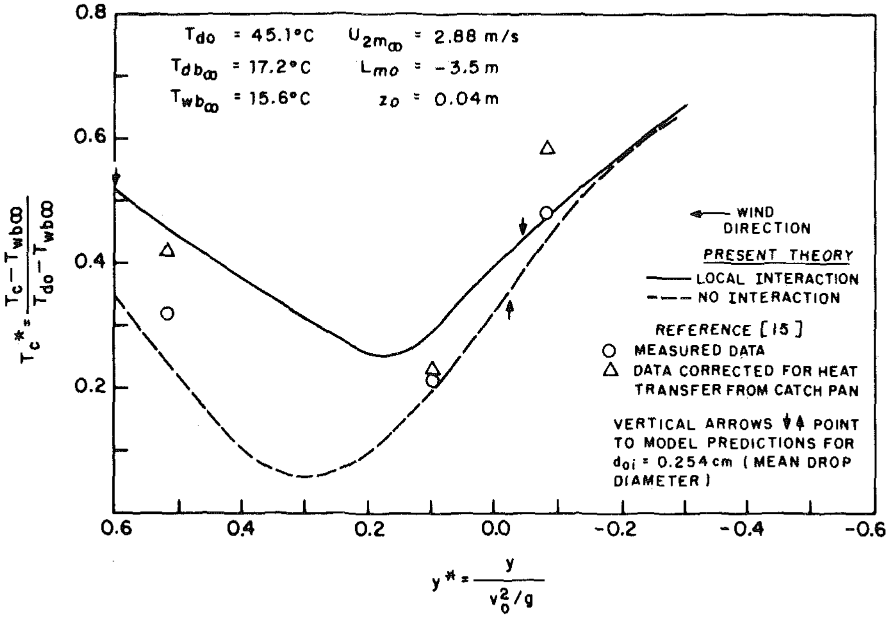

Fig. 7 Centerline droplet return temperature for Spraco 1751 nozzle ($U_{2m\infty}$ = 2.88 m/s)

The discharge velocity v_{0i}, for each droplet size is given by:

$$v_{0i} = v_{0z}/\sin \phi_i \qquad (21)$$

where

v_{0z} = initial vertical component of droplet velocity.

The initial vertical velocity component of the droplets discharged by ramp-bottom swirl nozzles (e.g., Spraco 1751) is a constant for all droplet sizes at a given spray flow rate, and is found empirically. For the Spraco 1751 nozzle discharging 200.6 1/min, v_{0z} = 8.093 m/s, as given by Chen [15].

For all model predictions, the atmosphere was assumed to be unstable under strong solar insolation. The surface roughness was set at z_0 = 0.04 m (30 cm high weeds). These assumptions were made in the absence of any specification of atmospheric turbulence conditions in the data.

Figures 6 and 7 are example comparisons between predicted and measured values of dimensionless cold spray temperature ($T_c^* = (T_c - T_{wb\infty})/(T_{do} - T_{wb\infty})$) of the water collected by the catch pans versus dimensionless distance ($y^* = yg/v_0^2$) along the spray centerline in the wind direction (y-axis). Additional comparisons of model predictions with data can be found in [11]. Also shown is the same data corrected for heat and mass transfer losses from the water in the catch pans [15].

The no-interaction theory, depicted by the dashed curves, gives the maximum amount of cooling that can be experienced by the droplets under the given ambient air conditions and wind speed. That is, the environment of the drops during their entire time of flight is ambient-air absolute humidity, dry-bulb temperature and velocity. The no-interaction predictions were obtained from the lowest order droplet solutions in the computer generated results.

In general, the local interaction theory shows good agreement with the corrected data, while the no-interaction theory predicts more cooling than the measured data. Since the local air in the spray domain is progressively heated and humidified as it passes through the spray, it is expected that the droplets do not experience the amount of cooling predicted by the no-interaction theory. This is indicated by the data.

Equal size droplets ejected upwind and downwind from the nozzle at the same discharge angle will not be cooled by equal amounts. The droplet ejected upwind will experience a large relative velocity to the wind and see air close to ambient conditions. A large relative velocity translates into a large Reynolds number and greater convective and evaporative heat transfer from the upwind droplet. Local air close to ambient conditions also results in greater heat transfer from the upwind droplet. The downwind droplet experiences a smaller relative velocity to the local wind and substantially heated and humidified local air. It therefore experiences less cooling. Since the downwind droplets were discharged at a lower angle, one would expect even less cooling than for equal upwind and downwind discharge angles. This results from the shorter time of flight at smaller discharge angles. The up and down arrows in Figs. 6 and 7 show the cooling experienced by a droplet of initial diameter equal to 0.254 cm (mean size drop). In each case, the downwind drop experienced less cooling (higher $T_c{}^*$) than the upwind drop. It may also be noticed that the points at which the droplets strike the pond surface are shifted to the right (against the wind) if one takes local interaction into account. This effect is due to the blockage of incoming air by the spray, slowing down the air due to momentum exchange with the droplets. The decreased drag on the drops resulting from the lower air velocity allows the drops to strike the pond further upwind.

Conclusions

A three-dimensional model that examines the detailed two-phase flow field of a spray unit has been presented. The model is capable of predicting the local properties of both the air-vapor phase and the drops in the entire domain of the spray without recourse to design-dependent empirical factors.

The model was used to generate solutions for the spray characteristics of a single PSM spray. At low wind ($U_{2m\infty} = 1.16$ m/s), significant entrainment of ambient air by the spray takes place, while at high wind ($U_{2m\infty} = 5.82$ m/s) less air interacts with the spray than initially enters the spray domain. Theoretical predictions of the model compare favorably with experimental data on centerline droplet return temperature for the Spraco 1751 nozzle.

The new model for spray units can be extended to determine the cooling performance of a pass of sprays aligned in the wind direction. The performance of an entire spray canal can be obtained by incorporating the model for a pass of sprays into a system model.

Acknowledgment

This work was supported by the National Science Foundation—Grant No. ENG. 78-20709. Appreciation is extended to the City University of New York Computer Center, for the use of their facilities. The above work was done in partial fulfillment of the requirements of the Ph.D. degree of S. Palaszewski from the School of Engineering of the City College of the City University of New York.

References

1 Ryan, P. J., and Myers, D. M., "Spray Cooling: A Review of Thermal Performance Models," *Proceedings of the American Power Conference*, Vol. 38, 1976, pp. 1473–1481.

2 Soo, S. L., "Power Spray Cooling—Unit and System Performance," ASME Paper No. 75-WA/Pwr-8, Nov. 1975.

3 Elgawhary, A. M., "Spray Pond Mathematical Model for Cooling Fresh Water and Brine," Ph.D. Dissertation, Oklahoma State University, Stillwater, Aug. 1969.

4 Frediani, H. A., and Smith, N., "Mathematical Model for Spray Cooling Systems," ASME *Journal of Engineering for Power*, Vol. 99, No. 2, Apr. 1977, pp. 279–283.

5 Berger, M. H., and Taylor, R. E., "An Atmospheric Spray Cooling Model," *Environmental Effects of Atmospheric Heat/Moisture Releases*, The Second AIAA/ASME Thermophysics and Heat Transfer Conference, Palo Alto, Calif., May 1978, pp. 59–64.

6 Porter, R. W., and Chen, K. H., "Heat and Mass Transfer from Spray Canals," ASME JOURNAL OF HEAT TRANSFER, Vol. 96, No. 3, Aug. 1974, pp. 286–291.

7 Chen, K. H., and Trezek, G. J., "Spray Energy Release (SER) Approach to Analyzing Spray System Performance," *Proceedings of the American Power Conference*, Vol. 38, 1976, pp. 1435–1448.

8 Chaturvedi, S., and Porter, R. W., "Air-Vapor Dynamics in Large-Scale Atmospheric Spray Cooling Systems," *Journal of Fluids Engineering*, Vol. 100, No. 1, March 1978, pp. 65–72.

9 Porter, R. W., Jain, M., and Chaturvedi, S. K., "Unit Thermal Performance of Atmospheric Spray Cooling Systems," ASME JOURNAL OF HEAT TRANSFER, Vol. 102, No. 2, May 1980, pp. 210–214.

10 Ranz, W. D., and Marshall, W. R., Jr., "Evaporation from Drops," *Chemical Engineering Progress*, Vol. 48, No. 3, February 1952, pp. 141–146, 173–180.

11 Palaszewski, S. J., "An Air-Vapor-Droplet Local Interaction Model for Spray Units," Ph.D. Dissertation, The City University of New York, New York, 1980.

12 Wallis, G. B., *One-Dimensional Two-Phase Flow*, McGraw Hill, New York, 1969.

13 Panofsky, H. A., "The Atmospheric Boundary Layer Below 150 Meters," *Annual Review of Fluid Mechanics*, Vol. 6, 1974, pp. 147–177.

14 Wilson, D. C., "Thermal Performance of Powered Spray Modules," Masters Thesis, University of Illinois, Urbana-Champaign, 1972.

15 Chen, K., "Heat and Mass Transfer from Power Plant Spray Cooling Ponds," Doctoral Dissertation, University of California, Berkeley, 1975.

B. Farouk[1]
Graduate Student.

S. İ. Güçeri
Assistant Professor.

Mechanical and Aerospace Engineering Department,
University of Delaware,
Newark, Del. 19711

Natural Convection from a Horizontal Cylinder—Laminar Regime

A finite-difference numerical method has been adopted to generate flow patterns and heat transfer characteristics for laminar, steady-state, two-dimensional natural convection around a circular cylinder submerged in an unbounded Boussinesq fluid. The approach allows the use of nonuniform as well as uniform specified temperature and heat flux distributions over the cylindrical surface. Part of the results are generated for reverse convective flows with recirculation zones which occur when part of the cylinder is below the ambient temperature while the remaining part is above. The results for uniform temperature boundary condition are in good agreement with the experimental data and other solutions available in literature.

Introduction

Natural convection from a horizontal cylinder has been the subject of several research studies. This configuration has applications over a wide range of engineering problems. Empirical relations, which are based on extensive experimental data have been presented by McAdams [1]. Temperature fields around heated single horizontal cylinders have been measured by interference fringes [2]. Earlier, photographs based on the same technique, illustrating the temperature field around horizontal cylinders in laminar flow have been obtained by Eckert and Soehngen [3]. Attempts were also made to analytically predict the local and overall heat transfer rates from the surface of heated, horizontal cylinders. Analytical studies are mostly based on the boundary layer approach. In general, these studies concern the nature of the portions of such flows attached to the surface. The subsequent regions where the flow may separate from the surface and rise as a buoyant plume were not considered in detail. One of the earliest works in this area was by Hermann [4] who obtained a solution for the differential equations under the assumption of a thin (as compared with the cylinder diameter) heated laminar layer for diatomic gases and small temperature differences. Due to the boundary layer approximation, his results are valid for moderately high Grashof numbers (10^4 to 3×10^8). Merk and Prins [5] presented analytical results of the heat transfer around horizontal cylinders and spheres. Chiang, et al. [6, 7] used a Blasius series expansion method to predict the heat transfer coefficients for laminar, natural convection from horizontal cylinders and spheres. Nakai and Okazaki [8] studied free convection from horizontal wires at uniform temperatures for the case when the thickness of the boundary layer around the cylinder is sufficiently large compared with its diameter. The near and far fields around the cylinder were considered separately. A comprehensive review of boundary layer flow with body forces including nonisothermal surfaces is given by Ostrach and Moore [9]. An account is given of the boundary layer analysis of the vertical flat plate problem with prescribed heat flux and the vertical cylinder where the surface temperature is permitted to vary linearly with the axial coordinate. In the latter case a similarity solution becomes possible. Churchill and Chu [10] presented correlating equations for both laminar and turbulent flow conditions, based on boundary-layer theory and compilation of experimental data. Kuehn and Goldstein [11] gave expressions for average Nusselt numbers over a wide range of Rayleigh numbers as a special case of correlating equations for natural convection between concentric horizontal cylinders.

Numerical solutions of the boundary layer equations for natural convection around horizontal cylinders have been obtained by Mucogulu and Chen [12], Merkin [13] and Fujii, et al. [14].

As in the present work, no boundary layer approximations were made in the finite element approach of Holster and Hale [15] and in the finite difference approach of Kuehn and Goldstein [16]. In the latter, the numerical solutions are compared with extensive experimental data for the temperature and velocity fields as well as the Nusselt number distribution.

This study is primarily concerned with the natural convection heat transfer from a horizontal circular cylinder with uniform and nonuniform boundary conditions, placed in an unbounded Boussinesq fluid. The surface temperature distribution is considered in such a way that the resulting buoyancy forces vary in magnitude around the cylinder. If this variation is large enough, flow reversal may occur. These temperature variations are frequently observed in solar energy applications such as the Thermal Wall Panel passive heating concept [17, 18], where the thermal storage materials are contained in horizontal cylinders and partially subjected to solar irradiation. Due to the complex flow fields, boundary layer approximations lose their validity and the complete Navier-Stokes and energy equations need to be solved. The special case of isothermal cylinder solutions are compared with available data in literature to verify the accuracy of the approach.

Problem Statement

The steady-state, two-dimensional laminar natural convection from horizontal cylinders is governed by the three conservation principles, viz., the conservation of mass, the conservation of momentum and the conservation of energy. The equations describing these principles are as follows:

Conservation of mass,

$$\frac{\partial v_r}{\partial r} + \frac{v_r}{r} + \frac{1}{r}\frac{\partial v_\theta}{\partial \theta} = 0 \tag{1}$$

conservation of momentum, r − direction,

$$\rho\left[v_r\frac{\partial v_r}{\partial r} + \frac{v_\theta}{r}\frac{\partial v_r}{\partial \theta} - \frac{{v_\theta}^2}{r}\right] = -\frac{\partial p}{\partial r} + \mu\left[\frac{\partial^2 v_r}{\partial r^2} + \frac{1}{r}\frac{\partial v_r}{\partial r} + \frac{1}{r^2}\frac{\partial^2 v_r}{\partial \theta^2} - \frac{v_r}{r^2} - \frac{2}{r^2}\frac{\partial v_\theta}{\partial \theta}\right] - g\rho\beta(T' - T_\infty)\cos\theta \tag{2}$$

conservation of momentum, θ − direction,

$$\rho\left[v_r\frac{\partial v_\theta}{\partial r} + \frac{v_\theta}{r}\frac{\partial v_\theta}{\partial \theta} + \frac{v_r v_\theta}{r}\right] = -\frac{1}{r}\frac{\partial p}{\partial \theta} + \mu\left[\frac{\partial^2 v_\theta}{\partial r^2} + \frac{1}{r}\frac{\partial v_\theta}{\partial r} + \frac{1}{r^2}\frac{\partial^2 v_\theta}{\partial \theta^2} - \frac{v_\theta}{r^2} + \frac{2}{r^2}\frac{\partial v_r}{\partial \theta}\right] + g\rho\beta(T' - T_\infty)\sin\theta \tag{3}$$

---

[1] Presently, Assistant Professor, Drexel University, Philadelphia, Pa.

Contributed by the Heat Transfer Division for publication in the JOURNAL OF HEAT TRANSFER. Manuscript received by the Heat Transfer Division, August 11, 1980.

conservation of energy,

$$\rho c_p \left[v_r \frac{\partial T}{\partial r} + \frac{v_\theta}{r}\frac{\partial T}{\partial \theta}\right] = k\left[\frac{\partial^2 T}{\partial r^2} + \frac{1}{r}\frac{\partial T}{\partial r} + \frac{1}{r^2}\frac{\partial^2 T}{\partial \theta^2}\right] \tag{4}$$

These equations can be put into a more convenient form by using the definitions for the stream function and vorticity as

$$v_r = \frac{1}{\rho r}\frac{\partial \psi}{\partial \theta}; \quad v_\theta = -\frac{1}{\rho}\frac{\partial \psi}{\partial r} \tag{5}$$

and

$$\omega = \frac{1}{r}\left[\frac{\partial}{\partial r}(r v_\theta) - \frac{\partial v_r}{\partial \theta}\right] \tag{6}$$

Also due to variable temperature boundary condition, it becomes impossible to define a meaningful Grashof number; therefore, the expressions are not non-dimensionalized. Substituting the expressions given by equations (5) into equation (6), the following expression is obtained:

$$\frac{\partial}{\partial r}\left[\frac{r}{\rho}\frac{\partial \psi}{\partial r}\right] + \frac{\partial}{\partial \theta}\left[\frac{1}{\rho r}\frac{\partial \psi}{\partial \theta}\right] = -r\omega \tag{7}$$

The two momentum equations, i.e., equations (2) and (3) can be reduced to a single equation by using the definitions of stream function and vorticity. Following substitutions, equation (2) is differentiated with respect to θ and equation (3) is differentiated with respect to r. After adding and simplifying,

$$\left[\frac{\partial}{\partial r}\left(\omega\frac{\partial \psi}{\partial \theta}\right) - \frac{\partial}{\partial \theta}\left(\omega\frac{\partial \psi}{\partial r}\right)\right] - \left[\frac{\partial}{\partial r}\left(r\frac{\partial(\mu\omega)}{\partial r}\right)\right.$$
$$\left. + \frac{\partial}{\partial \theta}\left(\frac{1}{r}\frac{\partial(\mu\omega)}{\partial \theta}\right)\right] - g\rho\beta\left[\frac{\partial T}{\partial \theta}\cos\theta + \frac{\partial T}{\partial r} r \sin\theta\right] = 0 \tag{8}$$

Also the energy equation with proper substitutions becomes,

$$\left[\frac{\partial}{\partial r}\left(T\frac{\partial \psi}{\partial \theta}\right) - \frac{\partial}{\partial \theta}\left(T\frac{\partial \psi}{\partial r}\right)\right] - \left[\frac{\partial}{\partial r}\left(\frac{k}{c_p} r\frac{\partial T}{\partial r}\right) + \frac{\partial}{\partial \theta}\left(\frac{k}{c_p}\frac{1}{r}\frac{\partial T}{\partial \theta}\right)\right] = 0 \tag{9}$$

The advantage of the stream function—vorticity formulation is that the pressure variable is eliminated and the number of equations to be solved is reduced to three. The solution to equations (7, 8) and (9), with appropriate boundary conditions, yields the desired distribution of ψ, ω and T in the flow field.

Boundary Conditions

Solution of elliptic equations requires that the conditions be specified along the entire boundary which encloses the flow field. In the present problem, two of the most important boundary sections are the cylindrical wall and a pseudo boundary sufficiently far away from the cylinder. A third section may be the vertical symmetry plane which exists only for symmetrical wall temperature or heat flux boundary conditions. However, in this study, even for such boundary conditions the entire flow field is considered and the need for the boundary conditions on the symmetry plane is eliminated. The two boundary sections are handled as follows:

a. Boundary Conditions on the Surface of the Cylinder. Temperature is specified over this boundary section. For the purpose of demonstrating the effects of nonuniform temperature distribution, an artificial temperature generation function is formulated as

$$T|_R = \sqrt{T_0^2 - e^2\cos^2\theta} - T_\infty + e\sin\theta \tag{10}$$

With this expression, the temperature distribution can be envisioned as being proportional to the spacing between two concentric/eccentric circles, having radii proportional to T_0 and T_∞, respectively. When the eccentricity factor e is zero, the case corresponds to an isothermal cylinder. It is possible that for sufficiently large values of e, the two circles intersect each other, indicating that the cool side of the cylinder is at a lower temperature than the ambient while the remaining section is higher.

Since the cylinder surface is assumed to be nonpermeable, it follows that for the stream function

$$\psi|_R = 0 \quad \text{for} \quad 0 \le \theta \le 2\pi \tag{11}$$

The boundary condition for the vorticity is not quite so easy to specify since it requires information on the gradients of velocities which are not known a priori. An expression for the vorticity boundary condition can be obtained by expanding the stream function near the wall, using a three term Taylor series and making use of the continuity and the no-slip condition. It is given as

$$\omega|_R = \frac{-2\psi}{\rho(\Delta r)^2} \tag{12}$$

where ψ is the value of the stream function at a short distance Δr into the fluid. An alternate boundary condition for vorticity at the wall which is based on the assumption that the gradients with respect to θ are negligible in the vicinity of the cylinder surface is presented in the Appendix. The formula for the vorticity at the wall is obtained by expressing its value in terms of the dependent variable values at and adjacent to the cylinder surface.

b. Boundary Conditions at the Far Field. The necessity to limit the size of the solution domain requires that a pseudo boundary be defined in the far field. To establish these conditions, a procedure suggested in reference [15] is followed. This approach considers the horizontal cylinder as a pump whereby the pumping is provided by the buoyancy forces. Any realistic model must allow for fluid to cross the pseudo boundary. It is assumed that the velocity component in the circumferential direction, along the pseudo boundary is zero implying that in the far field, all flow must be in the radial direction. If the domain is a large circle, the stream lines become normal to the boundary hence the boundary conditions for the stream function and vorticity become

$$\left.\frac{\partial \psi}{\partial r}\right|_{R_\infty} = 0; \quad \left.\frac{\partial \omega}{\partial r}\right|_{R_\infty} = 0 \quad 0 \le \theta \le 2\pi \tag{13}$$

and temperature of the fluid drawn into the flow field is the same as the ambient temperature. However, a generalization along the entire boundary cannot be made since the temperature distribution along

Nomenclature

c_p = specific heat at constant pressure
e = eccentricity factor for temperature distribution
g = gravitational acceleration
Gr = Grashof Number, $8\rho^2 g\beta R^3(T_0 - T_\infty)/\mu^2$
Gr$_m$ = mean Grashof Number, $8\rho^2 g\beta R^3(T_m\ T_\infty)/\mu^2$
k = thermal conductivity of fluid
Nu = Nusselt number
p = pressure
Pr = Prandtl number
r = radial coordinate
R = radius of circular cylinder
Ra = Rayleigh number (Gr · Pr)
R_∞ = radius of pseudo boundary
T' = local temperature
T_m = mean temperature at the surface
T_∞ = ambient temperature
T_0 = reference temperature as used in equation (10)
$T = T' - T_\infty$
v_r = radial velocity component
v_θ = circumferential velocity component
β = thermal coefficient of volume expansion
θ = circumferential (angle) coordinate
μ = dynamic fluid viscosity
ρ = density
ψ = stream function
ω = vorticity component parallel to cylinder axis

Subscripts

N,S,E,W,NE,SE,NW,SW = compass point location of nodes with respect to node P
n,s,e,w = compass point locations of the integration cell

the section of the boundary where the *plume* crosses, is not known a priori. It is assumed that the temperature gradient normal to the pseudo boundary is zero implying that the heat carrying action of the fluid is done purely by convection rather than by conduction, i.e.,

$$\left.\frac{\partial T}{\partial r}\right|_{R_\infty} = 0; \quad 0 \le \theta \le 2\rho \tag{14}$$

Solution Procedure

The equations of the previous sections are transformed into difference equations by using a finite-difference method in polar coordinates, presented by Gosman, et al. [19] and recently applied to forced flow across tube bundles by Launder and Massey [20]. A successive-substitution technique is employed to solve the finite difference equations. Instead of using standard Taylor series expansions, the finite difference equations are obtained by integration over finite cells. After creating a mesh in r and θ, these cells are obtained around each nodal point P through the half-distance points (Fig. 1). This method ensures that the conservation laws are obeyed over arbitrarily large or small portions of the field and it lends itself better to physical interpretation and hence to ease of understanding. Since the details of the procedure are given in reference [19], only the integration of the source terms will be presented briefly. The integral of the source term for T is zero. For ψ, following the assumption that ω is uniform over the integration cell,

$$I_{\text{sor}}^{\psi} = \omega_p(r_E - r_W)(\theta_N - \theta_S)r_p/4 \tag{15}$$

For vorticity, ω, the source term for equation (8) becomes

$$I_{\text{sor}}^{\omega} = -g\rho\beta \int_{r_w}^{r_e} \int_{\theta_s}^{\theta_n} r \frac{\partial T}{\partial r} \sin\theta \, d\theta \, dr - g\rho\beta \int_{r_w}^{r_e} \int_{\theta_s}^{\theta_n} \frac{\partial T}{\partial \theta} \cos\theta \, d\theta \, dr \tag{16}$$

The above equation can be integrated by parts. After integrating once, the temperature T appears as a multiplier within the integrand; it is then assigned the value T_P. Also noting that,

$$\cos\theta_n \simeq (\cos\theta_N + \cos\theta_P)/2, \text{ etc.,}$$

the discretized form of the source term integral for vorticity becomes

$$\begin{aligned} I_{\text{sor}}^{\omega} = \frac{g\rho\beta}{8} \{ & (\cos\theta_N - \cos\theta_S)[(r_E + r_P)(T_E + T_P) \\ & - (r_P + r_W)(T_W + T_P) - 2T_P(r_E - r_W)] \\ & - (r_E - r_W)[(\cos\theta_N + \cos\theta_P)(T_N + T_P) \\ & - (\cos\theta_S + \cos\theta_P)(T_S + T_P) - 2T_P(\cos\theta_N - \cos\theta_S)]\} \end{aligned} \tag{17}$$

These results, along with similar derivations for the diffusive and convective terms can be organized in such a way that each variable can be expressed as a successive substitution formula [19].

In the point iteration process employed here, the grid is systematically scanned node by node and the successive substitution formula is used to update the values of the variables (ψ, ω, T) at each node. The iteration sweep for the region $0 \le \theta \le \pi$ was carried out in the anti-clockwise direction and for the region $\pi \le \theta \le 2\pi$ it was carried out in the clockwise direction. When a symmetry plane is not considered in the flow domain, the above sweep directions were found to give better convergence. For a typical problem, with zero initial distributions of the dependent variables, converged solutions were obtained after about 400 iterations requiring a total of about 30 minutes of CPU time on a Burroughs' 7700 computer.

Results and Discussion

The nonlinear coupled partial differential equations are solved by considering a grid of 41 × 100 ($r \times \theta$) for the entire domain. The node spacing in the r-direction is reduced by a factor of 2 for $R \le r \le (R + R_\infty)/2$ region as compared to the remaining region to obtain a better accuracy in evaluating the local Nusselt number given as

$$\text{Nu}(\theta) = \left| \frac{2R}{T|_R} \left.\frac{\partial T}{\partial r}\right|_R \right| \tag{18}$$

which is calculated by using a two-point difference scheme for the temperature gradient at the wall. An important parameter for the finite difference method described herein is R_∞/R, the ratio of the radius of the pseudo boundary to the cylinder radius. A ratio of $R_\infty/R = 8$ was used in obtaining the results presented for variable temperature boundary condition because the local and mean Nusselt numbers become independent of R_∞/R when $R_\infty/R > 6$.

For uniform temperature boundary condition consistent with reference [16], it was observed that for larger Rayleigh numbers the boundary layer becomes thinner necessitating a finer mesh close to the boundary but allowing smaller R_∞/R to be adequate. When R_∞/R is decreased without changing the number of nodal points in the r-direction, it automatically provided a finer mesh. For $\text{Ra} \le 10^4$, $R_\infty/R = 8$ was used but for larger Ra, it was gradually decreased to 4 for the case of $\text{Ra} = 10^7$. All results were generated by considering air as the fluid with $\text{Pr} = .721$. Figure 2 shows the distribution of the local Nusselt number and its comparison with those obtained by other researchers. A 5°C difference was used between the uniform wall temperature and the ambient temperature. The agreement is quite satisfactory. Figure 3 shows the effect of the Rayleigh number on the angular distribution of the Nusselt number for cylinders with uniform wall temperature. Figure 4 indicates the variation of the average Nusselt number with Rayleigh number and its comparison with data from [16]. Temperature and flow field plots are not presented for the isothermal case since they are given in [16] along with comparison of experimental and numerically calculated temperature fields. Agreement of our results with those presented in [16] is satisfactory.

The main advantages of the present approach are that it can easily take into account the nonuniform boundary conditions and flows with recirculation. The results for natural convection from a cylinder with

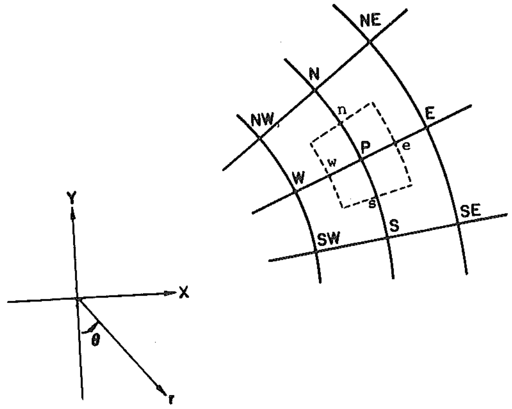

Fig. 1 Typical node "*P*" with its surrounding integration cell

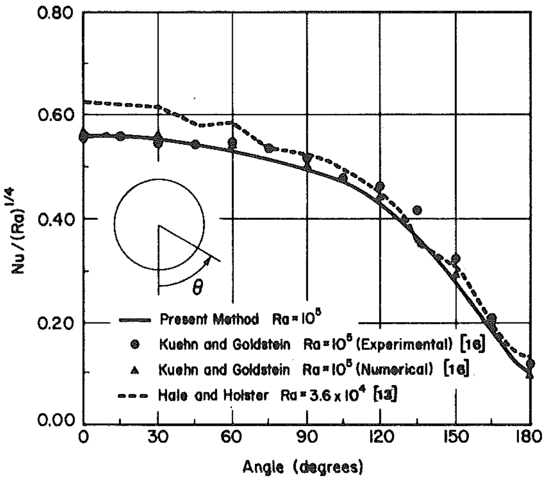

Fig. 2 Distribution of local heat transfer rates for an isothermal cylinder

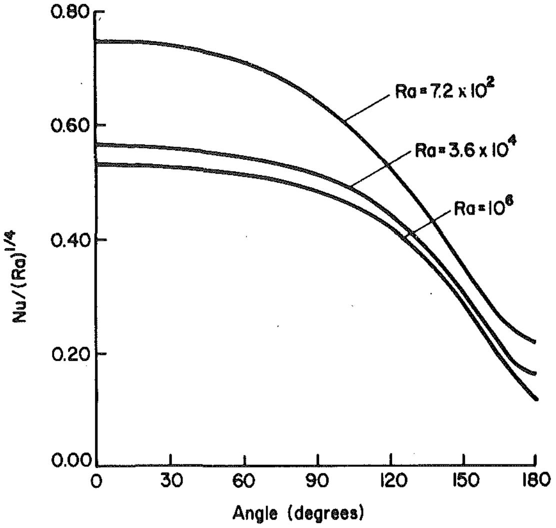

Fig. 3 Influence of Rayleigh number on local heat transfer coefficients for an isothermal cylinder

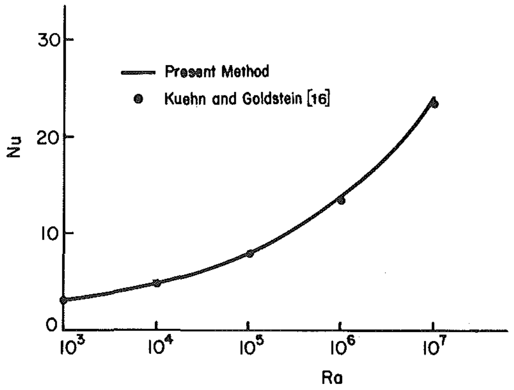

Fig. 4 Average Nusselt number as a function of Rayleigh number for an isothermal cylinder

prescribed nonuniform wall temperature are investigated with two cases, where the degree of nonuniformity is varied by the eccentricity factor e as introduced earlier. Figures 5 and 6 show the temperature and stream function distribution in the case where the difference between the ambient and surface temperatures vanish at the $\theta = 3\pi/2$ point. The surface temperature distribution is given by equation (10) with $e = 5.0°C$, $T_0 = 23.85°C$ and $T_\infty = 18.85°C$. The mean Grashof number is found to be $Gr_m = 50{,}000$. Comparing Figs. 5 and 6 with figures in [16], it is observed that the plume shifts to the right because of higher surface temperature of the cylinder on this side. Since no point on the cylinder surface is colder than the ambient temperature, no recirculation was observed for this case. Recirculation was not found for the isothermal cylinder as well. In the next example, a value of $e = 15.0°C$ was used along with the same values of T_0 and T_∞ used previously. The resulting surface temperature is such that reverse buoyancy forces occur on the two sides of the cylinder. On the cylindrical surface the largest positive and negative temperature differences with the ambient are 20°C and −10°C at the $\theta = \pi/2$ and $\theta = 3\pi/2$ locations respectively. The isotherms for this case are presented in Fig. 7. The streamlines in Fig. 8 indicate that recirculation is pronounced. For the above two examples, a meaningful definition of the Nusselt number becomes difficult to make. The local Nusselt number as given by equation (18) goes to infinity in regions where the temperature difference between the surface and the ambient vanishes. The Nusselt number may again vanish when $\partial T/\partial r|_R$ becomes close to zero. The polar plots of the local Nusselt number distribution for the above two cases as well as for the uniform surface temperature case are given in Fig. 9 for the purpose of comparison.

With this study, the use of a finite difference technique [19] in solving natural convection problems is demonstrated. The results

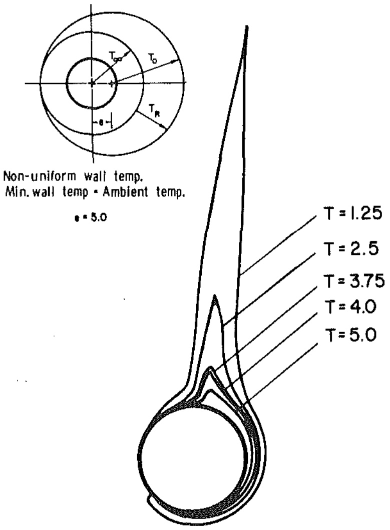

Fig. 5 Isotherms for natural convection with prescribed nonuniform surface temperature, $e = 5.0$, $T_0 = 23.85°C$, $T = 18.85°C$

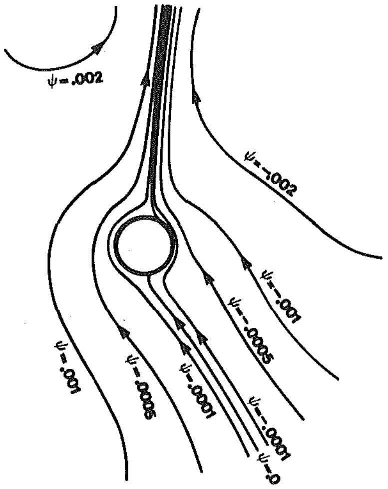

Fig. 6 Streamlines for the case of Fig. 5

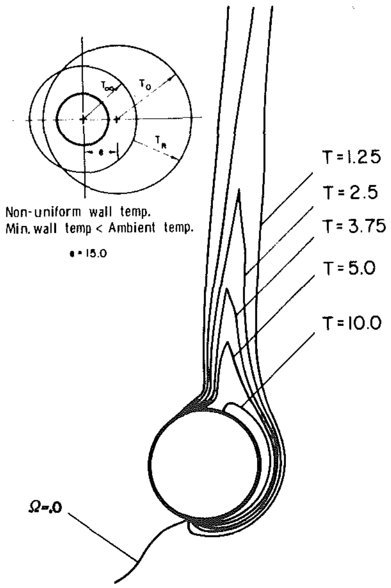

Fig. 7 Isotherms for natural convection with prescribed nonuniform surface temperature, $e = 15.0$, $T_0 = 23.85°C$, $T = 18.85°C$

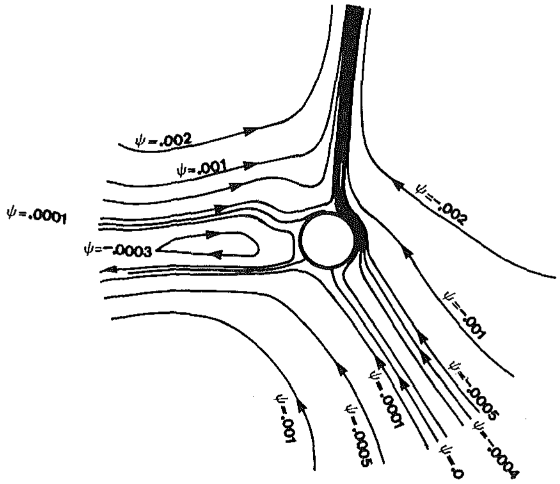

Fig. 8 Streamlines for the case of Fig. 7

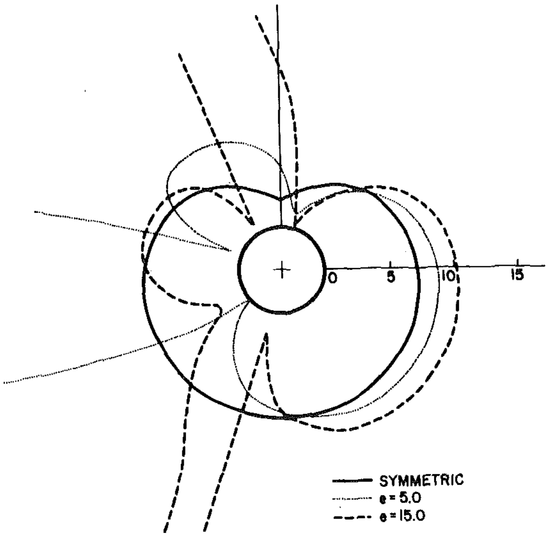

Fig. 9 Polar plots of the local Nusselt number distributions for natural convection with $e = 0.0$, $e = 5.0$ and $e = 15.0$

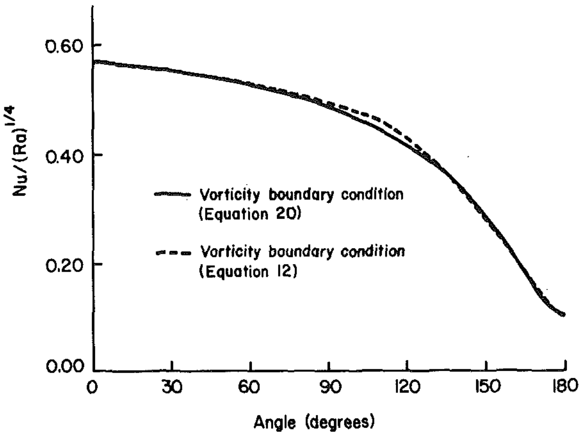

Fig. 10 Comparison of the distribution of local heat transfer rates for an isothermal cylinder with vorticity boundary conditions given by equation (12) and equation (20)

agree well with the available data and other solutions. The method presented works efficiently and quite satisfactorily in analyzing the regions such as the plume and recirculation zones if they exist. Furthermore, nonuniform boundary conditions which occur in many engineering problems can be accounted for. The present method also provides far more detail about the flow than is usually obtainable in an experimental study.

Acknowledgments

The authors thank Mr. Joseph Quigley for his expert help in computer graphics and Mr. Mark Deshon for his carefully done drawings.

References

1 McAdams, W. H., *Heat Transmission*, 3d. ed., McGraw-Hill, New York, 1954.

2 Kennard, R. B., *Natl. Bur. Standards J. Research*, 8,787, 1932, "Temperature, Its Measurement and Control in Science and Industry," Reinhold, New York, 1941, pp. 685–706.

3 Eckert, E. R. G., and Soehngen, E., "Studies on Heat Transfer in Laminar Free Convection with Zehnder-Mach Interferometer," USAF Tech. Report 5747, Dec. 1948.

4 Hermann, R., "Heat Transfer by Free Convection from Horizontal Cylinders in Diatomic Gases," NACA TM 1366, 1954.

5 Mark, H. J., and Prins, J. A., "Thermal Convection in Laminar Boundary Layers, I, II, III," *Applied Scientific Research*, Vol. 4A, 1953–54, pp. 11–24, 195–206, 207–224.

6 Chiang, T., and Kay, J., "On Laminar Free Convection From a Horizontal Cylinder," *Proceedings of 4th National Congress of Applied Mechanics*, 1962, pp. 1213–1219.

7 Chiang, T., Ossin, A., and Tien, C. L., "Laminar Free Convection From a Sphere," ASME JOURNAL OF HEAT TRANSFER, Vol. 86, 1964, pp. 537–542.

8 Nakai, S. and Okazaki, T., "Heat Transfer From a Horizontal Circular Wire at Small Reynolds and Grashof Numbers, Pts. I and II," *International Journal of Heat Mass Transfer*, Vol. 18, 1975, pp. 387–413.

9 Moore, F. .,K. (ed), *Theory of Laminar Flows*, Vol. 4, Princeton University Press, 1964.

10 Churchill, S. W., and Chu, H. H. S., "Correlating Equations for Laminar and Turbulent Free Convection from a Horizontal Cylinder," *International Journal of Heat Mass Transfer*, Vol. 18, 1975, pp. 1049–1053.

11 Kuehn, T. H., and Goldstein, R. J., "Correlating Equations for Natural Convection Heat Transfer Between Horizontal Circular Cylinders," *International Journal of Heat Mass Transfer*, Vol. 19, 1976, pp. 1127–1134.

12 Mucoglu, A., and Chen, T. S., "Analysis of Combined Forced and Free Convection Across a Horizontal Cylinder," *The Canadian Journal of Chemical Engineering*, Vol. 5, June 1977, pp. 265–279.

13 Merkin, J. H., "Free Convection Boundary Layers on Cylinders of Elliptic Cross-Section," ASME JOURNAL OF HEAT TRANSFER, Vol. 99, Aug. 1977, pp. 453–457.

14 Fujii, T., Fujii, M., and Matsunaga, T., "A Numerical Analysis of Laminar Free Convection Around an Isothermal Horizontal Circular Cylinder," *Numerical Heat Transfer*, Vol. 2, 1979, pp. 329–344.

15 Holster, J. L., and Hale, L. A., "Finite Element Simulation of Transient Free Convection From a Horizontal Cylinder," ASME Paper No. 79-HT-49.

16 Kuehn, T. H., and Goldstein, R. J., "Numerical Solution to the Navier-Stokes Equations for Laminar Natural Convection About a Horizontal Isothermal Circular Cylinder," *International Journal of Heat Mass Transfer*, 23, 1980, pp. 971–979.

17 Güçeri, S. İ., and Faunce, S. F., "Modeling of a Thermal Wall Panel Using Phase Change Material," *ENERGY—The International Journal*, Vol. 4, No. 4, Sept. 1979.

18 Faunce, S. F., Sliwkowski, J. J., and Güçeri, S. İ., "An Application of PCM in Passive Solar Systems," International Solar Energy Society Annual Meeting, Atlanta, May 1979. *Proceedings*.

19 Gosman, A. D., Pun, W. M., Runchal, A. K., Spalding, D. B., and Wolfshtein, M. W., *Heat and Mass Transfer in Recirculating Flows*, Academic Press, London, 1969.

20 Launder, B. E., and Massey, T. H., "The Numerical Prediction of Viscous Flow and Heat Transfer in Tube Banks," ASME JOURNAL OF HEAT TRANSFER, Vol. 100, 1978, pp. 565–571.

APPENDIX

An alternative to equation (12) can be derived as boundary condition for ω over the cylindrical surface by noting that the gradients near the boundary, along the θ-direction are negligible, when compared with those in the direction perpendicular to the surface. With this assumption, integrating equation (9) twice, substituting into equation (8) for the temperature, integrating the resulting equation twice and rearranging,

$$\omega = \left\{ \frac{g\rho\beta}{\mu} \frac{T}{r}\bigg|_R R^2 \sin\theta + R \frac{\omega}{r}\bigg|_R \right\} \ln r - \frac{g\rho\beta\sin\theta}{\mu} Rr \frac{\partial T}{\partial r}\bigg|_R$$

$$+ \omega|_R - R\frac{\partial \omega}{\partial r}\bigg|_R \ln R - \frac{g\rho\beta\sin\theta}{\mu} R^2 \frac{\partial T}{\partial r}\bigg|_R \ln R$$

$$+ \frac{g\rho\beta R^2 \sin\theta}{\mu} \frac{\partial T}{\partial r}\bigg|_R \qquad (19)$$

Finally, substituting for the vorticity in equation (7), performing the integration from the boundary surface to a point r adjacent in the flow field and making use of the no-slip condition yields

$$\omega|_R = \frac{\dfrac{r\omega}{r-R}\alpha + \dfrac{g\rho\beta\gamma R^2\sin\theta}{\mu} \dfrac{T - T|_R}{r-R} + \dfrac{\psi - \psi|_R}{\rho}}{\dfrac{R}{r-R}\alpha - \kappa} \qquad (20)$$

where

$$\alpha = \frac{r^2 + R^2}{4} \ln \frac{r}{R} + \frac{R^2 - r^2}{4}; \quad \kappa = \frac{R^2}{2} \ln \frac{R}{r} + \frac{r^2 - R^2}{4}$$

$$\gamma = \frac{3r^2 + R^2}{12} \ln \frac{r}{R} + \frac{R^3 - r^3}{9R}$$

In equation (20) ψ, ω and T are evaluated at the near wall node. The drawback of this formulation is that it is valid only if the angular derivatives of the dependent variables are negligible near the wall. A comparison of the local Nusselt number distribution around the cylinder for the case of Ra = 10^5 is given in Fig. 10 with both boundary conditions as given by equations (12) and (20).

ERRATUM

Erratum: C. E. Hickox, "Thermal Convection at Low Rayleigh Number from Concentrated Sources in Porous Media," published in the May 1981 issue of the *Journal of Heat Transfer*, pp. 232–236.

Figures 2, 5(*a*) and 8 were not reproduced properly for publication.

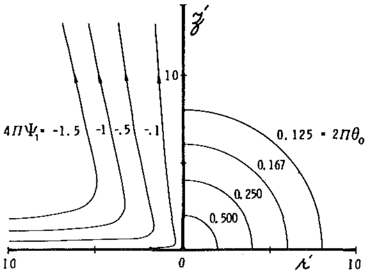

Fig. 2 Steady-state streamlines and isotherms for a point source at the base of a semi-infinite region ($L = k^{1/2}$)

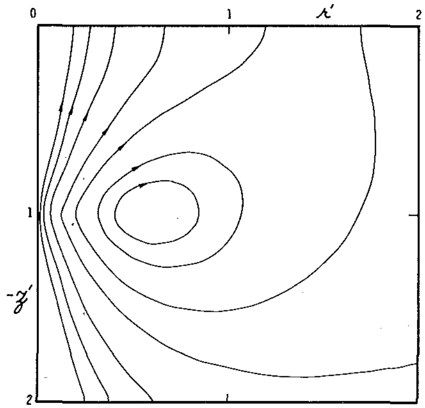

Fig. 5(*a*) Transient streamlines for a point source located below a permeable boundary (Ra = 0.5, $\tau = 0.1$. $L = D$, $\psi_1 \times 10^3 = 0.25, 0.5, 1, 2, 3, 4, 4.5$)

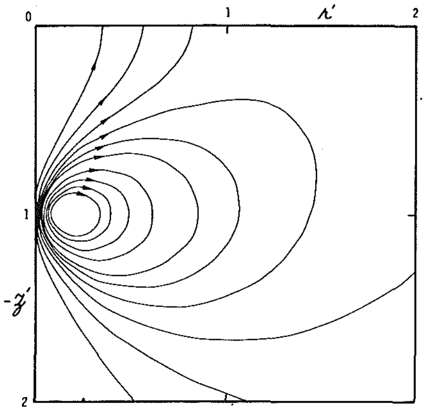

Fig. 8 Transient streamlines at one year for sub-seabed disposal of nuclear waste (Ra = 10^{-3}, $\tau = 4.8 \times 10^{15}$, $L = D$; $\psi_1 \times 10^{-4} = 1, 2, 3, 4, 5, 6, 7, 8, 9, 10, 12, 14$)

Transient Natural Convection Heat Transfer of Water with Maximum Density Effect and Supercooling

L. Robillard
P. Vasseur

Ecole Polytechnique,
Université de Montréal,
Department of Civil Engineering,
Montréal, P.Q., Canada, H3C 3A7

Transient two-dimensional laminar convective cooling of water in an enclosed rectangular cavity with a convective boundary condition is approached by a numerical method. The maximum density effect and supercooling are considered in order to understand the flow and temperature fields in a mass of water cooled to a temperature near its freezing point. The time dependent flow and temperature fields, mixed mean, center point, maximum wall temperature and the heat transfer rate on each wall are presented. The computations are performed mainly for the case of a square cavity but the influence of the aspect ratio of the cavity is also discussed.

1 Introduction

Many studies on natural convection heat transfer related to the cooling of a mass of water near its freezing point have been performed in the past [1–3]. Those studies were undertaken because of the importance of water in atmospheric and terrestrial problems. Furthermore, the fact that water is affected by a density anomaly near 4°C [4] introduces an additional complexity in the study of the transient natural convection heat transfer, the latter case being considerably different from that of a fluid without maximum density [5].

The effect of maximum density on the free convection induced by an isothermal vertical flat plate adjacent to a mass of cold water was first studied by Schechter [6]. The existence of dual motion (both up and down) in the boundary layer was demonstrated experimentally and theoretically and it was found that the resulting heat transfer coefficient was considerably affected by this particular flow motion. Because of their importance to certain freezing processes, a number of theoretical and experimental investigations were conducted on convective heat transfer occuring near an isothermal vertical flat plate [7, 8], between horizontal water layers [9–11], and inside enclosed cavities [12–17]. In all these investigations it was shown that the rates of heat transfer by free convection in water at 4°C are usually less than those occuring at other temperatures.

Most of the past investigations concerning the cooling of a mass of water have only been performed at temperatures above 0°C. However, it is well known [3] that water will normally supercool substantially below 0°C before the occurrence of ice nucleation. For instance, measurements by Dorsey [18] on the nucleation temperature in quiescent tap water show that the typical nucleation temperature is in the range of −4 to −7°C. The growth of ice inside supercooled water results in the formation of dentritic ice which may be responsible, under certain conditions, for the complete blockage of a water pipe subjected to a freezing environment [3, 13]. It is thus desirable to have a better understanding of the natural convection processes occuring during the supercooling of water.

The purpose of this investigation is to study numerically the transient two-dimensional laminar convection resulting from the cooling of a mass of water enclosed in a rectangular cavity subjected to convective boundary conditions. The cooling of water from the initial uniform temperature greater than 4°C passing through the maximum density point and finally in the supercooling range is considered. The present study is an extension of the works of Cheng, et al. [13] and Gilpin [16] concerning cooling in water pipes. Numerical studies of natural convection inside a rectangular cavity, in the absence of maximum density effect, have been carried out in the past by many investigators; that of Newell and Schmidt [19] contains a comprehensive bibliography.

2 Mathematical Statement of the Problem

A geometry of the problem is given in Fig. 1. The aspect ratio of the half cavity is denoted by $E = \ell/b$. The initial fluid temperature T_i is assumed to be uniform and at time $t = 0$ the cavity is suddenly exposed to a constant ambient temperature maintained at $T_\infty \leq 0$°C. The resistance and capacitance of the cavity walls are neglected. The cavity is supposed to be sufficiently long in the direction normal to the plane of Fig. 1 to assume a two-dimensional motion. It is also assumed that the motion is laminar. The governing equations for the transient natural convection, using the Boussinesq approximation [20] and neglecting viscous dissipation and compressibility effects, are then given in nondimensional form as:

$$\frac{\partial \Omega}{\partial \tau} + \frac{\partial U\Omega}{\partial X} + \frac{\partial V\Omega}{\partial Y} = \left(\frac{gb^3}{\alpha^2}\right)\frac{\partial \Delta\bar{\rho}}{\partial Y} + \Pr \nabla^2 \Omega \qquad (1)$$

$$\frac{\partial \theta}{\partial \tau} + \frac{\partial U\theta}{\partial X} + \frac{\partial V\theta}{\partial Y} = \nabla^2 \theta \qquad (2)$$

$$\Omega = -\nabla^2 \Psi \qquad (3)$$

$$U = \frac{\partial \Psi}{\partial Y} \qquad V = -\frac{\partial \Psi}{\partial X} \qquad (4)$$

where

$$\begin{aligned} &\tau = \frac{\alpha t}{b^2} \qquad U = \frac{ub}{\alpha} \qquad V = \frac{vb}{\alpha} \\ &\theta = \frac{T - T_\infty}{\Delta T} \qquad X = \frac{x}{b} \qquad Y = \frac{y}{b} \\ &\Psi = \frac{\psi}{\alpha} \qquad \Omega = \frac{\omega b^2}{\alpha} \qquad \nabla^2 = \frac{\partial}{\partial X^2} + \frac{\partial}{\partial Y^2} \\ &\Delta\bar{\rho} = \frac{\bar{\rho} - \rho(\theta)}{\bar{\rho}} \qquad \Pr = \frac{\nu}{\alpha} \qquad \mathrm{Bi} = \frac{hb}{k} \\ &\Delta T = T_i - T_\infty \end{aligned} \qquad (5)$$

and all other symbols are defined in Nomenclature.

The initial and boundary conditions are:

$$\begin{aligned} &U = V = \Psi = \Omega = 0 \quad &;\quad &\theta = 1 \quad &\text{at } \tau = 0 \\ &U = V = \Psi = 0 \quad &;\quad &\frac{\partial \theta}{\partial X} = \mathrm{Bi}\,\theta_w \quad &\text{at } X = 0 \\ &U = V = \Psi = 0 \quad &;\quad &\frac{\partial \theta}{\partial X} = -\mathrm{Bi}\,\theta_w \quad &\text{at } X = E \\ &\frac{\partial U}{\partial Y} = V = \Psi = \Omega = 0 \quad &;\quad &\frac{\partial \theta}{\partial Y} = 0 \quad &\text{at } Y = 0 \\ &U = V = \Psi = 0 \quad &;\quad &\frac{\partial \theta}{\partial Y} = -\mathrm{Bi}\,\theta_w \quad &\text{at } Y = 1 \end{aligned} \qquad (6)$$

It is noted in the boundary conditions that use has been made of the symmetry of the problem with respect to a vertical plane passing through $Y = 0$. The particular case with $U = V = 0$ in energy equation

---

Contributed by the Heat Transfer Division and presented at the 19th AIChE/ASME National Heat Transfer Conference, July 27 to 30, 1980, Orlando, Fla. Revised manuscript received by the Heat Transfer Division November 14, 1980. Paper No. 80-HT-74.

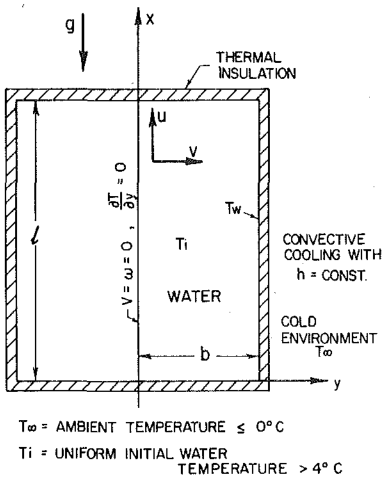

Fig. 1 Coordinate system and boundary conditions

(2) corresponds to the unsteady heat conduction in an infinite rectangular slab for which the exact solution is well known [21]. Furthermore the dimensionless time τ defined in equation (5) is similar in form to Fourier number in unsteady heat conduction.

The density-temperature relationship of water can be approximated by the following equation [22, 23]:

$$\frac{\rho - \rho_0}{\rho_0} = -\sum_{i=1}^{4} \beta_i T^i \tag{7}$$

where the density at 0°C is $\rho_0 = 0.9998396$ (gr/cm^3). The values of the constants are given in reference [13], for the temperature ranges 0 ~ 20°C and −10 ~ 10°C.

The mean temperature $\overline{T}$ of water is defined as

$$\overline{T} = T_\infty + \frac{\Delta T}{E} \int_0^1 \int_0^E \theta \, dX \, dY \tag{8}$$

It is noted that the quantity $(\overline{T} - T_\infty)/\Delta T$ represents the ratio of excess energy based on the initial state. It is also seen that the ratio $(T_i - \overline{T})/\Delta T$ represents the total heat loss with respect to the initial heat content and attains a value of 1 when the water is cooled to T_∞.

By assuming a perfect mixing of the fluid at any time, the mixed mean temperature T_b is given by:

$$T_b = T_\infty + \Delta T \exp[-\tau \mathrm{Bi}(1 + 2/E)] \tag{9}$$

The time-dependent heat transfer rates on each wall of the cavity are of practical interest. The local wall heat flux q can be computed by considering the wall temperature gradient $(\partial\theta/\partial N)_{N=0}$, where N is dimensionless normal to the boundary. The dimensionless local wall heat flux, defined as $\mathrm{Nu} = (qb)/(k\Delta T) = -(\partial\theta/\partial N)_{N=0}$, may thus be integrated over a given boundary. For example, integration over the top boundary gives:

$$\phi_T = -\int_0^1 \left(\frac{\partial\theta}{\partial X}\right)_{X=E} dY \tag{10}$$

in which ϕ_T is the dimensionless heat flux relative to that boundary. Similar results may be obtained for the side and bottom boundaries ϕ_L and ϕ_B.

The sum of the heat fluxes across boundaries is related to $\overline{\theta}_w$, the dimensionless temperature averaged over the boundary and to $\overline{\theta}$, the dimensionless temperature averaged over the cavity, by:

$$[\phi_T + \phi_B + E\,\overline{\theta}_L] = \mathrm{Bi}\,(2 + E)\,\overline{\theta}_w = \left[-E\,\frac{\partial\overline{\theta}}{\partial\tau}\right] \tag{11}$$

Thus the sum of the dimensionless average wall heat fluxes can be evaluated once the average wall temperature $\overline{\theta}_w$ is known.

3 Numerical Solution

The coupled vorticity transport and energy equations (1) and (2) may be solved by different numerical methods such as standard explicit method, alternating implicit Dufort-Frankel method and others [24]. In this study, the alternating direction implicit (A.D.I.) method is employed because of its simplicity and unconditional stability regardless of time step $\Delta\tau$ for linear parabolic equation. The first and second derivative were approximated by central differences and the time derivative by a first order forward difference. The finite difference forms of the equations were written in conservative form for the advective terms in order to preserve the transportive properties.

The specification of computational boundary conditions greatly affects the accuracy of the solution of the vorticity equation. Thus to be consistent with the accuracy of the scheme utilized in this study the wall vorticity was specified by a formulation similar to that developed by Woods [25]. Furthermore it should be noted that, in conjunction with Woods's form, a consistent formulation of the velocity field for the grid points nearest the wall requires the use of a three points special form obtained by a cubic equation [26]. The velocity components computed in this way extrapolate smoothly to the wall.

The elliptic equation (3) was solved by a successive over-relaxation (S.O.R.) procedure. For the present problem it was found that a relaxation factor of 1.8 was an optimum value. The iterative procedure was repeated until the ratio of the maximum change in stream function occuring in the field as a result of one approximation to the maximum value of the stream function was smaller than 5×10^{-4}. In most of the calculations presented in this paper it was observed that the number of iterations required decreases rapidly from 30 immediately after the start of the cooling to 2–5 for most other time steps. It was also found that the number of iterations reaches as high as 20 when the maximum density effect appears.

The effect of grid size on the accuracy of the present numerical solution has been studied for different mesh sizes. As noticed by Rubel and Landis [27] indications that a given mesh size will become inadequate as Grashof number increases are most easily given by the appearance of local temperature peak and by the unexpected rapid rise

Nomenclature

b = enclosure width
Bi = Biot number bh/k
E = aspect ratio of the half cavity ℓ/b
Gr = Grashof number $(gb^3/\nu^2)\,(\rho_4 - \rho_i)/\overline{\rho}$
h = constant heat transfer coefficient
k = thermal conductivity
ℓ = enclosure height
Nu = Nusselt number
Pr = Prandtl number ν/α
q = local heat flux by unit area
T = water temperature
t = time
u,v = velocities in x and y directions
$U,V,$ = dimensionless velocities in X and Y directions
x,y = cartesian coordinates
X,Y = dimensionless cartesian coordinates
α = thermal diffusivity
$\beta_1 \ldots \beta_4$ = constants (see equation (7))
ν = kinematic viscosity
ρ = water density
$\Delta\overline{\rho} = (\overline{\rho} - \rho)/\overline{\rho}$
$\Delta T = T_i - T_\infty$
τ = dimensionless time
ϕ_T,ϕ_L,ϕ_B = dimensionless average heat transfer at the top, side and bottom wall
ψ = stream function
Ψ = dimensionless stream function
ω = vorticity
Ω = dimensionless vorticity
θ = dimensionless temperature

Superscripts

$*$ = pure conduction case
$-$ = mean temperature condition

Subscripts

i = initial condition
∞ = ambient air temperature
w = wall condition
b = mixed mean water condition
c = the center of the cavity
max = maximum value
min = minimum value
4 = condition at 4°C.

of the average heat transfer. The mesh size used in this study ranged, depending on the aspect ratio E of the cavity, from 1/10 to 1/15 in the Y direction and $E/20$ or $E/30$ in the X direction. Numerical results have shown that the use of a finer grid mesh made relatively little difference to the final results although increasing sensibly the computer time. In particular the vortex formation was not affected by a mesh refinement. It was also verified that the vortex formation was not influenced by the sweep direction in the S.O.R. solution as it does for instance in a bottom-heated cavity. Typical values of the dimensionless time step were 0.0001, 0.0005 and 0.001. The total time steps ranged from 1600 to 2500, and the corresponding computing time was from 330 to 480 s on the IBM 360/70 computer.

To expedite plotting of the results, an auxiliary computer program was developed to locate points lying on specified isotherms and streamlines by linear interpolation of the computed values at the grid points. All graphs were performed using a CALCOMP 563 automatic plotter.

In order to check the validity of the present numerical method, comparisons have been made with other existing solutions. An excellent agreement was observed, for low Rayleigh numbers, with the analytical Poot's solution [28]. For higher Rayleigh numbers, the numerical results from Wilkes [29], for the case of heat transfer into a rectangular cavity, were integrally reproduced. Another means of checking that the present method was numerically conservative with sufficient accuracy was to evaluate the sum of the wall heat fluxes from equation (11). Simpson's rule was used for numerical integration and a three point finite difference approximation for $\partial\bar{\theta}/\partial\tau$. The agreement between the results obtained by the two alternative relations given in equation (11) was found to be within 1 to 2 percent.

4 Results and Discussion

In view of the number of parameters involved in the present problem, namely Bi, Pr, T_i, T_∞, E and gb^3/α^2, numerical solutions are presented only for typical cases. Previous investigations on transient natural convection in enclosed rectangular cavities with maximum density effects are concerned with walls having uniform temperature [12, 16]. However it is of interest to extend these studies to the case of a convective boundary condition where thermal insulation effect, for example, can be considered. This type of boundary condition gives rise to nonuniform wall temperature.

4.1 The Inversion Effect. Consideration will be given first to the case of a square cavity ($E = 2$) with initial water temperature $T_i = 8°\text{C}$, ambient temperature $T_\infty = 0°\text{C}$, $gb^3/\alpha^2 = 5.42 \times 10^8$, (i.e. Gr $= 6.72 \times 10^4$) and Bi = 2. The Prandtl number Pr is taken to be 11.6, corresponding to the average temperature 4°C. The calculated mean temperature $\bar{\theta}$, average wall temperature $\bar{\theta}_w$ and the heat transfer ϕ_T, ϕ_B and ϕ_L related to the top, lower and lateral boundaries respectively are presented in Fig. 2. The results for the two limit cases of pure conduction and perfect mixing are also plotted on this graph for comparison.

The contours for time dependent stream function and isotherms, corresponding to different times τ, are represented in Fig. 3, for flow visualization studies. The maximum and minimum values of the stream function Ψ and the contour intervals $\Delta\Psi$ for each graph are given for reference purpose. The 4°C isotherm, when it exists, is shown as a heavy dashed line on the isotherm and streamline plots. The symbols A, B, C, etc., shown in Fig. 2, correspond to the sequence of the transient streamline pattern and isotherms in Fig. 3.

At the very beginning, the cooling process is characterized by a pure conduction heat transfer. The departure from the initial uniform temperature T_i occurs near the walls, giving rise to an important temperature gradient in that region. A resulting motion of the boundary layer type is thus set up near the vertical walls. This motion is directed downward since it is associated with a horizontal density gradient having the heavier fluid near the wall. As a consequence of the symmetry and the continuity, the resulting fluid motion inside the whole cavity consists of two counterrotating vortices. Figure 3(a) only shows the right clockwise vortex. The isotherms represented on this figure indicate that the convection has not yet exerted a sensible effect on the temperature field. Therefore the top and bottom corners are approximately at the same temperature, this latter being naturally a minimum. However, as time progresses, the convective motion progressively stratifies the core region, as shown in Fig. 3(b). It is noted that the resulting isotherm configuration, closely spaced near the top wall but sparely spaced near the bottom one, produces respectively large and poor heat transfer on those two boundaries.

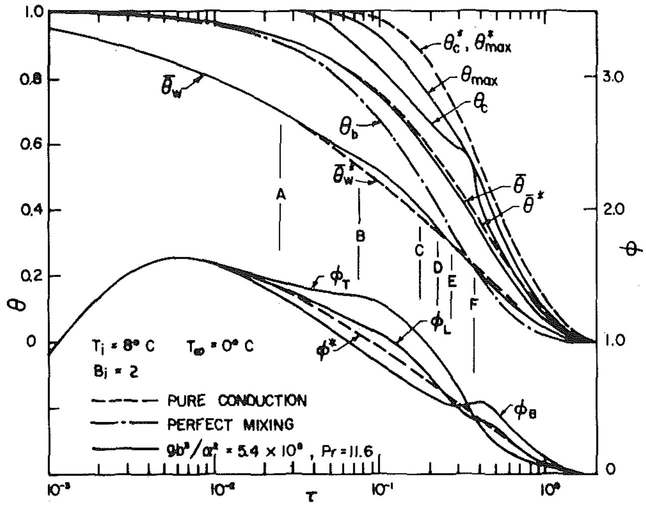

Fig. 2 Transient distributions for θ and ϕ, with results from pure conduction and perfect mixing for $T_i = 8°\text{C}$, $T_\infty = 0°\text{C}$, Bi = 2, $E = 2$, $gb^3/\alpha^2 = 5.42 \times 10^8$ and Pr = 11.6

The inversion process starts with the appearance of a 4°C isotherm in the temperature field, as shown in Fig. 3(b). As a result, the density of water decreases in the layer of fluid near the bottom of the cavity, leading to a situation where the flow field is potentially unstable because of the top heavy situation. This particular density field, related to the occurrence of the 4°C isotherm, gives rise to an additional pair of vortices rotating opposite to the existing ones. The resulting flow pattern is depicted in Fig. 3(c). With the progression of the inversion process, the lower vortex gradually increases its strength and displaces progressively the original vortex, as shown on sketches (c, d) and (e) of Fig. 3. The combined vortex action has two main effects. Firstly, it perturbs the isotherm pattern by carrying the cooler water from the side wall directly into the core region. Secondly, it improves the bottom heat transfer ϕ_B by transporting the warmer core water in the lower portion of the cavity. Thus when $\tau \geqslant 0.3$, ϕ_B becomes even larger than ϕ_T. The inversion process comes to an end when the original clockwise vortex has been completely overtaken by the vortex originating from below. In Fig. 3(f), i.e. at $\tau = 0.375$, the original clockwise circulation is completely reversed. The new motion brings gradually the warm core in the lower region of the cavity. Consequently the stratification of water is now characterized by weak gradients at the top and strong gradients at the bottom. Results obtained for higher values of τ (not presented here) show that the momentum of the eddy motion is slowly dissipated by the opposing viscous forces and that the fluid motion vanishes asymptotically with time.

The above description of the cooling process contains many aspects that are common to the other cases discussed in the present article. Thus the next sections will be limited to the description of the particular features characterizing those cases.

4.2 The Biot Number effect. In this section, the effect of a relatively large Biot number (Bi = 20.) on the heat transfer is presented. Except for the Biot number, the other governing parameters remain the same as in the preceeding section. The computed temperature and heat transfer curves are shown in Fig. 4. In order to understand the effect of the Biot number combined to the maximum density effect, it is worth to consider first the simpler problem of pure conduction. In this case, an increase of the Biot number enhances the heat transfer ϕ^* as it can be seen from Figs. 2 and 4 where the temperature curves θ_c^*, $\bar{\theta}^*$ and θ_w^* decrease faster toward zero with time. When convection is allowed, in the absence of a maximum density

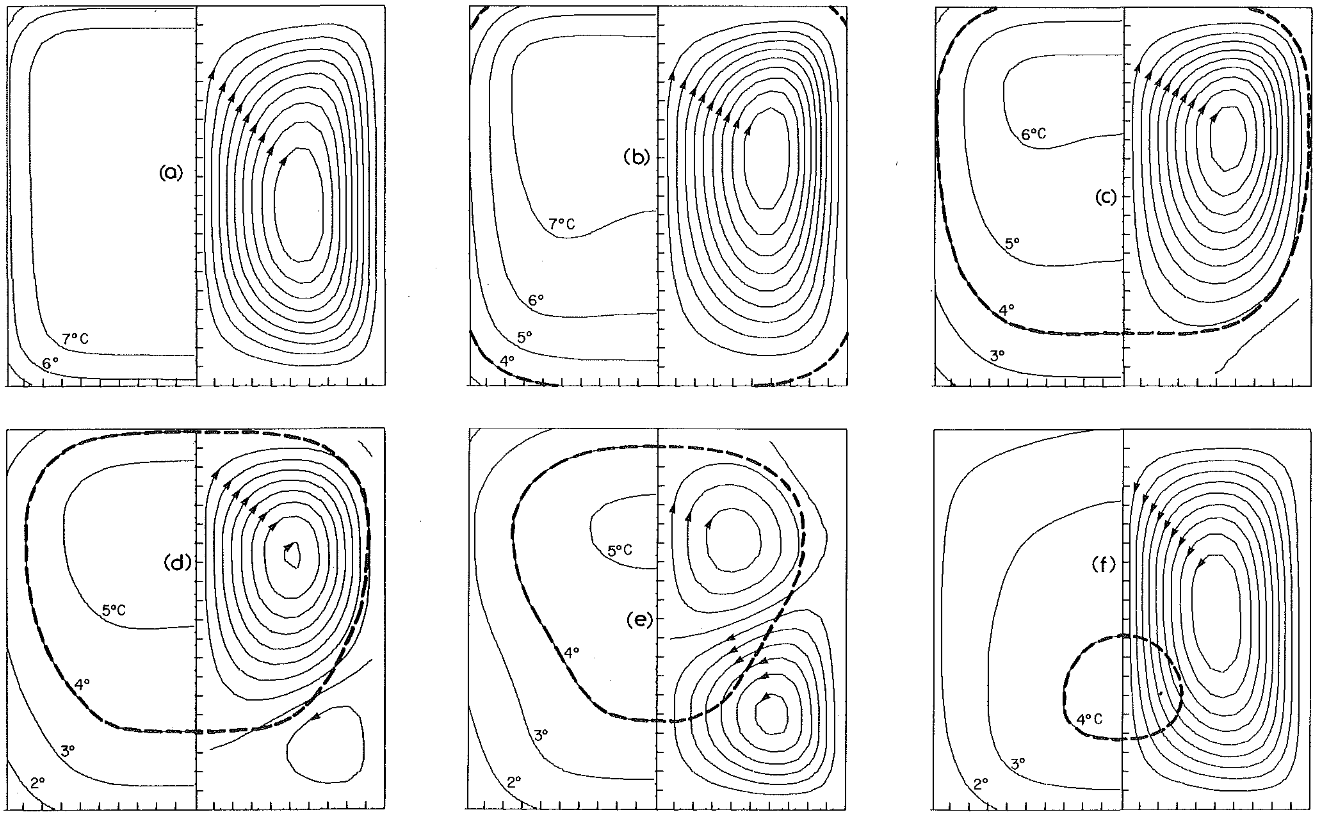

Fig. 3 Transient streamline pattern and isotherms for $T_i = 8°C$, $T_\infty = 0°C$, Bi = 2, $E = 2$, $gb^3/\alpha^2 = 5.42 \times 10^8$ and Pr = 11.6 at various time τ. The centerline and walls have value $\Psi = 0$. The values of τ, Ψ_{max}, Ψ_{min} and $\Delta\Psi$ are (*a*) $\tau = 0.025$, $\Psi_{max} = 9.9$, $\Delta\Psi = 0.99$; (*b*) $\tau = 0.075$, $\Psi_{max} = 9.5$, $\Delta\Psi = 0.95$; (*c*) $\tau = 0.175$, $\Psi_{max} = 4.6$, $\Psi_{min} = -0.2$, $\Delta\Psi = 0.48$; (*d*) $\tau = 0.225$, $\Psi_{max} = 3.1$, $\Psi_{min} = -0.7$, $\Delta\Psi = 0.39$; (*e*) $\tau = 0.275$, $\Psi_{max} = 1.2$, $\Psi_{min} = -2.1$, $\Delta\Psi = 0.33$; (*f*) $\tau = 0.375$, $\Psi_{min} = -5.5$, $\Delta\Psi = 0.55$.

effect, the fluid motion taking place inside the cavity enhances ϕ_T and attenuates ϕ_B. An increase of the Biot number promotes the convection, thus amplifying its effect on ϕ_T and ϕ_B. The presence of a maximum density introduces an additional complexity. In fact an increase of the Biot number has two opposing effects: one is the initial circulation inside the cavity which is strengthened and the other is the inversion process which occurs earlier and acts against the initial circulation. There are situations where the inversion process takes place so quickly that it annihilates almost completely the initial circulation.

It is noted that a Biot number equal to infinity corresponds to the case of non-insulated walls. The situation is equivalent to abruptly lowering T to T_∞ at the initiation of the cooling process. This type of situation has already been discussed in reference [30].

4.3 The Aspect Ratio Effect. The influence of the aspect ratio E on the present problem has been studied for elongated cavities with $E = 1$ and 4, respectively. In both cases the other parameters of the problem were kept equal to those of case 4.1

The results obtained (see reference [31]) with both cavities have shown that the general features of the density inversion remain qualitatively similar to those of the square cavity. However, for the vertically elongated cavity ($E = 4$), it was observed from numerical results that, when E is increased, the inversion process requires a longer period of time to be a accomplished. The growing and spreading of the counter clockwise vortex in the entire cavity was found to be a slower process than in the case of a square cavity. The results obtained with the horizontally elongated cavity ($E = 1$) have shown that the convective motion inside the cavity was considerably reduced as compared to the case with $E = 4$. This is due to the fact that in both cases the parameter value gb^3/α^2 was kept constant and that a decrease of E implies a reduction of the overall area of the cavity and thus a proportional decrease of the convection. It has to be noted that a cavity with $E < 2$ is more difficult to treat numerically than one with $E > 2$ because of the inherent relative importance of the unstable layer associated with this type of configuration [9]. A vertically elongated cavity is more stable since the instability zones related to the vertical density gradient along the horizontal walls are less important than the driving forces generated by the horizontal density gradient near the vertical wall.

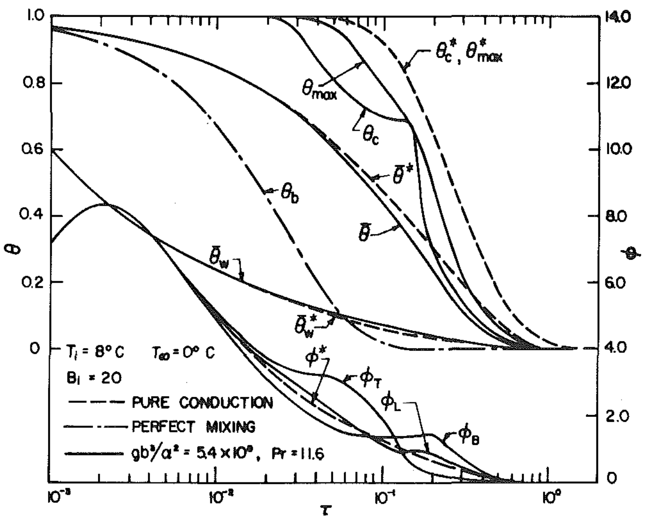

Fig. 4 Transient distribution for θ and ϕ, with results from pure conduction and perfect mixing, for $T_i = 8°C$, $T_\infty = 0°C$, Bi = 20, E = 2, $gb^3/\alpha^2 = 5.42 \times 10^8$ and Pr = 11.6

4.4 The Physical Parameter Effect. The effect of an increase of the physical parameter gb^3/α^2 on the present problem may be observed by comparing the sequence of Fig. 5 to that of Fig. 3. It is seen from Fig. 5(*a*) that the flow starts with the usual pair of counterrotating vortices. However at time $\tau = 0.035$, it is observed from Fig. 5(*b*)

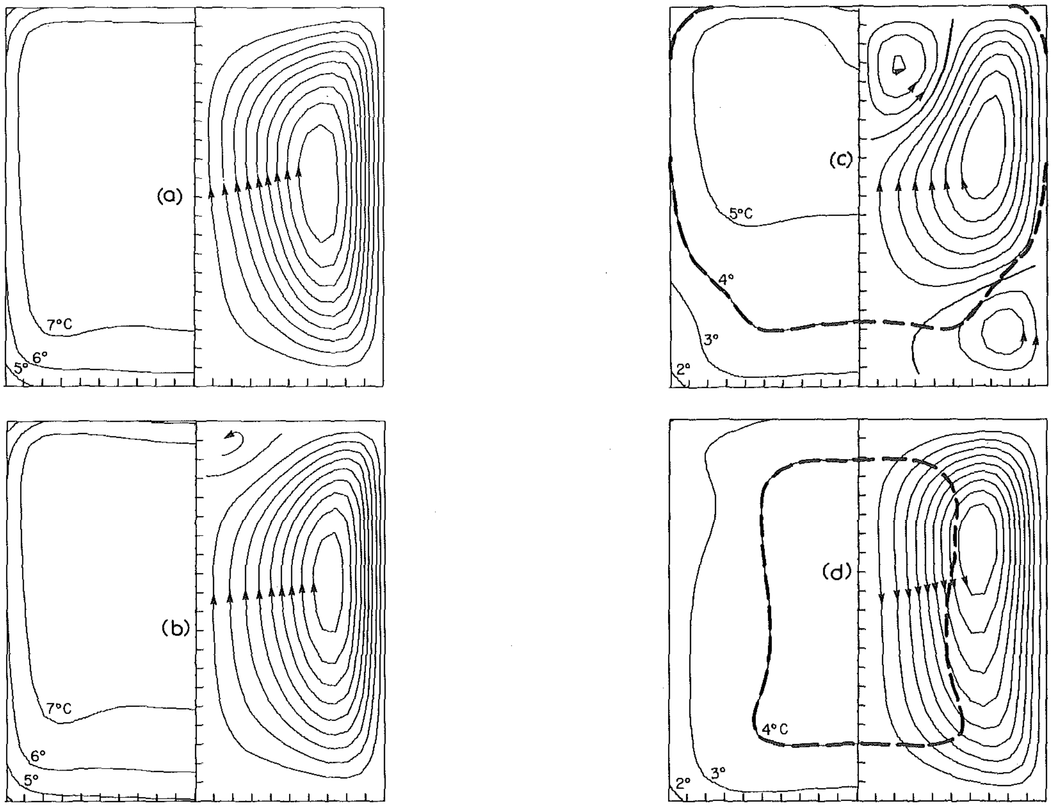

Fig. 5 Transient streamline pattern and isotherms for $T_i = 8°\mathrm{C}$, $T_\infty = 0°\mathrm{C}$, Bi = 2, $E = 2$, $gb^3/\alpha^2 = 4.3 \times 10^9$ and Pr = 11.6 at various time τ. The centerline and walls have value $\Psi = 0$. The values of τ, $\Psi_{\max}$, $\Psi_{\min}$ and $\Delta\Psi$ are (*a*) $\tau = 0.025$, $\Psi_{\max} = 30.1$, $\Delta\Psi = 3.01$; (*b*) $\tau = 0.035$, $\Psi_{\max} = 22.9$, $\Psi_{\min} = -0.7$, $\Delta\Psi = 2.36$; (*c*) $\tau = 0.150$, $\Psi_{\max} = 8.4$, $\Psi_{\min} = -4.4$, $\Delta\Psi = 1.28$; (*d*) $\tau = 0.250$, $\Psi_{\min} = -11.2$, $\Delta\Psi = 1.12$

that an additional pair of secondary vortices symmetrically located on the axis of symmetry occurs near the top boundary. The appearance of these secondary vortices is directly related to the unstable situation resulting from the particular temperature field prevailing near the top wall. As the cooling progresses, the secondary vortex pair increases its strength. At time $\tau = 0.15$, the inversion process starts with the occurence of the lower corner vortex and develops as already described in Section 4.1. At time $\tau = 0.25$ the lower vortex has completely overtaken the two original vortices and the circulation inside the cavity is completely reversed. Results obtained at higher values of τ show that the motion vanishes asymptotically with time.

The existence of the additional vortex pair of Fig. 5(*b*) must be dissociated from the inversion process since it appears before the occurrence of the 4°C isotherm in the temperature field. Moreover the existence of this additional vortex is not a result of the nonlinearity effects since it has also been observed in the present investigation for situations in which the relationship between the water density and its temperature was linear. For this case it was found that for relatively low Rayleigh numbers, i.e. for a low intensity of the convective motion, the flow inside the cavity developed into a standard counterrotating vortex pair. However, when the Rayleigh number was sufficiently high, the previous flow pattern was modified by the superposition of the two secondary vortices. Therefore, it is not suprising that for the present problem the second mode of convection does occur prior to the inversion process since the convective motion has been enhanced by the increase of the physical parameter, gb^3/α^2, as compared with the situation involved in Section 4.1.

The effect of density inversion on steady free convection of cold water contained in a rectangular cavity with isothermal vertical walls at different temperatures has been studied numerically and experimentally by Seki, et al. [17]. In that analysis a two-dimensional approach was assumed and verified experimentally for cavities with aspect ratio $E = 2$ to 10.

When the first mode of convection is involved in the present problem, the mechanism giving rise to the inversion process is quite similar to that studied by Seki and it is believed that a two-dimensional approach describes adequately the flow. However, the second mode of convection is characterized by the presence of additional rolls near the top boundary, those vortices resulting from the vertical density gradient prevailing in this region. This situation is similar to the case of a cavity heated from below for which a rich variety of flow structures have been observed in the past, as discussed for instance by Lindhorst, et al. [32]. It was found that, depending on the aspect ratio of the cavity and the Rayleigh number, the resulting flow pattern could be stationary or nonstationary. For stationary flow, three dimensional torus like roll or rolls parallel to the shorter side of the cavity [33] could be observed. Although similar, the present situation is complicated by the fact that the secondary rolls result from the interaction between an unstable layer of fluid and an already established flow field generated by the vertical walls. It is thus believed that in the physically realized flow three-dimensional motion is likely to occur when those rolls are present. For such a situation, the present numerical analysis will not predict adequately the flow field in this region.

4.5 The Case with Supercooling. The sequence of Fig. 6 illustrates a case in which the convective motion is relatively important prior (Gr = 1.17×10^6) and after the inversion process. Shortly after the initiation of the cooling process a secondary motion occurs, as seen on Fig. 6(*a*), in a way comparable to the case described in Section 4.4. At time $\tau = 0.05$, the inversion process gives rise to the usual inversion vortex near the lower corner of the cavity (Fig. 6(*b*)). As the cooling progresses, the relatively intense convective motion interacts with the unstable layer of fluid located between the 4°C isotherm and the lower boundary. As a result a new pair of secondary vortices appears in the lower central portion of the cavity (see Fig. 6(*c*)). This additional vortex pair was not present in the case described in Section 4.4 due to the fact that the convective motion was not sufficiently strong during the inversion process. It is interesting to note that this new vortex is connected to the original main one and that both rotate in the same clockwise direction. However, at time $\tau = 0.10$, Fig. 6(*d*)

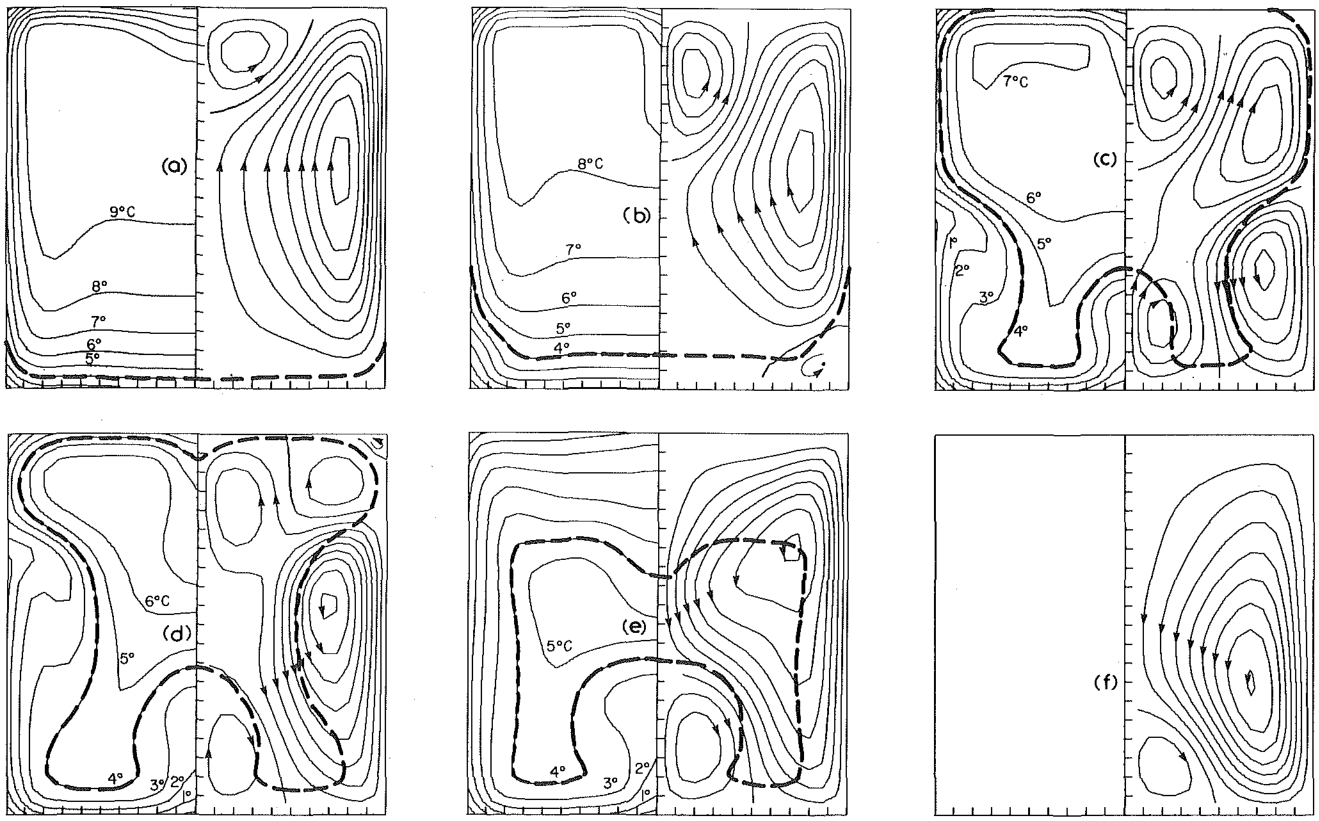

Fig. 6 Transient streamline pattern and isotherms for $T_i = 10$°C, $T_\infty = -10$°C, Bi = 2, $E = 2$, $gb^3/\alpha^2 = 4.3 \times 10^9$ and Pr = 13.7 at various time τ. The centerline and walls have value $\Psi = 0$. The values of τ, Ψ_{max}, Ψ_{min} and $\Delta\Psi$ are (a) $\tau = 0.025$, $\Psi_{max} = 32.1$, $\Psi_{min} = -12.0$, $\Delta\Psi = 4.41$; (b) $\tau = 0.050$, $\Psi_{max} = 22.1$, $\Psi_{min} = -12.3$, $\Delta\Psi = 3.44$; (c) $\tau = 0.085$, $\Psi_{max} = 14.2$, $\Psi_{min} = -15.9$ $\Delta\Psi = 3.11$; (d) $\tau = 0.100$, $\Psi_{max} = 5.1$, $\Psi_{min} = -22.1$, $\Delta\Psi = 2.72$; (e) $\tau = 0.125$, $\Psi_{max} \approx 7.6$, $\Psi_{min} = -18.9$, $\Delta\Psi = 2.65$; (f) $\tau = 1.300$, $\Psi_{max} = 1.5$, $\Psi_{min} = -6.4$ $\Delta\Psi = 0.79$

shows that this connection is broken by the growth of the inversion vortex. Thus the upper secondary vortex connects now with the inversion vortex, both rotating counter-clockwise. A very small eddy in the upper right corner of the cavity may also be observed on the same figure. With progression of cooling the original clockwise vortex gradually fades away due to the continuous growing of the inversion vortex. Thus at time $\tau = 0.125$ only two vortices are present inside the cavity. The flow pattern of Fig. 6(*e*) is now opposite to that of Fig. 6(*a*) and the inversion process is over. The remaining secondary vortex in the bottom of the cavity is similar in character to the initial secondary vortex. In fact its presence is maintained by the combined action of the existing unstable layer near the bottom boundary and the intense convective motion which follows the inversion. Fig. 6(*f*) indicates that the time required for the secondary motion to disappear is very long. Thus at time $\tau = 1.3$, the secondary vortex is still present, although greatly reduced in strength, as indicated by the value of Ψ_{min}. In fact a value $\tau \approx 2$ is required for this secondary vortex to disappear completely.

4.6 Comparison with Existing Experimental Studies. The cooling of a mass of water through its maximum density at 4°C has been studied experimentally in the past for different flow geometries and boundary conditions. For instance, Seki, et al. have investigated the effect of density inversion on the steady natural convection of a mass of water contained between two horizontal concentric cylinders maintained at different constant temperatures [34] and in a confined rectangular vessel in which different temperatures were imposed on the opposing vertical walls [17]. Furthermore the transient natural convection heat transfer of a horizontal cylinder of water cooled through its maximum density has been considered by Gilpin for two types of thermal boundary conditions, namely a convective cooling [3] and a constant cooling rate [35]. Due to the differences in geometries or boundary conditions a direct quantitative comparison between the results of those experimental studies and the present numerical investigation is not possible. Nevertheless, a few qualitative comparisons can be made in particular with Gilpin's results. For instance the transient behavior of the inversion process, as described in Section 4.1 of the present paper, is quite similar to that observed experimentally by Gilpin [16] in a pipe. In particular detailed observations of the flow pattern during the transition show that for relatively low intensity of convection, the inversion begins with a reversal of the flow direction in the boundary layer near the bottom of the cylinder. This reversal spreads to the top of the cylinder and then begins the reverse flow in the core. It is interesting to note that the secondary convection rolls predicted by the present theory have not been observed numerically or experimentally in the case of a horizontal pipe. The formation of a secondary vortex over a horizontal circular ice cylinder located in quiescent water of constant temperature has however been reported by Saitoh, et al. [35].

Experiments concerning the supercooling of water inside a circular pipe have been performed by Gilpin [3]. Results were obtained for Biot number of 0.2 and 15, respectively. It was observed that in both cases, following the inversion process, dentritic ice started to form at the top of the pipe, due to the presence of cold water at a temperature of approximately −4°C in this region. However, the overall growth of ice inside the pipe was considerably affected by the Biot number. For the higher Biot number the rapid cooling rate produced large temperature differences in the water and dentritic ice only grew adjacent to the pipe walls. For the lower Biot number, the cooling process was more uniform inside the cavity, and, as a result, dentritic ice blocked the entire section of the pipe. Numerical results obtained in the present study, but not presented here, concerning the supercooling of a rectangular cavity at various Biot numbers were qualitatively in agreement with Gilpin's results. However, the present case is characterized by the fact that the corners of the cavity cool down more rapidly than the rest of the boundary. It is thus expected that ice formation will generally start at corners.

5 Conclusions

A numerical solution is obtained for the transient natural convection of water, enclosed in rectangular cavities with a convective boundary condition, and cooled through the maximum density point at 4°C. The numerical solution, based on an implicit finite difference method, yields detailed streamline patterns and isotherms readily for flow visualization. The results obtained in the present study may be summarized as follows:

1 Convection in the absence of maximum density effect is enhanced by an increase of the parameters gb^3/α^2 and Bi. An additional vortex pair was observed to appear near the upper boundary for sufficiently high convective motion.

2 The effect of maximum density consists in slowing down the initial circulation inside the cavity and subsequenty in reversing it. The resulting heat transfer is thus reduced in comparison to a standard situation without maximum density effect. A consequence of the maximum density is the switch of the maximum heat transfer from the top wall to the bottom one during the cooling process.

3 The temperature in the water can depart significantly from those that would be predicted on the basis of simplifying assumptions such as "pure conduction" or "perfect mixing". This result implies that the prediction of the characteristics of the freezing of a mass of water will be in error if either of those simplifying assumptions is used. These errors will be particularly important at large Biot numbers.

4 The results obtained in this study for supercooling conditions involve a relatively high convective motion with secondary vortex pairs prior and after the inversion process, giving rise to complex flow patterns.

Acknowledgment

This research was supported by the National Research Council of Canada through grants NRC A-4197 and NRC A-9201, for which the authors are grateful.

References

1 Farhadieh, R., and Tankin, R. S., "A Study of the Freezing of Sea Water," *Journal of Fluid Mechanics*, Vol. 71, part 2, 1975, pp. 293–304.

2 Tankin, R. S., and Farhadieh, R., "Effects of Thermal Convection Currents on Formation of Ice," *International Journal of Heat and Mass Transfer*, Vol. 14, 1971, pp. 953–961.

3 Gilpin, R. R., "The Effect of Cooling Rate on the Formation of Dentritic Ice in a Pipe with no Main Flow," ASME JOURNAL OF HEAT TRANSFER, Vol. 99, 1977, pp. 419–424.

4 Goren, S. L., "On Ice Convection in Water at 4°C," *Chemical Engineering Science*, Vol. 21, 1966, pp. 515–518.

5 Schechter, R. S., and Isbin, H. S., "Natural Convection Heat Transfer in Regions of Maximum Density," *American Institute of Chemical Engineering Journal*, Vol. 4, No. 1, 1958, pp. 81–89.

6 Schechter, R. S., "Natural Convection Heat Transfer in Regions of Maximum Density," Ph.D. Thesis, University of Minnesota, 1956.

7 Vanier, C. R., and Tien, C., "Effect of Maximum Density and Melting on Natural Convection Heat Transfer from a Vertical Plate," *Chemical Engineering Progress Symposium Series*, Vol. 64, No. 82, 1968, pp. 240–254.

8 Vasseur, P., and Robillard, L., "Natural Convection of Water near the Freezing Point," *IARH Symposium on Ice Problems*, Luela, Sweden, 1978, pp. 257–270.

9 Merker, G. P., Waas, P., and Grigul, U., "Onset of Convection in a Horizontal Water Layer with Maximum Density Effects," *International Journal of Heat and Mass Transfer*, Vol. 22, 1979, pp. 505–515.

10 Cheng, K. C., and Wu, R. S., "Maximum Density Effects on Thermal Instability of Horizontal Laminar Boundary Layers," *Applied Sciences Research*, Vol. 31, 1976, pp. 465–479.

11 Sugawara, M., Fukusako, S., and Seki, N., "Experimental Studies on the Melting of a Horizontal Ice Layer," *Bulletin of the Japanese Society of Mechanical Engineering*, Vol. 18, No. 121, 1975, pp. 714–721.

12 Cheng, K. C., and Takeuchi, M., "Transient Natural Convection of Water in a Horizontal Pipe with Constant Cooling Rate through 4°C," ASME JOURNAL OF HEAT TRANSFER, Vol. 98, 1976, pp. 581–587.

13 Cheng, K. C., Takeuchi, M., and Gilpin, R. R., "Transient Natural Convection in Horizontal Water Pipes with Maximum Density Effect and Supercooling," *Numerical Heat Transfer*, Vol. 1, 1978, pp. 101–115.

14 Gilpin, R. R., "The Effects of Dentritic Ice Formation in Water Pipes," *International Journal of Heat and Mass Transfer*, Vol. 20, 1977, pp. 693–699.

15 Robillard, L. and Vasseur, P., "Effet du maximum de densité sur la convection libre dans une cavité fermée," *Canadian Journal of Civil Engineering*, Vol. 6, No. 4, 1979, pp. 481–493.

16 Gilpin, R. R., "Cooling of a Horizontal Cylinder of Water through its Maximum Density Point at 4°C," *International Journal of Heat and Mass Transfer*, Vol. 18, 1975, pp. 1307–1315.

17 Seki, N., Fukusako, S. and Inaba, H., "Free Convective Heat Transfer with Density Inversion in a Confined Rectangular Vessel," *Wärme-und Stoffübertragung*, Vol. 11, 1978, pp. 145–146.

18 Dorsey, N. E., "The Freezing of Supercooled Water," *Transactions of the American Society of Philosophical Society*, Vol. 38, 1948, pp. 248–325.

19 Newell, M. E. and Schmidt, J., "Heat Transfer by Laminar Natural Convection within Rectangular Enclosures," ASME JOURNAL OF HEAT TRANSFER, Vol. 92, 1970, pp. 159–168.

20 Gray, D. D., and Giorgini, A., "The Validity of the Bousinesq Approximation for Liquids and Gases," *International Journal of Heat and Mass Transfer*, Vol. 19, 1976, pp. 545–551.

21 Kreith, F., *Principles of Heat Transfer*, Intext Educational Publishers, New York, 1973.

22 Fujii, T., "Fundamentals of Free Convection Heat Transfer," *Progresses in Heat Transfer Engineering*, Vol. 3, 1974, pp. 66–67.

23 Weast, R. C., *Handbook of Chemistry and Physics*, 52nd ed., Chemical Rubber Co., Cleveland, Ohio 1972, p. F5.

24 Roache, P., *Computational Fluid Dynamics*, Hermosa Publishers, 1976.

25 Woods, L. C., "A Note on the Numerical Solution of Fourth Order Differential Equations," *Aeronautical Quarterly*, Vol. 5, Part 3, 1954, p. 176.

26 Briley, W. R., "A Numerical Study of Laminar Separation Bubbles Using the Navier-Stokes Equations," Report J110614-1, United Aircraft Research Laboratories, East Hartford, Conn, 1970.

27 Rubel, A. and Landis, F., "Numerical Study of Natural Convection in a Vertical Rectangular Enclosure," *High Speed Computational Fluid Dynamics*, Vol. II, 1969, pp. 208–213.

28 Poots, G., "Heat Transfer by Laminar Free Convection in Enclosed Plane Gas Layer," *Quarterly Journal of Mechanics and Applied Mathematics.*, Vol. 11, 1958, pp. 257–273.

29 Wilkes, J. D., "The Finite difference Computation of Natural Convection in an Enclosed Rectangular Cavity," Ph.D. thesis, University of Michigan, 1963.

30 Vasseur, P. and Robillard, L., "Transient Natural Convection Heat Transfer in a Mass of Water Cooled through 4°C," *International Journal of Heat and Mass Transfer*, Vol. 23, no. 9, 1980, pp. 1195–1205.

31 Robillard, L. and Vasseur, P., "Transient Natural Convection Heat Transfer of Water with Maximum Density Effect and Supercooling," ASME/AICHE National Heat Transfer Conference, Orlando, Fla, July 27–30, 1980, Paper No. 80-HT-74.

32 Linthorst, S. J. M., Schinkel, W. M. M. and Hoogendoorn, G. J., "Flow Structure with Natural Convection in Inclined Air-Filled Enclosures," A.I.Ch.E./ASME National Heat Transfer Conference, Orlando, Fla, July 27–30, HTD- Vol. 8, 1980, pp. 39–46.

33 Stork, K. and Muller, U., "Convection in Boxes: Experiments," *Journal Fluid Mechanics*, Vol. 54, Part 4, 1972, pp. 599–611.

34 Seki, N., Fukusako, S. and Nakaoka, M., "Experimental Study on Natural Convection Heat Transfer with Density Inversion of Water Between Two Horizontal Concentric Cylinders," ASME JOURNAL OF HEAT TRANSFER, Vol. 97, 1975, pp. 556–561.

35 Saitoh, T. and Hirose, T., "Thermal Instability of Natural Convection flow over a Horizontal Ice Cylinder Encompassing a Maximum Density Point," ASME JOURNAL OF HEAT TRANSFER, Vol. 102, 1980, pp. 261–267.

Flow Structure with Natural Convection in Inclined Air-Filled Enclosures

S. J. M. Linthorst
Research Scientist.

W. M. M. Schinkel[1]
Research Scientist.

C. J. Hoogendoorn
Professor.

University of Technology,
Delft, Holland

Flow visualization observations are described for natural convection flow in rectangular inclined enclosures. Observations are made in air-filled enclosures of small and moderate aspect ratio (0.25 $\leqslant A_x \leqslant$ 7), angles of inclination from 0 to 90 deg and Rayleigh number between 5 × 10^3 and 2.5 × 10^5. For the range of parameters considered we determined the transition from stationary to nonstationary flow and the transition from two-dimensional to three-dimensional flow. Also, the different stationary flow structures are described. In addition measurements of the velocity profile of the stationary flow have been performed by means of a laser doppler anemometer. Special attention has been given to the side wall boundary condition of the enclosure.

Introduction

For several years increasing attention has been paid to the problem of natural convection in inclined enclosures. Recently an excellent review was given by Catton [1]. Most investigations deal with the dependence of heat transfer on the relevant parameters. Relatively little attention has been given to the flow behavior, especially for low ($A_x \leqslant 1$) and moderate ($1 < A_x \leqslant 7$) aspect ratios.

However, knowledge of flow behavior is important for a number of reasons. It has been observed [2] that a transition from one flow pattern into another causes a discontinuity in the slope of the Nusselt number relations. Moreover, it is necessary for calculation purposes to know in what range of a parameter the flow is stationary and two-dimensional or three-dimensional. The transition to nonstationary and to turbulent flow is important from the more fundamental point of view.

The objective of this experimental investigation is the determination of natural convection flow characteristics, including secondary motion, the transition from two-dimensional to three-dimensional flow and the transition from stationary to nonstationary flow in air-filled enclosures of small and moderate aspect ratio. Two types of experiments have been done. In order to investigate the flow qualitatively flow visualization experiments have been performed. Secondly velocity measurements with a laser doppler anemometer (lda) have been carried out in order to obtain quantitative results.

In our experiments, the Rayleigh number (Ra), based on the plate distance D, varied from 5 × 10^3 to 2.5 × 10^5 and the angle of inclination ϕ from 0 to 90 deg. The value of the height to width aspect ratio A_x was between 0.25 and 7, the depth to width aspect ratio A_z was, dependent on the plate distance D, either 5 or 10. For notation see Fig. 1.

Flow Regimes

Most studies of the flow behavior have been done in the horizontal ($\phi = 0$ deg, heated from below) orientation and the vertical orientation ($\phi = 90$ deg). For notation see Fig. 1 Krishnamurti did flow visualization experiments for large aspect ratio and $\phi = 0$ deg [3, 4, 5] Stork and Müller [6] considered the aspect ratio dependence of the flow for $A_z \leqslant 6$ and $A_z \leqslant 6$ for the horizontal orientation.

In the vertical orientation ($\phi = 90$ deg) flow visualization has been done by Elder [7] for aspect ratios of 1 to 60, while recently Morrison and Tran [8] performed velocity measurements of the natural convection flow for $A_x = A_z = 5$ at Ra = 5 × 10^4.

For the inclined orientation some flow visualization experiments are done by Ozoe [9].

It is generally known that for small Ra numbers there is an unicellular two-dimensional motion, commonly referred to as the conductive base flow. The heat transfer in this situation is mainly due to conduction. With increasing Rayleigh number this base flow becomes unstable. It appears that two types of instabilities can be distinguished. For angles of inclination smaller than a certain transition angle ϕ', the instability is mainly buoyancy driven and leads to longitudinal rolls superposed on the base flow. Longitudinal rolls have their axes upslope and the rotation direction of a longitudinal roll is opposite to the direction of rotation of its direct neighbors. For angles of inclination between $\phi = \phi'$ and $\phi = 90$ deg the instability is mainly hydrodynamic and leads to transverse rolls (small and moderate Prandtl number) or travelling waves (high Prandtl number). A further increase of the Ra number causes a transition to nonstationary flow.

At moderate and small aspect ratios there are only a few investigations of the flow structure. Ozoe, et al. [9, 10, 11] investigated the flow and heat transfer both theoretically and experimentally. The aspect ratio varied between 1–15.5 and Ra between 3 × 10^3 and 10^5. In most experiments large Prandtl number fluids have been used. For $A_x \geqslant 8$ air was the working fluid. For $A_x = 1$ Ozoe, et al. obtained a unicellular two-dimensional motion for 10 deg $\leqslant \phi \leqslant$ 90 deg. At $\phi =$ 10 deg a transition to a complex three-dimensional stationary flow has been observed. Also the heat transfer results showed this transition: A minimum value of the Nusselt number occurred for $\phi = 10$ deg. At larger aspect ratio A_x a similar behavior has been observed. However the angle of transition (ϕ') increases with increasing aspect ratio.

Experimental Setup

Both the flow visualization experiments and the laser doppler anemometer measurements are performed with the same model (see Fig. 2). The model consisted of one copper plate and one aluminium plate (0.20 × 0.30 m^2) for the isothermal hot wall and isothermal cold wall, respectively. The distance between the walls could be varied by in-

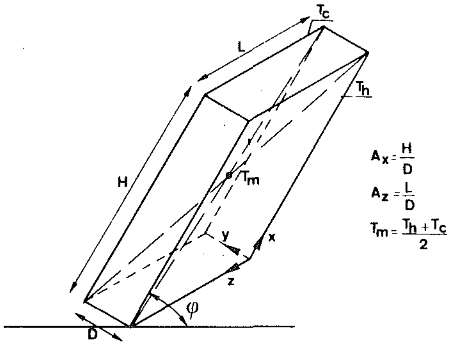

Fig. 1 A schematic view of the enclosure

---

[1] Present address: Shell/Amsterdam.

Contributed by the Heat Transfer Division and presented at the 19th AIChE/ASME National Heat Transfer Conference, July 27–30, 1980, Orlando, Fla. Revised manuscript received by the Heat Transfer Division October 17, 1980.

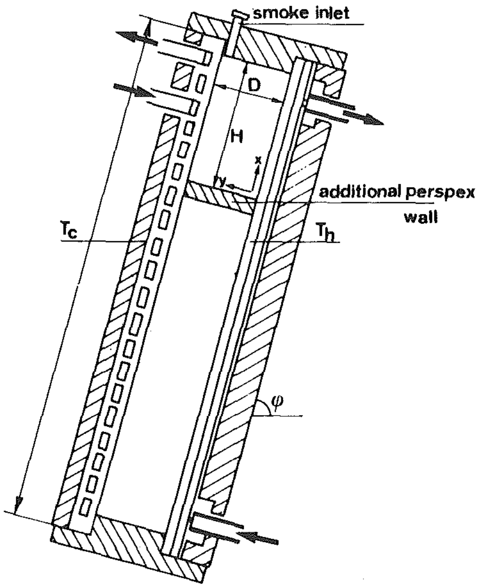

Fig. 2 The experimental model

serting two different covers, one for a plate distance of 0.02 m and one for $D = 0.04$ m. So the depth to width aspect ratio, A_z, was either 10 or 5. All the sidewalls were made of perspex to make flow visualization and lda measurements possible. The temperature of the isothermal walls could be controlled by means of two thermostatbaths. The temperature difference of the isothermal walls was varied up to 50 K. Both walls were isothermal to within 2 percent of the temperature difference at $\Delta T = 40$ K and within 8 percent for $\Delta T = 5$ K. To vary A_x, perspex walls could be placed at different heights in the enclosure. For $A_x < 1$ a slit structure, made of Lexan, was inserted in the cavity. At one of the shorter side walls small inlets were placed to inject smoke to visualize the flow pattern.

To illuminate a yz or xy-plane of the enclosure we created a parallel lightbeam by means of an optical setup and a Hg source of 500 W power. The model was placed on an apparatus to vary the angle of inclination with increments of 10 deg. The exposure time for making photographs varied between $\frac{1}{8}$ to 2 s for a film of 400 ASA (27 DIN). The camera we used was an Asahi Pentex ES II with a SMC Takumar f 1.8/55 mm lens. Close-up and wide-angle lenses were added.

The lda was used in the reference beam mode and only velocity profiles of stationary flows could be measured. We used a 5 mW He-Ne laser. A grating divides the laser beam into an intense 0^{th} order scattering beam and a weak first order reference beam. Instead of smoke, we used particles of aluminium oxide with a mean diameter of 1 μm for the lda measurements. The light, scattered from a particle passing the measuring volume, interferes with the first order beam on the photodiode. After passing a frequency filter, an amplifier and a Schmitt trigger, eight periods of the signal of the photodiode are counted which gives the value of the velocity component of the flow. Details of the lda experimental set-up can be found in Schinkel [12].

Flow Visualization Results

Vertical Orientation. For $A_x = 7$ and $A_z = 5$ unicellular two-dimensional motion was still observed at Ra = 3.6×10^4 (see Fig. 3(a)). At this Rayleigh number the flow is in the so-called transition regime. With increasing Rayleigh number a gradual transition to the boundary layer regime has been observed. The first secondary motion appeared at Ra = 1.5×10^5 (see Fig. 3(b) for clarity a photo is shown for Ra = 2×10^5) near the side wall regions. Secondary motion has the same rotation direction as the base flow. Further increase of Ra leads to additional secondary motion in the center of the enclosure. At Ra = 2.5×10^5 a weak tertiary motion located between the secondary motion, is observed (see Fig. 3(c)). The tertiary motion rotates in a direction opposite to the base flow. The secondary and tertiary motions have also been obtained in numerical calculations of Schinkel [12, 13].

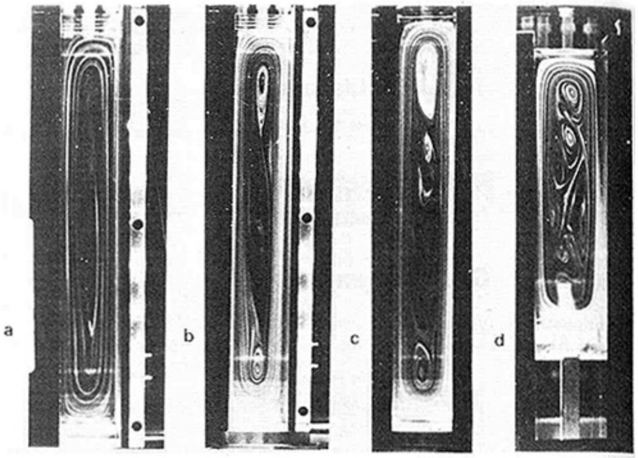

Fig. 3 Flow structure in the vertical orientation: (a) Ra = 3.6×10^4, A_x = 7; (b) Ra = 2.0×10^5, A_x = 7; (c) Ra = 2.5×10^5, A_x = 7; (d) Ra = 2.5×10^5, A_x = 4

He explains that the secondary motion in the side wall regions is caused by the stratification of the flow in this region. The secondary motion in the center is buoyancy driven as explained by Mallinson and de Vahl Davis [14]. The tertiary motion is a result of the interaction between the secondary motion in the side wall region and in the center.

At Ra = 2.5×10^5 the aspect ratio A_x has been decreased. It appeared that the secondary and tertiary motions became more pronounced (Fig. 3(d)) with decreasing aspect ratio up to $A_x = 2$. For $A_x < 2$ the tertiary motion disappeared and for $A_x = 1$ only two secondary rolls remain. For $A_x < 1$ no secondary motion was observed.

For $A_x \leqslant 7$ the flow remained stationary for all Ra numbers considered. It appeared that for $A_x \leqslant 7$ transverse rolls, as predicted and observed for large aspect ratios (Korpela [15]) never occured. This fact is in agreement with the stability theory of Bergholz [16]. In his analysis he took the effect of stratification in the core region into account and found that the stratification causes an increase of the critical Rayleigh number for the onset of transverse rolls. Our results confirmed by numerical results of Schinkel [13], show that the region of transverse rolls is never entered.

Horizontal Orientation. Our experiments in the horizontal orientation ($\phi = 0$ deg) are generally in good agreement with other investigations.

For $A_x = 0.5$ and $A_x = 0.25$ the flow appeared to be stationary for all Rayleigh numbers considered. For $A_x \geqslant 1$ the flow becomes nonstationary when the Rayleigh number exceeds a critical value. The dependence of the critical Rayleigh number on A_x has been given in Fig. 4. With increasing A_x the critical Rayleigh number decreases, which is expected according to the theory of Clever and Busse [17].

For $A_x \leqslant 1$ we observed longitudinal rolls with the rotation axis parallel to the x-axis. For $A_z = 5$, four rolls were observed at $A_x = 1$ and Ra = 5×10^4 (Fig 5(a)); for $A_x = 0.5$ we observed six rolls. For $A_x = 0.25$ situations of both six and eight rolls were obtained (see Fig. 5(b) and (c)). The fact that the number of rolls increases with decreasing aspect ratio A_x is in agreement with Stork [6]. However, the number of rolls is not in agreement with his results. Also the flow behavior for $A_x > 1$ that we observed in our experiments is not according his results. We obtained for $A_x > 1$ a torus like roll with fluid moving down at the four side walls and moving up in the center of the enclosure. This flow pattern has also been obtained by Krishnamurti [3, 4, 5] who mentioned that curved rolls are the rule rather than the exception. This particular flow behavior can be explained by side wall effects. If the mean temperature T_m ($= (T_h + T_c)/2$) of the fluid is not equal to the ambient temperature a net heat transfer will occur through the side walls to the surroundings. In our case the mean temperature T_m is greater than the ambient temperature T_a and the net heat transfer is positive. This effect forces the fluid to move downwards at the side walls.

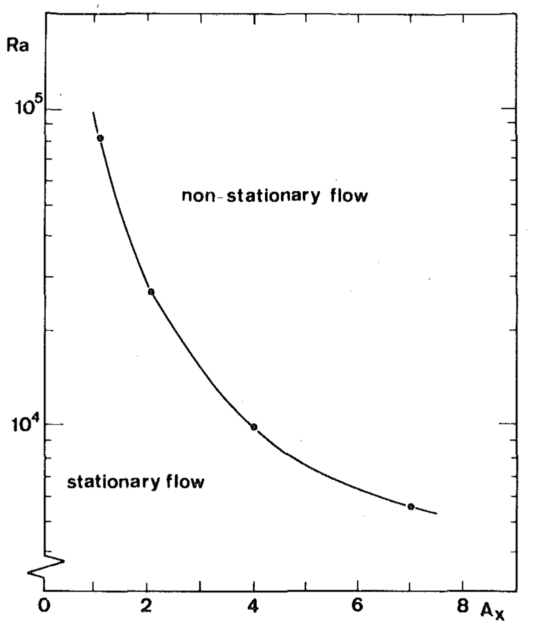

Fig. 4 The Ra_c for transition from stationary to nonstationary flow for the horizontal orientation ($\phi = 0$ deg) dependent on A_x

For $A_x \leqslant 1$ this effect results always in an even number of longitudinal rolls while for $A_x > 1$ the torus shaped roll appears.

For $A_x = 1$ and $A_z = 10$ we observed as expected ten equal sized longitudinal rolls (Fig. 5(*d*)).

The Inclined Situation. If we decrease the angle of inclination from $\phi = 90$ deg, we find a similar change in the flow pattern for aspect ratios $1 \leqslant A_x \leqslant 7$.

With decreasing angle, the tertiary and secondary motion tends to disappear before the flow becomes nonstationary or three-dimensional.

An example of the change in the flow pattern with ϕ can be seen in Fig. 6 for $A_x = 1$. By decreasing ϕ and Ra, we obtained the transition curves for each aspect ratio for stationary to nonstationary flow and for two-dimensional to three-dimensional flow. In Fig. 7 the transition curves are given for each aspect ratio. With decreasing aspect ratio the flow remains stationary for higher Ra number and smaller ϕ. Even for $A_x = 0.5$ and 0.25 only stationary flow was observed for the range of parameters considered. The transition from stationary two-dimensional to stationary three-dimensional flow occurs with increasing A_x for increasing ϕ for $A_x \geqslant 1$. This is in agreement with experiments of Ozoe [10]. For $A_x < 1$ the transition occurs for increasing ϕ with decreasing A_x (for example $\phi' = 40$ deg for $A_x = 0.5$ and $\phi' = 60$ deg for $A_x = 0.25$ at Ra $= 2 \times 10^5$). The angle of transition for transition to three-dimensional flow is only slightly dependent on Ra.

For a plate distance of 0.02 m no significant change for the two-dimensional flow has been observed. This indicates that for $D = 0.04$ m the depth aspect ratio ($A_z = 5$) is yet great enough to insure two-dimensionality of the base flow at the midplane of the enclosure. But, as already explained for the horizontal orientation, it effects the number of longitudinal rolls. This number is also influenced by the heat transport through the sidewalls as explained before.

At Ra $= 2 \times 10^5$, $\phi = 60$ deg and $A_x = 1$ we observed a particular flow pattern, i.e., two different orientations of the flow in different cross sections (see Fig. 6): one more or less horizontal and one vertical. In the z-direction there are 14 recirculating cells, seven for each orientation. For a smaller value of Ra, only the unicellular base flow remains.

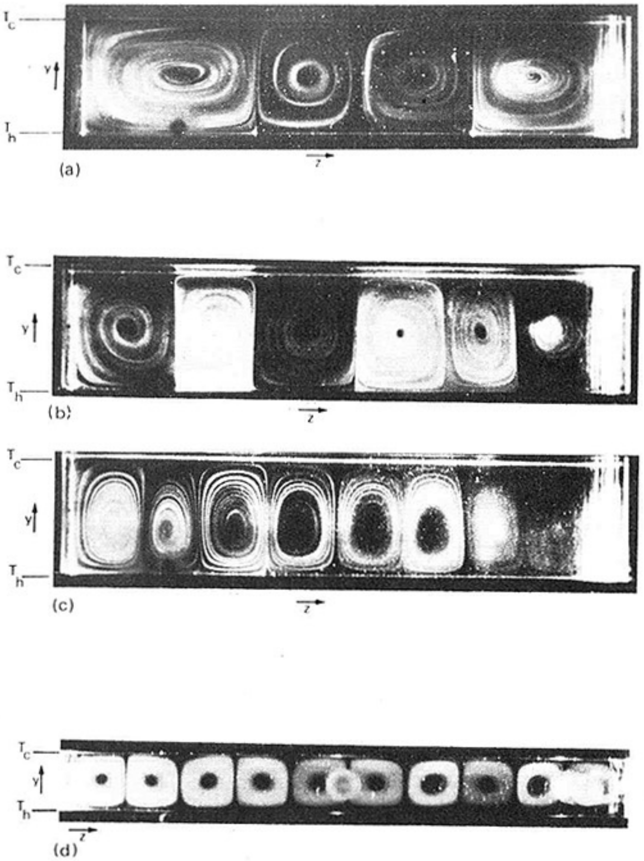

Fig. 5 Longitudinal rolls in the horizontal orientation ($\phi = 0$ deg): (*a*) $A_x = 1$, $A_z = 5$; (*b*) $A_x = 0.25$, $A_z = 5$; (*c*) $A_x = 0.25$, $A_z = 5$; (*d*) $A_x = 1$, $A_z = 10$

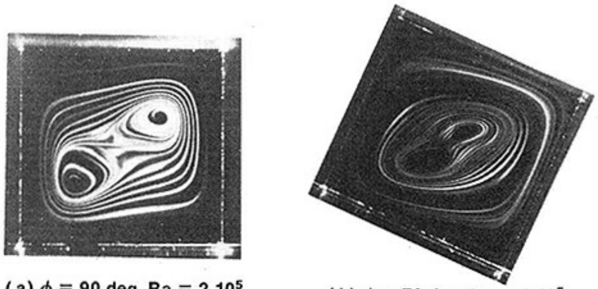

(*a*) $\phi = 90$ deg, Ra $= 2.10^5$ **(*b*) $\phi = 70$ deg, Ra $= 2.10^5$**

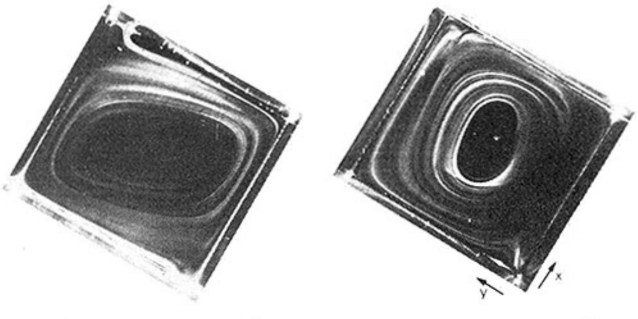

(*c*) $\phi = 60$ deg, Ra $= 2.10^5$ **(*d*) $\phi = 60$ deg, Ra $= 2.10^5$**

Fig. 6 Observed flow for $A_x = 1$, $\tilde{A}_z = 5$, for different angle of inclination

Results of Laser Doppler Measurements

Velocity profiles were measured for stationary flows. In Fig. 8 the u-velocity profile (velocity in the x-direction) dependence on y is given at the midplane of the enclosure ($x = 0.5\ A_x$, $z = 0.5\ A_z$) for $A_x = 7$ and different Rayleigh numbers. One can clearly see that the flow develops from a creeping flow at low Ra number to the boundary layer regime. With increasing Rayleigh number, the maximum velocity increases and the flow is concentrated near the hot and cold walls while the center of the enclosure is relatively tranquil. This development is in agreement with the theory described by Batchelor [18].

For Ra $= 2.2 \times 10^5$ u-velocity profiles are measured for different

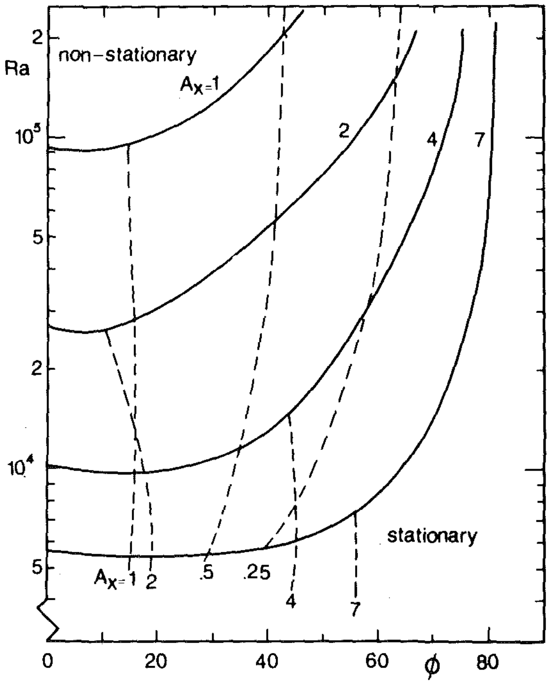

Fig. 7 Transition curves for different A_x dependent on Ra and ϕ: —— stationary to nonstationary flow; - - - two-dimensional to three-dimensional flow

aspect ratio A_x = 1, 2, 3, 4 and 5 (see Fig. 9). With increasing A_x the maximum velocity and the thickness of the boundary layer increases. In Fig. 10, the measured velocity profiles are given for A_x = 1 for different angles of inclination. It appears that with decreasing angle of inclination the maximum velocity remains approximately the same when $\phi > 60$ deg. Moreover, the velocities in the core region increase the decreasing angle of inclination.

To determine the influence of the heat transfer through the side walls on the flow, we measured at different depths in the enclosure the velocity profile (Fig. 11). The temperature T_a was smaller than the mean temperature T_m during the measurements. So we expected a downward directed flow near the side walls. In Fig. 11 this downward directed flow can be seen. Also we notice that for z/L = 0.3 to 0.5 the velocity profiles are equal which indicates that here the influence of the side walls is negligible. However, the velocity profiles at the cold and the hot wall are not fully symmetrical. Because of the net downward directed flow at the side walls the upward flow in the center of the enclosure should compensate this effect. Therefore, the net upward flow is positive. Measurements with insulated side walls (0.03 m polystyre) give a much more symmetrical velocity profile (see Fig. 12), which is in good agreement with measurements of Morrison and Tran [8]. This side wall boundary effect is less for smaller aspect ratio A_x, indicating that the heat transfer effect decreases with decreasing aspect ratio.

Conclusions

Flow visualization observations for the vertical orientation for small and moderate aspect ratio $0.25 \leqslant A_x \leqslant 7$ and $5 \times 10^3 \leqslant \mathrm{Ra} \leqslant 2.5 \times 10^5$ did not show transverse rolls. Instead for high Rayleigh number ($\mathrm{Ra} > 1.4 \times 10^5$) and $A_x \geqslant 1$ secondary and tertiary motion occurred.

In the horizontal situation we observed for $A_x \leqslant 1$ longitudinal rolls. The number of rolls is influenced by the side wall boundary condition. For $A_x > 1$ we obtained a torus-like flow pattern also due to the side wall boundary condition of the enclosure.

For all angles of inclination we determined the transition curves for the transition of stationary flow to nonstationary flow and for transition of two-dimensional flow to three-dimensional flow. We observed only stationary flow for $A_x < 1$ at the parameter range considered. For $A_x \geqslant 1$ the onset of nonstationary flow occured for the three-dimensional flow at a smaller value of the Rayleigh number

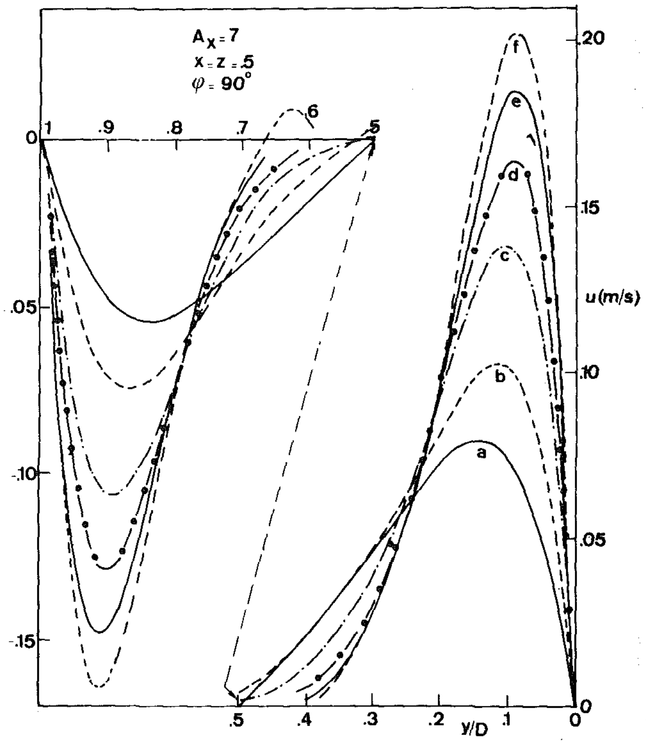

Fig. 8 u—velocity profiles for different Ra numbers for A_x = 7, ϕ = 90 deg: (a) Ra = $3.6.10^4$; (b) Ra = $6.8.10^4$; (c) Ra = $1.3.10^5$; (d) Ra = $1.8.10^5$; (e) Ra = $2.2.10^5$; (f) Ra = $2.5.10^5$

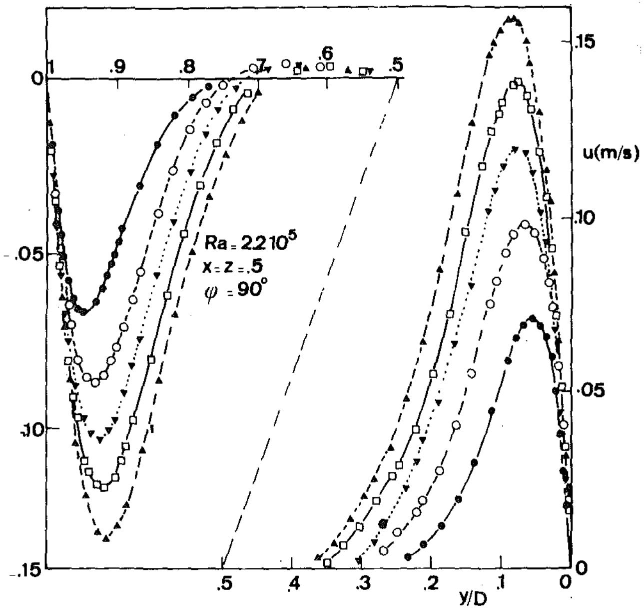

Fig. 9 u—velocity profiles for different A_x, ϕ = 90 deg: ● A_x = 1; ○ A_x = 2; ▼ A_x = 3; □ A_x = 4; ▲ A_x = 5

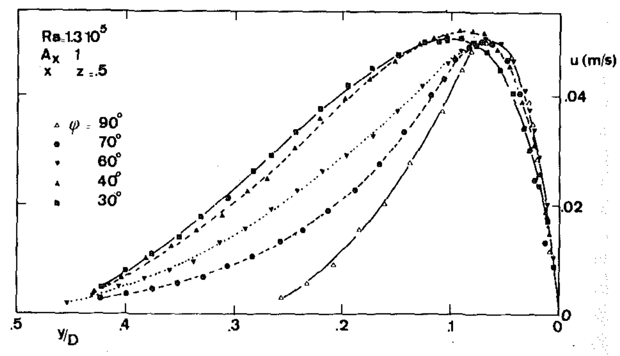

Fig. 10 u—velocity profiles for different ϕ, A_x = 1

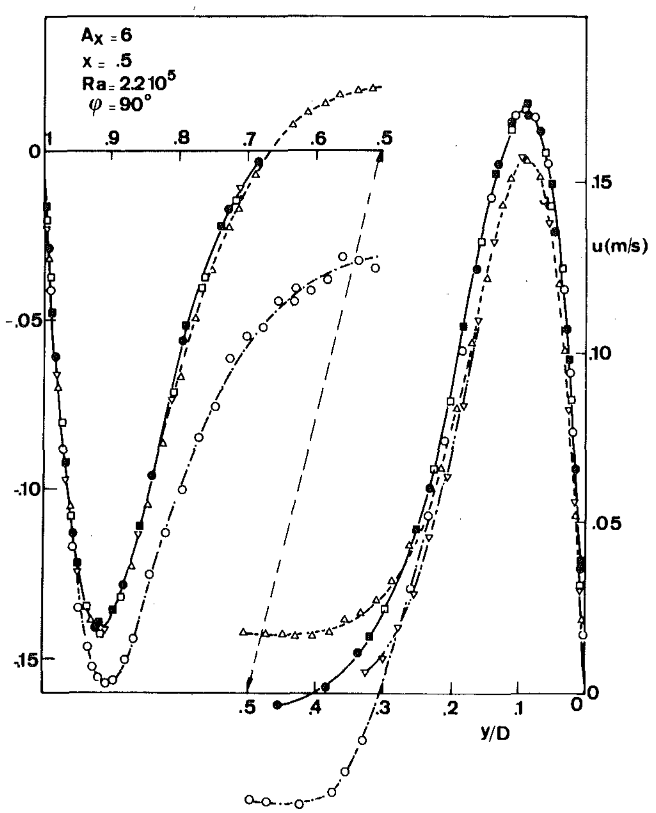

Fig. 11 u—velocity profiles at different depths in the enclosures: ● $z/L = 0.5$; ■ $z/L = 0.4$; □ $z/L = 0.3$; ▽ $z/L = 0.2$; △ $z/L = 0.1$, ○ $z/L = 0.05$

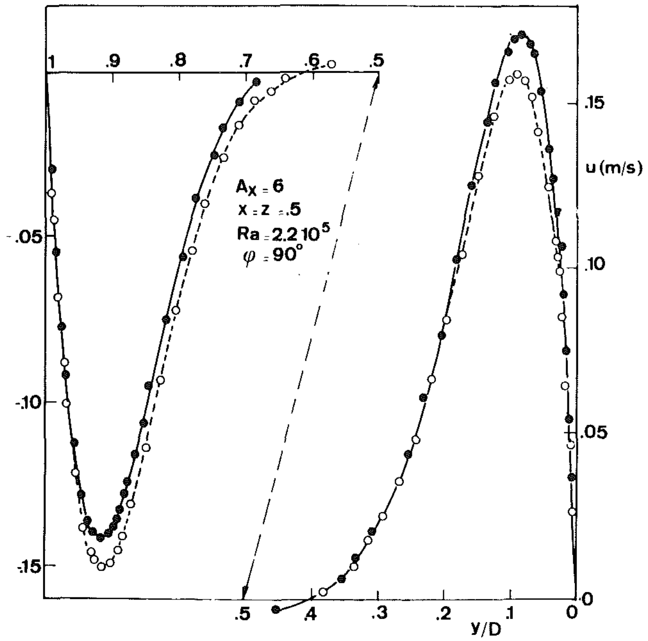

Fig. 12 u—velocity profiles with different side wall boundary condition: ● noninsolated; ○ insolated

than for the two-dimensional flow. The critical Rayleigh number for onset to nonstationary flow increased with decreasing A_x.

From the lda measurements it can be concluded that the value of the depth to width aspect ratio ($A_z = 5$) is great enough to insure two-dimensional flow at the midplane. For increasing Ra numbers the flow develops to a boundary layer flow. For decreasing ϕ the flow loses the boundary layer behavior and the velocities in the core region increase.

Acknowledgment

This work was supported by the Dutch Foundation for Pure Scientific Research (ZWO).

References

1 Catton, I., "Natural Convection in Enclosures," *Proceedings Sixth International Heat Transfer Conference*, Toronto, Canada, Aug. 7–11, Vol. 6, 1978, pp. 13–31.

2 Arnold, J. N., Catton, I., Edwards, D. K., "Experimental Investigation of Natural Convection in Inclined Rectangular Regions of Different Aspect-Ratios," ASME JOURNAL OF HEAT TRANSFER, Vol. 98, No. 1, 1976, pp. 67–71.

3 Krishnamurti, R., "On the Transition to Turbulent Convection. Part 1. The transition from Two- to Three-Dimensional Flow," *Journal of Fluid Mechanics*, Vol. 42, Part 2, 1970, pp. 295–307.

4 Krishnamurti, R., "On the Transition to Turbulent Convection. Part 2. The Transition to Time-Dependent Flow," *Journal of Fluid Mechanics*, Vol. 42, Part 2, 1970, pp. 309–320.

5 Krishnamurti, R., "Some Further Studies on the Transition to Turbulent Convection," *Journal of Fluid Mechanics*, Vol. 60, Part 2, 1973, pp. 285–303.

6 Stork, K., Müller, U., "Convection in Boxes: Experiments," *Journal of Fluid Mechanics*, Vol. 54, Part 4, 1972, pp. 599–611.

7 Elder, J. W., "Laminar Free Convection in a Vertical Slot," *Journal of Fluid Mechanics*, Vol. 23, Part 1, 1965, pp. 77–98.

8 Morrison, G. I., Tran, V. Q., "Laminar Flow in Vertical Free Convective Cavities," *International Journal of Heat and Mass Transfer*, Vol. 21, 1978, pp. 203–213.

9 Ozoe, H., Sayama, H., Churchill, S., "Natural Convection in a Long Inclined Rectangular Box Heated from Below," *International Journal of Heat and Mass Transfer*, Vol. 20, 1977, pp. 123–129.

10 Ozoe, H., Sayama, H., Churchill, S., "Natural Convection in an Inclined Rectangular Channel at Various Aspect-Ratios: Experimental Measurements," *International Journal of Heat and Mass Transfer*, Vol. 18, 1975, pp. 1425–1431.

11 Ozoe, H., Sayama, H., Churchill, S., "Natural Circulation in an Inclined Rectangular Channel Heated on one Side and Cooled on the Opposing Side," *International Journal of Heat and Mass Transfer*, Vol. 17, 1974, pp. 1209–1217.

12 Schinkel, W. M. M., "Natural Convection in Inclined Air-Filled Enclosures," Ph.D.-thesis, Delft University of Technology, 1980.

13 Schinkel, W. M. M., Linthorst, S. J. M., Hoogendoorn, C. J., "The Stratification in Natural Convection in Vertical Enclosures," *Proceedings 19th National Heat Transfer Conference*, session Natural Convection in Enclosures, Orlando, Fla, July 1980, pp. 31–38.

14 Mallinson, G. D., De Vahl Davis, G., "Three-Dimensional Natural Convection in a Box: a Numerical Study," *Journal of Fluid Mechanics*, Vol. 83, Part 1, 1977, pp. 1–31.

15 Korpela, S. A., Gözüm, D., Baxi, C. B., "On the Stability of the Conduction Regime of Natural Convection in a Vertical Slot," *International Journal of Heat and Mass Transfer*, Vol. 16, 1973, pp. 1683–1690.

16 Bergholz, R. F., "Instability of Steady Natural Convection in a Vertical Fluid Layer," *Journal Fluid Mechanics*, Vol. 84, 1978, pp. 743–768.

17 Clever, R. M., Busse, F. H., "Instabilities of Longitudinal Convection Rolls in an Inclined Layer," *Journal of Fluid Mechanics*, Vol. 81, Part 1, 1977, pp. 107–127.

18. Batchelor, G. K., "Heat Transfer by Free Convection Across a Closed Cavity Between Vertical Boundaries at Different Temperatures," *Quarterly Journal of Applied Mathematics*, Vol. 12, 1954, pp. 209–233.

W. D. Bennon[1]
F. P. Incropera
Heat Transfer Laboratory,
School of Mechanical Engineering,
Purdue University,
West Lafayette, IN 47907

Mixed Convection Heat Transfer from Horizontal Cylinders in the Crossflow of a Finite Water Layer

Heat transfer measurements and flow visualization studies have been performed for a single horizontal cylinder, a single row of six horizontal cylinders, and two rows of 13 horizontal cylinders submerged in an open channel flow. Regimes associated with free convection, combined convection, and forced convection have been delineated, and the effects of finite boundaries have been resolved. For a restricted set of space ratios, correlations of heat transfer data have been developed for the combined convection regime.

Introduction

Although frequently neglected, buoyancy effects can strongly influence convection heat transfer from circular cylinders under forced flow conditions. The effects are particularly significant for low velocity, high heat flux conditions and may influence the performance of systems involving waste heat utilization, nuclear waste disposal, reactor cooling, and sensible energy storage.

Several experimental studies have been performed to develop general heat transfer correlations for mixed convection conditions. Zijnen [1] was partially successful in using a vectorial addition of natural and forced convection results to correlate data obtained for air in crossflow over horizontal cylinders. There is little physical basis for such an approach, however, and more emphasis has been placed on the use of an equivalent Reynolds number to correlate results for a variety of fluids and flow conditions [2–4]. Other efforts [5, 6] have concentrated on identifying regions associated with natural, forced, and mixed convection. The regions have been delineated in terms of a Grashof number-Reynolds number ratio of the form Gr/Re^n, where n is typically in the range from 2 to 3, and some success has been achieved in using this ratio to correlate heat transfer data. In addition, several theoretical studies have been performed [7–9] and have been useful in delineating regimes for which mixed convection effects are significant.

Despite the foregoing efforts there remains a need for heat transfer correlations which apply over a wide range of mixed convection conditions and for which the effects of finite boundaries have been determined. Moreover, all studies performed to date have been concerned with a single cylinder, when, in fact, most applications involve an array of cylinders. Accordingly, the primary objective of this study has been to measure and to correlate heat transfer parameters under combined convection conditions for a single cylinder and for horizontal cylinder arrays. The experiments have been performed in a water channel for which the water layer height and cylinder placement may be varied, and measurements have been performed for the parameter range $0 \le Re_D \lesssim 2300$ and $0.04 \lesssim (Gr_D/Re_D^2) < \infty$. The effects of finite boundaries have been determined, and the data corresponding to the combined convection regimes have been correlated.

Experimental Procedures

The experiments were conducted in an open water channel which is 2.36 m long and constructed of 12.7 mm plexiglass. The channel has a fixed width of 280 mm, and up to 13 horizontal copper cylinders may be inserted according to the arrangement of Fig. 1. The first cylinder of the array is located 1 m from the channel entrance and each cylinder is drilled along its axis to permit insertion of an electrical heater. Power to each heater is regulated by a voltage controller and is monitored using a digital wattmeter calibrated to an accuracy of ±1 W over the range 0 to 300 W.

As shown in the insert of Fig. 1, four rectangular grooves are milled in each cylinder surface at 90 deg intervals, extending from one end to the midplane. Thermocouple leads are inserted in the grooves, with junctions attached to the surface at the midplane. The grooves are filled with a mixture of epoxy and finely ground copper filings, and the cylinder is polished with an abrasive cloth to provide a smooth surface condition. The cylinder surface temperature is taken to be the arithmetic mean of the four readings.

Inlet (upstream) and outlet (downstream) water temperatures are measured using two vertical arrays of five thermocouples, each mounted directly in the channel sidewall and extending 25.4 mm from the interior channel surface. The temperatures are evaluated by taking the arithmetic mean of the five values for an array. All thermocouple data are recorded and stored using an Esterline Angus Model PD-2064 programmable data acquisition system with a Kennedy Model 1610 magnetic tape recorder. An uncertainty of ±0.5°C is assigned to each thermocouple measurement.

A closed flow system, which permitted variation of the water layer height and the flow velocity, was used for all of the experiments, with tests performed under darkened laboratory conditions. The ambient air and inlet water temperatures were approximately 21°C, with temperature differences between the cylinder surface and the water ranging up to 21°C.

The upstream velocity field in the channel was measured by using the hydrogen bubble technique. A 50 mm long, 0.025 mm dia platinum wire was attached to a support frame which could be traversed vertically and in the flow direction. The wire was electronically pulsed, and the local velocity was inferred from photographs of the bubble traces. From repetitive measurements made for velocities in the range of interest (0 to 65 mm/s), the uncertainty associated with this pro-

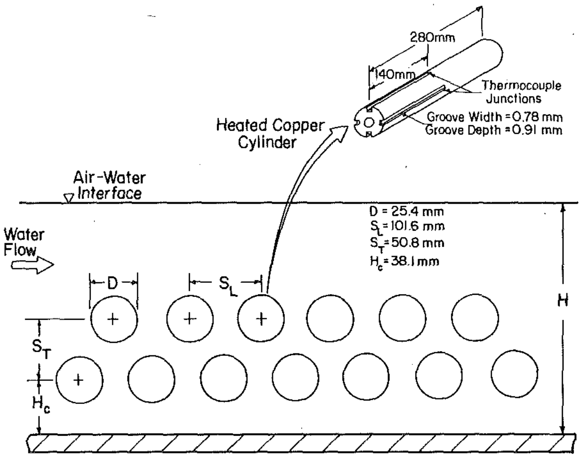

Fig. 1 Longitudinal section of water channel with 13 cylinder array

---

[1] Presently with Alcoa Technical Center, Alcoa, PA.

Contributed by the Heat Transfer Division for publication in the JOURNAL OF HEAT TRANSFER. Manuscript received by the Heat Transfer Division October 17, 1980.

cedure was estimated to be ±10 percent. The vertical distribution of the velocity was characterized by a central core of uniform velocity and upper and lower regions, approximately 25 mm thick, in which the velocity decreases with increasing distance from the core. Typically, however, conditions were dominated by the central core, whose velocity, U_0, was used to calculate the Reynolds number.

Observation of thermal plume development from the heated cylinders was achieved by using the shadowgraph technique. Collimated light from a 100 W mercury arc lamp was focused and passed through the channel sidewalls, and the transmitted light was cast on a thin sheet of frosted glass. Shadows appearing as a result of density variations were used to infer qualitative features of the plume development.

The average heat transfer coefficient for an N cylinder array may be obtained from an expression of the form

$$\bar{h} = \frac{1}{N}\sum_{j=1}^{N}\bar{h}_j = \frac{1}{N}\sum_{j=1}^{N}\frac{P_j}{A(T_{c,j} - T_{w,i})} \qquad (1)$$

where $\bar{h}_j$, P_j and $T_{c,j}$ are the average convection coefficient, the power dissipation, and the average surface temperature associated with a single cylinder. A Nusselt number for the array may then be expressed as $\overline{\mathrm{Nu}}_D = \bar{h}D/k$, and, for the conditions of the study, may be presumed to have a functional dependence of the form

$$\overline{\mathrm{Nu}}_D = f(\mathrm{Re}_D, \mathrm{Gr}_D, H/D, H_c/D, S_L/D, S_T/D) \qquad (2)$$

The Reynolds and Grashof numbers account for flow field effects related to inertia and buoyancy forces, respectively, while the space ratios account for cylinder spacing and finite medium effects. All water properties appearing in these parameters were evaluated at a mean film temperature defined as $\overline{T}_f = [\overline{T}_c + (T_{w,i} + T_{w,o})/2]/2$.

Three sets of experiments have been performed, corresponding to a single cylinder, a horizontal array of six cylinders in a single row, and a horizontal array of thirteen cylinders in two rows. For the single cylinder, data have been obtained over the parameter range $0 \le \mathrm{Re}_D \le 2300$ and $0.025 \le \mathrm{Gr}_D/\mathrm{Re}_D{}^2 \le \infty$, as well as for four different conditions related to cylinder placement and water layer height ($H = 240$ mm, $H_c = 38.1$ mm; $H = 100$ mm, $H_c = 38.1$ mm; $H = 75$ mm, $H_c = 38.1$ mm; $H = 240$ mm, $H_c = 88.9$ mm). For the six cylinder horizontal array, the parameter ranges were $0 \le \mathrm{Re}_D \le 2000$ and $0.040 \le \mathrm{Gr}_D/\mathrm{Re}_D{}^2 \le \infty$, with three different combinations of cylinder placement and water layer height ($H = 240$ mm, $H_c = 38.1$ mm; $H = 100$ mm, $H_c = 38.1$ mm; $H = 240$ mm, $H_c = 88.9$ mm); while for the 13 cylinder array, the ranges were $140 \le \mathrm{Re}_D \le 2050$ and $0.026 \le \mathrm{Gr}_D/\mathrm{Re}_D{}^2 \le 53$, with $H = 240$ mm and $H = 130$ mm. The cylinder diameter was fixed at $D = 25.4$ mm for all experiments, while the longitudinal pitch was fixed at $S_L = 101.6$ mm for both the six and 13 cylinder arrays and the transverse pitch was fixed at $S_T = 50.8$ mm for the 13 cylinder array.

An experimental uncertainty analysis was performed according to established procedures [10], and uncertainties in the parameters Re_D and $\mathrm{Gr}_D/\mathrm{Re}_D{}^2$ were determined to be approximately 10 and 20 percent, respectively, for the single cylinder experiments. The corresponding uncertainty in $\overline{\mathrm{Nu}}_D$ depends strongly on U_0 and P_j, varying from a high of 20 percent for large values of U_0 and small values of P_j to a low of 4 percent for small values of U_0 and large values of P_j. These high and low values increase to approximately 40 and 10 percent, respectively, for the six cylinder array and to approximately 60 and 15 percent, respectively, for the 13 cylinder array.

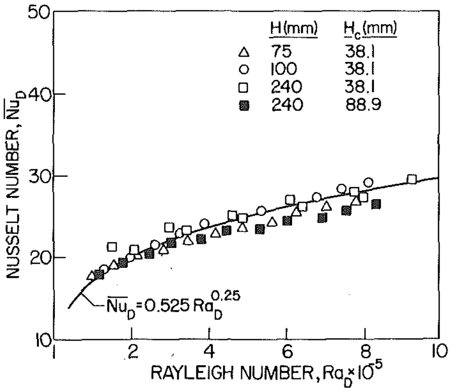

Fig. 2 Single cylinder Nusselt number as a function of Rayleigh number for pure free convection

Experimental Results: Single Cylinder

Results obtained for $\mathrm{Re}_D = 0$ ($\mathrm{Gr}_D/\mathrm{Re}_D{}^2 = \infty$) correspond to free convection and are plotted as a function of Rayleigh number in Fig. 2. The data are compared with the widely used correlation of McAdams [11] for an infinite medium, and the excellent agreement (to within ±15 percent) suggests that the finite geometry of the experiments has little effect on the results. There is no consistent variation of the data with the water layer height, H, and although the Nusselt number appears to increase slightly with decreasing distance, H_c, between the cylinder and the channel bottom, the trend is weak and well within experimental uncertainties. Although free convection heat transfer from a cylinder in a finite medium is known to be enhanced by the establishment of recirculating flows [12, 13], such flows require the presence of a finite width, as well as a finite height, and are hence absent from the present experiments.

The effect of Reynolds number is illustrated in Fig. 3, where representative data are plotted for $H = 100$ mm and $H_c = 38.1$ mm. For small values of the Reynolds number, $\mathrm{Re}_D \lesssim 200$, the Nusselt number is independent of Re_D, depending entirely on the heater power input and hence on the Rayleigh number. Accordingly, free convection correlations may be applied without error. With increasing Reynolds number, however, there is a gradual reduction in the dependence of $\overline{\mathrm{Nu}}_D$ on Ra_D and an increasing dependence on Re_D. The same trends were obtained for each of the other cylinder and water layer height

Nomenclature

A = cylinder surface area, m^2
C_i = constants in the heat transfer correlation
D = cylinder diameter, m
g = acceleration due to gravity, m/s^2
Gr_D = Grashof number, $g\beta(T_c - T_{w,i})D^3/\nu^2$
H = water layer height, m
H_c = distance from cylinder centerline to channel bottom, m
$\bar{h}$ = average heat transfer coefficient for the array of cylinders, W/m^2·K
$\bar{h}_j$ = average heat transfer coefficient for a single cylinder, W/m^2·K
k = thermal conductivity, W/m·K
N = number of cylinders in the array (1, 6 or 13)
$\overline{\mathrm{Nu}}_D$ = average Nusselt number for the array of cylinders, $\bar{h}D/k$
$\overline{\mathrm{Nu}}_{D,f}$ = average Nusselt number based on forced convection correlation
P_j = heater power dissipation, W
P_L, P_T = dimensionless longitudinal and transverse pitch ($P \equiv S/D$)
Pr = Prandtl number
Ra_D = Rayleigh number, $\mathrm{Gr}_D\mathrm{Pr}$
Re_D = Reynolds number, U_0D/ν
S_L, S_T = longitudinal and transverse pitch, m
$\overline{T}_c$ = average surface temperature for an array of cylinders, $\left(\sum_{j=1}^{N} T_{c,j}\right)/N$, K
$T_{c,j}$ = average surface temperature for a single cylinder, K
T_f = film temperature, K
$T_{w,i}$ = water inlet (upstream) temperature, K
$T_{w,o}$ = water outlet (downstream) temperature, K
U_0 = uniform core velocity associated with channel flow, mm/s
β = thermal expansion coefficient, K^{-1}
ν = kinematic viscosity, m^2/s

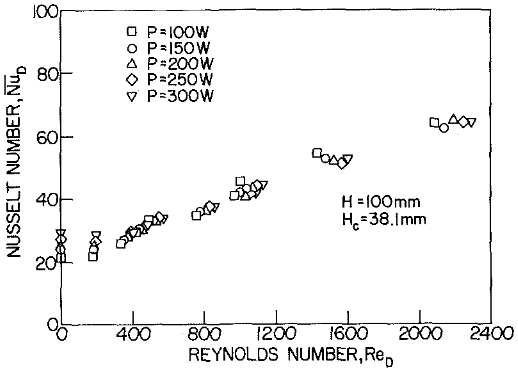

Fig. 3 Single cylinder Nusselt number as a function of Reynolds number for different heater power setting

combinations. Although the data revealed a slight increase in $\overline{\mathrm{Nu}}_D$ with decreasing H for large Re_D, differences were within the experimental uncertainty and space effects could again be neglected.

Figure 4 reveals the error associated with using a forced convection correlation to predict the mixed convection results of this study. Heat transfer data obtained for $P = 300$ W and two of the geometrical conditions are plotted as $(\overline{\mathrm{Nu}}_D - \overline{\mathrm{Nu}}_{D,f})/\overline{\mathrm{Nu}}_D$, where $\overline{\mathrm{Nu}}_{D,f}$ is obtained from a standard forced convection correlation of the form [11, 14]

$$\overline{\mathrm{Nu}}_{D,f} = (0.35 + 0.56\mathrm{Re}_D^{0.52})\mathrm{Pr}^{0.30} \qquad (3)$$

The discrepancy is large for $\mathrm{Re}_D = 200$, where buoyancy effects enhance heat transfer by approximately 50 percent, and decreases with increasing Re_D. Even for $\mathrm{Re}_D \simeq 2000$, however, the data remain consistently underpredicted by the correlation.

The ratio $\mathrm{Gr}_D/\mathrm{Re}_D^2$ may be used to delineate the data according to zones. In Fig. 5 representative raw data are plotted in terms of flow velocity and temperature difference, and the four zone boundaries determined by Fand and Keswani [6] are superposed on the plot. For a prescribed power, P, the value of $(T_c - T_{w,i})$ provides a measure of the average cylinder heat transfer coefficient through equation (1). For a fixed P and values of $U_0 \lesssim 10$ mm/s, the value of $(T_c - T_{w,i})$ is independent of U_0. Hence $\overline{\mathrm{Nu}}_D$ is independent of Re_D, and the range of $\mathrm{Gr}_D/\mathrm{Re}_D^2 > 40$ is one of free convection. For $2 < \mathrm{Gr}_D/\mathrm{Re}_D^2 < 40$, forced convection effects become discernable, and for a prescribed heater power, the trend is generally one of decreasing $(T_c - T_{w,i})$, and hence increasing $\bar{h}$, with increasing U_0. This trend is also characteristic of the region $\mathrm{Gr}_D/\mathrm{Re}_D^2 < 2$, although the effect becomes less pronounced for $\mathrm{Gr}_D/\mathrm{Re}_D^2 < 0.5$, which is a region associated with domination by forced convection effects [6].

Transition from free to forced convection is also characterized by significant changes in flow conditions. For free convections at low to moderate values of Gr_D, it is known [15, 16] that a laminar boundary layer originates at the lower stagnation point, develops around the cylinder, and merges at the upper stagnation point without separation. A plume is formed above the cylinder and rises vertically until it is deflected by the air-water interface. This behavior was also observed with the shadowgraph, along with changes which occur due to superposition of a horizontal, forced flow. In particular, with decreasing $\mathrm{Gr}_D/\mathrm{Re}_D^2$, the point of boundary layer merger and plume detachment is shifted clockwise. For values of $\mathrm{Gr}_D/\mathrm{Re}_D^2 \approx 40$, this shift is slight, as the cylinder boundary layer development remains dominated by buoyancy forces. With decreasing $\mathrm{Gr}_D/\mathrm{Re}_D^2$, inertia forces become more prominent, as the angle associated with plume detachment increases, and eventually $(\mathrm{Gr}_D/\mathrm{Re}_D^2 \lesssim 0.5)$ inertia forces dominate over those associated with buoyancy. Boundary layer separation is then observed to occur, as a wake develops downstream of the cylinder.

In view of the foregoing results and the fact that the data are only weakly dependent on H and H_c, it is reasonable to seek a heat transfer correlation of the form

$$\overline{\mathrm{Nu}}_D = [C_1 + C_2\mathrm{Re}_D^{C_3} + C_4(\mathrm{Gr}_D/\mathrm{Re}_D^2)^{C_5}]\mathrm{Pr}^{1/3} \qquad (4)$$

where the first two terms on the right-hand side resemble the form of typical forced convection correlations and the third term accounts for free convection effects. The constants C_1 to C_5 were evaluated from a nonlinear regression analysis of the data, and the resulting correlation is of the form

$$\overline{\mathrm{Nu}}_D = [4.11 + 0.20\,\mathrm{Re}_D^{0.65} + 0.71(\mathrm{Gr}_D/\mathrm{Re}_D^2)^{0.52}]\mathrm{Pr}^{1/3} \qquad (5)$$

All of the data which are in the range $175 \leq \mathrm{Re}_D \leq 2300$ and $0.025 \leq \mathrm{Gr}_D/\mathrm{Re}_D^2 \leq 48$ are correlated by this expression to within ±15 percent, irrespective of the values of H and H_c, and 93 percent of the data are correlated to within ±10 percent. For $\mathrm{Re}_D < 175$, the data are correlated to within ±15 percent by the free convection correlation of McAdams [11].

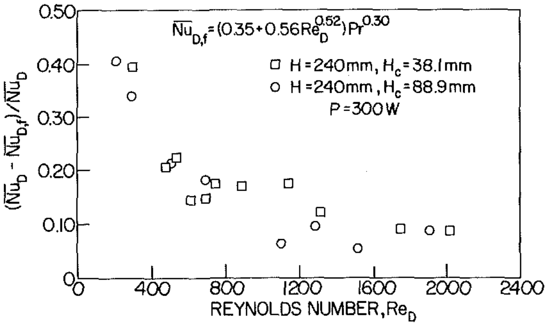

Fig. 4 Variation with Reynolds number of the difference between experimental single cylinder Nusselt numbers and predictions from a standard forced convection correlation [11,14]

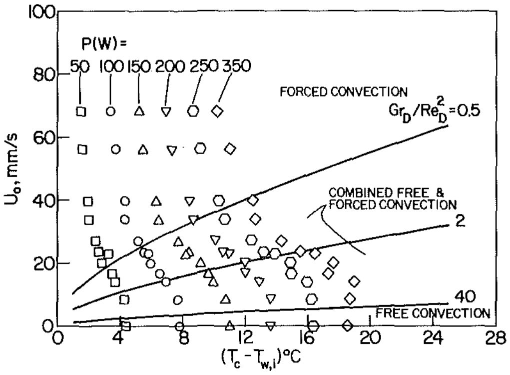

Fig. 5 Single cylinder heat transfer data corresponding to *H* = 240 mm and *H*$_c$ = 38.1 mm, with mixed convection boundaries delineated by the criteria of Fand and Keswani [6]

The foregoing results may be compared with those of Fand and Keswani [6], who divided their data into four regions according to the value of $\mathrm{Gr}_D/\mathrm{Re}_D^2$. For $\mathrm{Gr}_D/\mathrm{Re}_D^2 < 0.5$, heat transfer is primarily by forced convection and their data were correlated by an expression of the form

$$\overline{\mathrm{Nu}}_D = (0.255 + 0.699\,\mathrm{Re}_D^{0.5})\mathrm{Pr}^{0.29} \qquad (6)$$

All comparable data obtained in this study are correlated to within ±20 percent by this expression, although 95 percent of the data exceed the predictions. Natural convection effects begin to become significant for $0.5 < \mathrm{Gr}_D/\mathrm{Re}_D^2 < 2.0$ and are comparable to those of forced convection for $2.0 < \mathrm{Gr}_D/\mathrm{Re}_D^2 < 40$. Although Fand and Keswani propose the following correlation for the first of these regimes,

$$\overline{\mathrm{Nu}}_D = [0.255 + 0.699\mathrm{Re}_D^{0.5} + 0.188(\mathrm{Gr}_D/\mathrm{Re}_D^2)\mathrm{Gr}_D^{0.25}]\mathrm{Pr}^{0.29} \qquad (7)$$

no correlation is presented for the second regime. The data of this study are within ±17 percent of predictions based on equation (7), although 94 percent of the data exceed the predictions. For $\mathrm{Gr}_D/\mathrm{Re}_D^2 > 40$, free convection effects dominate and Fand and Keswani recommend an expression of the form

$$\overline{\mathrm{Nu}}_D = 0.406(1.7\mathrm{Gr}_D + \mathrm{Re}_D^2)^{1/4}\mathrm{Pr}^{1/4} \qquad (8)$$

The limited data obtained in this study are correlated to within ±9 percent by this expression. Accordingly, the results of this study are consistent with those of Fand and Keswani, although equation (5) is more versatile through its applicability to a wider range of Gr_D/Re_D^2.

Experimental Results: Six Cylinder Array

The shadowgraph was also used to observe hydrodynamic effects associated with the six cylinder array. For free convection ($Gr_D/Re_D^2 = \infty$), a laminar, vertical plume originates from each cylinder and rises to the air-water interface, where it is deflected to form a thin surface layer of warm water. Although plume oscillation and recirculation effects have been observed in similar experiments [16], no such effects could be discerned in this study. With the superposition of small to moderate forced flows, ($0.5 \lesssim Gr_D/Re_D^2$), the point at which the plumes detach from the cylinders is shifted clockwise and the plumes are cantered at an angle which increases with decreasing Gr_D/Re_D^2. Plumes generated by each of the six cylinders do not interact with the other cylinders, but mix in the free stream (above the array) as they ascend to the air-water interface. For $Gr_D/Re_D^2 \lesssim 0.5$, however, plume cylinder interactions begin to occur until each cylinder downstream of the lead cylinder is submerged in a turbulent flow originating from the wakes of the preceding cylinders.

The influence of the foregoing hydrodynamic effects on the cylinder Nusselt number is shown in the representative results of Fig. 6. For (Gr_D/Re_D^2) $\gtrsim 0.5$, there is little difference between cylinder Nusselt numbers, and it may be concluded that the cylinders act as isolated heat sources for which mutual thermal and hydrodynamic interactions are negligible. For (Gr_D/Re_D^2) = 0.20, however, the Nusselt number of the second cylinder in the array is approximately 10 percent larger than that of the lead cylinder, which may be attributed to flow separation from the lead cylinder. The gradual decline in the Nusselt number from cylinders three to six can be attributed to a progressive warming of the water, which causes the cylinder surface temperature to rise for a fixed heat dissipation. Since the upstream water temperature is also fixed, the Nusselt number must decline.

Effects on the average array Nusselt number of the Reynolds number, water layer height, and the separation of the array from the channel bottom are shown in Fig. 7. For $Re_D \lesssim 300$, the Nusselt number is only weakly dependent on Re_D and is independent of H and H_c. Variations in the data are due entirely to different values of the power input. Moreover, the results agree well with those obtained for the single cylinder (Fig. 3), supporting the supposition that each cylinder acts as an isolated heat source and is unaffected by the presence of other cylinders. For $Re_D \gtrsim 300$, however, the Nusselt number increases with increasing Reynolds number, and for $Re_D \gtrsim 700$ the results are influenced by H and H_c. In particular, there is a small, but discernable increase in $\overline{Nu}_D$ with increasing H_c, although differences are within experimental uncertainties. There is a larger increase in $\overline{Nu}_D$ with decreasing H, and differences are most pronounced for the range $700 \lesssim Re_D \lesssim 1500$. This increase in Nusselt number with decreasing water layer height may be attributed to recirculation effects. With decreasing H, the space available for free-stream plume mixing is reduced and the probability of recirculating plumes interacting with downstream cylinders increases. With increasing Reynolds numbers above 1500, however, all plumes are swept horizontally in the direction of the forced flow and the probability of freestream mixing and recirculation from above the array is reduced. Hence the effect of H on $\overline{Nu}_D$ should diminish.

If the effects of H and H_c on the heat transfer data are neglected, a correlation of the form prescribed by equation (4) may be attempted for the average array Nusselt number. Obtaining the constants C_1 to C_5 from a nonlinear regression analysis of the data for $Re_D > 140$, the following expression was found to correlate all results to within ±26 and 94 percent of the data to within ±15 percent

$$\overline{Nu}_D = [7.34 + 0.019 Re_D^{0.94} + 0.92 (Gr_D/Re_D^2)^{0.47}] Pr^{1/3} \qquad (9)$$

For $Re_D < 140$, the data are correlated to within ±15 percent by the free convection correlation of McAdams [11].

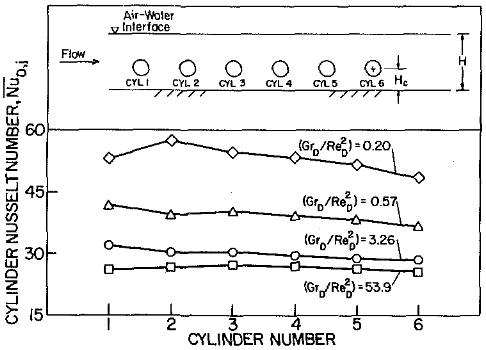

Fig. 6 Distribution of Nusselt numbers for the six cylinder array (H = 240 mm, H_c = 38.1 mm, P = 300 W)

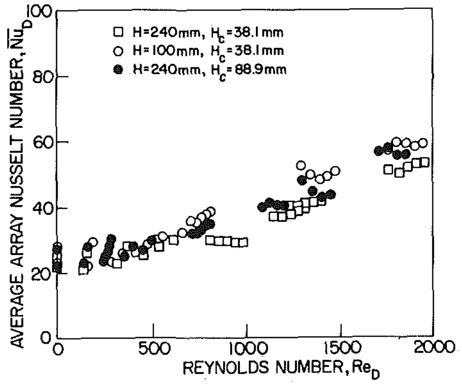

Fig. 7 Effects of Reynolds number, water layer height, and array placement on the average Nusselt number for the six cylinder array

Experimental Results: Thirteen Cylinder Array

Hydrodynamic effects associated with the thirteen cylinder array have also been observed shadowgraphically. As for the single cylinder and the six cylinder array, free convection ($Gr_D/Re_D^2 = \infty$) is characterized by laminar plumes which rise to the air-water interface and form a thin surface layer of warm water. Hence each cylinder acts as an isolated heat source. For small to moderate forced flows ($0.5 \lesssim Gr_D/Re_D^2 \lesssim 40$), the rear stagnation points are shifted clockwise and the plumes leave the cylinders cantered at angles which increase with decreasing Gr_D/Re_D^2. Plumes generated by the lower row of cylinders interact with the upper row, and above the array the plumes mix and are carried downstream as they ascend to the air-water interface. For $Gr_D/Re_D^2 \lesssim 0.5$, each cylinder downstream of the leading cylinders is submerged in a turbulent flow originating from the wakes of the preceding cylinders.

The influence of the foregoing hydrodynamic effects on the cylinder Nusselt number is shown by the representative results of Fig. 8. For (Gr_D/Re_D^2) = 40.4, Nusselt numbers associated with cylinders in a given row are approximately the same, although the Nusselt numbers associated with the upper row are approximately 25 percent less than those of the lower row. This result is due to the fact that, although free convection effects are dominant, the forced flow is sufficient to deflect plumes from the lower row into cylinders of the upper row. Accordingly, surface temperatures associated with cylinders of the upper row are larger than those of cylinders in the lower row, and the Nusselt number must be correspondingly smaller. Similar results have been observed by Eckert and Soehngen [17] for free convection from heated cylinders in a vertical array. With decreasing (Gr_D/Re_D^2) differences between results for the top and bottom rows diminish, as the effects of the forced flow become more significant. For (Gr_D/Re_D^2) = 0.18, forced flow effects become dominant and the results are characterized by increasing Nusselt number for the first few cylinders and a gradual decline for the cylinders which follow. The increase for the leading cylinders may be attributed to flow separation effects, while the subsequent decline may be attributed to increases in the cylinder surface temperature due to the rising water temperature.

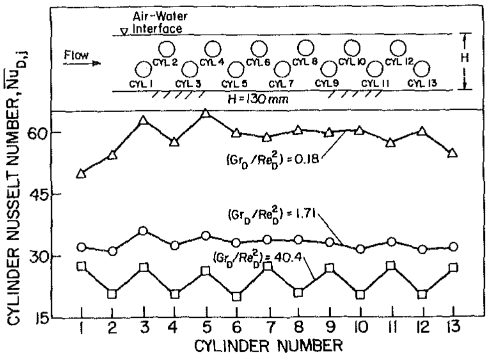

Fig. 8 **Distribution of Nusselt numbers for the 13 cylinder array (*H* = 130 mm, *P* = 250 W)**

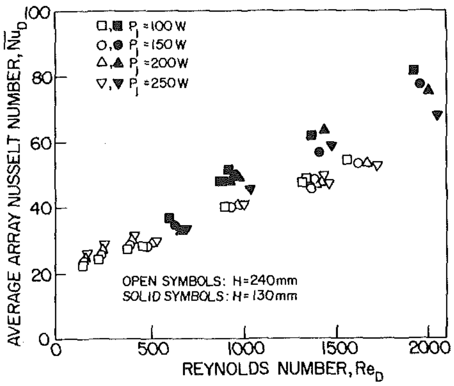

Fig. 9 **Effects of Reynolds number, cylinder power dissipation, and water layer height on the average Nusselt number for the 13 cylinder array**

The effects of Reynolds number, cylinder power dissipation, and water layer height on the average array Nusselt number are shown in Fig. 9. For $H = 240$ mm, the Reynolds number dependence is typical of that obtained for the six cylinder array and the results are only weakly dependent on the cylinder power dissipation. The strongest dependence occurs at low values of Re_D and the increase in $\overline{Nu}_D$ with increasing P_j is due to the importance of free convection effects. The same trends characterize the low Reynolds data, which do not appear in the figure, for the shallow water layer ($H = 130$ mm). However, at larger values of Re_D, $\overline{Nu}_D$ begins to decrease significantly with increasing P_j for the shallow layer. This trend is attributed to the effect which both increasing Re_D and decreasing H have on increasing the probability of warm water heated by the lead cylinders interacting with the downstream cylinders. Note that, for moderate to large values of Re_D, the average array Nusselt number increases with decreasing water layer height, which is consistent with results obtained for the six cylinder array.

If space ratio effects are neglected, a correlation of the form prescribed by equation (4) may also be obtained for the 13 cylinder array. Applying the nonlinear regression analysis to the data, it follows that

$$\overline{Nu}_D = [9.97 + 0.039\,Re_D^{0.83} + 0.54(Gr_D/Re_D^2)^{-0.84}]Pr^{1/3} \quad (10)$$

All of the data which are in the range $143 \leq Re_D \leq 2046$ and $0.026 \leq (Gr_D/Re_D^2) \leq 53$ are correlated to within ±23 percent by this expression and 92 percent of the data are correlated to within ±15 percent. Much of this discrepancy may be attributed to the ignored effects of H on $\overline{Nu}_D$. Note that, unlike the preceding correlations, the exponent on the (Gr_D/Re_D^2) term is negative, indicating that buoyancy acts to reduce the overall heat transfer from the array. This result is due to the effect of plume-cylinder interactions within the array. For $Gr_D/Re_D^2 > 53$, plume deflection is negligible and, because of the staggered arrangement, each cylinder behaves as an isolated heat source for which the standard free convection correlation may be applied.

Summary

Heat transfer measurements have been performed for a single horizontal cylinder and for horizontal arrays of six and 13 cylinders submerged in an open water channel flow. Major conclusions of the study are as follows:

1 For $Re_D \lesssim 150$ and $Gr_D/Re_D^2 \gtrsim 50$, forced convection effects are negligible, and in all cases the cylinders behave as isolated heat sources. Heat transfer data are correlated to within ±15 percent by the standard expression for free convection in an infinite medium [11].

2 For the single cylinder in the range $175 \leq Re_D \leq 2300$ and $0.025 \leq Gr_D/Re_D^2 \leq 48$, combined convection effects must be considered and the data are correlated to within ±15 percent by equation (5). For $Re_D > 2300$ and $Gr_D/Re_D^2 < 0.025$, buoyancy effects may be neglected, and a standard forced convection correlation, such as equation (3) or (6), may be used with ±20 percent accuracy.

3 For $Gr_D/Re_D^2 \gtrsim 0.5$ in the six cylinder array, each cylinder may be approximated as an isolated heat source characterized by the same Nusselt number. For $Gr_D/Re_D^2 \lesssim 0.5$, however, interactions between cylinder flow fields induce a small increase in the Nusselt number of the second cylinder, which is followed by a gradual decline in the Nusselt number of subsequent cylinders. For the 13 cylinder array, isolated heat source behavior may not be assumed for $Gr_D/Re_D^2 \lesssim 50$. For larger values of Gr_D/Re_D^2 associated with this range, thermal plumes generated in the bottom row of cylinders interact with the top row to significantly reduce Nusselt numbers associated with this row. With decreasing (Gr_D/Re_D^2) differences in the Nusselt numbers between rows diminish; while in the lower range of (Gr_D/Re_D^2), there is an increase in the Nusselt number for cylinders immediately downstream of the lead cylinders. This increase is followed by a gradual decline in the Nusselt number associated with subsequent cylinders.

4 Neglecting space ratio effects, the average Nusselt number for the six cylinder array is correlated to within ±26 percent by equation (9) for $140 < Re_D < 2000$ and $0.04 < (Gr_D/Re_D^2) < 54$. Similarly, the average Nusselt number for the thirteen cylinder array is correlated to within ±23 percent by equation (10) for $140 < Re_D < 2050$ and $0.026 < Gr_D/Re_D^2 < 53$.

Because they pertain to a restricted set of space ratios, caution should be exercised in using the correlations of this study. For each of the three geometries, the correlations are applicable when $H/D \geq 2.95$ and $H_c/D \gtrsim 1.5$. However, if the cylinders are placed close to the air-water interface ($H/D < 2.95$) and/or close to the channel bottom ($H_c/D < 1.5$), thermal and hydrodynamic interactions may introduce significant error.

Although results obtained for the six cylinder array pertain to a single longitudinal pitch ($P_L = 4$), they should be applicable to a wider range of P_L, so long as each cylinder in the array continues to behave as an isolated heat source. It is only for small values of $P_L \rightarrow 1$ that the results may become suspect. The same may not be said for the thirteen cylinder array, for which the results pertain to fixed longitudinal and transverse pitches of $P_L = 4$ and $P_T = 2$, respectively. With decreasing P_L and P_T, thermal and hydrodynamic interactions are enhanced; while for increasing P_L and P_T, the cylinders behave more like isolated heat sources. In each case the effect on heat transfer is likely to be significant.

Acknowledgments

The authors wish to express their appreciation to Mr. Gregory Terpay for his assistance in performing the flow visualization studies.

References

1 Zijnen, B. G. Van der Hegge, "Modified Correlation Formulae for Heat Transfer by Natural and Forced Convection from Horizontal Cylinders," *Applied Scientific Research*, Vol. A6, No. 1, 1956, pp. 129–140.

2. Börner, H., "Über den Wärme-und Stoffübergang an Umspülten Einzelkörpern bei Überlagerung von Freier und Erzwungener Strömung," *Verins Deutscher Ingenieur Forschung.*, No. 512, 1965.

3 Hatton, A. P., James, D. D., and Swire, H. W., "Combined Forced and Natural Convection with Low-Speed Air Flow over Horizontal Cylinders,"

Journal of Fluid Mechanics, Vol. 42, Part 1, 1970, pp. 17–31.

4 Morgan V. T., "The Overall Heat Transfer from Smooth Circular Cylinders," J. P. Hartnett and T. F. Irvine, Jr., eds., *Advances in Heat Transfer*, Vol. 11, 1975, pp. 199–264.

5 Sharma, G. K. and Sukhatme, S. P., "Combined Free and Forced Convection Heat Transfer from a Heated Tube to a Transverse Air Stream," ASME JOURNAL OF HEAT TRANSFER, Vol. 91, No. 3, 1969, pp. 457–459.

6 Fand, R. M. and Keswani, K. K., "Combined Natural and Forced Convection Heat Transfer from Horizontal Cylinders to Water," *International Journal of Heat and Mass Transfer*, Vol. 16, 1973, pp. 1175–1191.

7 Sparrow, E. M. and Lee, L., "Analysis of Mixed Convection about a Horizontal Cylinder," *International Journal of Heat and Mass Transfer*, Vol. 19, 1976, pp. 229–232.

8 Mucoglu, A., and Chen, T. S., "Analysis of Mixed Convection across a Horizontal Cylinder with a Uniform Surface Heat Flux," ASME Paper No. 77-HT-45, AIChE-ASME Heat Transfer Conference, Salt Lake City, Aug. 15–17, 1977.

9 Merkin, J. K., "Mixed Convection from a Horizontal Circular Cylinder," *International Journal of Heat and Mass Transfer*, Vol. 20, 1977, pp. 73–77.

10 Kline, S. J. and McClintock, F. A., "Describing Uncertainties in Single-Sample Experiments," *Mechanical Engineering*, Vol. 11, 1953, pp. 3–8.

11 McAdams, W. H., *Heat Transmission*, McGraw-Hill, 1954, pp. 175–177.

12 Marsters, G. F., "Natural Convective Heat Transfer from a Horizontal Cylinder in the Presence of Nearby Walls," *Canadian Journal of Chemical Engineering*, Vol. 53, 1975, pp. 144–149.

13 Yaghoubi, M. A. and Incropera, F. P., "Natural Convection from a Heated Horizontal Cylinder in a Shallow Water Layer," *Proceedings of the Sixth International Heat Transfer Conference*, Vol. 2, NC-15, 1978, pp. 269–274.

14 Fand, R. M., "Heat Transfer by Forced Convection from a Clyinder to Water in Cross Flow," *International Journal of Heat and Mass Transfer*, Vol. 8, 1965, pp. 995–1010.

15 Pera, L. and Gebhart, B., "Experimental Observations of Wake Formation over Cylindrical Surfaces in Natural Convection Flows," *International Journal of Heat and Mass Transfer*, Vol. 15, 1972, pp. 175–177.

16 Incropera, F. P. and Yaghoubi, M. A., "Buoyancy Driven Flows Originating from Heated Cylinders Submerged in a Finite Water Layer," *International Journal of Heat and Mass Transfer*, Vol. 23, 1980, pp. 269–278.

17 Eckert, E. R. G. and Soehngen, E., "Studies on Heat Transfer in Laminar Free Convection with the Zehnder-Mach Interferometer," USAF Tech. Rep. 5747, 1948.

L. S. Yao
F. F. Chen
Graduate Student.

Department of Mechanical and
Industrial Engineering,
University of Illinois at Urbana-Champaign,
Urbana, Ill. 61801

A Horizontal Flow Past a Partially Heated, Infinite Vertical Cylinder

The free-convection boundary layer along a partially heated infinitely long vertical cylinder disturbed by a steady horizontal flow is studied. The asymptotic solution indicates that the boundary layer is mainly induced by the buoyancy force in the neighborhood of the thermal leading edge. The effect of the horizontal free stream on the boundary layer gradually increases as one moves upward away from the thermal leading edge along the cylinder. The boundary-layer separation does not occur in the neighborhood of the thermal leading edge. However, the asymptotic solution shows that the forced convection tends to separate the boundary layer along the aft body of the cylinder. The importance of the effect of the forced convection is governed by the parameter $\epsilon z^{1/2}$ *where* ϵ *is the inverse of the square root of the Richardson number. The asympotic solution is valid as long as the value of* $\epsilon z^{1/2}$ *is small, and is not explicitly restricted by the Richardson number.*

1 Introduction

Owing to the shortage of oil and natural gas, and their ever increasing prices, solar power is increasingly being considered as one of the viable alternate energy resources in electricity generation. One of the preliminary designs of solar power plants contains a central receiver which is constructed by a series of vertical pipes and looks like a large vertical cylinder [1]. The receiver is designed as a once through heat exchanger to boil the water by solar heating. The surface temperature of the receivers is much higher than the ambient temperature. A significant free convection is induced by the density stratification of air inside the thermal boundary layer. Simultaneously, a breeze may pass by the receiver and disturb the free convection around the receiver. The resulting free and forced convection flow is three-dimensional. The distributions of temperature and flow are needed to design the structure for rigidity and to estimate the free-forced convective heat loss.

Due to the large dimension of the receiver and the likely high ambient turbulence level, the boundary-layer flow around the receiver is expected to be turbulent. In particular, the vertical pipes of small radius, which form the receiver, behave as roughened surfaces. In this paper, however we concentrate on the interaction of the free and the forced convections around the receiver by studying the laminar flow along an infinitely long vertical cylinder.

The free-forced convection is a fundamentally interesting problem in convective heat transfer. Oosthnizen and Leung [2, 3] have studied the problem for an infinite cylinder with a finite heating length experimentally and numerically. They have found that the accuracy of the numerical solution deteriorates in the region of the thermal leading edge. Their computation was started a short distance above the thermal leading edge. Consequently, an error due to mistreating the leading-edge conditions is to be expected. A detailed analysis is carried out in this paper to describe the flow development and heat transfer mechanism in this region. Before we start describing the physical model, a brief review of some relevant works is summarized.

Free convection has been extensively studied for the past half century, since Schmidt and Beckmann [4] measured the thermal boundary layer along a heated vertical plate. Pohlhausen demonstrated that the similarity solution exists for the free-convection boundary layer. Since then, series solutions have been thoroughly developed for free convections over arbitrary shape bodies. A comprehensive review can be found in Lin and Chao [5].

Two-dimensional combined free and forced convection has also attracted substantial attention. Most of them are either by a method of parameter perturbation on the forced convection, or by a numerical method. The expansion parameter is the Richardson number. A review of the works can be found in Joshi and Sukhatme [6]. Joshi and Sukhatme studied the combined free and forced convection from a horizontal cylinder and suggested that the expansion parameter for a free-convection dominant flow is the inverse of the Richardson number.

Three-dimensional combined free and forced convection has not received much detailed study. Young and Yang [7] studied the effect of small cross-flow and surface temperature variation on laminar free convection along a vertical plate. By coincidence, Eichhorn and Hason [8] and Plumb [9] report their studies of the mixed convection about a vertical surface in cross-flow at the same time. The asymptotic solutions for a forced-convection dominant flow for both internal flow (pipe flow) [10] and external flow [11, 12] have been obtained by perturbations on the forced convection. The expansion parameter is still the Richardson number. The numerical solution of the boundary layer along a heated horizontal cylinder shows that the range of validity of the asymptotic solution is limited to a small region close to the leading edge of the cylinder [13] where the free-convection effect is small. However, the importance of the free convection grows downstream even for a small Richardson number.

In this paper, we study the free-convection dominant flow on a partially heated infinite vertical cylinder. The forced convection is considered due to a steady breeze and is treated as a perturbed effect.

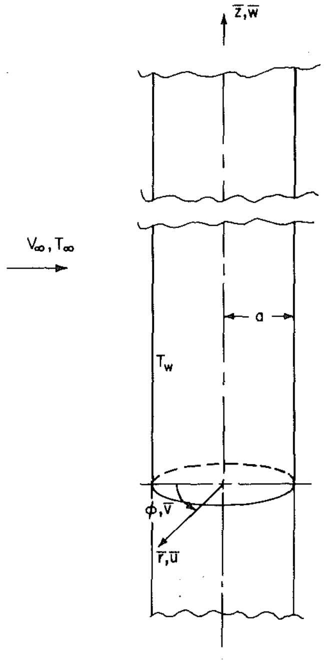

Fig. 1 Physical model and coordinates

Contributed by the Heat Transfer Division for publication in the JOURNAL OF HEAT TRANSFER. Manuscript received by the Heat Transfer Division September 9, 1981.

The perturbation parameter is the inverse of the square root of the Richardson number; Reynolds number, Re, and Grashof number, Gr, are the implicit parameters for this problem. In this paper, we assume Re is large to insure the existence of a forced-convection boundary layer. It can be shown that the displacement effect of the free-convection boundary layer is $O(\mathrm{Re}/\mathrm{Gr}^{3/2})$. In the following analysis, we assume that Re is smaller than $\mathrm{Gr}^{3/2}$. This rules out the possibility that the axial pressure gradient induced by the free-convection boundary layer becomes $0(1)$. Besides the restriction stated above, the perturbation solution is not limited by the value of ϵ; instead, it is valid as long as $\epsilon \cdot z^{1/2}$ is small. This implies that the smaller ϵ is the larger region (or large z) where the perturbation solution can be applied. It is worthy to point out that $\epsilon \cdot z^{1/2}$ can be rewritten as $(\mathrm{Re}/\sqrt{\mathrm{Gr}_{\bar{z}}}) \cdot (\bar{z}/a)^2$ where $\mathrm{Gr}_{\bar{z}}$ is the Grashof number in terms of $\bar{z}$. This indicates that the characteristic length of the free convection is $\bar{z}$.[1] Since the thermal leading edge provides a division line for $z \geq 0$ and $z < 0$, and the flow development for $z < 0$ has little practical interest, our study is concentrated for $z \geq 0$.

The asymptotic solution shows that the free convection dominates the heat loss in the region close to the thermal leading edge. However, the importance of the forced convection increases as one moves vertically upward away from the thermal leading edge even when the magnitude of the breeze is small compared with the buoyancy effect. The region in which the free convection is the dominant flow component shrinks as the magnitude of the breeze increases. No flow separation along the aft body of the cylinder is found in the region where the free convection is dominant. However, the solution does indicate the flow separation can occur as one moves vertically upward where the forced convection gradually becomes important. Numerical solution [14] shows that, however, the separation starts from the rear stagnation point about $\bar{z} = 0.0056 \cdot a/\epsilon^2$ for Prandtl number, Pr, equal to 10, and $\bar{z} = 0.0044 \cdot a/\epsilon^2$ for Pr = 0.733.

2 Physical Model and Analysis

The physical model considered is an infinite vertical cylinder of radius a, shown in Fig. 1. A uniform horizontal free stream is flowing by the cylinder. The velocity and the temperature of the free stream are U_∞ and T_∞, respectively. The surface temperature of the cylinder for $\bar{z} \geq 0$ is held constant at T_w, which is larger than T_∞. For $\bar{z} < 0$, it is unheated. The governing equations in cylindrical polar coordinates, Fig. 1, are

$$\frac{\partial \bar{u}}{\partial \bar{r}} + \frac{\bar{u}}{\bar{r}} + \frac{1}{r}\frac{\partial \bar{v}}{\partial \phi} + \frac{\partial \bar{w}}{\partial \bar{z}} = 0 \tag{1a}$$

$$\bar{u}\frac{\partial \bar{u}}{\partial \bar{r}} + \frac{\bar{v}}{\bar{r}}\frac{\partial u}{\partial \phi} - \frac{\bar{v}^2}{\bar{r}} + \bar{w}\frac{\partial \bar{u}}{\partial \bar{z}} = \frac{-1\partial \bar{p}}{\rho \partial \bar{r}} + \nu\left[\frac{\partial^2 \bar{u}}{\partial \bar{r}^2} + \frac{1}{\bar{r}}\frac{\partial \bar{u}}{\partial \bar{r}} - \frac{\bar{u}}{\bar{r}^2} + \frac{1}{\bar{r}^2}\frac{\partial^2 \bar{u}}{\partial \phi^2} - \frac{2}{\bar{r}^2}\frac{\partial \bar{v}}{\partial \phi} + \frac{\partial^2 \bar{u}}{\partial \bar{z}^2}\right] \tag{1b}$$

$$\bar{u}\frac{\partial \bar{v}}{\partial \bar{r}} + \frac{\bar{v}}{\bar{r}}\frac{\partial \bar{v}}{\partial \phi} + \frac{\overline{uv}}{\bar{r}} + \bar{w}\frac{\partial \bar{v}}{\partial \bar{z}} = \frac{-1}{\rho \bar{r}}\frac{\partial \bar{p}}{\partial \phi} + \nu\left[\frac{\partial^2 \bar{v}}{\partial \bar{r}^2} + \frac{1}{\bar{r}}\frac{\partial \bar{v}}{\partial \bar{r}} - \frac{\bar{v}}{\bar{r}^2} + \frac{1}{\bar{r}^2}\frac{\partial^2 \bar{v}}{\partial \phi^2} + \frac{2}{\bar{r}^2}\frac{\partial \bar{u}}{\partial \phi} + \frac{\partial^2 \bar{v}}{\partial \bar{z}^2}\right] \tag{1c}$$

$$\bar{u}\frac{\partial \bar{w}}{\partial \bar{r}} + \frac{\bar{v}}{\bar{r}}\frac{\partial \bar{w}}{\partial \phi} + \bar{w}\frac{\partial \bar{w}}{\partial \bar{z}} = \frac{-1}{\rho}\frac{\partial \bar{p}}{\partial \bar{z}} + \nu\left[\frac{\partial^2 \bar{w}}{\partial \bar{r}^2} + \frac{1}{\bar{r}}\frac{\partial \bar{w}}{\partial \bar{r}} + \frac{1}{\bar{r}^2}\frac{\partial^2 \bar{w}}{\partial \phi^2} + \frac{\partial^2 \bar{w}}{\partial \bar{z}^2}\right] + \beta g(T - T_\infty) \tag{1d}$$

$$\bar{u}\frac{\partial T}{\partial \bar{r}} + \frac{\leq v}{\bar{r}}\frac{\partial T}{\partial \phi} + \bar{w}\frac{\partial T}{\partial z} = \alpha\left[\frac{\partial^2 T}{\partial \bar{r}^2} + \frac{1}{\bar{r}}\frac{\partial T}{\partial \bar{r}} + \frac{1}{\bar{r}^2}\frac{\partial^2 T}{\partial \phi^2} + \frac{\partial^2 T}{\partial \bar{z}^2}\right] \tag{1e}$$

The fluid density variation due to heating is considered to be only important in the form of the buoyancy force, equation (1*d*). This is known as the Boussinesq approximation.

The flow and thermal conditions considered in the paper are that the Grashof number is large to insure the existence of the thermal boundary layer; however, its value should not be too large to cause the free-convection boundary layer to be turbulent. The magnitude of the Reynolds number (defined in equation (2)) is not explicitly restricted, as long as its value is not too large to make the Richardson number small. This implies that $\mathrm{Re}^2 < \mathrm{Gr}$.

The flow close to the leading edge ($z = 0$) is very complicated. Since the heat conduction in the z direction is important, the thermal boundary layer starts a small distance ahead of the leading edge. The thermal penetration depth, δ, is proportional to $[\beta g \cdot (T_w - T_\infty)/\nu]^{-1/3}$ and is independent of the geometric length (the variables are defined in equation (2)). The induced velocity is proportional to $\nu/\delta = [\beta g(T_w - T_\infty)\nu^2]^{1/3}$. This is much smaller than the thermal boundary layer velocity whose magnitude is proportional to $\sqrt{\beta g(T_w - T_\infty)\bar{z}}$. This has been verified by comparing Pohlhausen's solution with the Schmidt and Beckmann's data. In the analysis, we do not consider the leading-edge effect; therefore, the result cannot be applied to the immediate neighborhood of the leading edge.

For a free-convection dominant flow, the magnitude of the buoyancy force should be the same order as that of the inertial force. The dimensionless variables are introduced in equation (2).

$$\left.\begin{array}{ll}
z = \dfrac{\bar{z}}{a}, \quad r = \dfrac{\bar{r}}{a} & \text{(coordinates)} \\
u, v, w = \bar{u}, \bar{v}, \bar{w}/(\sqrt{\mathrm{Gr}} \cdot \nu/a) & \text{(velocities)} \\
p = \bar{P}/(\rho\, \mathrm{Gr}\, \nu^2/a^2) & \text{(pressure)} \\
\theta = (T - T_\infty)/(T_w - T_\infty) & \text{(temperature)} \\
\mathrm{Re} = (V_\infty a)/\nu & \text{(Reynolds number)} \\
\mathrm{Gr} = [\beta g(T_w - T_\infty)a^3]/\nu^2 & \text{(Grashof number)} \\
\epsilon = \mathrm{Re}/\sqrt{\mathrm{Gr}} & \text{(the inverse of the square root of Richardson number)} \\
\mathrm{Pr} = \nu/\alpha & \text{(Prandtl number)}
\end{array}\right\} \tag{2}$$

where ν is the kinematic viscosity; α, thermal diffusivity; β, the thermal expansion coefficient.

Inviscid Flow. Complete solution of equations (1) may be obtained by a numerical method, such as finite-difference method. It is well known that the required number of nodes for flows of large Reynolds numbers is usually beyond the capacity of the current generation computers; in particular, a thin boundary layer exists along

---

[1] The authors wish to acknowledge that the referee pointed out this important fact.

Nomenclature

a = radius of the cylinder
f = stream functions, equations (17–21)
g = gravitational acceleration
G = temperature functions, equations (17–21)
Gr = Grashof number, equation (2)
Nu = Nusselt number
P = pressure
Pr = Prandtl number
r = radial coordinate

Re = Reynolds number
T = temperature
u, v, w = boundary-layer velocities
U, V, W = inviscid flow velocities
z = axial coordinate
β = thermal expansion coefficient
ϵ = expansion parameter, equation (2)
η = similarity variable, equation (17*e*)
θ = dimensionless temperature, equation (2)
ν = kinematic viscosity

ϕ = azimuthal coordinate
τ = shear stress

Subscripts

ω = surface
∞ = free stream

Superscripts

$-$ = dimensional quantities
$\cdot$ = derivative with respect to η

the cylinder for the considered problem. On the following, we apply the method of matched asymptotic expansion to solve equations (1).

The zeroth-order outer solution is the potential flow with the slip conditions on the cylinder. The zeroth-order inner solution is the boundary-layer flow with the nonslip conditions on the cylinder and matching with the zeroth-order outer solution far away from the cylinder. The expansion procedures for the outer and the inner flows are described below in detail.

The dimensionless equations governing the flow outside of the thermal boundary layer can be obtained by substituting equations (2) into equations (1) and are

$$\frac{\partial u}{\partial r}+\frac{u}{r}+\frac{1}{r}\frac{\partial v}{\partial \phi}+\frac{\partial w}{\partial z}=0 \qquad (3a)$$

$$u\frac{\partial u}{\partial r}+w\frac{\partial u}{\partial r}+\frac{v}{r}\frac{\partial u}{\partial \phi}-\frac{v^2}{r}=-\frac{\partial p}{\partial r}+0(1/\sqrt{\mathrm{Gr}}) \qquad (3b)$$

$$u\frac{\partial v}{\partial r}+w\frac{\partial v}{\partial z}+\frac{v}{r}\frac{\partial v}{\partial \phi}+\frac{uv}{r}=\frac{-1}{r}\frac{\partial p}{\partial \phi}+0(1/\sqrt{\mathrm{Gr}}) \qquad (3c)$$

$$u\frac{\partial w}{\partial r}+w\frac{\partial w}{\partial z}+\frac{v}{r}\frac{\partial w}{\partial \phi}=-\frac{\partial p}{\partial z}+0(1/\sqrt{\mathrm{Gr}}) \qquad (3d)$$

Since it is isothermal outside of the thermal boundary layer, the energy equation can be ignored. The associated boundary conditions are

$$\text{as } r\rightarrow\infty: w=v\cos\phi+u\sin\phi\rightarrow 0, \text{ and } v\sin\phi-u\cos\phi\rightarrow\epsilon \qquad (4a)$$

$$\text{at } r=1: u=0 \text{ (slip-condition).} \qquad (4b)$$

Boundary conditions (4*a*) and (4*b*) suggest that the solution of equations (3) can be expanded in a series of ϵ, which is the inverse of the square root of the Richardson number. Knowing that the value of ϵ is small, the solution of equations (3) is sought in the following form.

$$\begin{aligned} u&=U_0+\epsilon U_1+\epsilon^2U_2+\epsilon^3U_3+\ldots\\ w&=W_0+\epsilon W_1+\epsilon^2W_2+\epsilon^3W_3+\ldots\\ v&=V_0+\epsilon V_1+\epsilon^2V_2+\epsilon^3V_3+\ldots\\ p&=P_0+\epsilon P_1+\epsilon^2P_2+\epsilon^3P_3+\ldots \end{aligned} \qquad (5)$$

The governing equations of the components in equation (5) are obtained by substituting equation (5) into equations (3) and then collecting the terms of equal ϵ order. The equations and their solution are given below.

$$(\epsilon^0): U_0\frac{\partial U_0}{\partial r}+W_0\frac{\partial U_0}{\partial z}+\frac{V_0}{r}\frac{\partial U_0}{\partial \phi}-\frac{V_0^2}{r}=-\frac{\partial P_0}{\partial r} \qquad (6a)$$

$$U_0\frac{\partial W_0}{\partial r}+W_0\frac{\partial W_0}{\partial z}+\frac{V_0}{r}\frac{\partial W_0}{\partial \phi}=-\frac{\partial P_0}{\partial z} \qquad (6b)$$

$$U_0\frac{\partial V_0}{\partial r}+W_0\frac{\partial V_0}{\partial z}+\frac{V_0}{r}\frac{\partial V_0}{\partial \phi}+\frac{U_0V_0}{r}-\frac{-1}{r}\frac{\partial P_0}{\partial \phi} \qquad (6c)$$

$$\frac{\partial U_0}{\partial r}+\frac{U_0}{r}+\frac{1}{r}\frac{\partial V_0}{\partial \phi}+\frac{\partial W_0}{\partial z}=0. \qquad (6d)$$

The solutions of equations (6) which satisfy the homogeneous boundary conditions are zero, i.e.,

$$V_0=U_0=W_0=0 \text{ and } P_0=\text{constant}. \qquad (7)$$

$$(\epsilon^1): \frac{\partial P_1}{\partial r}=\frac{\partial P_1}{\partial z}=\frac{\partial P_1}{\partial \phi}=0 \qquad (8a)$$

$$\frac{\partial U_1}{\partial r}+\frac{U_1}{r}+\frac{\partial W_1}{\partial z}+\frac{1}{r}\frac{\partial V_1}{\partial \phi}=0 \qquad (8b)$$

Equations (8*a*) and (7) indicate that

$$P_1=0 \qquad (9)$$

$$(\epsilon^2): U_1\frac{\partial U_1}{\partial r}+W_1\frac{\partial U_1}{\partial z}+\frac{V_1}{r}\frac{\partial U_1}{\partial \phi}-\frac{V_1^2}{r}=-\frac{\partial P_2}{\partial r}, \qquad (10a)$$

$$U_1\frac{\partial V_1}{\partial r}+W_1\frac{\partial V_1}{\partial z}+\frac{V_1}{r}\frac{\partial V_1}{\partial \phi}+\frac{U_1V_1}{r}=\frac{-1}{r}\frac{\partial P_2}{\partial \phi}, \qquad (10b)$$

$$U_1\frac{\partial W_1}{\partial r}+W_1\frac{\partial W_1}{\partial z}+\frac{U_1}{r}\frac{\partial W_1}{\partial \phi}=-\frac{\partial P_2}{\partial z}, \qquad (10c)$$

$$\frac{\partial U_2}{\partial r}+\frac{U_2}{r}+\frac{\partial W_2}{\partial z}+\frac{1}{r}\frac{\partial V_2}{\partial \phi}=0 \qquad (10d)$$

The boundary conditions associated with equations (8*b*) and (10*a*–10*c*) are

$$W_1 \text{ and } V_1\cos\phi+U_1\sin\phi\rightarrow 0, \text{ and } V_1\sin\phi-U_1\cos\phi\rightarrow 1 \text{ as } r\rightarrow\infty; \qquad (11a)$$

$$U_1=0 \text{ at } r=1 \qquad (11b)$$

For an infinite cylinder, the inviscid flow does not depend on the *z*-coordinate; its solution is well known. The velocity and the pressure gradient along the surface of the cylinder ($r = 1$) are

$$V_1=2\sin\phi, \qquad (12a)$$

$$W_1=0, \qquad (12b)$$

and

$$-\frac{\partial P_2}{\partial \phi}=4\sin\phi\cos\phi \qquad (12c)$$

When Re is not very small, the forced-convection boundary layer separates along the aft body of the cylinder. The flow separation can affect the inviscid flow; therefore, the solution (12) is valid only along the forebody of the cylinder for a forced-convection flow. We will, however, demonstrate later that the boundary layer does not separate in the region where the free convection is dominant.

The solution (12) shows that forced convection affects the free-convection boundary layer in two ways. The viscous shear, equation (12*a*) drives the boundary layer along the ϕ direction. Its order of magnitude is ϵ, and is proportional to $\sin\phi$. The pressure gradient along the ϕ direction, equation (12*c*), has a smaller effect than that of the viscous shear. Its order of magnitude is ϵ^2 and is proportional to $\sin 2\phi$. This feature probably shares by the cavity flows driven by the surface forces or by the body forces near the boundary.

The equations of ϵ^3 with equation (10*d*) can be solved to obtain U_2, W_2, V_2 and P_3. However, the homogeneous boundary conditions insure a zero solution, i.e.,

$$U_2=V_2=W_2=P_3=0 \qquad (13)$$

Boundary Layer. The boundary-layer equations can be obtained by stretching the coordinate normal to the surface of the cylinder. The stretched coordinate is

$$y=(r-1)\cdot\mathrm{Gr}^{1/4} \text{ and } u_b=U\cdot\mathrm{Gr}^{1/4} \qquad (14)$$

and the rest of the dimensionless variables are identical to those defined for the inviscid flow. Substitution of the dimensionless variables into equations (1), after evaluating the pressure gradient from the inviscid solution, gives

$$\frac{\partial u_b}{\partial y}+\frac{\partial w}{\partial z}+\frac{\partial v}{\partial \phi}=0, \qquad (15a)$$

$$u_b\frac{\partial v}{\partial y}+w\frac{\partial v}{\partial z}+v\frac{\partial v}{\partial \phi}=\epsilon^2\cdot(2\sin 2\phi)+\frac{\partial^2 v}{\partial y^2}+0(\mathrm{Gr}^{-1/4}), \qquad (15b)$$

$$u_b\frac{\partial w}{\partial y}+w\frac{\partial w}{\partial z}+v\frac{\partial w}{\partial \phi}=\theta+\frac{\partial^2 w}{\partial y^2}+0(\mathrm{Gr}^{-1/4}), \qquad (15c)$$

$$u_b\frac{\partial \theta}{\partial y}+w\frac{\partial \theta}{\partial z}+v\frac{\partial \theta}{\partial \phi}=\frac{1}{\mathrm{Pr}}\frac{\partial^2 \theta}{\partial y^2}+0(\mathrm{Gr}^{-1/4}). \qquad (15d)$$

The momentum equation in the r direction shows that the pressure gradient normal to the surface of the cylinder is of order of $\mathrm{Gr}^{-1/4}$ and is negligible. The associated boundary conditions are

$$w=\theta=0 \text{ and } v=\epsilon\cdot(2\sin\phi) \text{ at } z=0. \qquad (16a)$$

$$u_b = v = w = 0, \text{ and } \theta = 1 \text{ at } y = 0, \tag{16b}$$

$$w = \theta = 0, \text{ and } v \rightarrow \epsilon \cdot (2 \sin \phi) \text{ as } y \rightarrow \infty. \tag{16c}$$

Following the expansion procedure used in solving the inviscid flow, the solution of the boundary layer can be expressed as a series of ϵ. In terms of the stream functions, they are

$$\begin{aligned} w = {} & (4z)^{1/2} \cdot f_0'(\eta) + (\epsilon) \cdot 5 \cdot (4z) \cdot f_1'(\eta) \cdot (2 \cos \phi) \\ & + (\epsilon^2) \cdot (4z)^{3/2} \cdot [f_{3c}'(\eta) \cdot (4 \cos^2 \phi) + f_{3s}'(\eta) \cdot (4 \sin^2 \phi)] \\ & + \ldots \end{aligned} \tag{17a}$$

$$v = (\epsilon) \cdot f_2'(\eta) \cdot (2 \sin \phi) + (\epsilon^2) \cdot (4z)^{1/2} \cdot f_4'(\eta) \cdot (2 \sin 2\phi) + \ldots \tag{17b}$$

$$\begin{aligned} u_b = {} & (4z)^{-1/4} \cdot (\eta f_0' - 3f_0) + (\epsilon) \cdot (4z)^{1/4} \cdot (\eta f_1' - f_1 + f_2) \cdot (2 \cos \phi) \\ & + (\epsilon^2) \cdot (4z)^{3/4} \cdot [(\eta f_{3c}' - 7f_{3c} + f_2) \cdot (4 \cos^2 \phi) \\ & + (\eta f_{3s}' - 7f_{3s} + f_4) \cdot (4 \sin^2 \phi)] + \ldots \end{aligned} \tag{17c}$$

$$\begin{aligned} \theta = {} & G_0(\eta) + (\epsilon) \cdot (4z)^{1/2} \cdot G_1(\eta) \cdot (2 \cos \phi) \\ & + (\epsilon^2) \cdot (4z) \cdot [G_{2c}(\eta) \cdot (4 \cos^2 \phi) + G_{2s} \cdot (4 \sin^2 \phi)] + \ldots, \end{aligned} \tag{17d}$$

where

$$\eta = y/(4z)^{1/4} \tag{17e}$$

and the prime denotes the derivative with respect to η. The governing equations of the stream functions, f's, and the temperature functions, G's, are obtained by substituting equations (17) into equations (15) and collecting the terms of equal ϵ. They are

$$(\epsilon^0): f_0''' + 3f_0 f_0'' - 2(f_0')^2 = -G_0, \tag{18a}$$

$$G_0'' + 3 \cdot \mathrm{Pr} \cdot f_0 \cdot G_0' = 0, \tag{18b}$$

$$(\epsilon^1): f_1''' + 3f_0 f_1'' - 6f_0' f_1' + 5f_0'' f_1 = -G_1 - f_0'' f_2, \tag{19a}$$

$$f_2''' + 3f_0 f_2'' = 0, \tag{19b}$$

$$\frac{1}{\mathrm{Pr}} \cdot G_1'' + 3f_0 G_1' - 2f_0' G_1 = -G_0' \cdot (5f_1 + f_2) \tag{19c}$$

$$\begin{aligned} (\epsilon^2): & f_4''' + 3f_0 f_4'' - 2f_0' f_4 \\ & = -1 - 5\eta f_2'' f_1' + (\eta f_1' - f_1 + f_2) \cdot f_2'' + (f_2')^2 \end{aligned} \tag{20a}$$

$$\begin{aligned} & f_{3c}''' + 3f_0 f_{3c}'' - 8f_0' f_{3c}' + 7f_0'' f_{3c} \\ & = -G_{2c} - f_0'' \cdot f_4 - 5 \cdot (4\eta f_1' + f_1) \cdot f_1'' \\ & \quad + 5 \cdot f_1'' \cdot f_2 + 100 \cdot (f_1')^2 \end{aligned} \tag{20b}$$

$$f_{3s}''' + 3f_0 f_{3s}'' - 8f_0' f_{3s}' + 7f_0'' f_{3s} = -G_{2s} - 5f_1' f_2' - f_0'' f_4 \tag{20c}$$

$$\begin{aligned} & \frac{1}{\mathrm{Pr}} \cdot G_{2c}'' + 3f_0 G_{2c}' - 4f_0' G_{2c} \\ & = -G_0' \cdot (f_4 + 7 \cdot f_{3c}) - (4\eta f_1' + f_1 - f_2) \cdot G_1' + 10 \cdot f_1' \cdot G_1 \end{aligned} \tag{20d}$$

$$\frac{1}{\mathrm{Pr}} G_{2s}'' + 3 \cdot f_0 \cdot G_{2s}' - 4f_0' G_{2s} = -G_0' \cdot (f_4 + 7 \cdot f_{3s}) - f_2' \cdot G_1. \tag{20e}$$

The transformed boundary condition associated with equations (18–20) are

$$\begin{aligned} \text{at } \eta = 0: & f_0 = f_0' = f_1 = f_1' = f_2 = f_2' = f_{3c} = f_{3c}' = f_{3s} = f_{3s}' \\ & = f_4 = f_4' = G_1 = G_{2c} = G_{2s} = 0, \text{ and } G_0 = 1; \end{aligned} \tag{21a}$$

$$\text{as } \eta \rightarrow \infty: f_0', f_{3c}', f_{3s}', f_4', G_0, G_{2c}, G_{2s} \rightarrow 0, \quad \text{and } f_2' \rightarrow 1. \tag{21b}$$

The solution of equations (18) is the free-convection flow, and is known as the Schmidt-Beckmann-Pohlhausen solution. In the limit that the Reynolds number approaches zero, equations (17) show that the flow is free convection.

Equations (17) show that the effects of the forced convection are proportional to $\epsilon z^{1/2}$. This indicates that ϵ is not the actual parameter for the perturbation solution; instead, the parameter should be $\epsilon z^{1/2}$. Therefore, the perturbation is valid for arbitrary value of ϵ as long as the value of $\epsilon z^{1/2}$ is small. The upper limit $\epsilon z^{1/2}$ for which the perturbation solution may be applied can be found by comparing the perturbation solution with the downstream numerical solution which is discussed in [14].

Equations (18–20) with the boundary conditions (21) are solved by numerical integration. The results are given and discussed in the next section.

3 Results and Discussion

Equation (17a) shows that the axial velocity can be estimated in terms of the stream functions f_0, f_1, f_{3c} and f_{3s}. The values of f_0 and f_0' are presented in Fig. 2 for Pr = 0.01, 1 and 10, respectively. This solution is known as the Schmidt-Beckmann-Pohlhausen solution, and represents the free convection along a heated vertical cylinder (or plate). The magnitude of the free convection is inversely proportional to the Prandtl number. Functions f_1 and f_1', given in Fig. 3, represent the first-order effect of the forced convection on the free convection. Values of f_1 and f_1' are negative. This is a consequence of the forced convection suppressing the free-convection boundary layer in the neighborhood of the forward stagnation point ($\phi = 0$), and thus thinning the boundary layer. The amplitudes of f_1 and f_1' are also inversely proportional to the Prandtl number. Values of f_{3c}, f_{3c}', f_{3s} and f_{3s}', given respectively in Figs. 4 and 5, are the effects of the forced convection driven by the azimuthal pressure gradient. The amplitude of these functions increase with Prandtl number. The functional shapes of f_{3c} and f_{3s} are similar, but are different in magnitudes. This shows that the second-order solution of w is not proportional to cos 2ϕ.

The azimuthal velocity, v, can be estimated in terms of f_2 and f_4 as shown in equation (17b). Values for f_2, f_2', f_4 and f_4' are shown in Figs. 6 and 7, respectively. f_2 and f_2' represent the forced convection driven by the viscous force; f_4 and f_4' are due to the azimuthal pressure gradient. Function f_4' shows a wave structure which pushes the fluid

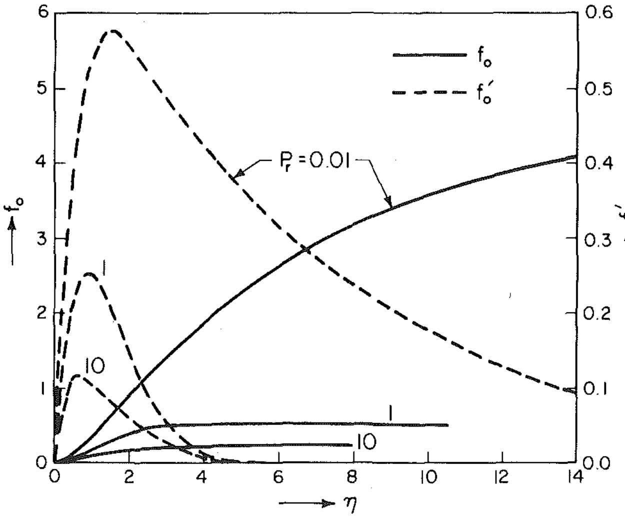

Fig. 2 Stream functions f_0 and f_0'

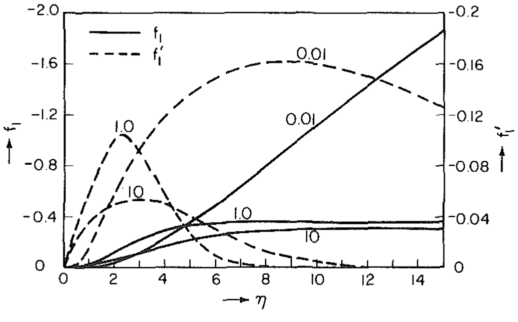

Fig. 3 Stream function f_1 and f_1'

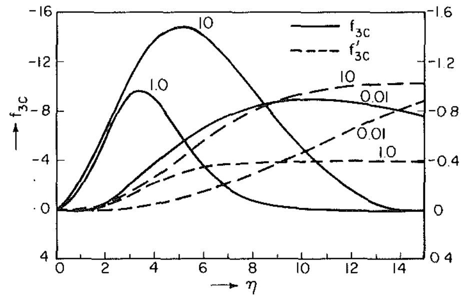

Fig. 4 Stream functions f_{3c} and f_{3c}'

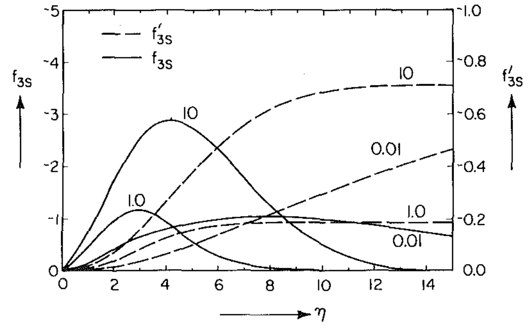

Fig. 5 Stream functions f_{3s} and f_{3s}'

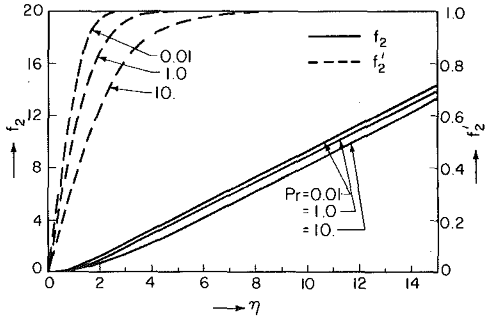

Fig. 6 Stream functions f_2 and f_2'

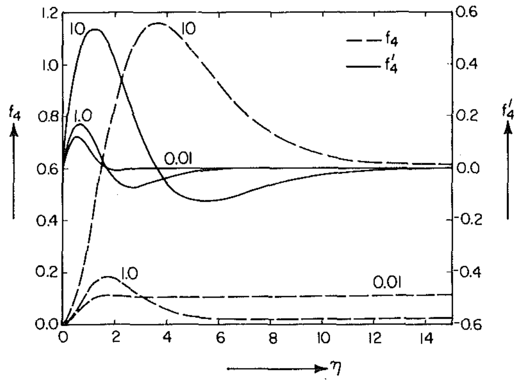

Fig. 7 Stream functions f_4 and f_4'

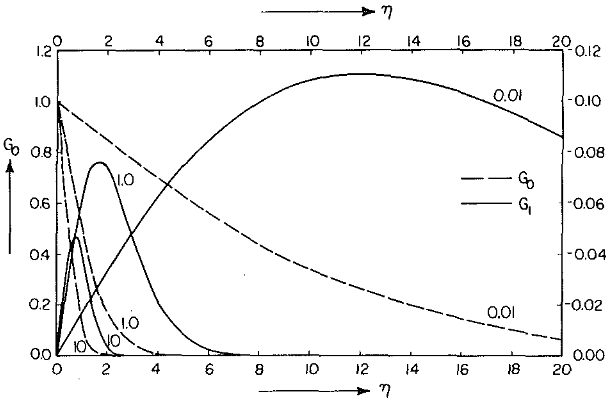

Fig. 8 Temperature functions G_0 and G_1

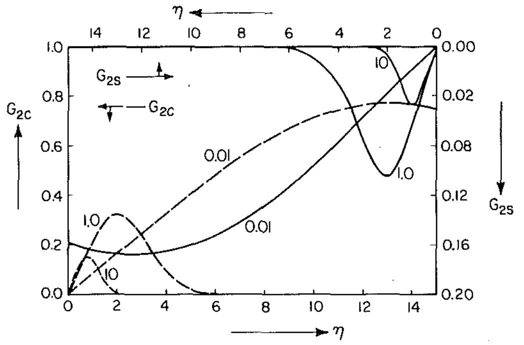

Fig. 9 Temperature functions G_{2c} and G_{2s}

along the positive direction close to the cylinder surface and retards the fluid close to the free stream.

Function G_0, given in Fig. 8, is the temperature distribution due to the free convection. The first-order temperature distribution, G_1, due to the forced convection is also shown in Fig. 8 for Pr = 0.01, 1, and 10, respectively. The second-order temperature distribution due to the azimuthal pressure gradient is contributed to two parts: G_{2_c} represents the temperature distribution proportional to $\cos^2\phi$ and G_{2_s} is proportional to $\sin 2\phi$, as shown in Fig. 9.

Shear Stress and Nusselt Number. The shear stresses along z and ϕ directions can be estimated from equations (17a) and (17b), respectively. They are

$$\frac{\tau_{rz}}{\rho\nu^2/a^2} = \mathrm{Gr}^{3/4}\cdot(4z)^{1/4}\cdot\{f_0''(0) + 10\epsilon(4z)^{1/2}\cdot f_1''(0)\cdot\cos\phi + 4\epsilon^2(4z).\,[f_{3c}''(0)\cdot\cos^2\phi + f_{3s}''(0)\cdot\sin^2\phi] + \ldots\} \quad (22a)$$

$$\frac{\tau_{r\phi}}{\rho\nu^2/a^2} = \mathrm{Re}\cdot\mathrm{Gr}^{1/4}\cdot(4z)^{-1/4}\cdot[2\cdot f_2''(0)\cdot\sin\phi + 2\epsilon(4z)^{1/2}\cdot f_4''(0)\cdot\sin^2\phi + \ldots] \quad (22b)$$

Coefficients of f'' s are listed in Table 1. The last two terms of equation (22a) represent the effects of the azimuthal pressure gradient. Except for Pr = 0.01, the values of $f_{3s}''(0)$ and $f_{3c}''(0)$ are negative. The azimuthal pressure gradient has the effect of decreasing the value of τ_{rz}. The second term on the right-hand side of equation (22a) is contributed due to the azimuthal inviscid velocity, which increases the value of τ_{rz} for $0 \le \phi < 90$ deg and decreases it for 90 deg $< \phi \le 180$ deg. The first order azimuthal shear stress, $\tau_{r\phi}$, is proportional to $\sin\phi$ and the second order effect is proportional to $\sin^2\phi$. The second-order effect is due to the azimuthal pressure gradient whose value is positive for 0 deg $\le \phi < 90$ deg and is negative for 90 deg $< \phi \le 180$ deg. This indicates that the forced-convection separation for 90 deg $< \phi \le 180$ deg can occur when the value of $\epsilon^2 z$ becomes large, as expected.

Nusselt number with respect to a and $(T_w - T_\infty)$ can be derived from equation (17d) and is

$$\mathrm{Nu} = -[\mathrm{Gr}/(4z)]^{1/4}\cdot\{G_0'(0) + 2\epsilon(4z)^{1/2}G_1'(0)\cdot\cos\phi + 4\epsilon^2(4z)\cdot[G_{2c}'(0)\cdot\cos^2\phi + G_{2s}'(0)\cdot\sin^2\phi] + \ldots\} \quad (23)$$

With Table 1, equation (23) shows that the first-order forced-convection effect increases the heat transfer rate for $0 \le \phi < 90$ deg and decreases it for 90 deg $< \phi \le 180$ deg. The second-order forced-convection effects, due to the azimuthal pressure gradient, constantly decrease the heat transfer rate. Since $G_0'(0)$ represents the free-convection heat transfer, the heat transfer rate due to the free and forced convection is always smaller than that due to the free convection alone for $\phi \ge 90$ deg. This type of Nusselt-number distribution has been demonstrated by the numerical solution for Pr = 10 [3].

Table 1 Coefficients for shear stress and Nusselt number

	Pr				
Functions	0.01	0.1	0.733	1.0	10
$f_0''(0)$	0.987543	0.858704	0.674175	0.642178	0.419160
$f_1''(0)$	−0.001392	−0.036508	−0.059129	−0.059208	−0.044931
$f_{3c}''(0)$	0.030153	−0.029042	−0.130256	−0.139573	−0.202793
$f_{3s}''(0)$	−0.014563	−0.052309	−0.074680	−0.076463	−0.133325
$f_2''(0)$	0.768148	0.705665	0.591001	0.567147	0.377088
$f_4''(0)$	0.480285	0.483977	0.547409	0.575214	1.00187
$G_0'(0)$	−0.080623	−0.230175	−0.507904	−0.567134	−1.16926
$G_1'(0)$	−0.016694	−0.040675	−0.063274	−0.065802	−0.085290
$G_{2c}'(0)$	0.079404	0.180094	0.224638	0.210649	0.246207
$G_{2s}'(0)$	0.018833	0.044503	0.063753	0.059811	0.051344

However, the numerical solution for Pr = 0.7 indicates that the Nusselt number along $\phi = 90$ deg is larger than that due to the free convection which is inconsistent with that of Pr = 10. This is due to the fact that the numerical solution was not started at $z = 0$; instead, it was started at a small value of z. The error induced by mistreating the initial condition propagates along the cylinder. The error might be gradually damped out as the value of z increases; however, the error can be significant in the neighborhood of the thermal leading edge.

Equations (17) show that the length scale further upward along the cylinder is $a \cdot \mathrm{Gr}/\mathrm{Re}^2$. It can be shown that the solution in the region $\bar{z} \sim 0(a \cdot \mathrm{Gr}/\mathrm{Re}^2)$ is valid at $\bar{z} = 0$, and the similarity solution of the free-convection boundary layer is the initial condition for this problem. However, $z = 0$ is a singular point, and a stable numerical solution can only be found by transforming the governing equations to the parabolic coordinates which remove the singularity at $z = 0$. The computational procedure is very similar to the case of free-forced convection on a longitudinal and horizontal cylinder [13].

References

1 Clausing, A. M., Clark, G. L., and Mueller, M. H., *Modeling, Simulating, Testing, and Measurements for Solar Energy System*, edited by Nash, J. M., et al., ASME, New York, 1978, p. 73.

2 Oosthuizen, P. H., and Leung, R. K., "Combined Convective Heat Transfer from Vertical Cylinders in a Horizontal Flow," Paper No. 78-WA/HT-45, ASME Winter Annual Meeting, San Francisco, Calif., 1978.

3 Oosthuizen, P. H., "Numerical Study of Combined Convective Heat Transfer from a Vertical Cylinder in a Horizontal Flow," *Proceedings of the 6th International Heat Transfer Conference*, Toronto, Canada, MC-4, 1978, pp. 19–24.

4 Schlicting, H., *Boundary-Layer Theory*, McGraw-Hill, New York, 1968, p. 300.

5 Lin, F. N., and Chao, B. T., "Laminar Free Convection over Two-Dimensional and Axizymmetric Bodies of Arbitrary Contour," ASME JOURNAL OF HEAT TRANSFER, Vol. 96, 1974, pp. 435–442.

6 Joshi, N. D., and Sukhatme, S. P., "An Analysis of Combined Free and Forced Convection Heat Transfer from a Horizontal Circular Cylinder to a Transverse Flow," ASME JOURNAL OF HEAT TRANSFER, Vol. 93, No. 4, 1971, pp. 441–448.

7 Young, R. J., and Yang, K. T., "Effect of Small Cross Flow and Surface Temperature Variation on Laminar Free Convection Along a Vertical Plate," JOURNAL OF APPLIED MECHANICS, Vol. 30, 1963, pp. 252–256.

8 Eichhorn, R., and Hasan, M. M., "Mixed Convection about a Vertical Surface in Cross-Flow: A Similarity Solution," ASME Paper No. 80-H-129, 1980.

9 Plumb, O. A., "The Effect of Crossflow on Natural Convection from Vertical Heated Surfaces," ASME Paper No. 80-HT-71.

10 Yao, L. S., "Free-Forced Convection in the Entry Region of a Heated Straight Pipe," ASME JOURNAL OF HEAT TRANSFER, Vol. 100, 1978, pp. 212–219.

11 Yao, L. S., "Variable Viscosity Effect on the Laminar Water Boundary Layer on Heated Cones," *Journal of Applied Mechanics*, Vol. 45, 1978, pp. 481–486.

12 Yao, L. S., and Catton, I., "Buoyancy Cross-Flow Effects in the Boundary Layer on a Heated Longitudinal Horizontal Cylinder," ASME JOURNAL OF HEAT TRANSFER, Vol. 99, 1977, pp. 122–124.

13 Yao, L. S:, Catton, I., and McDonough, J. M., "Free-Forced Convection along a Horizontal Cylinder," *Number of Heat Transfer*, Vol. 1, 1978, pp. 255–266.

14 Yao, L. S., "Buoyancy Effects on a Boundary Layer Along an Infinite Cylinder with a Step Change of Surface Temperature," ASME Paper No. 80 WA/HT-25, 1980.

Developing Laminar Free Convection in an Open Ended Vertical Annulus with a Rotating Inner Cylinder

M. A. I. El-Shaarawi
Lecturer.

A. Sarhan
Asst. Lecturer.

Mechanical Engineering Department,
Alazhar University,
Nasr City, Cairo
Egypt

A finite-difference scheme is developed for solving the boundary layer equations governing the laminar free convection flow in open ended vertical concentric annuli with rotating inner walls. Numerical results are presented for a fluid of $Pr = 0.7$ *in an annulus of radius ratio 0.5 under the thermal boundary conditions of one wall being isothermal and the opposite wall adiabatic. Comparing the present results for the development of* δ_θ *(tangential boundary layer displacement thickness) with those corresponding results of forced flows shows that heating the inner cylinder has always stabilizing effects while heating the outer cylinder has either destabilizing or stabilizing effects.*

Introduction

Free convection heat transfer and its associated fluid motion in an open ended vertical concentric annulus whose inner cylinder rotates is an idealization of many frequently occurring engineering situations. In vertical electric machines, the heat resulting from the iron and copper losses is conducted to the rotor surface where it is transferred to the air in the annular gap between the rotor and the stator. The transfer of heat by natural convection and radiation is always a factor in the cooling of an electric machine and may be the sole means for cooling some small types of electric apparatus. Therefore, the design of cooling systems for such types of electric machines requires a knowledge of the hydrodynamic behavior of the free convection flow to limit the rotor temperature to less than the maximum permitted value. Beside other applications in chemical mixing processes, fiber coating applications and drying machinery, there are possibilities of future applications for compact rotary heat exchangers and combustion chambers.

These possible future applications depend on the fact that when an isothermal viscous fluid is contained in an annular duct with a rotating inner cylinder, there is a possibility for the existing Couette flow to become hydrodynamically unstable and Taylor vortices [1], a secondary laminar flow regime, may appear. This instability occurs when the rotational speed of the inner cylinder becomes sufficiently large such that the ratio of destabilizing centrifugal forces to restraining viscous forces reaches a critical value at which breakdown of the original Couette laminar regime occurs, and vortices appear. These vortices, occuring within the fluid on a macroscopic scale, will increase the efficiency of convective heat transfer mechanism if one or both of the annulus boundaries were heated.

However, heating one or both of the annulus boundaries creates a radial temperature gradient which affects the stability of a Couette flow between two rotating concentric cylinders. In the absence of axial fluid flow, neglecting gravitational body forces (i.e., neglecting free convection effects), and assuming constant physical fluid properties except the density which is allowed to vary according to the Boussinesq approximation in only the centrifugal acceleration term, Yih [2], Becker and Kaye [3] and Walowit, et al. [4] have shown that positive and negative radial temperature gradients are destabilizing and stabilizing, respectively.

The presence of an axial velocity component has also significant effects on the hydrodynamic stability of a Couette flow. Most of the available investigations into this problem are limited to the case of the onset of hydrodynamic instability in fully developed Couette flows with a superimposed steady or fully developed axial flow (e.g., [5–8]). These investigations showed that the presence of a superimposed low axial flow has a stabilizing effect on the onset of Taylor vortices.

In reality, the tangential velocity profile for an axial viscous flow in an annulus with a rotating inner cylinder is a function of the axial distance, not withstanding the superimposed axial velocity profile [9–12]. Therefore, there is an axial length required for the tangential velocity profile to approach the well known fully developed Couette profile. Astill [9–10] showed, by means of a visualization technique and hot wire measurements, that transition in a tangentially developing flow starts near the rotating inner cylinder as oscillating waves within the tangential boundary layer. He also developed the unique stability criterion available to date for the onset of instability in tangentially developing flows. His empirical stability criterion, which has recently been confirmed by Payne and Martin [13], is a Taylor number based on the tangential boundary layer displacement thickness (δ_θ) rather than the gap width.

According to Astill's stability criterion, knowledge of the axial growth of δ_θ for tangentially developing flows is essential to locate the axial position of the point of origin of instability. Therefore, one of the main aims of the present investigation is to determine the development of the tangential boundary layer displacement thickness for tangentially developing flows created by buoyancy effects only. Also, the lack of either theoretical or experimental investigations concerning the development of laminar free convection in open ended vertical concentric annuli, with either stationary or rotating inner walls, represents another motive for the present work. Two thermal boundary conditions are considered in this investigation; namely, case *I* in which the inner wall is isothermal while the outer wall is adiabatic, and case *O* in which the outer wall is isothermal while the inner wall is adiabatic.

Governing Equations

The fluid is assumed to have constant physical properties but obeys the Boussinesq approximation, according to which its density is constant except in the buoyancy term of the vertical momentum equation. The flow is steady, axisymmetric and without internal heat generation. Viscous dissipation and axial diffusion of heat are neglected. Further, applying the Prandtl boundary layer assumptions and checking the order of magnitude of each term [10], the equations governing the free convection fluid motion and heat transfer in the entry region of a vertical concentric annulus with a rotating inner cylinder reduce to the following equations

$$\frac{\partial(rv)}{\partial r} + \frac{\partial(ru)}{\partial z} = 0 \qquad (1)$$

$$\rho_0 \frac{w^2}{r} = \frac{\partial p}{\partial r} \qquad (2)$$

Contributed by the Heat Transfer Division for publication in the JOURNAL OF HEAT TRANSFER. Manuscript received by the Heat Transfer Division, July 7, 1980.

$$\rho_0\left(v\frac{\partial w}{\partial r}+u\frac{\partial w}{\partial z}\right)=\mu\frac{\partial}{\partial r}\left[\frac{1}{r}\frac{\partial}{\partial r}(rw)\right] \tag{3}$$

$$\rho_0\left(v\frac{\partial u}{\partial r}+u\frac{\partial u}{\partial z}\right)=-\frac{\partial p}{\partial z}-\rho_0 g[1-\beta(t-t_0)]+\frac{\mu}{r}\frac{\partial}{\partial r}\left(r\frac{\partial u}{\partial r}\right) \tag{4}$$

$$\rho_0 c_p\left(v\frac{\partial t}{\partial r}+u\frac{\partial t}{\partial z}\right)=\frac{k}{r}\frac{\partial}{\partial r}\left(r\frac{\partial t}{\partial r}\right) \tag{5}$$

Defining a pressure defect p' as

$$p'=p-p_s \tag{6}$$

equations (2) and (4) can be written

$$\rho_0\frac{w^2}{r}=\frac{\partial p'}{\partial r} \tag{7}$$

$$\rho_0\left(v\frac{\partial u}{\partial r}+u\frac{\partial u}{\partial z}\right)=-\frac{\partial p'}{\partial z}+\rho_0 g\beta(t-t_0)+\frac{\mu}{r}\frac{\partial}{\partial r}\left(r\frac{\partial u}{\partial r}\right) \tag{8}$$

Introducing the dimensionless parameters given in the Nomenclature, equations (1, 3, 5, 7) and (8) can be replaced by the following dimensionless forms

$$\frac{\partial V}{\partial R}+\frac{V}{R}+\frac{\partial U}{\partial Z}=0 \tag{9}$$

$$\frac{W^2}{R}=\frac{8(1-N)^5}{1+N}\frac{\mathrm{Gr}^2}{\mathrm{Ta}}\frac{\partial P}{\partial R} \tag{10}$$

$$V\frac{\partial W}{\partial R}+U\frac{\partial W}{\partial Z}=\frac{\partial^2 W}{\partial R^2}+\frac{1}{R}\frac{\partial W}{\partial R}-\frac{W}{R^2} \tag{11}$$

$$V\frac{\partial U}{\partial R}+U\frac{\partial U}{\partial Z}=-\frac{\partial P}{\partial Z}+\frac{T}{16(1-N)^4}+\frac{\partial^2 U}{\partial R^2}+\frac{1}{R}\frac{\partial U}{\partial R} \tag{12}$$

$$V\frac{\partial T}{\partial R}+U\frac{\partial T}{\partial Z}=\frac{1}{\mathrm{Pr}}\left(\frac{\partial^2 T}{\partial R^2}+\frac{1}{R}\frac{\partial T}{\partial R}\right) \tag{13}$$

These five coupled equations (9–13) are subject to the following boundary conditions:

for $Z = 0$ and $N < R < 1$, $V = W = T = 0$, $U = U_0$ and $P = P_0 = -U_0{}^2/2$

for $Z \geqslant 0$ and $R = N$, $U = V = 0$, $W = 1$ and $T = 1$ for case I or $\dfrac{\partial T}{\partial R} = 0$ for case O

for $Z \geqslant 0$ and $R = 1$, $U = V = W = 0$ and $\dfrac{\partial T}{\partial R} = 0$ for case I and $T = 1$ for case O

for $Z = L$ and $R = 1$, $P = 0$ (14)

It is noteworthy that the initial pressure at the duct entrance in the above conditions (14) is obtained by applying Bernoulli's equation, i.e., taking into consideration the acceleration of the fluid to the channel inlet.

Using the boundary conditions (14), equation (9) can be written in the following integral form

$$Q=(1-N^2)U_0=2\int_N^1 RU\,dR \tag{15}$$

The tangential boundary layer displacement thickness, the heat absorbed by the fluid from entrance up to a particular elevation, and the mixing cup temperature can respectively be given, in dimensionless forms, by the following equations

$$\delta_\theta{}^*=\int_N^1 W\,dR/(1-N) \tag{16}$$

$$H=\int_N^1 UTR\,dR \tag{17}$$

$$T_m=\int_N^1 UTR\,dR\Big/\int_N^1 UR\,dR \tag{18}$$

Also, the local Nusselt number and the average Nusselt number over the annulus height can respectively be given by the following two equations

$$\mathrm{Nu}=2(1-N)\left.\frac{\partial T}{\partial R}\right|_w/(1-T_m) \tag{19}$$

$$\overline{\mathrm{Nu}}=\mathrm{Ra}^*\bar{H}\,D/D_w \tag{20}$$

The fully developed flow, which occurs if the channel is sufficiently high and uniform temperature is achieved before the fluid reaches the top, provides an analytical check on the finite difference solution to be obtained. Noting that for fully developed flow, $T = 1$, $\partial/\partial Z = 0$ and $V = 0$, the inertia terms on the left hand sides of equations (11) and (12) vanish and the resulting reduced two equations give, respectively, the following fully developed tangential (Couette) and axial velocity profiles

$$W_{fd}=\frac{N}{1-N^2}\left(\frac{1}{R}-R\right) \tag{21}$$

$$U_{fd}=\frac{1-R^2-(1-N^2)(\ln R/\ln N)}{64(1-N)^4} \tag{22}$$

Nomenclature

a = local heat transfer coefficient based on area of heated surface, $-k\left.\dfrac{\partial t}{\partial r}\right|_w/(t_m-t_w)$

$\bar{a}$ = average heat transfer coefficient over the annulus height, $\bar{h}/\pi D_w l(t_m-t_0)$

b = annular gap width (r_2-r_1)

c_p = specific heat of fluid at constant pressure

D = hydraulic diameter of annulus $(2b)$

D_w = diameter of the heated wall

g = gravitational body force per unit mass

h = heat absorbed by fluid from entrance up to any particular elevation in the annulus, $\displaystyle\int_{r_1}^{r_2} 2\pi c_p\rho_0 ru(t_m-t_0)\,dr$

$\bar{h}$ = heat absorbed by fluid from entrance up to annulus exit, i.e., value of h at $z = l$

H = dimensionless heat absorbed from entrance up to any particular elevation, $h/\pi\rho_0 c_p l\gamma \mathrm{Gr}^*(t_w-t_0)$

$\bar{H}$ = dimensionless heat absorbed from entrance up to annulus exit, i.e., value of H at $z = l$

H_{fd} = fully developed value of H

k = thermal conductivity of fluid

ℓ = height of annulus

L = dimensionless height of annulus, $1/\mathrm{Gr}^*$

N = annulus radius ratio, r_1/r_2

n = number of radial increments in the numerical mesh network

p = pressure of fluid at any point

p' = pressure defect at any point, $p-p_s$

p_0 = pressure of fluid at annulus entrance

p_{w0} = pressure of fluid at the outer wall of annulus

p_s = hydrostatic pressure, $-\rho_0 gz$

P = dimensionless pressure defect at any point, $p'r_2{}^4/\rho_0 l^2\gamma^2\,\mathrm{Gr}^{*2}$

P_0 = dimensionless pressure defect at annulus entrance, $p_0 r_2{}^4/\rho_0 l^2\gamma^2\,\mathrm{Gr}^{*2}$

P_{w0} = dimensionless pressure defect at outer wall, $(p_{w0}-p_s)r_2{}^4/\rho_0 l^2\gamma^2\,\mathrm{Gr}^{*2}$

q = volumetric flow rate, $\displaystyle\int_{r_1}^{r_2} 2\pi ru\,dr$

Q = dimensionless volumetric flow rate, $q/\pi l\gamma\,Gr^*$

Q_{fd} = fully developed value of Q

r = radial coordinate

r_1 = inner radius of annulus

r_2 = outer radius of annulus

R = dimensionless radial coordinate, r/r_2

t = fluid temperature at any point

t_m = mixing cup temperature over any cross section, $\displaystyle\int_{r_1}^{r_2} utr\,dr\Big/\int_{r_1}^{r_2} ur\,dr$

(Continued on next page)

Also, since for fully developed flow, $T = 1$, equations (15) and (17) show that the limiting values of the dimensionless volumetric flow rate and heat absorbed (Q and H) are equal and given by

$$Q_{fd} = H_{fd} = 2\int_N^1 RU_{fd}\,dR$$

$$= \frac{1-N^2}{128(1-N)^4}\left[1 + N^2 + \frac{1-N^2}{\ln N}\right] \quad (23)$$

Numercial Analysis and Method of Solution

Considering the mesh network of Fig. 1, and by an indirect extension of the work of Bodoia and Osterle [14], equations (9–14) can be written in the following finite difference forms

$$\frac{V_{i+1,j+1} - V_{i,j+1}}{\Delta R} + \frac{V_{i+1,j+1} + V_{i,j+1}}{2[N + (i - \frac{1}{2})\Delta R]} + \frac{U_{i+1,j+1} + U_{i,j+1} - U_{i+1,j} - U_{i,j}}{2\Delta Z} = 0 \quad (24)$$

$$\frac{W_{i,j}W_{i,j+1}}{N + (i-1)\Delta R} = \frac{8(1-N)^5}{1+N}\frac{\mathrm{Gr}^2}{\mathrm{Ta}}\frac{P_{i,j+1} - P_{i-1,j+1}}{\Delta R} \quad (25)$$

$$V_{i,j}\frac{W_{i+1,j+1} + W_{i+1,j} - W_{i-1,j} - W_{i-1,j+1}}{4\Delta R} + U_{i,j}\frac{W_{i,j+1} - W_{i,j}}{\Delta Z}$$

$$= \frac{W_{i+1,j+1} + W_{i+1,j} - 2W_{i,j+1} - 2W_{i,j} + W_{i-1,j+1} + W_{i-1,j}}{2(\Delta R)^2} + \frac{1}{N + (i-1)\Delta R}$$

$$\frac{W_{i+1,j+1} + W_{i+1,j} - W_{i-1,j} - W_{i-1,j+1}}{4\Delta R} - \frac{W_{i,j+1} + W_{i,j}}{2[N + (i-1)\Delta R]^2} \quad (26)$$

$$V_{i,j}\frac{U_{i+1,j+1} - U_{i-1,j+1}}{2\Delta R} + U_{i,j}\frac{U_{i,j+1} - U_{i,j}}{\Delta Z} = \frac{P_{i,j} - P_{i,j+1}}{\Delta Z} + \frac{T_{i,j+1}}{16(1-N)^4} + \frac{U_{i+1,j+1} - 2U_{i,j+1} + U_{i-1,j+1}}{(\Delta R)^2} + \frac{1}{N + (i-1)\Delta R}\frac{U_{i+1,j+1} - U_{i-1,j+1}}{2\Delta R} \quad (27)$$

$$V_{i,j}\frac{T_{i+1,j+1} - T_{i-1,j+1}}{2\Delta R} + U_{i,j}\frac{T_{i,j+1} - T_{i,j}}{\Delta Z} = \frac{1}{\mathrm{Pr}}\left(\frac{T_{i+1,j+1} - 2T_{i,j+1}}{(\Delta R)^2} + \frac{T_{i-1,j+1}}{(\Delta R)^2} + \frac{1}{N + (i-1)\Delta R}\frac{T_{i+1,j+1} - T_{i-1,j+1}}{2\Delta R}\right) \quad (28)$$

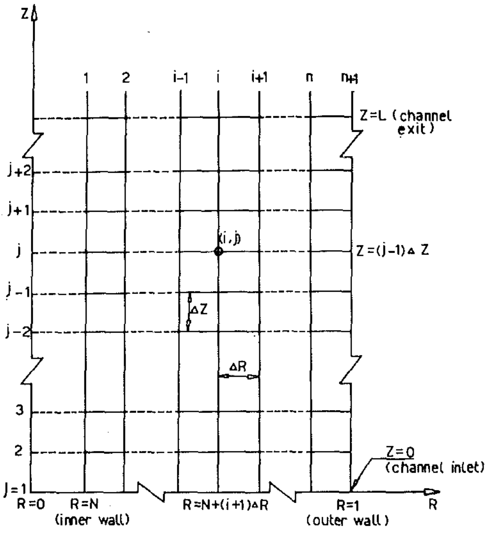

Fig. 1 Mesh network for finite difference representation

$$Q = 2\Delta R \sum_{i=2}^{n} U_{i,j}[N + (i-1)\Delta R] \quad (29)$$

It should be noted that the above finite difference equations are linearized by assuming that, where the product of two unknowns occurs, one of them is given approximately by its value at the previous axial step. The variables with subscript $j + 1$ represent the unknowns and those with subscript j are knowns. Also, applying the available numerical stability theories summerized in [15] shows that the finite difference equations (24–28) are consistent representations of the boundary layer equations (9–13) and are stable for all mesh sizes as long as the downstream axial velocity is non-negative. Moreover, the chosen finite difference approximations are not perfectly symmetrical nor are they of the same form in all the equations. This is done so as to insure stability of the numerical solution and to enable the equations to be solved in the following manner.

For an annulus of a given N, the numerical solution of the foregoing finite difference equations is obtained by first selecting values of Pr, Q and $\mathrm{Gr}^2/\mathrm{Ta}$. Using the value of Q and applying (15) we get the inlet velocity U_0 and hence the inlet pressure P_0 is obtained. Then, starting at the $j = 1$ column (annulus entrance cross section) and applying (26) to points $i = 2, 3, \ldots, n$ and (28) to points $i = 2, 3, \ldots, n + 1$, we get $(2n - 1)$ simultaneous linear equations which when solved (e.g., by Thomas' method [16]) give the values of the $(2n - 1)$ unknowns ($W_{2,2}$,

Nomenclature Continued

$\bar{t}_m$ = mixing cup temperature over the exit cross section, i.e., value of t_m at $z = l$
t_0 = fluid temperature at annulus entrance
t_w = isothermal wall temperature
T = dimensionless temperature at any point, $(t - t_0)/(t_w - t_0)$
T_m = dimensionless mixing cup temperature, $(t_m - t_0)/(t_w - t_0)$
u = axial velocity component at any point
u_{fd} = fully developed axial velocity component
u_0 = entrance axial velocity, $\int_{r_1}^{r_2} 2\pi ru\,dr/\pi(r_2^2 - r_1^2)$
U = dimensionless axial velocity at any point, $ur_2^2/l\gamma\,\mathrm{Gr}^*$
U_{fd} = dimensionless fully developed axial velocity component, $u_{fd}r_2^2/l\gamma\,\mathrm{Gr}^*$
v = radial velocity component at any point
V = dimensionless radial velocity component, vr_2/γ
w = tangential velocity component at any point
W = dimensionless tangential velocity component, $w/\Omega r_1$
W_{fd} = dimensionless fully developed tangential velocity component
z = axial coordinate
Z = dimensionless axial coordinate, $z/\ell\,\mathrm{Gr}^*$
β = volumetric coefficient of thermal expansion
ϵ = dimensionless axial coordinate, $2z(1 - N)/r_2\,\mathrm{Re}$
ρ = fluid density
ρ_0 = fluid density at inlet fluid temperature
μ = dynamic viscosity of fluid
γ = kinematic viscosity of fluid, μ/ρ_0
Ω = angular velocity of inner cylinder
δ_θ = tangential boundary layer displacement thickness, $\int_{r_1}^{r_2} w\,dr/\Omega r_1$
δ_θ^* = dimensionless tangential boundary layer displacement thickness, δ_θ/b
Gr = Grashof number, $g\beta(t_w - t_0)D^3/\gamma^2$
Gr* = modified Grashof number, D Gr$/l$
Nu = local Nusselt number, aD/k
$\overline{\mathrm{Nu}}$ = average Nusselt number, $\bar{a}D/k$
$\overline{\mathrm{Nu}}_i$ = average Nusselt number for case I, $(1 - N)\bar{H}\,\mathrm{Ra}^*/N$
$\overline{\mathrm{Nu}}_0$ = average Nusselt number for case O, $(1 - N)\bar{H}\,\mathrm{Ra}^*$
Pr = Prandtl number, $\mu c_p/k$
Ra = Rayleigh number, Gr · Pr
Ra* = modified Rayleigh number, Gr* · Pr
Re = axial Reynolds number, u_0D/γ
Ta = Taylor number, $2\Omega^2 r_1^2 b^3/\gamma^2(r_1 + r_2)$
Ta* = modified Taylor number, Ta $(b/l)^2$

$W_{3,2}, \ldots, W_{n,2}, T_{2,2}, T_{3,2}, \ldots, T_{n+1,2}$) at all points of the second column. Now, applying (25) with $i = 2, 3, \ldots, n + 1$ and (27) with $i = 2, 3, \ldots, n$ and (29) to the entire column we obtain $2n$ equations which when solved (e.g., by a special form of Gauss-Jordan elimination scheme [15]) give the values of the $2n$ unknowns ($U_{2,2}, U_{3,2}, \ldots, U_{n,2}, P_{1,2}, P_{2,2}, \ldots, P_{n+1,2}$) at all points of the second column. Using the computed values of U's and applying (24) we get the values of V's at all points of the second column. Repeating this procedure, we advance column by column along the annulus until the pressure P at the outer wall of the annulus ($P_{n+1,j}$) returns to zero. This cross section (at which $P_{n+1,j} = 0$) establishes the unknown dimensionless heated length L, which, by definition, is the reciprocal of the unknown modified Grashof number. Hence, both the dimensionless heat absorbed by the fluid from entrance up to the channel exist ($\overline{H}$) and the average Nusselt number ($\overline{\text{Nu}}$) can be calculated from equations (17) and (20), respectively.

It may be worth mentioning that, in practice, for a confined free convection flow, such as that given under consideration, the channel height ℓ is normally known (i.e., L is given) while the volumetric flow rate q (hence Q) is unknown. In fact, the present model and method of solution are handling the problem in a reversed manner, i.e., obtaining an unknown channel height for a given volumetric flow rate. Therefore, the last condition stated in equation (14), i.e., $P = 0$ at $Z = L$ and $R = 1$, is not explicitly imposed on the solution, but continually checked for satisfaction. However, taking into consideration that its satisfaction establishes the unknown channel height, this condition could be regarded as being implicitly imposed.

On the other hand, it is known that near the annulus entrance large gradients exist. For this reason, all the computer runs were made by taking 40 radial increments and very small axial steps ($\Delta Z = 10^{-7}$ for values of $Q \leqslant 0.0025$ and $\Delta Z = 10^{-6}$ for values of $Q > 0.0025$) near the entrance. Further downstream only 20 radial increments were used and the axial step was increased several times as the flow moves away from the entrance.

Results and Conclusions

Comparing the dimensionless equations and boundary conditions (9–14) with those corresponding equations and boundary conditions governing the case of developing laminar forced flows [17–18], three main differences might be noted. Firstly, the energy and momentum equations are coupled in the present case. Secondly, the inlet velocity U_0 and the inlet pressure P_0 are not predetermined initial conditions independent of the channel height as in the case of forced flows. Rather, each of them is dependent upon the channel height and the initial driving temperature difference ($t_w - t_0$). Thirdly, the number of similarity parameters describing the present case exceeds by one those corresponding similarity parameters describing the purely forced convection case.

For this last reason, it was possible, for a given Pr and a given N, to obtain solutions for those equations which govern the forced flow by varying only one parameter, viz Re^2/Ta [17–18]. On the other hand, numerical solutions for the present case are only possible by varying the magnitudes of two parameters, namely Gr^2/Ta and Q. However, there are limitations, as will be clarified, on the magnitude of each of these two parameters.

Computations were carried out for an annulus of $N = 0.5$ with $\text{Pr} = 0.7$. For this particular radius ratio, equation (23) yields the following limiting fully developed value for both Q and H

$$Q_{fd} = H_{fd} = 0.015748 \tag{30}$$

Equation (30) merely states that it is impossible, in the purely laminar free convection regime and irrespective of the value of Gr^2/Ta, to have a dimensionless volumetric flow rate (Q) greater than 0.015748 through an annulus of $N = 0.5$, otherwise there must be an external force aiding the buoyancy driving force. In other words, the dimensionless volumetric flow rate (Q) reaches an upper asymptotic value (Q_{fd}) as the annulus height approaches infinity. A special computer run was made for $Q = Q_{fd}$ and $\text{Gr}^2/\text{Ta} = \infty$ and it has been found that, even though both U and T approach asymptotically their fully developed values, it was impossible to compute a value of Z at which the pressure P returns back to zero. Therefore, the present case was solved for values of Q ranged from 0.001 to 0.015, at various values of the parameter Gr^2/Ta.

On the other hand, more than 80 computer runs were made but it has been found that, at sufficiently low values of Gr^2/Ta, a numerical solution, for a given Q, is available up to a certain axial distance from the annulus entrance afterwhich a divergence from the laminar solution, similar to that reported in [18], occurs. For such unsuccessful computer runs the dimensionless pressure defect (P) failed to return back to zero and hence the determination of the annulus dimensionless height (L) was impossible. Also, the point at which the solution starts to diverge, in such unsuccessful runs, always moves toward the entrance as the value of Gr^2/Ta further decreases. Moreover, as the value of Q decreases, the lowest value of Gr^2/Ta, for which a laminar solution could be obtained over the entire annulus height, increases. Taking into consideration the relationship which links together the parameters Gr^2/Ta, Q and Re^2/Ta, the reader may refer to [18] for a discussion on the phenomenon of a nonexistant laminar solution, for a given Q, at low values of Gr^2/Ta. Also, Schlichting [19] explained the physical reasons due which one "must not expect" laminar solutions to be available "for arbitrary large $\Omega r_1/u_0$," i.e., for high spin, low buoyancy cases.

Apart from those nonexistant solutions at sufficiently low values of Gr^2/Ta, the following sections present samples of the most important results which have been obtained from the successful computer runs.

Effect of the Parameters Q and Gr^2/Ta on the Characteristics of the Developing Flow. It is worth mentioning that choosing a value of $Q \ll Q_{fd}$ implies a short annulus of a large hydraulic diameter with a large temperature difference ($t_w - t_0$). In other words, it implies a case of a large modified Grashof number (Gr*) and that the flow leaves the annulus top exit before reaching the fully developed flow conditions. Thus, for a given value of $\text{Gr}^{*2}/\text{Ta}^*$ (for $N = 0.5$, $\text{Gr}^{*2}/\text{Ta}^* = 4\ \text{Gr}^2/\text{Ta}$), decreasing the value of Q implies also an increase in the value of Taylor number.

Figures 2(a) and 2(b) show, for $Q = 0.005$ and 0.014, respectively, the variations of the dimensionless outer wall pressure defect (P_{w0}) and the dimensionless heat absorbed by the fluid (H) with the dimensionless axial distance (Z), for both thermal boundary conditions (I) and (O), at various selected values of the parameter Gr^2/Ta. It could be seen from these two figures that, for a given Q and for either case I or case O, increasing the value of the parameter Gr^2/Ta causes an increase in the length required for the pressure defect at the outer wall to return back to zero, i.e., an increase in the dimensionless annulus height (L). This means that, for a given mass flow rate, increasing the rotational speed of the inner cylinder reduces the required annulus height. However, provided that laminar solutions exist, it has been found that the Q-L variation in the range of $10^3 \leqslant \text{Gr}^2/\text{Ta} \leqslant \infty$ could be considered, with a maximum deviation of less than 10 percent, equivalent to the Q-L relationship shown in Fig. 3 for the stationary walls case.

Another conclusion to be drawn from Fig. 2(a) is that, the inner cylinder rotation causes the heat absorbed by the fluid (H) to be slightly increased for case I and slightly decreased for case O. At large values of Q, such an effect is so slight that it is unremarkable in Fig. 2(b). Therefore, the $\overline{H}$-L variation for the stationary walls case, given in Fig. 3, could also be used, irrespective of the value of the parameter Gr^2/Ta, for the case with rotating inner walls. These slight effects of the core rotation on H are attributed, as may be seen from Fig. 4, to the increase in the outer wall and the decrease in the inner wall velocity boundary layer thicknesses [18].

Other unpresented results indicate that, for a given Q, the parameter Gr^2/Ta has very slight effects on the local Nusselt number, the mixing cup temperature, the development of the tangential velocity component and the dimensionless tangential boundary layer displacement thickness. In general, the slight effects of the parameter Gr^2/Ta on the characteristics of the developing free convection flow are qualitatively similar to those effects of the parameter Re^2/Ta on the characteristics of developing forced flows [17–18].

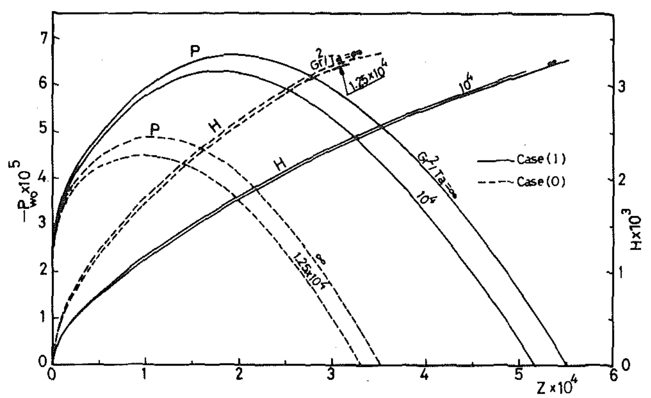

Fig. 2(*a*) Variations of the heat absorbed by fluid and the outer wall pressure defect with the axial distance at various values of Gr^2/Ta, $N = 0.5$, $Q = 0.005$, $Pr = 0.7$

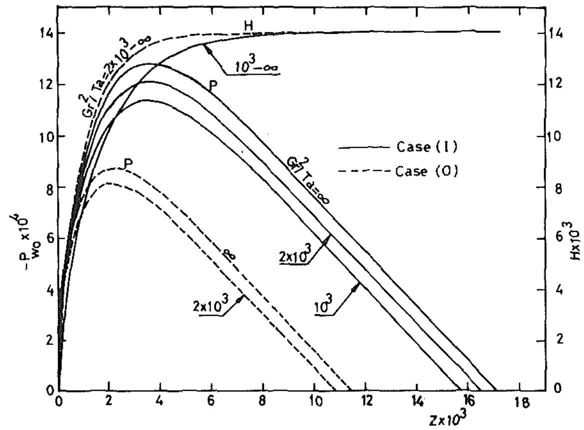

Fig. 2(*b*) Variations of the heat absorbed by fluid and the outer wall pressure defect with the axial distance at various values of Gr^2/Ta, $N = 0.5$, $Q = 0.014$, $Pr = 0.7$

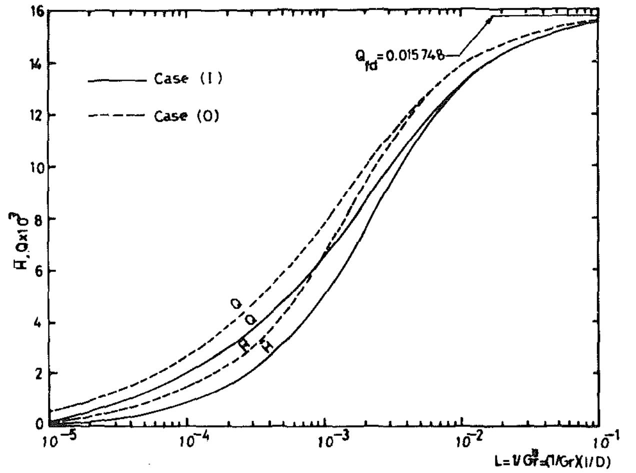

Fig. 3 Variations of dimensionless volumetric flow rate and dimensionless heat absorbed with the dimensionless annulus height, $Pr = 0.7$, $N = 0.5$, $Gr^2/Ta = \infty$

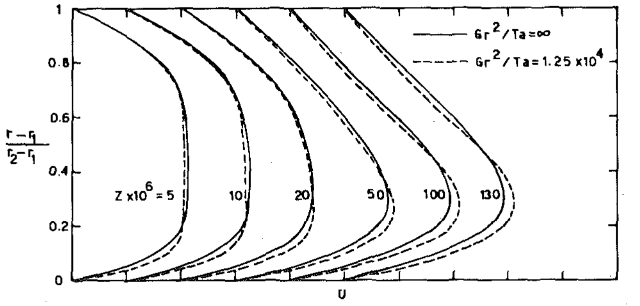

Fig. 4 Effect of the parameter Gr^2/Ta on the development of the axial velocity component, $N = 0.5$, $Q = 0.0025$, $Pr = 0.7$, Case *I*

Figure 5 present the developing tangential velocity profiles corresponding to two chosen values of Q. For $Q = 0.001$, this figure shows that the zero tangential velocity profile at the annulus entrance is developed at the exit into a profile which is similar to that about a single vertical cylinder rotating in a flow parallel to its axis. On the other hand, for $Q = 0.012$, Fig. 5 shows that the tangential velocity profile near the annulus exit tends to approach the fully developed profile given by equation (21).

The effect of the parameter Q on the development of the radial velocity component could be seen from Fig. 6. While, for high values of Q, the radial velocity transfers fluid from regions close to the two boundaries to the core fluid, it mainly transfers, for low values of Q, fluid from the region close to the adiabatic wall to that region close to the heated wall.

Effect of Thermal Boundary Conditions on the Characteristics of the Developing Flow. In Fig. 7 a comparison is made, for a given value of Q and a given value of Gr^2/Ta, between the pressure distribution across the annulus for case I and for case O. It is clear from this figure that, for the same value of Z, the effect of inner cylinder rotation on the pressure distribution across the annulus is more strong for case O than for case I. Actually, this is due to the fact that, for a given Q, the dimensionless annulus height (L) for case O is shorter than that for case I, i.e., the modified Grashof number for case O is larger than that for case I. Hence, for a given Gr^2/Ta, i.e., for a given Gr^{*2}/Ta^*, case O has a higher value of Ta^* than case I.

In order to explain the effect of thermal boundary conditions on the development of the tangential velocity component, it should be noted that the tangential momentum is transported by two mechanisms. Firstly, by the transport created by the radial velocity component and, secondly, by the molecular diffusion due to the viscosity of the fluid. At low values of Q (e.g., $Q = 0.001$), it can be seen from Fig. 6 that the radial velocity component for case O mainly transfers fluid from regions close to the rotating inner wall to the region close to the heated outer wall and thus transporting tangential momentum from fluid near the inner rotating cylinder to the fluid far from it. On the other hand, it can also be seen that, for this value of Q, the radial velocity component for case I mainly transfers fluid from regions close to the stationary outer wall to the region close to the rotating inner wall. Therefore, the tangential momentum transport due to the radial velocity is bigger in case O than in case I and hence one can easily understand why the tangential velocity profiles, presented in Fig. 5 for $Q = 0.001$, develop in case O quicker than in case I.

Also, at high values of Q (e.g., $Q = 0.015$), the same previously mentioned effects of the thermal boundary conditions on the developing radial and tangential velocity components are present, as could be seen from Figs. 5 and 6. However, such effects become decreasingly significant as the value of Q increases, i.e., as the value of Gr^* decreases.

The dimensionless tangential boundary layer displacement thickness is drawn in Fig. 8 against the dimensionless axial distance ϵ for various values of the parameter Q. The dimensionless axial distance ϵ, rather than Z, has been chosen in order that the forced flow results [17] could easily be compared with the present free convection results. It is clear from this figure that for case I the value of δ_θ^* is lower, at the same value of ϵ and for all values of Q, than its corresponding value of the forced flow case. Also, from the same figure, for a given annulus under thermal boundary conditions (I) and at the same value of ϵ, decreasing the value of Q, i.e., increasing the value of Gr^* and consequently increasing the corresponding value of $(t_w - t_0)$, causes a decrease in the value of δ_θ^*. So, combining these results with Astill's stability criterion for tangentially developing flows [9–10] leads to the conclusions that: (1) A purely laminar free convection flow under thermal boundary conditions (I) has, for all values of Q and at the same value of ϵ, a more stable tendency than a forced flow. (2) At

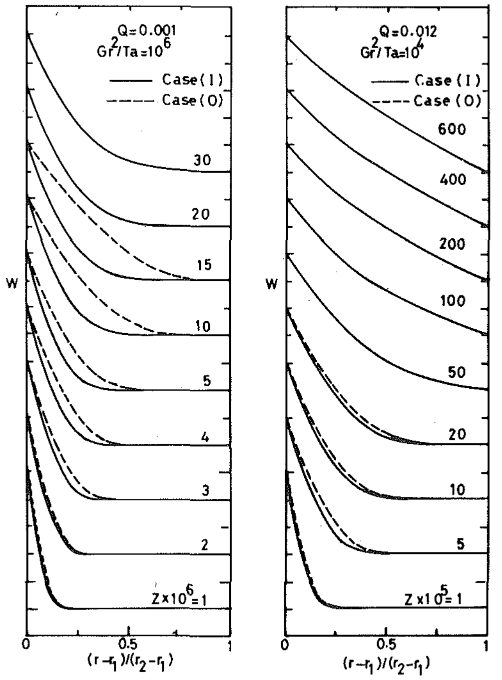

Fig. 5 Effect of the thermal boundary conditions and the parameter Q on the developing tangential velocity profiles, $N = 0.5$, $\mathrm{Pr} = 0.7$

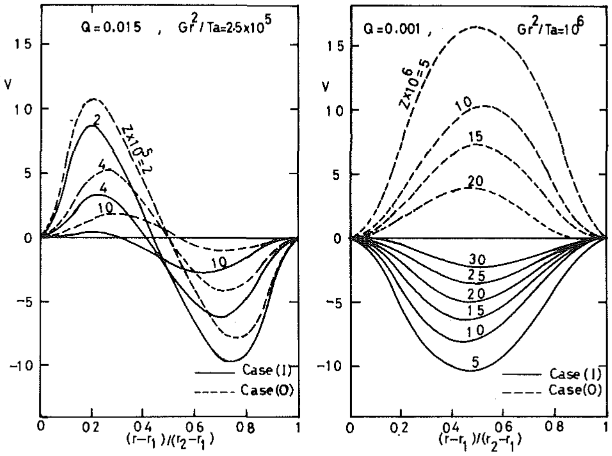

Fig. 6 Effect of the parameter Q and thermal boundary conditions on the developing radial velocity component, $N = 0.5$, $\mathrm{Pr} = 0.7$

the same value of ϵ, this tendency for stability increases as the value of Q decreases, i.e., as the value of $(t_w - t_0)$ and hence the corresponding radial negative temperature gradient increase. These results and conclusions are as might be expected since in case of a pure free convection under thermal boundary conditions (I) a negative radial temperature gradient and an axial flow are present; both have stabilizing effects as was mentioned in the introduction of the paper.

On the other hand, in case of a pure free convection under thermal boundary condition (O) a positive radial temperature gradient, which has destabilizing effects, is present beside the axial flow, which is stabilizing. Therefore, depending upon the relative magnitudes of the stabilizing axial flow and the destabilizing positive radial temperature gradient, i.e., depending upon the values of both Q (which is proportional to Re/Gr) and Re (which is inversely proportional to ϵ), it is expected in case O to have either stabilizing or destabilizing effects. Again, the combination of Astill's stability criterion and the present predictions, shown in Fig. 8, for the development of δ_θ^* for case O, confirm these expectations. As could be seen from this figure, for a given annulus under thermal boundary conditions (O) and at the same value of ϵ, decreasing the value of Q causes an increase in the value of δ_θ^* i.e., an increase in the tendency of the flow for destabilization. Also, for very low values of Q (e.g., $Q = 0.001$) the purely laminar free convection flow under thermal boundary conditions (O) has a more unstable tendency than a forced flow, while for high values of Q (e.g., $Q = 0.015$) the reverse is true.

Finally, in order to check the adequacy of the present numerical predictions against the present fully developed analytical solution and also against the available numerical and analytical results for parallel plate channels and circular tubes [14, 20, 21] and [22], the practically important correlation between the average Nusselt number and the modified Rayleigh number is drawn in Fig. 9. It is noteworthy that this figure could be used for any value of $\mathrm{Gr}^2/\mathrm{Ta}$, provided that the flow remains in the purely laminar free convection regime. This is because it has been found that, for a given value of Q, the parameter $\mathrm{Gr}^2/\mathrm{Ta}$ has slight negligible effects on $\overline{\mathrm{Nu}}$. From this figure, it is clear that at low values of Ra*, the two curves of the present results for case I and case O approach respectively the lines A and $\overline{A}$ which are plots of equation (20) at full development. Also, at high values of Ra* these two curves approach, respectively, lines B and $\overline{B}$ which represent the limiting case of an infinite hydraulic diameter (D) and thus the $\frac{1}{4}$ power law of heated vertical plates or ciruclar tubes applies.

On the other hand, the present results for case O are in good agreement at low values of Ra* with the results of [22] for circular tubes, but at high values of Ra* the results of [22] are higher by about 8 percent than the present results. Also, the present results for case I are clearly different, at low values of Ra*, from the results of [21] for parallel plate channels. However, at high values of Ra*, the present results for case I are, in fact, lower by about 2 percent than the results of [14] and [20].

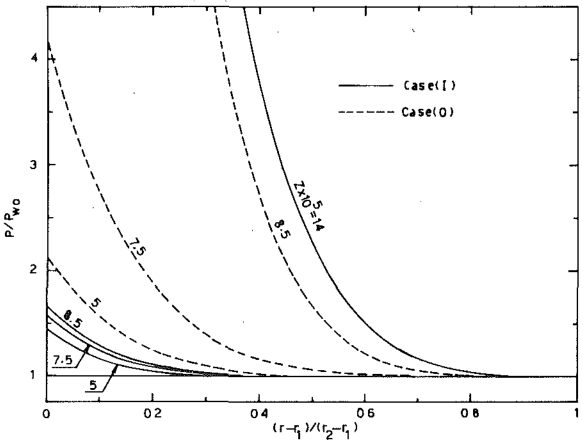

Fig. 7 Effect of thermal boundary conditions on the pressure distribution across an annulus of $N = 0.5$, $\mathrm{Pr} = 0.7$, $Q = 0.0025$, $\mathrm{Gr}^2/\mathrm{Ta} = 10^5$

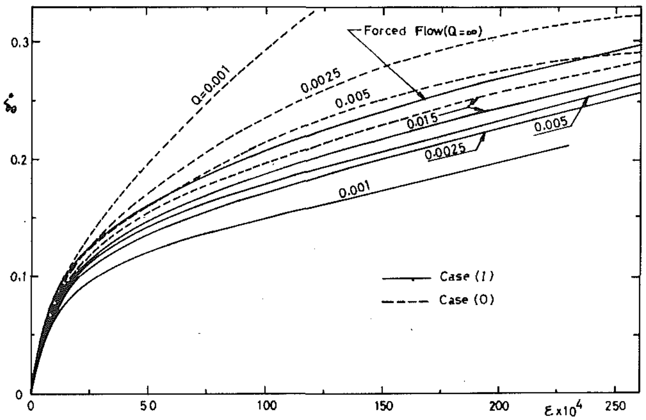

Fig. 8 Dimensionless tangential boundary layer displacement thickness against dimensionless axial distance, $N = 0.5$, $\mathrm{Pr} = 0.7$

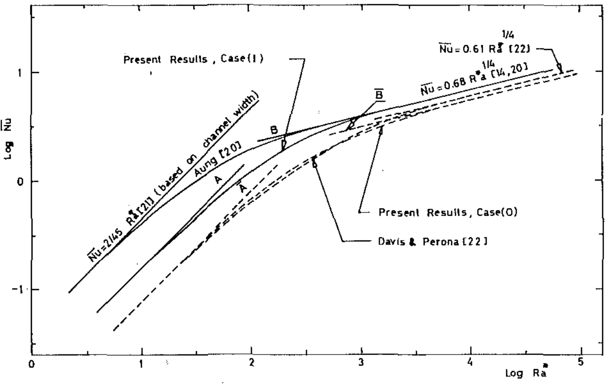

Fig. 9 Comparison of $\overline{Nu}$ against Ra* with data of [14, 20, 21, 22]

Acknowledgment

The financial support of Alazhar University, which allowed us to carry out this investigation on the ICL 1900 computer of Cairo University, is gratefully acknowledged.

References

1 Taylor, G. I., "Stability of a Viscous Liquid Contained Between Two Rotating Cylinders," *Philosophical Transactions*, Series A, Vol. 223, 1923, pp. 289–343.

2 Yih, C., "Dual Role of Viscosity in the Instability of Revolving Fluids of Variable Density," *The Physics of Fluids*, Vol. 4, No. 7, July 1961, pp. 806–811.

3 Becker, K. M., and Kaye, J., "The Influence of a Radial Temperature Gradient on the Instability of Fluid Flow in an Annulus with an Inner Rotating Cylinder," ASME JOURNAL OF HEAT TRANSFER, May 1962, pp. 106–110.

4 Walowit, J., Tsao, S., and DiPrima, R. C., "Stability of Flow Between Arbitrarily Spaced Concentric Surfaces Including the Effect of a Radial Temperature Gradient," ASME *Journal of Applied Mechanics*, Vol. 31, Dec. 1964, pp. 585–593.

5 DiPrima, R. C., "The Stability of a Viscous Fluid Between Rotating Cylinders with an Axial Flow," *Journal of Fluid Mechanics*, Vol. 9, 1960, pp. 621–631.

6 Elliot, L., "Stability of a Viscous Fluid Between Rotating Cylinders with Axial Flow and Pressure Gradient Round the Cylinders," *The Physics of Fluids*, Vol. 16, No. 5, May 1973, pp. 577–580.

7 Chung, K. C., and Astill, K. N., "Hydrodynamic Instability of Viscous Flow Between Rotating Coaxial Cylinders With Fully Developed Axial Flow," *Journal of Fluid Mechanics*, Vol. 81, 1977, pp. 641–655.

8 Hasoon, M. A., and Martin, B. W., "The Stability of Viscous Axial Flow in an Annulus with a Rotating Inner Cylinder," *Proceedings of Royal Society of London*, Series A, Vol. 352, 1977, pp. 351–381.

9 Astill, K. N., "Studies of the Developing Flow Between Concentric Cylinders With the Inner Cylinder Rotating," ASME JOURNAL OF HEAT TRANSFER, Vol. 86, 1964, pp. 383–391.

10 Astill, K. N., "Modes of Adiabatic Flow in the Entrance Region of an Annulus with an Inner Rotating Cylinder," Ph.D. dissertation, Massachusetts Institute of Technology, 1961.

11 Astill, K. N., Ganley, J. T., and Martin, B. W., "The Developing Tangential Velocity Profile for Axial Flow in an Annulus with a Rotating Inner Cylinder," *Proceedings of the Royal Society of London*, Series A, Vol. 307, 1968, pp. 55–69.

12 Martin, B. W., and Payne, A., "Tangential Flow Development for Laminar Axial Flow in an Annulus with a Rotating Inner Cylinder," *Proceedings of the Royal Society of London*, Series A, Vol. 328, 1972, pp. 123–141.

13 Payne, A., and Martin, B. W., "Heat Transfer to Laminar Axial Flow in a Concentric Annulus from a Rotating Inner Cylinder," *Proceedings of the Fifth International Heat Transfer Conference*, Japan Society of Mechanical Engineers. and Society of Chemical Engineers, Japan, Heat Transfer 1974, II, FC 2.7, pp. 80–84.

14 Bodoia, J. R., and Osterle, J. F., "The Development of Free Convection Between Heated Vertical Plates," ASME JOURNAL OF HEAT TRANSFER, Vol. 84, 1962, pp. 40–44.

15 Carnahan, B., Luther, H. A., and Wilkes, J. O., *Applied Numerical Methods*, John Wiley & Sons, New York, pp. 449–475.

16 Lapidus, L., *Digital Computation for Chemical Engineers*, McGraw-Hill, New York, 1962, pp. 254–255.

17 Coney, J. E. R., and El-Shaarawi, M. A. I., "A Contribution to the Numerical Solution of Developing Laminar Flow in the Entrance Region of Concentric Annuli With Rotating Inner Walls," ASME *Journal of Fluids Engineering*, Vol. 96, No. 4, Dec. 1974, pp. 333–340.

18 Coney, J. E. R., and El-Shaarawi, M. A. I., "Laminar Heat Transfer in the Entrance Region of Concentric Annuli With Rotating Inner Walls," ASME JOURNAL OF HEAT TRANSFER, No. 4, Vol. 96, Nov. 1974, pp. 560–562.

19 Schlichting, H., "Laminar Flow About a Rotating Body of Revolution in an Axial Airstream," NACA, TM 1415, 1956.

20 Aung, W., Fletcher, L. S., and Sernas, V., "Developing Laminar Free Convection Between Vertical Flat Plates With Asymmetric Heating," *International Journal of Heat and Mass Transfer*, Vol. 15, No. 11, Nov. 1972, pp. 2293–2308.

21 Aung, W., "Fully Developed Laminar Free Convection Between Vertical Plates Heated Asymmetrically," *International Journal of Heat and Mass Transfer*, Vol. 15, No. 8, Aug. 1972, pp. 1577–1580.

22 Davis, L. P., and Perona, J. J., "Development of Free Convection Flow of a Gas in a Heated Vertical Open Tube," *International Journal of Heat and Mass Transfer*, Vol. 14, 1971, pp. 889–903.

Laminar Mixed Convection in a Shrouded Fin Array

S. Acharya
S. V. Patankar
Department of Mechanical Engineering,
University of Minnesota,
Minneapolis, MN 55455

An analytical study is made to investigate the effect of buoyancy on laminar forced convection in a shrouded fin array. Two heating conditions are considered; in one, the fins and the base surface are hotter than the fluid, and in the other, they are colder. The results are obtained numerically for a wide range of the governing buoyancy parameter. It is found that with a hot fin and base, the secondary flow pattern is mostly made up of a single eddy. The influence of buoyancy is significant and leads to Nusselt numbers and friction factors which are much higher than for pure forced convection. With a cold fin and base, the presence of a tip clearance between the fins and the shroud generates a multiple eddy pattern. The resulting stratification is responsible for the existence of high axial velocity and temperature in the clearance region relative to that in the inter-fin space. Compared to the hot fin case, the secondary flow is weaker, and therefore a relatively smaller increase in the friction factor is obtained. The Nusselt number is found to increase only in the absence of tip clearance. The distribution of the heat transfer coefficient along the fin and the base for both heating situations is found to be highly nonuniform.

Introduction

The heat transfer from fins is often strongly influenced by the details of the flow field in which they are placed. An example of such a situation is the forced convection through a shrouded fin array, which was analyzed by Sparrow, et al. [1]. They demonstrated that the heat transfer from the fin is greatly altered by the presence or the absence of a clearance between the fin tip and the shroud. Another factor that is likely to exert a substantial influence on the fin heat transfer is the presence of secondary flows induced by the buoyancy forces. Such influence has been established for laminar convection in a circular tube with circumferentially uniform heating [2–6] or nonuniform heating [7] of the tube walls. The purpose of this paper is to evaluate the effect of buoyancy on the flow and heat transfer through a shrouded fin array.

The geometry to be considered is shown schematically in Fig. 1. Fluid flows in the direction perpendicular to the plane of diagram. Although a fin thickness t is shown in the schematic representation, the flow field is calculated from the thin-fin assumption, i.e., the thickness t is regarded as negligibly small in comparison with the fin height H or the inter-fin spacing s.

The analysis is performed for laminar flow and for thermally and hydrodynamically developed conditions. The shroud is considered as adiabatic, while the base surface and the fins transfer heat at a uniform rate per unit axial length to (or from) the fluid flowing through the array. Compared to the convection resistance, the conduction resistance of the solid material of the base and the fins is supposed to be negligible, so that, at a given cross section, there is a uniform temperature along the fin and the base surface. Since the buoyancy effects will depend on whether heat is transferred from or to the fluid, two separate situations are considered. In one, the fins and the base are maintained at a temperature higher than that of the fluid. This situation will be referred to as the "hot fin" case. In the other situation, designated as the "cold fin" case, the fins and the base are maintained at a temperature lower than that of the fluid. Further, it is interesting to note that the effects of buoyancy are identical for the hot fin case for the geometry shown in Fig. 1 and the cold fin case with the geometry inverted, and vice versa.

The governing equations for the situation were solved numerically. The procedure described in [8], in particular the *SIMPLER* algorithm, was used. Solutions were obtained over a wide range of values of the governing buoyancy parameter, such that substantial natural convection effects were encountered at the high end of the range. The Prandtl number was assigned the value of 0.7 (for air).

Analysis

The geometrical symmetry of the physical situation shown in Fig. 1 can be used to confine the analysis to a typical module, which is also shown in Fig. 1, where one may observe the use of the thin fin assumption $t \ll H$ and $t \ll s$.

The first step in the specialization of the conservation equations for mass, momentum and energy is the formulation of the buoyancy term. This term is contained in the equation expressing the conservation of momentum in the y direction and may be written as

$$-\frac{\partial p}{\partial y} - \rho g \tag{1}$$

The density appearing in (1) can be related to temperature by means of the Boussinesq model, which gives

$$\rho = \rho_w\,(1 - \beta(T - T_w)) \tag{2}$$

Here T_w denotes the temperature of the fin and the base surface, and ρ_w is the corresponding density. At this stage, a modified pressure p' is defined as

$$p' = p + \rho_w g y \tag{3}$$

With this definition, expression (1) can be rewritten as

$$-\frac{\partial p'}{\partial y} + \rho g \beta (T - T_w) \tag{4}$$

where, in accordance with the constant-density assumption, ρ_w has been replaced by ρ.

The fully developed conditions imply that the velocity components u, v, and w do not change with the axial coordinate z, and that the axial pressure gradient $\partial p/\partial z$ is equal to $d\overline{p}/dz$, where $\overline{p}$ is the mean pressure over a cross section. For the thermal boundary condition considered, all temperatures rise linearly with z, so that

$$\frac{\partial T}{\partial z} = \frac{dT_w}{dz} = \frac{Q'}{\rho c_p (s/2)\,(H + c)\overline{w}} \tag{5}$$

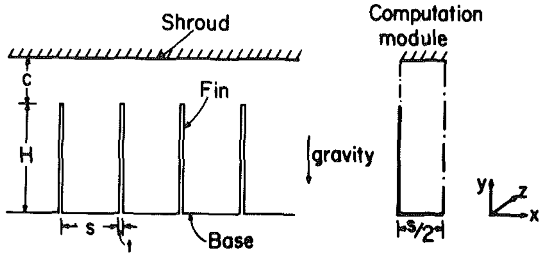

Fig. 1 Shrouded fin array and the computation module

Contributed by the Heat Transfer Division for publication in the JOURNAL OF HEAT TRANSFER. Manuscript received by the Heat Transfer Division October 7, 1980.

where Q' is the heat input per unit axial length for the computation module shown in Fig. 1. Equation (5) has been obtained from an overall heat balance for the domain.

With the dimensionless variables defined by

$$X = x/H, \quad Y = y/H, \quad S = s/H, \quad C = c/H \tag{6a}$$

$$U = \frac{u}{(\nu/H)}, \quad V = \frac{v}{(\nu/H)}, \quad W = \frac{w}{(-d\bar{p}/dz)\,(H^2/\mu)} \tag{6b}$$

$$P = \frac{p'}{\rho(\nu/H)^2}, \quad \phi = \frac{T - T_w}{Q'/k} \tag{6c}$$

the equations expressing the conservation of mass, momentum, and energy become

$$\frac{\partial U}{\partial X} + \frac{\partial V}{\partial Y} = 0 \tag{7}$$

$$U\frac{\partial U}{\partial X} + V\frac{\partial U}{\partial Y} = -\frac{\partial P}{\partial X} + \frac{\partial^2 U}{\partial X^2} + \frac{\partial^2 U}{\partial Y^2} \tag{8}$$

$$U\frac{\partial V}{\partial X} + V\frac{\partial V}{\partial Y} = -\frac{\partial P}{\partial Y} + \frac{\partial^2 V}{\partial X^2} + \frac{\partial^2 V}{\partial Y^2} + \mathrm{Gr}^+ \phi \tag{9}$$

$$U\frac{\partial W}{\partial X} + V\frac{\partial W}{\partial Y} = 1 + \frac{\partial^2 W}{\partial X^2} + \frac{\partial^2 W}{\partial Y^2} \tag{10}$$

$$U\frac{\partial \phi}{\partial X} + V\frac{\partial \phi}{\partial Y} = \frac{1}{\mathrm{Pr}}\left(\frac{\partial^2 \phi}{\partial X^2} + \frac{\partial^2 \phi}{\partial Y^2}\right) - \frac{2}{\mathrm{Pr}}\frac{W/\overline{W}}{S(1 + C)} \tag{11}$$

Equations (7) to (11) contain two independent parameters, Gr^+ and Pr. Gr^+ is a modified Grashof number defined as

$$\mathrm{Gr}^+ = \frac{g\,\beta Q' H^3}{\nu^2 k} \tag{12}$$

For a fixed duct height and inter-fin spacing, it is the magnitude of Gr^+ alone that governs the heat transfer results for a particular fluid. The second parameter is the Prandtl number Pr, which has been set equal to 0.7 in this investigation.

It is worth noting that, since a fully developed flow is considered here, the cross-stream flow field and the associated heat transfer are governed only by the Grashof number and are not influenced by the Reynolds number of the axial flow. This is a characteristic of all fully developed flows (see [7] for an additional example), in which, since the axial velocity does not change with the axial distance, the inertia of the axial flow plays no role. In a *developing* flow, however, the Reynolds number must be considered in addition to the Grashof number.

The boundary of the computation module shown in Fig. 1 is made of solid walls and symmetry lines. All velocities are equal to zero on the solid walls. At a symmetry line, the normal velocity is zero, and the normal gradients of the two other velocity components are zero. For the temperature equation, the appropriate boundary conditions are given by $\phi = 0$ on the fin and the base surface and the normal gradient $\partial\phi/\partial n = 0$ on the shroud and on the symmetry lines.

Computational experiments were conducted to determine the grid spacing required for sufficient accuracy. It was found that a 22 × 28 grid gave solutions for which the reported results are accurate to 0.5 percent. A higher density of points was employed close to the solid boundaries and near the fin tip ($Y = 1$).

Results and Discussion

Results are presented for the two kinds of heating situation and for Grashof numbers ranging from 10^4 to 10^7. Results beyond a Gr^+ of 10^7 have not been shown, since it is unlikely that the flow will remain laminar under those conditions. The inter-fin spacing $S(= s/H)$ is held fixed at 0.5, while the tip clearance $C(= c/H)$ is assigned the values of 0, 0.4 and 1.0. As stated before, all results pertain to a Prandtl number of 0.7.

Streamline Patterns. Information about the secondary flow pattern can be best obtained from the streamline maps, which will now be presented. The stream function is obtained from the velocity field solution by evaluating the integral

$$\psi = \int_0^Y U\,dY \tag{13}$$

along constant-X lines and with $\psi = 0$ at $X = Y = 0$. The streamline patterns are shown for both kinds of heating situations—the hot fin case in Figs. 2, 3 and 4 and the cold fin case in Figs. 5, 6 and 7. The contours have been drawn for all three values of the clearance parameter ($C = 0, 0.4, 1$) and for Grashof number Gr^+ of 10^4, 10^6 and 10^7. The value of ψ_m below each streamline map stands for the maximum value of ψ, which is a measure of the vigor of the secondary flow.

For the hot fin case, the streamlines corresponding to Gr^+ of 10^4 and 10^6 (Figs. 2 and 3) have a single eddy structure. At Grashof number of 10^7 and for $C = 0$ (Fig. 4), a small counter-rotating eddy, akin to a "thermal" is created. For greater clearances, the stronger secondary flows produce a more homogeneous distribution of axial velocity and temperature, thereby restoring the single eddy pattern.

In the cold fin case, depicted in Figs. 5, 6 and 7, there is a tendency for temperature stratification as evidenced by the multiple eddies

Nomenclature

A_f = fin surface area
A_{ht} = heat transfer area of fin and base
C = clearance parameter, c/H
c = tip clearance
c_p = specific heat at constant pressure
D_e = equivalent diameter, equation (16)
f = friction factor, equation (15)
Gr^+ = modified Grashof number, $g\beta Q'H^3/k\nu^2$
g = acceleration due to gravity
H = fin height
h_b = local heat transfer coefficient along the base, $q_b/(T_w - T_B)$
$\bar{h}_b$ = average heat transfer coefficient along base, $\bar{q}_b/(T_w - T_B)$
h_f = local fin heat transfer coefficient, $q_f/(T_w - T_B)$
$\bar{h}_f$ = average fin heat transfer coefficient, $\bar{q}_f/(T_w - T_B)$
$\bar{h}$ = average heat transfer coefficient for fin and base surface, equation (14)
k = thermal conductivity of fluid
$\dot{m}$ = total mass flow rate
$\dot{m}_f$ = mass flow rate in inter-fin space
$\overline{\mathrm{Nu}}$ = average Nusselt number for fin and base surface, $\bar{h}H/k$
$(\overline{\mathrm{Nu}})_0$ = forced convection value of $\overline{\mathrm{Nu}}$
P = dimensionless pressure, equation (6c)
Pr = Prandtl number of the fluid
p = pressure
p' = modified pressure, equation (3)
$\bar{p}$ = mean pressure over a cross section
Q' = prescribed uniform heat transfer rate for the computation module per unit axial length
Q_f' = the part of Q' that is transferred by the fin
q_b = local base surface heat flux
$\bar{q}_b$ = average base surface heat flux
q_f = local fin heat flux
$\bar{q}_f$ = average fin heat flux
Re = Reynolds number, $\bar{w}D_e/\nu$
S = inter-fin spacing parameter, s/H
s = inter-fin spacing
T = temperature
T_B = bulk temperature
T_w = fin and base surface temperature
t = fin thickness
U, V, W = dimensionless velocities, equation (6b)
u, v, w = velocity components in x, y, z directions
$\overline{W}$ = mean value of W
$\bar{w}$ = mean axial velocity
X, Y = dimensionless coordinates, x/H, y/H
x, y = cross-sectional coordinates
z = axial Coordinate
β = thermal expansion coefficient
μ = viscosity
ν = kinematic Viscosity
ρ = density
ϕ = dimensionless temperature, equation (6c)
ψ = dimensionless stream function, equation (13)
ψ_m = maximum value of ψ

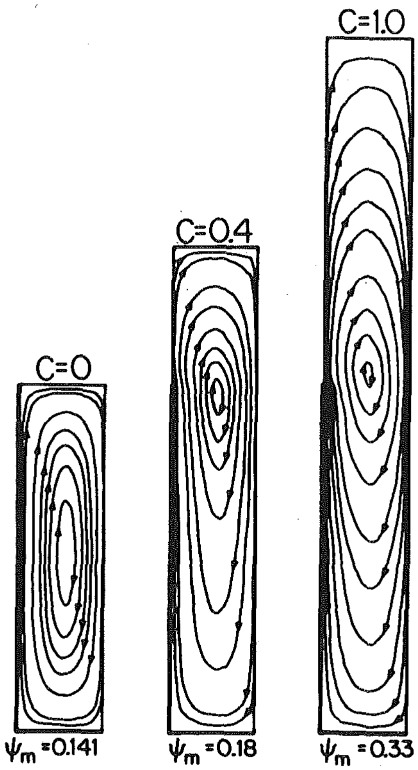

Fig. 2 Streamline pattern for the hot fin case ($Gr^+ = 10^4$)

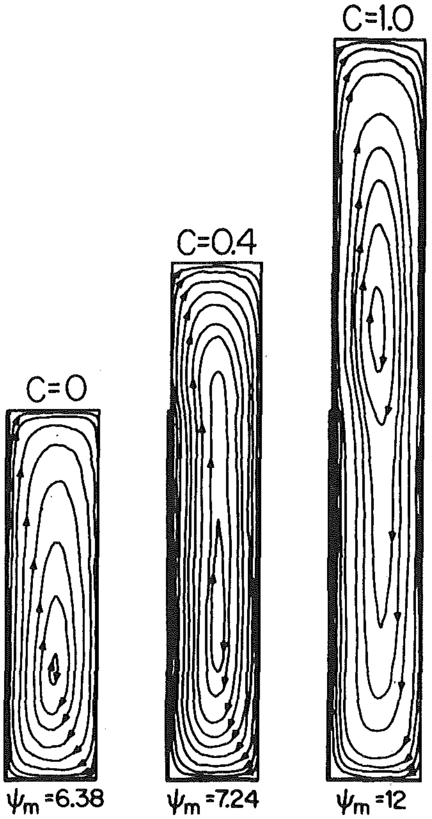

Fig. 3 *Streamline pattern for the hot fin case* ($Gr^+ = 10^6$)

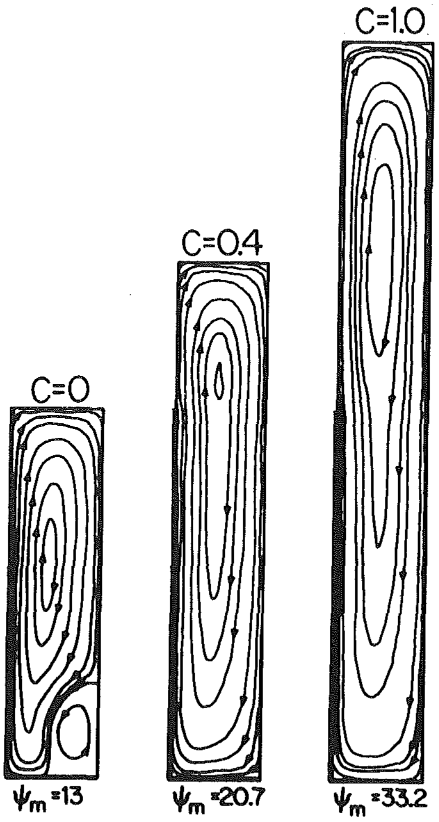

Fig. 4 Streamline pattern for the hot fin case ($Gr^+ = 10^7$)

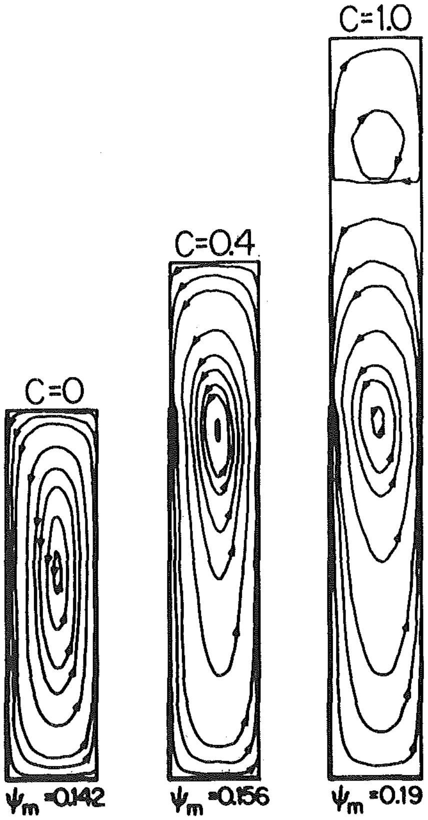

Fig. 5 Streamline pattern for the cold fin case ($Gr^+ = 10^4$)

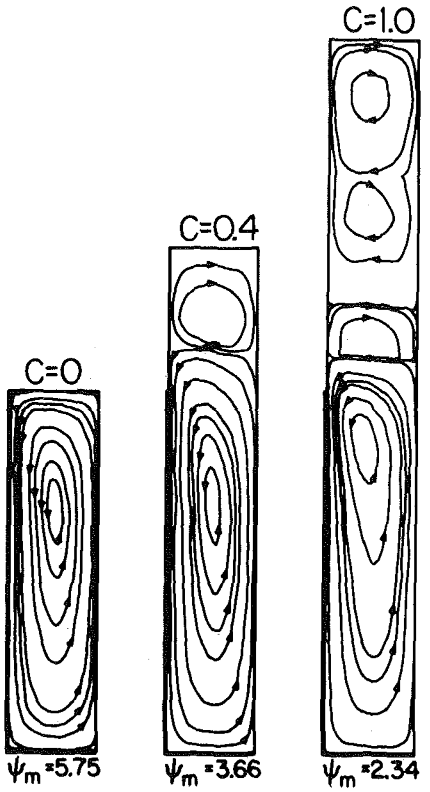

Fig. 6 *Streamline pattern for the cold fin case ($Gr^+ = 10^6$)*

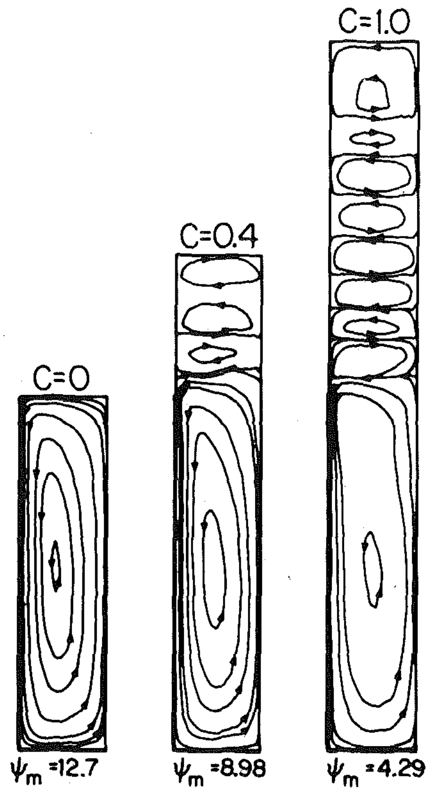

Fig. 7 **Streamline pattern for the cold fin case ($Gr^+ = 10^7$)**

formed in the clearance region. The stratification is further enhanced with an increase in either Gr^+ or C. Such an effect reduces the cross-sectional temperature difference in the inter-fin region and thus diminishes the strength of the secondary flow.

Centerline Profiles of Axial Velocity. Figure 8 shows the normalized axial velocity profile along the base bisector for the hot fin case. For both values of C (i.e., 0 and 1) the curve for $Gr^+ = 10^4$ lies remarkably close to the curve corresponding to pure forced convection, thereby implying the presence of only a very weak secondary flow. This effect can be repeatedly observed in many of the graphs to be presented later and indicates that a certain threshold value of Gr^+ (around 10^4) has to be crossed before buoyancy can cause any detectable change in the results relative to those for pure forced convection.

For zero tip clearance ($C = 0$), the symmetrical distribution in absence of natural convection becomes left-skewed (Fig. 8) at higher Grashof numbers. This is caused by the downflow leg of the main eddy carrying with it the high axial velocity fluid from the interior of the duct. With tip clearance ($C = 1$) and in the absence of secondary flow, the fluid in seeking the path of least resistance attains higher axial velocity in the clearance region than in the inter-fin space. With stronger secondary currents (at higher Gr^+), the axial velocity distribution becomes more homogeneous as evidenced in Fig. 8.

For the cold fin case (Fig. 9), the secondary flow is downward along the fin and upward along the base bisector. Thus, for $C = 0$, the symmetrical distribution in absence of natural convection becomes right-skewed when buoyancy is present. In the presence of tip clearance, high axial velocities in the clearance region are preserved due to the occurrence of temperature stratification which confines the main secondary eddy in the inter-fin region.

Overall Heat Transfer Results. The overall heat transfer characteristics of the system will be presented through two dimensionless groups: the ratio of average Nusselt number to its forced convection value, $\overline{Nu}/(\overline{Nu})_0$ and the ratio Q_f'/Q', where Q_f' is the surface integrated fin heat loss (or gain) and Q' is the total heat loss (or gain) from the fin and the base surface. The average Nusselt

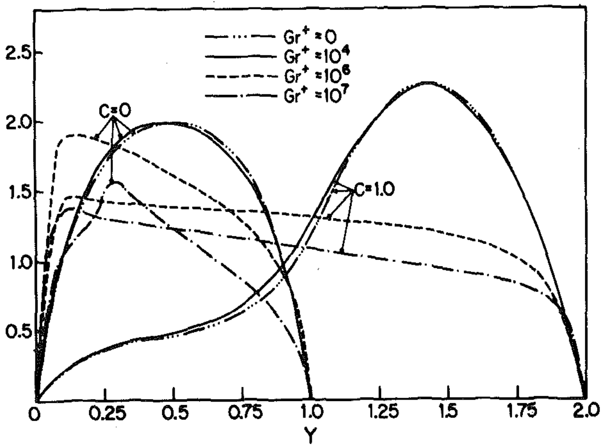

Fig. 8 **Axial velocity distribution along the base bisector for hot fin case**

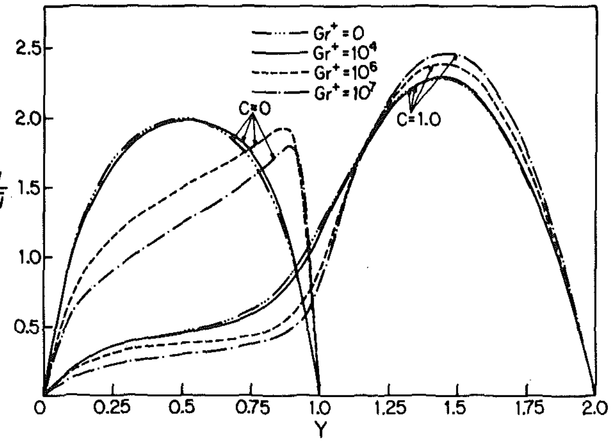

Fig. 9 **Axial velocity distribution along the base bisector for the cold fin case**

number is evaluated as

$$\bar{h} = \frac{Q'}{(H + s/2)(T_w - T_B)}, \overline{\mathrm{Nu}} = \frac{\bar{h}H}{k} \tag{14}$$

where T_B is the bulk temperature of the fluid.

Figures 10 and 11 show the distributions of $\overline{\mathrm{Nu}}/(\overline{\mathrm{Nu}})_0$ and Q_f'/Q' with respect to Gr^+. The solid lines correspond to the hot fin case and are referred to the left hand ordinate. The dashed curves are for the cold fin case and are keyed to the right hand ordinate.

For the hot fin case, the Nusselt number (Fig.10) increases with Gr^+ and also with the tip clearance, in accordance with the strengthening of the buoyancy-induced secondary flow. For the results presented, a Nusselt number as high as 24 times its forced-convection value is encountered. In the cold fin case, Nusselt number increases only in absence of tip clearance. Both for $C = 0.4$ and $C = 1.0$ the curves fall slightly below the $\overline{\mathrm{Nu}}/(\overline{\mathrm{Nu}})_0 = 1$ line thereby implying a small adverse effect of buoyancy on the overall heat transfer. Such an effect is understood by noting that the stratification at the top is responsible for reduced temperatures and axial velocities in the inter-fin region. In addition, the major contribution to the value of the bulk temperature T_B, used in the definition of Nusselt number $\overline{\mathrm{Nu}}$, comes from the hot fluid in the clearance region, which however does not play an active role in the heat transfer process from the thermally active walls.

The ratio Q_f'/Q' plotted in Fig. 11 for the hot fin case is seen to decrease with Gr^+ up to $\mathrm{Gr}^+ = 10^6$, followed by a slight increase. The initial decrease is due to the presence of secondary flow which causes the fluid to become thermally saturated as it flows along the base, and thus, the fluid reaching the fin is not particularly heat receptive. As the velocity of the secondary flow increases, the thermal saturation effect diminishes, and this manifests itself beyond Gr^+ of 10^6 through an increase in Q_f'/Q'.

It should be noted, that up to a Gr^+ of about 5×10^5, Q_f'/Q' exceeds $A_f/A_{ht} = 0.8$, thereby implying that, on a unit area basis, the fins constitute a more effective heat transfer surface than the base. However, beyond a Gr^+ of 5×10^5, the presence of strong secondary flows make the base a more effective heat transfer surface.

In the cold fin case, the fin is always a more effective heat transfer surface than the base. This is because the base receives fluid which is precooled by the fin. With increasing Gr^+, this thermal saturation effect becomes particularly pronounced leading to higher Q_f'/Q'.

Friction Factor. The friction factor is evaluated from the standard definition

$$f = -(d\bar{p}/dz)\, D_e/(\tfrac{1}{2}\rho\bar{w}^2) \tag{15}$$

in which the equivalent diameter D_e for the computation module is

$$D_e = 4(s/2)\,(H + c)/(H + s) \tag{16}$$

If equation (15) is rewritten in terms of the dimensionless variables, there results

$$f\mathrm{Re} = (8/\overline{W})\,\{S(1 + C)/(1 + S)\}^2 \tag{17}$$

with

$$\mathrm{Re} = \bar{w}D_e/\nu \tag{18}$$

Figure 12 shows the variation of $(f\mathrm{Re})/(f\mathrm{Re})_0$ with Gr^+. Here $(f\mathrm{Re})_0$ is the forced convection value of $f\mathrm{Re}$. The results for the hot fin case are shown by solid lines and are referred to the left hand ordinate, while the results for the cold fin case drawn with respect to the right hand ordinate are shown by dashed lines.

Stronger secondary flows are associated with increasing values of Gr^+ and higher (lower) values of clearance C for the hot (cold) fin case. As expected, the greater the vigor of the secondary flow, the higher is the axial pressure gradient or the value of $f\mathrm{Re}$. Since the buoyancy effects are more vigorous for the hot fin case, the increase in $f\mathrm{Re}$ values is also proportionately higher. Further, it is interesting to note that, whereas the Nusselt number for the hot fin case is increased by as much as 24 times, the corresponding friction factor is increased only about four times.

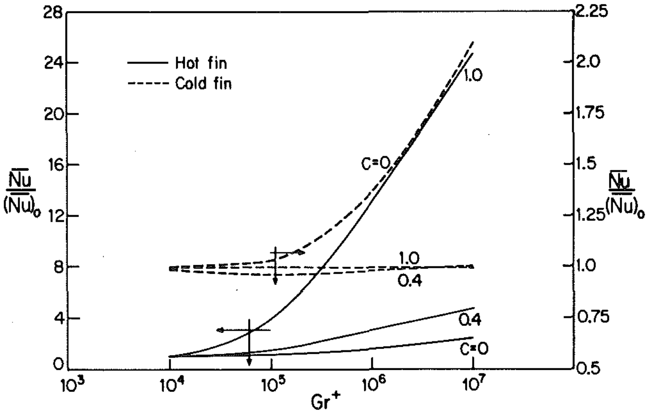

Fig. 10 The Nusselt number ratio as a function of the Grashof number

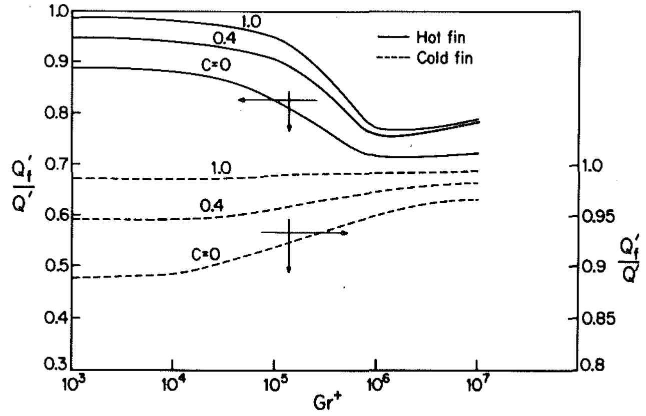

Fig. 11 Fractional fin heat loss as a function of the Grashof number

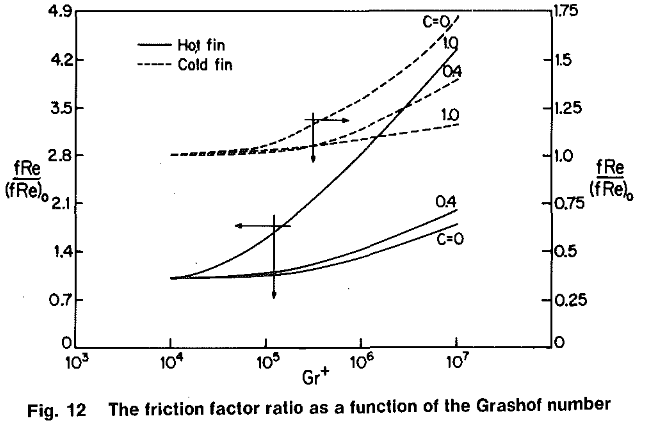

Fig. 12 The friction factor ratio as a function of the Grashof number

Mass Flow Ratios. To characterize the flow distribution, the ratio $\dot{m}_f/\dot{m}$ was evaluated, where $\dot{m}_f$ is the mass flow rate in the inter-fin space and $\dot{m}$ is the total mass flow rate in the module.

For $C = 0$, the mass flow ratio $\dot{m}_f/\dot{m}$ is obviously equal to unity (Fig. 13). For the hot fin case with $C \neq 0$, the secondary flow becomes more vigorous with higher Gr^+, leading to a more homogeneous axial velocity distribution and thus a higher $\dot{m}_f/\dot{m}$ value. For the cold fin case, an increase of Gr^+ produces more stratification thereby retaining high axial velocities in the clearance zone and thus reducing the $\dot{m}_f/\dot{m}$ values.

Local Heat Transfer Rates. The distributions of the normalized heat transfer coefficient along the fin $h_f/\bar{h}_f$ are presented in Figs. 14 and 15 for the hot fin case and the cold fin case respectively. The results for pure forced convection were found to lie very close to those for $\mathrm{Gr}^+ = 10^4$, while the results for $\mathrm{Gr}^+ = 10^6$ display a trend exactly similar to that predicted with $\mathrm{Gr}^+ = 10^7$. Hence results have been

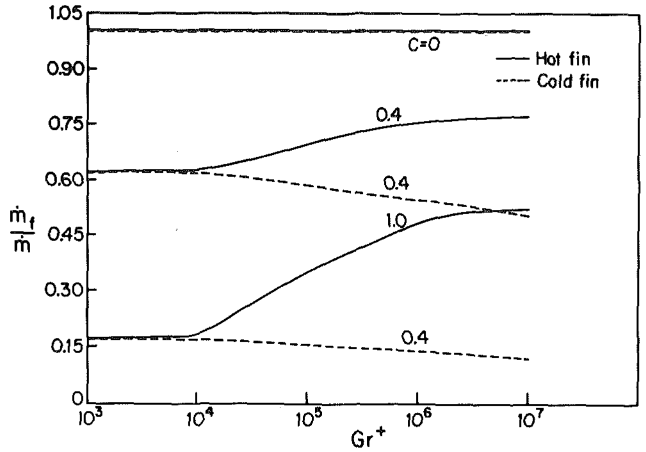

Fig. 13 Fraction of mass flow rate through the inter-fin region as a function of the Grashof number

presented for Gr^+ values of 10^4 and 10^7 and for all three values of C.

The heat transfer coefficient along the fin h_f and the average fin heat transfer coefficient $\bar{h}_f$ were evaluated from the following definitions

$$h_f = q_f/(T_w - T_B) \qquad \bar{h}_f = \bar{q}_f/(T_w - T_B) \qquad (19)$$

where only q_f varies along the isothermal fin. It should be noted that $h_f/\bar{h}_f = q_f/\bar{q}_f$.

For the hot fin case, the results for pure forced convection or for low Gr^+ are identical to those presented by Sparrow, et al. [1]. For $C = 0$, h_f has its maximum value midway along the fin where the fluid axial velocity is a maximum. In the presence of tip clearance, h_f increases monotonically to the tip, which is washed by high axial velocity fluid. Under the action of buoyancy ($Gr^+ = 10^7$), the maximum heat transfer coefficient in the presence of tip clearance occurs at two locations characterized by the presence of high axial velocities. One such location is at the fin tip and the other is between the mid span of the fin and the base. With $C = 0$, the maximum axial velocity and therefore the maximum value of $h_f/\bar{h}_f$ occur at the midplane of the fin.

For the cold fin case (Fig. 15), the secondary flows are rather weak at a Gr^+ of 10^4, resulting in a $h_f/\bar{h}_f$ distribution similar to that in Fig. 14. With a more vigorous secondary flow, the heat transfer coefficient in the presence of tip clearance increases monotonically to the tip. This effect is attributable to the occurrence of temperature stratification, which confines the high axial velocity fluid in the proximity of the fin tip. With $C = 0$, the upflow leg of the secondary flow eddy carries the high axial velocity from the midplane towards the fin tip. Since at the fin tip the resistance to flow is relatively large, the maximum heat transfer coefficient occurs close to, but not at, the fin tip.

The distribution of $h_b/\bar{h}_b$, which represents the ratio of the local base heat transfer coefficient h_b to the average base heat transfer coefficient $\bar{h}_b$, is presented in Figs. 16 and 17. The coefficients h_b and $\bar{h}_b$ are defined in the same way as the fin heat transfer coefficients h_f and $\bar{h}_f$.

For the hot fin case (Fig. 16), the flow is in a clockwise direction. Thus, the fluid becomes less and less amenable to heat transfer as it flows towards the fin, which explains why $h_b/\bar{h}_b$ decreases away from the base mid point. For $Gr^+ = 10^7$ and in the absence of any clearance, $h_b/\bar{h}_b$ is maximum at the separation streamline between the two eddies (i.e., at $x/H \simeq 0.125$. See Fig. 4). This is due to the convection of high axial velocity and low temperature fluid along the separation streamline. With tip clearance, secondary flows are strengthened thereby removing the small eddy and the effect of the separation streamline on the nature of the $h_b/\bar{h}_b$ distribution.

Figure 17 shows the $h_b/\bar{h}_b$ distribution for the cold fin case. Since the fluid flows down the fin and then over the base, regions of the base closer to the fin can transfer more heat than the regions away from

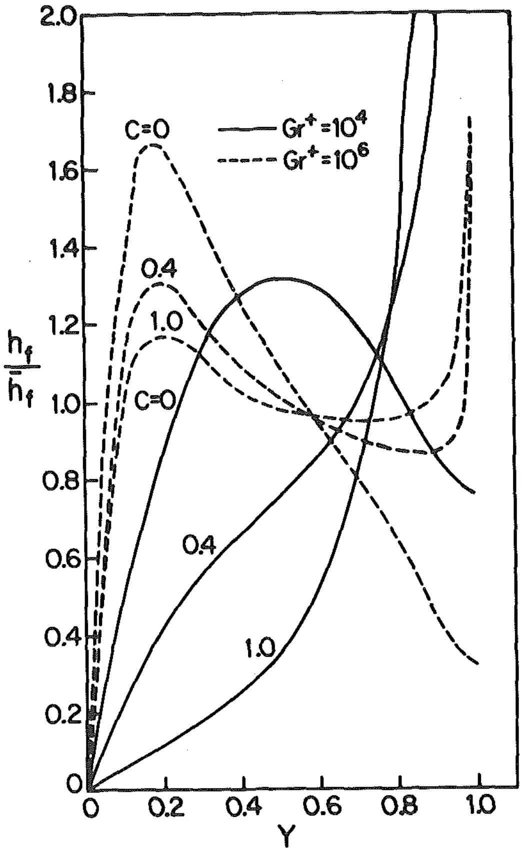

Fig. 14 Variation of the fin heat transfer coefficient for the hot fin case

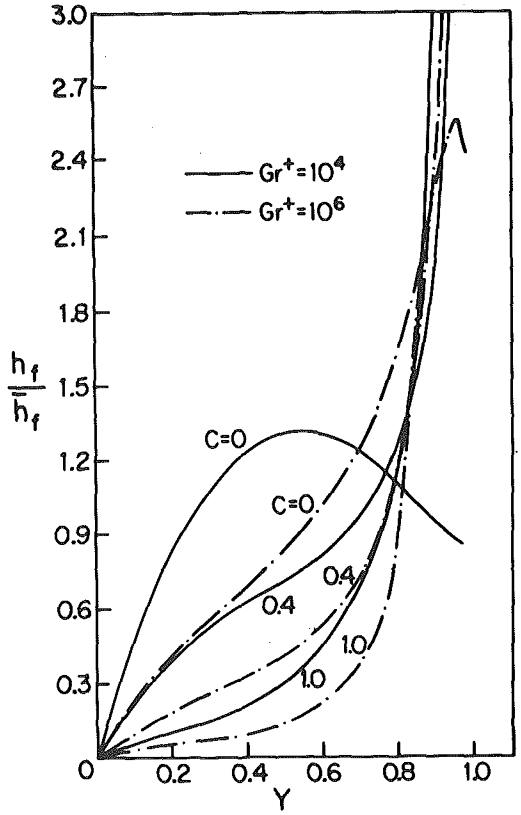

Fig. 15 Variation of the fin heat transfer coefficient for the cold fin case

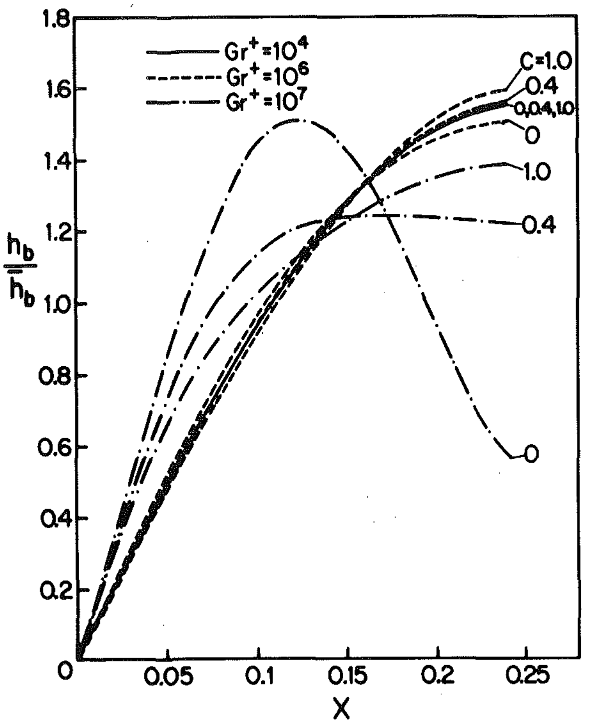

Fig. 16 Variation of the base heat transfer coefficient for the hot fin case

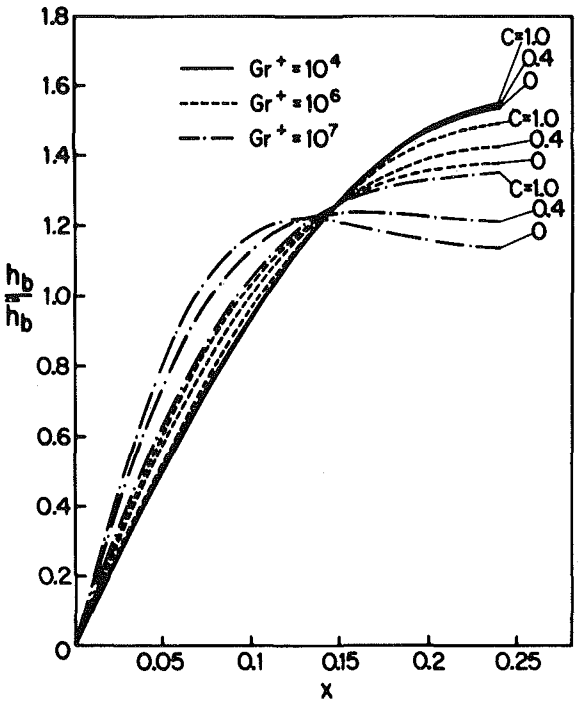

Fig. 17 Variation of the base heat transfer coefficient for the cold fin case

the fin. Thus a more uniform distribution of $h_b/\bar{h}_b$ relative to the forced convection distribution is obtained.

Concluding Remarks

The results of this investigation have demonstrated that the buoyancy forces significantly affect the heat transfer characteristics of laminar forced convection in a shrouded fin array.

For the hot fin case, the flow pattern is in general made up of a single eddy. Secondary flows, which become stronger when either Gr^+ or C is increased, produce a more homogenized axial velocity and temperature distribution. The strengthening of the secondary flows produces a substantial increase in both friction factor and the Nusselt number relative to their forced convection values, but causes a decline in the relative effectiveness of the fin as a heat transfer surface.

For the cold fin case, the presence of a tip clearance produces a multiple-eddy flow pattern. The secondary flows are weaker than those in the hot fin case and are further dampened with increased stratification at high Grashof numbers. The axial velocity and temperature are higher in the clearance region than in the interfin space. While the friction factor value increases with Gr^+, the Nusselt number does so only in the absence of any clearance. The fin is almost always a more effective heat transfer surface than the base.

Acknowledgment

This research was performed under the auspices of NSF Grant ENG 75-18141 A01.

References

1 Sparrow, E. M., Baliga, B. R., and Patankar, S. V., "Forced Convection Heat Transfer from a Shrouded Fin array with and without Tip Clearance," JOURNAL OF HEAT TRANSFER, Nov. 1978, Vol. 100, pp. 572–579.

2 Cheng, K. C., and Hong, S. W., "Combined Free and Forced Laminar Convection in Inclined Tubes," *Applied Scientific Research*, Vol. 27, 1972, pp. 19–38.

3 Newell, P. H., and Bergles, A. E., "Analysis of Combined Free and Forced Convection for Fully Developed Laminar Flow in Horizontal Tubes," ASME JOURNAL OF HEAT TRANSFER, Vol. 90, 1970, pp. 83–93.

4 Farris, G. N., and Viskanta, R., "An Analysis of Laminar Combined Forced and Free Convection Heat Transfer in a Horizontal Tube," *International Journal of Heat and Mass Transfer*, Vol. 10, 1967, pp. 1625–1629.

5 Hussain, N. A., and McComas, S. T., "Experimental Investigation of Combined Convection in a Horizontal Circular Tube with Uniform Heat Flux," *Heat Transfer*, Vol. 4, Paper No. NC 3.4, Elsevier Publishing, Amsterdam, 1970.

6 Bergles, A. E., and Simonds, R. R., "Combined Forced and Free Convection for Laminar Flow in Horizontal Tubes with Uniform Heat Flux," *International Journal of Heat and Mass Transfer*, Vol. 14, 1971, pp. 1989–2000.

7 Patankar, S. V., Ramadhyani, S., and Sparrow, E. M., "Effect of Circumferentially Non-Uniform Heating on Laminar Combined Convection in a Horizontal Tube," ASME JOURNAL OF HEAT TRANSFER, Vol. 100, Feb. 1978, pp. 63–69.

8 Patankar, S. V., *Numerical Heat Transfer and Fluid Flow*, McGraw-Hill—Hemisphere, 1980.

Combined Free and Forced Convection in Vertical Tubes with Radial Internal Fins

C. Prakash
S. V. Patankar
Department of Mechanical Engineering,
University of Minnesota,
Minneapolis, MN 55455

An analysis is made of the fully developed laminar flow and heat transfer in vertical tubes with radial internal fins to determine the influence of the buoyancy forces. The governing equations for velocity and temperature are solved by a finite difference technique which incorporates a special scheme for treating the two coupled variables. Results are presented for a range of the Rayleigh number and for various values of the fin height and the number of fins. The buoyancy force is found to increase significantly both friction and heat transfer in the finned tube; augmentation factors in the range of 5 to 10 are encountered. The effect of buoyancy is particularly strong when the number of fins is small and the fins are short.

Introduction

Internally finned tubes have found wide use in compact heat exchangers. The main purpose of the fins is to provide additional surface area for augmenting the heat transfer. An extensive review of heat transfer enhancement techniques has been presented by Bergles [1], in which different internal fin arrangements are described. The fins are usually radial and they may be straight or spiral. The present work is restricted to straight radial fins.

The problem of fully developed laminar flow in circular tubes with radial internal fins has been studied analytically [2] and numerically [3, 4]. However, the effect of buoyancy on the forced convection has not been investigated so far. For finless circular tubes, the problem of fully developed combined free and forced convection has been solved analytically [5, 6] and investigated experimentally [7]. The purpose of the present paper is to obtain numerical solutions for the free and forced convection in vertical internally finned circular tubes.

Only certain thermal boundary conditions admit fully developed solutions for the buoyancy-affected flow. One such boundary condition is that of uniform heat input per unit axial length. Because of its practical relevance, this boundary condition was chosen for the present study. Further, the tube wall and the fins were supposed to be of high thermal conductivity so that they would assume a uniform temperature over any cross section.

For a *heated* tube, the buoyancy forces *assist* the wall-near flow if the fluid flows upwards. In a cooled tube, on the other hand, an upward flow is opposed near the wall. Further, it may be noted that a heated upflow behaves identically to a cooled downflow. Similarly, a cooled upflow is equivalent to a heated downflow.

For finless circular tubes, the cooled upflow (or heated downflow) is known [5] to give useful solutions only for very small values of the Rayleigh number. At a Rayleigh number of about 33, the centerline velocity approaches infinity and the solution is said to "run away." Since a similar behavior is expected also for the finned tubes, the present investigation was restricted to only heated upflow (or cooled downflow). For this situation the effect of buoyancy is to accelerate the flow near the wall while retarding the flow in the core. At a critical value of the Rayleigh number, this retardation tends to cause reverse flow. Since fully developed solutions involving reverse flows are not expected to occur in practical situations, the numerical computations were not carried out beyond the critical Rayleigh number.

In addition to the Rayleigh number, two geometrical parameters, namely the fin height and the number of fins govern the problem. The number of fins was varied between 4 and 32, and the fin height was increased up to 80 percent of the tube radius.

Analysis

Statement of the Problem. The problem to be investigated is that of fully developed laminar combined free and forced convection through a vertical internally finned circular tube, the cross section of which is shown in Fig. 1. The fins are straight, continuous, and equally distributed around the tube circumference. The thickness of the fins is assumed to be negligible. The tube receives a uniform heat input per unit axial length, and at any axial location, a uniform temperature is taken to prevail at all points on the fins and the tube wall. This assumption implies that the fins and the tube are made of a highly conducting material. The fluid properties are assumed constant except for the variation of density in the buoyancy term. Finally, viscous dissipation and compression work terms are neglected in the energy equation. For a fully developed flow, the velocity components in the cross-sectional plane are zero and the axial velocity is itself independent of the axial distance. Further, for the thermal boundary condition considered, all temperatures rise linearly in the axial direction at the same rate.

Governing Equations. Under the foregoing assumptions, the equations governing the problem are:

$$\frac{\mu}{r}\frac{\partial}{\partial r}\left(r\frac{\partial W}{\partial r}\right)+\frac{\mu}{r^2}\frac{\partial^2 W}{\partial \theta^2}=\left(\frac{dp}{dz}\right)+\rho g \tag{1}$$

$$\frac{\alpha}{r}\frac{\partial}{\partial r}\left(r\frac{\partial T}{\partial r}\right)+\frac{\alpha}{r^2}\frac{\partial^2 T}{\partial \theta^2}=W\frac{\partial T}{\partial z} \tag{2}$$

where W is the axial velocity and T is the temperature; other symbols are defined in the Nomenclature. The effect of natural convection is introduced through the Boussinesq approximation:

$$\rho=\rho_W\left(1+\beta\left(T_W-T\right)\right) \tag{3}$$

where $T_W(z)$ is the wall (or fin) temperature at an axial location z, ρ_W the corresponding density, and β the coefficient of volumetric expansion. Since T_W rises linearly with z, ρ_W is a function of z. However, in accordance with the constant-density approximation, ρ_W will now be interpreted as a constant density corresponding to some reference location.

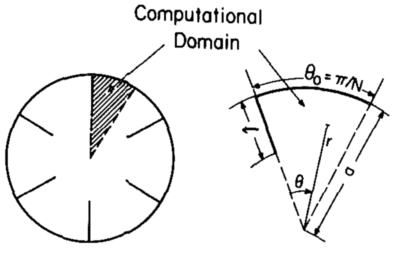

Fig. 1 Circular tube with fins and the computational domain

Contributed by the Heat Transfer Division for publication in the JOURNAL OF HEAT TRANSFER. Manuscript received by the Heat Transfer Division October 7, 1980.

For an arrangement of N equally spaced fins, the required calculation domain is shown in Fig. 1. It can be seen to be a sector of angle π/N extending from one fin to a location half-way towards the next fin. The boundary conditions for this domain are straightforward. On the tube wall and the fin surface, the velocity W is zero and the temperature equals T_W. The remaining boundaries of the domain (shown by dashed lines) are lines of symmetry implying $\partial W/\partial\theta$ and $\partial T/\partial\theta$ to be zero there.

The axial gradient of temperature $\partial T/\partial z$ can be related to the heat input Q_t per unit axial length by an overall heat balance:

$$\frac{\partial T}{\partial z} = \frac{dT_W}{dz} = \frac{dT_b}{dz} = \frac{Q_t}{\dot{m}c} \tag{4}$$

where T_b is the bulk temperature defined by:

$$T_b = \iint WTrdrd\theta / \iint Wrdrd\theta \tag{5}$$

the integration being over the whole cross section of the tube. $\dot{m}$ is the mass flow rate through the tube and is given by

$$\dot{m} = \rho\overline{W}(\pi a^2) = \rho \iint Wrdrd\theta \tag{6}$$

where a is the radius of the tube. Incidentally, equation (6) defines the mean velocity $\overline{W}$ as well.

The problem can be nondimensionalized by introducing

$$\Theta = (T - T_W)/(Q_t/k) \tag{7}$$

$$\Omega = (W\mu) \bigg/ \left[a^2\left(-\frac{dp}{dz} - \rho_W g\right)\right] \tag{8}$$

and

$$R = r/a \tag{9}$$

where k is the thermal conductivity of the fluid. These definitions lead to the following dimensionless form of the governing equations.

$$\frac{1}{R}\frac{\partial}{\partial R}\left(R\frac{\partial\Omega}{\partial R}\right) + \frac{1}{R^2}\frac{\partial^2\Omega}{\partial\theta^2} + \pi\overline{\Omega}\,\mathrm{Ra}\,\Theta + 1 = 0 \tag{10}$$

and

$$\frac{1}{R}\frac{\partial}{\partial R}\left(R\frac{\partial\Theta}{\partial R}\right) + \frac{1}{R^2}\frac{\partial^2\Theta}{\partial\theta^2} - \Omega/(\pi\overline{\Omega}) = 0 \tag{11}$$

in which $\overline{\Omega}$ is the mean value of Ω and is related to $\overline{W}$ by:

$$\overline{\Omega} = \overline{W}\mu \bigg/ \left[a^2\left(-\frac{dp}{dz} - \rho_W g\right)\right] \tag{12}$$

From a given distribution of Ω, $\overline{\Omega}$ can be calculated from

$$\overline{\Omega} = \iint \Omega R dR d\theta / \iint R dR d\theta \tag{13}$$

where the integrals are taken over the tube cross section. Another important quantity appearing in equation (10) is the Rayleigh number Ra defined by

$$\mathrm{Ra} = (\rho_W \beta g a^4 dT_b/dz)/(\alpha\mu) \tag{14}$$

The presence of $\pi\overline{\Omega}$ in equations (10) and (11) can be suppressed by introducing a new variable ϕ defined by

$$\phi = \pi\overline{\Omega}\Theta \tag{15}$$

As a result, equations (10) and (11) become

$$\nabla^2\Omega + \mathrm{Ra}\phi + 1 = 0 \tag{16}$$

and

$$\nabla^2\phi - \Omega = 0 \tag{17}$$

where ∇^2 is the two-dimensional Laplacian operator given by

$$\nabla^2 = \frac{1}{R}\frac{\partial}{\partial R}\left(R\frac{\partial}{\partial R}\right) + \frac{1}{R^2}\frac{\partial^2}{\partial\theta^2} \tag{18}$$

As regards the boundary conditions, Ω and ϕ are both zero on the tube wall and the fin surfaces, while their normal gradient is zero on the remaining boundaries of the domain.

Heat Transfer and Pressure Drop Parameters. Results of pressure drop due to friction may be presented through the value of $f\mathrm{Re}$ where,

$$\text{friction factor } f = D_e\left(-\frac{dp}{dz} - \rho_W g\right) \bigg/ \left(\frac{1}{2}\rho_W \overline{W}^2\right) \tag{19}$$

and

$$\text{Reynolds number } \mathrm{Re} = \rho_W \overline{W} D_e/\mu \tag{20}$$

Here D_e is the equivalent hydraulic diameter defined by:

$$D_e = 4 \times \text{cross-sectional area/wetted perimeter}$$

which for the finned tube is given by:

$$D_e = 2a/((Nh/\pi) + 1) \tag{21}$$

where h is the dimensionless fin height ℓ/a. A combination of equations (12, 19) and (20) leads to

$$f\mathrm{Re} = 2\,D_e{}^2/(\overline{\Omega}a^2) \tag{22}$$

Thus, after a solution for Ω has been obtained, $f\mathrm{Re}$ can be obtained from the value of $\overline{\Omega}$.

The heat transfer coefficient is based on the difference between the wall temperature and the bulk temperature. This temperature difference is given by

$$T_W - T_b = -\overline{\Theta}\,Q_t/k \tag{23}$$

Nomenclature

a = tube radius
A_f = fin heat transfer area
A_t = total (fin plus circular tube) heat transfer area
c = specific heat of the fluid
D = tube diameter $2a$
D_e = equivalent hydraulic diameter of channel, equation (21)
f = friction factor, equation (19)
$(f\mathrm{Re})_0$ = $f\mathrm{Re}$ at zero Rayleigh number
g = acceleration due to gravity
h = dimensionless fin height
h_T = heat transfer coefficient, equation (25)
k = thermal conductivity of the fluid
ℓ = fin height
$\dot{m}$ = total mass flow rate
N = number of fins
Nu = Nusselt number
Nu_0 = Nusselt number at zero Rayleigh number
Q_f = heat transferred by the fin per unit axial length
Q_t = total heat input per unit axial length
r = radial coordinate
R = dimensionless radial coordinate r/a
Re = Reynolds number $(\rho_W \overline{W} D_e)/\mu$
Ra = Rayleigh number $(\rho_W \beta g a^4 dT_b/dz)/(\alpha\mu)$
T = fluid temperature
T_b = bulk temperature of the fluid, equation (5)
T_W = tube wall and fin temperature
W = axial velocity of the fluid
$\overline{W}$ = average velocity of the fluid, equation (6)
z = axial coordinate
α = thermal diffusivity of the fluid
β = coefficient of volumetric expansion of the fluid
θ = angular coordinate
θ_0 = half the angular spacing between the fins
Θ = dimensionless temperature, equation (7)
μ = fluid viscosity
ρ = fluid density
ρ_W = fluid density at wall temperature
ϕ = the variable $\pi\overline{\Omega}\Theta$, equation (15)
Ω = dimensionless axial velocity, equation (8)
$\overline{\Omega}$ = average dimensionless velocity, equation (13)

where

$$\overline{\Theta} = \iint \Omega\Theta R dR d\theta / \iint \Omega R dR d\theta \quad (24)$$

the integration being performed over the tube cross section.

With external heating being applied on the circular tube of diameter D ($= 2a$), the heat transfer coefficient h_T is defined as

$$h_T = Q_t/(\pi D(T_W - T_b)) \quad (25)$$

and thus the Nusselt number Nu is given by

$$\mathrm{Nu} = \frac{h_T D}{k} = -1/(\pi\overline{\Theta}) \quad (26)$$

Computational Procedure

The computational task consists of the solution of equations (16) and (17). These can be seen to be the familiar Poisson equations, which are coupled through their source terms. They can be solved by any standard finite-difference technique. At first it appears that the coupling between the equations can be handled by an iterative technique with successive substitution. Thus, with a guessed field of ϕ, equation (16) is solved to obtain a field of Ω; this, in turn, is substituted into equation (17), which is then solved to obtain new values of ϕ. The process is repeated until the values of Ω and ϕ cease to change.

Such a simple-minded scheme, however, was found to converge for only small values of the Rayleigh number. At large values of Ra, for which the equations are strongly coupled, the successive-substitution technique tended to diverge. At times, convergence could be obtained by heavy underrelaxation, but then the approach to convergence was extremely slow resulting in excessive computer time.

To describe a more satisfactory solution procedure, the differential equations (16) and (17) are first written in finite-difference form as follows.

$$a_{ij}\Omega_{ij} = p_{ij}\Omega_{i+1,j} + q_{ij}\Omega_{i-1,j} + b_{ij}\Omega_{i,j+1} + c_{ij}\Omega_{i,j-1} + d_{ij}\phi_{ij} + r_{ij} \quad (27)$$

and

$$a_{ij}\phi_{ij} = p_{ij}\phi_{i+1,j} + q_{ij}\phi_{i-1,j} + b_{ij}\phi_{i,j+1} + c_{ij}\phi_{i,j-1} + g_{ij}\Omega_{ij} \quad (28)$$

Here, the subscripts i and j denote grid locations in the θ and r directions respectively. Equation (27) expresses Ω_{ij} in terms of the Ω values at the four neighboring grid points and in terms of the value of ϕ_{ij}. Similarly, equation (28) gives ϕ_{ij} in terms of its neighbors and Ω_{ij}. All the coefficients in these equations, except d_{ij}, depend simply on geometrical properties of the grid, and the expressions for them can be obtained from any suitable finite difference formulation. The actual formulation used in this study has been described in detail in [8]. The term r_{ij} arises from the constant source term of unity in equation (16); there is no corresponding term, it is worth noting, in equation (28). The coefficients d_{ij} and g_{ij} represent the coupling between the two equations; d_{ij} depends on the Rayleigh number Ra.

The procedure for solving the algebraic equations (27) and (28) is based on the practice of solving them by a line-by-line method [8]. The method involves solving simultaneously for all the variable values along one grid line, which can be accomplished by an efficient algorithm. In the present work, the line method is extended to the simultaneous solution of two coupled variables. The complete details of the algorithm (which may also be found in other places, for example [9]) are given in Appendix A. The central idea of the algorithm is as follows.

If equations (27) and (28) are written for a line identified by a certain value of i, then the algebraic equations connecting the grid points along that line read

$$a_j\Omega_j = b_j\Omega_{j+1} + c_j\Omega_{j-1} + d_j\phi_j + e_j \quad (29)$$

and

$$a_j\phi_j = b_j\phi_{j+1} + c_j\phi_{j-1} + g_j\Omega_j + f_j \quad (30)$$

where the subscript i has been dropped for convenience and the quantities e_j and f_j are given by

$$e_j = r_{ij} + p_{ij}\Omega_{i+1,j} + q_{ij}\Omega_{i-1,j} \quad (31)$$

$$f_j = p_{ij}\phi_{i+1,j} + q_{ij}\phi_{i-1,j} \quad (32)$$

The Ω and ϕ values entering in the definitions of e_j and f_j are the current values available in the iterative procedure.

Equations (29) and (30) with the current estimates of e_j and f_j represent sufficient equations for finding the values of Ω and ϕ at all the grid points along the chosen line. After the simultaneous solution for these equations has been obtained (by the method of Appendix A), the next line is handled in a similar manner. In this way, lines for all values of i are visited and the Ω and ϕ values updated there. The procedure is then repeated for lines identified by the values of j. Sufficient repetitions of this scheme finally lead to the converged solution. It may be noted that, since the line equations treat Ω and ϕ as simultaneous variables, convergence is obtained even when the coupling is strong.

Although the procedure described so far converged satisfactorily in most cases, rather slow convergence was encountered when the number of fins was large and the fin height was small. This results from the fact that, when the angular width of the calculation domain is small, the circumferential coefficients p_{ij} and q_{ij} in equations (27) and (28) are much greater than the radial coefficients b_{ij} and c_{ij}. Further, with small fin height, the boundaries normal to the θ direction are largely symmetry lines and do not provide direct information about the values of Ω and ϕ there.

This difficulty was eliminated by supplementing the line-by-line scheme by a block-correction procedure, which uses the concepts of "additive corrections" generalized by Settari and Aziz [10]. The algebraic details of the block correction are given in Appendix B. The central idea of the procedure is to update given fields of Ω_{ij} and ϕ_{ij} by adding corrections Ω'_j and ϕ'_j which are uniform over a line of constant r (i.e., for a given value of j). These corrections are obtained by solving the integral conservation equations derived by summing equations (27) and (28) for all values of i. The integral equations for Ω'_i and ϕ'_j are also coupled in the same manner as the line equations (29) and (30) and are therefore solved by the procedure of Appendix A. It is possible to use block correction also in the other direction with Ω'_j and ϕ'_i as uniform corrections over a radial line. However, for the geometry and the boundary conditions of the present problem, this did not seem particularly helpful.

To summarize, the coefficients in the finite-difference equations (27) and (28) are first calculated. These equations are then solved by an iterative technique. One overall iteration cycle includes the block correction and the line-by-line solution of the coupled equations on all radial and circumferential lines. The iteration process is continued till convergence.

Results

The computations were performed on a 32 × 14 grid in the $r - \theta$ coordinates. A nonuniform grid spacing was used; the grid lines were closely packed near the fin, the fin tip, and the tube wall. Exploratory calculations on finer grids and on grids of different nonuniformity were used to establish that the presented results are accurate to at least 0.1 percent. No underrelaxation was necessary while solving the coupled equations by the method just described. About 25 iterations were needed to attain convergence to at least five significant figures. It is interesting to note that the number of iterations was independent of the value of the Rayleigh number; this is a direct result of the simultaneous solution for the two coupled variables.

A range of values of fin height and number of fins was considered. For each value of fin height and number of fins, solutions were obtained for increasing values of the Rayleigh number. The Rayleigh number was gradually increased till reverse flows started appearing in the solution. As stated before, fully developed solutions beyond this critical Rayleigh number are not expected to occur in practical situations.

Velocity Profiles. Figure 2 shows the effect of natural convection

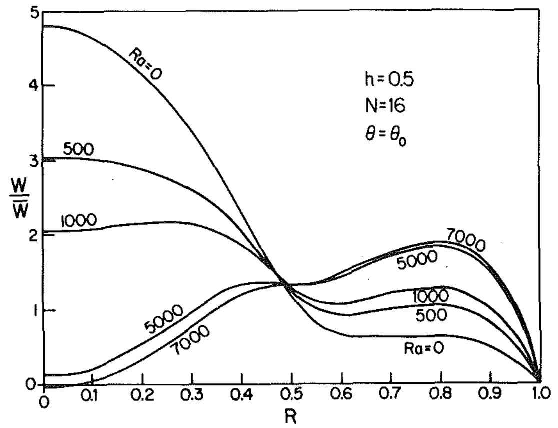

Fig. 2 Effect of natural convection on velocity profile on a radial line midway between two adjacent fins

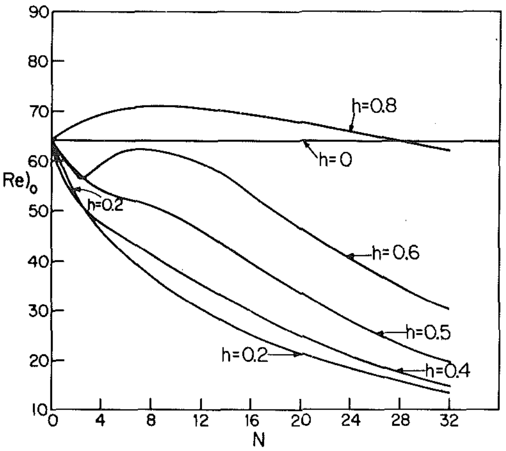

Fig. 4 *f*Re as a function of fin height and number of fins for zero Rayleigh number, i.e., no natural convection

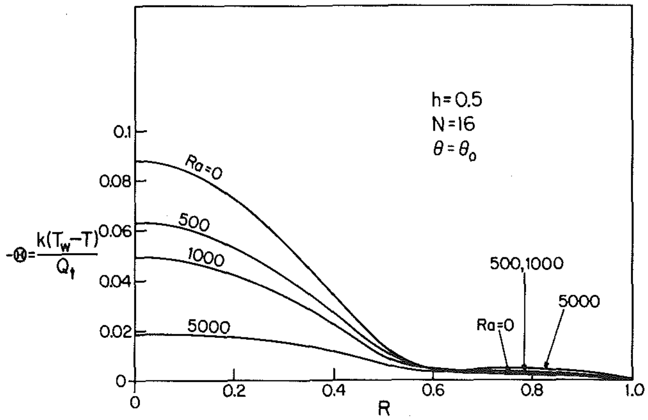

Fig. 3 Effect of natural convection on temperature distribution on a radial line midway between two adjacent fins

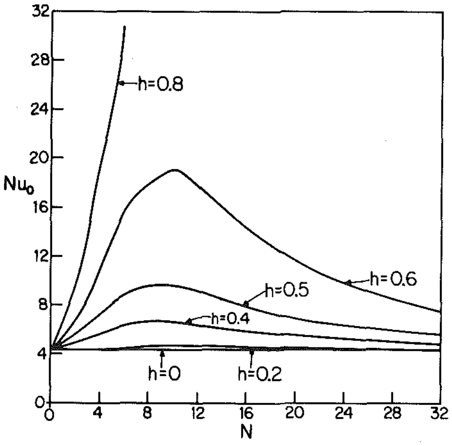

Fig. 5 Nusselt number as a function of fin height and number of fins for zero Rayleigh number, i.e., no natural convection

on the flow velocity for a typical case. Here, $W/\overline{W}$ is plotted as a function of the radial coordinate R at $\theta = \theta_0$ which corresponds to the symmetry line between two adjacent fins. The dimensionless fin height h is 0.5. At zero Rayleigh number (no natural convection), the smaller velocities in the outer region are caused by the greater resistance provided by the presence of the fins. Most of the flow, therefore, remains in the main core. As the Rayleigh number increases, the hotter fluid near the tube wall and the fins is accelerated by the buoyancy force. Consequently, for a given flow rate, the velocity in the center of the tube decreases in comparison. At very large Rayleigh numbers, value of $W/\overline{W}$ in the center of the tube can be seen to become very small and even negative. Further, it can be noted that an increase in the Rayleigh number makes the velocity profile steeper at the tube wall leading to greater friction.

Temperature Profiles. Temperature profiles for the same location and conditions are shown in Fig. 3. For the shown case of sixteen fins, the temperature of the wall (and fins) seems to prevail in the outer region beyond $R = 0.5$; this is expected because of the close proximity of the fins, which have a dimensionless height $h = 0.5$. In the main core, the temperature is significantly different from the wall temperature. At low Rayleigh numbers, the central region of the tube is able to sustain much lower temperatures since the velocity there is high. As the Rayleigh number increases, the temperature distribution tends to become more uniform because the low-velocity core region is now unable to maintain substantially lower temperatures.

Friction and Heat Transfer. It is convenient to present the results for the friction factor and the Nusselt number with reference to their values for zero Rayleigh number. These reference values, therefore, are first presented in Figs. 4 and 5, where the variation of $(f\text{Re})_0$ and Nu_0 with the number of fins N and the fin height h is shown. The subscript 0 identifies the case of zero Rayleigh number. The results for non-zero Rayleigh number are normalized with these basic values. The $(f\text{Re})_0$ curves are the same as those given by Hu and Chang [2]. The Nusselt number Nu_0 cannot be directly compared with the values in [2] because of a different thermal boundary condition used there. The data presented in Figs. 4 and 5 have also been given in a tabular form by Masliyah and Nandakumar [4]. (In Fig. 5 only a part of the curve for $h = 0.8$ has been included; the remaining part would go far beyond the scale chosen for the figure.)

Figure 6 shows the effect of natural convection on Nu and fRe for a moderate number of fins ($N = 6$) for four different fin heights. For each case, the Rayleigh number range is limited by the appearance of reverse flow. The larger the value of the fin height, the higher is the value of this critical Rayleigh number. Both fRe and Nu increase with the Rayleigh number with fRe increasing faster. At a given Rayleigh number, shorter fins tend to have a higher $f\text{Re}/(f\text{Re})_0$ and Nu/Nu_0 than longer fins. This behavior can be understood by noting that the shorter fins require, due to their smaller area, greater nonuniformity of cross-sectional temperature to transfer a given heat input Q_t. The effect of buoyancy is thus stronger for shorter fins. The curves marked $h = 0$ in Fig. 6 correspond to the finless tube, for which the friction factor is seen to rise very rapidly with the Rayleigh number. Also, compared to the finned tubes, a finless tube is seen to sustain a rather small Rayleigh number, which is around 600.

Figure 7 presents the same results as Fig. 6 except that the number of fins is 16. For such a large number of fins, the fin height used in practice is expected to be smaller. Therefore, the values of h beyond 0.5 were not included in the computations. The results for sixteen fins can be seen to be similar to those in Fig. 6.

The striking conclusion from Figs. 6 and 7 is that the buoyancy forces have a significant effect on friction and heat transfer. Aug-

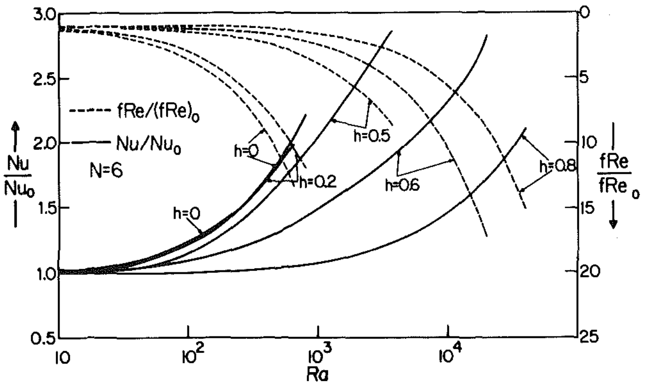

Fig. 6 Effect of natural convection on fRe and Nusselt number for tubes with six fins of varying fin heights

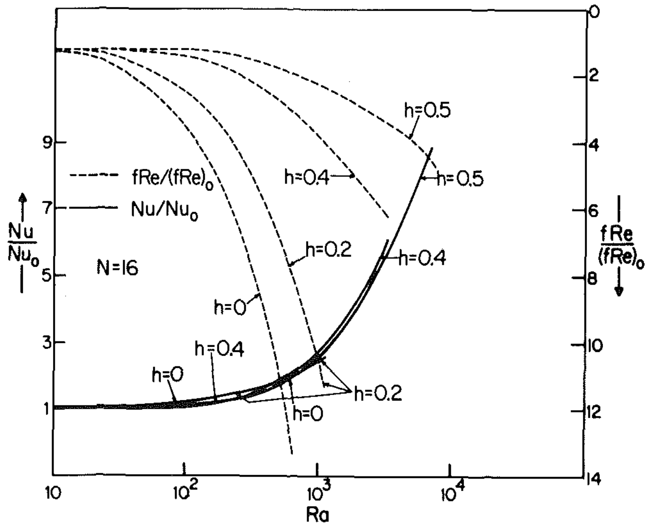

Fig. 7 Effect of natural convection on fRe and Nusselt number for tubes with sixteen fins of varying fin heights

mentation factors of 5 to 10 are easily encountered.

Figures 8 and 9 compare the effect of natural convection on tubes with different number of fins for the same fin height. The fins considered in Fig. 8 are rather short, the dimensionless fin height being 0.2. As can be seen, for a given Rayleigh number, the quantities $f\text{Re}/(f\text{Re})_0$ and Nu/Nu_0 are not very strongly dependent on the number of fins. Figure 9 shows the results for longer fins, with $h = 0.5$. The overall behavior is the same as in Fig. 8. The curve for $N = 6$ showing the variation of $f\text{Re}/(f\text{Re})_0$, however, indicates a faster rise of $f\text{Re}$ with the Rayleigh number. The combination of $h = 0.5$ and $N = 6$ is such that there is substantial heat transfer in the circumferential direction. This leads to greater nonuniformity of temperature and consequent stronger buoyancy forces. An increase in N and a decrease in h both tend to make the heat transfer predominantly radial. Further perspective is added by the curves marked $N = 0$ in Figs. 8 and 9, which represent a finless tube.

In summary, Figs. 6–9 illustrate that the effect of natural convection is to increase both the $f\text{Re}$ and the Nusselt number Nu. At any given Rayleigh number, the ratio $f\text{Re}/(f\text{Re})_0$ is greater than the ratio Nu/Nu_0. The effect of natural convection, seen in terms of $f\text{Re}/(f\text{Re})_0$ and Nu/Nu_0, seems to be more pronounced on tubes with a small number of fins and small fin heights. Another noteworthy characteristic is that the influence of the Rayleigh number on the heat transfer performance for both finned and finless tubes is about the same; however, the frictional resistance of the finless tube increases more rapidly than that of the finned tubes. In this sense, a finned tube becomes even more attractive as an augmentation device when the natural convection effects are significant.

Of the total heat input to the tube, a part is carried by the fin and the remainder by the tube wall. If Q_f is the amount of heat carried by the fin out of a total amount of heat Q_t, then the ratio Q_f/Q_t represents the relative contribution made by the fin. Further, if the separate areas of the fin and the tube plus fins, A_f and A_t respectively, are taken into account, $(Q_f/A_f)/(Q_t/A_t)$ stands for the fin effectiveness on an equal area basis. Table 1 shows these quantities for the situation in the absence of natural convection. The subscript 0 has been added to emphasize that the quantities are for zero Rayleigh number. The first set shows that, for a given fin height, increasing the number of fins reduces the fin effectiveness. The second set shows that, for a specified number of fins, shorter fins are more effective than longer ones.

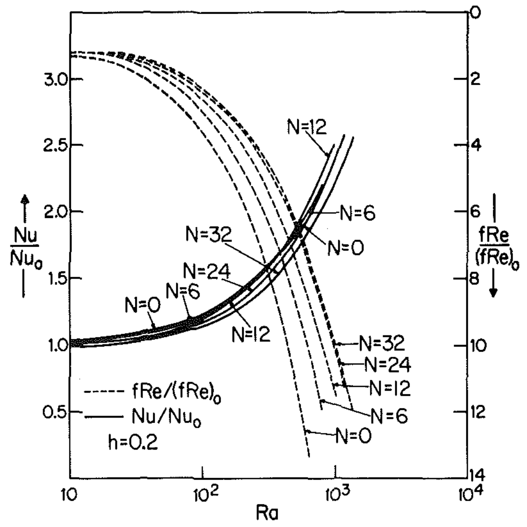

Fig. 8 Effect of natural convection on fRe and Nusselt number for tubes with fins of dimensionless fin height h = 0.2 and different number of fins

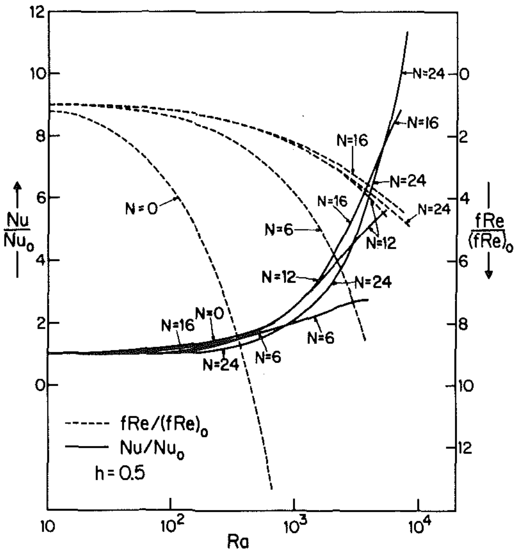

Fig. 9 Effect of natural convection on fRe and Nusselt number for tubes with fins of dimensionless fin height h = 0.5 and different number of fins

Figure 10 shows the effect of natural convection on fin effectiveness for all combinations of fin height and number of fins given in Table 1. As can be seen, the fin effectiveness is considerably reduced in the presence of natural convection. For a given Rayleigh number and fin height, the smaller the number of fins, the greater is the reduction in the fin effectiveness expressed in terms of $(Q_f/Q_t)/(Q_f/Q_t)_0$. For a given Rayleigh number and number of fins, the effect of fin height is not very strong, but the general trend is that fins with greater fin height have a greater reduction in effectiveness. These trends can be understood from the fact that the buoyancy forces accelerate the flow near the tube wall, while retarding the flow near the tube axis. Thus, the tube wall carries a greater share of the total heat transfer as the Rayleigh number increases.

Table 1 Fin effectiveness at zero Rayleigh number (no natural convection)

N	h	$(Q_f/Q_t)_0$	A_f/A_t	$\dfrac{(Q_f/A_f)_0}{(Q_t/A_t)_0}$
6	0.5	0.7183	0.4884	1.4708
12	0.5	0.9077	0.6563	1.3832
16	0.5	0.9471	0.7179	1.3192
24	0.5	0.9768	0.7925	1.2326
16	0.2	0.7671	0.5045	1.5205
16	0.3	0.9053	0.6043	1.4981
16	0.4	0.9494	0.6707	1.4156
16	0.5	0.9471	0.7179	1.3192

Concluding Remarks

The equations governing fully developed laminar combined free and forced convection through vertical internally finned circular tubes have been solved using a finite difference technique. For all values of fin height, number of fins, and Rayleigh number, the Nusselt number and the friction factor are found to increase significantly with the Rayleigh number. The effect of natural convection is particularly pronounced when the number of fins is small and when the fins are short. For each geometry, there exists a critical value of the Rayleigh number beyond which a reverse flow would occur at the tube centerline. The critical Rayleigh numbers for the finned tubes were found to be greater than the critical Rayleigh number for a finless tube. This means that, for a given mass flow rate and heat input, the formation of recirculating cells is less likely with a finned tube than with a finless tube. Also, since the friction of the finless tube is more strongly enhanced by buoyancy, the finned tubes appear as more attractive augmentation devices when the influence of natural convection is significant.

Acknowledgment

This research was performed under the auspices of NSF Grant ENG 75-18141 A01.

References

1 Bergles, A. E., "Survey and Evaluation of Techniques to Augment Convective Heat and Mass Transfer," *Progress in Heat and Mass Transfer*, Vol. 1, Pergamon Press, Elmsford, N. Y., 1969, pp. 331–424.

2 Hu, M. H., and Chang, Y. P., "Optimization of Finned Tubes for Heat Transfer in Laminar Tube Flow," ASME JOURNAL OF HEAT TRANSFER, Vol. 95, 1975, pp. 332–338.

3 Nandakumar, K., and Masliyah, J. H., "Fully Developed Viscous Flow in Internally Finned Tubes," *Chemical Engineering Journal*, Vol. 10, 1975, pp. 113–120.

4 Masiliyah, J. H., and Nandakumar, K., "Heat Transfer in Internally Finned Tubes," ASME JOURNAL OF HEAT TRANSFER, Vol. 98, 1976, pp. 257–261.

5 Morton, B. R., "Laminar Convection in Uniformly Heated Pipes," *Journal of Fluid Mechanics*, Vol. 12, 1959, pp. 227–240.

6 Tao, L. N., "Heat Transfer of Combined Free and Forced Convection in Circular and Sector Tubes," *Applied Scientific Research* (A), Vol. 9, 1960, pp. 357–368.

7 Kemeny, G. A., and Somers, E. V., "Combined Free and Forced-Convective Flow in Vertical Circular Tubes—Experiments with Water and Oil," ASME JOURNAL OF HEAT TRANSFER, Vol. 84, 1962, pp. 339–346.

8 Patankar, S. V., *Numerical Heat Transfer and Fluids Flow*, McGraw-Hill—Hemisphere, New York, 1980.

9 Deshpande, M. D., and Giddens, D. P., "Direct Solution of Two Linear Systems of Equations Forming Coupled Tridiagonal-Type Matrices," *International Journal of Numerical Methods in Engineering*, Vol. 11, 1977, pp. 1049–1052.

10 Settari, A., and Aziz, K., "A Generalization of the Additive Correction Methods for the Iterative Solution of Matrix Equations," *SIAM Journal of Numerical Analysis*, Vol. 10, 1973, pp. 506–521.

APPENDIX A

Simultaneous Solution for Two Coupled Variables

Here the task is to solve the following equations:

$$a_j\Omega_j = b_j\Omega_{j+1} + c_j\Omega_{j-1} + d_j\phi_j + e_j \qquad \text{(A-1)}$$

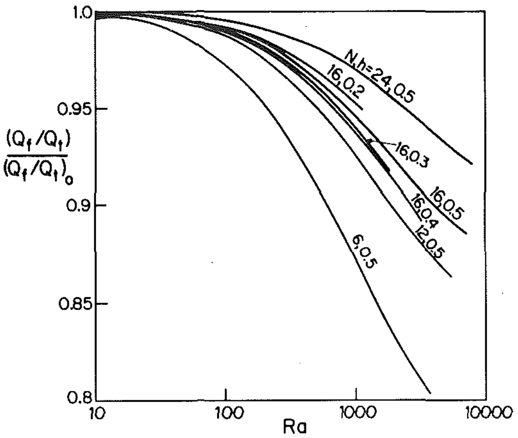

Fig. 10 Effect of natural convection on fin effectiveness

$$a_j\phi_j = b_j\phi_{j+1} + c_j\phi_{j-1} + g_j\Omega_j + f_j \qquad \text{(A-2)}$$

for $j = 2, M$, internal points

where it is assumed that there are $M + 1$ grid points along the line. These equations have been written such that the boundary values of Ω and ϕ at $j = 1$ and $j = M + 1$ do not appear explicitly. In other words,

$$c_2 = 0 \quad \text{and} \quad b_M = 0 \qquad \text{(A-3)}$$

This can be achieved in the following manner. If a boundary value is known, it can be absorbed in the constant term e_j or f_j. If the boundary value is not known, the corresponding boundary condition (such as zero gradient) can be used to eliminate the boundary value from the finite difference equations for the internal points. The first step in the algorithm is to recast equations (A-1) and (A-2) as

$$\Omega_j = P_j\Omega_{j+1} + R_j\phi_{j+1} + Q_j \qquad \text{(A-4)}$$

$$\phi_j = P_j\phi_{j+1} + T_j\Omega_{j+1} + U_j \qquad \text{(A-5)}$$

When the above equations are written for $j - 1$ and used to substitute for Ω_{j-1} and ϕ_{j-1} into equations (A-1) and (A-2), the result is

$$(a_j - c_j P_{j-1})\Omega_j - (c_jR_{j-1} + d_j)\phi_j = b_j\,\Omega_{j+1} + (e_j + c_jQ_{j-1})$$

$$(a_j - c_j P_{j-1})\phi_j - (c_jT_{j-1} + g_j)\Omega_j = b_j\,\phi_{j+1} + (f_j + c_jU_{j-1})$$

These two simultaneous equations can be solved for Ω_j and ϕ_j in terms of Ω_{j+1} and ϕ_{j+1}. Comparison of the expressions so obtained with equations (A-4) and (A-5) leads to the recurrence relations for P_j, R_j, Q_j, T_j and U_j. These are given as follows:
Let

$$\alpha_j = a_j - c_jP_{j-1} \qquad \text{(A-6)}$$

$$\beta_j = d_j + c_jR_{j-1} \qquad \text{(A-7)}$$

$$\eta_j = g_j + c_jT_{j-1} \qquad \text{(A-8)}$$

$$\xi_j = (\alpha_j{}^2 - \beta_j\eta_j) \qquad \text{(A-9)}$$

then

$$P_j = b_j\alpha_j/\xi_j \qquad \text{(A-10)}$$

$$R_j = b_j\beta_j/\xi_j \qquad \text{(A-11)}$$

$$Q_j = (\alpha_j(e_j + c_jQ_{j-1}) + \beta_j(f_j + c_jU_{j-1}))/\xi_j \qquad \text{(A-12)}$$

$$T_j = b_j\eta_j/\xi_j \qquad \text{(A-13)}$$

$$U_j = (\eta_j(e_j + c_jQ_{j-1}) + \alpha_j(f_j + c_jU_{j-1}))/\xi_j \qquad \text{(A-14)}$$

Since $c_2 = 0$, the values of P_2, R_2, Q_2, etc. can be calculated without knowing P_1, R_1, Q_1, etc. Then the recurrence relations can be used for $j = 3, 4 \ldots M$. Also, since b_M is zero, P_M, R_M and T_M would turn out to be zero. Hence $\Omega_M = Q_M$ and $\phi_M = U_M$.

Summary of the Algorithm

i Calculate P_j, Q_j, R_j, T_j and U_j for $j = 2$ to M using equations (A-6) through (A-14).

ii Set $\Omega_M = Q_M$ and $\phi_M = U_M$.

iii Back-substitute into equations (A-4) and (A-5) to obtain Ω_j and ϕ_j for $j = M - 1, M - 2, \ldots, 4, 3, 2$.

APPENDIX B

Block-Correction Procedure

The equations for the block-correction procedure are derived from the basic finite difference equations (27) and (28) for the Ω and ϕ fields. Further, it is assumed that these equations have been modified such that the boundary values do not appear in them. It is proposed that

$$\Omega_{ij} = \Omega^*_{ij} + \Omega'_j \tag{B-1}$$

$$\phi_{ij} = \phi^*_{ij} + \phi'_j \tag{B-2}$$

for all internal grid points.

Here Ω^*_{ij} and ϕ^*_{ij} are the current values of Ω_{ij} and ϕ_{ij}, and Ω'_j and ϕ'_j are the proposed block corrections. Equations (B-1) and (B-2) are first substituted into equations (27) and (28), and then the resulting equations are summed over all internal values of i, i.e., from $i = 2$ to $i = N$; the result is:

$$V_j\Omega'_j = X_j\Omega'_{j+1} + W_j\Omega'_{j-1} + Y_j\phi'_j + Z_j \tag{B-3}$$

$$V_j\phi'_j = X_j\phi'_{j+1} + W_j\phi'_{j-1} + M_j\Omega'_j + N_j \tag{B-4}$$

for $j = 2$ to M

where

$$V_j = \sum_{i=2}^{N} (a_{ij} - p_{ij} - q_{ij}) \tag{B-5}$$

$$X_j = \sum_{i=2}^{N} b_{ij} \tag{B-6}$$

$$W_j = \sum_{i=2}^{N} c_{ij} \tag{B-7}$$

$$Y_j = \sum_{i=2}^{N} d_{ij} \tag{B-8}$$

$$M_j = \sum_{i=2}^{N} g_{ij} \tag{B-9}$$

$$Z_j = \sum_{i=2}^{N} (p_{ij}\Omega^*_{i+1,j} + q_{ij}\,\Omega^*_{i-1,j} + b_{ij}\,\Omega^*_{i,j+1} + c_{ij}\,\Omega^*_{i,j-1} - a_{ij}\,\Omega^*_{ij} + d_{ij}\,\phi^*_{ij} + r_{ij}) \tag{B-10}$$

$$N_j = \sum_{i=2}^{N} (p_{ij}\,\phi^*_{i+1,j} + q_{ij}\,\phi^*_{i-1,j} + b_{ij}\,\phi^*_{i,j+1} + c_{ij}\,\phi^*_{i,j-1} - a_{ij}\,\phi^*_{ij} + g_{ij}\,\Omega^*_{ij}) \tag{B-11}$$

It is interesting to note that the expressions for Z_j and N_j represent the summations of the residuals of equations (27) and (28) respectively; when these residuals are zero, no block correction is obviously needed.

The coupled equations (B-3) and (B-4) are solved for the values of Ω'_j and ϕ'_j by the use of the algorithm given in Appendix A.

Krishna P. Singh
Vice President—Engineering
Joseph Oat Corporation,
Camden, N. J. 08104
Mem. ASME

Some Fundamental Relationships for Tubular Heat Exchanger Thermal Performance

Some basic relationships to characterize tubular heat exchanger thermal performance are derived in terms of the well-known state variables. It is shown that the knowledge of η (NTU), R (heat capacity rate ratio), and partial derivatives of the temperature efficiency P with respect to η and R enables complete characterization of the exchanger performance around an operating point. Thus, the exchanger performance can be readily predicted for the so-called "subdesign" conditions. Likewise, additional criteria to compare various exchanger styles for a given range of operating conditions can be developed. Two such criteria are developed in this paper.

1 Introduction

Heat exchangers are designed to deliver a certain heat transfer rate for a certain specified condition of flow rates and temperatures. This specified condition is often labeled as the "design point" for the heat exchanger [1]. However, there are few exchangers which are confined to operating at the design point only. Conditions of service result in variation in the input quantities to the exchanger (namely, flow rates and inlet temperatures) resulting in quite different outlet temperatures and heat duty. Furthermore, the heat exchanger operator may seek to set the input quantities to obtain a desired output. Thus, the "subdesign" characteristics of heat exchangers are undoubtedly of great value to the operator and the system engineer.

A similar motivation for quantifying subdesign characteristics arises when selecting the exchanger style [2] during the design stage. If an exchanger is designated to perform under more than one set of conditions, then it is obviously meaningful to compare the candidate designs for their subdesign characteristics rather than focusing the attention exclusively on the design point. In order to make a meaningful comparison between various exchanger geometries "around" a design point, the concept of the "exchanger effectiveness gradient vector" and "LMTD correction factor gradient vector" are proposed. Their practical significance is illustrated by comparing some commonly used designs.

In contrast to other process equipment such as pumps and turbines, operating curves for heat exchangers are seldom generated. This is presumably due to the large number of variables involved (two flow rates, four terminal temperatures, heat transfer coefficients and heat transfer surface). However, it is possible to derive explicit relationships to predict exchanger performance when any or some of the principal variables are changed. Such expressions are obviously of value to the user: they also help the designer evaluate a host of operating conditions which ordinarily necessitate use of a computer program.

The expression for the exchanger effectiveness gradient vector is derived in the next section, followed by the development of expressions for predicting performance under subdesign conditions in Section 3. The concept of the LMTD correction factor gradient vector is introduced in Section 4. These concepts are further illustrated in Section 5, followed by a brief conclusion in Section 6.

2 Exchanger Effectiveness

There are several definitions of efficiency associated with heat exchanger performance. Of these, exchanger heat transfer effectiveness[1] as defined by Kays and London [3] is perhaps most meaningful. The effectiveness of a heat exchanger is defined as the ratio of the actual heat duty to the thermodynamically maximum possible heat duty, i.e.

$$\epsilon = \frac{Q}{Q_{\max}} \tag{1}$$

where

$$Q = M_s(T_1 - T_2) = M_t(t_2 - t_1) \tag{2}$$

and

$$Q_{\max} = M_{\min}(T_1 - t_1) \tag{3}$$

where

$$M_{\min} = \text{Min}\,(M_s, M_t) \tag{4}$$

ϵ can be conveniently expressed in terms of commonly used dimensional parameters; namely temperature efficiency P, and heat capacity rate ratio R, defined as follows:

$$P = \frac{t_2 - t_1}{T_1 - t_1} \tag{5}$$

$$R = \frac{M_t}{M_s} = \frac{T_1 - T_2}{t_2 - t_1} \tag{6}$$

It can be shown using the foregoing equations, that

$$\begin{aligned} \epsilon &= P; \quad R \le 1 \\ &= RP; \quad R \ge 1 \end{aligned} \tag{7}$$

Equation (7) leads to some interesting corollaries: (a) Since ϵ must be less than or equal to 1, it follows that P must *always* be less than the lesser of 1 and $1/R$. (b) The temperature efficiency P is always less than or equal to the effectiveness, ϵ.

Another important dimensionless variable that occurs in the formulations of heat exchanger performance analysis is the so-called number of transfer units (NTU) or η,[2] defined as

$$\eta = \frac{UA}{M_t} \tag{8}$$

In fact, it can be shown that η and R can be treated as two independent variables that completely characterize the thermal performance of a heat exchanger; i.e.

$$P = f(\eta, R) \tag{9a}$$

---

[1] Also referred to as "temperature efficiency" in the literature.

Contributed by the Heat Transfer Division for publication in the JOURNAL OF HEAT TRANSFER. Manuscript received by the Heat Transfer Division October 23, 1980.

[2] Some texts [3] define NTU as $UA/M_{\min}$; where $M_{\min}$ is lesser of M_t and M_s. In this paper the definition implied by equation (8) is used throughout the text.

It thus follows from equation (7) that ϵ can also be considered to be a function of η and R; i.e.

$$\epsilon = h(\eta, R) \tag{9b}$$

Thus

$$d\epsilon = dh = \frac{\partial h}{\partial \eta} d\eta + \frac{\partial h}{\partial R} dR$$

$$d\epsilon = dP = \frac{\partial P}{\partial \eta} d\eta + \frac{\partial P}{\partial R} dR; \quad R \leq 1 \tag{10}$$

$$\begin{aligned} d\epsilon &= PdR + RdP \\ &= PdR + R\left(\frac{\partial P}{\partial \eta} d\eta + \frac{\partial P}{\partial R} dR\right) \end{aligned}$$

$$\text{or } d\epsilon = \left(P + R\frac{\partial P}{\partial R}\right) dR + R\frac{\partial P}{\partial \eta} d\eta; \quad R \geq 1 \tag{11}$$

Equations (10) and (11) define the incremental change in ϵ as a function of partial derivatives of P with respect to η and R. We have

$$d\epsilon = a\, dR^* + b\, d\eta^* \tag{12}$$

where

$$a = \begin{cases} R\dfrac{\partial P}{\partial R}, & R < 1 \\ R\left(P + R\dfrac{\partial P}{\partial R}\right); & R > 1 \end{cases} \tag{a}$$

$$b = \begin{cases} \eta\dfrac{\partial P}{\partial \eta}, & R \leq 1 \\ \eta R\dfrac{\partial P}{\partial \eta}; & R \geq 1 \end{cases} \qquad (b) \qquad (13)$$

and

$$dR^* = \frac{dR}{R} \tag{c}$$

$$d\eta^* = \frac{d\eta}{\eta} \tag{d}$$

Thus dR^* and $d\eta^*$ are fractional changes in R and η, respectively. Hence, we have

$$d\epsilon = \nabla\epsilon . \bar{n}$$

where

$$(\bar{n}) = (d\eta^*, dR^*) \quad \text{and}$$

$\nabla\epsilon$ is the gradient of ϵ surface in the coordinate system consisting of dR^* and $d\eta^*$. The magnitude of this gradient vector is given by

$$\chi = |\nabla\epsilon| = (a^2 + b^2)^{1/2} \tag{14}$$

As discussed later, χ can be used as a direct measure of the perturbation in exchanger performance due to small variations in the input variables. We note that a and b are readily computed if the derivatives of P with respect to η and R are known.

Before proceeding to illustrate the usefulness of the above relationships, we will consider similar concepts for another measure of exchanger performance: the so-called LMTD temperature correction factor.

3 Temperature Correction Factor

Whereas ϵ is a measure of the exchanger effectiveness corresponding to thermodynamically maximum attainable heat transfer rate, the LMTD temperature correction factor F, is the gage of exchanger performance vis-a-vis a countercurrent heat exchanger. It is defined as the ratio of the heat transfer surface area required in a countercurrent heat exchanger to that in the subject heat exchanger for a given set of heat duty and flow conditions. It is expressed in terms of the foregoing parameters η and R as follows

$$F = \frac{1}{\eta(R-1)} \ln \frac{1-P}{1-PR} \tag{15}$$

P appears explicitly in equation (15). However, F can also be viewed as an implicit function of η and R by virtue of equation (9a).

Derivatives of F with respect to η, P, and R are directly obtained from equation (15). We have

$$\frac{\partial F}{\partial \eta} = -\frac{1}{\eta^2 (R-1)} \ln \frac{1-P}{1-PR} = \frac{-F}{\eta} \tag{16}$$

$$\frac{\partial F}{\partial P} = \frac{1}{\eta(1-P)(1-PR)} \tag{17}$$

$$\frac{\partial F}{\partial R} = \frac{-F}{(R-1)} + \frac{P}{\eta(R-1)(1-PR)} \tag{18}$$

Furthermore

$$dF = \frac{\partial F}{\partial P} dP + \frac{\partial F}{\partial \eta} d\eta + \frac{\partial F}{\partial R} dR \tag{19}$$

Substituting for dP from equation (10), we have

$$dF = \left(\frac{\partial F}{\partial P}\frac{\partial P}{\partial \eta} + \frac{\partial F}{\partial \eta}\right) d\eta + \left(\frac{\partial F}{\partial P}\frac{\partial P}{\partial R} + \frac{\partial F}{\partial R}\right) dR$$

$$\text{or} \quad dF = \left(B\frac{\partial P}{\partial \eta} + A\right) d\eta + \left(B\frac{\partial P}{\partial R} + C\right) dR \tag{20}$$

where

$$(A, B, C) = \left(\frac{\partial F}{\partial \eta}, \frac{\partial F}{\partial P}, \frac{\partial F}{\partial R}\right)$$

Thus

$$dF = \eta\left(B\frac{\partial P}{\partial \eta} + A\right) d\eta^* + R\left(B\frac{\partial P}{\partial R} + C\right) dR^* \tag{21}$$

$$\text{or} \quad dF = \nabla F . \bar{n} \tag{22}$$

∇F is the gradient of F vector in the coordinate space consisting of η^* and R^*. The norm of this vector can be used as a direct measure of the susceptibility of the exchanger performance due to perturbations in the input data. It is to be noted that computation of the norm

Nomenclature

A = total heat transfer surface area, m^2
a = coefficient of dR^*
b = coefficient of $d\eta^*$
F = LMTD temperature correction factor, dimensionless
M_s = shellside heat capacity rate (mass flow rate times the specific heat of shellside fluid), W/K
M_t = tubeside heat capacity rate, W/K
P = temperature effectiveness, dimensionless
Q = total heat duty, W
$Q_{\max}$ = thermodynamic maximum heat duty, W
R = heat capacity rate ratio (equation (6)), dimensionless
T_1, T_2 = shellside inlet and outlet temperatures, respectively, K
t_1, t_2 = tubeside inlet and outlet temperatures, respectively, K
U = overall heat transfer coefficient, W/m^{2}K
ϵ = exchanger heat transfer effectiveness (equation (1)), dimensionless
η = number of heat transfer units (NTU) (equation (8)), dimensionless
χ = norm of exchanger effectiveness gradient vector

of ∇F requires evaluating $\partial P/\partial\eta$ and $\partial P/\partial R$ as was the case for $\nabla\epsilon$ (equation (13)).

The functional relationship for most heat exchanger configurations have the general form

$$\eta = \phi(P, R) \tag{23}$$

where ϕ is an explicit function in P and R. $\partial\eta/\partial P$ (and hence $\partial P/\partial\eta$) can be obtained directly from equation (23) by differentiation. $\partial P/\partial R$ is computed by observing that

$$\psi(\eta, P, R) = \eta - \phi(P, R) = 0 \tag{24}$$

Treating ψ to be a function of η and R directly, and also explicitly through P, we have

$$\frac{\partial\psi}{\partial R} + \frac{\partial\psi}{\partial P}\frac{\partial P}{\partial R} = 0 \tag{25}$$

Noting that

$$\frac{\partial\psi}{\partial R} = \frac{-\partial\phi}{\partial R};\quad \frac{\partial\psi}{\partial P} = \frac{-\partial\phi}{\partial P}$$

we have

$$\frac{-\partial\phi}{\partial R} - \frac{\partial\phi}{\partial P}\frac{\partial P}{\partial R} = 0$$

$$\text{or}\quad \frac{\partial P}{\partial R} = \frac{-\partial\phi}{\partial R}\Big/\frac{\partial\phi}{\partial P} \tag{26}$$

$\partial\phi/\partial R$ and $\partial\phi/\partial P$ are directly obtained from equation (23). In this manner, the expression for $\partial P/\partial R$ is obtained.

We will now examine some common heat exchanger geometries.

(a) Countercurrent Heat Exchanger. The functional relationship is given by [4]

$$\eta = \frac{\ln\dfrac{1-P}{1-PR}}{R-1} \tag{27}$$

We have, by direct differentiation

$$\partial\eta/\partial P = \frac{1}{(1-P)(1-PR)} \qquad (a)$$

$$\partial P/\partial R = \frac{e^{\eta(R-1)}[\eta(R-1) + 1 - e^{\eta(R-1)}]}{[1 - Re^{\eta(R-1)}]^2} \qquad (b) \quad (28)$$

The norms of $\nabla\epsilon$ and ∇F can now be directly obtained by substituting above relationships into equations (13) and (20), respectively.

(b) One Shell Pass—Two Tube Pass Heat Exchangers. The functional relationship is well-known [4].

$$\eta = \frac{1}{(1+R^2)^{1/2}} \ln\left[\frac{2 - P[R + 1 - (1+R^2)^{1/2}]}{2 - P[R + 1 + (R^2+1)^{1/2}]}\right] \tag{29}$$

This expression can be recast to give P as a function of η and R

$$P = \frac{2[1 - e^{\eta R'}]}{R + 1 - R' - e^{\eta R'}(1 + R + R')} \tag{30}$$

where

$$R' = (1+R^2)^{1/2} \tag{31}$$

The derivatives $\partial P/\partial\eta$ and $\partial P/\partial R$ are obtained by direct differentiation. We have, after some manipulation

$$\partial P/\partial\eta = 1 - PR - P + 0.5P^2R \tag{32}$$

$$\frac{\partial P}{\partial R} = -\frac{1}{YR'}[2\eta \mathrm{Re}^{\eta R'} + P\{R'(1 - e^{\eta R'}) - R(1 + e^{\eta R'}) - \eta \mathrm{Re}^{\eta R'}(R + 1 + R')\}] \tag{33}$$

where

$$Y = R + 1 - R' - e^{\eta R'}(R + 1 + R') \tag{34}$$

(c) Two Shell Pass—Four Tube Pass. The functional relationship is [4]

$$\eta = \frac{2}{R'}\ln\left[\frac{\dfrac{2}{P} - 1 - R + \dfrac{2}{P}[(1-P)(1-PR)]^{1/2} + R'}{\dfrac{2}{P} - 1 - R + \dfrac{2}{P}[(1-P)(1-PR)]^{1/2} - R'}\right] \tag{35}$$

In this case evaluation of the partial derivatives is quite tedius. It is preferable to obtain the derivatives numerically on a digital computer, i.e.

$$\frac{\partial\eta}{\partial P} = \lim_{\Delta P\to 0}\frac{\eta(P+\Delta P) - \eta(P)}{\Delta P} \qquad (a)$$

$$\frac{\partial\eta}{\partial R} = \lim_{\Delta R\to 0}\frac{\eta(R+\Delta R) - \eta(R)}{\Delta R} \qquad (b) \quad (36)$$

Having determined $\partial\eta/\partial P$ and $\partial\eta/\partial R$; equation (26) can now be utilized to evaluate $\partial P/\partial R$.

Prior to illustrating the application of the concepts of effectiveness gradient and LMTD gradient vectors, we will derive general expressions for predicting subdesign performance of tubular exchangers. These expressions are also shown to require evaluation of the same set of partial derivatives, namely $\partial P/\partial\eta$ and $\partial P/\partial R$.

4 Subdesign Relationships

First of all, we observe that P is independent of temperatures (equation (9)). It thus follows that P will remain invariant with respect to changes in the inlet or outlet temperatures.[3] Thus, it should be possible to determine exchanger performance for subdesign cases involving changes in temperature data if the value of P for the design point is given. Explicit expressions for the four possible cases are readily obtained as follows:

(*a*) *Input temperatures* T_1 *and* t_1 *varied (to new values, say* $T_1{}^*$ *and* $t_1{}^*$*)*:[4]

Noting that

$$P = \frac{t_2 - t_1}{T_1 - t_1} = \frac{t_2{}^* - t_1{}^*}{T_1{}^* - t_1{}^*}$$

We have

$$t_2{}^* = P(T_1{}^* - t_1{}^*) + t_1{}^* \tag{37}$$

Heat balance yields

$$R(t_2{}^* - t_1{}^*) = T_1{}^* - T_2{}^* \tag{38}$$

This, together with equation (37) yield

$$T_2{}^* = T_1{}^* - PR(T_1{}^* - t_1{}^*) \tag{39}$$

(*b*) *Hot fluid inlet* T_1 *and cold fluid outlet* t_2 *varied (to new values* $T_1{}^*$ *and* $t_2{}^*$*, respectively).*

Equation (37) gives

$$t_1{}^* = \frac{PT_1{}^* - t_2{}^*}{P - 1} \tag{40}$$

$T_2{}^*$ is expressed in terms of $T_1{}^*$ and $t_2{}^*$ by using equation (38) as follows:

$$T_2{}^* = \frac{1}{(P-1)}[(P - 1 + PR)T_1{}^* - PRt_2{}^*] \tag{41}$$

(*c*) *Hot fluid outlet* T_2 *and cold fluid inlet* t_1 *varied:* Similar analysis is performed to give the following relationship for $T_1{}^*$ and $t_2{}^*$:

---

[3] It is presumed that the coefficient U is not affected by temperature changes. For most practical cases, this assumption can be adopted without significant error as long as temperature changes are small.

[4] Subdesign temperatures are indicated with *a* * superscript in this section.

$$T_1^* = \frac{1}{(1 - PR)}\left[-PRt_1^* + T_2^*\right] \tag{42}$$

$$t_2^* = \frac{1}{(1 - PR)}\left[PT_2^* - t_1^*(PR + P - 1)\right] \tag{43}$$

(*d*) *Both outlet temperatures varied:* Given the new values of T_2^* and t_2^*, the associated values of T_1^* and t_1^* are obtained by a similar procedure. The final results are:

$$T_1^* = \frac{t_2^*RP - (1 - P)T_2^*}{P + PR - 1} \tag{44}$$

$$t_1^* = \frac{PT_2^* + PRt_2^* - t_2^*}{P + PR - 1} \tag{45}$$

Equations (37, 39–45) give the eight required relationships to compute two unknown terminal temperatures for each of the four possible cases of combinations of specified temperatures.

(*e*) *Flow rates varied:* As opposed to "modest" variation in terminal temperatures, changes in flow rates, and surface area directly affect the values of η and/or R (and also η indirectly through possible changes in U). Thus flow rate changes alter the heat exchanger performance variables in an explicit manner. It is important to know how the exchanger will respond to changes in flow rates within the expected range of variation. Using Taylor series [5], assuming P to be continuous in η and R, we have

$$\begin{aligned} P(\eta^*, R^*) = P(\eta, R) &+ \left(\frac{\partial P}{\partial \eta}\Delta\eta + \frac{\partial P}{\partial R}\Delta R\right) \\ &+ \frac{1}{2}\left(\frac{\partial^2 P}{\partial \eta^2}\Delta\eta^2 + 2\frac{\partial^2 P}{\partial \eta \partial R}\Delta\eta\,\Delta R \right. \\ &\left. + \frac{\partial^2 P}{\partial R^2}\Delta R^2\right) + \text{Terms of higher order} \end{aligned} \tag{46}$$

For moderate changes in η and R (ΔR and $\Delta\eta$ small), sufficiently accurate value of P (η^*, R^*) (referred hence forth as P^*) can be obtained by using only the first order derivatives. Thus

$$P^* \doteq P + \frac{\partial P}{\partial \eta}\Delta\eta + \frac{\partial P}{\partial R}\Delta R \tag{47}$$

The partial derivatives $\partial P/\partial\eta$ and $\partial P/\partial R$ are evaluated in accordance with the procedure described in the preceding section. Thus, P^* is computed. Having determined P^*, the two unknown terminal temperatures can be determined using the appropriate set of equations (out of equations (37–45)).

5 Effectiveness and Correction Factor Gradient Vectors

It was shown in the foregoing that computation of the partial derivatives of P with respect to η and R directly leads to the determination of $\nabla\epsilon$ and ∇F. Evaluation of $\nabla\epsilon$ and ∇F provide important insight into the stability and sensitivity characteristics of a heat exchanger at the operating point under consideration. Tube pluggings and tube surface fouling are a fact of life in heat exchanger operation. A pertinent question is: How will the heat duty hold up in face of a declining U (fouling) or decreasing surface area (plugged tubes)? The magnitudes of $\nabla\epsilon$ and ∇F provide direct answers to this question. To verify this fact we refer to Fig. 1 which gives χ ($= |\nabla\epsilon|$) and ϵ as a function of η for countercurrent (curve A) and one shell pass-two tube pass (curve B) designs for a specific value of R. We note that χ for "one-two" design is smaller than that for the countercurrent design for the same value of ϵ. For example, corresponding to $P = \epsilon = 0.5$, $\chi_A = .312$, $\chi_B = .285$. This indicates that the effectiveness for the one-two design will vary less rapidly with respect to changes in input data than the countercurrent design. Table 1 gives numerical values of the derivatives to enable a direct comparison. By way of comparison, let us compute the decline in the exchanger effectiveness for a 1 percent reduction in U (and hence η) in a countercurrent heat exchanger operating at $P = \epsilon = 0.5$ ($R = 0.5$). Table 1 yields (by interpolation)

$$\partial\epsilon/\partial\eta = 0.375$$

Equation (10) gives

$$d\epsilon = \eta\frac{\partial\epsilon}{\partial\eta}d\eta^* = -(0.8)(0.375)(0.01) = -0.0030$$

A one-two exchanger operating at identical conditions ($P = 0.5$, $\eta = 0.867$, $R = 0.5$), subject to 1 percent reduction in η has (by interpolation, Table 1)

$$\frac{\partial\epsilon}{\partial\eta} = 0.278$$

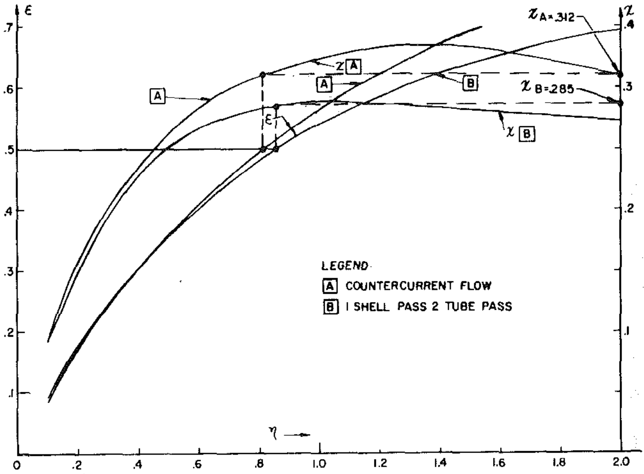

Fig. 1 ϵ and χ versus η ($\dot{R} = 0.5$)

Table 1 Derivatives of *P* with respect to η and R[†], countercurrent and one-two heat exchangers ($R = 0.5$)

NTU, η	Countercurrent Heat Exchanger P	$\frac{\partial\epsilon}{\partial\eta}$	$\frac{\partial\epsilon}{\partial R}$	One Shell Pass—Two Tube Pass Heat Exchanger P	$\frac{\partial\epsilon}{\partial\eta}$	$\frac{\partial\epsilon}{\partial R}$
0.1	0.093	0.865	−0.425 E-2	0.093	0.863	−0.44 E-2
0.2	0.174	0.754	−0.146 E-1	0.173	0.748	−0.155 E-1
0.4	0.307	0.587	−0.440 E-1	0.304	0.567	−0.492 E-1
0.6	0.412	0.467	−0.763 E-1	0.403	0.436	−0.894 E-1
0.8	0.496	0.379	−0.107	0.480	0.337	−0.130
1.0	0.565	0.312	−0.133	0.540	0.263	−0.169
1.1	0.595	0.285	−0.145	0.565	0.233	−0.187
1.2	0.622	0.260	−0.155	0.587	0.206	−0.205
1.4	0.670	0.220	−0.173	0.623	0.162	−0.236
1.6	0.710	0.187	−0.186	0.652	0.128	−0.264
1.8	0.745	0.160	−0.196	0.675	0.101	−0.288

[†] Note: $\frac{\partial P}{\partial \eta} = \frac{\partial\epsilon}{\partial\eta}; \frac{\partial P}{\partial R} = \frac{\partial\epsilon}{\partial R}$ (from equation (10)) for $R \le 1.0$.

Hence

$$d\epsilon = -(0.867)(0.278)(0.01) = -0.0024$$

Therefore, the loss of effectiveness in the one-two design is 80 percent of that in a countercurrent design when both designs are subject to 1 percent reduction in the NTU. Thus the one-two design may be considered to be more stable and less sensitive to perturbations in the input data than an identical service countercurrent heat exchanger.

To demonstrate another variation of the same concept, let us investigate the increase in the shellside flow rate required to nullify the loss in heat duty due to a given decrease in NTU. Let us consider the following operating condition:

$$R = 0.5, P = 0.565, \Delta\eta = -0.05$$

The data for the countercurrent design is found from Table 1:

$$\eta = 1.0, \frac{\partial\epsilon}{\partial\eta} = 0.312, \frac{\partial\epsilon}{\partial R} = -0.133$$

From equation (10)

$$d\epsilon = 0 = \frac{\partial\epsilon}{\partial\eta} d\eta + \frac{\partial\epsilon}{\partial R} dR$$

Hence

$$dR = \frac{-\frac{\partial\epsilon}{\partial\eta} d\eta}{\frac{\partial\epsilon}{\partial R}}$$

Substituting numbers we have

$$dR|_{cc} = -0.1173$$

Hence

$$R* = R + dR = 0.3827$$

Percentage increase in M_s required

$$= \left(\frac{R}{R*} - 1\right)(100) = 30.65 \text{ percent}$$

Similar procedure for one-two design yields

$$\eta = 1.1, \frac{\partial\epsilon}{\partial\eta} = 0.233; \quad \frac{\partial\epsilon}{\partial R} = 0.187$$

$$dR|_{1\text{-}2} = -0.0623$$

$$R* = 0.5 - 0.0623 = 0.4377$$

Thus, percentage increase in M_s required is computed to be 14.23 percent.

This comparison clearly shows the superiority of one-two design over its countercurrent counterpart from the standpoint of stability of performance.

Questions like the ones raised above can be readily answered if $\nabla\epsilon$ is known, which merely implies computing $\partial P/\partial\eta$ and $\partial P/\partial R$.

Evaluation of these derivatives is a simple matter, especially since most design work is performed on digital computers.

The above example mathematically proves what is intuitively obvious. The decline in performance of a countercurrent heat exchanger due to deterioration in U, reduction in A or flow rates is steeper than it is in a one-two exchanger. The magnitudes of χ and the components of $\nabla\epsilon$ mathematically confirm this intuitive result. $\nabla\epsilon$ is a simple, yet definitive measure of relative sensitivities between two non-countercurrent designs. It is also a convenient tool to predict subdesign performance of operating equipment.

Knowledge of ∇F provides understanding of the equipment response from another vantage point. ∇F for a countercurrent heat exchanger is by definition zero. Large values of ∇F correspond to small value of F. Figures 2 and 3 show ∇F plotted against F for two different heat exchanger geometries. We note that $\nabla F \to 0$ as $F \to 1$ for both designs. This is seen to be true for all heat exchanger configurations. ∇F is thus a second measure of deviation from countercurrency. A sharp decrease in F coincides with a sharp increase in ∇F (Fig. 4).

If two exchanger thermal geometries possess identical values of F at the design point, then ∇F provides the basis for judging their relative merits for subdesign conditions. In this sense, ∇F provides a tool for sensitivity studies in the same manner as $\nabla\epsilon$. Figure 5 shows the coefficients of ∇F vector as a function of P. We note that both derivatives are negative and both increase with P (as F decreases, refer to Fig. 4), although $\partial F/\partial R$ has a well defined maximum point. These curves point to the plausible conclusion that the LMTD correction factor in inefficient designs respond more sharply to perturbation in input data. Thus if the heat transfer surface area in a "low F" is reduced, the attendant increase is F will be greater than that in a "high F" unit subject to a similar surface area reduction. On the other hand, the decrease in F due to input data change (such as decreased shellside flow rate) is also liable to be greater in a low F geometry compared to a high F one. The conditions for each heat exchanger are unique to its function. Therefore, the considerations in regard to subdesign performance will dictate as to how to interpret the coefficients of the LMTD gradient vector, or the effectiveness gradient vector. Our objective herein is merely to formulate their definition and illustrate their possible use. Perhaps not all designs require their evaluation; nonetheless their knowledge certainly yields additional insights into the hardware characteristics.

6 Conclusions

Expressions to evaluate the performance of a heat exchanger under subdesign operating conditions have been derived. It has been shown that the partial derivatives $\partial P/\partial\eta$ and $\partial P/\partial R$ are central to the

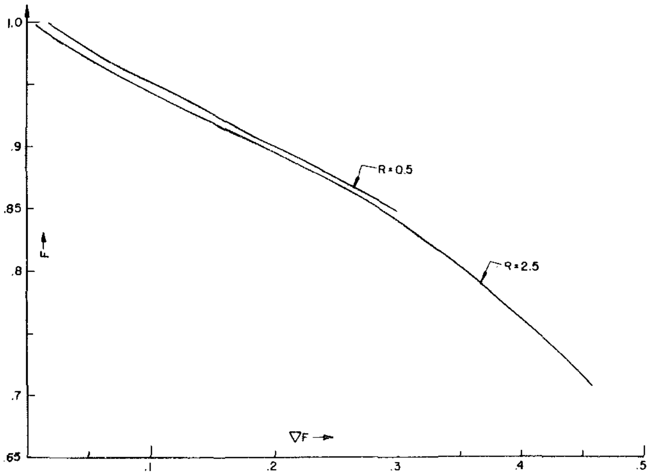

Fig. 2 F versus ∇F for 1 shell pass-2 tube pass heat exchanger

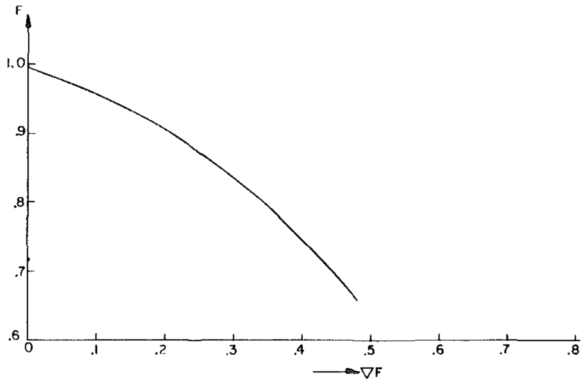

Fig. 3 ∇F versus F; two shell pass-4 tube pass (R = 0.5)

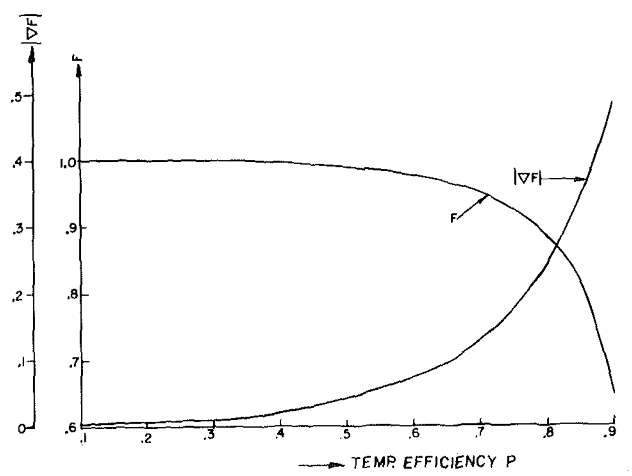

Fig. 4 F and $|\nabla F|$ versus P (two shell pass-4 tube pass $H.X.$)

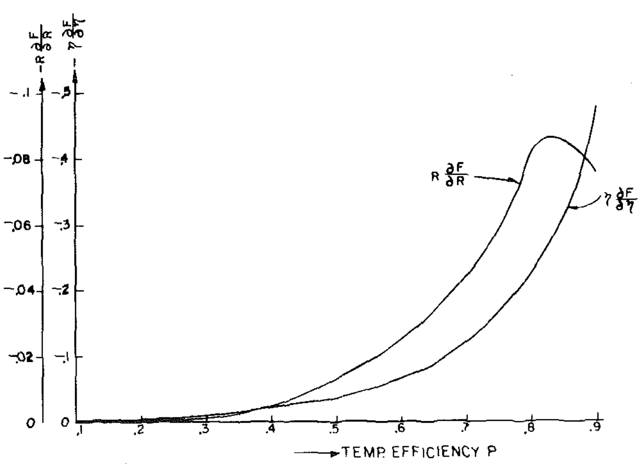

Fig. 5 Derivatives of F versus P (two shell pass-4 tube pass $H.X.$)

characterization of the exchanger response in the vicinity of an operating point. The effectiveness gradient vector or the temperature correction factor gradient vector can be readily evaluated if $\partial P/\partial\eta$ and $\partial P/\partial R$ are known. The components of these vectors (in the $\eta - R$ plane) and their norms yield valuable insight into the exchanger characteristics around the design point. Comparison of these quantities may be useful in selecting the most suitable candidate design for a given set of operating data.

References

1 *Standard For Closed Feedwater Heaters*, Heat Exchange Institute, Third Edition, 1979.

2 *Standard for Tubular Exchanger Manufacturers Association*, Sixth Edition, New York, 1978, p. 5.

3 Kays, W. M., and London, A. L., *Compact Heat Exchangers*, McGraw-Hill, New York, 1964.

4 Kern, D. Q., *Process Heat Transfer*, McGraw-Hill, New York, 1950.

5 Hildebrand, F. B., *Advanced Calculus for Applications*, Prentice Hall, New York, 1962, p. 348.

I. L. Maclaine-cross
Broken Hill Division,
University of New South Wales,
Broken Hill, N.S.W. 2880, Australia

P. J. Banks
Division of Mechanical Engineering,
Commonwealth Scientific and Industrial Research
Organization,
Highett, Victoria 3190, Australia

A General Theory of Wet Surface Heat Exchangers and its Application to Regenerative Evaporative Cooling

Wet surface heat exchangers such as cooling towers and wet plate heat exchangers are important in air conditioning. A linear approximate model of wet surface heat exchangers is proposed. The equations of the model are rearranged, enabling solutions for wet bulb depression and wet bulb temperature to be obtained independently, by analogy from published solutions for dry bulb temperature in dry surface heat exchangers. Performance predictions by this method for a crossflow cooling tower are found to agree with those from a prevous finite difference solution. Published performance measurements for a crossflow wet plate heat exchanger are lower than predicted by the method possibly due to poor wetting or excessive water flow. Excellent performance is predicted for a proposed regenerative evaporative cooler using such an exchanger.

1 Introduction

In wet surface heat exchangers, heat is transferred between a fluid stream and a moist air stream through a water film on the moist air side of the heat transfer surface. In air conditioning, simple evaporative coolers, water cooling towers, finned coils with condensation and sprayed coil or evaporative condensers are commercially important types of wet surface heat exchanger [1]. The fluid stream is either water or a primary or secondary refrigerant in these examples.

Air-to-air plate heat exchangers with the surfaces of one set of passages wet are used as indirect and regenerative evaporative coolers. Regenerative evaporative coolers offer lower energy consumption than vapor compression or closed cycle coolers and better performance and lower water consumption than simple evaporative coolers. These were sold in the south western United States during the 1930's [2]. Later they did not compete with vapor compression or simple evaporative coolers. The large size of the metal plate heat exchangers was an important disadvantage.

Pescod [3] has more recently developed compact crossflow plastic plate heat exchanger designs. His pin fin surfaces have small diameter pins at large spacings to minimize pressure drag. At high laminar flow Reynolds numbers, he measured pressure drops and heat transfer coefficients over three times those for parallel plates [4, 5]. The ratio of measured pressure drop to heat transfer coefficient was similar to that for parallel plates. Pescod [5] has also reported measurements of effectiveness for his plate heat exchangers with the surfaces of one set of passages wet.

Mickley [6] recognized that all wet surface heat exchangers could be represented by a single mathematical model which he solved using a partly graphical method. Mickley assumed that the Lewis relation is satisfied which is approximately true for water-air systems with good wetting, and that the water mass flow rate and the specific heat of moist air are constant. These assumptions allow the differential equations of the model to be expressed and solved in terms of moist air specific enthalpy, which is equivalent for the degree of approximation used to solution in terms of adiabatic saturation or thermodynamic wet bulb temperature.

Baker and Shryock [7] used an electronic digital computer to solve finite difference equations for a cooling tower with water film heat transfer resistance. Like Mickley they assumed that the Lewis relation is satisfied, but, except in their equations (9, 10) for film resistance, did not assume constant water mass flow rate or moist air specific heat. The water film heat transfer resistance for their examples was small so that the implied assumptions in their equations (9, 10) affected their results only slightly. Computer results such as these can be as accurate as the equations solved, but they give no understanding of the processes occurring. If results are required for a different design at another place or time, another computer program must usually be written, which can be laborious.

The theory of wet surface heat exchangers presented here is intended to improve understanding and simplify calculations. A linear approximation to the saturation line, together with assumptions like those of Mickley [6] mentioned above, are used to give linear partial differential equations (Section 2). These equations are rearranged, enabling solutions for wet bulb depression and wet bulb temperature to be obtained independently, by analogy from published solutions [8] for dry bulb temperature in dry surface heat exchangers (Section 3). This approximate theory is found to agree with Baker and Shryock's [7] finite difference solutions for a crossflow cooling tower (Section 4).

Predictions of the efficiencies of Pescod's plate heat exchangers with wet passages, using dry surface results [4, 5] and the theory presented here, are found to be significantly greater than reported measurements [5] (Section 5). Poor wetting of Pescod's plastic plates is suspected. The wettability of parallel plates of woven cloth has been found excellent in evaporative coolers [9, 10]. The performance of a proposed regenerative evaporative cooler (Section 6) using a plate heat exchanger with a Pescod surface for the dry passages and woven cloth parallel plates for the wet passages is predicted (Section 7). Detailed calculations are given in Section 8 to illustrate the use of Sections 2 and 3. The predicted performance compares favorably with that of vapor compression and simple evaporative coolers.

All the authors' calculations in Sections 3, 4, 5, 7 and 8 were made using a Hewlett-Packard 97A programmable electronic calculator. The program for calculating crossflow heat exchanger temperature efficiency used Baclic's equation [11] with all Bessel functions evaluated simultaneously by a recurrence relation [12]. For capacity rate ratios less than unity, temperature efficiency equals the effectiveness defined in [8].

The theory of wet surface heat exchangers presented here was suggested to the authors by the analogy theory of coupled heat and mass transfer in porous media, which they have applied to regenerative heat and water vapour exchangers [13, 14, 15]. In this analogy theory, the coupled heat and mass transfer is described by two combined potentials acting independently, which correspond to wet bulb temperature and web bulb depression in a wet surface heat exchanger. The possible accuracy of the theory presented here was indicated by the close agreement found between performance predictions from the analogy theory in linearized form and from finite difference solutions for practical energy recovery regenerators used in air conditioning [14, 15].

2 A Model of the Wet Surface Heat Exchanger

Partial differential equations including terms for all significant

---

Contributed by the Heat Transfer Division for publication in the JOURNAL OF HEAT TRANSFER. Manuscript received by the Heat Transfer Division October 7, 1980.

effects in a wet surface heat exchanger may be solved using an electronic digital computer. Solution using a hand calculator and literature tables or charts requires simplified equations. Therefore the actual wet surface heat exchanger will be replaced by a mathematical model satisfying conditions which give a set of linear algebraic and partial differential equations to be solved simultaneously. The model structure is shown schematically in Fig. 1.

The model satisfies the following conditions, which correspond to those used for heat transfer alone in heat exchangers:

1 zero wall, air and fluid thermal and moisture diffusivity in the flow directions;
2 no heat transfer to the surroundings occurs;
3 the passage walls are impervious to mass transfer;
4 pressures and mass flow rates are constant and uniform for both streams;
5 c_f, c_a, h_c, h_D, h_g, h_{fg} and U are constant and uniform;
6 the passage geometry is uniform throughout the heat exchanger.

The model also satisfies the following condition, used previously for wet surface heat exchangers [6, 7]:

7 the Lewis relation is satisfied, that is

$$h_D = h_{ca}/c_a \tag{1}$$

Mickley's assumptions [6] (Section 1) are replaced by the following conditions:

8 the specific enthalpy of moist air h_a is a linear function of t_a and w_a, thus

$$h_a = h_{ao} + c_a t_a + h_g w_a \tag{2}$$

where h_{ao} is a constant;

9 the evaporating water film is stationary and continuously replenished at its surface with water at the same temperature;
10 the moisture content w_w of the air in equilibrium with the water surface is a linear function of the water surface temperature t_w, so that the model saturation line is given by

$$w_w = d + e\,t_w \tag{3}$$

The linear equations (4–8) below may be derived from conditions 1 to 10. The approximate psychrometer equation is

$$w_a = w_a{}' + (t_a{}' - t_a)c_a/h_{fg} \tag{4}$$

where ′ indicates the adiabatic saturation state defined using the linearized or model saturation line of condition 10, equation (3).

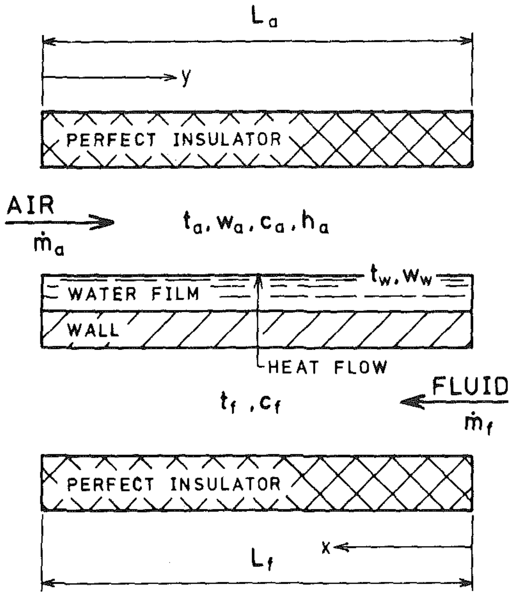

Fig. 1 Structure of mathematical model of the wet surface heat exchanger

For conservation of energy in the fluid stream

$$c_f \dot{m}_f L_f \frac{\partial t_f}{\partial x} = UA\,(t_w - t_f) \tag{5}$$

For conservation of energy and water at the air–water interface

$$h_{ca}A_a(t_a - t_w) + h_D A_a h_{fg}\,(w_a - w_w) + UA\,(t_f - t_w) = 0 \tag{6}$$

For conservation of water vapor in the moist air stream

$$\dot{m}_a L_a \frac{\partial w_a}{\partial y} = h_D A_a\,(w_w - w_a) \tag{7}$$

For conservation of energy in the moist air stream

$$\dot{m}_a L_a \frac{\partial h_a}{\partial y} = h_{ca}A_a\,(t_w - t_a) + h_D h_g A_a\,(w_w - w_a) \tag{8}$$

The boundary conditions satisfied by the model and to be used in solving equations (1–8) are that the inlet fluid temperature and the inlet air temperature and moisture content are known and constant.

Nomenclature

a_p, a_w = thickness of plate or of water film (m)
A, A_a = surface area associated with U or with h_c and h_D (m^2)
A_c = minimum free flow area of passage (m^2)
b_a, b_f = plate spacing for air or for fluid passage (m)
c = specific heat capacity (J/kg K)
$c_{wb} = (c_a + eh_{fg})$, wet bulb specific heat capacity (J/kg dry air K)
d, e = constants in equation (3) (kg/kg dry air, kg/kg dry air K)
ET^* = effective temperature [16] (°C)
f_s = 1.005, correction factor for presence of air (dimensionless)
h_a = specific enthalpy of moist air (J/kg dry air)
h_{ao} = constant in equation (2) (J/kg dry air)
h_c = heat transfer coefficient (W/m^{2}K)
h_D = water vapor transfer coefficient of moist air stream (kg dry air/m^{2}s)
h_{fg} = latent heat of vaporization of water (J/kg)
h_g = specific enthalpy of water vapour (J/kg)
$h_{wb} = (1 + eh_{fg}/c_a)h_{ca}$, wet bulb heat transfer coefficient (W/m^{2}K)
k_p, k_w = thermal conductivity of plate or of water film (W/m K)
L = passage length in flow direction (m)
$\dot{m}_a$, $\dot{m}_f$ = mass flow rate of moist air (kg dry air/s) or of fluid (kg/s)
Nu = Nusselt number (dimensionless)
Pr = Prandtl number (dimensionless)
Re = $2\,\dot{m}\,(1 + w)b/(A_c\mu)$, parallel plate Reynolds number (dimensionless)
St = $h_cA_c/(c\,\dot{m})$, Stanton number (dimensionless)
t = temperature (°C)
U = overall heat transfer coefficient between water surface and fluid (W/m^{2}K)
w = humidity ratio (kg/kg dry air)
W = overall width of plate heat exchanger (m)
x,y = distance from fluid inlet, or from moist air inlet, in flow direction (m)
η_f, η_ℓ, η_u = temperature efficiency, $\eta_z = (t_{z\,\text{out}} - t_{f\,\text{in}})/(t_a{}'_{\text{in}} - t_{f\,\text{in}})$, where $z = f, \ell$ or u (dimensionless)
$\eta_{wc} = (t_{f\,\text{out}} - t_{f\,\text{in}})/(t_a{}^*{}_{\text{in}} - t_{f\,\text{in}})$, water cooling efficiency (dimensionless)
μ = dynamic viscosity (Pa s)

Superscripts

$*$ = at adiabatic saturation relative to true or actual saturation line
′ = at adiabatic saturation relative to linearized or model saturation line

Subscripts

a = moist air stream
f = fluid stream
in = inlet
ℓ = lower fluid stream
max = maximum value
mean = mean value
min = minimum value
out = outlet
u = upper fluid stream
w = at water surface

For a parallel flow exchanger $y = xL_a/L_f$, for a counterflow exchanger $y = (1 - x/L_f)L_a$ and for a crossflow exchanger x and y are not related.

Conditions 1, 2 and 3 are approximately satisfied by many actual wet surface heat exchangers. The model will approximate actual performance if appropriately chosen mean values are used for the constants in conditions 4, 5, 6 and 8. Condition 7 will be approximately satisfied if the surface is wet by a continuous film of water.

Condition 9 is closely approximated in evaporative coolers and finned coils with condensation. It is also closely approximated in sprayed coils and wet plate heat exchangers if the wetting water mass flow rate is negligible compared with the air mass flow rate. For cooling towers with high inlet water temperature and low inlet air wet bulb temperature, a significant fraction of the water mass flow may be evaporated. In this case, it is assumed here that the model water mass flow rate is constant and equal to the average of the actual inlet and outlet water flow rates.

Condition 10 is not satisfied in an actual exchanger. The model represents actual performance if constants d and e in equation (3) are chosen to give an approximate least squares fit to the true or actual saturation line over the range of water surface temperatures. The recommended values are

$$e = (w_{w\,\max} - w_{w\,\min})/(t_{w\,\max} - t_{w\,\min}) \tag{9}$$

$$d = (2(w_{w\,\min} + w_{w\,\mathrm{mean}}) - w_{w\,\max})/3 - e\,t_{w\,\min} \tag{10}$$

where $t_{w\,\min}$ is an estimate of the minimum water surface temperature, $t_{w\,\max}$ of the maximum, and $t_{w\,\mathrm{mean}} = (t_{w\,\min} + t_{w\,\max})/2$. Also, $w_{w\,\min}$, $w_{w\,\max}$ and $w_{w\,\mathrm{mean}}$ are the actual saturation moisture contents at the corresponding temperatures. Equations (9) and (10) would be an exact least squares fit if the saturation line were a parabola.

This model saturation line may be constructed graphically on a psychrometric chart as shown in Fig. 2. First, the estimated values of $t_{w\,\min}$, $t_{w\,\max}$ and $t_{w\,\mathrm{mean}}$ are used to plot the points w min, w max and w mean on the actual saturation line. The straight line joining w min and w max is drawn, then, parallel to this line and two thirds of the way from it towards point w mean, another line is drawn. This is the model saturation line.

3 Solution of the Model Equations

In Section 3.1, the equations of Section 2 are rearranged to form an ordinary differential equation for web bulb depression, and in Section 3.2 an independent set of partial differential equations for wet bulb temperature. The equations are seen to be similar to those for dry bulb temperature in dry surface exchangers, which have been solved elsewhere [8].

3.1 The Model Wet Bulb Depression, $t_a - t_a'$. Substituting equation (2) in (8) and subtracting h_g times (7) gives

$$c_a\dot{m}_aL_a\frac{\partial t_a}{\partial y} = h_{ca}A_a\,(t_w - t_a) \tag{11}$$

Now the wet bulb depression

$$\begin{aligned} t_a - t_a' &= (w_a' - w_a)\,h_{fg}/c_a \quad \text{(rearranging equation (4))}\\ &= (d + e\,t_a' - w_a)\,h_{fg}/c_a \quad \text{(by equation (3) since } t_a', w_a' \text{ on the saturation line)}\\ &= -\,(t_a - t_a')\,h_{fg}e/c_a + (d + e\,t_a - w_a)\,h_{fg}/c_a \quad \text{(rearranging)} \end{aligned}$$

so

$$t_a - t_a' = (d + e\,t_a - w_a)h_{fg}/(c_a + e\,h_{fg}) \tag{12}$$

Multiplying equation (11) by $e\,h_{fg}/(c_a + e\,h_{fg})$ and subtracting equation (7) multiplied by $c_a\,h_{fg}/(c_a + e\,h_{fg})$ gives

$$c_a\dot{m}_aL_a\frac{\partial}{\partial y}\left(\frac{(e\,t_a - w_a)\,h_{fg}}{c_a + e\,h_{fg}}\right) = \frac{A_ah_{fg}(h_{ca}e\,(t_w - t_a) - c_ah_D(w_w - w_a))}{c_a + e\,h_{fg}}$$

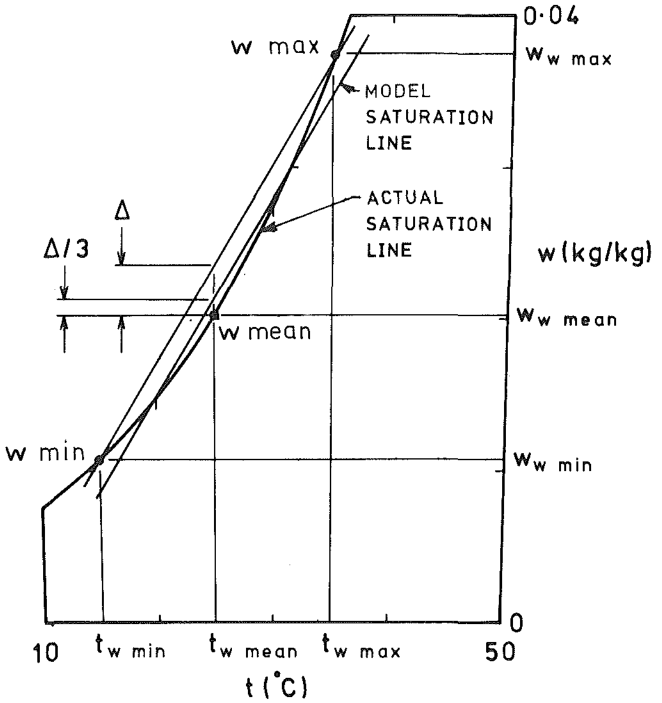

Fig. 2 Graphical construction of the model saturation line

Since d is constant, substituting equations (1) and (3) gives

$$c_a\dot{m}_aL_a\frac{\partial}{\partial y}\left(\frac{(d + e\,t_a - w_a)\,h_{fg}}{c_a + e\,h_{fg}}\right) = -h_{ca}A_a\frac{(d + e\,t_a - w_a)\,h_{fg}}{c_a + e\,h_{fg}}$$

Substituting from equation (12) gives

$$c_a\dot{m}_aL_a\frac{\partial(t_a - t_a')}{\partial y} = -h_{ca}A_a\,(t_a - t_a') \tag{13}$$

The solution of this ordinary differential equation is

$$t_a - t_a' = (t_{a\,\mathrm{in}} - t'_{a\,\mathrm{in}})\exp\,(-\,h_{ca}A_ay/(c_a\dot{m}_aL_a))$$

which predicts that the wet bulb depression decays exponentially with distance y from the air inlet. At the outlet,

$$y = L_a \text{ and } t_a - t_a' = t_{a\,\mathrm{out}} - t'_{a\,\mathrm{out}}$$

so the solution becomes

$$t_{a\,\mathrm{out}} - t'_{a\,\mathrm{out}} = (t_{a\,\mathrm{in}} - t'_{a\,\mathrm{in}})\exp\,(-h_{ca}A_a/(c_a\dot{m}_a)) \tag{14}$$

where $h_{ca}A_a/(c_a\dot{m}_a)$ is the number of heat transfer units for the moist air stream and may be calculated using heat transfer literature [8]. The solution is analogous to that for the difference between dry bulb temperature and wall temperature in a dry surface exchanger with constant wall temperature.

3.2 The Model Wet Bulb Temperature t_a'. Rearranging equation (12) gives

$$(1 + e\,h_{fg}/c_a)\,t_a' = t_a + (w_a - d)\,h_{fg}/c_a \tag{15}$$

Substituting equations (1, 3, 15) in (6) and defining a wet bulb heat transfer coefficient by $h_{wb} = (1 + e\,h_{fg}/c_a)h_{ca}$ gives

$$h_{wb}A_a(t_a' - t_w) + UA\,(t_f - t_w) = 0 \tag{16}$$

Substituting equation (11) in (13), multiplying by $(1 + h_{fg}/c_a)$ and defining a wet bulb specific heat by $c_{wb} = c_a + e\,h_{fg}$ gives

$$c_{wb}\dot{m}_aL_a\frac{\partial t_a'}{\partial y} = h_{wb}A_a(t_w - t_a') \tag{17}$$

Equations (5, 16, 17) have been solved in the literature [8] for parallel flow, counterflow and crossflow heat transfer alone exchangers. The literature solutions allow the outlet wet bulb temperature $t'_{a\,\mathrm{out}}$ to be calculated by replacing dry bulb temperature t_a in the dimensionless parameters of the solutions by wet bulb temperature t_a', moist air heat transfer coefficient h_{ca} by wet bulb heat transfer coefficient h_{wb} and moist air specific heat c_a by wet bulb specific heat c_{wb}.

The values of c_{wb} and $(1 + e\, h_{fg}/c_a)$ for calculating h_{wb} may be estimated using Table 1 at $t_{w\ \mathrm{mean}}$, or using equation (9) for e with c_a and h_{fg} evaluated at state w mean. Table 1 was calculated using simplified psychrometric equations from [14] with the correction factor $f_s = 1.005$ and the latent heat of water

$$h_{fg} = 2\,501\,000 - 2\,412\, t_w \text{ J/kg}$$

where $0°\mathrm{C} < t_w < 90°\mathrm{C}$.

4 Comparison of Model with Finite Difference Solution

Table 2 compares some crossflow cooling tower finite difference solutions of Baker and Shryock [7] with the model (Section 2) and its solution (Section 3). The model shown in Fig. 1 represents a cooling tower when the flowing fluid is water and the wall is removed.

The first four columns of Table 2 are the first four columns of Baker and Shryock's Table 2, and the fifth column is Baker and Shryock's third last column which is for finite water film heat transfer resistance and water mass flow decreasing with evaporation. The mean mass flow ratio $\dot{m}_{f\ \mathrm{mean}}/\dot{m}_a$ in column 6 and the water cooling efficiency η_{wc} in column 8 were calculated using the model. The water cooling efficiency η_{wc} in column 7 was calculated from the first three columns using the definition

$$\eta_{wc} = (t_{f\ \mathrm{out}} - t_{f\ \mathrm{in}})/(t_a{}^*{}_{\mathrm{in}} - t_{f\ \mathrm{in}}).$$

The percentage difference in water cooling efficiencies predicted using the two methods is shown in the last column. The difference increases with the water temperature range but is less than 1.5 percent in all cases.

Minor differences between the predictions of the model presented in Section 2 and Baker and Shryock's [7] model are caused by conditions 4, 5, 8, and 9. Also, Baker and Shryock [7] did not report their vapor pressure and thermodynamic data which may have differed from those used here (Section 3.2). Furthermore, for the calculations in their Table 2, they gave only the wet bulb temperature of the inlet air. However, for the calculations in their Tables 1(*b*) and 1(*c*), saturated inlet air was used; therefore the inlet air was assumed to be saturated for the calculations in their Table 2.

Table 1 Wet bulb specific heat c_{wb} and its ratio to moist air specific heat, $c_{wb}/c_a = h_{wb}/h_{ca} = 1 + e\, h_{fg}/c_a$

t °C	$1 + e\, h_{fg}/c_a$	c_{wb} J/g K	t °C	$1 + e\, h_{fg}/c_a$	c_{wb} J/g K
0	1.686	1.707	30	4.758	5.034
2	1.779	1.803	32	5.159	5.491
4	1.882	1.910	34	5.597	5.999
6	1.996	2.029	36	6.077	6.562
8	2.123	2.162	38	6.601	7.188
10	2.264	2.310	40	7.175	7.885
12	2.420	2.474	42	7.802	8.662
14	2.592	2.656	44	8.489	9.531
16	2.782	2.859	46	9.241	10.50
18	2.992	3.083	48	10.06	11.60
20	3.222	3.331	50	10.97	12.83
22	3.475	3.606	52	11.96	14.23
24	3.753	3.911	54	13.06	15.81
26	4.058	4.248	56	14.26	17.62
28	4.392	4.621	58	15.59	19.70

The major difference between the two models is the linear saturation line of condition 10. As defined by equations (3, 9, 10), condition 10 is accurate for actual exchangers with only a small water surface temperature range because a straight line can accurately approximate a smooth curve only over a small distance. The comparison with Baker and Shryock's finite difference solutions suggests that the model and condition 10 are satisfactory for appreciable water surface temperature ranges.

5 Prediction of Wet Plate Heat Exchanger Performance from that Measured When Dry

Measurements on plastic plate heat exchangers with two cross flow air streams, one with dry passages and the other wet by water sprays, have been reported by Pescod [5]. The passages were otherwise identical and the dry air mass flow rates of the two streams were equal, $\dot{m}_a = \dot{m}_f$. Pescod gave equations for the wet bulb temperature efficiency of the dry stream η_f, which he called wet effectiveness, as a function of passage velocity for three pin fin surfaces and one corrugated surface ([5], Table 3). The full lines on Fig. 3 are these efficiencies plotted against passage Reynolds number.

Predictions of the wet bulb temperature efficiency η_f were made using the model in Section 2 and its solution in Section 3. The heat transfer coefficients used were those calculated by Pescod [5] from measurements made with all heat exchanger surfaces dry. For evaluating properties, a mean air temperature of 27°C and a mean water surface temperature of 22°C were assumed. The thickness of the polyvinyl chloride plates was 0.2 mm [4] and the water film thickness was assumed as 0.2 mm. The long dashed lines on Fig. 3 are the predictions, which are all over 10 percent higher than the measurements with some over 20 percent higher.

The difference between the measurements and predictions considerably exceeds the claimed experimental error. One or more of the model conditions must not apply to the measurements. Pescod [5] does not report the spray water mass flow rates. If they are excessive, the water film would have a significant velocity and condition 9 would not apply. If the water film does not cover the wet plates completely, the effective value of h_D may be significantly less than that of h_{ca}/c_a and condition 7 will not apply.

The effect of excessive spray water mass flow rate may be examined by replacing condition 9 by the extreme case of constant water surface temperature throughout the exchanger. The short dashed line in Fig. 3 shows this prediction for the first pin fin surface. At low Reynolds numbers the measurements are higher than these predictions but at high Reynolds numbers they are lower. Assuming that constant water mass flow rate was maintained while varying the air flow rates, the water flow rates would be most excessive and measurements lowest

Table 2 Comparison of finite difference solution and model for a cooling tower with finite water film resistance

Data from Baker and Shryock ([7], Table 2)					Calculated values			
Temperature °F								
$t_{f\ \mathrm{in}}$	$t_{f\ \mathrm{out}}$	$t_a{}^*{}_{\mathrm{in}}$	$\dot{m}_{f\ \mathrm{in}}/\dot{m}_a$	$h_DA_a/\dot{m}_{f\ \mathrm{in}}$	$\dot{m}_{f\ \mathrm{mean}}/\dot{m}_a$	η_{wc} [7]	η_{wc} model	percent diff.
69.2	62.3	47.7	1.088	1.049	1.086	0.3209	0.3225	0.48
85.1	71.7	47.7	1.09	1.032	1.085	0.3583	0.3570	−0.35
99.6	78.5	46.6	1.09	1.061	1.082	0.3981	0.3951	−0.76
119.1	86.8	46.8	1.12	1.049	1.108	0.4467	0.4404	−1.43
78.9	71.4	47.5	1.96	0.763	1.955	0.2389	0.2405	0.71
90.1	79.1	48.9	1.99	0.766	1.983	0.2670	0.2664	−0.21
102.0	86.8	51.2	2.04	0.761	2.029	0.2992	0.2966	−0.87
108.5	89.8	46.1	2.04	0.742	2.027	0.2997	0.2972	−0.84
88.0	71.6	44.3	0.954	1.073	0.9492	0.3753	0.3743	−0.26
99.1	77.3	47.4	0.928	1.099	0.9214	0.4217	0.4190	−0.64
111.6	84.6	54.6	0.964	1.071	0.9550	0.4737	0.4668	−1.45

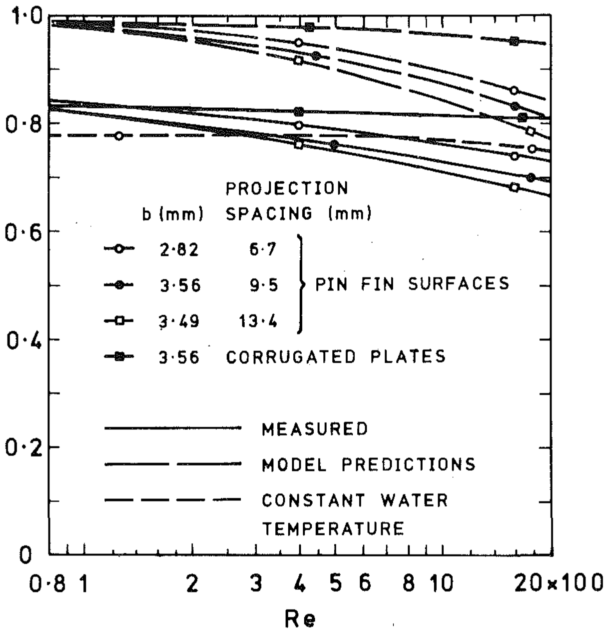

Fig. 3 Comparison of measured and predicted wet bulb temperature efficiencies η_f for plate heat exchangers as functions of passage Reynolds number, Re

relative to the predictions at low Reynolds numbers. Hence, excessive water flow rates, and thus condition 9, are not the sole cause of efficiency measurements lower than predicted by the model of Section 2. Poor wetting and thus condition 7 must be a significant cause of low measured η_f efficiencies.

6 A Proposal for an Improved Regenerative Evaporative Cooler

The precursors of the regenerative evaporative cooler analyzed in Section 7 were a cycle attributed by Watt ([2], p. 210, Fig. 29*A*] to Carl Boester and a related regenerative evaporative cooler due to Pescod ([5], Fig. 10). Boester's cycle consisted of a dry finned coil precooling air to a water cooling tower. The water flow in the coil was taken from the tower sump and returned to the tower water inlet. Chilled tower water flow not required for the coil was used for air conditioning. A simple modification of Boester's cycle is to increase the size of the finned coil so it uses all the water circulating in the cooling tower and to use the excess cooled air directly for air conditioning. Pescod's regenerative evaporative cooler uses this cycle but the finned coil and water cooling tower are replaced by a single wet plate heat exchanger.

For the three related cycles mentioned in the last paragraph, if appropriate mass flows are chosen and the number of transfer units increased, the cooled air or water supplied to the load approaches the dew point temperature of the ambient air even if the temperature rise across the load is constant and finite. The cycle analyzed was chosen because it satisfies this condition. The minimum temperature does not approach the dew point with a constant and finite load for the other indirect evaporative cooling cycles described by Watt [2]. The minimum temperature for simple evaporative coolers is the often much higher wet bulb temperature. The analyzed cycle however retains the advantage of supplying all fresh air to the room like a simple evaporative cooler.

Figure 4 shows schematically the cooler to be analyzed. There are three principal modifications to Pescod's cooler ([5], Fig. 10). The first is that a simple woodwool evaporative cooler pad has been placed in the room inlet stream to improve performance and balance the pressure drops of the two streams. The wet results for Pescod's pin fin surfaces discussed in Section 5 are inconsistent with theory and their pressure drop is excessive for the wet passages in Fig. 4. Therefore, the second modification is that the parallel plate passages tested in evaporative coolers [9, 10] will be used here as shown in the Fig. 4 passage detail. To insure wettability, the walls of these passages are unsized woven nylon, rayon or fiberglass cloth fastened horizontally by adhesive at approximately 30 mm vertical intervals to leave a capillary space with a strong horizontal wicking action between the cloth and plate. The third modification, intended to minimize the overall volume of the cooler, is the irregular pentagonal shape for the plates, shown in Fig. 4, instead of the rectangular shape used by Pescod. The shape would be designed and optimized using a computer.

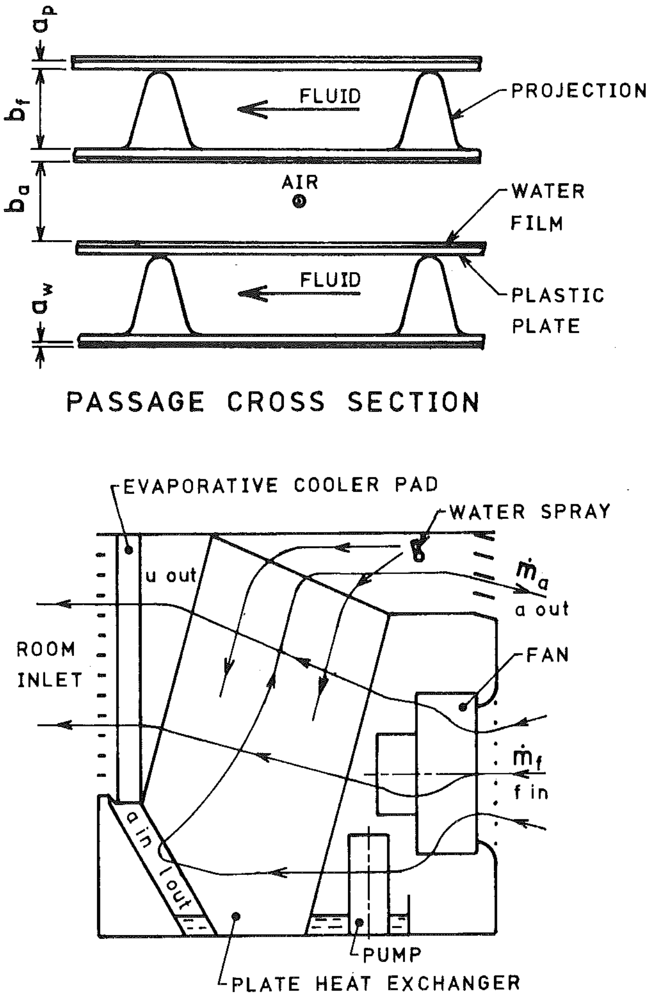

Fig. 4 Proposed regenerative evaporative cooler using wet plate heat exchanger

7 Predicted Performance of the Proposed Regenerative Evaporative Cooler

The rectangular model of the proposed cooler shown in Fig. 5 is used below. The moist air flowing horizontally on the dry side of the plates is referred to as the fluid stream with subscript f, and that flowing vertically on the wet side of the plates as the air stream with subscript a. The upper part of the fluid stream which enters the evaporative cooler pad and eventually the room is denoted by the subscript u and the lower part which becomes the air stream by ℓ.

The data used for the calculations detailed in Section 8 are tabulated below, except for the external dimensions of the plate heat exchanger model which are shown in Fig. 5:

width of fluid passages	$b_f = 2$ mm
overall plate thickness	$a_p = 0.2$ mm
water film thickness	$a_w = 0.1$ mm
width of air passages	$b_a = 2$ mm
fluid stream mass flow rate	$\dot{m}_f = 0.500$ kg dry air/s
air stream mass flow rate	$\dot{m}_a = 0.167$ kg dry air/s

absolute pressure	$p_t = 101.325$ kPa
inlet fluid dry bulb temperature	$t_{f\ \text{in}} = 35°\text{C}$
inlet fluid wet bulb temperature	$t_f{}^*{}_{\text{in}} = 24°\text{C}$

The results of the calculations in Section 8 and others not given in detail are summarized here. The room air state was chosen to be an effective temperature $ET^* = 27°\text{C}$. The $ET^* = 27°\text{C}$ line is shown on Fig. 6 and passes through 25°C at 100 percent relative humidity and 27°C at 50 percent relative humidity [16]. The pressure drop in the fluid passages was 93 Pa, air passages 60 Pa and evaporative cooler pad 50 Pa. The fan efficiency was assumed as 0.50 and the fan motor efficiency 0.70 to estimate the fan power consumption at 189 W. The pump power consumption was assumed to be 60 W giving a total electric power consumption of 249 W. Inlet fluid state A, 35°C DB, 24°C WB, gave a room air inlet temperature of 21.2°C DB, and room state of 26.2°C DB, 71 percent RH, equivalent to a cooling capacity of 1.73 kW. Inlet fluid state B, 46°C DB, 24°C WB gave a room air inlet temperature of 18.1°C DB, 17.0°C WB and room state of 26.9°C DB, 53 percent RH, equivalent to a cooling capacity of 3.03 kW.

Simple evaporative coolers with humidifying efficiencies typically 0.80 are not capable of producing the design room condition $ET^* = 27°\text{C}$. The volume of a commercial vapour compression unit with coefficient of performance approximately 2 would be smaller than the regenerative evaporative cooler for state A but larger for state B. The electric power consumption of the proposed regenerative evaporative cooler is less than 30 percent of vapor compression power consumption even for inlet state A. For state B, its manufacturing cost could be considerably less than that of a vapor compression unit if manufactured in comparable numbers.

8 Sample Calculation Details for the Performance Prediction

Details of the calculation of the mean outlet temperature of the upper fluid stream $t_{u\ \text{out}}$ for inlet state A are given in subsections 8.1, 8.2, 8.3 and 8.4 below to illustrate the use of Sections 2 and 3. The calculated outlet temperature $t_{u\ \text{out}} = 23.1°\text{C}$ is below the inlet wet bulb temperature $t_f{}^*{}_{in} = 24°\text{C}$. On passing through the evaporative cooler pad with humidifying efficiency 0.80, the temperature is further reduced to 21.2°C, Fig. 6, which is close to the inlet fluid dew point of 19.7°C.

8.1 Evaluation of Thermodynamic and Transport Properties. Initially the minimum water surface temperature will be assumed $t_{w\ \text{min}} = 21°\text{C}$ and the maximum water surface temperature $t_{w\ \text{max}} = 31°\text{C}$. The mean water surface temperature

$$t_{w\ \text{mean}} = (t_{w\ \text{min}} + t_{w\ \text{max}})/2 = (21 + 31)/2 = 26°\text{C},$$

and this temperature will be used for evaluating all fluid and air stream properties.

From a psychrometric chart [17], $w_{w\ \text{mean}} = 21.3$ g/kg and the inlet fluid humidity ratio $w_{f\ \text{in}} = 14.2$ g/kg. From Table 1, $c_{wb} = 4\,248$ J/kg K and $(1 + e\,h_{fg}/c_a) = 4.058$. From equations (65, 66, 67) in [14], $c_f = 1\,033$ J/kg K. From dry air property tables [18], Pr = 0.707 and $\mu_a = \mu_f = 18.46\ \mu\text{Pa s}$. From water property tables [18], $k_w = 0.606$ W/m K, and from plastics properties tables [19], $k_p = 0.178$ W/m K.

8.2 Calculation of Stanton Numbers and Heat Transfer Coefficients. Neglecting pin surface and cross-sectional areas, following Pescod [4, 5],

$$A_{cf} = L_a W\, b_f/(b_f + 2\,(a_p + a_w) + b_a)$$

$$= 0.6 \times 0.6 \times 2/(2 + 2(0.2 + 0.1) + 2) = 0.1565\ \text{m}^2$$

$$\text{Re}_f = 2\dot{m}_f\,(1 + w_{f\ \text{in}})\, b_f/(A_{cf}\,\mu_f)$$

$$= 2 \times 0.500\,(1 + 0.0142)2 \times 10^{-3}/(0.1565 \times 18.46 \times 10^{-6}) = 702.1$$

From ([5], Fig. 3) $\text{St}_f\,\text{Pr}^{2/3} = 0.027$ so $\text{St}_f = 0.027 \times 0.707^{-2/3} = 0.034\,02$ and $h_{cf} = \text{St}_f c_f \dot{m}_f/A_{cf} = 0.034\,02 \times 1\,033 \times 0.500/0.1565 = 112.3\ \text{W/m}^2\,\text{K}$

Similarly

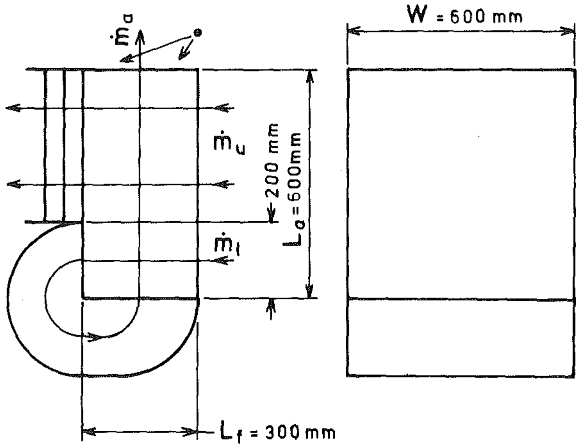

Fig. 5 Model of proposed regenerative evaporative cooler using rectangular wet plate heat exchanger

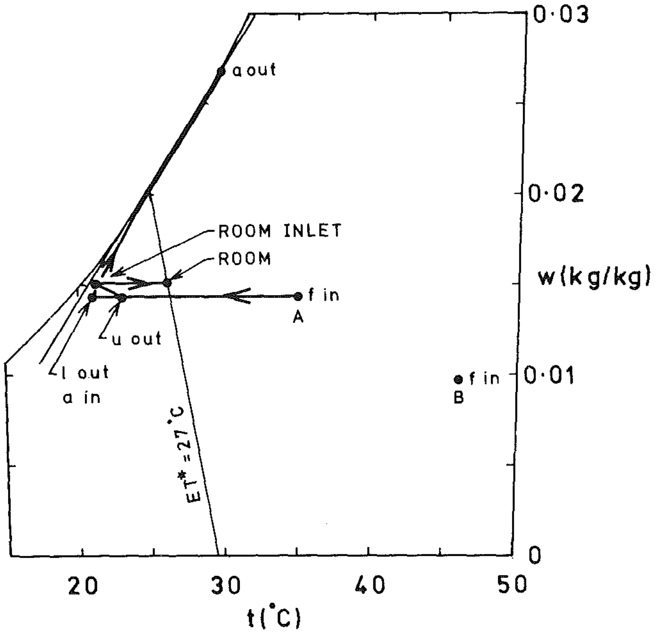

Fig. 6 Cycle of proposed regenerative evaporative cooler on psychrometric chart

$$A_{ca} = L_f W\, b_a/(b_f + 2(a_p + a_w) + b_a)$$

$$= 0.3 \times 0.6 \times 2/(2 + 2(0.2 + 0.1) + 2) = 0.078\,26\ \text{m}^2$$

$$\text{Re}_a = 2\dot{m}_a\,(1 + w_{w\ \text{mean}})\, b_a/(A_{ca}\mu_f)$$

$$= 2 \times 0.167\,(1 + 0.0213)2 \times 10^{-3}/(0.078\,26 \times 18.46 \times 10^{-6})$$
$$= 472.2$$

From ([8], p. 103) $\text{Nu}_a = 8.235$

$$\text{so St}_a = \text{Nu}_a/(Pr\,Re_a) = 8.235/(0.707 \times 472.2)$$

$$= 0.024\,67$$

$$\text{and } h_{wb} = (1 + e\,h_{fg}/c_a)\,h_{ca}$$
$$= (1 + e\,h_{fg}/c_a)\,\text{St}_a c_a \dot{m}_a/A_{ca}$$

$$= \text{St}_a c_{wb} \dot{m}_a/A_{ca}$$

$$= 0.024\,67 \times 4\,248 \times 0.167/0.078\,26$$
$$= 223.6\ \text{W/m}^2\text{K}.$$

8.3 Calculation of Dimensionless Parameters and Temperature Efficiencies. The overall number of heat transfer units for using literature crossflow heat exchanger solutions as described in Section 3.2 is

$$\frac{A}{c_f\dot{m}_f\,(1/U + 1/h_{wb})} = \frac{h_{cf}A}{c_f\dot{m}_f\,(1 + h_{cf}(a_p/k_p + a_w/k_w + 1/h_{wb}))}$$

$$\left(\frac{1}{U} = \frac{1}{h_{cf}} + \frac{a_p}{k_p} + \frac{a_w}{k_w}\right)$$

$$= \frac{2\,\mathrm{St}_f L_f}{b_f\,(1 + h_{cf}\,(a_p/k_p + a_w/k_w + 1/h_{wb}))}$$

$$\left(\mathrm{St}_f = \frac{h_{cf} A_{cf}}{c_f \dot{m}_f} \text{ and } \frac{A}{A_{cf}} = \frac{2L_f}{b_f}\right)$$

$$= \frac{2 \times 0.034\,02 \times 0.3}{2 \times 10^{-3}\,(1 + 112.3\,(0.2 \times 10^{-3}/0.178 + 0.1 \times 10^{-3}/0.606 + 1/223.6))}$$

$$= 6.197$$

The capacity rate ratio for the lower half of the exchanger is $c_f \dot{m}_\ell/(c_{wb} \dot{m}_a) = 1\,033 \times 0.167/(4\,248 \times 0.167) = 0.2432$.

The lower half temperature efficiency

$$\eta_\ell = (t_{\ell\ \mathrm{out}} - t_{f\ \mathrm{in}})/(t_a{}'_{\mathrm{in}} - t_{f\ \mathrm{in}})$$

may be calculated from the above two dimensionless parameters as described towards the end of Section 1 as $\eta_\ell = 0.9768$.

The capacity rate ratio for the whole exchanger is $c_f \dot{m}_f/(c_{wb} \dot{m}_a) = 1\,033 \times 0.500/(4\,248 \times 0.167) = 0.7281$.

The fluid stream temperature efficiency η_f may be calculated similarly to η_ℓ as $\eta_f = 0.8637$.

By conservation of dry air $\dot{m}_\ell = \dot{m}_a$ and $\dot{m}_f = \dot{m}_u + \dot{m}_\ell$, and by conservation of energy $\dot{m}_f \eta_f = \dot{m}_u \eta_u + \dot{m}_\ell \eta_\ell$, so solving simultaneously

$$\eta_u = (\dot{m}_f \eta_f - \dot{m}_a \eta_\ell)/(\dot{m}_f - \dot{m}_a)$$

$$= (0.500 \times 0.8637 - 0.167 \times 0.9768)/(0.500 - 0.167) = 0.8070$$

8.4 Calculation of Upper Stream Outlet Temperature $t_{u\ \mathrm{out}}$. From the approximate saturation line in Fig. 6, $t_f{}'_{\mathrm{in}} = 23.8$°C.

Subtracting equation (12) for the air inlet from equation (12) for the fluid inlet and $w_{a\ \mathrm{in}} = w_{\ell\ \mathrm{out}} = w_{f\ \mathrm{in}}$ gives

$$t_{f\ \mathrm{in}} - t_f{}'_{\mathrm{in}} - (t_{a\ \mathrm{in}} - t_a{}'_{\mathrm{in}}) = -\,(t_{a\ \mathrm{in}} - t_{f\ \mathrm{in}})\,e\,h_{fg}/(c_a + e\,h_{fg})$$

which on rearranging becomes

$$t_a{}'_{\mathrm{in}} - t_{f\ \mathrm{in}} = -\,(t_{f\ \mathrm{in}} - t_f{}'_{\mathrm{in}}) + (t_{a\ \mathrm{in}} - t_{f\ \mathrm{in}})/(1 + e\,h_{fg}/c_a)$$

$$= -\,(t_{f\ \mathrm{in}} - t_f{}'_{\mathrm{in}}) + (t_a{}'_{\mathrm{in}} - t_{f\ \mathrm{in}})\,\eta_\ell/(1 + e\,h_{fg}/c_a)$$

$$\text{(from definition of } \eta_\ell\text{)}$$

$$= -\,(t_{f\ \mathrm{in}} - t_f{}'_{\mathrm{in}})/(1 - \eta_\ell/(1 + e\,h_{fg}/c_a))$$

From definition of η_u

$$t_{u\ \mathrm{out}} = t_{f\ \mathrm{in}} + (t_a{}'_{\mathrm{in}} - t_{f\ \mathrm{in}})\,\eta_u$$

$$= t_{f\ \mathrm{in}} - (t_{f\ \mathrm{in}} - t_f{}'_{\mathrm{in}})\eta_u/(1 - \eta_\ell/(1 + e\,h_{fg}/c_a))$$

$$\text{(substituting } t_a{}'_{\mathrm{in}} - t_{f\ \mathrm{in}} \text{ from equation above)}$$

$$= 35 - (35 - 23.8)\ 0.8070/(1 - 0.9768/4.058)$$

$$= 23.1\,^\circ\mathrm{C}$$

9 Conclusion

The linearized approximate theory presented in Sections 2 and 3 extends the "enthalpy potential" theory [6, 7] of wet surface heat exchangers, showing that wet bulb temperature and wet bulb depression may be considered as independent driving potentials in the operation of such exchangers, enabling performance prediction by analogy from that of dry surface heat exchangers.

The theory presented may be expected to predict accurately wet surface heat exchanger performance provided that the water surface temperature range is less than 20 K and the Lewis relation (condition 7) is satisfied (Sections 4 and 5). This theory predicts excellent performance for a regenerative evaporative cooler using a wet plate heat exchanger (Section 7).

The measured performance of wet plate heat exchangers reported by Pescod [5] is substantially less than that predicted (Section 5). This deviation may be reduced if the water film were made continuous and the water mass flow rate small in these exchangers. Water mass flow rate and wet passage outlet state should be measured simultaneously with other flows and states. Improved understanding of heat transfer alone and pressure drop in Pescod's pin fin surfaces (Section 1) is also desirable. Predicted regenerative evaporative cooler performance can be obtained only if predicted wet plate heat exchanger performance is achieved.

Acknowledgments

The authors are grateful to Mr. D. Pescod and Dr. J. G. van Leersum, of the CSIRO Division of Mechanical Engineering, for helpful suggestions.

The first author is grateful to the Department of Mechanical Engineering, Monash University, Australia for the use of their facilities while this paper was being written. Financial support was received from the Australian Government under grant number F74/15117 awarded by the Australian Research Grants Committee.

References

1 *ASHRAE Handbook and Product Directory*, Equipment volume, American Society of Heating, Refrigerating and Air-Conditioning Engineers, New York, 1979.

2 Watt, J. R., "Indirect Evaporative Cooling," *Evaporative Air Conditioning*, The Industrial Press, New York, 1963, pp. 204–224.

3 Pescod, D., "Unit Air Cooler Using Plastic Heat Exchanger with Evaporatively Cooled Plates," *Australian Refrigeration, Air Conditioning and Heating*, Vol. 22, No. 9, Sept. 1968, pp. 22–26.

4 Pescod, D., "Effects of Turbulence Promoters on the Performance of Plate Heat Exchangers," *Heat Exchangers: Design and Theory Sourcebook*, McGraw-Hill, New York, 1974, pp. 601–615.

5 Pescod, D., "A Heat Exchanger for Energy Saving in an Air-Conditioning Plant," *Transactions of the American Society of Heating, Refrigerating and Air-Conditioning Engineers*, Vol. 85, Part 2, 1979, pp. 238–251.

6 Mickley, H. S., "Design of Forced Draft Air Conditioning Equipment," *Chemical Engineering Progress*, Vol. 45, No. 12, Dec. 1949, pp. 739–745.

7 Baker, D. R. and Shryock, H. A., "A Comprehensive Approach to the Analysis of Cooling Tower Performance," ASME JOURNAL OF HEAT TRANSFER, Vol. 83, No. 3, 1961, pp. 339–350.

8 Kays, W. M., and London, A. L., *Compact Heat Exchangers*, 2nd ed., McGraw-Hill, New York, 1964.

9 Hollands, K. G. T., and Pott, P., "Development and Testing of Evaporative Cooler Pads," *Mechanical and Chemical Engineering Transactions of The Institution of Engineers, Australia*, Vol. MC7, No. 2, Nov. 1971, pp. 66–72.

10 Deutscher, K. O., Dunkle, R. V., and Megler, V. R., "A Fundamental Study of Heat, Mass and Momentum Transfer in a Parallel Passage Evaporative Cooler Pad," *First Australasian Conference on Heat and Mass Transfer*, Monash University, Melbourne, 1973, Section 5.2, pp. 7–14.

11 Baclic, B. S., "A Simplified Formula for Cross-Flow Heat Exchanger Effectiveness," ASME JOURNAL OF HEAT TRANSFER, Vol. 100, No. 4, Nov. 1978, pp. 746–747.

12 *HP-67/HP-97 MATH PAC 1*, Hewlett-Packard Company, Corvallis, 1976, pp. 18-01–18-02.

13 Maclaine-cross, I. L. and Banks, P. J., "Coupled Heat and Mass Transfer in Regenerators—Prediction Using an Analogy with Heat Transfer," *International Journal of Heat and Mass Transfer*, Vol. 15, No. 6, June 1972, pp. 1225–1242.

14 Maclaine-cross, I. L., "A Theory of Combined Heat and Mass Transfer in Regenerators," Ph.D. Thesis, Department of Mechanical Engineering, Monash University, Australia, 1974.

15 Banks, P. J., "Prediction of Heat and Water Vapour Exchanger Performance from That of a Similar Heat Exchanger," *Compact Heat Exchangers—History, Technological Advancement and Mechanical Design Problems*, Conference Proceedings, HTD-Vol. 10, The American Society of Mechanical Engineers, New York, 1980, pp. 57–64.

16 *ASHRAE Handbook and Product Directory*, Fundamentals volume, American Society of Heating, Refrigerating and Air-Conditioning Engineers, New York, 1977, p. 8.21.

17 "What's in a Chart?," *Australian Refrigeration, Air Conditioning and Heating*, Vol. 28, No. 9, Sept. 1974, pp. 17–18.

18 Mayhew, Y. R and Rogers, G. F. C., *Thermodynamic and Transport Properties of Fluids SI Units*, 2nd ed., Blackwell, Oxford, 1974.

19 "Resins and Molding Compounds," *Modern Plastics Encyclopedia edition*, Vol. 54, No. 10A, Oct. 1977, p. 483.

A Parametric Study of a Particulate Direct Contact Heat Exchanger

Ruth Letan
Associate Professor,
Department of Mechanical Engineering,
Ben-Gurion University of the Negev,
Beer-Sheva, Israel

The function performed by a direct contact heat exchanger is by definition a heat interaction between two media without an interfering wall between them. The direct contact heat exchanger analyzed herein refers to the restricted definition of systems in which temperatures of the contacted media vary without change of phase. This class involves the particulate systems of immiscible liquids, solid particles in fluids, gas bubbles in liquids, and droplets in gases. The applicability of direct contact heat exchangers has been considered for use in fouling and crystallizing systems, sea-water heating, geothermal brines, as well as in nuclear and MHD power plants. An analytic way to evaluate the performance of a direct contact heat exchanger is applied to examine the effects of operational variables upon length and diameter of a heat exchanger. The heat exchanger becomes shorter as the particle size decreases, and heat capacity ratio, flow rate ratio and approach temperature increase. The diameter of the column decreases with the particle size, and the density ratio of the contacted media. It increases with the flow rate ratio. All the evaluations made, correspond to the laminar bulk flow in the heat exchanger, and to particle Reynolds numbers in the range of 20–500.

Introduction

Direct contact heat exchangers have attracted attention mainly because of their applicability to fouling and corrosive fluids, clogging suspensions, and solid media of granular character. Development of the heat exchangers has been initiated for desalination processes [1] and carried on to geothermal systems [2], to crystallizing brines [3, 4], to nuclear reactors [5], and considered for application in MHD combustion systems [6].

In this paper, a direct contact heat exchanger is parametrically analyzed, namely the effects of operational parameters upon the geometry design variables are examined. These parameters relate to flow rates, temperatures, physical properties of the contacted media, and size of the dispersed medium.

By definition, in a direct contact system heat is transferred between media without an interfering wall between them. Presently, the study is concerned with a direct contact heat exchanger within its conventional, restricted definition which applies to a heat interaction between two media of different temperatures, taking place without change of phase, mass transfer, or reaction in the contacted media. However, the principle to be demonstrated, is applicable to direct contact heat exchangers in their broader definition [4].

Operationally, a direct contact heat exchanger is a container of any shape or configuration which provides good contact between the process and working media. The conventional shape, configuration, and operation relate to a tubular vertical column in which the process and working media move countercurrently to each other, with one of them being particulately dispersed. The dispersion may consist of solid particles, liquid droplets or gas bubbles. The character of the dispersion is usually determined by the process medium, although in some processes, an optimization may dictate the choice. For example, coal preheating requires the process medium of solid particles to be contacted with gases. On the other hand, a geothermal brine may be contacted with a working medium of liquid droplets or solid pebbles.

The present parametric analysis is concerned with a vertical tubular heat exchanger operated in a counterflow with particles uniformly dispersed in a fluid. The physical properties of the contacted media remain the same along, and across the column, and so does the particle size. The assumption of uniform size, or a representative average size, applies to a variety of systems in which change of phase does not take place. Systems with widely distributed sizes across or along the exchanger may be analyzed accordingly, by applying the general principles underlined herein.

The question to be considered relates to the size of the heat exchanger, namely the diameter and length of the exchanger, needed to affect a temperature change, ΔT, in the process medium supplied at a flow rate, Q. The effects imposed on the exchanger geometry by the variation of the operational conditions and the physical properties of the contacted media are investigated.

Geometry Variables

The main contact volume of the two media is the column proper. Therefore, the elemental geometry variables are the diameter of the column proper and the length of the column proper. Other geometry variables such as inlets and outlets vary in design with the character of the contacted media and are not presently considered.

Diameter. In the analysis, the process medium is considered to be a continuous fluid in the direct contact heat exchanger.

The diameter, D, of the column proper of the exchanger may be calculated for a specified flow rate of the process fluid, Q_c [7],

$$D = 2\left(\frac{Q_c}{\pi \cdot u_c}\right)^{1/2} \tag{1}$$

where, u_c is the superficial velocity. The evaluation of u_c is to be achieved through the following relations:

(*a*) The superficial velocities in a counterflow are related to the slip velocity [8],

$$u_s = \frac{u_d}{\phi} + \frac{u_c}{1-\phi} = u_c\left(\frac{R}{\phi} - \frac{1}{1-\phi}\right) \tag{2}$$

(*b*) Slip velocity is related to holdup. The semi-empirical expression [9],

$$u_s = u_T(1-\phi)^n \tag{3}$$

fits with reasonable accuracy a wide range of experimental results found in the literature [10]. For the presently considered range of $20 \leqslant \mathrm{Re}_o \leqslant 500$, we obtain the exponent, n, [9] as,

$$n = 4.45\ \mathrm{Re}_o^{-0.1} - 1 \tag{4}$$

The terminal velocity, u_T, may be expressed as,

Contributed by the Heat Transfer Division and presented at the Winter Annual Meeting, December 10–15, 1978, San Francisco, Calif. of THE AMERICAN SOCIETY OF MECHANICAL ENGINEERS. Revised manuscript received by the Heat Transfer Division June 3, 1980. Paper No. 78-WA/HT-16.

$$u_T = 0.268\,\mathrm{Re}_o{}^{0.3}\left(g\left|\frac{\rho_d}{\rho_c} - 1\right|d_p\right)^{0.5} \tag{5}$$

by using the drag coefficient relationship for smooth spheres [7].

(c) The operation holdup, ϕ, at any flow rate ratio, $R(= u_d/u_c)$, is usually chosen as a fraction of the holdup at flooding, ϕ_f [7]. The *state of flooding corresponds to the onset of disruption of stable flow* conditions, and therefore the holdup at flooding represents the maximum achievable holdup at any specified flow rate ratio.

The relationship between ϕ_f and R, has been previously derived [7] in an implicit form. In an explicit form, the relationship is expressed as,

$$\phi_f = \frac{-(n+2) \pm [(n+2)^2 + 4(n+1)(1/R - 1)]^{1/2}}{2(n+1)(1/R - 1)} \tag{6}$$

where $0 < \phi_f < 1$ within $0 < R < \infty$.

For $R = \infty (u_c = 0)$ we obtain

$$\phi_f|_{\max} = \frac{1}{n+1} \tag{7}$$

whereas, for $R = 1$, the original expression [7] reduces to,

$$\phi_f = \frac{1}{n+2} \tag{8}$$

Thus, equations (6–8) yield,

$$\phi_f = \phi_f(n, R) = \phi_f(\mathrm{Re}_o, R) \tag{9}$$

with, n, defined by equation (4).

(d) Combining equations (1–5) leads to,

$$D = \frac{2.18 Q_c{}^{1/2}}{g^{1/4}} \frac{[R(1/\phi - 1) + 1]^{1/2}}{(1 - \phi)^{(n+1)}}\, x\, \frac{\mathrm{Re}_o}{\left[d_p\left|\frac{\rho_d}{\rho_c} - 1\right|\right]^{1/4}} \tag{10}$$

where, ϕ, as a fraction of ϕ_f is obtainable from equations (6–8).

In a study of the relationship expressed by equation (10), ϕ_f may be substituted for ϕ.

Equation (10) provides us with the tools to follow the variation of the exchanger diameter by varying the flow rates and properties of the working medium for any specified flow rate of the process fluid.

Length. The methods of approach to direct contact heat exchangers based upon an area heat transfer coefficient or volumetric overall heat transfer coefficient were previously discussed in detail [7, 11]. Their applicability to specific cases was outlined [7]. A more generalized relationship and thereupon a general method of evaluation of an exchanger length necessitated an analysis of the flow regime imposed upon the moving particles, and knowledge of the mechanism of heat transfer between the particles and the fluid. In a particulate uniform system, of solid particles, liquid droplets or gas bubbles in a fluid, where the particle flow regime corresponds to $20 \leqslant \mathrm{Re}_o \leqslant 500$, and the bulk flow in the column is laminar, the mechanism of transfer by wake shedding [7, 11] dominates.

The relationship between temperatures and length was formulated for the wake dominated system [7] as,

$$\frac{T_{do} - T_{co}}{T_{di} - T_{co}} = \left[\frac{mS}{r\alpha_2}\left[1 - \left(\frac{r}{m}\alpha_2 + 1\right)\exp(\alpha_2 L)\right] + 1\right] \cdot \exp\left(-\frac{M}{r}\right) \tag{11}$$

where, $L \gg 0$ and,

$$P = M + 1/R \tag{12}$$

with

$$\alpha_{1,2} = -\frac{m}{2}\left[\frac{1}{M} + \frac{1}{r} - \frac{1}{P} \pm \left[\left(\frac{1}{M} + \frac{1}{r} + \frac{1}{P}\right)^2 - \frac{1}{Mr}\right]^{1/2}\right] \tag{13}$$

and

$$S = \frac{\alpha_1 + \frac{m}{r} - \frac{mr}{PM}\left[\exp\left(\frac{M}{r}\right) - 1\right],}{\alpha_2 - \alpha_1} \tag{14}$$

Specifying the inlet and outlet temperatures of the process fluid, T_{ci}, and T_{co}, respectively, and choosing as a parameter the approach temperature between the two media at one end of the column, for example $\Delta T_b = T_{di} - T_{co}$, determines also T_{do} by the relationship,

$$T_{co} - T_{ci} = Rr(T_{di} - T_{do}) \tag{15}$$

The parameters involved in equation (11) may be classified as free parameters and wake parameters.

The free parameters relate to r, R, and T_{di}. Each of those may serve as a free variable in the design of an exchanger.

The wake parameters, M and m, vary with the flow regime in the particulate system and have to be evaluated or measured. The method of evaluation adopted herein, relates to the general flow characteristics of a particle and their extension to a particulate system.

For evaluation of wake parameters, let us define, Re_s,

$$\mathrm{Re}_s = \frac{d_p \cdot u_s}{\nu_c} = \mathrm{Re}_o(1 - \phi)^n \tag{16}$$

Obviously, Re_s, is always smaller than, Re_o.

Within the presently considered flow range of $20 \leqslant \mathrm{Re}_o \leqslant 500$ let us restrict our analysis to

$$24 \leqslant \mathrm{Re}_s \leqslant 500(1 - \phi)^{1.4}$$

where, the upper limit corresponds to $\mathrm{Re}_o \leqslant 500$ [4].

Thus, the relative wake volume, M, is evaluated as follows (equation (14) of [4]). For $24 \leqslant \mathrm{Re}_s \leqslant 150$,

$$M = 0.25(1 - \cos\alpha_s)(\cos\alpha_s - \cos 2\alpha_s) + (1.05\,\mathrm{Re}_s - 1.45)\sin^2\alpha_s \tag{17}$$

For $150 \leqslant \mathrm{Re}_s \leqslant 500(1 - \phi)^{1.4}$

$$M = 0.25(1 - \cos\alpha_s)(\cos\alpha_s - \cos 2\alpha_s) + 0.835\sin^2\alpha_s \tag{18}$$

α_s, the point of boundary layer separation on a sphere, was measured and graphically presented [12] as a unique function of Re_s namely

Nomenclature

c_p = specific heat capacity, J/kg °C
D = diameter of column proper, m
d_p = particle diameter, m
$g = 9.8$ m/s^2
L = length of column proper, m
M = relative volume of wake to particle
m = volume of wake elements shed per volume of particle and unit length of column, m^{-1}
n = defined by equation (4)
Q = volumetric flow rate, m^3/s
R = volumetric flow rate ratio, $Q_d/Q_c = u_d/u_c$
$r = (c_p\rho)_d/c_p\rho)_c$
Re_o = single particle Reynolds number, $d_p u_T/\nu_c$
Re_s = particle Reynolds number, $d_p u_s/\nu_c$
S = defined by equation (14)
T = temperature, °C
u = superficial velocity, $Q/(\pi D^2/4)$, m/s
u_s = slip velocity, equation (2), m/s
u_T = terminal velocity, m/s
$\alpha_{1,2}$ = defined by equation (13)
α_s = angle of separation from rear stagnation point
μ = dynamic viscosity, kg/m-s
ν = kinematic viscosity, m^2/s
ρ = density, kg/m^3
ϕ = holdup, volumetric fraction of particles in a column

Subscripts

b = bottom of the column
c = continuous
d = dispersed
f = flooding
i = inlet
o = outlet

$$\alpha_s = \alpha_s(\mathrm{Re}_s) \tag{19}$$

The other wake parameter, the relative wake shedding m, is evaluated as (equation (25) of [4])

$$m \cdot d_p = \frac{K}{\mathrm{Re}_o{}^{1/2}} \frac{1 + \phi/R(1-\phi)}{(1-\phi)^{n/2}} \frac{\sin^2 \alpha_s}{(\cos \alpha_s)^{1/2}} \tag{20}$$

K, is an experimental constant. It may be obtained by a single experiment in any particulate system in which, m, is measurable [11] at specified flow conditions (R, ϕ) of the particular process fluid (μ_c, ρ_c) and the working medium (d_p, ρ_d).

The relationship obtainable combining equations (11–15, 20), and (17–18) will show us that the length of an exchanger for a specified temperature change in the process fluid, may be designed by varying inlet temperatures, flow rates, and properties of the working medium.

Volume. The two elemental geometry variables, the diameter, D, and the length, L, determine the volume of the heat exchanger required to affect a temperature change, ΔT_c, in the process fluid supplied at a volumetric flow rate, Q_c. The volume of the exchanger, ($\pi LD^2/4$), may be followed through the term, LD^2, where, L, is calculated by equations (11–20), and D, by equations (10) and (6).

All the equations derived so far, relate solely to a particulate system of constant physical properties and uniform particle size in the exchanger. The analysis is also limited to a particle flow regime within the range of $20 \leqslant \mathrm{Re}_o \leqslant 500$, and a laminar bulk flow in the exchanger.

Effect of Operational Variables

The operational variables presently considered relate to a single heat exchanger designed for a process fluid of a specified flow rate and temperature change. In the analysis of an industrial plant, which involves several heat exchangers and other types of equipment, additional variables have to be accounted for. In an optimization of a single heat exchanger, the geometry considerations play a major role. However, the cost function may dictate a length to diameter ratio away from the geometrical optimum.

The operational variables may be divided into four groups: physical properties, particle size, flow rates, and temperatures. Their effect upon the column geometry varies, and may be followed by assigning numerical values to all variables involved in the governing equations (equations (10) and (11)). The physical fundamentals of those equations were outlined in their original formulations [7, 11]. Presently of interest to us are the trends exhibited by the geometry variables, which result from those formulations. Some numerical examples are presented in Figs. 1–5.

The physical phenomena responsible for diameter variation relate to the relative velocity between the phases, while those responsible for length variation relate to the rate of heat transfer between the phases.

With respect to column diameter the physical picture, in a simplified way, may be illustrated as follows. The faster particles move in a column, the smaller is the cross section required for a specified flow rate. The larger a spherical particle is, the higher is its velocity in a medium. Hence, for any flow rate, the column diameter is reduced as the particle size is increased. Figure 1 shows us that effect clearly. The effect of density ratio is explicit within the terminal velocity (equation (5)). From equation (10) it is apparent that the column diameter increases infinitely as the density ratio approaches unity. By physical reasoning we may expect that effect. In counterflow, vertical movement between phases is due to their difference in density. The closer their densities are, the slower the phases move, and a larger cross section is needed for a given flow rate. This trend is obvious in Fig. 1.

The flow rate ratio, R, is another operational variable which affects the column geometry. Increasing the flow rate ratio of the two phases, for a specified flow rate of one phase, means a higher total flow rate. That explicitly requires a larger cross section. However, the implicit physical phenomenon related to flow rate ratio expresses itself in holdup of particles. It increases with the flow rate ratio [7], and that in turn brings upon a smaller slip velocity between the phases. Again, a larger cross-section is required for a given flow rate. Namely, diameter increases with flow rate ratio, as presented in Fig. 2.

Variables which govern heat transfer rates between the phases, determine the exchanger length. Particle size has a complex effect upon these rates. The larger a particle is, the larger is the amount of heat to be transfered to it. That calls upon a longer contact time with the continuous medium, namely a longer heat exchanger.

Additionally to that, a spherical particle increases in velocity with its size, and needs a longer column for a given contact time. The wake parameters, M, and, m, also affect the rates of heat transfer, although implicitly. The overall effect, as observed in Fig. 3, makes the heat exchanger longer, as the particle size becomes larger.

Figure 3 shows also that increasing the heat capacity ratio, r, makes the column shorter. This effect may be physically analyzed as follows: For a specified temperature change in the continuous phase, and a higher capacity ratio, the particle temperature change is smaller. A higher temperature difference is preserved along the exchanger, the rate of heat transfer is higher, and for a given amount of heat to be transferred, a shorter column is needed.

The effect of approach temperature, ΔT_b, between the contacted media is exhibited in Fig. 4. It is unidirectional and related to length only. The larger the difference, the higher is the heat transfer rate, and the shorter is the exchanger needed for a specified operation to take place.

With regard to flow rate ratio, R, the same physical phenomena, which bring upon a larger diameter of the column, make it shorter. With flow rate ratio increases the holdup of particles, and their slip velocity, decreases. The slower particles require a shorter column to transfer an amount of heat to their surrounding medium. The actual picture is much more complex, as the mechanism of transfer between the phases is governed by the flow characteristics. However, the overall trend, as illustrated in Fig. 4, follows the above indicated direction.

The effect of other variables upon length and diameter can be examined by physical reasoning in a similar way. However, an overall effect of the non-unidirectional variables, upon the heat exchanger volume, cannot be qualitatively predicted by such interpretation.

The volume of the heat exchanger is determined by the combination LD^2, which may be investigated with respect to any physical or operational variation in the exchanger. As an example, the particle size and density ratio variations have been chosen for the illustration. As may be observed in Fig. 5, the role of density ratio, and thereupon of the exchanger diameter is decisive in the vicinity of, $\rho_d/\rho_c = 1$. Away from that value the effect of the particle size upon exchanger length is reflected in the volume of the exchanger.

The graphical presentations numerically provide an approximation of the effects to be expected. The inaccuracy is mainly due to the uncertainty involved in the evaluation of the wake parameters, M, and, m, and to a smaller extent in the flow characteristics. The constant, K, of equation (20) was evaluated as, $K = 0.1$, for the present computational program of the column length. The numerical evaluation was based on experimental data obtained in a kerosene-water system [11], with 3×10^{-3}m, sized droplets. The accuracy of K and its general applicability has to be experimentally tested in systems of different physical properties, and long exchangers. K, obtained in a specific system for which the exchanger is designed, may considerably improve the estimates of length.

With respect to the column diameter, a closer evaluation may be achieved through the information of the slip velocity-holdup relationship in the actual system.

The analysis carried so far, corresponds solely to a laminar bulk flow, and a particle flow regime, where phenomena of wake formation and shedding behind particles dominate. The study was mainly intended to gain some more insight into the nature of particulate direct contact heat exchangers.

Conclusions

The geometry of a direct contact heat exchanger of particulate character operated countercurrently, varies with the physical prop-

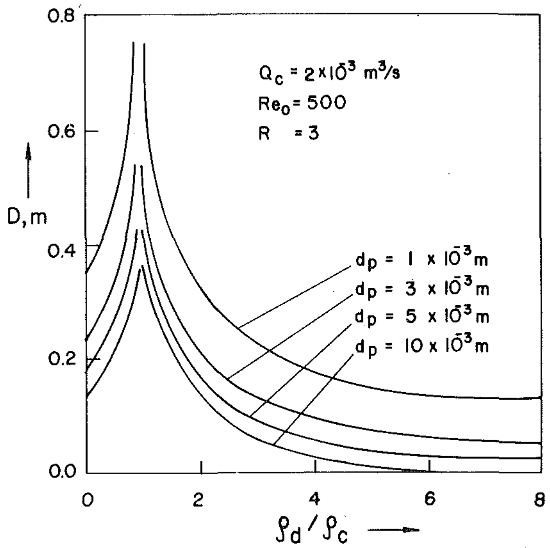

Fig. 1 Effect of particle size and density ratio on diameter

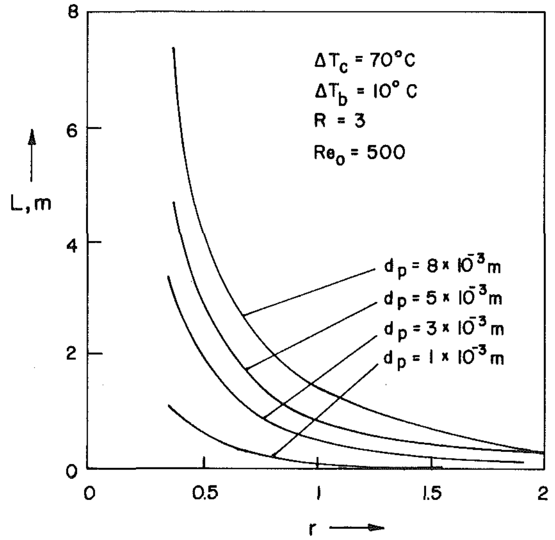

Fig. 3 Effect of particle size and heat capacity ratio on length

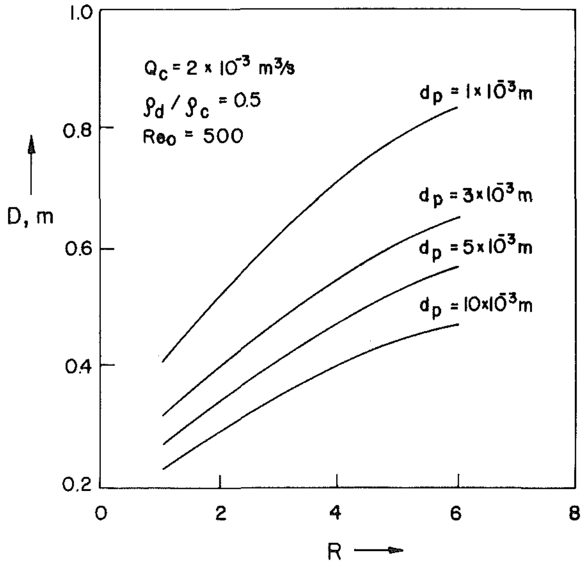

Fig. 2 Effect of particle size and flow rate ratio on diameter

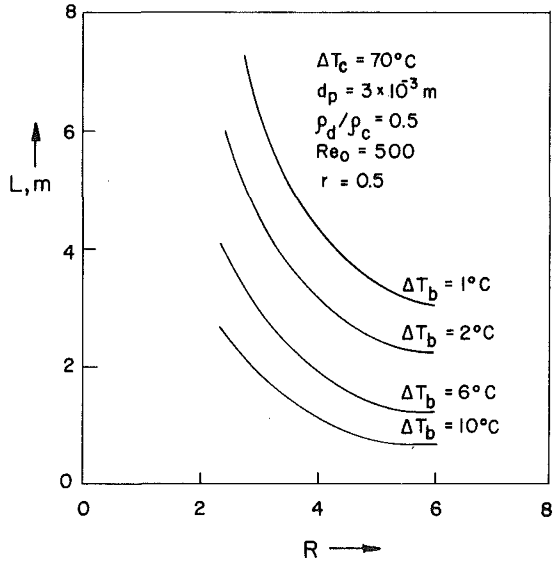

Fig. 4 Effect of approach temperature and flow rate ratio on length

erties of the contacted media, their flow rate ratio, the approach temperature between them, and the particle size of the dispersed phase.

For a process fluid of a specified flow rate, and temperature change, the column length decreases with approach temperature, and with flow rate and heat capacity of the working medium. It increases with particle size.

The column diameter becomes larger with the flow rate of the working medium and with the density ratio as it approaches unity. The diameter becomes smaller as the particle size increases.

The volume of the heat exchanger is determined by the combined effects of diameter and length. The volume increases with the particle size, and with the density ratio of the contacted media as it approaches unity.

All the evaluations made, correspond to a laminar bulk flow in the exchanger and to particle Reynolds numbers in the range of 20–500.

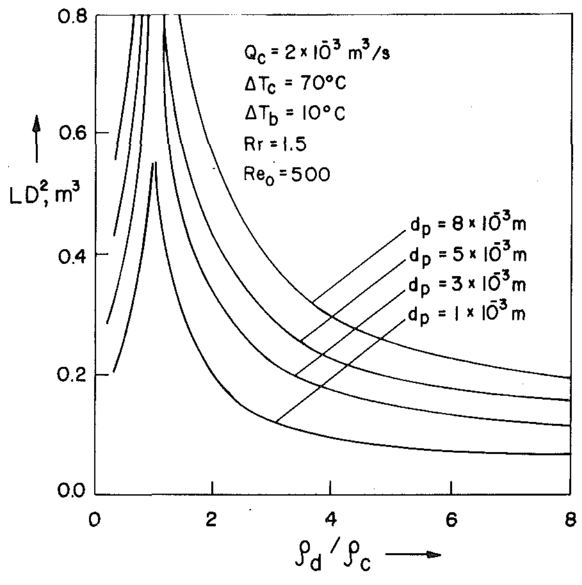

Fig. 5 Effect of particle size and density ratio on volume

Acknowledgment

The computational work presented graphically was carried out by Mr. E. Hoch.

References

1 Woodward, T., "Heat Transfer in a Spray Column," *Chemical Engineering Progress*, Vol. 57, 1961, pp. 52–57.

2 Surrat, W. B., and Hart, G. K., "Testing of Direct Contact Heat Exchangers for Geothermal Brines," ASME Paper 77-HT-4, 17th National Heat Transfer Conference, Salt Lake City, Utah, Aug. 14–17, 1977.

3 Letan, R., "A Direct Contact Cooled Crystallizer," *Industrial and Engineering Chemistry Process Design and Development*, Vol. 12, No. 3, 1973, pp. 300–305.

4 Zmora, J., and Letan, R., "Direct Contact Cooling of a Crystallizing Brine," *Proceedings of the International Heat Transfer Conference*, Vol. 4, 1978, pp. 61–65.

5 Pierce, R. D., Dwyer, O. E., and Martin J. J., *Journal of American Institute of Chemical Engineers*, Vol. 5, 1959, pp. 257–261.

6 Eustis, R. H., Private Communication, Mechanical Engineering Department, Stanford University, Stanford, Calif.

7 Letan, R., "Design of a Particulate Direct Contact Heat Exchanger: Uniform Countercurrent Flow," ASME Paper 76-HT-27, 16th National Heat Transfer Conference, St. Louis, Mo., Aug. 9–11, 1976.

8 Lapidus, L., and Elgin, J. C., "Mechanics of Vertical-Moving Fluidized Systems," *Journal of American Institute of Chemical Engineers*, Vol. 3, No. 1, 1957, pp. 63–68.

9 Richardson, J. F., and Zaki, W. N., "Sedimentation and Fluidization," *Transactions of Institution of Chemical Engineers*, Vol. 32, 1954, pp. 35–53.

10 Letan, R., "On Vertical Dispersed Two-Phase Flow," *Chemical Engineering Science*, Vol. 29, 1974, pp. 621–624.

11 Letan, R., and Kehat, E., "The Mechanism of Heat Transfer in a Spray Column Heat Exchanger," *Journal of American Institute of Chemical Engineers*, Vol. 14, No. 3, 1968, pp. 398–405.

12 Taneda, S., "Experimental Investigation of the Wake behind a Sphere at Low Reynolds Numbers," *Reports of Research Institute of Applied Mechanics*, Kyushu University, Vol. 4, 1956, pp. 99–105.

Conduction of Heat across Rectangular Cellular Enclosures

J. Eftekhar
G. Darkazalli
Mem. ASME

A. Haji-Sheikh
Mem. ASME

Mechanical Engineering Department,
University of Texas at Arlington,
Arlington, Tex.

A simplified analytical model for the computation of thermal conduction across rectangular-celled enclosures based on the assumption of quasi-one-dimensional conduction in the cell partitions is presented. The rectangular enclosures may contain solid or liquid for which the conduction is two or three-dimensional depending on the geometrical configuration. Additional assumptions concerning radiation interchange between participating surfaces are necessary when the enclosure contains a stagnant gas. This analytical model leads to a closed form solution for temperature distribution in the partitions and the multidimensional conductive region. A parametric study of heat flux is presented. The numerical data define a range of parameters for which a one-dimensional conduction model is satisfactory.

Introduction

Numerous experimental and numerical computational studies dealing with free convection within enclosures have been reported in the literature. As early as 1954, Batchelor [1] presented the results of the experimental investigations of free convection across a cavity with opposite vertical boundaries maintained at two different temperatures. Additional research includes the study of free convection within air filled enclosed rectangular cavities by Davis [2] and Yin, et al [3]. Recent studies concerning free convection heat transfer across rectangular-celled honeycombs are reported in references [4] through [9]. It is reported in reference [9] that when the Rayleigh number is less than 10^4 to 10^5 (or more) depending on various parameters, heat transfer is by combined conduction and radiation. This condition is highly desirable if rectangular-celled cavities are used in order to reduce the rate of heat loss from a wall. Hexagonal or rectangular-celled honeycombs are used to reduce the transfer of heat across skylights and doubleglazed windows by suppressing the free convection of heat in the trapped air layer.

The experimental data in reference [9] are obtained for carefully controlled laboratory conditions where heat transfers across cavities located between two isothermal plates. At low Rayleigh number this situation leads to an identical linear temperature distribution in the fluid layer and partitions. However, in many situations, one surface, e.g., plate 1, Fig. 1, can be considered isothermal, while the other surface, e.g., plate 2, Fig. 1, transfers heat to the inside of a conditioned space by free convection. The temperature distribution in the fluid layer is no longer one-dimensional. The rate of heat transfer depends on the geometrical dimensions, thermal conductivity of all participating surfaces, and the heat transfer coefficient between the exterior of plate 2 and an external fluid. This paper provides reference values (low Rayleigh number) for heat flux across rectangular-celled cavities when plate 2 is not isothermal, and will enhance the range of usefulness of available information on this subject. An analytical model for the calculation of heat loss is presented and an analytical solution is derived for conduction of heat in a composite medium which consists of two homogeneous regions; a quasi-one-dimensional and a multidimensional. This solution is valid when both regions are solid as well as when the rectangular cell cavities are filled with a fluid, provided the corresponding Rayleigh number for the latter case is below the onset of free convection. A parametric study describing the effect of two-dimensional conduction in the fluid layer is discussed. A closed form two-dimensional solution is obtained when the enclosures are separated by horizontal partitions, Fig. 1(a). The generalization is made to include the conduction of heat across rectangular celled regions, Fig. 1(b).

Analysis

The analytical model consists of a two-dimensional region bounded between thin partitions, a constant temperature plate, and a thin plate (plate 2, Fig. 1(a)) parallel to the constant temperature plate. The partitions and plate 2 are assumed to be sufficiently thin (see Appendix) so that the conduction of heat within them is quasi-one-dimensional. The geometrical configuration for this model is shown in Fig. 1. The differential equation which governs the steady state conduction of heat across a two-dimensional air layer is the Laplace equation, which may be obtained from any standard heat transfer text, e.g. reference [10].

$$\frac{\partial^2 T_a}{\partial x^2}+\frac{\partial^2 T_a}{\partial y^2}=0 \tag{1}$$

where T_a is the temperature of the two-dimensional region; e.g., air.

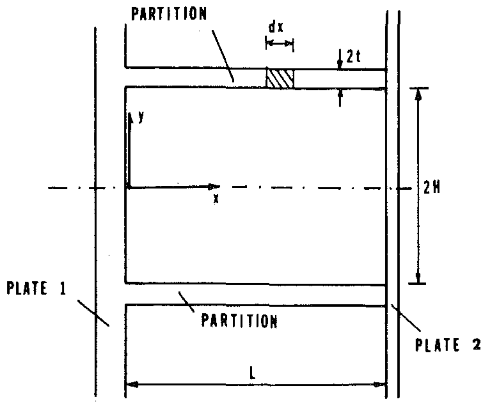

Fig. 1(a)

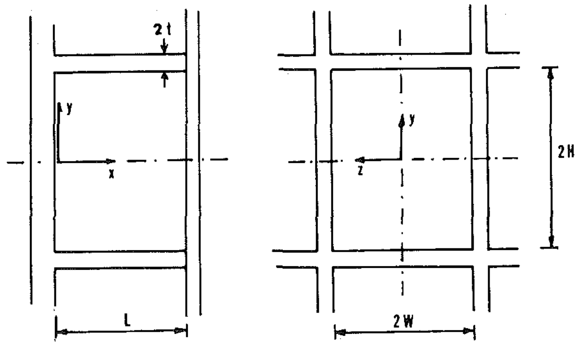

Fig. 1(b)

Fig. 1 Schematic of a two and three-dimensional rectangular-celled cavity

---

Contributed by the Heat Transfer Division for publication in the JOURNAL OF HEAT TRANSFER. Manuscript received by the Heat Transfer Division July 10, 1980.

The boundary conditions which should be satisfied are

$$T = T_0 \text{ at } x = 0,$$

$$\frac{\partial T_a}{\partial y} = 0 \text{ at } y = 0, \tag{2}$$

$$-k_a\left(\frac{\partial T_a}{\partial y}\right) = U_a(T - T_\infty) \text{ at } x = L$$

including continuity of temperature and heat flux at the interface of air and partition which will be discussed later. The thermal conductivity of air is k_a and the overall heat transfer coefficient is U_a which includes the contribution of the thermal resistance of plate 2 and convection coefficient of the cooling fluid on the external surface of plate 2. A considerable simplification is realized by introducing the transformation

$$\frac{T_0 - T_a}{T_0 - T_\infty} = (x/L)B_a/(1 + B_a) + \theta_a \tag{3}$$

The solution of the function θ_a using standard separation of variables solution technique is

$$\theta_a = \sum_{n=1}^{\infty} C_n \sin(\lambda_n x)\cosh(\lambda_n y) \tag{4}$$

In which λ_n is the eigenvalue obtained from the equation

$$\tan(\lambda L) = -\lambda L/B_a \tag{5}$$

The quasi-one-dimensional conduction of heat in the partitions is derived by applying the energy conservation law to the material element in Fig. 1.

$$k_f t\left(\frac{\partial^2 T_f}{\partial x^2}\right) = k_a\left(\frac{\partial T_a}{\partial y}\right)_{\text{at } y = H} \tag{6}$$

The transformation

$$\frac{T_0 - T_f}{T_0 - T_\infty} = (x/L)B_f/(1 + B_f) + \theta_f \tag{7}$$

in conjunction with equation (3) and (4) reduces equation (6) to the following form

$$\frac{\partial^2\theta_f}{\partial x^2} = \frac{r}{t}\sum_{n=1}^{\infty} C_n\lambda_n \sin(\lambda_n x)\sinh(\lambda_n H) \tag{8}$$

wherein $r = k_a/k_f$. The solution for this equation after using the appropriate boundary conditions

$$\theta_f = 0 \quad \text{at } x = 0$$

and

$$-k_f\frac{\partial\theta_f}{\partial x} = U_f\theta_f \quad \text{at } x = L \tag{9}$$

takes the following form

$$\theta_f = -\frac{r}{t}\sum_{n=1}^{\infty}\frac{C_n}{\lambda_n}\sin(\lambda_n x)\sinh(\lambda_n H) + \frac{x}{L}\sum_{n=1}^{\infty} C_n\zeta_n \sinh(\lambda_n H) \tag{10}$$

where

$$\zeta_n = \frac{rL}{t}\,\frac{1 - B_f/B_a}{1 + B_f}\cos(\lambda_n L) \tag{10a}$$

Cognizance should be taken of the continuity of heat flux at the interface used in the derivation of equation (6). The continuity of temperature at the interface was utilized for evaluation of the constant C_n in equations (4) and (10); that is,

$$\frac{A_m\eta_m}{\beta_m} = \sum_{n=1}^{\infty} A_n\zeta_n + R;\ m = 1,2.\dots \tag{11}$$

in which

$$A_m = C_m \sinh(\lambda_m H) \tag{11a}$$

$$\beta_m = \frac{-(1 + B_a)\cos(\lambda_m L)}{B_a\lambda_m L} \tag{11b}$$

$$\gamma_m = \frac{1}{2} - \frac{\sin(2\lambda_m L)}{4\lambda_m L} \tag{11c}$$

$$\eta_m = \gamma_m \coth(\lambda_m H) + \frac{\gamma_m r}{\lambda_m t} \tag{11d}$$

and

$$R = \frac{B_f}{1 + B_f} - \frac{B_a}{1 + B_a} \tag{11e}$$

It should be mentioned that the coordinate x was eliminated from equation (10) using orthogonal properties of the sine function. Equation (11) appears to require a simultaneous solution of infinite equations, but the solution is accomplished analytically. It is common practice to obtain a series solution, and then study the convergence of the solution. However, here it is assumed that equation (11) contains a convergent series. Based on this assumption, the right hand side of equation (11) is constant and independent of m.

$$\frac{A_1\eta_1}{\beta_1} = \frac{A_2\eta_2}{\beta_2} = \cdots = \frac{A_m\eta_m}{\beta_m} = \frac{A_n\eta_n}{\beta_n} = \sum_{n=1}^{\infty} A_n\zeta_n + R \tag{12}$$

which leads to the equation

$$A_n = (A_m\eta_m/\beta_m)(\beta_n/\eta_n) \tag{13}$$

The substitution of A_n from equation (13) in equation (11) results in the evaluation of A_m (which is related to C_m, equation (11a)).

$$A_m = \frac{R\beta_m/\eta_m}{1 - \sum_{n=1}^{\infty}\beta_n\zeta_n/\eta_n} \tag{14}$$

The final solution hence becomes

$$\theta_a = \sum_{m=1}^{\infty} A_m \sin(\lambda_m x)\cosh(\lambda_m y)/\sinh(\lambda_m H) \tag{14a}$$

and

$$\theta_f = -\frac{r}{t}\sum_{m=1}^{\infty}\frac{A_m}{\lambda_m}\sin(\lambda_m x) + \frac{x}{L}\sum_{m=1}^{\infty} A_m\zeta_m \tag{14b}$$

Now the examination of the convergence becomes necessary. As λ_m goes to infinity, β_m goes to zero since $1/\lambda_m$ goes to zero. All other quantities converge to finite limits.

Nomenclature

A_n, B_n, C_n = Fourier coefficients
$B_a = U_aL/k_a$
$B_f = U_fL/k_f$
H = cell height, Fig. 1
k = thermal conductivity
L = cell length, Fig. 1
$\overset{\circ}{\overline{\text{Nu}}}$ = heat flux ratio, $Q_{T,2}/Q_{T,1}$
$r = k_a/k_f$
R = constant, equation (11e)
q_r = radiant heat flux
Q = heat transfer rate
$Q_T = Q_a + Q_f$
$t = \frac{1}{2}$ thickness of partition, Figs. 1
U = conductance at $x = L$, equation (2)
W = cell width, Fig. 1
x,y,z = coordinate, Fig. 1
β = equation (11b)
γ = equation (11c)
ζ = equation (10a)
η = equation (11d)
λ = eigenvalue, equation (15)
θ = temperature function, equation (3)

Subscripts

a = air
f = fin-type partition
m,n = indices
1 = one-dimensional solution
2 = two-dimensional solution

The examination of equation (14) reveals that these series converge uniformly [11] over the entire domain. Numerically, it was observed that 300 terms are sufficient, in most cases, to achieve an accuracy of greater than four significant figures.

Rectangular Cells. The temperature distribution in a rectangular-celled cavity, Fig. 1(*b*), can be derived following the transformation given by equation (2). The function θ_a can be decomposed into two functions, θ_{a1} and θ_{a2}.

$$\theta_a(x, y, z) = \theta_{a1}(x, y) + \theta_{a2}(x, z) \tag{15}$$

The substitution of θ_a into the three-dimensional Laplace equation results in two distinct two-dimensional Laplace equations. Applying the appropriate boundary conditions similar to derivation of equation (4) results in

$$\theta_{a1}(x, y) = \sum_{m=1}^{\infty} A_m \sin(\lambda_m x) \cosh(\lambda_m y)/\sinh(\lambda_m H) \tag{16a}$$

and

$$\theta_{a2}(x, z) = \sum_{m=1}^{\infty} B_m \sin(\lambda_m x) \cosh(\lambda_m z)/\sinh(\lambda_m W) \tag{16b}$$

The solution for quasi-one-dimensional temperature distributions in the partitions remains unchanged; that is, at $y = H$ partition

$$\theta_{f1} = -\frac{r}{t}\sum_{m=1}^{\infty} \frac{A_m}{\lambda_m} \sin(\lambda_m x) + \frac{x}{L}\sum_{m=1}^{\infty} A_m \zeta_m \tag{17a}$$

and at $z = W$ partition,

$$\theta_{f2} = -\frac{r}{t}\sum_{m=1}^{\infty} \frac{B_m}{\lambda_m} \sin(\lambda_m x) + \frac{x}{L}\sum^{\infty} B_m \zeta_m \tag{17b}$$

The Fourier coefficients A_m and B_m in equations (16) and (17) can be determined by satisfying the condition of continuity of temperature at the interface of air and partitions. Unlike the two-dimensional solution, the three-dimensional solution requires an additional assumption in order to satisfy the basic assumption of quasi-one-dimensional conduction in the partitions. This assumption is included in the following relations

$$\theta_{a1}(x, H) + \bar{\theta}_{a2}(x, W) = Rx/L + \theta_{f1}(x);\ \text{at } y = H \text{ partition} \tag{18a}$$

$$\bar{\theta}_{a1}(x, H) + \theta_{a2}(x, W) = Rx/L + \theta_{f2}(x);\ \text{at } y = W \text{ partition} \tag{18b}$$

where

$$\bar{\theta}_{a1}(x, H) = \frac{1}{H}\int_0^H \theta_{a1} dy \text{ and } \bar{\theta}_{a2}(x, W) = \frac{1}{W}\int_0^W \theta_{a2} dz$$

Substitution of θ_{a1}, θ_{a2}, θ_{f1}, and θ_{f2} from equations (16) and (17) in the above equations and utilization of the orthogonality properties of the sin $(\lambda_m x)$ function results in

$$A_m\left[\frac{\gamma_m \coth(\lambda_m H)}{\beta_m} + \frac{r\gamma_m}{\beta_m t \lambda_m}\right] + B_m \frac{\gamma_m}{\lambda_m W \beta_m} = R + \sum_{n=1}^{\infty} A_n \zeta_n \tag{19a}$$

$$A_m \frac{\gamma_m}{\lambda_m H \beta_m} + B_m\left[\frac{\gamma_m \coth(\lambda_m W)}{\beta_m} + \frac{r\gamma_m}{\beta_m t \lambda_m}\right] = R + \sum_{n=1}^{\infty} B_n \zeta_n \tag{19b}$$

The method used for calculating the Fourier coefficient A_m from equation (11), for the two-dimensional problem, now can be utilized for determination of A_m and B_m for the three-dimensional case. The result is

$$\begin{aligned} A_m = R &\left\{\left(\frac{\eta_m{}^{(2)}}{\beta_m} - \frac{\xi_m{}^{(1)}}{\beta_m}\right) - \sum_{n=1}^{\infty} (\Delta_{m,n}{}^{(2)} - \Delta_{m,n}{}^{(1)})\zeta_n\right\} \Big/ \\ &\left\{\left[\frac{\eta_m{}^{(1)}}{\beta_m} - \sum_{n=1}^{\infty} \Lambda_{m,n}{}^{(1)}\zeta_n\right]\left[\frac{\eta_m{}^{(2)}}{\beta_m} - \sum_{n=1}^{\infty} \Delta_{m,n}{}^{(2)}\zeta_n\right]\right. \\ &\left. - \left[\frac{\xi_m{}^{(1)}}{\beta_m} - \sum_{n=1}^{\infty} \Delta_{m,n}{}^{(1)}\zeta_n\right]\left[\frac{\xi_m{}^{(2)}}{\beta_m} - \sum_{n=1}^{\infty} \Lambda_{m,n}{}^{(2)}\zeta_n\right]\right\} \end{aligned} \tag{20a}$$

$$\begin{aligned} B_m = R &\left\{\left(\frac{\eta_m{}^{(1)}}{\beta_m} - \frac{\xi_m{}^{(2)}}{\beta_m}\right) - \sum_{n=1}^{\infty} (\Lambda_{m,n}{}^{(1)} - \Lambda_{m,n}{}^{(2)})\zeta_n\right\} \Big/ \\ &\left\{\left[\frac{\eta_m{}^{(1)}}{\beta_m} - \sum_{n=1}^{\infty} \Lambda_{m,n}{}^{(1)}\zeta_n\right]\left[\frac{\eta_m{}^{(2)}}{\beta_m} - \sum_{n=1}^{\infty} \Delta_{m,n}{}^{(2)}\zeta_n\right]\right. \\ &\left. - \left[\frac{\xi_m{}^{(1)}}{\beta_m} - \sum_{n=1}^{\infty} \Delta_{m,n}{}^{(1)}\zeta_n\right]\left[\frac{\xi_m{}^{(2)}}{\beta_m} - \sum_{n=1}^{\infty} \Lambda_{m,n}{}^{(2)}\zeta_n\right]\right\} \end{aligned} \tag{20b}$$

where

$$\Lambda_{m,n}{}^{(1)} = \Gamma_{m,n}(\eta_n{}^{(2)}\eta_m{}^{(1)} - \xi_n{}^{(1)}\xi_m{}^{(2)}) \tag{21a}$$

$$\Delta_{m,n}{}^{(1)} = \Gamma_{m,n}(\eta_n{}^{(2)}\xi_m{}^{(1)} - \xi_n{}^{(1)}\eta_m{}^{(2)}) \tag{21b}$$

$$\Lambda_{m,n}{}^{(2)} = \Gamma_{m,n}(\eta_n{}^{(1)}\xi_m{}^{(2)} - \xi_n{}^{(2)}\eta_m{}^{(1)}) \tag{21c}$$

$$\Delta_{m,n}{}^{(2)} = \Gamma_{m,n}(\eta_n{}^{(1)}\eta_m{}^{(2)} - \xi_n{}^{(2)}\xi_m{}^{(1)}) \tag{21d}$$

$$\Gamma_{m,n} = \frac{\beta_n}{\beta_m}\frac{1}{\eta_n{}^{(1)}\eta_n{}^{(2)} - \xi_n{}^{(1)}\xi_n{}^{(2)}} \tag{21e}$$

$$\eta_m{}^{(1)} = \gamma_m\left[\coth(\lambda_m H) + \frac{r}{t\lambda_m}\right] \tag{21f}$$

$$\eta_m{}^{(2)} = \gamma_m\left[\coth(\lambda_m W) + \frac{r}{t\lambda_m}\right] \tag{21g}$$

$$\xi_m{}^{(1)} = \frac{\gamma_m}{\lambda_m W} \text{ and } \xi_m{}^{(2)} = \frac{\gamma_m}{\lambda_m H} \tag{21h}$$

Parametric Example: The total heat flux leaving the constant temperature plate, at $x = 0$, per unit width of the plate is calculated by the application of the Fourier equation to the temperature solutions, equations (14), (14*a*) and (14*b*). The result is

$$\frac{LQ_a}{k_a H(T_0 - T_\infty)} = \frac{B_a}{1 + B_a} + \frac{L}{H}\sum_{n=1}^{\infty} A_n \tag{22a}$$

and

$$\frac{LQ_f}{k_{ft}(T_0 - T_\infty)} = \frac{B_f}{1 + B_f} + \sum_{n=1}^{\infty} A_n\zeta_n - \frac{rL}{t}\sum_{n=1}^{\infty} A_n \tag{22b}$$

The total heat transfer, Q_T, is the sum of Q_a and Q_f which may be written in the following form

$$\frac{LQ_T}{k_a H(T_0 - T_\infty)} = \frac{Q_a L}{k_a H(T_0 - T_\infty)} + \frac{Q_f L}{k_f t(T_0 - T_\infty)}\frac{t}{rH} \tag{23}$$

A simpler solution which disregards the transfer of heat from the slats to the trapped air may be derived by the equivalent parallel electrical network method

$$\frac{LQ_{T,1}}{k_a H(T_0 - T_\infty)} = \frac{B_a}{1 + B_a} + \frac{B_f}{1 + B_f}\frac{t}{rH} \tag{24}$$

The ratio of $\overline{\text{Nu}}^{\circ} = Q_T/Q_{T,1}$, using equations (23) and (24), is computed and presented in Table 1. The entries in Table 1 are prepared for a range of r between 0.025 and 1, fluid layer aspect ratio H/L between 0.05 and 2, and partition aspect ratio L/t between 50 and 5000. It is reasonable to assume that the external heat transfer coefficient on plate 2 is constant, at least within a small region $-(H + t) < y < (H + t)$. Since $U_a = U_f$ is a reasonable selection for most of the practical applications, it is selected for this parametric study. For the sake of brevity, data for only $B_a = 1, 2, 5$, and 10 are reported. When $B_a \to \infty$, the analytical solution degenerates into ($\lambda_n \to n\pi/L$ and $\zeta_n \to 0$) a linear one-dimensional solution.

An in-depth study of the influence of thermal radiation requires a solution of an integro-differential equation and is beyond the scope of this paper. However, the radiation interchange among internal surfaces of the cavity and exchange of radiation between plate 2 and surroundings will not influence the entries in Table 1 if the following conditions are satisfied. The gas (air) does not participate in radiation exchange, the partitions are reradiating surfaces, and the net energy, q_r, leaving surface 2 is constant (independent of y). Accordingly, the boundary condition at $x = L$, equation (2), must be replaced by

$$-k_a \cdot \frac{\partial T_a}{\partial y} = U_a(T - T_\infty) + q_r$$

Table 1 $\overline{\mathrm{Nu}}^{o} = Q_{T,2}/Q_{T,1}$ for $B_a = 1$

H/L	r	L/t=50	100	200	500	1000	5000
0.05	0.025	1.431	1.500	1.489	1.367	1.248	1.067
0.05	0.050	1.358	1.386	1.341	1.220	1.135	1.033
0.05	0.100	1.256	1.249	1.196	1.111	1.063	1.014
0.05	0.200	1.140	1.122	1.086	1.044	1.024	1.005
0.05	0.250	1.106	1.089	1.061	1.030	1.016	1.004
0.05	0.500	1.026	1.020	1.013	1.006	1.003	1.001
0.05	1.000	1.000	1.000	1.000	1.000	1.000	1.000
0.10	0.025	1.477	1.469	1.391	1.242	1.146	1.035
0.10	0.050	1.370	1.329	1.245	1.133	1.075	1.017
0.10	0.100	1.240	1.191	1.127	1.063	1.034	1.007
0.10	0.200	1.118	1.084	1.052	1.024	1.013	1.003
0.10	0.250	1.086	1.060	1.036	1.016	1.009	1.002
0.10	0.500	1.019	1.012	1.007	1.003	1.002	1.000
0.10	1.000	1.000	1.000	1.000	1.000	1.000	1.000
0.20	0.025	1.433	1.365	1.264	1.142	1.080	1.018
0.20	0.050	1.308	1.232	1.151	1.073	1.039	1.008
0.20	0.100	1.181	1.123	1.074	1.033	1.017	1.004
0.20	0.200	1.081	1.051	1.029	1.012	1.006	1.001
0.20	0.250	1.058	1.035	1.020	1.008	1.004	1.001
0.20	0.500	1.012	1.007	1.004	1.002	1.001	1.000
0.20	1.000	1.000	1.000	1.000	1.000	1.000	1.000
0.25	0.025	1.401	1.324	1.226	1.117	1.065	1.014
0.25	0.050	1.278	1.200	1.126	1.060	1.032	1.007
0.25	0.100	1.159	1.103	1.061	1.027	1.014	1.003
0.25	0.200	1.069	1.042	1.023	1.010	1.005	1.001
0.25	0.250	1.049	1.029	1.016	1.007	1.004	1.001
0.25	0.500	1.010	1.006	1.003	1.001	1.001	1.000
0.25	1.000	1.000	1.000	1.000	1.000	1.000	1.000
0.50	0.025	1.277	1.201	1.129	1.062	1.033	1.007
0.50	0.050	1.178	1.116	1.069	1.031	1.016	1.003
0.50	0.100	1.095	1.057	1.032	1.014	1.007	1.001
0.50	0.200	1.040	1.023	1.012	1.005	1.003	1.001
0.50	0.250	1.028	1.015	1.008	1.003	1.002	1.000
0.50	0.500	1.005	1.003	1.002	1.001	1.000	1.000
0.50	1.000	1.000	1.000	1.000	1.000	1.000	1.000
1.00	0.025	1.159	1.109	1.067	1.032	1.017	1.004
1.00	0.050	1.099	1.062	1.035	1.016	1.008	1.002
1.00	0.100	1.051	1.030	1.016	1.007	1.004	1.001
1.00	0.200	1.021	1.012	1.006	1.003	1.001	1.000
1.00	0.250	1.014	1.008	1.004	1.002	1.001	1.000
1.00	0.500	1.003	1.002	1.001	1.000	1.000	1.000
1.00	1.000	1.000	1.000	1.000	1.000	1.000	1.000
2.00	0.025	1.082	1.056	1.034	1.016	1.008	1.002
2.00	0.050	1.051	1.031	1.018	1.008	1.004	1.001
2.00	0.100	1.026	1.015	1.008	1.003	1.002	1.000
2.00	0.200	1.011	1.006	1.003	1.001	1.001	1.000
2.00	0.250	1.007	1.004	1.002	1.001	1.000	1.000
2.00	0.500	1.001	1.001	1.000	1.000	1.000	1.000
2.00	1.000	1.000	1.000	1.000	1.000	1.000	1.000

Table 1 $\overline{\mathrm{Nu}}^{o} = Q_{T,2}/Q_{T,1}$ for $B_a = 2$

H/L	r	L/t=50	100	200	500	1000	5000
0.05	0.025	1.637	1.760	1.743	1.536	1.348	1.090
0.05	0.050	1.499	1.544	1.476	1.297	1.178	1.042
0.05	0.100	1.328	1.319	1.249	1.138	1.078	1.017
0.05	0.200	1.162	1.140	1.099	1.051	1.028	1.006
0.05	0.250	1.118	1.099	1.068	1.034	1.018	1.004
0.05	0.500	1.026	1.020	1.013	1.006	1.003	1.001
0.05	1.000	1.000	1.000	1.000	1.000	1.000	1.000
0.10	0.025	1.715	1.706	1.574	1.339	1.199	1.046
0.10	0.050	1.517	1.457	1.332	1.175	1.097	1.021
0.10	0.100	1.306	1.242	1.160	1.077	1.042	1.009
0.10	0.200	1.136	1.097	1.060	1.027	1.014	1.003
0.10	0.250	1.096	1.066	1.040	1.018	1.010	1.002
0.10	0.500	1.019	1.012	1.007	1.003	1.002	1.000
0.10	1.000	1.000	1.000	1.000	1.000	1.000	1.000
0.20	0.025	1.639	1.531	1.373	1.193	1.106	1.023
0.20	0.050	1.422	1.313	1.200	1.095	1.051	1.011
0.20	0.100	1.227	1.153	1.091	1.041	1.021	1.004
0.20	0.200	1.092	1.058	1.033	1.014	1.007	1.002
0.20	0.250	1.063	1.039	1.022	1.009	1.005	1.001
0.20	0.500	1.012	1.007	1.004	1.002	1.001	1.000
0.20	1.000	1.000	1.000	1.000	1.000	1.000	1.000
0.25	0.025	1.587	1.465	1.315	1.158	1.086	1.019
0.25	0.050	1.377	1.268	1.166	1.077	1.041	1.009
0.25	0.100	1.198	1.128	1.075	1.033	1.017	1.004
0.25	0.200	1.079	1.048	1.027	1.011	1.006	1.001
0.25	0.250	1.054	1.032	1.018	1.008	1.004	1.001
0.25	0.500	1.010	1.006	1.003	1.001	1.001	1.000
0.25	1.000	1.000	1.000	1.000	1.000	1.000	1.000
0.50	0.025	1.392	1.279	1.175	1.082	1.044	1.009
0.50	0.050	1.236	1.152	1.089	1.040	1.021	1.004
0.50	0.100	1.117	1.070	1.039	1.017	1.009	1.002
0.50	0.200	1.045	1.026	1.014	1.006	1.003	1.001
0.50	0.250	1.030	1.017	1.009	1.004	1.002	1.000
0.50	0.500	1.005	1.003	1.002	1.001	1.000	1.000
0.50	1.000	1.000	1.000	1.000	1.000	1.000	1.000
1.00	0.025	1.220	1.149	1.091	1.042	1.022	1.005
1.00	0.050	1.130	1.080	1.046	1.020	1.010	1.002
1.00	0.100	1.063	1.037	1.020	1.008	1.004	1.001
1.00	0.200	1.024	1.013	1.007	1.003	1.001	1.000
1.00	0.250	1.016	1.009	1.005	1.002	1.001	1.000
1.00	0.500	1.003	1.002	1.001	1.000	1.000	1.000
1.00	1.000	1.000	1.000	1.000	1.000	1.000	1.000
2.00	0.025	1.114	1.076	1.046	1.021	1.011	1.002
2.00	0.050	1.067	1.041	1.023	1.010	1.005	1.001
2.00	0.100	1.032	1.019	1.010	1.004	1.002	1.000
2.00	0.200	1.012	1.007	1.004	1.001	1.001	1.000
2.00	0.250	1.008	1.004	1.002	1.001	1.000	1.000
2.00	0.500	1.001	1.001	1.000	1.000	1.000	1.000
2.00	1.000	1.000	1.000	1.000	1.000	1.000	1.000

$$= U_a(T - T^*_\infty)$$

where $T_\infty{}^* = T_\infty - q_r/U_a$. Therefore, throughout the calculations, $T_\infty{}^*$ instead of T_∞ must be used. While Q_T and $Q_{T,1}$ are affected by $T_\infty{}^*$, the entries in Table 1 remain unchanged.

The fin effect at the partition causes the heat flux at the base of the partition ($x = 0$) to increase and the heat flux at $x = 0$ in the two-dimensional layer to decrease. Therefore, the entries in Table 1 are a measure of departure from one-dimensionality due to net fin effect. According to Table 1, the fin effect is negligible when $B_a \to 0$, $B_a \to \infty$, $H/L \to \infty$, and $r \to 1$. The largest increase in heat flux is observed for B_a in the neighborhood of 5. As $H/L \to 0$, $\overline{\mathrm{Nu}}^{o}$ approaches unity if H/t remains constant. The value of $H/t = (L/t)\cdot(H/L)$ for a few entries in Table 1 is small for some applications. Moreover, it should be noted that even for a small H/t the quasi-one-dimensional criterion is satisfied (see Appendix). According to entries in Table 1, when the two-dimensional region is air and the partition is nonmetallic, the departure from one-dimensionality may exceed 25 percent for certain variables. The high thermal conductivity partitions cause a larger departure from one-dimensionality. Therefore, the one-dimensional solution defined by equation (24) is generally satisfactory except for small values of r and H/L, and $L/t < 1000$.

The computations were carried out on the IBM 370/155 digital computer. The total computation time, using a double precision code, for one value of B_a and 500 eigenvalues, was 15 min.

References

1 Batchelor, G. K., "Heat Transfer by Free Convection Across a Closed Cavity between Vertical Boundaries at Different Temperatures," *Quarterly of Applied Mathematics*, Vol. 12, No. 3, 1954, pp. 209–233.

2 Davis, G. D., "Laminar Natural Convection in an Enclosed Rectangular Cavity," *International Journal of Heat and Mass Transfer*, Vol. 11, 1968, pp. 1675–16.

3 Yin, S. H., Wang, T. Y., and Chen, K., "Natural Convection in an Air Layer Enclosed within Rectangular Cavities," *International Journal of Heat and Mass Transfer*, Vol. 21, 1978, pp. 307–315.

4 Arnold, J. N., Edwards, D. K., Catton, I., and Edward, D. K., "Experimental Investigation of Natural Convection in a Finite Rectangular Region Inclined at Various Angles from 0° to 180°," *Proceedings of the 1974 Heat Transfer and Fluid Mechanics Institute*, edited by L. R. Davis and R. E. Wilson, Stanford University Press, 1974, pp. 321–329.

5 Arnold, J. N., Edwards, D. K., and Catton, I., "Effect of Tilt and Horizontal Aspect Ratio on Natural Convection in Rectangular Honeycombs," ASME JOURNAL OF HEAT TRANSFER, Vol. 99, 1977, pp. 120–122.

6 Hollands, K. G. T., "Natural Convection in Horizontal Thin-Walled Honeycomb Panels," ASME JOURNAL OF HEAT TRANSFER, Vol. 95, 1973, pp. 439–444.

7 Cane, R. L. D., Hollands, K. G. T., Raithby, G. D., Unny, T. E., "Free Convection Heat Transfer Across Inclined Honeycomb Panels," ASME JOURNAL OF HEAT TRANSFER, Vol. 99, 1977, pp. 86–91.

8 Hollands, K. G. T., Unny, T. E., Raithby, G. D., Konicel, L., "Free Convection Across Inclined Air Layers," ASME JOURNAL OF HEAT TRANSFER, Vol. 98, 1976, pp. 189–193.

9 Smart, D. R., Hollands, K. G. T., and Raithby, G. D., "Free Convection Heat Transfer Across Rectangular-Celled Diathermanous Honeycombs," ASME JOURNAL OF HEAT TRANSFER, Vol. 102, 1980, pp. 75–80.

10 Arpaci, Vedat, *Conduction Heat Transfer*, Addison-Wesley, 1966.

11 Kaplan, Wilfred, Advanced Calculus, Addison-Wesley, 1956.

APPENDIX

The partitions, Fig. 1, should be sufficiently thin so that the average temperature variation $\Delta\overline{T}$ across the partition in y-direction is small in comparison with the size of $T_0 - T_\infty$. A bound on the value of $|\Delta\overline{T}|$ can be estimated if we consider T_f not to be one-dimensional

$$\frac{L}{t}\,|\Delta\overline{T}| < \int_0^L \left|\frac{\partial T_f}{\partial y}\right|_{y=H} dx = t\left[\left|\frac{\partial T_{f,2}}{\partial x}\right|_{x=0} - \left|\frac{\partial T_{f,2}}{\partial x}\right|_{x=L}\right]$$

Table 1 $\overline{\mathrm{Nu}}^{\circ} = Q_{T,2}/Q_{T,1}$ for $B_a = 5$

H/L	r	L/t=50	100	200	500	1000	5000
0.05	0.025	1.798	1.988	1.974	1.682	1.430	1.106
0.05	0.050	1.558	1.619	1.543	1.335	1.198	1.046
0.05	0.100	1.317	1.313	1.246	1.138	1.078	1.017
0.05	0.200	1.135	1.118	1.085	1.044	1.024	1.005
0.05	0.250	1.094	1.079	1.055	1.028	1.015	1.003
0.05	0.500	1.018	1.014	1.009	1.004	1.002	1.000
0.05	1.000	1.000	1.000	1.000	1.000	1.000	1.000
0.10	0.025	1.902	1.908	1.730	1.418	1.240	1.054
0.10	0.050	1.575	1.515	1.373	1.195	1.107	1.023
0.10	0.100	1.295	1.236	1.158	1.077	1.041	1.009
0.10	0.200	1.113	1.082	1.051	1.024	1.013	1.003
0.10	0.250	1.076	1.053	1.033	1.015	1.008	1.002
0.10	0.500	1.013	1.005	1.005	1.002	1.001	1.000
0.10	1.000	1.000	1.000	1.000	1.000	1.000	1.000
0.20	0.025	1.797	1.665	1.459	1.231	1.126	1.027
0.20	0.050	1.465	1.349	1.222	1.105	1.056	1.012
0.20	0.100	1.219	1.150	1.090	1.041	1.021	1.004
0.20	0.200	1.077	1.049	1.028	1.012	1.006	1.001
0.20	0.250	1.050	1.031	1.018	1.008	1.004	1.001
0.20	0.500	1.008	1.005	1.003	1.001	1.001	1.000
0.20	1.000	1.000	1.000	1.000	1.000	1.000	1.000
0.25	0.025	1.727	1.577	1.385	1.189	1.102	1.022
0.25	0.050	1.415	1.297	1.184	1.085	1.045	1.009
0.25	0.100	1.191	1.126	1.074	1.033	1.017	1.004
0.25	0.200	1.066	1.041	1.023	1.010	1.005	1.001
0.25	0.250	1.043	1.026	1.014	1.006	1.003	1.001
0.25	0.500	1.007	1.004	1.002	1.001	1.000	1.000
0.25	1.000	1.000	1.000	1.000	1.000	1.000	1.000
0.50	0.025	1.479	1.339	1.210	1.098	1.052	1.011
0.50	0.050	1.260	1.168	1.098	1.044	1.023	1.005
0.50	0.100	1.114	1.069	1.039	1.017	1.009	1.002
0.50	0.200	1.037	1.022	1.012	1.005	1.003	1.001
0.50	0.250	1.024	1.014	1.007	1.003	1.002	1.000
0.50	0.500	1.004	1.002	1.001	1.000	1.000	1.000
0.50	1.000	1.000	1.000	1.000	1.000	1.000	1.000
1.00	0.025	1.271	1.182	1.109	1.050	1.026	1.006
1.00	0.050	1.144	1.089	1.050	1.022	1.011	1.002
1.00	0.100	1.062	1.036	1.020	1.008	1.004	1.001
1.00	0.200	1.020	1.011	1.006	1.003	1.001	1.000
1.00	0.250	1.013	1.007	1.004	1.002	1.001	1.000
1.00	0.500	1.002	1.001	1.001	1.000	1.000	1.000
1.00	1.000	1.000	1.000	1.000	1.000	1.000	1.000
2.00	0.025	1.143	1.093	1.055	1.025	1.013	1.003
2.00	0.050	1.075	1.046	1.026	1.011	1.006	1.001
2.00	0.100	1.032	1.018	1.010	1.004	1.002	1.000
2.00	0.200	1.010	1.006	1.003	1.001	1.001	1.000
2.00	0.250	1.006	1.004	1.002	1.001	1.000	1.000
2.00	0.500	1.001	1.001	1.000	1.000	1.000	1.000
2.00	1.000	1.000	1.000	1.000	1.000	1.000	1.000

Table 1 $\overline{\mathrm{Nu}}^{\circ} = Q_{T,2}/Q_{T,1}$ for $B_a = 10$

H/L	r	L/t=50	100	200	500	1000	5000
0.05	0.025	1.726	1.914	1.918	1.656	1.417	1.104
0.05	0.050	1.458	1.515	1.461	1.293	1.176	1.042
0.05	0.100	1.234	1.235	1.189	1.109	1.063	1.014
0.05	0.200	1.091	1.081	1.059	1.031	1.017	1.004
0.05	0.250	1.061	1.053	1.037	1.019	1.011	1.002
0.05	0.500	1.011	1.008	1.005	1.003	1.001	1.000
0.05	1.000	1.000	1.000	1.000	1.000	1.000	1.000
0.10	0.025	1.810	1.841	1.693	1.404	1.233	1.053
0.10	0.050	1.467	1.431	1.322	1.172	1.096	1.021
0.10	0.100	1.217	1.179	1.123	1.061	1.033	1.007
0.10	0.200	1.075	1.056	1.036	1.017	1.009	1.002
0.10	0.250	1.049	1.036	1.022	1.010	1.005	1.001
0.10	0.500	1.008	1.005	1.003	1.001	1.001	1.000
0.10	1.000	1.000	1.000	1.000	1.000	1.000	1.000
0.20	0.025	1.721	1.624	1.440	1.225	1.123	1.027
0.20	0.050	1.383	1.298	1.195	1.094	1.050	1.011
0.20	0.100	1.163	1.115	1.071	1.033	1.017	1.004
0.20	0.200	1.052	1.034	1.020	1.009	1.005	1.001
0.20	0.250	1.033	1.021	1.012	1.005	1.003	1.001
0.20	0.500	1.005	1.003	1.002	1.001	1.000	1.000
0.20	1.000	1.000	1.000	1.000	1.000	1.000	1.000
0.25	0.025	1.663	1.545	1.370	1.184	1.100	1.022
0.25	0.050	1.344	1.256	1.162	1.076	1.041	1.009
0.25	0.100	1.143	1.097	1.058	1.026	1.014	1.003
0.25	0.200	1.044	1.028	1.016	1.007	1.004	1.001
0.25	0.250	1.028	1.017	1.010	1.004	1.002	1.000
0.25	0.500	1.004	1.002	1.001	1.001	1.000	1.000
0.25	1.000	1.000	1.000	1.000	1.000	1.000	1.000
0.50	0.025	1.449	1.326	1.204	1.096	1.051	1.011
0.50	0.050	1.221	1.148	1.087	1.039	1.021	1.004
0.50	0.100	1.087	1.054	1.031	1.014	1.007	1.001
0.50	0.200	1.025	1.015	1.008	1.004	1.002	1.000
0.50	0.250	1.016	1.009	1.005	1.002	1.001	1.000
0.50	0.500	1.002	1.001	1.001	1.000	1.000	1.000
0.50	1.000	1.000	1.000	1.000	1.000	1.000	1.000
1.00	0.025	1.263	1.178	1.107	1.049	1.026	1.005
1.00	0.050	1.126	1.079	1.045	1.020	1.010	1.002
1.00	0.100	1.048	1.029	1.016	1.007	1.004	1.001
1.00	0.200	1.014	1.008	1.004	1.002	1.001	1.000
1.00	0.250	1.008	1.005	1.003	1.001	1.001	1.000
1.00	0.500	1.001	1.001	1.000	1.000	1.000	1.000
1.00	1.000	1.000	1.000	1.000	1.000	1.000	1.000
2.00	0.025	1.142	1.093	1.055	1.025	1.013	1.003
2.00	0.050	1.067	1.041	1.023	1.010	1.005	1.001
2.00	0.100	1.025	1.015	1.008	1.003	1.002	1.000
2.00	0.200	1.007	1.004	1.002	1.001	1.000	1.000
2.00	0.250	1.004	1.002	1.001	1.001	1.000	1.000
2.00	0.500	1.001	1.000	1.000	1.000	1.000	1.000
2.00	1.000	1.000	1.000	1.000	1.000	1.000	1.000

It can be noted that

$$\left|\frac{\partial T_{f,2}}{\partial x}\right|_{x=0} < \left|\frac{\partial T_{a,1}}{\partial x}\right| \text{ and } \left|\frac{\partial T_{f,2}}{\partial x}\right|_{x=L} > \left|\frac{\partial T_{f,1}}{\partial x}\right|,$$

then

$$\frac{\Delta \overline{T}}{|T_0 - T_\infty|} < \left(\frac{t}{L}\right)^2 \left[\left|\frac{LQ_{a,1}}{Hk_a(T_0 - T_\infty)}\right| - \left|\frac{LQ_{f,1}}{tk_f(T_0 - T_\infty)}\right|\right]$$

The terms in the square brackets are readily available by elementary methods, hence, the final result is

$$\frac{|\Delta \overline{T}|}{|T_0 - T_\infty|} < \left(\frac{t}{L}\right)^2 \left[\frac{B_a}{1 + B_a} - \frac{B_f}{1 + B_f}\right]$$

when $U_f = U_a$ and $k_f \to k_a$, the quantity in the square brackets will vanish and since this quantity is always less than unity, the relation

$$\frac{|\Delta \overline{T}|}{|T_0 - T_\infty|} < \left(\frac{t}{L}\right)^2$$

is used as a guideline for satisfying the quasi-one-dimensional condition in the partitions. The largest $|\Delta \overline{T}|/|T_0 - T_\infty|$ for entries in Table 1 is less than 0.0004.

Journal of Heat Transfer
Technical Notes

A Closed-Form Analytical Solution for Freezing Adjacent to a Plane Wall Cooled by Forced Convection

C. F. Hsu[1] and E. M. Sparrow[1]

Nomenclature

Bi = Biot number, hW/k
c_p = specific heat
Fo = Fourier number, $\alpha t/W^2$
h = coolant heat transfer coefficient
k = thermal conductivity
St = Stanton number, $h/\bar{u}(\rho c_p)_c$
Ste = Stefan number, $c_p(T^* - T_{bi})/\lambda$
T_b = coolant bulk temperature
T_{bi} = inlet coolant temperature
T_w = temperature at channel wall on which freezing occurs
T^* = fusion temperature
t = time
$\bar{u}$ = mean velocity of coolant
W = channel width, Fig. 1
X = dimensionless axial coordinate, x/W
x,y = coordinates, Fig. 1
α = thermal diffusivity
Δ = dimensionless layer thickness, δ/W
δ = frozen layer thickness, Fig. 1
η = transformed coordinate, equation (7)
θ = dimensionless temperature, $(T - T^*)/(T_{bi} - T^*)$
λ = latent heat of fusion
ρ = density
τ = dimensionless time, FoSte
Ω = coolant heat-capacity parameter, equation (6)

Subscripts

c = properties of coolant
properties of frozen layer are unsubscripted

Introduction

The analysis of multi-dimensional freezing on a wall that is convectively cooled from the rear has evoked recent interest because of its relevance to phase-change thermal energy storage (e.g., [1, 2]). The published solutions have involved either finite difference calculations or other numerical work. There is, however, a particular case for which a closed-form analytical solution can be obtained, subject to certain reasonable and widely accepted assumptions about the physical model. The case in point is the two-dimensional freezing on a plane wall wherein the rear face of the wall is one of the boundaries of a parallel plate channel through which a coolant passes.

A schematic diagram of the physical situation is pictured in Fig. 1. As shown there, a liquid phase-change medium at its saturation temperature T^* is contained in a space which is relatively long in the direction into and out of the plane of the figure. The space is bounded at the left by a parallel plate channel having an interplate spacing W. For times $t < 0$, the entire system is at a uniform temperature T^* and, in addition, there is no flow in the channel. Then, at $t = 0$, a coolant with an inlet temperature $T_{bi} < T^*$ is caused to flow in the channel, and freezing takes place along the wall.

Figure 1 shows an instantaneous view of the frozen layer. Owing to the rise of the bulk temperature in the streamwise direction, the thickness of the frozen layer will diminish in that direction, as portrayed in the figure. Note also that there will be no natural convection in the liquid phase-change medium since its temperature is uniform.

The closed-form solution given here should be useful in its own right as a guide to design and, in addition, it can serve as a standard of comparison against which to test approximate solution methods.

Analysis

The first step in the analysis is to write an energy balance for a control volume which spans the channel cross section and is of length dx in the flow direction. The relevant energy quantities include the enthalpy convected into and out of the control volume, the heat stored in the fluid, and the convective heat transfer from the wall to the fluid. In mathematical terms,

$$(\rho c_p)_c W(\bar{u}\partial T_b/\partial x + \partial T_b/\partial t) = h(T_w - T_b) \qquad (1)$$

where the subscript c denotes properties of the coolant fluid. As indicated in Fig. 1, both T_w and T_b are variables and are unknown. The coolant flow is assumed to be fully turbulent and hydrodynamically developed, and h will be assumed to be constant. Note that h may also encompass the transverse conductance of the wall.

For the freezing problem, two highly plausible simplifications will be made. The first is that for moderate values of the Stefan number that lie in the practical range (Ste ≤ 0.5), sensible heat effects do not materially affect the freezing-induced heat flow through the solid. The

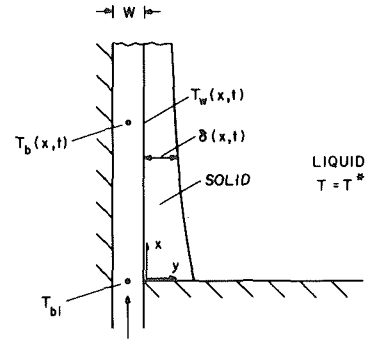

Fig. 1 Freezing on a wall that is convectively cooled from the rear

---

[1] Department of Mechanical Engineering, University of Minnesota, Minneapolis, Minn. 55455

Contributed by the Heat Transfer Division for publication in the JOURNAL OF HEAT TRANSFER. Manuscript received by the Heat Transfer Division September 12, 1980.

second is that the axial conduction through the solid is negligible compared with the transverse conduction, a condition akin to the well-established boundary layer model. This condition should be fully satisfied for channels that are not too short.

A consequence of the foregoing simplifications is that at any x

$$\partial T/\partial y = (T^* - T_w)/\delta \tag{2}$$

and, in addition,

$$h(T_w - T_b) = k(\partial T/\partial y) = \rho\lambda(\partial\delta/\partial t) \tag{3}$$

The solution task involves the three coupled partial differential equations (1) and (3) which contain T_b, T_w, and δ as unknowns and x and t as independent variables. Dimensionless variables are first introduced as

$$X = x/W,\ \Delta = \delta/W,\ \theta = (T - T^*)/(T_{bi} - T^*),\ \tau = \text{FoSte} \tag{4}$$

where

$$\text{Fo} = \alpha t/W^2, \quad \text{Ste} = c_p(T^* - T_{bi})/\lambda \tag{5}$$

Unsubscripted properties correspond to the solid. The dimensionless parameters which are needed to characterize the solution are

$$\text{St} = h/\bar{u}(\rho c_p)_c,\ \text{Bi} = hW/k,\ \Omega = ((\rho c_p)_c/\rho c_p)(\text{Ste}/\text{Bi}) \tag{6}$$

Care should be taken not to confuse the Stefan number Ste and the Stanton number St.

In addition to the dimensionless variables and parameters, a major step forward toward the solution is accomplished by a change of variables from X,τ to X,η such that

$$X = X, \quad \eta = \tau - (\text{St}\Omega)X \tag{7}$$

Application of the change of variables to equations (1) and (3) yields

$$(\partial\theta_b/\partial X)/\text{St} = \theta_w - \theta_b \tag{8}$$

$$\text{Bi}(\theta_b - \theta_w) = \theta_w/\Delta = \partial\Delta/\partial\eta \tag{9}$$

where, by dint of the $-(\text{St}\Omega)X$ part of η, the storage term has been eliminated from equation (8). Then, upon rearrangement of equation (9)

$$\theta_w = \tfrac{1}{2}(\partial\Delta^2/\partial\eta), \quad \theta_b = \tfrac{1}{2}(\partial\Delta^2/\partial\eta) + (1/\text{Bi})(\partial\Delta/\partial\eta) \tag{10}$$

By employing equations (9) and (10), θ_w and θ_b can be eliminated from equation (8) in favor of Δ. The result of these eliminations yields an equation of the form $\partial/\partial\eta(\ldots) = 0$, which, after integration, becomes

$$\frac{1}{\text{St}}\frac{\partial}{\partial X}\left[\frac{\Delta^2}{2} + \frac{\Delta}{\text{Bi}}\right] + \frac{\Delta}{\text{Bi}} = F(X) \tag{11}$$

where $F(X)$ is a function of integration. Thus, although Δ and $\partial\Delta/\partial X$ are functions of η as well as of X, equation (11) states that the left-hand side is independent of η. Thus, it can be evaluated at any convenient value of η, i.e., where Δ and $\partial\Delta/\partial X$ are known.

It will now be shown that $\Delta = \partial\Delta/\partial X = 0$ at $\eta = 0$, so that $F(X) = 0$. It can easily be verified that $\eta = 0$ corresponds to an axial station $x = \bar{u}t$. If account is taken of the slug-flow model implied by equation (1), then $x = \bar{u}t$ corresponds to the penetration distance of the coolant into the channel at time t. Since there is no freezing for $x > \bar{u}t$ in the absence of axial conduction, the foregoing assertion is substantiated.

With $F(X) = 0$, equation (11) can be integrated to give

$$\Delta/\text{St} + \ln\Delta/\text{BiSt} + X/\text{Bi} = G(\eta) \tag{12}$$

where $G(\eta)$, the function of integration, states that the left-hand side is independent of X. It is especially convenient to evaluate the left-hand side at $X = 0$ and, thereby, to find G. The solution for Δ at $X = 0$ is denoted by Δ_0. It is found by setting $\theta_b = 1$ in equation (10) and integrating, with the end result

$$\Delta_0 = -1/\text{Bi} + ((1/\text{Bi})^2 + 2\eta)^{1/2} \tag{13}$$

Once G has been found, the closed-form solution for Δ follows from (12) as

$$\Delta + \ln\Delta/\text{Bi} = -(\text{St}/\text{Bi})X + \Delta_0 + \ln\Delta_0/\text{Bi} \tag{14}$$

Furthermore, considering equations (10), it is seen that the solutions for θ_w and θ_b are obtained by differentiating equation (14), so that

$$\theta_w = \Delta(\partial\Delta_0/\partial\eta)g(\Delta_0)/g(\Delta), \quad \theta_b = \Delta(\partial\Delta_0/\partial\eta)g(\Delta_0) \tag{15}$$

where

$$g(\psi) = 1 + 1/\text{Bi}\psi, \quad \partial\Delta_0/\partial\eta = ((1/\text{Bi})^2 + 2\eta)^{-1/2} \tag{16}$$

Equations (14) and (15) convey the closed-form solutions for Δ, θ_w, and θ_b. The only visible parameters are the Stanton and Biot numbers, St and Bi, but the Ω parameter is embedded in the η variable.

If E denotes the energy extracted from the freezing solid during a time interval $t = 0$ to $t = t$ and over a length of channel from $x = 0$ to $x = x$, then

$$E/\rho\lambda W^2 = \int_0^X \Delta dX \tag{17}$$

which requires numerical integration for its evaluation.

Results and Discussion

In view of the space limitations inherent in a Note, only illustrative results will be presented in order to identify trends. It should be noted, however, that the availability of the closed-form algebraic solution, as detailed in the foregoing, enables results to be readily obtained for any values of the three parameters St, Bi, and Ω.

Figure 2 deals with parameter ranges representative of turbulent gas flows (e.g., air) as coolants. The figure is subdivided into two panels, respectively for Bi = 2 and 20. In each panel, for each of a succession of parametric times τ, the frozen layer thickness Δ is plotted as a function of the distance X along the channel (τ, Δ, and X are dimensionless quantities defined in equation (4)). The solid and dashed curves correspond respectively to Stanton numbers St = 0.002 and 0.004.

It is relevant to note that the parameter Ω does not appear in Fig. 2. The absence of Ω can be traced back to its role as a measure of the heat capacity of the coolant. On physical grounds, it can be expected that the heat capacity of a gaseous coolant will play a negligible role. To verify this expectation numerically, results were obtained for Ω values representative of the conditions for the left-hand and right-hand panels, $\Omega = 0.0002$ and 0.00002, respectively, and for $\Omega = 0$ as a comparison case. Within the scale of the figure, the Δ versus X results for $\Omega \neq 0$ and $\Omega = 0$ are coincident.

By inspecting the figure, it is seen that for the conditions of the left-hand panel, the frozen layer thickness decreases in the flow direction at any fixed time. Whereas this same trend is in evidence in the right-hand panel, the extent of the decrease is much smaller. The decrease of the layer thickness is a reflection of the increase of the

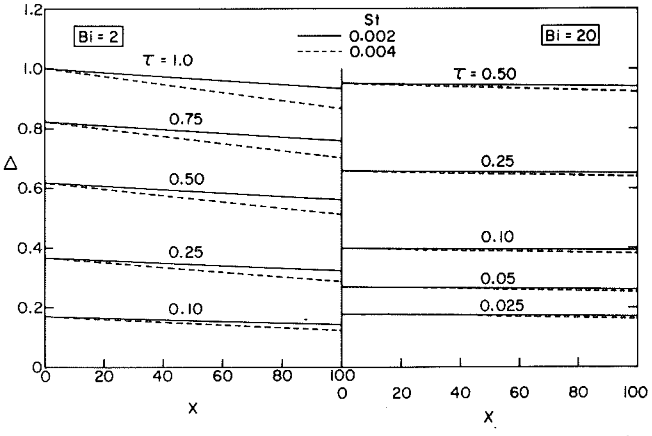

Fig. 2 Distributions of frozen layer thickness for conditions representative of turbulent gas flows as coolants

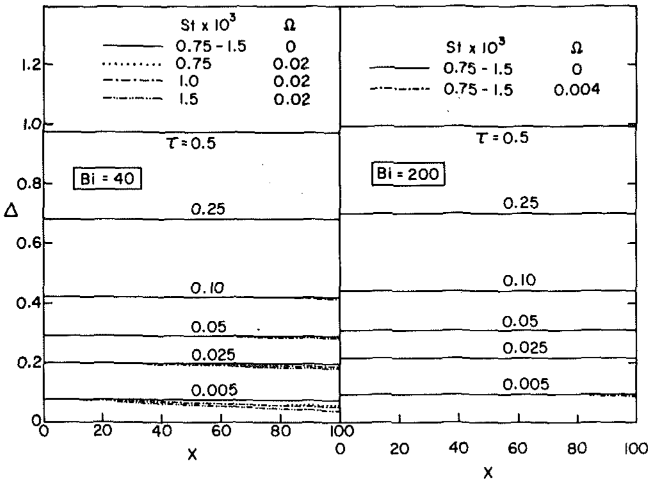

Fig. 3 Distributions of frozen layer thickness for conditions representative of turbulent liquid flows as coolants

coolant temperature in the flow direction. The coolant temperature rise becomes larger at lower Reynolds numbers (i.e., larger Stanton numbers), and this is why the dashed curves drop off to a greater extent than do the solid curves.

At larger Biot numbers (right-hand panel), the thermal resistance of the frozen layer controls the rate of heat transfer, and this diminishes the impact of the coolant temperature rise on the freezing rate. Consequently, there is only a slight dropoff in the frozen layer thickness in the streamwise direction.

Attention is now turned to Fig. 3, where results are plotted for the case in which the coolant is a liquid such as water and the flow is turbulent. The structure of the figure is similar to that of Fig. 2. For the conditions depicted in the left-hand panel, the coolant heat capacity parameter Ω is ~ 0.02, while an appropriate Ω value for the right-hand panel is ~ 0.004. Results for these Ω values are shown in the respective panels along with those for which the coolant heat capacity is neglected ($\Omega = 0$).

The figure shows that only for very short times does the coolant heat capacity play a role, and that role is heightened at higher Stanton numbers (i.e., lower Reynolds numbers). However, as the freezing process proceeds (i.e., at larger times), the heat capacity effect wanes. Note also that at higher Biot numbers, the dominance of the solid-side resistance blunts the heat capacity effect, even at early times.

It may also be noted from the figure that aside from the aforementioned early-time heat capacity effect, the frozen layer thickness is nearly independent of x. This behavior is due to the relatively slight streamwise temperature rise experienced by the liquid coolant and to the dominance of the solid- side thermal resistance. With increasing Biot number, the results tend to approach those of the one-dimensional Stefan solution, which gives $\Delta = (2\tau)^{1/2}$.

Acknowledgment

This research was performed under the auspices of the U.S. Department of Energy (DOE/DE-ACO2-79ER10343).

References

1 Green, T. F., and Vliet, G. C., "Thermal Response of a Latent Heat Storage Unit: An Analytical and Experimental Investigation," ASME Paper No. 79-HT-36, 1979.

2 Shamsundar, N., and Srinivasan, R., "Effectiveness-NTU Charts for Latent Heat Storage Units," ASME *Journal of Solar Energy Engineering*, Vol. 102, No. 4, 1980, pp. 263–271.

Phase Change around a Circular Cylinder

V. J. Lunardini[1]

Nomenclature

A = area of phase change interface
c = mass specific heat
k = thermal conductivity
ℓ = latent heat of fusion, mass basis
q = surface heat transfer rate
$q^* = \dfrac{qc_1}{2\pi k_1 \ell}$, dimensionless heat transfer
r = radial coordinate
r_0 = radius of cylinder
R = radius of phase change location
$S_T = \begin{cases} c_1(T_f - T_s)/\ell \text{ freeze} \\ c_1(T_s - T_f)/\ell \text{ thaw} \end{cases}$
t = time
T = temperature
x_ℓ = volumetric water content of soil
α = thermal diffusivity
$\alpha_{12} = \alpha_1/\alpha_2$
$\beta = R/r_0$ dimensionless phase change position
δ = temperature penetration radius
$\phi = \dfrac{T_0 - T_f}{T_f - T_s}$ superheat or subcooling parameter
$\Omega = \delta/R$
ρ = density
$\tau = \dfrac{\alpha_1 t}{r_0^2} S_T$, dimensionless time

Subscripts

0 = initial
1 = region 1
2 = region 2
f = fusion of frozen
s = surface
t = thawed

Introduction

The question of freezing and thawing of soil systems is important for engineering design in permafrost regions. Thus solutions to conduction problems with moving boundaries are sought for application to analysis and synthesis. Interest in these problems has also been stimulated by the requirements of latent heat storage in solar energy systems.

The homogeneous, semi-infinite medium, initially at a temperature different than the fusion value, has a general solution for a step change of surface temperature, Neumann [1], generalized in Carslaw and Jaeger [2]. Recently, Lunardini and Varotta [3] derived an accurate, but approximate, solution to this problem by using the heat balance integral technique. Yuen [14] also used the heat balance integral with collocation to generate a less accurate approximation.

Unfortunately, there are no general solutions for phase change in cylindrical coordinates. Since this is an important geometry for practical applications a significant effort has been expended upon approximate and numerical solutions. The geometry of the system, Fig. 1, is that of a circular cylinder surrounded by an infinite, homogeneous, medium. Tien and Churchill [4] numerically solved the freezing problem using interpolation near the phase change nodes. More recently, Sparrow, et al. [5] examined the same problem for

---

[1] U.S. Army Cold Regions Research and Engineering Laboratory, Hanover, N.H.

Contributed by the Heat Transfer Division and presented at the 19th AIChE/ASME Heat Transfer Conference, Orlando, Fla., July 27–30, 1980. Revised manuscript received by the Heat Transfer Division December 15, 1980.

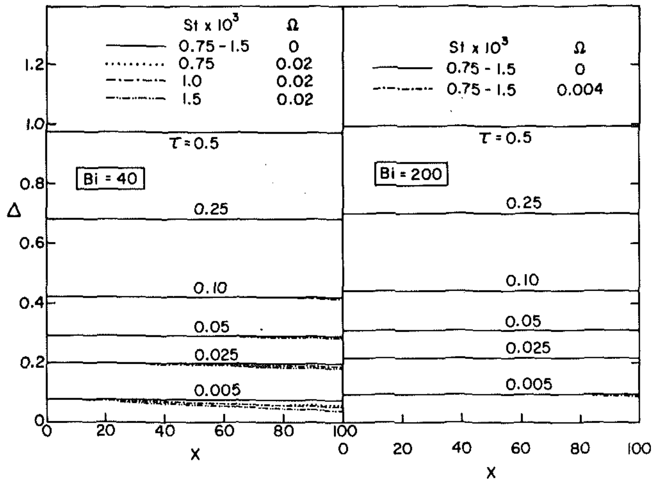

Fig. 3 **Distributions of frozen layer thickness for conditions representative of turbulent liquid flows as coolants**

coolant temperature in the flow direction. The coolant temperature rise becomes larger at lower Reynolds numbers (i.e., larger Stanton numbers), and this is why the dashed curves drop off to a greater extent than do the solid curves.

At larger Biot numbers (right-hand panel), the thermal resistance of the frozen layer controls the rate of heat transfer, and this diminishes the impact of the coolant temperature rise on the freezing rate. Consequently, there is only a slight dropoff in the frozen layer thickness in the streamwise direction.

Attention is now turned to Fig. 3, where results are plotted for the case in which the coolant is a liquid such as water and the flow is turbulent. The structure of the figure is similar to that of Fig. 2. For the conditions depicted in the left-hand panel, the coolant heat capacity parameter Ω is ~ 0.02, while an appropriate Ω value for the right-hand panel is ~ 0.004. Results for these Ω values are shown in the respective panels along with those for which the coolant heat capacity is neglected ($\Omega = 0$).

The figure shows that only for very short times does the coolant heat capacity play a role, and that role is heightened at higher Stanton numbers (i.e., lower Reynolds numbers). However, as the freezing process proceeds (i.e., at larger times), the heat capacity effect wanes. Note also that at higher Biot numbers, the dominance of the solid-side resistance blunts the heat capacity effect, even at early times.

It may also be noted from the figure that aside from the aforementioned early-time heat capacity effect, the frozen layer thickness is nearly independent of x. This behavior is due to the relatively slight streamwise temperature rise experienced by the liquid coolant and to the dominance of the solid- side thermal resistance. With increasing Biot number, the results tend to approach those of the one-dimensional Stefan solution, which gives $\Delta = (2\tau)^{1/2}$.

Acknowledgment

This research was performed under the auspices of the U.S. Department of Energy (DOE/DE-ACO2-79ER10343).

References

1 Green, T. F., and Vliet, G. C., "Thermal Response of a Latent Heat Storage Unit: An Analytical and Experimental Investigation," ASME Paper No. 79-HT-36, 1979.

2 Shamsundar, N., and Srinivasan, R., "Effectiveness-NTU Charts for Latent Heat Storage Units," ASME *Journal of Solar Energy Engineering*, Vol. 102, No. 4, 1980, pp. 263–271.

Phase Change around a Circular Cylinder

V. J. Lunardini[1]

Nomenclature

A = area of phase change interface
c = mass specific heat
k = thermal conductivity
ℓ = latent heat of fusion, mass basis
q = surface heat transfer rate
$q^* = \dfrac{qc_1}{2\pi k_1 \ell}$, dimensionless heat transfer
r = radial coordinate
r_0 = radius of cylinder
R = radius of phase change location
$S_T = \begin{cases} c_1(T_f - T_s)/\ell \text{ freeze} \\ c_1(T_s - T_f)/\ell \text{ thaw} \end{cases}$
t = time
T = temperature
x_ℓ = volumetric water content of soil
α = thermal diffusivity
$\alpha_{12} = \alpha_1/\alpha_2$
$\beta = R/r_0$ dimensionless phase change position
δ = temperature penetration radius
$\phi = \dfrac{T_0 - T_f}{T_f - T_s}$ superheat or subcooling parameter
$\Omega = \delta/R$
ρ = density
$\tau = \dfrac{\alpha_1 t}{r_0^2} S_T$, dimensionless time

Subscripts

0 = initial
1 = region 1
2 = region 2
f = fusion of frozen
s = surface
t = thawed

Introduction

The question of freezing and thawing of soil systems is important for engineering design in permafrost regions. Thus solutions to conduction problems with moving boundaries are sought for application to analysis and synthesis. Interest in these problems has also been stimulated by the requirements of latent heat storage in solar energy systems.

The homogeneous, semi-infinite medium, initially at a temperature different than the fusion value, has a general solution for a step change of surface temperature, Neumann [1], generalized in Carslaw and Jaeger [2]. Recently, Lunardini and Varotta [3] derived an accurate, but approximate, solution to this problem by using the heat balance integral technique. Yuen [14] also used the heat balance integral with collocation to generate a less accurate approximation.

Unfortunately, there are no general solutions for phase change in cylindrical coordinates. Since this is an important geometry for practical applications a significant effort has been expended upon approximate and numerical solutions. The geometry of the system, Fig. 1, is that of a circular cylinder surrounded by an infinite, homogeneous, medium. Tien and Churchill [4] numerically solved the freezing problem using interpolation near the phase change nodes. More recently, Sparrow, et al. [5] examined the same problem for

---

[1] U.S. Army Cold Regions Research and Engineering Laboratory, Hanover, N.H.

Contributed by the Heat Transfer Division and presented at the 19th AIChE/ASME Heat Transfer Conference, Orlando, Fla., July 27–30, 1980. Revised manuscript received by the Heat Transfer Division December 15, 1980.

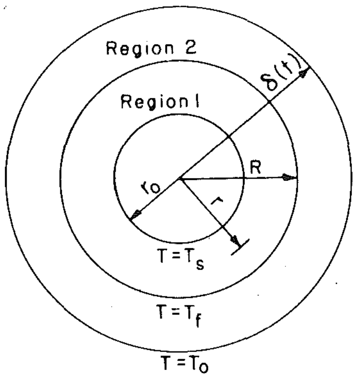

Fig. 1 Geometry of cylindrical system

melting via a finite difference solution with phase boundary immobilization although the properties of the two phases were assumed equal. Both used the plane (Neumann) solution to start the calculation and both illustrate the usual problem of elaborate programming necessary for numerical solutions to Stefan problems. Bell [6] used the heat balance integral method, with an arbitrary number of regions, to solve the solidification problem when the initial temperature was at the fusion value. The technique simplifies the choice of the assumed temperature profile, but introduces a set of simultaneous, first order differential equations to solve. This tends to negate the basic simplicity of the heat balance integral technique and the single phase problem is not a good test of the computational complexity.

The heat balance integral method is used here to reduce the numerical computation to an elementary form. Solutions can easily be generated for a range of parameters, when freezing or thawing occurs.

Approximate Solution

The derivation of the heat balance integral method and applications have been described previously, Goodman [7, 8]. The equations for a melting system are,

$$\frac{\partial}{\partial r}\left(r\frac{\partial T_1}{\partial r}\right)=\frac{r}{\alpha_1}\frac{\partial T_1}{\partial t} \tag{1}$$

$$T_1(R,t)=T_f \tag{1a}$$

$$T_1(r_0,t)=T_s \tag{1b}$$

$$\frac{\partial}{\partial r}\left(r\frac{\partial T_2}{\partial r}\right)=\frac{r}{\alpha_2}\frac{\partial T_2}{\partial t} \tag{2}$$

$$T_2(R,t)=T_f \tag{2a}$$

$$T_2(\delta,t)=T_0 \tag{2b}$$

$$\frac{\partial T_2(\delta,t)}{\partial r}=0 \tag{2c}$$

The depth of penetration of the temperature wave is $\delta(t)$ and beyond this radius the temperature is T_0. The energy balance at the phase change interface is

$$-k_1\frac{\partial T_1(R,t)}{\partial r}+k_2\frac{\partial T_2(R,t)}{\partial r}=\rho_1\ell\frac{dR}{dt} \tag{3}$$

The solution method consists of choosing approximations for the temperatures which will satisfy all of the conditions in terms of the unknown parameters $\delta(t)$ and $R(t)$. Lardner and Pohle [9] noted that a logarithmic temperature approximation is most appropriate when the area is varying with r. An approximation for T_1 that satisfies equations (1a,b) is

$$T_1=T_s-\frac{(T_s-T_f)\ell n\left(\dfrac{r}{r_0}\right)}{\ell n\dfrac{R}{r_0}} \tag{4}$$

A similar approximation for T_2 that satisfies equations (2a–c) is

$$T_2=T_0+(T_f-T_0)\frac{\delta-r}{\delta-R}\frac{\ell n\left(\dfrac{r}{\delta}\right)}{\ell n\left(\dfrac{R}{\delta}\right)} \tag{5}$$

Equation (4) exhibits the correct analytical form for the quasi-steady solution of equation (1). This is valid as $S_T \rightarrow 0$, contributes to the accuracy of the results, and suggests a method to choose the temperature approximation.

Equations (1–5) lead to the following two coupled equations, written in nondimensional form.

$$\alpha_{12}S_T\frac{dF}{d\tau}=\frac{1}{\Omega-1}+\frac{1}{\ell n\Omega} \tag{6}$$

$$\left[S_T\left(\frac{\beta}{2\ell n\beta}-\frac{\beta^2-1}{4\beta(\ell n\beta)^2}\right)+\beta\right]\frac{d\beta}{d\tau}=\frac{1}{\ell n\beta}-k_{21}\phi\left(\frac{1}{\Omega-1}+\frac{1}{\ell n\Omega}\right) \tag{7}$$

$$F(\beta,\Omega)=\frac{\beta^2}{2}+\frac{\beta^2}{(1-\Omega)\ell n\Omega}\left[-\frac{\Omega}{4}(\Omega^2-1)+\left(\frac{\Omega}{2}-\frac{1}{3}\right)\ell n\Omega+\frac{1}{9}(\Omega^3-1)\right] \tag{8}$$

The instantaneous heat flow from the cylinder is given by

$$q=-k_1A\frac{\partial T_1(r_0,t)}{\partial r} \tag{9}$$

Using equation (4), the nondimensional heat flow is

$$q^*=\frac{qc_1}{2\pi k_1\ell}=\frac{S_T}{\ell n\beta} \tag{10}$$

Solution and Application to Soil Systems

Equations (6–8) were solved with a fourth order Runge-Kutta, predictor-corrector technique. Since the problem is initially singular at the origin, the Neumann solution was used to start the solution. Sparrow, et al. [5] solved this problem numerically, with $\alpha_{12}=k_{12}=1$, for a range of S_T and ϕ. The results of the much simpler method presented here are within 5 percent of these values. The completely different numerical solution of Tien and Churchill [4] is also in close agreement as can be seen in Fig. 2. The comparison of the heat flow from the cylinder can be seen from Fig. 3. The calculations have been generalized for a range of α_{12}, k_{12}, appropriate for soil systems, and are presented in Lunardini [13]. The property ratios for soils can be expressed as a function of x_ℓ, the volumetric fraction of water in the soil. These property ratios can be obtained using the method of Lunardini and Varotta [3] and references [10–12]. For $x_\ell=0$, $\alpha_{12}=k_{12}=1.0$. The curves are valid for any medium with the same property ratios.

For a soil the value of $x_\ell=0$ denotes zero latent heat and no phase change. However, in general, the $x_\ell=0$ curves could characterize any material with constant thermal properties and arbitrary latent heat. At the other extreme, when $x_\ell=1$, the case of pure water occurs and the effects of convection should be considered. For a soil, even if x_ℓ is quite high, the nature of the soil solid skeleton minimizes free convection distortions.

Discussion

The heat balance integral method reduces the partial differential equations of heat flow to ordinary differential equations. The numerical solution is then greatly simplified and can be carried out with elementary computer systems and algorithms. The accuracy is related to the choice of the temperature approximations. For the cylindrical system it has been shown that the results are essentially identical to two different, complete, numerical solutions. The heat balance integral method is practical for two phase, Stefan problems.

The effect of the property ratios is quite significant. For the same values of ϕ, S_T, as α_{21}, k_{21} increase, the thaw rate increases and the freeze rate decreases. For the same values of x_ℓ, ϕ, S_T, the freeze rate will exceed the thaw rate at any time, excepting the case for $x_\ell=0$.

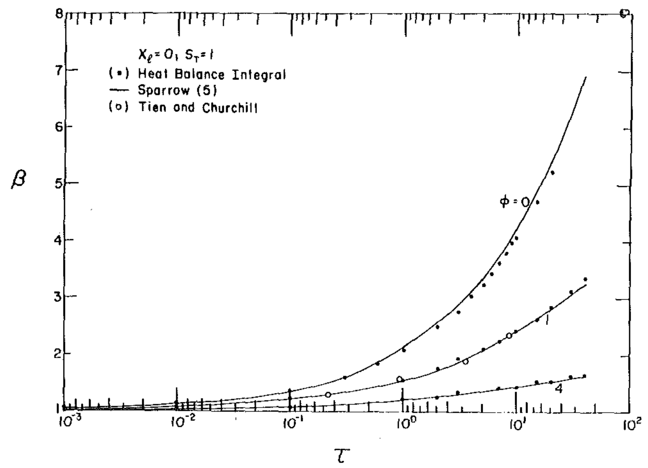

Fig. 2 Accuracy of phase change radius, $S_T = 1.0$, $\alpha_{12} = k_{12} = 1.0$

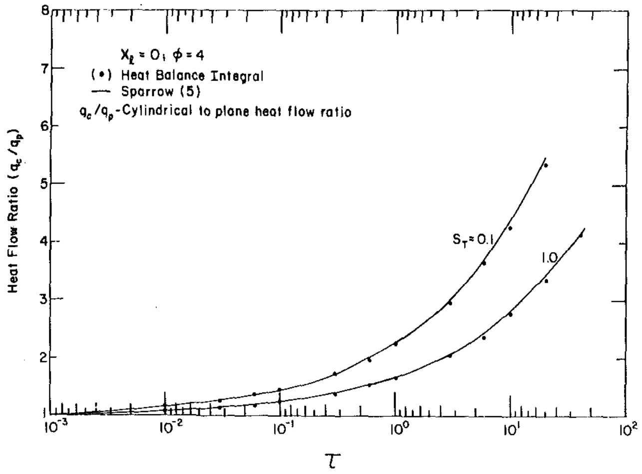

Fig. 3 Accuracy of cylinder heat flow, $\alpha_{12} = k_{12} = 1.0$, $\phi = 4.0$

References

1 Neumann, F., Lectures given in the 1860's C. F. Riemann-Weber, *Die partiellen Differential-gleichungen Physik*, 5th ed., Vol. 2, p. 121.

2 Carslaw, H. S., and Jaeger, J. C., *Conduction of Heat in Solids*, 2nd ed., Clarendon Press, Oxford, 1959.

3 Lunardini, V., and Varotta, R., "Approximate Solution to Neumann Problem for Soil Systems,"ASME *Journal of Energy Resources Technology*, Vol. 103, No. 1, 1981, pp. 76–81.

4 Tien, L. C., and Churchill, S. W., "Freezing Front Motion and Heat Transfer Outside an Infinite, Isothermal Cylinder," *AIChE Journal*, Vol. 11, No. 5, 1965, pp. 790–793.

5 Sparrow, E. M., Ramadhyani, S., and Patankar, S. V., "Effect of Subcooling on Cylindrical Melting," ASME JOURNAL OF HEAT TRANSFER, Vol. 100, No. 3, 1978, pp. 395–402.

6 Bell, G. E., "Solidification of a Liquid About a Cylindrical Pipe," *International Journal of Heat Mass Transfer*, Vol. 22, 1979, pp. 1681–1686.

7 Goodman, T. R., "The Heat-Balance Integral and Its Application to Problems Involving a Change of Phase," *Trans. ASME*, Vol. 80, 1958, pp. 335–342.

8 Goodman, T. R., "Application of Integral Methods to Transient Nonlinear Heat Transfer," *Advances in Heat Transfer*, Vol. 1, T. F. Irvine and J. P. Hartnett, Eds., Academic Press, New York, 1964, pp. 52–122.

9 Lardner, T. J., and Pohle, F. V., "Application of the Heat Balance Integral to Problems of Cylindrical Geometry," *Trans. ASME*, Vol. 83, No. 2, 1961, pp. 310–312.

10 Gold, L. W., and Lachenbruch, A. H., "Thermal Conditions in Permafrost—A Review of North American Literature," *Proceedings of Second International Permafrost Conference*, National Academy of Science, 1973, pp. 3–25.

11 Kersten, M. S., "Thermal Properties of Soils," University of Minnesota Experiment Station, Bulletin No. 28, 1949, 227 pages.

12 Lunardini, V. J., "Presentation of Some Thermal Properties of Soil Systems," Canadian Society of Mechanical Engineers, paper 71-CSME-38, *Engineering Institute of Canada Meeting*, 1971, Quebec City.

13 Lunardini, V. J., "Phase Change Around a Circular Pipe," CRREL Rept. 80-27, Dec. 1980.

14 Yuen, W. W., "Application of the Heat Balance Integral to Melting Problems with Initial Subcooling," *International Journal of Heat Mass Transfer*, Vol. 23, 1980, pp. 1157–1160.

Heat Conduction through "Yin-Yang" Bodies

John H. Lienhard[1]

Consider steady two-dimensional heat conduction through bodies whose boundaries are either maintained at one of two temperatures, or are insulated. If such a body has a geometrical axis of symmetry; if one piece of the left side is insulated and the other piece of it is held at a temperature, T_1; if the right side is either insulated or isothermal at T_2, with the positions of the insulated and isothermal segments inverted from those on the left; then the shape factor, S, is unity.

To see why this is true, consider two such cases in Figs. 1(a) and 1(b). The symmetry specified above obviously requires that the isothermal lines are mirror images of the adiabatic lines. The number of isothermal increments will therefore match the number of adiabatic increments so $S = 1$. We shall refer to such shapes as *Yin-Yang*[2] figures. Actually any Yin-Yang figure must be the result of conformally mapping Fig. 1(a). Accordingly it is sufficient that it be simply-connected with only one piece of its boundary at each temperature. It can also be doubly-connected (since Fig. 1(a) can be mapped into an infinite region with a single hole in it) as long as the point at infinity is not singular. Two other restrictions are that the thermal conductivity, k, must be constant, and there should be no heat sources.

Nine more Yin-Yang figures are presented in Fig. 2: (a) is a semi-infinite strip; (b), (c), and (g) have double axes of Yin-Yang symmetry although (b) and (g) are infinite in extent and (c) is finite; (d), (f), and (i) are semi-infinite bodies, (e) and (h) are finite; however, (i) can be viewed as the inverted limit of case (h) as the piece of boundary at T_1 is shrunk. Each of these situations would be hard to deal with analytically or numerically. Since $S = 1$ in each case we can express the heat transfer, Q (W/m), as simply

$$Q = k(T_1 - T_2)$$

The number of possibilities is, of course, unlimited, and they include many potentially useful configurations. Anyone doing a two-dimensional heat conduction calculation should first look at it to see if it resolves into a Yin-Yang figure. If it does, Q can be obtained without calculation.

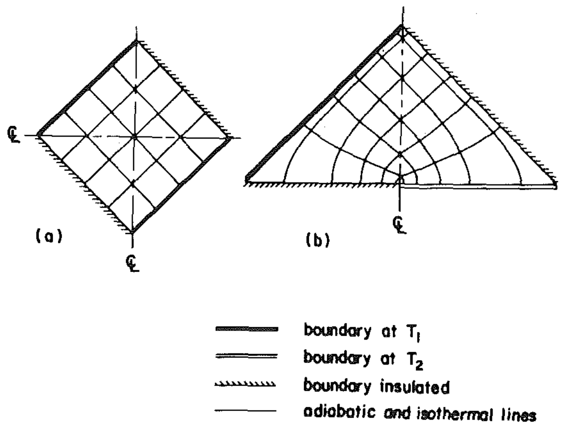

Fig. 1 Two Yin-Yang figures

---

[1] Professor, Mechanical Engineering Department, University of Houston, Houston, Tex. 77004, Fellow ASME.

[2] We use the Chinese term to evoke the sort of inverted symmetry involved, although the actual Yin-Yang figure does not really have the required mirror-image geometrical symmetry.

Contributed by the Heat Transfer Division for publication in the JOURNAL OF HEAT TRANSFER. Manuscript received by the Heat Transfer Division November 24, 1980.

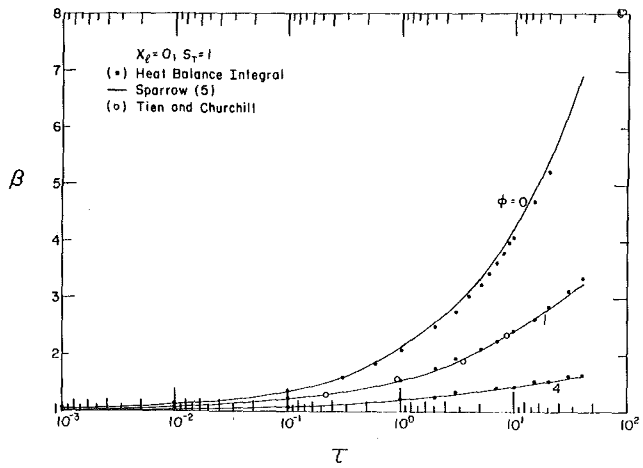

Fig. 2 Accuracy of phase change radius, $S_T = 1.0$, $\alpha_{12} = k_{12} = 1.0$

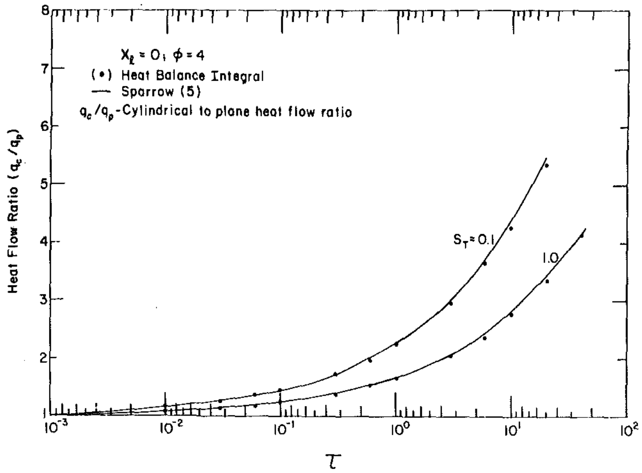

Fig. 3 Accuracy of cylinder heat flow, $\alpha_{12} = k_{12} = 1.0$, $\phi = 4.0$

References

1 Neumann, F., Lectures given in the 1860's C. F. Riemann-Weber, *Die partiellen Differential-gleichungen Physik*, 5th ed., Vol. 2, p. 121.

2 Carslaw, H. S., and Jaeger, J. C., *Conduction of Heat in Solids*, 2nd ed., Clarendon Press, Oxford, 1959.

3 Lunardini, V., and Varotta, R., "Approximate Solution to Neumann Problem for Soil Systems,"ASME *Journal of Energy Resources Technology*, Vol. 103, No. 1, 1981, pp. 76–81.

4 Tien, L. C., and Churchill, S. W., "Freezing Front Motion and Heat Transfer Outside an Infinite, Isothermal Cylinder," *AIChE Journal*, Vol. 11, No. 5, 1965, pp. 790–793.

5 Sparrow, E. M., Ramadhyani, S., and Patankar, S. V., "Effect of Subcooling on Cylindrical Melting," ASME JOURNAL OF HEAT TRANSFER, Vol. 100, No. 3, 1978, pp. 395–402.

6 Bell, G. E., "Solidification of a Liquid About a Cylindrical Pipe," *International Journal of Heat Mass Transfer*, Vol. 22, 1979, pp. 1681–1686.

7 Goodman, T. R., "The Heat-Balance Integral and Its Application to Problems Involving a Change of Phase," *Trans. ASME*, Vol. 80, 1958, pp. 335–342.

8 Goodman, T. R., "Application of Integral Methods to Transient Nonlinear Heat Transfer," *Advances in Heat Transfer*, Vol. 1, T. F. Irvine and J. P. Hartnett, Eds., Academic Press, New York, 1964, pp. 52–122.

9 Lardner, T. J., and Pohle, F. V., "Application of the Heat Balance Integral to Problems of Cylindrical Geometry," *Trans. ASME*, Vol. 83, No. 2, 1961, pp. 310–312.

10 Gold, L. W., and Lachenbruch, A. H., "Thermal Conditions in Permafrost—A Review of North American Literature," *Proceedings of Second International Permafrost Conference*, National Academy of Science, 1973, pp. 3–25.

11 Kersten, M. S., "Thermal Properties of Soils," University of Minnesota Experiment Station, Bulletin No. 28, 1949, 227 pages.

12 Lunardini, V. J., "Presentation of Some Thermal Properties of Soil Systems," Canadian Society of Mechanical Engineers, paper 71-CSME-38, *Engineering Institute of Canada Meeting*, 1971, Quebec City.

13 Lunardini, V. J., "Phase Change Around a Circular Pipe," CRREL Rept. 80-27, Dec. 1980.

14 Yuen, W. W., "Application of the Heat Balance Integral to Melting Problems with Initial Subcooling," *International Journal of Heat Mass Transfer*, Vol. 23, 1980, pp. 1157–1160.

Heat Conduction through "Yin-Yang" Bodies

John H. Lienhard[1]

Consider steady two-dimensional heat conduction through bodies whose boundaries are either maintained at one of two temperatures, or are insulated. If such a body has a geometrical axis of symmetry; if one piece of the left side is insulated and the other piece of it is held at a temperature, T_1; if the right side is either insulated or isothermal at T_2, with the positions of the insulated and isothermal segments inverted from those on the left; then the shape factor, S, is unity.

To see why this is true, consider two such cases in Figs. 1(a) and 1(b). The symmetry specified above obviously requires that the isothermal lines are mirror images of the adiabatic lines. The number of isothermal increments will therefore match the number of adiabatic increments so $S = 1$. We shall refer to such shapes as *Yin-Yang*[2] figures. Actually any Yin-Yang figure must be the result of conformally mapping Fig. 1(a). Accordingly it is sufficient that it be simply-connected with only one piece of its boundary at each temperature. It can also be doubly-connected (since Fig. 1(a) can be mapped into an infinite region with a single hole in it) as long as the point at infinity is not singular. Two other restrictions are that the thermal conductivity, k, must be constant, and there should be no heat sources.

Nine more Yin-Yang figures are presented in Fig. 2: (a) is a semi-infinite strip; (b), (c), and (g) have double axes of Yin-Yang symmetry although (b) and (g) are infinite in extent and (c) is finite; (d), (f), and (i) are semi-infinite bodies, (e) and (h) are finite; however, (i) can be viewed as the inverted limit of case (h) as the piece of boundary at T_1 is shrunk. Each of these situations would be hard to deal with analytically or numerically. Since $S = 1$ in each case we can express the heat transfer, Q (W/m), as simply

$$Q = k(T_1 - T_2)$$

The number of possibilities is, of course, unlimited, and they include many potentially useful configurations. Anyone doing a two-dimensional heat conduction calculation should first look at it to see if it resolves into a Yin-Yang figure. If it does, Q can be obtained without calculation.

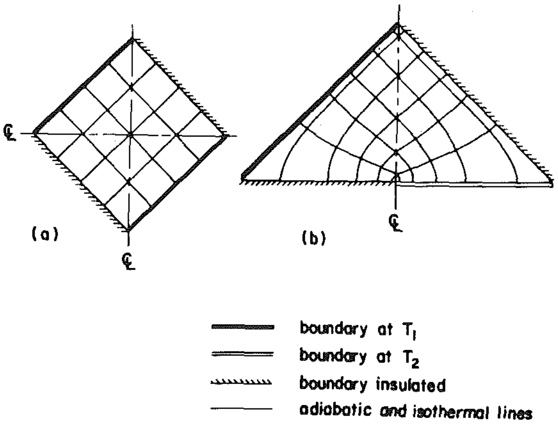

Fig. 1 Two Yin-Yang figures

---

[1] Professor, Mechanical Engineering Department, University of Houston, Houston, Tex. 77004, Fellow ASME.

[2] We use the Chinese term to evoke the sort of inverted symmetry involved, although the actual Yin-Yang figure does not really have the required mirror-image geometrical symmetry.

Contributed by the Heat Transfer Division for publication in the JOURNAL OF HEAT TRANSFER. Manuscript received by the Heat Transfer Division November 24, 1980.

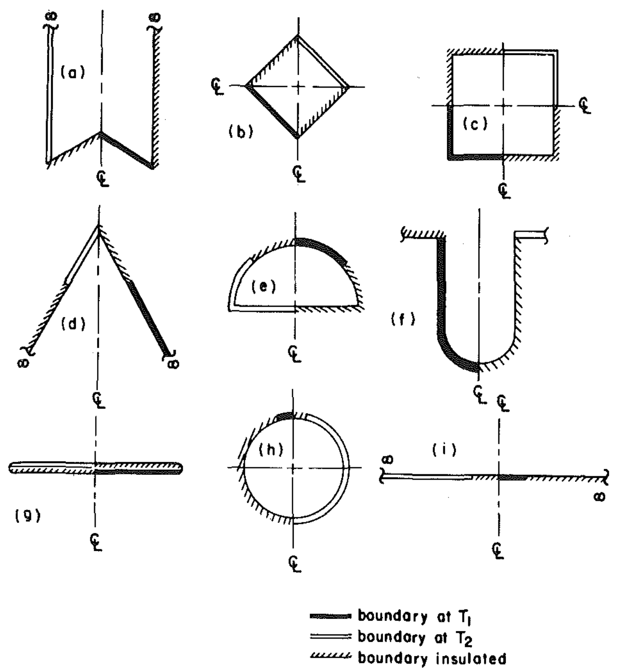

Fig. 2 Nine more Yin-Yang figures

Acknowledgment

I am grateful to the Lloyds Trefethen and to Lewis Wheeler for useful criticism and discussion of this problem. Lloyd N. Trefethen pointed out the simply-connected restriction.

Transient Thermal Expansion of Solids During Inert Heating, Phase Change, and Surface Gasification

L. W. Hunter[1]

Introduction

A difficulty in calculating heat conduction in an expanding solid is that the boundary locations are unknown in advance. However, by recognizing that some energy is carried by the internal motion in the solid, we show here that the governing equations (in one dimension) may be reduced to an ordinary fixed boundary heat conduction problem in a new coordinate. When phase changes and surface gasification occur with thermal expansion, the same approach reduces the equations to constant density form.

Transient thermal expansion has a number of important effects. A substantial resistance to heat flow can develop between two solids initially in contact, when one of the solids cools and recedes [1]. When a solid is constrained from expanding, a large stress can result. Thermal expansion in ramjet insulators [2, 3] and intumescent coatings [4] significantly reduces their heat throughput. As a last example, the velocity of a subsurface phase change front can be affected by thermal expansion [5, 6].

Governing Equations

To combine a number of possibilities in one example, Fig. 1, we consider a solid slab which insulates a metal from heating on one side. The back face of the slab (at $x = 0$) is held fixed while the front face (initially at $x = X_0$) is heated uniformly. We assume that the solid, initially at temperature $T = T_0$, undergoes inert expansion until the exposed surface reaches a phase change temperature, T_{pc}. Then a new solid phase forms and an interface begins to move toward $x = 0$. (Another possibility that may be treated just as well is the melting of a horizontal slab, under uniform heating from above to avoid buoyant convection currents.) The new solid phase warms up further until $T = T_{pyr}$ say, when gasification begins by surface pyrolysis or sublimation. We neglect transient internal stresses, and assume that the kinetic energy of the solid is small. The pressure is assumed to be uniform.

This model should not be applied when the heating rate is too high. Super-heating could occur, resulting in a variable composition zone between the two solid phases and subsurface gas flows near the exposed face. With a high radiant influx, subsurface absorption would be expected. If the expansion speed approaches the speed of sound, then the kinetic energy of the solid may become important, and internal pressure variations and transient stresses should be considered.

In the interior of each phase, the temperature and velocity vary in accordance with heat conservation

$$\frac{\partial T}{\partial t} + v\frac{\partial T}{\partial x} = \frac{1}{\rho \hat{C}}\frac{\partial}{\partial x}\left(k\frac{\partial T}{\partial x}\right), \qquad (1)$$

and mass conservation,

$$\frac{\partial \rho}{\partial t} + \frac{\partial}{\partial x}(\rho v) = 0, \qquad (2)$$

where $\hat{C} = \hat{C}(T)$ is the specific heat at constant pressure, $k = k(T)$ is the thermal conductivity, and $\rho = \rho(T)$ is the density. We now define a quantity

$$\xi = \int_0^x dx'\rho/\rho(T_0), \qquad (3)$$

reminiscent of the Dorotnitzyn-Stewartson transformation [7]. In equation (3), we integrate across the phase interface if necessary, so that ξ is continuous even when ρ changes abruptly at the interface. We make ξ a new coordinate and write $T = T(\xi, t)$. It is then found that equation (1) simplifies to

$$\frac{\partial T}{\partial t} = \frac{1}{\rho(T_0)\hat{C}}\frac{\partial}{\partial \xi}\left(k^*\frac{\partial T}{\partial \xi}\right), \qquad (4)$$

where $k^* = k^*(T)$ is an effective thermal conductivity defined by

$$k^*(T) = k(T)\rho(T)/\rho(T_0). \qquad (5)$$

The free boundary difficulty that arises in the usual formulation of inert thermal expansion [1] is avoided in ξ-coordinates. The value of ξ at the exposed surface, $\xi = \Xi(t)$ say, is simply the initial thickness of the slab, $\Xi(t) = X_0$. The value remains X_0 during the subsurface phase change.

We now list the remaining auxiliary conditions necessary to completely determine the temperature. In these conditions, it may be noted for later use that the density ρ appears explicitly only in the effective thermal conductivity, k^*, as in equation (4).

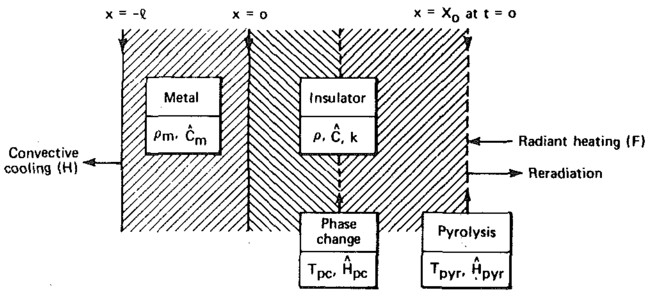

Fig. 1 A swelling insulator which protects a metal from heating on one side

---

[1] Applied Physics Laboratory, The Johns Hopkins University, Laurel, MD 20810.

Contributed by the Heat Transfer Division for publication in the JOURNAL OF HEAT TRANSFER. Manuscript received by the Heat Transfer Division, October 20, 1980.

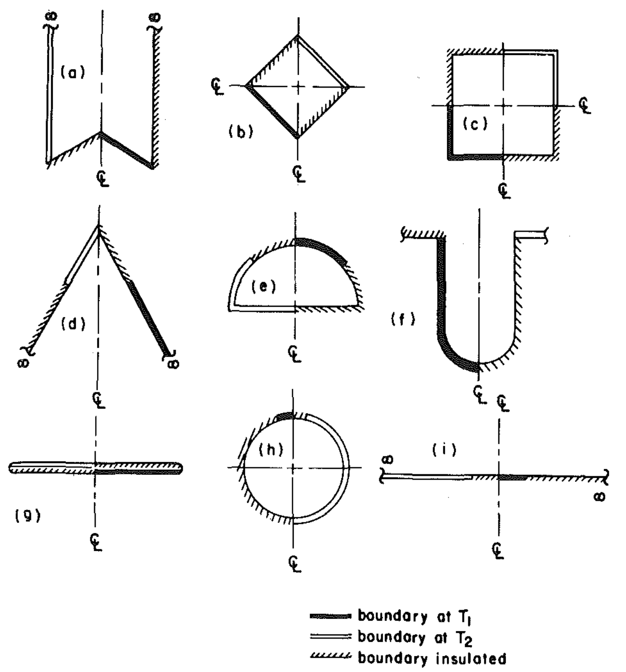

Fig. 2 Nine more Yin-Yang figures

Acknowledgment

I am grateful to the Lloyds Trefethen and to Lewis Wheeler for useful criticism and discussion of this problem. Lloyd N. Trefethen pointed out the simply-connected restriction.

Transient Thermal Expansion of Solids During Inert Heating, Phase Change, and Surface Gasification

L. W. Hunter[1]

Introduction

A difficulty in calculating heat conduction in an expanding solid is that the boundary locations are unknown in advance. However, by recognizing that some energy is carried by the internal motion in the solid, we show here that the governing equations (in one dimension) may be reduced to an ordinary fixed boundary heat conduction problem in a new coordinate. When phase changes and surface gasification occur with thermal expansion, the same approach reduces the equations to constant density form.

Transient thermal expansion has a number of important effects. A substantial resistance to heat flow can develop between two solids initially in contact, when one of the solids cools and recedes [1]. When a solid is constrained from expanding, a large stress can result. Thermal expansion in ramjet insulators [2, 3] and intumescent coatings [4] significantly reduces their heat throughput. As a last example, the velocity of a subsurface phase change front can be affected by thermal expansion [5, 6].

Governing Equations

To combine a number of possibilities in one example, Fig. 1, we consider a solid slab which insulates a metal from heating on one side. The back face of the slab (at $x = 0$) is held fixed while the front face (initially at $x = X_0$) is heated uniformly. We assume that the solid, initially at temperature $T = T_0$, undergoes inert expansion until the exposed surface reaches a phase change temperature, T_{pc}. Then a new solid phase forms and an interface begins to move toward $x = 0$. (Another possibility that may be treated just as well is the melting of a horizontal slab, under uniform heating from above to avoid buoyant convection currents.) The new solid phase warms up further until $T = T_{pyr}$ say, when gasification begins by surface pyrolysis or sublimation. We neglect transient internal stresses, and assume that the kinetic energy of the solid is small. The pressure is assumed to be uniform.

This model should not be applied when the heating rate is too high. Super-heating could occur, resulting in a variable composition zone between the two solid phases and subsurface gas flows near the exposed face. With a high radiant influx, subsurface absorption would be expected. If the expansion speed approaches the speed of sound, then the kinetic energy of the solid may become important, and internal pressure variations and transient stresses should be considered.

In the interior of each phase, the temperature and velocity vary in accordance with heat conservation

$$\frac{\partial T}{\partial t} + v\frac{\partial T}{\partial x} = \frac{1}{\rho\hat{C}}\frac{\partial}{\partial x}\left(k\frac{\partial T}{\partial x}\right), \tag{1}$$

and mass conservation,

$$\frac{\partial \rho}{\partial t} + \frac{\partial}{\partial x}(\rho v) = 0, \tag{2}$$

where $\hat{C} = \hat{C}(T)$ is the specific heat at constant pressure, $k = k(T)$ is the thermal conductivity, and $\rho = \rho(T)$ is the density. We now define a quantity

$$\xi = \int_0^x dx'\rho/\rho(T_0), \tag{3}$$

reminiscent of the Dorotnitzyn-Stewartson transformation [7]. In equation (3), we integrate across the phase interface if necessary, so that ξ is continuous even when ρ changes abruptly at the interface. We make ξ a new coordinate and write $T = T(\xi, t)$. It is then found that equation (1) simplifies to

$$\frac{\partial T}{\partial t} = \frac{1}{\rho(T_0)\hat{C}}\frac{\partial}{\partial \xi}\left(k^*\frac{\partial T}{\partial \xi}\right), \tag{4}$$

where $k^* = k^*(T)$ is an effective thermal conductivity defined by

$$k^*(T) = k(T)\rho(T)/\rho(T_0). \tag{5}$$

The free boundary difficulty that arises in the usual formulation of inert thermal expansion [1] is avoided in ξ-coordinates. The value of ξ at the exposed surface, $\xi = \Xi(t)$ say, is simply the initial thickness of the slab, $\Xi(t) = X_0$. The value remains X_0 during the subsurface phase change.

We now list the remaining auxiliary conditions necessary to completely determine the temperature. In these conditions, it may be noted for later use that the density ρ appears explicitly only in the effective thermal conductivity, k^*, as in equation (4).

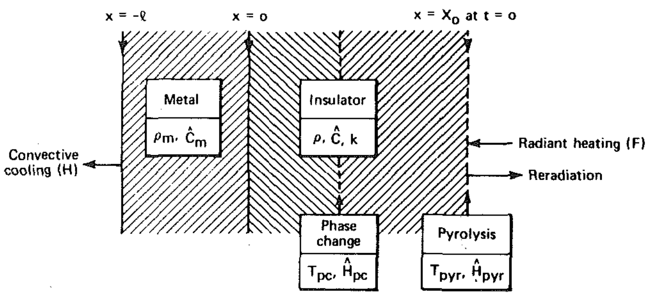

Fig. 1 A swelling insulator which protects a metal from heating on one side

---

[1] Applied Physics Laboratory, The Johns Hopkins University, Laurel, MD 20810.

Contributed by the Heat Transfer Division for publication in the JOURNAL OF HEAT TRANSFER. Manuscript received by the Heat Transfer Division, October 20, 1980.

During the pyrolysis, $\Xi(t)$ satisfies

$$F - \sigma T_{pyr}{}^4 - k^* \frac{\partial T}{\partial \xi} = -\hat{H}_{pyr}\rho(T_0)\frac{d\Xi(t)}{dt} \qquad (6)$$

at $\xi = \Xi(t)$, where F is the radiant influx, σ is the Stefan-Boltzmann constant, and $\hat{H}_{pyr}$ is the specific heat of pyrolysis. The location of the phase change interface $\xi = \Xi_{pc}(t)$ say, satisfies

$$\left(k^* \frac{\partial T}{\partial \xi}\right)_+ - \left(k^* \frac{\partial T}{\partial \xi}\right)_- = -\hat{H}_{pc}\rho(T_0)\frac{d}{dt}\Xi_{pc}(t), \qquad (7)$$

where $\hat{H}_{pc}$ is the specific heat of phase change.

The boundary condition at the metal ($\xi = 0$) is

$$\hat{C}_m \rho_m l \frac{\partial T}{\partial t} = k^* \frac{\partial T}{\partial \xi} - H(T - T_0) \text{ at } \xi = 0, \qquad (8)$$

where $\hat{C}_m$ is the (constant) specific heat, ρ_m the (constant) density, and l the thickness of the metal. In addition, H is the heat transfer coefficient for convective losses to air at temperature T_0. The boundary condition at the phase change front is $T = T_{pc}$. At the exposed surface, the condition is

$$F - \sigma T^4 - k^* \frac{\partial T}{\partial \xi} = 0 \text{ if } T < T_{pyr} \qquad (9)$$

and $T = T_{pyr}$ otherwise.

The solution of the last equations determines the x-location of the exposed face,

$$x = \int_0^{\Xi(t)} d\xi \rho(T_0)/\rho \qquad (10)$$

and of the phase change front similarly. The mass loss flux is

$$\dot{m}'' = -\rho(T_0)\frac{d}{dt}\Xi(t). \qquad (11)$$

Discussion

In the thermal expansion problem in ξ-coordinates, equations (4–9), the density appeared only in the effective thermal conductivity, k^*. Now suppose that the density is set constant without changing the other thermal properties. Then ξ becomes x and k^* becomes k and we can denote the temperature by $T^{(0)}(x, t; k)$, in which the dependence on $k = k(T)$ is indicated. It is seen that the variable density solution is just

$$T = T^{(0)}(\xi, t; k^*), \qquad (12)$$

in which ξ replaces x and k^* replaces k. It follows that variable density problems for a variety of boundary conditions including those in Fig. 1 may be reduced to equivalent constant density problems and solved by the usual methods.

References

1 Meyer, G. H., "A Numerical Method for Heat Transfer in an Expanding Rod," *International Journal of Heat and Mass Transfer*, Vol. 21, 1978, pp. 824–826.

2 Roberts, W., Laub, B., Suchsland, K., Shimizu, A., and Chambers, J., "Ramburner Internal Insulation Investigation. Modeling and Computer Programs," Marquardt Company Report AFAPL-TR-75-109-Vol.-1, 1975.

3 Chambers, J., Harkins, W., Roberts, W., and Meyers, G., "Ramburner Internal Insulation Investigation. Characterization and Tailoring of Silicone Elastomers," Marquardt Company Report AFAPL-TR-75-199-Vol.-2, 1975.

4 Cagliostro, D. E., Riccitiello, S. R., Clark, K. J., and Shimizu, A. B., "Intumescent Coating Modeling," *Journal of Fire and Flammability*, Vol. 6, 1975, pp. 205–221.

5 Danckwerts, P. V., "Unsteady-State Diffusion or Heat-Conduction with Moving Boundary," *Transactions of the Faraday Society*, Vol. 46, 1950, pp. 701–712.

6 Carslaw, H. S., and Jaeger, J. C., *Conduction of Heat in Solids*, 2nd ed. Oxford at the Clarendon Press, 1959, pp. 290–291.

7 Eckert, E. R. G., and Drake, R. M., Jr., *Analysis of Heat and Mass Transfer*, McGraw-Hill, 1972, p. 424.

Acknowledgment

The author thanks J. C. W. Rogers, L. L. Perini, and R. W. Hart for helpful discussions. Support for this work was provided by the Department of the Navy, Naval Sea Systems Command, under Contract N00024-78-C-5384.

Extension of the Adams-Welty Fluid Bed Heat Transfer Model to the Packed Bed Case

Ronald L. Adams[1]

Introduction

The purpose of this note is to propose a packed bed heat transfer model based upon the gas convection dominant fluid bed heat transfer model of Adams and Welty [1]. The assumption of large particle Reynolds number is retained and the resulting packed bed model seems to be valid for particle Reynolds number greater than about 50. The new packed bed heat transfer model can be combined with the original fluid bed heat transfer model such that analytical studies of heat transfer during the turndown phase of combustor operation can be carried out.

Model Description

The fundamental element of the gas convection dominant heat transfer model of Adams and Welty is analysis of flow within interstitial channels adjacent to the heat transfer surface. The model is based upon a boundary layer analysis of flow within these channels with separate treatment of the two-dimensional flow near the channel center and three-dimensional, but Stokes' flow in the cusped corners formed at particle contact points. For the fluidized regime, the thermal state of the average particle is assumed to be such that the temperature distribution along the particle surface (from the wall to the edge of the Stokes' region) is linear and this assumption yields reasonable agreement with experiment (see Catipovic, et al. [2]). The size of the Stokes' region is established by requiring the heat transfer be continuous across the channel and therefore depends upon the thickness of the two-dimensional boundary layer near the channel center.

When the bed is in the packed state, solid particles will remain at the heat transfer surface indefinitely and consideration must be given to the conditions under which the model of Adams and Welty remains valid. In particular, the model assumes that the influence of the heat transfer surface is confined to a single particle layer. This condition is satisfied as long as the major contribution to the heat transfer is convection due to the two-dimensional gas boundary layer forming on the tube wall. Thus the Reynolds number must be large enough such that boundary layer thickness within the interstitial channel is less than half a particle diameter and so that the Stokes' region does not encompass the entire width of the channel. Furthermore, the thermal state of the average particle will be different than under fluidized conditions and this difference is approximated by assuming that the portion of the particle surface near the wall and bounding the Stokes' region is at the wall temperature. The major difference between this model and those of Gabor [3] and Botterill and Denloye [4] is its fundamental approach to the details of the heat transfer processes rather than the use of empirical, effective conductivities. Also, heat transfer beyond the particle layer adjacent to the wall has been neglected and this confines the model to large particle Reynolds number.

---

[1] Assistant Professor, Department of Mechanical Engineering, Oregon State University, Corvallis, Ore. 97331.

Contributed by the Heat Transfer Division for publication in the JOURNAL OF HEAT TRANSFER. Manuscript received by the Heat Transfer Division, January 12, 1981.

During the pyrolysis, $\Xi(t)$ satisfies

$$F - \sigma T_{pyr}{}^4 - k^* \frac{\partial T}{\partial \xi} = -\hat{H}_{pyr}\rho(T_0)\frac{d\Xi(t)}{dt} \qquad (6)$$

at $\xi = \Xi(t)$, where F is the radiant influx, σ is the Stefan-Boltzmann constant, and $\hat{H}_{pyr}$ is the specific heat of pyrolysis. The location of the phase change interface $\xi = \Xi_{pc}(t)$ say, satisfies

$$\left(k^* \frac{\partial T}{\partial \xi}\right)_+ - \left(k^* \frac{\partial T}{\partial \xi}\right)_- = -\hat{H}_{pc}\rho(T_0)\frac{d}{dt}\Xi_{pc}(t), \qquad (7)$$

where $\hat{H}_{pc}$ is the specific heat of phase change.

The boundary condition at the metal ($\xi = 0$) is

$$\hat{C}_m \rho_m l \frac{\partial T}{\partial t} = k^* \frac{\partial T}{\partial \xi} - H(T - T_0) \text{ at } \xi = 0, \qquad (8)$$

where $\hat{C}_m$ is the (constant) specific heat, ρ_m the (constant) density, and l the thickness of the metal. In addition, H is the heat transfer coefficient for convective losses to air at temperature T_0. The boundary condition at the phase change front is $T = T_{pc}$. At the exposed surface, the condition is

$$F - \sigma T^4 - k^* \frac{\partial T}{\partial \xi} = 0 \text{ if } T < T_{pyr} \qquad (9)$$

and $T = T_{pyr}$ otherwise.

The solution of the last equations determines the x-location of the exposed face,

$$x = \int_0^{\Xi(t)} d\xi \rho(T_0)/\rho \qquad (10)$$

and of the phase change front similarly. The mass loss flux is

$$\dot{m}'' = -\rho(T_0)\frac{d}{dt}\Xi(t). \qquad (11)$$

Discussion

In the thermal expansion problem in ξ-coordinates, equations (4–9), the density appeared only in the effective thermal conductivity, k^*. Now suppose that the density is set constant without changing the other thermal properties. Then ξ becomes x and k^* becomes k and we can denote the temperature by $T^{(0)}(x, t; k)$, in which the dependence on $k = k(T)$ is indicated. It is seen that the variable density solution is just

$$T = T^{(0)}(\xi, t; k^*), \qquad (12)$$

in which ξ replaces x and k^* replaces k. It follows that variable density problems for a variety of boundary conditions including those in Fig. 1 may be reduced to equivalent constant density problems and solved by the usual methods.

References

1 Meyer, G. H., "A Numerical Method for Heat Transfer in an Expanding Rod," *International Journal of Heat and Mass Transfer*, Vol. 21, 1978, pp. 824–826.

2 Roberts, W., Laub, B., Suchsland, K., Shimizu, A., and Chambers, J., "Ramburner Internal Insulation Investigation. Modeling and Computer Programs," Marquardt Company Report AFAPL-TR-75-109-Vol.-1, 1975.

3 Chambers, J., Harkins, W., Roberts, W., and Meyers, G., "Ramburner Internal Insulation Investigation. Characterization and Tailoring of Silicone Elastomers," Marquardt Company Report AFAPL-TR-75-199-Vol.-2, 1975.

4 Cagliostro, D. E., Riccitiello, S. R., Clark, K. J., and Shimizu, A. B., "Intumescent Coating Modeling," *Journal of Fire and Flammability*, Vol. 6, 1975, pp. 205–221.

5 Danckwerts, P. V., "Unsteady-State Diffusion or Heat-Conduction with Moving Boundary," *Transactions of the Faraday Society*, Vol. 46, 1950, pp. 701–712.

6 Carslaw, H. S., and Jaeger, J. C., *Conduction of Heat in Solids*, 2nd ed. Oxford at the Clarendon Press, 1959, pp. 290–291.

7 Eckert, E. R. G., and Drake, R. M., Jr., *Analysis of Heat and Mass Transfer*, McGraw-Hill, 1972, p. 424.

Acknowledgment

The author thanks J. C. W. Rogers, L. L. Perini, and R. W. Hart for helpful discussions. Support for this work was provided by the Department of the Navy, Naval Sea Systems Command, under Contract N00024-78-C-5384.

Extension of the Adams-Welty Fluid Bed Heat Transfer Model to the Packed Bed Case

Ronald L. Adams[1]

Introduction

The purpose of this note is to propose a packed bed heat transfer model based upon the gas convection dominant fluid bed heat transfer model of Adams and Welty [1]. The assumption of large particle Reynolds number is retained and the resulting packed bed model seems to be valid for particle Reynolds number greater than about 50. The new packed bed heat transfer model can be combined with the original fluid bed heat transfer model such that analytical studies of heat transfer during the turndown phase of combustor operation can be carried out.

Model Description

The fundamental element of the gas convection dominant heat transfer model of Adams and Welty is analysis of flow within interstitial channels adjacent to the heat transfer surface. The model is based upon a boundary layer analysis of flow within these channels with separate treatment of the two-dimensional flow near the channel center and three-dimensional, but Stokes' flow in the cusped corners formed at particle contact points. For the fluidized regime, the thermal state of the average particle is assumed to be such that the temperature distribution along the particle surface (from the wall to the edge of the Stokes' region) is linear and this assumption yields reasonable agreement with experiment (see Catipovic, et al. [2]). The size of the Stokes' region is established by requiring the heat transfer be continuous across the channel and therefore depends upon the thickness of the two-dimensional boundary layer near the channel center.

When the bed is in the packed state, solid particles will remain at the heat transfer surface indefinitely and consideration must be given to the conditions under which the model of Adams and Welty remains valid. In particular, the model assumes that the influence of the heat transfer surface is confined to a single particle layer. This condition is satisfied as long as the major contribution to the heat transfer is convection due to the two-dimensional gas boundary layer forming on the tube wall. Thus the Reynolds number must be large enough such that boundary layer thickness within the interstitial channel is less than half a particle diameter and so that the Stokes' region does not encompass the entire width of the channel. Furthermore, the thermal state of the average particle will be different than under fluidized conditions and this difference is approximated by assuming that the portion of the particle surface near the wall and bounding the Stokes' region is at the wall temperature. The major difference between this model and those of Gabor [3] and Botterill and Denloye [4] is its fundamental approach to the details of the heat transfer processes rather than the use of empirical, effective conductivities. Also, heat transfer beyond the particle layer adjacent to the wall has been neglected and this confines the model to large particle Reynolds number.

---

[1] Assistant Professor, Department of Mechanical Engineering, Oregon State University, Corvallis, Ore. 97331.

Contributed by the Heat Transfer Division for publication in the JOURNAL OF HEAT TRANSFER. Manuscript received by the Heat Transfer Division, January 12, 1981.

The alteration of the boundary conditions on the Stokes' region described above will modify both the Stokes' region size and average Nusselt number. Following the analysis of Adams [5], the average Nusselt number for the Stokes' region when the particle surface is at the wall temperature is

$$\mathrm{Nu}_{p0} = \frac{2S_0}{(s_p/r_p)} \tag{1}$$

with

$$S_0 = \frac{1}{2}\left(1 + \frac{T_w}{T_B}\right)\left(\frac{T_w}{T_B}\right)^{1/2}\left(\frac{1 + A_1/T_B}{T_w/T_B + A_1/T_B}\right) \tag{2}$$

where T_B and T_w are bed and wall temperatures, respectively, A_1 is the Sutherland constant for the gas, S_p is half the particle spacing at the wall and r_p is the particle radius. While the Stokes' region matching criterion is modified such that the parameters k_1 and k_2 appearing in the approximations for the Stokes' region boundary are (see Adams [6])

$$(k_1)_{\text{packed}} = (k_1)_{\text{fluidized}}/1.4 \tag{3}$$

$$(k_2)_{\text{packed}} = [(k_2)_{\text{fluidized}}] \times 1.4 \tag{4}$$

Therefore,

$$k_1 = 5.26 - 7.72\left(\frac{s_p}{r_p} - 1\right) \tag{5}$$

$$k_2 = 0.0127 + 0.0222\left(\frac{s_p}{r_p} - 1\right) \tag{6}$$

Then, the channel Nusselt number (based upon particle diameter) follows from the previous analysis, i.e.,

$$\mathrm{Nu}_p \simeq \begin{cases} a\sqrt{\mathrm{Re}_p} + b + \mathrm{Nu}_{p0} & \mathrm{Re}_p \geq \mathrm{Re}_{p_m} \quad (7a) \\ c\mathrm{Re}_p + \mathrm{Nu}_{p0} & \mathrm{Re}_p < \mathrm{Re}_{p_m} \quad (7b) \end{cases}$$

with

$$a = 0.76\alpha \tag{8}$$

$$b = -k_1 S_0 \tag{9}$$

$$c = \frac{k_2\alpha^2}{S_0} \tag{10}$$

$$\alpha = \frac{1.58}{\mathrm{Pr}^{0.4}}\left[\frac{Q_g^+}{(s_p/r_p)(1.405 + 5.6e^{-0.0849u'}\sqrt{\mathrm{Re}_p Q_g^+})}\right]^{1/2} \tag{11}$$

where Pr is the gas Prandtl number, Q_g^+ is the interstitial gas velocity (nondimensionalized with superficial velocity), u' is the interstitial turbulence intensity and Re_p is the Reynolds number based upon particle diameter and supericial velocity. The maximum Reynolds number, Re_{p_m}, for quasi-linear behavior satisfies the nonlinear equation

$$\mathrm{Re}_{p_m}Q_g^+ = A + Be^{-C}\sqrt{\mathrm{Re}_{p_m}Q_g^+} \tag{12}$$

where

$$A = 1.405\beta \tag{13}$$

$$B = 5.6\beta \tag{14}$$

$$C = 0.0849u' \tag{15}$$

with

$$\beta = \left(\frac{1.79\mathrm{Pr}^{0.4}k_1 S_0\sqrt{1/2 s_p/r_p}}{0.76 - (0.578 - 4k_1k_2)^{1/2}}\right)^2 \tag{16}$$

Equation (7) together with a potential model of the interstitial flow with corrections for local voidage variation (to obtain Q_g^+) allows estimation of local and total heat transfer to immersed surfaces. In the case of a horizontal tube, the lower stagnation region exhibits a relatively high voidage such that the potential model is inaccurate; however, the heating there can be obtained by using the finite difference solutions for interstitial velocity obtained by George, et al. [7] and neglecting the Stokes' region contribution there.

Comparison with Experiment

Heat transfer data for a horizontal tube immersed in an atmospheric pressure packed bed reported by Catipovic [8] were selected to test the validity of the model. Other data for horizontal tubes immersed in large particle/high pressure beds have been reported by Chandron, et al. [9] but packed bed data are not included. Also, Botterill and Denloye [4] report data for a vertical cylinder immersed in a large particle bed under both packed and fluidized conditions.

Local and total Nusselt number calculations were made for particle sizes in the range 1.3–6.6 mm in a low temperature bed at atmospheric pressure. The parameters used in the calculations are listed in Table 1 and comparison of calculated results with Catipovic's data is made in Figs. 1 and 2. Figure 1 illustrates the accuracy of calculated local values for 4 mm dia particles. It appears from the figure that local fluidization and bubbling may be occurring near the side of the tube

Table 1 Calculation parameters

Bed Temperature	308 K
Wall Temperature	376 K
Bed Voidage	0.40
Surface Voidage	
Lower Stagnation	0.8 ($\theta = -0.452$ to 0.452 rad)
Remaining Surface	0.44
Particle Sphericity	0.97
Turbulence Intensity	0.20
Prandtl Number	0.70

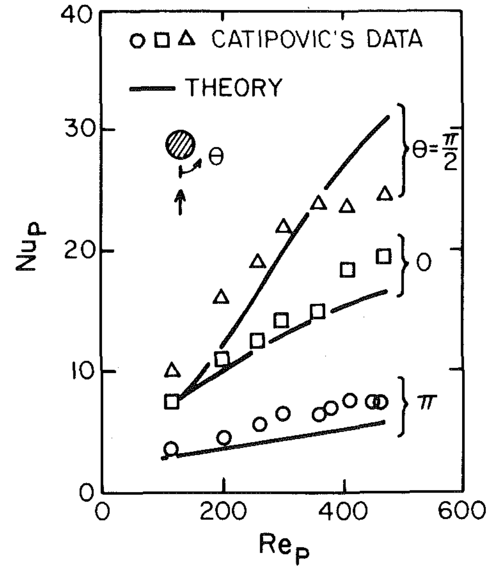

Fig. 1 Comparison of Catipovic's packed bed data for local Nusselt number with theory for 4 mm dia particles fluidized with air at 1 ATM

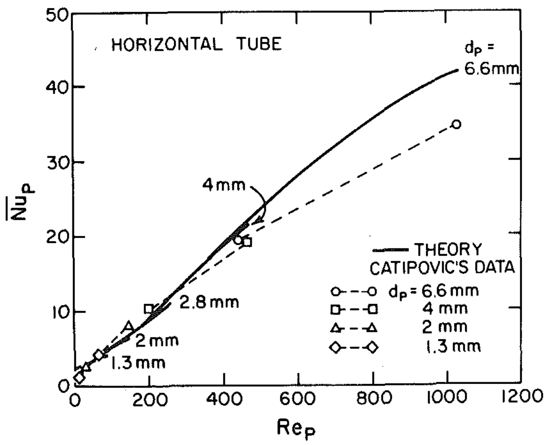

Fig. 2 Comparison of Catipovic's packed bed data for total Nusselt number with theory for particles fluidized with air at 1 ATM

$(\theta = \pi/2)$, resulting in poor agreement at the higher Reynolds number. The top and lower stagnation values agree reasonably well with the measurements though it is noted that the analytical value for the lower stagnation point is sensitive to the voidage assumed. Figure 2 is a comparison of calculated and measured total Nusselt number for the four particle sizes considered. Note that the theoretical curves are nearly coincident and linear with Reynolds number. The best agreement was obtained in the mid-range of Reynolds Number and worst agreement when local bubbling and fluidization effects seem to be present. Over the range of Reynolds number from 50 to 1000, the maximum difference between theory and experiment is about 20 percent.

Summary

The gas convection dominant heat transfer model of Adams and Welty has been extended to the case of a horizontal tube immersed in a large particle packed bed. This extension will allow analytical studies of heat transfer during turndown of a fluid bed combustor operating in the gas convection dominant regime. Comparison of the model with measurements made by Catipovic [8] shows reasonable agreement with both local and total Nusselt number for an immersed tube for the particle Reynolds number range of 50 to 1000.

Acknowledgments

The work reported herein was prepared, in part, for the U. S. Department of Energy under Contract No. EF-77-S-01-2714. Some support was also provided by the Battelle Memorial Institute Distributions to Universities Program.

References

1 Adams, R. L., and Welty, J. R., "A Gas Convection Model of Heat Transfer in Large Particle Fluidized Beds," *AIChE Journal*, Vol. 25, No. 3, May 1979, pp. 395–405.

2 Catipovic, N. M., Fitzgerald, T. J., George, A. H., and Welty, J. R., "Experimental Validation of the Adams-Welty Model for Heat Transfer in Large-Particle Fluidized Beds," submitted to *AIChE Journal*, 1980.

3 Gabor, J. D., "Heat Transfer to Particle Beds with Gas Flows Less Than or Equal to That Required for Incipient Fluidization," *Chemical Engineering Science*, Vol. 25, 1970, p. 979.

4 Botterill, J. S. M. and Denloye, A. O. O., "Gas Convective Heat Transfer to Packed and Fluidized Beds," *AIChE Symposium Series*, Vol. 74, No. 176, 1978.

5 Adams, R. L., "An Analytical Model of Heat Transfer to a Horizontal Cylinder Immersed in a Gas Fluidized Bed," Ph.D. Thesis, Oregon State University, Corvallis, Ore., 1977.

6 Adams, R. L., "An Approximate Formula for Gas Convection Dominant Heat Transfer in Large-Particle Fluidized Beds," ASME JOURNAL OF HEAT TRANSFER, Vol. 103, No. 2, 1981, pp. 395–397.

7 George, A. H., Catipovic, N. M., and Welty, J. R., "An Analytical Study of Heat Transfer to a Horizontal Cylinder in a Large Particle Fluidized Bed," ASME Paper No. 79-HT-78, Aug. 1979.

8 Catipovic, N. M., "Heat Transfer to Horizontal Tubes in Fluidized Beds: Experiment and Theory," Ph.D. Thesis, Oregon State University, Corvallis, Ore., 1979.

9 Chandron, R., Chen, J. C., and Staub, F. W., "Local Heat Transfer Coefficients Around Horizontal Tubes in Fluidized Beds," ASME JOURNAL OF HEAT TRANSFER, Vol. 102, No. 1, 1980. pp. 152–157.

Thermal Storage Regenerator Parameters for Almost Constant Gas Discharge Temperature

F. E. Romie[1]

Introduction

Regenerator parameters can be selected to satisfy two important criteria for thermal energy storage; first, a large fraction of the energy made available during the charge process should be returned during regenerator discharge and, second, the temperature of the discharge gas leaving the regenerator should be close to the constant entrance temperature of the gas used to charge the regenerator. The latter criterion has particular importance if the stored energy is to be used as the heat source for a heat engine because the loss in thermodynamic availability due to a decreased discharge gas temperature reduces the work that can be realized from the stored thermal energy.

The purpose of this note is to present regenerator parameters which satisfy both criteria. In particular, parameters are presented which give a normalized gas discharge temperature equal to 0.95 at the end of the discharge period. $(\tau_a(1,1) = 0.95)$.

Method and Results

The data presented are obtained by iteration ($\tau_a(1,1)$ is a dependent variable) of the solution method described in [1]. The solution is based on idealizations common to most treatments [2–8] of the steady-state periodic operation of the counterflow regenerator. The idealizations are:

1 The entrance temperatures, τ_{a1}' and τ_{b1}', of the discharge and charge gases are constant. (Actual temperatures are denoted by a prime.) The conductance, hA, for transfer of heat between the gas and solid is constant and uniform throughout the matrix as are the thermal capacity, WC, of the matrix solid and the capacity rate, wc, of the fluid. (The conductances and capacity rates for the two fluids and the flow periods, t_a and t_b, are in general different.)

2 No axial transfer of heat occurs in the matrix.

3 The thermal conductivity of the solid is infinite in the direction normal to fluid flow or, equivalently, the temperature of the matrix solid is uniform in any plane normal to fluid flow.

4 The ratio of the thermal capacity of the fluid contained in the matrix (at any instant) to the thermal capacity of the matrix is negligibly small (zero).

The fourth idealization will be satisfied for thermal storage regenerators when gases are used as the heat transfer agents [9]. The third idealization can be relaxed by use of approximate treatments of transverse conduction [10, 11]. In many cases, however, regenerators will be designed to have a very large heat transfer area per unit volume and the resultant fine subdivision of the matrix composing the regenerator implies that this idealization will be closely realized. The absence of axial transfer of heat required by the second idealization appears to be satisfied for axial conduction in pebble bed and similar constructions which offer no continuous path for conduction. However, with operation at sufficiently high temperature the axial transfer of heat by radiation can become significant with a consequent reduction of the thermal effectiveness and the gas discharge temperature. For constructions with continuous axial conduction paths [12] can be consulted.

Both the thermal effectiveness, $\bar{\tau}_a$, and the normalized final gas discharge temperature, $\tau_a(1,1)$, $(\tau_a(1,1) = (\tau_a'(1,1) - \tau_{a1}')/(\tau_{b1}' - \tau_{a1}'))$ are expressible in terms of four parameters: (1), the ratio of the thermal capacity of the mass of gas passed through the regenerator during discharge to the thermal capacity of the mass of gas passed during charge, $(wct)_a/(wct)_b$, (2), the ratio of the thermal capacity of the mass of gas passed during discharge to the thermal capacity of the matrix solid, $(wct)_a/WC$, (3), the ratio N_a/N_b which is equal to the ratio of the Stanton numbers for the two flows and, (4), the value of Ntu, the number of transfer units for the regenerator.

$$\mathrm{Ntu} = \left[\frac{1}{N_a} + \frac{(wct)_a}{(wct)_b}\frac{1}{N_b}\right]^{-1} \qquad (1)$$

The parameter N with suscripts a or b is the ratio of the thermal conductance, hA, to the capacity rate, wc, during the discharge and charge periods respectively.

Three regenerator properties are expressed in terms of the thermal effectiveness. The energy stored during charge and delivered during

---

[1] Assoc. Mem. ASME.

Contributed by the Heat Transfer Division for publication in the JOURNAL OF HEAT TRANSFER. Manuscript received by the Heat Transfer Division November 14, 1980.

($\theta = \pi/2$), resulting in poor agreement at the higher Reynolds number. The top and lower stagnation values agree reasonably well with the measurements though it is noted that the analytical value for the lower stagnation point is sensitive to the voidage assumed. Figure 2 is a comparison of calculated and measured total Nusselt number for the four particle sizes considered. Note that the theoretical curves are nearly coincident and linear with Reynolds number. The best agreement was obtained in the mid-range of Reynolds Number and worst agreement when local bubbling and fluidization effects seem to be present. Over the range of Reynolds number from 50 to 1000, the maximum difference between theory and experiment is about 20 percent.

Summary

The gas convection dominant heat transfer model of Adams and Welty has been extended to the case of a horizontal tube immersed in a large particle packed bed. This extension will allow analytical studies of heat transfer during turndown of a fluid bed combustor operating in the gas convection dominant regime. Comparison of the model with measurements made by Catipovic [8] shows reasonable agreement with both local and total Nusselt number for an immersed tube for the particle Reynolds number range of 50 to 1000.

Acknowledgments

The work reported herein was prepared, in part, for the U. S. Department of Energy under Contract No. EF-77-S-01-2714. Some support was also provided by the Battelle Memorial Institute Distributions to Universities Program.

References

1 Adams, R. L., and Welty, J. R., "A Gas Convection Model of Heat Transfer in Large Particle Fluidized Beds," *AIChE Journal*, Vol. 25, No. 3, May 1979, pp. 395–405.

2 Catipovic, N. M., Fitzgerald, T. J., George, A. H., and Welty, J. R., "Experimental Validation of the Adams-Welty Model for Heat Transfer in Large-Particle Fluidized Beds," submitted to *AIChE Journal*, 1980.

3 Gabor, J. D., "Heat Transfer to Particle Beds with Gas Flows Less Than or Equal to That Required for Incipient Fluidization," *Chemical Engineering Science*, Vol. 25, 1970, p. 979.

4 Botterill, J. S. M. and Denloye, A. O. O., "Gas Convective Heat Transfer to Packed and Fluidized Beds," *AIChE Symposium Series*, Vol. 74, No. 176, 1978.

5 Adams, R. L., "An Analytical Model of Heat Transfer to a Horizontal Cylinder Immersed in a Gas Fluidized Bed," Ph.D. Thesis, Oregon State University, Corvallis, Ore., 1977.

6 Adams, R. L., "An Approximate Formula for Gas Convection Dominant Heat Transfer in Large-Particle Fluidized Beds," ASME JOURNAL OF HEAT TRANSFER, Vol. 103, No. 2, 1981, pp. 395–397.

7 George, A. H., Catipovic, N. M., and Welty, J. R., "An Analytical Study of Heat Transfer to a Horizontal Cylinder in a Large Particle Fluidized Bed," ASME Paper No. 79-HT-78, Aug. 1979.

8 Catipovic, N. M., "Heat Transfer to Horizontal Tubes in Fluidized Beds: Experiment and Theory," Ph.D. Thesis, Oregon State University, Corvallis, Ore., 1979.

9 Chandron, R., Chen, J. C., and Staub, F. W., "Local Heat Transfer Coefficients Around Horizontal Tubes in Fluidized Beds," ASME JOURNAL OF HEAT TRANSFER, Vol. 102, No. 1, 1980. pp. 152–157.

Thermal Storage Regenerator Parameters for Almost Constant Gas Discharge Temperature

F. E. Romie[1]

Introduction

Regenerator parameters can be selected to satisfy two important criteria for thermal energy storage; first, a large fraction of the energy made available during the charge process should be returned during regenerator discharge and, second, the temperature of the discharge gas leaving the regenerator should be close to the constant entrance temperature of the gas used to charge the regenerator. The latter criterion has particular importance if the stored energy is to be used as the heat source for a heat engine because the loss in thermodynamic availability due to a decreased discharge gas temperature reduces the work that can be realized from the stored thermal energy.

The purpose of this note is to present regenerator parameters which satisfy both criteria. In particular, parameters are presented which give a normalized gas discharge temperature equal to 0.95 at the end of the discharge period. ($\tau_a(1,1) = 0.95$).

Method and Results

The data presented are obtained by iteration ($\tau_a(1,1)$ is a dependent variable) of the solution method described in [1]. The solution is based on idealizations common to most treatments [2–8] of the steady-state periodic operation of the counterflow regenerator. The idealizations are:

1 The entrance temperatures, τ_{a1}' and τ_{b1}', of the discharge and charge gases are constant. (Actual temperatures are denoted by a prime.) The conductance, hA, for transfer of heat between the gas and solid is constant and uniform throughout the matrix as are the thermal capacity, WC, of the matrix solid and the capacity rate, wc, of the fluid. (The conductances and capacity rates for the two fluids and the flow periods, t_a and t_b, are in general different.)

2 No axial transfer of heat occurs in the matrix.

3 The thermal conductivity of the solid is infinite in the direction normal to fluid flow or, equivalently, the temperature of the matrix solid is uniform in any plane normal to fluid flow.

4 The ratio of the thermal capacity of the fluid contained in the matrix (at any instant) to the thermal capacity of the matrix is negligibly small (zero).

The fourth idealization will be satisfied for thermal storage regenerators when gases are used as the heat transfer agents [9]. The third idealization can be relaxed by use of approximate treatments of transverse conduction [10, 11]. In many cases, however, regenerators will be designed to have a very large heat transfer area per unit volume and the resultant fine subdivision of the matrix composing the regenerator implies that this idealization will be closely realized. The absence of axial transfer of heat required by the second idealization appears to be satisfied for axial conduction in pebble bed and similar constructions which offer no continuous path for conduction. However, with operation at sufficiently high temperature the axial transfer of heat by radiation can become significant with a consequent reduction of the thermal effectiveness and the gas discharge temperature. For constructions with continuous axial conduction paths [12] can be consulted.

Both the thermal effectiveness, $\bar{\tau}_a$, and the normalized final gas discharge temperature, $\tau_a(1,1)$, ($\tau_a(1,1) = (\tau_a'(1,1) - \tau_{a1}')/(\tau_{b1}' - \tau_{a1}')$) are expressible in terms of four parameters: (1), the ratio of the thermal capacity of the mass of gas passed through the regenerator during discharge to the thermal capacity of the mass of gas passed during charge, $(wct)_a/(wct)_b$, (2), the ratio of the thermal capacity of the mass of gas passed during discharge to the thermal capacity of the matrix solid, $(wct)_a/WC$, (3), the ratio N_a/N_b which is equal to the ratio of the Stanton numbers for the two flows and, (4), the value of Ntu, the number of transfer units for the regenerator.

$$\text{Ntu} = \left[\frac{1}{N_a} + \frac{(wct)_a}{(wct)_b}\frac{1}{N_b}\right]^{-1} \tag{1}$$

The parameter N with suscripts a or b is the ratio of the thermal conductance, hA, to the capacity rate, wc, during the discharge and charge periods respectively.

Three regenerator properties are expressed in terms of the thermal effectiveness. The energy stored during charge and delivered during

---

[1] Assoc. Mem. ASME.

Contributed by the Heat Transfer Division for publication in the JOURNAL OF HEAT TRANSFER. Manuscript received by the Heat Transfer Division November 14, 1980.

Table 1 Single parameter variation of $\bar{\tau}_a$ and $\tau_a(1,1)$ about the point Ntu = 128, $(wct)_a/(wct)_b = 0.95$, $(wct)_a/WC = 0.7$ and $Na/Nb = 1.0$

	(Point)				
Ntu	64	90	128	180	256
$\bar{\tau}_a$	0.984	0.991	0.996	0.998	1.000
$\tau_a(1,1)$	0.873	0.914	0.950	0.976	0.992
Na/Nb	0.5	0.7	1.0	1.4	2.0
$\bar{\tau}_a$	0.996	0.996	0.996	0.996	0.996
$\tau_a(1,1)$	0.948	0.949	0.950	0.951	0.952
$(wct)_a/(wct)_b$	0.91	0.93	0.95	0.97	0.99
$\bar{\tau}_a$	0.999	0.998	0.996	0.992	0.986
$\tau_a(1,1)$	0.985	0.972	0.950	0.912	0.855
$(wct)_a/WC$	0.5	0.6	0.7	0.8	0.9
$\bar{\tau}_a$	0.999	0.998	0.996	0.992	0.983
$\tau_a(1,1)$	0.998	0.976	0.950	0.894	0.754

discharge is Q.

$$Q = (wct)_a \bar{\tau}_a (\tau_{b1}' - \tau_{a1}') \qquad (2)$$

The fraction of the energy made available during charge, $(wct)_b(\tau_{b1}' - \tau_{a1}')$, that is stored and thus returned on discharge is the storage effectiveness, R.

$$R = \frac{Q}{(wct)_b(\tau_{b1}' - \tau_{a1}')} = \bar{\tau}_a \frac{(wct)_a}{(wct)_b} \qquad (3)$$

The fraction of the matrix maximum energy storage capability, $WC(\tau_{b1}' - \tau_{a1}')$, that is used is the capacitance utilization, U.

$$U = \frac{Q}{WC(\tau_{b1}' - \tau_{a1}')} = \frac{(wct)_a}{WC} \bar{\tau}_a \qquad (4)$$

For a given thermal storage, Q, the required capacity, WC, of the matrix is inversely proportional to the capacitance utilization which cannot exceed unity.

Figure 1 presents, for $N_a/N_b = 1$, values of Ntu, $(wct)_a/(wct)_b$ and $(wct)_a/WC$ which correspond to a final normalized gas discharge temperature of 0.95. For all points on the curves of Fig. 1 the value of the thermal effectiveness, $\bar{\tau}_a$, is greater than 0.99. Hence, with an inaccuracy of less than 1 percent, the ordinate, $(wct)_a/(wct)_b$ can be read as the storage effectiveness, R, and the curve parameter, $(wct)_a/WC$, as the capacitance utilization, U. The data are insensitive to the value used for N_a/N_b. Calculations using $N_a/N_b = 0.5$ and 2.0 produce only slightly different results. The difference cannot be shown to the scale of Fig. 1.

Table 1 shows the effect on $\bar{\tau}_a$ and $\tau_a(1,1)$ of changing, one at a time, the values of the four parameters all of which, except the one being varied, remain at the point defined in the table heading. Inspection of the table shows, for example, that varying N_a/N_b from 0.5 to 2.0 has no effect (i.e., less than 0.1 percent) on the thermal effectiveness and produces only a 0.4 percent increase in the value of $\tau_a(1,1)$. The table also shows, for given values of $(wct)_a/(wct)_b$ and $(wct)_a/WC$, that a value of Ntu greater than that given by Fig. 1 produces a value of $\tau_a(1,1)$ greater than 0.95, and conversely.

Figure 2 shows the temperature histories of the charge, τ_b, and discharge, τ_a, gases leaving the regenerator for two cases corresponding to $\tau_a(1,1) = 0.95$. It may be noted that the discharge gas temperature decreases from 1.0 to 0.95 only towards the end of the discharge period. In Fig. 2 the area below a τ_a curve divided by the total area of the figure is the thermal effectiveness and the area above a τ_b curve divided by the total area of the figure is the storage effectiveness, R. Figure 3 shows the temperature distributions in the matrix at the beginning of the discharge (T_a) and charge (T_b) periods for the two cases defined in Fig. 2. The ratio of the area included between a pair of curves (both dashed or solid) to the total area of the figure is the capacitance utilization, U.

References

1 Romie, F. E., "Periodic Thermal Storage: The Regenerator," ASME Journal of Heat Transfer, Vol. 101, Nov. 1979, pp. 726–731.

2 Nusselt, W., "Der Beharrungszustand im Winderhitzer," *Zeitschrift des Vereins Deutscher Ingenieuw*, Vol. 72, July 1928, pp. 1052–1054.

3 Hausen, H., "Nahrungsverfahren zur Berechnung des Wärmeaustausches in Regeneratoren," *ZAMM*, Vol. 11, 1931, pp. 105–114.

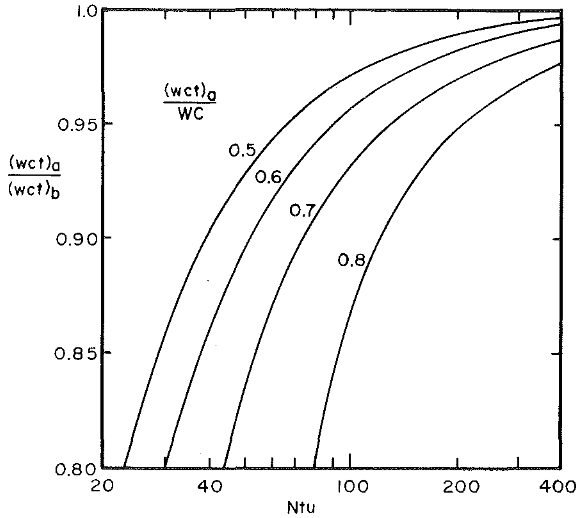

Fig. 1 Conditions for a normalized gas temperature equal to 0.95 at the end of the discharge period

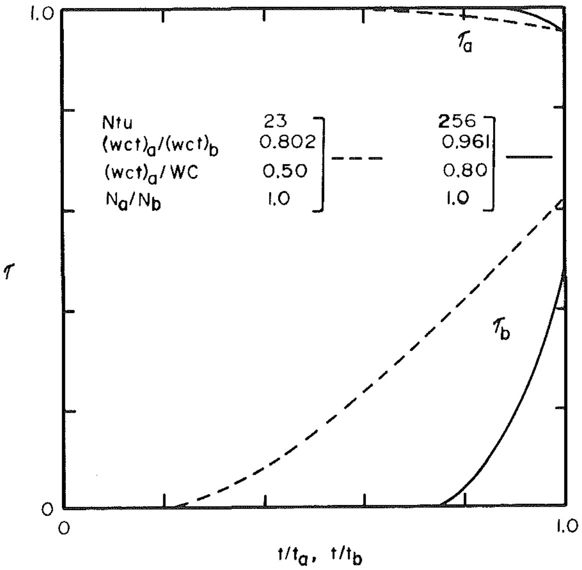

Fig. 2 Temperature histories of the leaving gases during discharge (τ_a) and charge (τ_b)

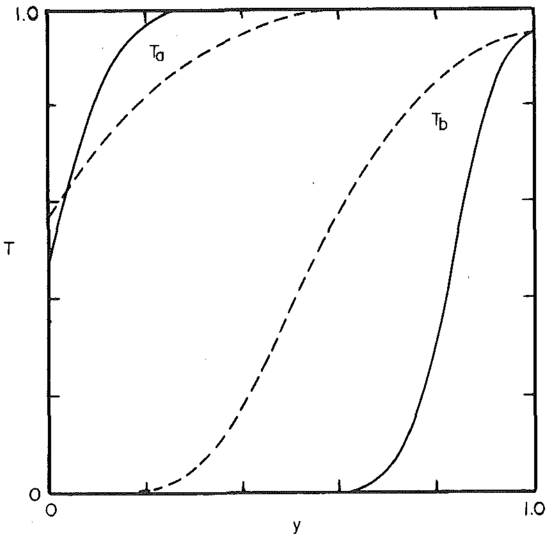

Fig. 3 Matrix temperature distributions at the beginning of discharge (τ_a) and the beginning of charge (τ_b). See Fig. 2 for key.

4 Iliffe, M. A., "Thermal Analysis of the Contra-Flow Regenerative Heat Exchanger," *Proceedings of the Institute of Mechanical Engineers*, Vol. 159, 1948, pp. 363–372.

5 Lambertson, T. J., "Performance Factors of a Periodic-Flow Heat Exchanger," *Trans. ASME*, Vol. 80, Apr. 1958, pp. 586–592.

6 Nahavandi, A. N., and Weinstein, A. S., "A Solution to the Periodic-Flow Regenerative Heat Exchanger Problem," *Applied Scientific Research*, Sec. A, Vol. 10, 1961, pp. 335–348.

7 Hausen, H., *Wärmeübertragung im Gegenstrom, Gleichstrom und Kreuzstrom*, Springer-Verlag, Berlin, 1950, pp. 262–444.

8 Jakob, M., *Heat Transfer*, Vol. 2, John Wiley & Sons, New York, 1957, pp. 261–341.

9 Maclaine-cross, I. L., "Effect of Interstitial Fluid Heat Capacity on Regenerator Performance," ASME JOURNAL OF HEAT TRANSFER, Vol. 102, Aug. 1980, pp. 572–574.

10 Hausen, H., "Survey of the Heat Transfer Theories in Regenerators," *Heat Exchangers: Design and Theory Sourcebook*, McGraw-Hill, New York, 1974, pp. 207–222.

11 Romie, F. E., "Approximate)Treatment of Transverse Conduction in Regenerators," ASME JOURNAL OF HEAT TRANSFER, Vol. 102, Aug. 1980, pp. 574–576.

12 Bahnke, G. D., and Howard, C. P., "The Effect of Longitudinal Heat Conduction on Periodic-Flow Heat Exchanger Performance," ASME *Journal of Engineering for Power*, Vol. 86, Apr. 1964, pp. 105–119.

Effect of Knudsen Number on Dropwise Condensation

Hiroaki Tanaka[1]

The purpose of this technical note is twofold. One is to point out the effect of a Knudsen number on dropwise condensation. The other is to give a clear physical sketch of the mechanism of heat transfer in dropwise condensation, which was discussed in previous papers [1, 2] in an exact but fairly sophisticated manner. We will begin with the second part.

It seems that, under dropwise condensation of steam, heat is mainly transferred by microscopic active droplets whose sizes are small enough for the heat flow rate through themselves to be virtually controlled by mass-transfer resistance at the liquid-vapor interface. As to this resistance, the kinetic theory of gases gives the following equivalent interfacial heat-transfer coefficient [3].

$$h_i = \frac{2\alpha}{2-\alpha}\,\frac{1}{(2\pi R T_s)^{1/2}}\,\frac{h_{fg}{}^2}{v_g T_s} \tag{1}$$

where α is the condensation coefficient, R the gas constant, T_s the saturation temperature, h_{fg} the heat of vaporization, and v_g the specific volume of the vapor. In Table 1, values of h_i are calculated for water and mercury at several saturation temperatures. It should be noted that in this calculation, the condensation coefficient α was assumed to be unity. Umur and Griffith [4] have achieved an analysis of heat conduction through a single drop of hemispherical shape of radius r, with a uniform subcooling ΔT at the base and the heat-transfer coefficient h_i at the liquid-vapor interface. Here, in order to make drop size r dimensionless, we may introduce a Biot number $R^* = h_i r \int \lambda_l$, where λ_l is the thermal conductivity of the liquid. Then Umur and Griffith's analytical result of heat-transfer rate through a single drop is as a first approximation divided into the following two regions by a characteristic size $R^* = 2$. Namely, as to a droplet in a region $R^* < 2$, the heat-transfer rate through the droplet can well be expressed as $Q = 2\pi r^2 h_i \Delta T$, because in this case thermal conduction resistance through the droplet is almost negligible yielding a uniform heat flux distribution of $h_i \Delta T$ over the whole liquid-vapor interface. As a result of this case the heat-transfer rate per unit base area of the droplet becomes $2h_i\Delta T$. On the other hand, for a drop within the region $R^* > 2$, the conduction inside the drop almost controls the heat transfer, resulting in a much lower value than $2h_i\Delta T$ for the heat-transfer rate per unit base area of the drop. The characteristic drop size in the actual dimension $r_1 = 2\lambda_l/h_i$, which corresponds to $R^* = 2$, is listed in the fourth column of Table 1.

The so-called steady dropwise condensation on an inclined surface is in reality composed of transient dropwise condensation which is taking place repeatedly on tracks left by departing drops. The instantaneous drop-size distribution during this transient dropwise condensation occurring locally on a newly exposed surface follows a form [2]:

$$\tilde{\alpha} = 1 - (R^*/\hat{R})^p \tag{2}$$

where $\tilde{\alpha}$ denotes the fraction of the area covered by drops with sizes greater than R^* and exponent p has a value around 0.3. $\hat{R}$ is the instantaneous, effective maximum drop size in the dimensionless form and it grows with time t elapsed from the beginning of the transient dropwise condensation as [1]

$$\hat{R} = \text{Bi}\left(\frac{t}{\tau}\right)^{1/(1+p)} \tag{3}$$

where $\text{Bi} = h_i R_{\max}/\lambda_l$ is the Biot number corresponding to the departing drop size $R_{\max}$ and τ is the time interval at which the condenser surface is swept by departing drops. Equation (2) is applicable to the following size range with the exception of the neighborhood of the extremely small end where droplet sizes are comparable either to the spacing between the nucleation sites or to the primary drop size.

$$R^*/\hat{R} \leqq 0.1 \tag{4}$$

When equation (2) is valid at the characteristic size $R^* = 2$, we can estimate the instantaneous fraction f of the condenser surface which can be utilized by the active droplets in the size range $R^* \leqq 2$ without being occupied by drops in the size range $R^* > 2$ as

$$f = 1 - \tilde{\alpha}(R^* = 2) = (2/\hat{R})^p$$

The time average $\bar{f}$ of this fraction is calculated with the aid of equation (3) as

$$\bar{f} = \frac{1}{\tau}\int_0^\tau f dt = \left(\frac{\text{Bi}}{2}\right)^{-p}\int_0^1\left(\frac{t}{\tau}\right)^{-p/(1+p)} d\left(\frac{t}{\tau}\right) = (1+p)\left(\frac{\text{Bi}}{2}\right)^{-p}$$

Here we consider the limiting case where the nucleation site density is infinitely high as well as the primary drop size is effectively zero. (As a matter of fact, the thermodynamic critical size of a water droplet is about 2×10^{-5} mm at a subcooling of $\Delta T = 1.0°\text{C}$. It is inversely proportional to ΔT and is almost invariable of the saturation temperature.) In this case, equation (2) can be applied down to zero radius and it predicts very naturally the complete coverage of the surface by drops. Then the fraction $\bar{f}$ is fully covered by the active droplets which convey heat at an almost uniform rate of $2h_i\Delta T$ per unit base area according to the foregoing solution by Umur and Griffith. Further, if we neglect the contribution to heat transfer of drops in the size range $R^* > 2$ as a first approximation, we have for the time-averaged heat-transfer coeffficient of dropwise condensation

Table 1

Substance; $R_{\max}$ observed	T_s K	h_i W/m²K	r_1 mm	L mm
Water; $R_{\max} = 1.2$ mm	295	8.55×10^5	1.42×10^{-3}	1.6×10^{-3}
	306	1.45×10^6	8.56×10^{-4}	8.8×10^{-4}
	321	2.78×10^6	4.60×10^{-4}	4.3×10^{-4}
	342	6.10×10^6	2.17×10^{-4}	1.8×10^{-4}
	373	1.57×10^7	8.69×10^{-5}	6.1×10^{-5}
Mercury; $R_{\max} = 0.15$ mm	378	4.35×10^3	4.88	1.4×10^{-1}
	412	1.74×10^4	1.30	3.0×10^{-2}
	452	6.62×10^4	0.362	6.9×10^{-3}
	492	1.95×10^5	0.129	2.0×10^{-3}

---

[1] Associate Professor, Department of Mechanical Engineering, The University of Tokyo, Bunkyo-ku, Tokyo, Japan.

Contributed by the Heat Transfer Division for publication in the JOURNAL OF HEAT TRANSFER. Manuscript received by the Heat Transfer Division December 29, 1980.

4 Iliffe, M. A., "Thermal Analysis of the Contra-Flow Regenerative Heat Exchanger," *Proceedings of the Institute of Mechanical Engineers*, Vol. 159, 1948, pp. 363–372.

5 Lambertson, T. J., "Performance Factors of a Periodic-Flow Heat Exchanger," *Trans. ASME*, Vol. 80, Apr. 1958, pp. 586–592.

6 Nahavandi, A. N., and Weinstein, A. S., "A Solution to the Periodic-Flow Regenerative Heat Exchanger Problem," *Applied Scientific Research*, Sec. A, Vol. 10, 1961, pp. 335–348.

7 Hausen, H., *Wärmeübertragung im Gegenstrom, Gleichstrom und Kreuzstrom*, Springer-Verlag, Berlin, 1950, pp. 262–444.

8 Jakob, M., *Heat Transfer*, Vol. 2, John Wiley & Sons, New York, 1957, pp. 261–341.

9 Maclaine-cross, I. L., "Effect of Interstitial Fluid Heat Capacity on Regenerator Performance," ASME JOURNAL OF HEAT TRANSFER, Vol. 102, Aug. 1980, pp. 572–574.

10 Hausen, H., "Survey of the Heat Transfer Theories in Regenerators," *Heat Exchangers: Design and Theory Sourcebook*, McGraw-Hill, New York, 1974, pp. 207–222.

11 Romie, F. E., "Approximate)Treatment of Transverse Conduction in Regenerators," ASME JOURNAL OF HEAT TRANSFER, Vol. 102, Aug. 1980, pp. 574–576.

12 Bahnke, G. D., and Howard, C. P., "The Effect of Longitudinal Heat Conduction on Periodic-Flow Heat Exchanger Performance," ASME *Journal of Engineering for Power*, Vol. 86, Apr. 1964, pp. 105–119.

Effect of Knudsen Number on Dropwise Condensation

Hiroaki Tanaka[1]

The purpose of this technical note is twofold. One is to point out the effect of a Knudsen number on dropwise condensation. The other is to give a clear physical sketch of the mechanism of heat transfer in dropwise condensation, which was discussed in previous papers [1, 2] in an exact but fairly sophisticated manner. We will begin with the second part.

It seems that, under dropwise condensation of steam, heat is mainly transferred by microscopic active droplets whose sizes are small enough for the heat flow rate through themselves to be virtually controlled by mass-transfer resistance at the liquid-vapor interface. As to this resistance, the kinetic theory of gases gives the following equivalent interfacial heat-transfer coefficient [3].

$$h_i = \frac{2\alpha}{2-\alpha} \frac{1}{(2\pi R T_s)^{1/2}} \frac{h_{fg}{}^2}{v_g T_s} \tag{1}$$

where α is the condensation coefficient, R the gas constant, T_s the saturation temperature, h_{fg} the heat of vaporization, and v_g the specific volume of the vapor. In Table 1, values of h_i are calculated for water and mercury at several saturation temperatures. It should be noted that in this calculation, the condensation coefficient α was assumed to be unity. Umur and Griffith [4] have achieved an analysis of heat conduction through a single drop of hemispherical shape of radius r, with a uniform subcooling ΔT at the base and the heat-transfer coefficient h_i at the liquid-vapor interface. Here, in order to make drop size r dimensionless, we may introduce a Biot number $R^* = h_i r \int \lambda_l$, where λ_l is the thermal conductivity of the liquid. Then Umur and Griffith's analytical result of heat-transfer rate through a single drop is as a first approximation divided into the following two regions by a characteristic size $R^* = 2$. Namely, as to a droplet in a region $R^* < 2$, the heat-transfer rate through the droplet can well be expressed as $Q = 2\pi r^2 h_i \Delta T$, because in this case thermal conduction resistance through the droplet is almost negligible yielding a uniform heat flux distribution of $h_i \Delta T$ over the whole liquid-vapor interface. As a result of this case the heat-transfer rate per unit base area of the droplet becomes $2h_i \Delta T$. On the other hand, for a drop within the region $R^* > 2$, the conduction inside the drop almost controls the heat transfer, resulting in a much lower value than $2h_i \Delta T$ for the heat-transfer rate per unit base area of the drop. The characteristic drop size in the actual dimension $r_1 = 2\lambda_l/h_i$, which corresponds to $R^* = 2$, is listed in the fourth column of Table 1.

The so-called steady dropwise condensation on an inclined surface is in reality composed of transient dropwise condensation which is taking place repeatedly on tracks left by departing drops. The instantaneous drop-size distribution during this transient dropwise condensation occurring locally on a newly exposed surface follows a form [2]:

$$\tilde{\alpha} = 1 - (R^*/\hat{R})^p \tag{2}$$

where $\tilde{\alpha}$ denotes the fraction of the area covered by drops with sizes greater than R^* and exponent p has a value around 0.3. $\hat{R}$ is the instantaneous, effective maximum drop size in the dimensionless form and it grows with time t elapsed from the beginning of the transient dropwise condensation as [1]

$$\hat{R} = \mathrm{Bi}\left(\frac{t}{\tau}\right)^{1/(1+p)} \tag{3}$$

where $\mathrm{Bi} = h_i R_{\max}/\lambda_l$ is the Biot number corresponding to the departing drop size $R_{\max}$ and τ is the time interval at which the condenser surface is swept by departing drops. Equation (2) is applicable to the following size range with the exception of the neighborhood of the extremely small end where droplet sizes are comparable either to the spacing between the nucleation sites or to the primary drop size.

$$R^*/\hat{R} \leqq 0.1 \tag{4}$$

When equation (2) is valid at the characteristic size $R^* = 2$, we can estimate the instantaneous fraction f of the condenser surface which can be utilized by the active droplets in the size range $R^* \leqq 2$ without being occupied by drops in the size range $R^* > 2$ as

$$f = 1 - \tilde{\alpha}(R^* = 2) = (2/\hat{R})^p$$

The time average $\bar{f}$ of this fraction is calculated with the aid of equation (3) as

$$\bar{f} = \frac{1}{\tau}\int_0^\tau f dt = \left(\frac{\mathrm{Bi}}{2}\right)^{-p} \int_0^1 \left(\frac{t}{\tau}\right)^{-p/(1+p)} d\left(\frac{t}{\tau}\right) = (1+p)\left(\frac{\mathrm{Bi}}{2}\right)^{-p}$$

Here we consider the limiting case where the nucleation site density is infinitely high as well as the primary drop size is effectively zero. (As a matter of fact, the thermodynamic critical size of a water droplet is about 2×10^{-5} mm at a subcooling of $\Delta T = 1.0°\mathrm{C}$. It is inversely proportional to ΔT and is almost invariable of the saturation temperature.) In this case, equation (2) can be applied down to zero radius and it predicts very naturally the complete coverage of the surface by drops. Then the fraction $\bar{f}$ is fully covered by the active droplets which convey heat at an almost uniform rate of $2h_i \Delta T$ per unit base area according to the foregoing solution by Umur and Griffith. Further, if we neglect the contribution to heat transfer of drops in the size range $R^* > 2$ as a first approximation, we have for the time-averaged heat-transfer coeffficient of dropwise condensation

Table 1

Substance; $R_{\max}$ observed	T_s K	h_i W/m²K	r_1 mm	L mm
Water; $R_{\max} = 1.2$ mm	295	8.55×10^5	1.42×10^{-3}	1.6×10^{-3}
	306	1.45×10^6	8.56×10^{-4}	8.8×10^{-4}
	321	2.78×10^6	4.60×10^{-4}	4.3×10^{-4}
	342	6.10×10^6	2.17×10^{-4}	1.8×10^{-4}
	373	1.57×10^7	8.69×10^{-5}	6.1×10^{-5}
Mercury; $R_{\max} = 0.15$ mm	378	4.35×10^3	4.88	1.4×10^{-1}
	412	1.74×10^4	1.30	3.0×10^{-2}
	452	6.62×10^4	0.362	6.9×10^{-3}
	492	1.95×10^5	0.129	2.0×10^{-3}

---

[1] Associate Professor, Department of Mechanical Engineering, The University of Tokyo, Bunkyo-ku, Tokyo, Japan.

Contributed by the Heat Transfer Division for publication in the JOURNAL OF HEAT TRANSFER. Manuscript received by the Heat Transfer Division December 29, 1980.

$$h = 2h_i(1 + p)\left(\frac{\text{Bi}}{2}\right)^{-p}$$

If we put $p = 0.3$, we finally have

$$h/h_i = 3.20\text{Bi}^{-0.3} \tag{5}$$

In the previous paper [2], the following equation (its original form is $\text{Nu} = 5.64\xi_1{}^{-0.7}$ where $\text{Nu} = hR_{\max}/\lambda_l$ and $\xi_1 = 2/\text{Bi}$) was derived for the limiting case of the complete coverage of the surface by drops after a fairly troublesome theoretical process.

$$h/h_i = 3.47\text{Bi}^{-0.3} \tag{6}$$

We find that the resultant equation (5) of the foregoing bold approximation agrees with the exact result (6) fairly well. Here it must be noted that equation (6) is valid with a collateral condition (7), because $R^*/\hat{R}$ with $R^* = 2$ and $\hat{R}$ in equation (3) has to satisfy condition (4) during a main portion of time t over the sweeping period τ.

$$\text{Bi} \gg 1 \tag{7}$$

This condition is well satisfied by water, while it completely fails of mercury (see Table 1 by taking note of $\text{Bi} = 2R_{\max}/r_1$).

In the previous paper [1, 2] the Nusselt number $hR_{\max}/\lambda_l$ was introduced to nondimensionalize the heat-transfer coefficient for dropwise condensation h. It seems more reasonable, however, to employ the ratio of the heat-transfer coefficients, h/h_i, as in equation (6), because this ratio is directly related to the fraction of the condenser surface covered by the active droplets, as has been made clear by the foregoing discussion.

Now we have come up to the stage to discuss the effect of Knudsen number. The interfacial matter transfer characterized by equation (1) is in its origin based on the kinetic theory of gases. Then we become aware that the foregoing theory [4] of heat conduction through a single drop by Umur and Griffith, in which a uniform heat-transfer coefficient h_i was assumed at the liquid-vapor interface, holds true in the case where the size of the drop r is much greater than the mean free path L of molecules in the vapor phase. In other words a Knudsen number defined by $\text{Kn} = L/r$ should be much smaller than unity. At this juncture, values of the mean free path are listed in the last column of Table 1 [5]. We find from Table 1 that, for the case of water, the mean free path L is almost equivalent to the characteristic drop size r_1. Therefore, as for the most of the active droplets in the size range $R^* \leqq 2$ i.e. $r \leqq r_1$, the Knudsen number becomes greater than unity and Umur and Griffith's theoretical result proves no longer applicable.

For the sake of brevity we may consider the case where $\text{Kn} > 1$ holds for all active droplets. Further, we assume as before the limit of the complete coverage of the surface by drops. Then, the fraction $\bar{f}$ of the condenser surface which is completely covered by active droplets conveys heat per unit area not at the foregoing rate of $2h_i\Delta T$ but at the reduced rate of $h_i\Delta t$, because in this case the whole microscopic area of the liquid-vapor interface is not uniformly effective but the macroscopic superficial area seems to be effectively concerned with mass transfer [6] (a hemisphere has a projected area equal to $\frac{1}{2}$ the outside area). As a result of this case, reducing the numerical constant of equation (6) by a factor of two, we have as a first approximation

$$h/h_i = 1.74\text{Bi}^{-0.3} \tag{8}$$

In the previous paper [2], the author estimated the condensation coefficient of water at around 0.2 by comparing available experimental data obtained at various pressures with the prediction from equation (6) on the assumption that the nucleation site density is infinitely high. However, if we employ equation (8) on this occasion, the condensation coefficient of water is $\alpha = 0.45$.

Finally the case of mercury will be briefly mentioned, as it offers a very special case. From Table 1, the characteristic size r_1 far exceeds the departing drop size $R_{\max}$ especially at low temperatures. This means that heat conduction resistance through any drop can be neglected as compared with the interfacial mass-transfer resistance. Further, at the lowest temperature in Table 1, the mean free path L is nearly the size of the departing drop. Hence, for the majority of droplets that exist on the condenser surface, the Knudsen numbers are greater than unity. As a result, the heat-transfer coefficient for dropwise condensation will take the same value as the interfacial heat-transfer coefficient h_i. This is the reason why there is no appreciable difference between the experimentally obtained heat-transfer coefficient for dropwise condensation and that for filmwise condensation of mercury at low temperatures [7].

References

1 Tanaka, H., "A Theoretical Study of Dropwise Condensation," ASME JOURNAL OF HEAT TRANSFER, Vol. 97, 1975, pp. 72–78.

2 Tanaka, H., "Further Developments of Dropwise Condensation Theory," ASME JOURNAL OF HEAT TRANSFER, Vol. 101, 1979, pp. 603–611.

3 Schrage, R. W., *A Theoretical Study of Interphase Mass Transfer*, Columbia University Press, New York, 1953.

4 Umur, A., and Griffith, P., "Mechanism of Dropwise Condensation," ASME JOURNAL OF HEAT TRANSFER, Vol. 87, 1965, pp. 275–282.

5 Kennard, E. H., *Kinetic Theory of Gases*, McGraw-Hill, New York, 1938.

6 Melville, H. W., "A Note on Evaporation from Irregular Surfaces," *Transactions of the Faraday Society*, Vol. 32, 1936, pp. 1017–1020.

7 Necmi, S., and Rose, J. W., "Heat-Transfer Measurements During Dropwise Condensation of Mercury," *International Journal of Heat and Mass Transfer*, Vol. 20, 1977, pp. 877–881.